STUDIES ON AEROSOL SIZE DISTRIBUTIONS, EMISSIONS, AND EXPOSURES

by

Tianren Wu

A Dissertation

Submitted to the Faculty of Purdue University

In Partial Fulfillment of the Requirements for the degree of

Doctor of Philosophy

Lyles School of Civil Engineering

West Lafayette, Indiana

May 2020

THE PURDUE UNIVERSITY GRADUATE SCHOOL
STATEMENT OF COMMITTEE APPROVAL

Dr. Brandon E. Boor, Chair

Lyles School of Civil Engineering, Purdue University

Dr. Ernest R. Blatchley III

Lyles School of Civil Engineering, Purdue University

Dr. Alexander Laskin

Department of Chemistry, Purdue University

Dr. Jeffrey A. Siegel

Department of Civil & Mineral Engineering, University of Toronto

Dr. Athanasios Tzempelikos

Lyles School of Civil Engineering, Purdue University

Approved by:

Dr. Dulcy M. Abraham

Head of the Graduate Program

Dedicated to My Family

ACKNOWLEDGMENTS

First, Dr. Boor — thank you for your mentorship and patient guidance throughout my doctoral studies. You really taught me how to construct complete and practical research projects with the big picture in mind, and I thoroughly enjoyed brainstorming with you on new research ideas. You taught me not only the technical details, but also every aspect of how to be an independent researcher, and I am very grateful to your encouragement for me to pursue a career in academia.

Danielle and Jinglin — thanks for all your help and hard work during our indoor air campaigns. You are excellent lab mates and I am very happy to work with you.

I am thankful to the members of the American Society of Heating, Refrigerating, and Air Conditioning Engineers (ASHRAE) Project Monitoring Subcommittee, Paolo Tronville, Geoff Crosby, Bruce McDonald, Brian Krafthefer, and Tom Justice, who provided us with important guidance and feedback on our ASHRAE RP-1734 project, and our collaborators in Finland, Martin Täubel, Rauno Holopainen, Sinikka Vainiotalo, Anna Kaisa Viitanen, Sampo Saari, and Jorma Keskinen, who helped us on the particle resuspension project. I also would like to thank the staff of the Herrick Laboratory Shop at Purdue for their amazing work in helping us with indoor air quality measurements in the Herrick Living Lab. I would like to acknowledge the grants that supported my doctoral studies: ASHRAE Grant-In-Aid and ASHRAE RP-1734.

I am so grateful to my family for their support and love. My parents, Meiyan and Chaogang — you are my strong support for my study abroad, both spiritually and financially. You are always being supportive of all the decisions I made in different steps of my life. My grandpa, Shihong — you are the most important educator in my life, who always encouraged me to strive for more and be better. I also would like to thank my bunnies, Tutu, Sesame and Fafa, who are my best companions when I work at late nights, and my friends, Wang Bingkai, Xu Weijun, Li Xinyu, Chen Xiaoyu and Liu Zhaoqing, for all the kindness and help. Lastly, I would like to thank my wife, Miaomiao — you are the most important person in my life. I feel so fortunate to meet you and get married to you, and I would never have made it to this point without your love and support.

TABLE OF CONTENTS

LIST OF TABLES

LIST OF FIGURES

ABSTRACT

Aerosols are solid or liquid particles that span in size from a few nanometers to tens of micrometers. They are important in both outdoor and indoor environments due to their impact on climate and human health. Many aerosol processes of interest to the environment, health, and filtration are strongly size-dependent. Aerosol particle size distributions (PSDs) provide a basis to better understand outdoor and indoor air pollution sources, evaluate human exposure to air pollution, and aerosol deposition in the human respiratory tract and filters in building ventilation systems. Monitoring the temporal evolution of aerosol PSDs enable for characterization of dynamic aerosol transport and transformation processes, such as direct emissions, nucleation, condensation, coagulation, resuspension, deposition, and filtration. This thesis presents three studies on the PSDs of: (i.) urban aerosols in cities around the world in order to identify geographical trends in the shape and magnitude of PSDs and to frame future research needs for PSD observations at a global-scale, (ii.) synthesized salt particles from a novel thermal aerosol generator to evaluate its suitability for air filter testing, and (iii.) indoor biological particulate matter (*bio*PM) to characterize transient inhalation exposures of infants and adults to resuspended *bio*PM from carpet dust induced by crawling and walking.

First, this thesis presents the current state-of-knowledge of urban aerosol PSDs by critically analyzing n=793 urban aerosol PSD observations made between 1998 to 2017 in n=125 cities in n=51 countries across the following regions of the world: Africa (AF), Central, South, and Southeast Asia (CSSA), East Asia (EA), Europe (EU), Latin America (LA), North America, Australia, and New Zealand (NAAN), and West Asia (WA). Prominent geographical variations in the shape and magnitude of urban aerosol number and mass PSDs were identified and significant variations in number PSDs were found between cities in EU and NAAN with those in CSSA and EA. Most PSD observations published in the literature are short-term, with only 14% providing data for longer than six months. There is a paucity of PSDs measured in AF, CSSA, LA, and WA, demonstrating the need for long-term aerosol measurements across wide size ranges in many cities around the globe. Inter-region variations in PSDs have important implications for population exposure, driving large differences in the urban aerosol inhaled deposited dose rate received in each region of the human respiratory system. Similarly, inter-region variations in the shape of PSDs impact the penetration of urban aerosols through filters in building ventilation systems,

which serve as an important interface between the outdoor and indoor atmospheres. The results of this critical review demonstrate that global initiatives are urgently needed to develop infrastructure for routine and long-term monitoring of urban aerosol PSDs spanning the nucleation to coarse modes.

Second, this thesis evaluates a newly designed commercially available thermal aerosol generator for ageing air filters in building heating, ventilation, and air-conditioning (HVAC) systems. The physical characteristics of the synthesized salt aerosol (NaCl and KCl) under different generator operational conditions were evaluated. The shape of the number and mass PSD output of the thermal aerosol generator are similar to those found in outdoor (urban) and indoor air and can be modulated by varying the rate at which the salt stick is fed into the flame. The morphology of the NaCl and KCl particles varied with size, with compact spherical or cubic structures observed below 100 nm and agglomerates observed above 100 nm. The thermal aerosol generator is a cost-effective technique for rapid ageing of HVAC filters with a PSD that more accurately represents, compared to conventional loading dusts, what filters encounter in real HVAC installations.

Lastly, this thesis characterizes infant and adult inhalation exposures and respiratory tract deposited dose rates of resuspended *bio*PM from carpets. Chamber experiments were conducted with a robotic crawling infant and an adult performing a walking sequence. Breathing zone (BZ) size distributions of resuspended fluorescent biological aerosol particles (FBAPs), a *bio*PM proxy, were monitored in real-time. FBAP exposures were highly transient during periods of locomotion. Both crawling and walking delivered a significant number of resuspended FBAPs to the BZ, with concentrations ranging from 0.5-2 cm^{-3}. Infants and adults are primarily exposed to a unimodal FBAP size distribution between 2 and 6 μm, with infants receiving greater exposures to super-10 μm FBAPs. In just one minute of crawling or walking, 10^2-10^3 resuspended FBAPs can deposit in the respiratory tract, with an infant receiving much of their respiratory tract deposited dose in their lower airways. Per kg body mass, an infant will receive nearly four times greater respiratory tract deposited dose of resuspended FBAPs compared to an adult.

1. INTRODUCTION

1.1 Aerosols and their size distributions

Aerosols are a key constituent of indoor and outdoor air pollution and include a diverse mixture of liquid and solid particles spanning in size from a single nanometer to tens of micrometers. Aerosol measurements are critical for monitoring the extent of air pollution, identifying pollutant sources, understanding aerosol transport and transformation mechanisms, and evaluating human exposure and health outcomes.[1–10] Human exposure to aerosols in urban and built environments is responsible for adverse health effects, including mortality and morbidity due to cardiovascular and respiratory diseases, asthma, and neural diseases.[6,11–17] Improved characterization of aerosols is needed to better understand the impact of aerosol exposure on human health and to evaluate the efficacy of current and future air quality legislation.

Aerosols can be classified into different modes according to theirs sizes: the nanocluster aerosol mode (NCA; <3 nm), nucleation mode (3-10 nm), Aitken mode (10-100 nm), accumulation mode (100-1000 nm), and coarse mode (>1000 nm). Sub-micron aerosol refers to particles with a diameter less than 1000 nm. In most environmental conditions, aerosols exist as an ensemble of particles with a variety of sizes. The size-resolved abundance of the aerosol is often statistically depicted as a continuous lognormal distribution function, which is referred to as the lognormal particle size distribution (PSD).[18,19] The PSD can be interpreted as the aerosol concentration normalized by the particle size on a logarithmic scale. The integrated area beneath the PSD within a given size range represents its total size-integrated concentration. The PSD can be expressed in terms of number, surface area, volume, or mass concentrations which allows one to translate across different domains.

1.2 Urban aerosol particle size distributions

Of particular importance are measurements of aerosol PSDs in the urban environment. Measurement of urban aerosol PSDs provides a basis for in-depth evaluation of size-resolved aerosol transport and transformation processes in the urban atmosphere, air pollution source apportionment, aerosol deposition in the human respiratory system, and associated toxicological

effects on the human body. Despite the atmospheric and health relevance of urban PSDs, long-term aerosol measurements are often focused on size-integrated concentration metrics, such as $PM_{2.5}$ (size-integrated mass concentration of particles with an aerodynamic diameter less than 2.5 μm), that lack essential size-resolved information. While urban aerosol PSD measurements have been conducted in cities around the globe, they are often short in duration and not performed as part of routine air quality monitoring. Urban PSDs provide a more complete assessment of an aerosol population, beyond what can be achieved with size-integrated metrics. Of particular importance are urban PSDs that capture the ultrafine particle regime (UFP, 1 to 100 nm). UFPs tend to dominate number PSDs, penetrate deep into the lung, and are associated with various deleterious human health outcomes.

Presently, there are no comprehensive literature reviews synthesizing urban aerosol PSD observations from around the globe in order to identify geospatial trends in the structure of number and mass PSDs. Previous literature reviews of urban aerosol PSDs have focused on major emission sources and source apportionment techniques[3] and the implications of urban aerosol PSDs on indoor air quality.[7] There has been a large number of urban aerosol PSD observations conducted over the past few decades. A comprehensive review of urban aerosol PSD observations from around the globe is needed to help us identify the current state-of-knowledge on urban aerosol PSDs in cities around the globe and help motivate future research efforts and frame forthcoming urban air pollution measurement needs. Such a review is the focus of Chapter 2.

1.3 Loading aerosols for HVAC filtration experiments

Outdoor aerosols are an important source of indoor aerosols as they can enter the building via the heating, ventilation, and air-conditioning (HVAC) system and through the cracks in the building envelope. Air filters are equipped in HVAC systems in commercial and residential buildings to remove indoor and outdoor aerosols and to improve indoor air quality. As aerosols are captured by HVAC filters, they will begin to form complex deposits of solid dendrites and liquid films within the filter fiber matrix.[20–22] A combination of depth filtration and cake formation across the filter restricts airflow and imposes a pressure drop that must be overcome by the blower in the air handling unit (AHU).[23–25] It is necessary to characterize the loading kinetics of HVAC filters aged with an aerosol representative of that found in outdoor (urban) and indoor

environments in order to better predict the trend in airflow resistance, and associated AHU blower power draw to overcome this pressure drop, during a filter's service life.

Loading aerosols typically used to age HVAC filters include ISO-12103-1-A2 Fine Test Dust, ISO-12103-1-A4 Coarse Test Dust, and ASHRAE Test Dust per ANSI/ASHRAE Standard 52.2-2017.[26,27] Such aerosols are primarily composed of coarse mode particles (1,000 to 100,000 nm). While useful for providing insights into differences in loading kinetics among filter media, coarse mode loading aerosols have a particle number and mass PSD unlike that found in outdoor (urban) and indoor environments.[7,18,26,28–30] Thus, the HVAC filter will undergo a much different loading process than what it will encounter in real HVAC installations.[26,31,32] To better characterize the loading kinetics of the HVAC filters, a new test method or aerosol generator, which can reproduce particles with the PSDs similar to indoor and outdoor (urban) PSDs, will be needed to enable for a more realistic simulation of how filters are aged in real environments. Such a generator is evaluated in Chapter 3.

1.4 Indoor biological particulate matter and resuspension

Biological particulate matter (*bio*PM) refers to particles of biological origin, including living or dead microorganisms (e.g. bacteria, archaea), biological dispersal items (e.g. pollen grains, fungal spores), biological excretions, and insect and plant debris.[33,34] House dust is enriched with *bio*PM of indoor and outdoor origin. They can be lifted up and become airborne by external forces, such as aerodynamic forces, electrostatic forces, and vibration of the deposit surface, of which the process is called resuspension.

Inhalation exposure to airborne *bio*PM has been associated with adverse health effects, including asthma, wheezing, respiratory infections, and several allergic symptoms.[35–41] On the other hand, protective health effects have been found to be associated with exposure to environmental microbes and specific allergens in numerous studies. Early-life exposures to a diversity of bacteria and fungi and high indoor dust concentrations of bacterial and fungal cells; bacterial lipopolysaccharides and muramic acid; polysaccharides of fungi, pollen, and plants; and allergenic proteins of dust mites and animal dander have been linked to a reduced prevalence of asthma, atopy, wheeze, hay fever, and allergies later in life.[42–52]

Human activities, such as simply walking across a carpet, can induce a large amount of indoor dust resuspension from surfaces.[53] Despite the health and environmental significance of

indoor dust, which is widely used as a long-term inhalation exposure surrogate, we have a limited understanding of the relationship between particle resuspension induced by age-dependent forms of locomotion, such as crawling and walking, with the transient exposures that are received by infants, children, and adults. Evaluating the respiratory tract deposited dose rate can help us better understand respiratory and allergic health outcomes of inhaled resuspended *bio*PM associated with different age-dependent forms of locomotion. Chapter 4 presents the results of an experimental investigation into *bio*PM resuspension and exposure.

1.5 Dissertation overview

This thesis advances our understanding of the current state-of-knowledge on geographical variations in urban aerosol PSDs in cities around the globe, physical characteristics of salt aerosol produced by a new thermal aerosol generator to be used for HVAC filtration testing, and inhalation exposure of infants and adults to the resuspended *bio*PM from carpets. The thesis focuses on the analysis of aerosol size distributions and their implications for exposure assessment, emission sources, and aerosol formation and transformation processes.

Chapter 2 presents a critical review of urban aerosol PSD measurements by synthesizing n=793 PSD observations from n=125 cities in n=51 countries measured from 1998 to 2017. Geographical variations in physical characteristics of the aerosol population was identified on a global scale. The geographical distribution of measurement locations and the categorization of the collected PSDs enables for identification of monitoring gaps in urban aerosol PSD measurements. The implications of geographical variations in urban aerosol number and mass PSDs on human inhalation exposure and aerosol filtration in buildings were evaluated to demonstrate the broad utility of routine PSD monitoring.

Chapter 3 provides the characterization of a high-output thermal flame aerosol generator for HVAC filtration experiments. The physical characteristics (e.g. size distribution, morphological features, and effective density) of the synthesized salt particles were characterized. The effect of operational conditions on the PSD of salt particles was investigated and the suitability for HVAC filtration experiments was validated.

Chapter 4 describes results from a study characterizing infant and adult inhalation exposures and respiratory tract deposited dose rates of resuspended *bio*PM from carpets. First, a brief review on the health effects of the inhalation exposure of *bio*PM and the laser-induced fluorescence (LIF)

technique for *bio*PM detection were provided. The chamber experiments are then introduced, which were conducted with a robotic crawling infant and an adult performing a walking sequence. A LIF instrument was deployed to measure the transient size distributions of resuspended fluorescent biological aerosol particles (FBAPs) at infant and adult breathing zone (BZ) height. The region-resolved respiratory tract deposited dose rates of the resuspended FBAPs associated with crawling and walking were estimated by using the Multiple-Path Particle Dosimetry (MPPD) model for infants and adults.

2. URBAN AEROSOL SIZE DISTRIBUTIONS: A GLOBAL PERSPECTIVE

2.1 Overview

This chapter presents a comprehensive critical review of the current state-of-knowledge on urban aerosol particle size distribution (PSD) observations by synthesizing *n*=793 measured PSDs between 1998 to 2017 from *n*=125 cities in *n*=51 countries around the globe. The geographical distribution of measurement locations and categorization of measurement information reveal significant gaps in urban aerosol PSD observations. An agglomerated analysis by geographical region enables for identification of geospatial variations in the shape and magnitude of urban aerosol number and mass PSDs. Inter-region variations in PSDs have important implications for population exposure, driving large differences in the urban aerosol inhaled deposited dose rate received in each region of the human respiratory system. Similarly, inter-region variations in the shape of PSDs impact the penetration of urban aerosols through filters in building ventilation systems, which serve as an important interface between the outdoor and indoor atmospheres. This critical review helps motivate future research efforts and frame forthcoming urban air pollution measurement needs.

2.2 Introduction

Urban air pollution is a major global environmental health challenge. Urban aerosol measurements are critical for monitoring the extent of urban air pollution, identifying pollutant sources, understanding aerosol transport and transformation mechanisms, and evaluating human exposure and health outcomes.[3,8,12,28] Human exposure to aerosols in urban environments is responsible for adverse health effects, including mortality and morbidity due to cardiovascular and respiratory diseases, asthma, and neural diseases.[11,14,17] Improved characterization of urban aerosols is needed to better understand the impact of aerosol exposure on human health and to evaluate the efficacy of current and future air quality legislation.

Measurement of urban aerosol PSDs are of particular interest as it provides a basis for in-depth evaluation of size-resolved aerosol transport and transformation processes in the urban atmosphere, air pollution source apportionment, aerosol deposition in the human respiratory

system, and associated toxicological effects on the human body. Presently, there are no comprehensive literature reviews synthesizing urban aerosol PSD observations from around the globe in order to identify geospatial trends in the structure of number and mass PSDs. Previous literature reviews of urban aerosol PSDs have focused on major emission sources and source apportionment techniques[3] and the implications of urban aerosol PSDs on indoor air quality.[7] There has been a large number of urban aerosol PSD observations conducted over the past few decades. The objective of this critical review is to provide a comprehensive overview of urban aerosol PSD observations from around the globe.

This study reviews n=793 urban aerosol PSD observations from n=125 cities in n=51 countries measured between 1998 to 2017. Urban aerosol PSD data spanning the nucleation to coarse modes (3 to 10,000 nm) was extracted from the literature, fit to multi-modal lognormal distribution functions, and agglomerated by geographical region in order to identify trends in the physical characteristics of aerosol populations from different regions. This represents the first attempt, to the authors' knowledge, to understand geographical variations in urban aerosol PSDs at a global scale. The geographical distribution of measurement locations and the categorization of the collected PSDs enables for identification of gaps in urban aerosol PSD measurements. This will help motivate future research efforts and frame forthcoming urban air pollution measurement needs. Along with urban aerosol PSDs, size-resolved urban aerosol effective densities were also reviewed. The effective density is an important aerosol morphological parameter that provides a basis to reliably translate measured number PSDs to mass PSDs. The implications of geographical variations in urban aerosol PSDs on human inhalation exposure and aerosol filtration in buildings were evaluated to demonstrate the broad utility of routine PSD monitoring.

2.3 Methodology for establishing the current state-of-knowledge on urban aerosol PSD observations

An expansive literature search was conducted on short- and long-term stationary and mobile measurements of urban aerosol number and mass PSDs between 1998 and 2017. The aim was to capture any potentially relevant peer-reviewed resources in which urban aerosol PSDs have been reported. Two academic search indices, Web of Science and ScienceDirect, along with Google Scholar, were used to conduct the literature search. Search terms included: urban aerosol, particle size distribution, urban aerosol size distribution, aerosol size distribution, urban particulate

matter, scanning mobility particle sizer urban, differential mobility particle sizer urban, and urban aerosol MOUDI, among others. Approximately 3,400 peer-reviewed journal articles and reports were initially screened to determine if they contained suitable information. Approximately 200 of them, which reported urban or semi-urban aerosol PSDs in the sub-micron regime (< 1000 nm), with some also covering the coarse regime (> 1000 nm), were selected for detailed analysis (Figure 2.1). These articles presented *n*=793 individual PSDs (182 of which covered both the sub-micron and coarse regime) from *n*=125 cities in *n*=51 countries around the globe (Table 2.1).

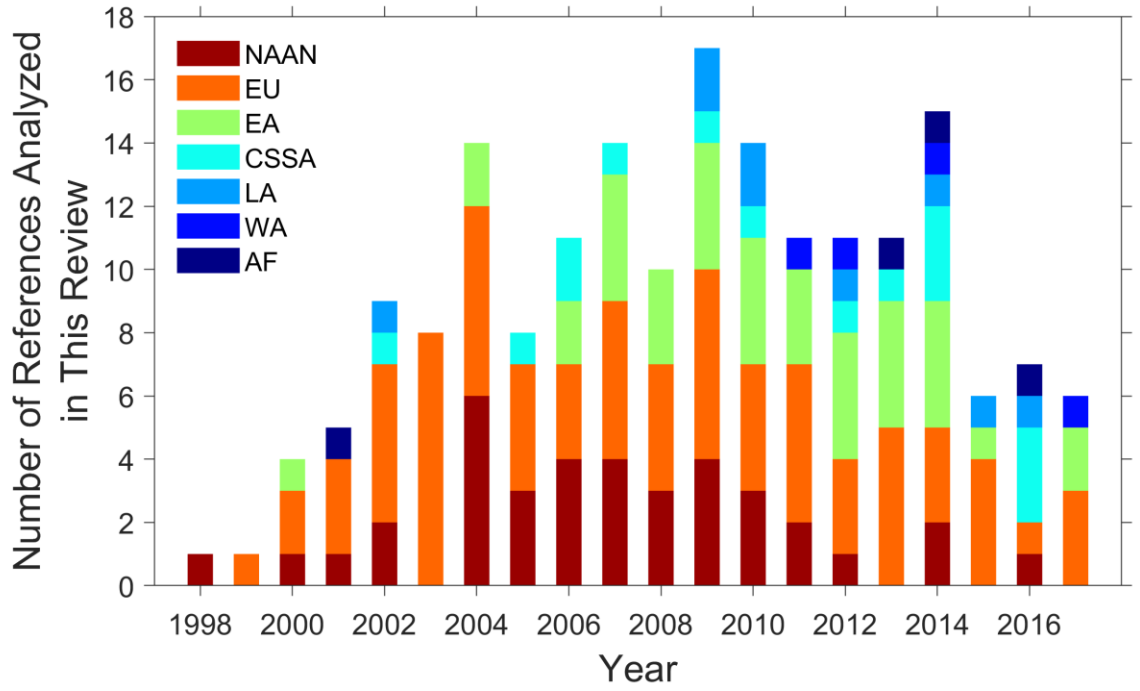

Figure 2.1 Temporal and geographical distribution by year of the urban PSD references analyzed in this study (1998-2017)

Most PSDs reported number-based concentrations (e.g. measured with a Scanning Mobility Particle Sizer (SMPS) or Aerodynamic Particle Sizer (APS)), while some report mass-based concentrations (e.g. measured by inertial impactors) or columnar volume concentrations (e.g. measured by sun/sky radiometers). For PSDs reported only in the form of figures without lognormal fitting parameters, as was most common among the references, the GRABIT tool in MATLAB (The MathWorks, Inc., Natick, MA, USA) and WebPlotDigitizer (https://automeris.io/WebPlotDigitizer, Version 4.0) were utilized to extract the data points of the PSDs. The PSDs were subsequently reproduced in MATLAB. A consistent particle size

definition, the electrical mobility diameter (D_{em}), was used for all PSDs, as described in Section 2.3 and 2.4.

The PSDs were classified by geographical region: Africa (AF), Central, South, and Southeast Asia (CSSA), East Asia (EA), Europe (EU), Latin America (LA), North America, Australia, and New Zealand (NAAN), and West Asia (WA) (Table 2.1). The PSDs in each geographical region were separated into two site types depending on the measurement location within the city. 'Urban' indicates that the measurement was conducted in urban areas that are not strongly affected by localized traffic emissions. 'Traffic (near-road)' indicates that the environment was strongly influenced by traffic emissions, e.g. street canyon or roadside.

2.4 Methodology for evaluating geographical trends in size-resolved urban aerosol effective densities

2.4.1 Introduction to size-resolved urban aerosol effective density functions

Evaluation of geographical variations in size-resolved aerosol morphological features is needed to better characterize urban aerosol populations around the world. This section outlines the development of size-resolved urban aerosol effective density (ρ_{eff}) functions from D_{em} = 3 to 10000 nm. Size-dependent differences in the aerosol particle density (ρ_p) and dynamic shape factor (χ) are best captured together through ρ_{eff}. The ρ_{eff} functions serve three purposes in this study: (1.) to translate urban aerosol number PSDs to mass PSDs, (2.) to convert aerodynamic diameter (D_a)-based PSDs to D_{em}-based PSDs, and (3.) to provide a summary of ρ_{eff} measurements in the urban atmosphere. (2.) is necessary to enable a consistent particle size definition to be used in compiling PSD observations from around the globe, as described in Section 2.4. The size-resolved ρ_{eff} functions include a combination of direct measurements of ρ_{eff} in the urban atmosphere (Section 2.3.2) and approximations for size fractions where direct measurements have not yet been reported in the literature, such as sub-10 nm and coarse mode particles (Section 2.3.3-2.3.5). The integration of the size-resolved ρ_{eff} functions with the urban aerosol PSD observations is presented in Section 2.3.6.

Different definitions of ρ_{eff} have been used in previous studies.[54] In the current study, ρ_{eff} is defined as the ratio of the measured particle mass (m_p) to the volume calculated from D_{em} assuming spheres[54–57] (Equation 2-1):

$$\rho_{eff} = \frac{6m_p}{\pi D_{em}^3} \quad (2\text{-}1)$$

Only empirical ρ_{eff} values defined in this manner were collected from the literature. The particle volume (V_p) is defined as the volume taken up by all of the solid and liquid material in the particle and void space enclosed within the particle envelope.[54] For an irregular particle, the volume equivalent diameter (D_{ve}) represents the diameter of a sphere that has the same volume as V_p [18,19,54] (Equation 2-2):

$$V_p = \frac{\pi}{6} D_{ve}^3 \quad (2\text{-}2)$$

The ratio of m_p to V_p is referred to as the particle density (ρ_p), as shown in Equation (2-3):

$$\rho_p = \frac{6m_p}{\pi D_{ve}^3} \quad (2\text{-}3)$$

The relationship between D_{em} and D_{ve} is given by DeCarlo et al. and Seinfeld and Pandis[18,54]:

$$\frac{D_{em}}{C_c(D_{em})} = \frac{D_{ve}\chi}{C_c(D_{ve})} \quad (2\text{-}4)$$

where C_c is the Cunningham Slip Correction Factor.[19,58,59]

2.4.2 Urban aerosol effective densities: summary of direct measurements

Direct measurements of ρ_{eff} in urban environments are limited. However, sufficient data is available in the literature to identify trends in ρ_{eff} among geographical regions and intra-city site types (urban or traffic). Size-resolved urban aerosol ρ_{eff} values were extracted from n=9 studies conducted in Denmark, China, United States, and Finland (Table 2.2). The studies report direct measurements of ρ_{eff}, primarily in the sub-micron regime through use of various aerosol instrument configurations, such as those evaluating the mass-mobility relationship of an aerosol population through a Differential Mobility Analyzer (DMA)-Aerosol Particle Mass Analyzer (APM) system (e.g. McMurry et al.[56]). The measured ρ_{eff} values and measurement information, including measurement technique, duration, and site (city, country), are summarized in Table 2.2.

As the PSD and direct ρ_{eff} measurements were conducted in different cities and at different site types within the city, it is reasonable to apply ρ_{eff} values which were measured under a condition consistent with a PSD measurement when converting number PSDs to mass PSDs and D_a to D_{em}. In order to apply the most reasonable ρ_{eff} to a PSD observation, the collected size-

resolved ρ_{eff} values were divided into three groups according to the geographical region where the direct measurement was conducted and the site type (urban or traffic). Direct measurements conducted in China in 'urban' environments were incorporated into Group A. Direct measurements in the United States in 'urban' environments were incorporated into Group B. Direct measurements conducted in the United States, Finland, and Denmark in 'traffic' environments were incorporated into Group C. None of the direct ρ_{eff} measurements in China were conducted in 'traffic' environments. The ρ_{eff} values for the size range of 3200 to 5600 nm reported by Hu et al.[55] were not included as the high ρ_{eff} values associated with the abundance of minerals in coarse particles in Beijing might bias the analysis.[60,61]

Representative size-resolved ρ_{eff} functions were estimated for Groups A, B, and C (Figure 2.9). For the direct ρ_{eff} measurements tabulated in Table 2.2, the collected values were often reported as a function of particle size discretely. In order to convert them to a continuous ρ_{eff} function with respect to size, which can be easily applied when converting number PSDs to mass PSDs and D_a to D_{em}, a few assumptions were made. For particles greater than 10 nm, if the particles at a certain diameter $D_{em,1}$ were reported to have an effective density of $\rho_{eff,1}$, we assume the particles in the size range from ($D_{em,1}$-50 nm) to ($D_{em,1}$+50 nm) also have the same effective density of $\rho_{eff,1}$. If the particles at diameter $D_{em,2}$ ($D_{em,2}>D_{em,1}$) were reported to have an effective density of $\rho_{eff,2}$ in the same study and $D_{em,2}$ is within the size range from $D_{em,1}$ to ($D_{em,1}$+50 nm), we assume the particles with the size from ($D_{em,1}$-50 nm) to ($D_{em,1}+D_{em,2}$)/2 to have the effective density of $\rho_{eff,1}$, while the particles with the size from ($D_{em,1}+D_{em,2}$)/2 to ($D_{em,2}$+50 nm) have the effective density of $\rho_{eff,2}$. By doing this, we obtained several continuous size-resolved ρ_{eff} functions ranging from approximately 10 nm to several hundred nanometers. We then took the mean of the size-resolved ρ_{eff} values derived from direct measurements in each of the three groups, illustrated as blue lines in the gray regions of Figure 2.9.

Table 2.1 Summary of direct measurements of size-resolved urban aerosol effective densities.

Country	City	Site Type	Measurement Duration	Measurement Technique	Size (nm)	Effective Density, ρ_{eff} (g cm^{-3})	Reference
Denmark	Copenhagen	Traffic (near road)	January - February 2012	DMA-APM	75	0.934	Rissler et al. (2014)[a]
					100	0.8078	
					150	0.4636	
					250	0.6432	
					350	0.276	
U.S.	Los Angeles[b]	Urban	September - October 2005	DMA-APM	50	1.14	Geller et al. (2006)
					118	1.12	
					146	1.21	
					202	1.14	
					322	0.86	
					414	0.73	
	Downey[c]	Traffic (near road)			50	1.13	
					118	1	
					146	0.94	
					202	0.78	
					322	0.49	
					414	0.31	
	Riverside	Urban			50	1.4	
					118	1.4	
					146	1.29	
					202	1.06	
China	Beijing	Urban	January 22 - 27 2007	SMPS/APS-MOUDI	56-100	2.085	Hu et al. (2012)[d]
					100-180	1.32	
					180-320	1.336	
					320-560	1.885	
					560-1000	1.75	
					1000-1800	1.655	
					1800-3200	1.38	
					3200-5600	2.23	
					5600-10000	-	
China	Shanghai	Urban	December 6 - January 12 2012	TDMA-APM	50	1.36	Yin et al. (2015)
					100	1.45	
					200	1.52	
					300	1.53	
					400	1.55	
					309	1.62	

Table 2.1 continued.

China	Shanghai	Urban	December 21 2014 - January 13 2015	DMA-APM	40	1.37	Xie et al. (2017)
					100	1.4	
					220	1.47	
					300	1.5	
U.S.	Houston	Urban	April 15 - May 31 2009	DMA-APM	46	1.55	Levy et al. (2013)[e]
					81	1.55	
					151	1.54	
					240	1.54	
					350	1.5	
Finland	Helsinki	Traffic (near road)	February 10 - 26 2003, January 28 - February 12 2004	ELPI-SMPS	20.3	1.04	Virtanen et al. (2006)
					72	1.5	
			August 12 - 27 2003, August 6 - 20 2004		18.9	0.96	
					75.1	1.8	
China	Beijing	Semi-Urban	May - June 2016	DMA-CPMA	50	1.56	Qiao et al. (2018)
					80	1.55	
					100	1.51	
					150	1.5	
					240	1.47	
					350	1.42	
U.S.	Atlanta	Urban	August 2009	TDMA-APM	107	1.58	McMurry et al. (2002)[f]
					309	1.62	

[a]Average of the soot and dense mode during Period I in Rissler et al.[62]
[b]Referred to as USC in Geller et al.[63]
[c]Referred to as 710-freeway in Geller et al.[63]
[d]Average of the polluted and clean episodes in Fig. 4 in Hu et al.[55]
[e]Average of the values in Fig. 11 in Levy et al.[66]
[f]Average of $\rho_{eff,2}$ in Table 3 in McMurry et al.[56]
DMA: Differential Mobility Analyzer
TDMA: Tandem Differential Mobility Analyzer
CPMA: Centrifugal Particle Mass Analyzer
APM: Aerosol Particle Mass Analyzer
ELPI: Electrical Low Pressure Impactor
SMPS: Scanning Mobility Particle Sizer
APS: Aerodynamic Particle Sizer
MOUDI: Micro-Orifice Uniform Deposit Impactor

2.4.3 Urban aerosol effective densities: considerations for sub-10 nm particles without direct measurements

Direct measurements of ρ_{eff} from D_{em} = 3 to 10 nm have not been previously reported in the literature. Particles in this size range are typically formed by homogeneous or heterogeneous nucleation, which can involve sulfuric acid (H_2SO_4), amines, ammonia, and organic vapors (e.g. Kulmala et al.[68]). H_2SO_4 and highly oxygenated molecules (HOMs) or extremely low volatility organic compounds (ELVOCs) are often involved in the nucleation and initial growth of particles

during an atmospheric new particle formation event. Previous studies have assumed nucleated particles formed in experimental chambers in the size range of 4 to 12 nm to have a density of 1.5 g cm^{-3}.[69] ELVOCs and HOMs are assumed to have a density of 1.5 g cm^{-3} and 1.4 g cm^{-3}, respectively.[70,71] For simplicity, we used the ρ_p of condensed ELVOCs[70] (1.5 g cm^{-3}) and the condensed phase density of H_2SO_4[72] (1.83 g cm^{-3}) to estimate the lower and upper limits of ρ_{eff} for particles from D_{em} = 3 to 10 nm, assuming the particles adopt a spherical shape with χ = 1. The mean value of the two limits was used as the representative ρ_{eff} for all three groups (dark red lines in light blue regions of Figure 2.9). Despite uncertainties in the assumed ρ_{eff} values, particles from D_{em} = 3 to 10 nm contribute negligibly to particle mass concentrations and are seldom measured with aerodynamic-based techniques, thus conversion from D_a to D_{em} is often unnecessary.

2.4.4 Urban aerosol effective densities: considerations for accumulation mode particles without direct measurements

There is a lack of direct measurements of ρ_{eff} in Groups B and C for particles greater than approximately 400 nm in size. Pitz et al.[73] conducted measurements of apparent particle density for particles with a $D_a \leq 2500$ nm ($PM_{2.5}$) at an urban background site in Germany. The apparent particle density ranged from 1.05 to 2.36 g cm^{-3}, with a mean value of 1.65 g cm^{-3}. As particles in the accumulation mode strongly contribute to urban aerosol mass concentrations (e.g. PM_1, $PM_{2.5}$), we assume the mean apparent particle density of 1.65 g cm^{-3} to be the representative ρ_{eff} for particles in the size range from D_{em} = 400 to 2500 nm in Group B (dark red line in yellow region of Figure 2.9). Rissler et al.[62] measured the ρ_{eff} of urban aerosols from 50 to 400 nm in a street canyon in central Copenhagen and identified two different groups of aerosols with distinctive ρ_{eff}: loose chain-like soot aggregates and more dense particles. The ρ_{eff} of the dense particles from D_{em} = 50 to 400 nm was in the range of 1.3 to 1.65 g cm^{-3}, of which the main constituents were inorganic salts, such as sulfate, nitrate, and ammonium, along with organics. Previous studies that have investigated the chemical composition of near-road aerosols indicated that the mass fraction of black carbon (elemental carbon) to the total mass of particles from D_{em} = 400 to 1000 nm was 6.4 to 26.7%.[74–78] Here, we assume that loose chain-like soot aggregates do not contribute significantly to particle mass concentrations in this size range and applied the mean value of ρ_{eff} for 'dense' particles as measured by Rissler et al.[62] as the representative ρ_{eff} for particles from D_{em} = 400 to 1000 nm in Group C (dark red line in orange region of Figure 2.9). Although soot particles,

which have a ρ_{eff} less than that of the dense particles, exist in the size range of D_{em} = 400 to 1000 nm, denser components, such as organics, mineral dusts, and crustal materials, may also exist in this size range.

2.4.5 Urban aerosol effective densities: considerations for coarse mode particles without direct measurements

Direct measurements of urban aerosol ρ_{eff} have been rarely conducted in the coarse mode, in part due to the difficulty of extending mass-mobility measurements (e.g. DMA-APM) to this size range. Coarse particles can be composed of organics, ions, dusts, crustal material, brake and tire wear, sea salt, black carbon, and other trace elements.[74–76,79–84] These materials are associated with a wide range in ρ_p. Secondary organic aerosol (SOA) synthesized in the laboratory are reported to have ρ_p ranging from 1 to 1.65 g cm^{-3}, depending on formation conditions and gas-phase precursors.[85–88] The ρ_p of $(NH_4)_2SO_4$ and NH_4NO_3, which represent sulfate and nitrate compounds dominant in ionic mass, were reported to be approximately 1.7 g cm^{-3}.[89–92] The ρ_p of dust varies with the associated components, including amorphous silicon oxide (2.1 to 2.3 g cm^{-3}), illite/muscovite (2.7 to 3.1 g cm^{-3}), montmorillonite (2.2 to 2.7 g cm^{-3}), and quartz (2.65 g cm^{-3}).[93] The inherent material density of diesel soot was measured to be 1.77 g cm^{-3}.[94]

The shape of coarse mode particles is often composition-dependent. The value of χ depends on the shape of the particle. For a sphere, χ = 1; for a cylinder with an axial ratio of 2, χ = 1.1; for a cylinder with an axial ratio of 5, χ = 1.35; and for a compact cluster of four spheres, χ = 1.17.[19] Some studies indicate that SOA has a spherical shape, suggestive of $\chi \sim 1$.[95–97] Coarse mode dust particles often exhibit large values of χ. The χ of Saharan mineral dusts measured in Morocco with a D_{em} = 1200 nm is 1.25.[98] Davies[99] reported χ to be 1.36 to 1.82 for quartz, 2.04 for talc, and 1.57 for sand. Soot particles typically exist as porous agglomerates, however, they can transform to spheres over several hours by condensation of H_2SO_4.[62,100–102] The complicated mixing state of urban aerosols introduces additional uncertainties in estimating the ρ_{eff} for coarse mode particles.[103]

ρ_{eff} values were estimated for coarse mode particles in Group C, for particles larger than 2500 nm in Group B, and for particles larger than 3200 nm in Group A. The ρ_p and χ of three types of aerosols, including inorganic aerosol, SOA, and mineral dust, were used to estimate a range of values for ρ_{eff}. $(NH4)_2SO_4$ and NH_4NO_3, with a ρ_p of approximately 1.7 g cm^{-3} and a χ of 1.01,[89–

[92,104] were selected as the representative inorganic aerosol to calculate ρ_{eff}. Nearly spherical SOA was assumed to adopt ρ_{eff} of 1 to 1.65 g cm^{-3}.[85–88] Illite, kaolinite, and montmorillonite were chosen to represent mineral dust, with ρ_p of 2.7 to 3.1 g cm^{-3}, 2.6 g cm^{-3}, and 2.2 to 2.7 g cm^{-3}, and with χ of 1.3, 1.05, and 1.11, respectively.[93,104,105]

Equation (2-4) presents the relationship between D_{em} and D_{ve}. For coarse mode particles, the value of $\frac{C_C(D_{ve})}{C_c(D_{em})}$ is approximately unity, such that the Cunningham slip correction factors in Equation (2-4) can be reasonably neglected. Therefore, Equation (2-4) becomes $D_{em} = D_{ve}\chi$. Plugging this into Equation (2-1), we arrive at Equation (2-5):

$$\rho_{eff} = \frac{6m_p}{\pi\chi^3 D_{ve}^3} \tag{2-5}$$

Combining Equation (2-3) and (2-5), we can derive Equation (2-6), which describes the relationship between ρ_{eff}, ρ_p, and χ for coarse mode particles (an example is given in Figure 2.2):

$$\rho_{eff} = \frac{\rho_p}{\chi^3} \tag{2-6}$$

With the different combinations of ρ_p and χ described above, Equation (2-6) was applied to calculate ρ_{eff} values for the three types of aerosols. The values span from 1 to approximately 2 g cm^{-3} (light green region of Figure 2.9). The ρ_{eff} values within this range are used as the representative ρ_{eff} for coarse mode particles in Group C, for particles larger than 2500 nm in Group B, and for particles larger than 3200 nm in Group A.

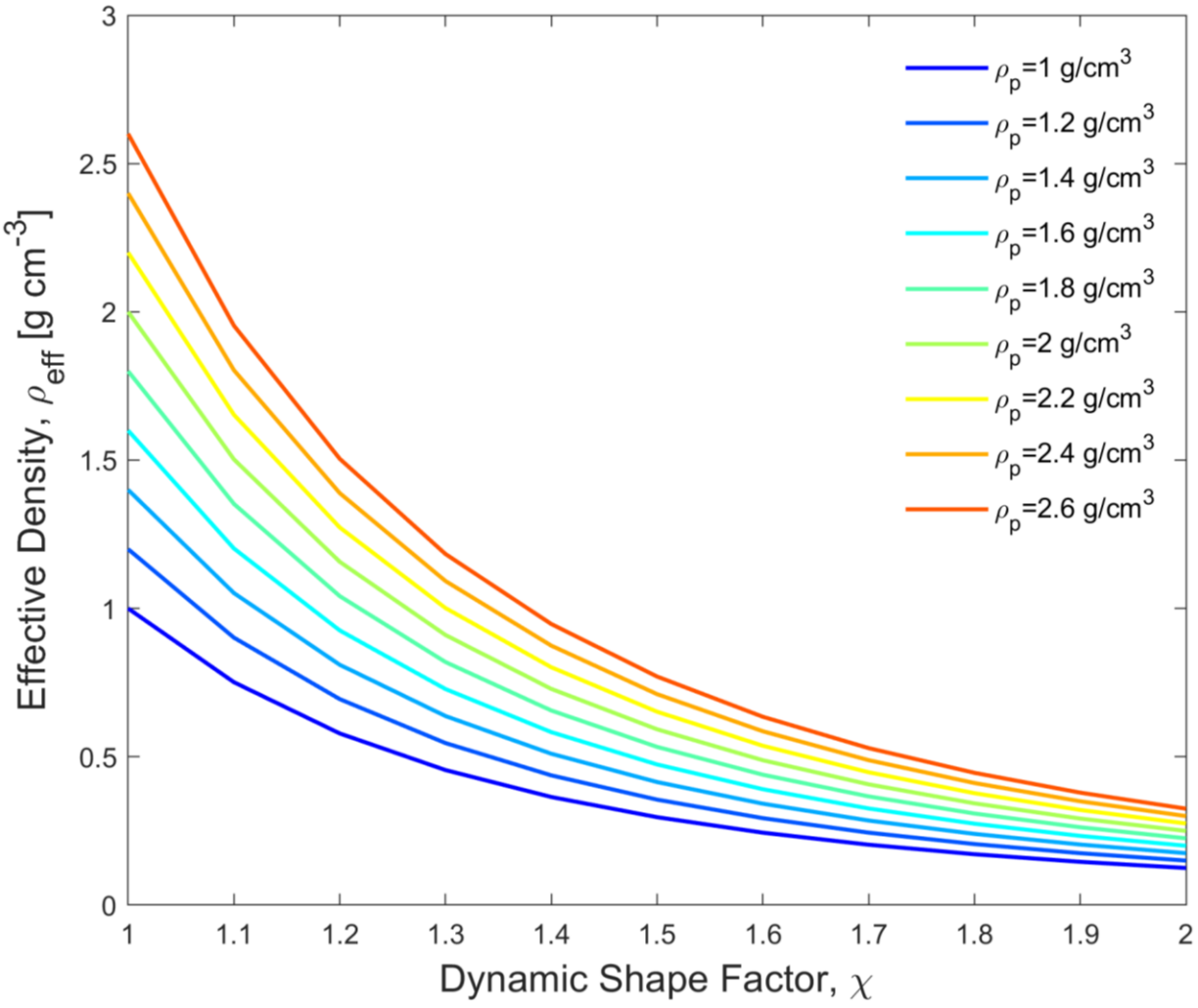

Figure 2.2 Effective densities (ρ_{eff}) as derived from different values of dynamic shape factors (χ) and particle densities (ρ_p), assuming the value of $C_c(D_{ve})/C_c(D_{em})$ is approximately unity for coarse particles.

2.4.7 Integration of size-resolved urban aerosol effective density functions with urban aerosol PSD observations

The combination of directly measured and estimated ρ_{eff} values between D_{em} = 3 to 10000 nm provides a basis to establish continuous, size-resolved urban aerosol ρ_{eff} functions for Groups A (ρ^A_{eff}), B (ρ^B_{eff}), and C (ρ^C_{eff}), as illustrated in Figure 2.9. When converting number PSDs to mass PSDs and D_a to D_{em}, ρ^A_{eff} was applied to number PSDs measured in the 'urban' environment in cities in CSSA, WA, LA, AF, and China. ρ^B_{eff} was applied to number PSDs measured in the 'urban' environment in cities in EU, NAAN, Japan, and Korea. ρ^C_{eff} was applied to number PSDs measured in the 'traffic' areas in cities around the globe, excluding China.

ρ^A_{eff} was applied to the number PSDs measured at both urban and traffic sites in China. The urban PSD measurements in China collected in this study were mainly from megacities, such as Beijing, Shanghai, and Guangzhou. Heavy-duty diesel trucks are prohibited to enter many urban areas during the daytime in these megacities.[4] In addition, the fraction of diesel-powered cars in cities in China are much lower than that in Europe or North America. It is shown that gasoline-powered passenger cars contribute 91% of the total amount of vehicles in Beijing.[4] Therefore, the relative fraction of soot particles in the near-road region was expected to be lower than that in North America and Europe. Previous studies suggest that the contribution of black carbon to $PM_{2.5}$ mass concentrations was less than 4% in Shanghai.[106,107] In addition, soot particles from gasoline engine vehicles might be more 'compact' due to the relatively sulfur 'rich' fuel used in China.[64] Soot particles may also be heavily aged or internally mixed with other condensable materials due to the higher pollution levels in megacities, resulting in a higher ρ_{eff} than freshly emitted soot particles. Huang et al.[108] indicated that the number fraction of pure black carbon was 1.9% in Shanghai during polluted periods. Therefore, the near-road size-resolved ρ_{eff} was assumed to be closer to the values compiled for ρ^A_{eff}, rather than those for ρ^C_{eff}.

2.5 Methodology for analyzing urban aerosol PSD observations

2.5.1 Introduction to multi-modal lognormal fitting and transformations of urban aerosol PSDs

The urban aerosol PSDs were fit to the multi-modal lognormal distribution function and translated across number (cm^{-3}), surface area ($\mu m^2\ cm^{-3}$), volume ($\mu m^3\ cm^{-3}$), and mass ($\mu g\ m^{-3}$) domains following different strategies depending on the measurement technique and size range, as described in Section 2.4.1.1-2.4.1.4. Lognormal fitting parameters, including the geometric mean diameter, geometric standard deviation, and concentration for each mode, along with measurement information, for all *n*=793 PSDs are compiled in the Appendix (Tables A1-A5). For a few selected studies where the measured PSDs were already fit to the multi-modal lognormal distribution function, the listed fitting parameters were used directly. The fitting parameters provide a basis to characterize the shape and magnitude of the PSDs, as well as a mathematical parameterization to re-produce the measured PSDs for subsequent analysis by the atmospheric aerosol research community.

2.5.1.1 Urban aerosol number PSDs in the sub-micron regime

Urban aerosol number PSDs that only included modes in the sub-micron regime (nucleation, Aitken, and accumulation) were typically measured via electrical mobility-based techniques as number-based concentrations (e.g. SMPS). The extracted measured data for these PSDs were fit to the multi-modal lognormal distribution function ($dN/dLogD_p$, cm^{-3}, Equation 2-7) by using a lognormal fitting code in MATLAB based on the nonlinear least-squares curve fitting function, lsqcurvefit.m:

$$\frac{dN}{dLogD_p} = \sum_{i=1}^{n} \frac{N_i}{(2\pi)^{1/2} log(\sigma_i)} exp[-\frac{(log\ D_p - log\ \overline{D_{p,i}})^2}{2log^2(\sigma_i)}] \quad (2\text{-}7)$$

The geometric mean diameter ($\overline{D_{p,i}}$), geometric standard deviation (σ_i), and particle number concentration or amplitude (N_i) for each mode (i) were determined. The number of modes was based upon what was needed to achieve the best fit to the measured data. Fitting parameters and measurement information for urban aerosol number PSDs in the sub-micron regime are provided in Table A.1, an example of which is shown in Figure 2.3. The fitted number PSDs were converted to surface area PSDs ($dS/dLogD_p$, $\mu m^2\ cm^{-3}$) and volume PSDs ($dV/dLogD_p$, $\mu m^3\ cm^{-}$

^{3}) assuming spherical particles and converted to mass PSDs (dM/dLogD$_p$, μg m^{-3}) using the representative size-resolved ρ_{eff} functions for Groups A, B, or C (Section 2.3, Figure 2.9). Size-integrated concentrations were also calculated.

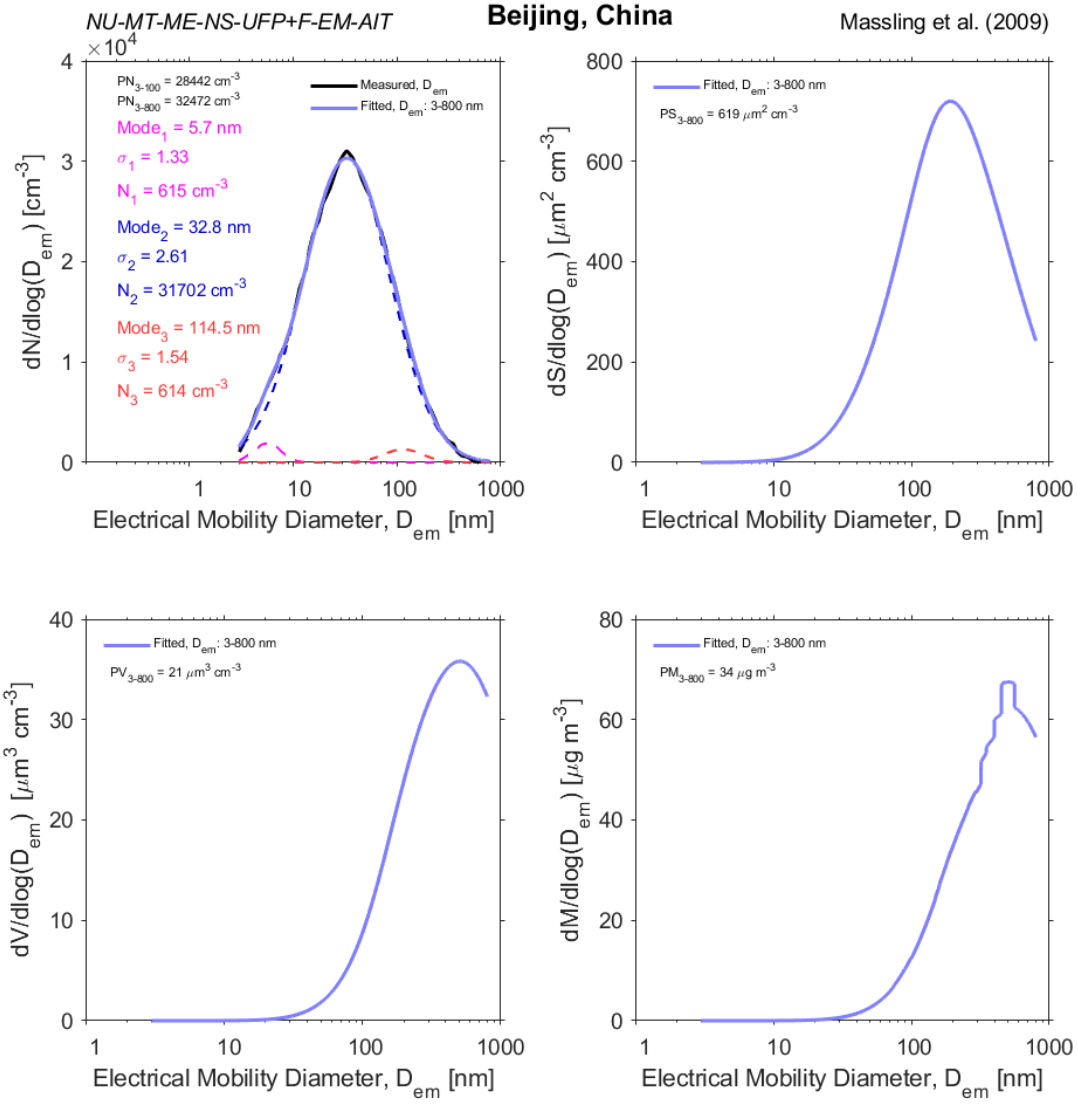

Figure 2.3 Example of urban aerosol number, surface area, volume, and mass PSDs measured by electrical mobility techniques. The upper left plot shows an urban aerosol number PSD with lognormal fitting parameters listed. The black curve indicates the measured data and the blue curve was reproduced with the multi-modal lognormal fitting parameters. The dashed curves represent each individual mode of the lognormal fitting. PN, PS, PV, and PM represent the size-integrated particle number, surface area, volume, and mass concentrations, respectively (the subscripts indicate the size range).

2.5.1.2 Urban aerosol number PSDs that cover both the sub-micron and coarse regimes

Urban aerosol number PSDs that cover both the sub-micron and coarse regimes typically utilize a combination of different aerosol measurement techniques. Electrical mobility-based techniques (e.g. SMPS) are often used for the sub-micron regime and aerodynamic-based techniques (e.g. APS) or optical-based techniques (e.g. Optical Particle Counter (OPC) or Optical Particle Sizer (OPS)) are used for the coarse regime and a fraction of the accumulation mode. The amplitude of number PSDs can span one to three orders of magnitude over the sub-micron and coarse regimes. When both regimes are measured concurrently, the coarse mode is often present as the tail of the accumulation mode in the number PSDs. Thus, the lognormal fitting of the number PSDs often ignores the coarse mode particles, which can result in an inaccurate estimation of the volume and mass concentrations of large particles when converting the fitted number PSDs to volume and mass PSDs. Therefore, the PSDs that cover both the sub-micron and coarse regimes were separated into two segments, each of which was individually fitted to the multi-modal lognormal distribution function in order to reproduce the measured data more accurately.

Electrical mobility-based techniques typically cover size fractions that contribute significantly to number PSDs in the urban atmosphere (e.g. $D_{em} \leq 100$ nm). Thus, the segment of the number PSDs measured by such techniques were directly fitted with the multi-modal lognormal distribution function by Equation (2-7), and the fitted number PSDs were converted to surface area, volume, and mass PSDs as described in Section 2.4.1.1. Size fractions measured by aerodynamic- or optical-based techniques often cover a fraction of the accumulation mode and the coarse mode, both of which contribute significantly to volume and mass PSDs. Therefore, to best reproduce the volume and mass PSDs, a different approach was employed to fit the PSDs measured by these two techniques.

For aerodynamic-based measurements, D_a needs to be converted to D_{em} so that a consistent particle size definition can be used. In some studies, the authors did this by converting the measured D_a-based PSD to a D_{em}-based PSD using the value for ρ_{eff} that gave the best fit between the converted D_{em}-based PSD with the measured D_{em}-based PSD in an overlap region (often the accumulation mode) that was covered by both electrical mobility- and aerodynamic-based techniques (e.g. Pitz et al.[109]). Most urban aerosol number PSDs measured with an APS were reported as D_a-based PSDs[9] or converted to Stoke's or geometric diameter-based PSDs by assuming values for χ and ρ_p.[4,110–114] For the latter, such diameters were first converted back to

D_a, and then to D_{em}. Equation (2-8) shows the relationship between D_a and D_{ve}[19,54], where ρ_0 is the standard density of 1 g cm^{-3}:

$$D_{ve} = D_a\sqrt{\frac{\chi\rho_0 C_c(D_a)}{\rho_p C_c(D_{ve})}} \quad (2\text{-}8)$$

For coarse mode particles, it is assumed that $\frac{C_C(D_{ve})}{C_c(D_a)}$ is approximately unity. As mentioned in Section 2.3.5, $D_{ve} = D_{em}/\chi$; combining this with Equation (2-8), we arrive at Equation (2-9):

$$\frac{\rho_p^{1/2}}{\chi^{3/2}\rho_0^{1/2}} = \frac{D_a}{D_{em}} \quad (2\text{-}9)$$

From Equation (2-9) and (2-6), we can derive the relationship between D_a and D_{em} (Equation 2-10), which is used to convert D_a to D_{em}:

$$\rho_{eff} = \rho_0(\frac{D_a}{D_{em}})^2 \quad (2\text{-}10)$$

As described in Section 2.3, a series of ρ_{eff} values were generated from different combinations of χ and ρ_p (Figure 2.2 and light green region of Figure 2.9) for a fraction of the coarse mode without direct ρ_{eff} measurements in Groups A, B, and C. When converting D_a to D_{em} for these particles, each D_a was converted to multiple D_{em} corresponding to a series of ρ_{eff} to account for the uncertainty in ρ_{eff}. Therefore, for each of the D_a-based number PSDs in the size range where direct ρ_{eff} data is lacking, a series of D_{em}-based number PSDs were determined. Figure 2.4 shows the ratio of D_a to D_{em} when translating between the two diameters for different values of χ and ρ_p (assuming $\frac{C_C(D_{ve})}{C_c(D_a)} \approx 1$). In general, D_a/D_{em} increases with decreasing χ and increasing ρ_p.

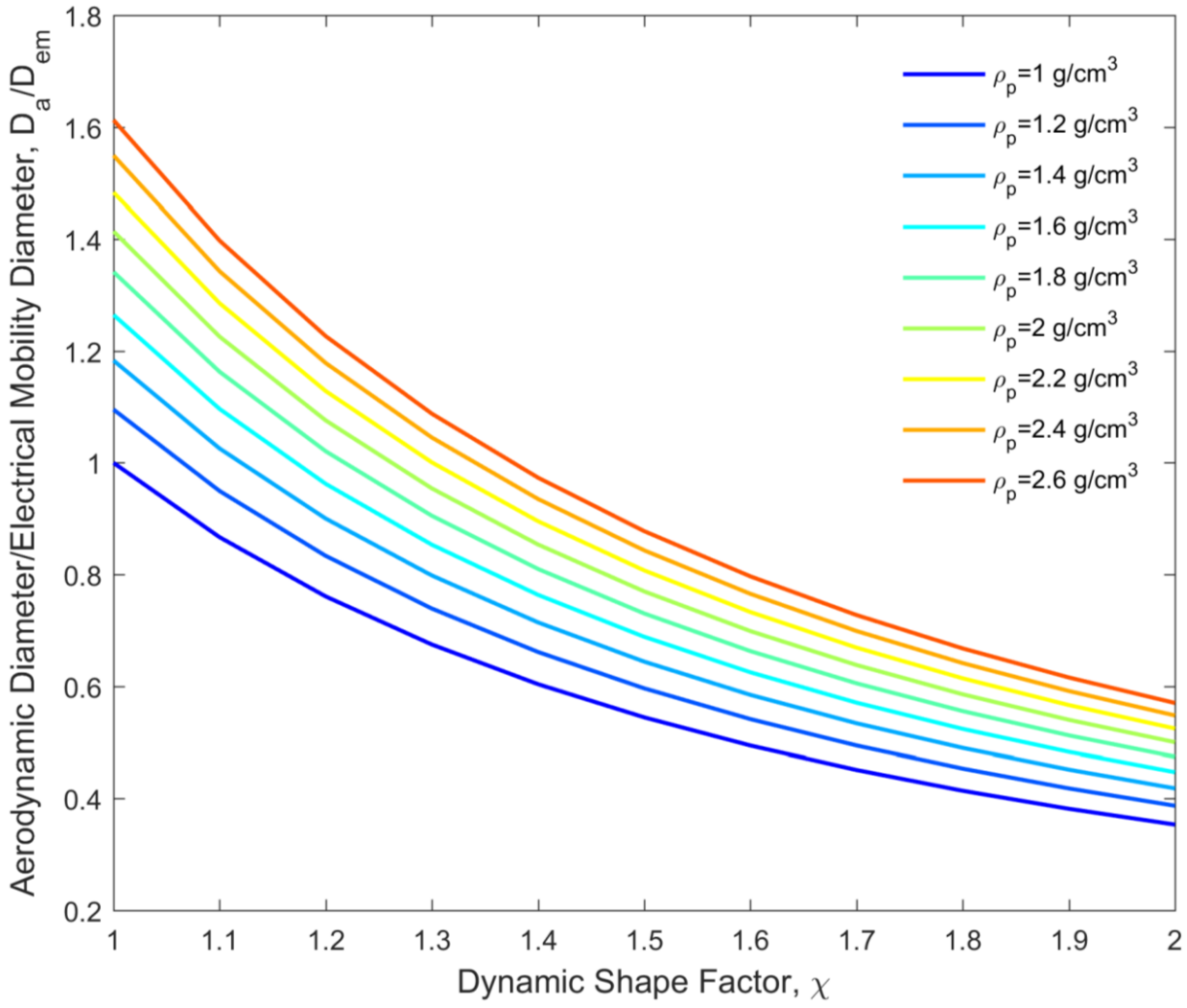

Figure 2.4 The ratio of aerodynamic diameter (D_a) to electrical mobility diameter (D_{em}) derived from different values of the dynamic shape factor (χ) and particle density (ρ_p).

The converted D_{em}-based number PSDs were transformed to D_{em}-based volume PSDs. For the size fraction of the coarse mode where the ρ_{eff} was estimated by different combinations of χ and ρ_p, multiple D_{em}-based volume PSDs were obtained from the series of D_{em}-based number PSDs. An example is shown in Figure 2.5. We took the mean D_{em}-based volume PSD of that series of D_{em}-based volume PSDs, and then conducted the multi-modal lognormal fitting via Equation (2-11):

$$\frac{dV}{dLogD_p} = \sum_{i=1}^{n} \frac{V_i}{(2\pi)^{1/2} log(\sigma_i)} exp[-\frac{(log\, D_p - log\, \overline{D_{p,i}})^2}{2log^2(\sigma_i)}] \quad (2\text{-}11)$$

where V_i is the volume concentration of mode i. The fitted D_{em}-based volume PSDs were then converted back to number and surface area D_{em}-based PSDs. This was done to prevent possible amplification in the difference between the measured and lognormally fitted PSDs when converting number PSDs to volume PSDs.

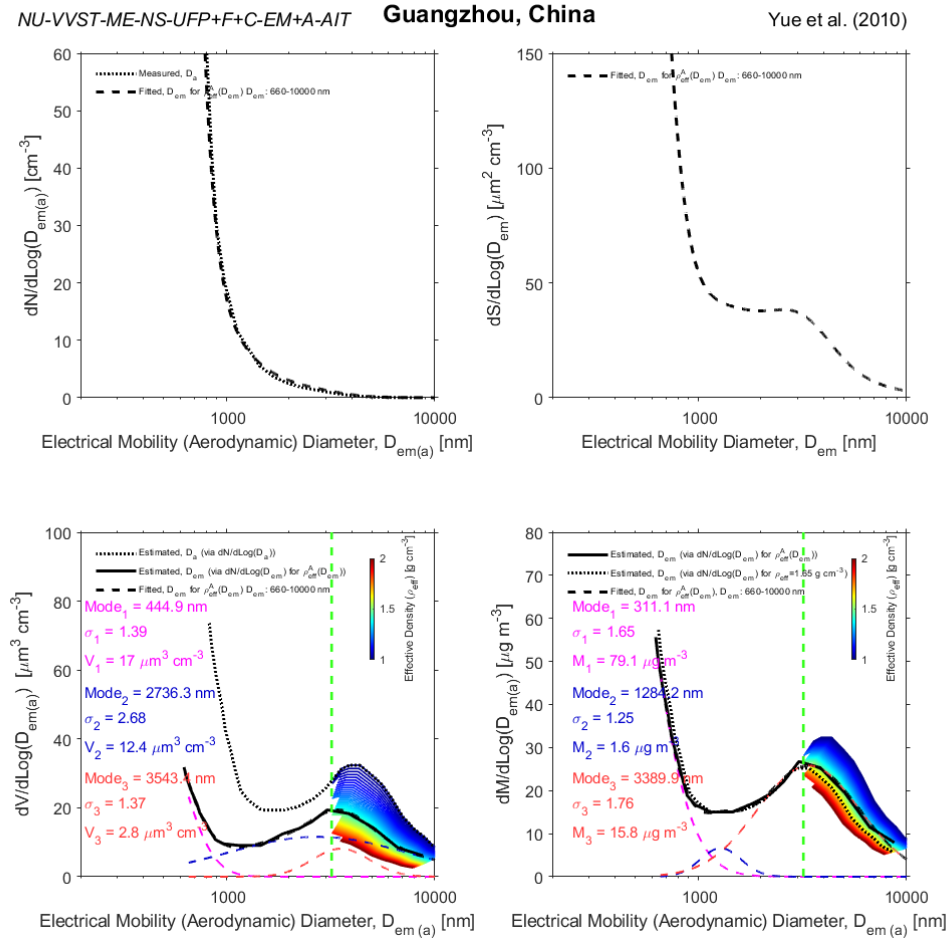

Figure 2.5 An example of urban aerosol number, surface area, volume, and mass PSDs measured by aerodynamic techniques. The black dotted curve in the number PSD indicates the measured data. The dotted line in the D_a-based volume PSD was converted from the measured D_a-based number PSD. The solid black lines in the volume and mass PSDs are D_{em}-based PSDs converted from the measured D_a-based number PSD. The rainbow color lines are the converted D_{em}-based volume and mass PSDs for a range of ρ_{eff} to account for the uncertainties in ρ_{eff} in the coarse regime. The relationship between the color and ρ_{eff} is shown in the color bar. The dotted color lines are the lognormal fitting curves for each mode. The dashed black lines in the volume and mass PSDs are the sum of the fitted sub-modes. The fitted volume PSD was converted back to number and surface area PSDs, which are shown as the dashed black lines. The effective size range for the lognormal fitting is indicated. The mass D_{em}-based PSD was also converted assuming a uniform apparent ρ_{eff} of 1.65 g cm^{-3} as the dotted black line. [109]

The converted D_{em}-based number PSDs were also transformed into D_{em}-based mass PSDs by applying the effective density functions ρ^{A}_{eff}, ρ^{B}_{eff}, or ρ^{C}_{eff}, according to the measurement location and site type (Section 3, Figure 2.9). For the size fraction of the coarse mode where the ρ_{eff} was estimated by different combinations of χ and ρ_p, multiple D_{em}-based mass PSDs were obtained from a series of D_{em}-based number PSDs. Similar to the volume PSDs, we took the mean D_{em}-based mass PSD of that series of D_{em}-based mass PSDs, and then conducted the multi-modal lognormal fitting via Equation (2-12):

$$\frac{dM}{dLogD_p} = \sum_{i=1}^{n} \frac{M_i}{(2\pi)^{1/2} log(\sigma_i)} exp\left[-\frac{\left(log\, D_p - log\, \overline{D_{p,i}}\right)^2}{2log^2(\sigma_i)}\right] \quad (2\text{-}12)$$

where M_i is the mass concentration of mode i. Now the number, surface area, volume, and mass PSDs in the size range covered both the electrical mobility- and aerodynamic-based techniques can be reproduced. The goal of this stage is to apply the most appropriate size-resolved ρ_{eff} to a given number PSD measurement, thereby accurately estimating its volume and mass PSD and taking into consideration the uncertainties of the unknown size-resolved ρ_{eff} values for the coarse mode. Fitting parameters and measurement information for urban aerosol PSD measurements made with both electrical mobility- and aerodynamic-based techniques covering the sub-micron and coarse regimes are provided in Table A.2.

For optical-based measurements, we assume the optical diameter is equivalent to D_{em} due to the lack of information needed to convert one to the other. The number PSDs measured by optical-based techniques were transformed to mass PSDs assuming a uniform apparent density of 1.65 g cm^{-3}.[73] The mass PSDs were then fitted with the multi-modal lognormal distribution function using Equation (2-12). The fitted mass PSDs were converted back to number, surface area, and volume PSDs. Fitting parameters and measurement information for urban aerosol PSD measurements made with both electrical mobility- and optical-based techniques covering the sub-micron and coarse regimes are provided in Table A.3.

2.5.1.3 Urban aerosol mass PSDs measured by gravimetric methods employing inertial impactors

For urban aerosol mass PSDs measured by gravimetric methods with inertial impactors, the D_a-based mass PSDs were converted to D_{em}-based mass PSDs to enable for comparison with the other electrical mobility-based measurements. According to the measurement location and site type, D_a was converted to D_{em} using the ρ_{eff} functions for Groups A, B, or C, via Equation (2-10). For the fraction of the coarse mode where a series of χ and ρ_p were used to estimate ρ_{eff}, each D_a-based mass PSD was converted to multiple D_{em}-based mass PSDs, with each PSD corresponding to a particular value of ρ_{eff}. Then, the mean D_{em}-based PSD was taken from the series of D_{em}-based mass PSDs and merged with the rest of the D_{em}-based mass PSD determined via the effective density functions ρ^A_{eff}, ρ^B_{eff}, or ρ^C_{eff}. The multi-modal lognormal fitting was conducted for the D_{em}-based mass PSDs by using Equation (2-12). An example is shown in Figure 2.6.

The D_a-based mass PSDs were also converted to D_{em}-based volume PSDs by using the ρ_{eff} functions for Groups A, B, or C. Similar to the conversion for mass PSDs, for the fraction of the coarse mode where a series of χ and ρ_p were used to estimate ρ_{eff}, each D_a-based mass PSD was converted to multiple D_{em}-based volume PSDs. The mean D_{em}-based volume PSD was taken from this series of D_{em}-based volume PSDs and merged with the rest of the D_{em}-based volume PSD. The multi-modal lognormal fitting was conducted for the D_{em}-based volume PSDs by using Equation (2-11). The fitted D_{em}-based volume PSDs were converted to D_{em}-based number and surface area PSDs. Fitting parameters and measurement information for urban aerosol PSD measurements made with gravimetric methods employing inertial impactors are provided in Table A.4.

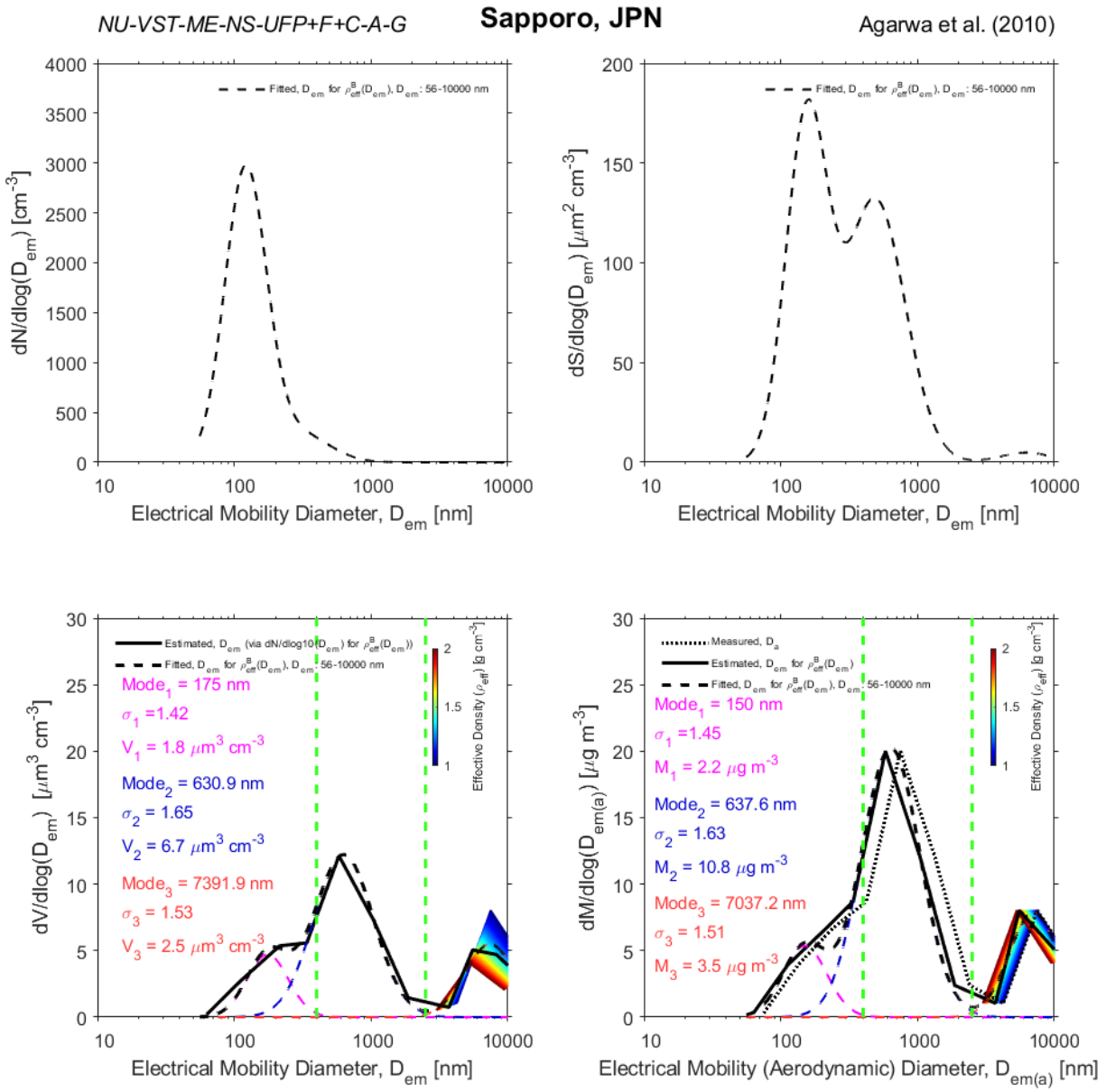

Figure 2.6 An example of urban aerosol number, surface area, volume, and mass PSDs measured by gravimetric methods employing inertial impactors. The black dotted curve in the mass PSD indicates the measured data. The solid black lines in the volume and mass PSDs are D_{em}-based PSDs converted from the measured D_a-based mass PSD by using ρ^B_{eff}. The rainbow color lines are the converted D_{em}-based volume and mass PSDs for a range of ρ_{eff} to account for the uncertainties in ρ_{eff} in the coarse regime. The relationship between the color and ρ_{eff} is shown in the color bar. The dotted color lines are the lognormal fitting curves for each mode. The dashed black lines in the volume and mass PSDs are the sum of the fitted sub-modes. The fitted volume PSD was converted to number and surface area PSDs, which are shown as the dashed black lines. The effective size range for the lognormal fitting is indicated.

2.5.1.4 Urban Aerosol Columnar Volume PSDs

Urban aerosol columnar volume PSDs measured by sun/sky radiometers were first converted to number PSDs assuming spherical particles. Then, the converted number PSDs and the columnar volume PSDs were separately fitted with multi-modal lognormal distribution functions, using Equation (2-7) and (2-11), respectively. The fitted number PSDs were transformed to surface area PSDs and the fitted volume PSDs were transformed to mass PSDs assuming a uniform apparent density of 1.65 g cm^{-3}.[73] As the columnar volume PSDs do not present the absolute aerosol concentration, they were plotted in arbitrary units. Fitting parameters and measurement information for urban aerosol columnar volume PSD measurements made with sun/sky radiometers are provided in Table A.5.

2.4.1.5 Considerations for Grouping Urban Aerosol PSD Observations by Geographical Region

The collection of urban aerosol PSD observations from around the globe offers a basis to identify geographical trends in number and mass PSDs. A few considerations were made in grouping the PSDs by geographical region. For urban aerosol number PSDs, the prominent peak is most often present in the UFP regime, which is captured very well by electrical mobility-based techniques (e.g. SMPS). However, PSD measurements made with aerodynamic-based techniques (e.g. APS, inertial impactors), optical-based techniques (e.g. OPC, OPS), or sun/sky radiometers typically cannot accurately characterize number PSDs down to the UFP regime. Thus, when grouping urban aerosol number PSDs by geographical region, only measurements made via electrical mobility-based techniques involving the UFP regime were used. More recent PSD observations of the sub-3 nm nanocluster aerosol mode made with diethylene glycol-based condensation particle counters, which can contribute significantly to sub-micron particle number concentrations, were not included in the global-scale analysis given the limited number of measurements that have been made (e.g. Rönkkö et al.[115]). For urban aerosol mass PSDs, the maximum value of the PSD typically exists in either the accumulation mode or the coarse mode. Therefore, urban aerosol PSD measurements made via electrical mobility-based techniques that only cover the sub-micron regime were not used in the analysis of geographical trends in mass PSDs. Only PSD measurements made with inertial impactors and those combining both electrical

mobility- and aerodynamic-/optical-based techniques to cover both the sub-micron and coarse regimes were incorporated into the global mass PSD analysis.

2.5.2 Categorization and presentation of urban aerosol PSD observations in the Appendix

The urban aerosol PSD observations were categorized by seven factors in order to better evaluate the shape and magnitude of an individual PSD and to provide a basis for historical interpretations of the PSDs: (1.) sampling location, (2.) sampling duration, (3.) time of day, (4.) event identification, (5.) target aerosol population, (6.) measurement type, and (7.) prominent mode. The categorization information is presented in the Appendix A in Tables A1-A5 as acronyms as: (1.) – (2.) – (3.) – (4.) – (5.) – (6.) – (7.) (e.g. Figure 2.3, 2.5, 2.6). Intra-city sampling locations include: traffic-influenced (TR), city center (CC), urban background (UB), sub-urban (SUB), and non-specific urban (NU). Non-specific urban represents an environment that is in the urban area, but all of the other indicators are not applicable. The sampling duration of the measurements were classified into several time-scales: long term (LT: > 6 months), moderate term (MT: 1 – 6 months), short term (ST: 1 week – 1 month), very short term (VST: 1 day – 1 week), and very, very short term (VVST: < 1 day). The time of the day includes: morning (M), afternoon (A), evening/night (E), daytime (D), and mean/median of the day (ME). Event identification includes: non-specific event (NS), new particle formation (NPF), biomass burning (BB), photochemical event (PC), combustion event (CB), dust storm (DS), and haze (HZ). The majority of PSDs were classified as NS as the reported observational period was not associated with a particular event. The target aerosol population indicates the size range covered by the measurement setup, including: UFP regime (UFP: $D_p \leq 100$ nm), fine regime (F: 100 nm < $D_p \leq$ 1000 nm), coarse regime (C: $D_p >$ 1000 nm), UFP and fine regimes (UFP+F), fine and coarse regimes (F+C), and UFP regime with both fine and coarse regimes (UFP+F+C). The measurement type includes aerosol instruments based on electrical mobility classification (EM), aerodynamic sizing (A), optical sizing (O), sun/sky radiometers (RS), and gravimetric methods using inertial impactors (A-G). The prominent mode indicates the location of the prominent peak in the number PSDs, including the nucleation mode (NUC), Aitken mode (AIT), and accumulation mode (ACC). In some cases, the peak is present at the border of the nucleation and Aitken modes (NUC-AIT), or at the border of the Aitken and accumulation modes (AIT-ACC).

For number PSDs measured with a combination of electrical mobility- and aerodynamic-/optical-based techniques covering the sub-micron and coarse regimes (Tables A.2, A.3), the PSDs were divided into two segments as outlined in Section 2.4.1.2; thus, a separate figure was generated for each segment. Figure 2.3 is representative of sub-micron urban aerosol number PSDs measured with electrical mobility-based techniques that are included in the Appendix A. The upper-left plot includes the measured/extracted data (black curve), which was fitted to the multi-modal lognormal distribution function. The lognormal fitting parameters are listed, with the colors corresponding to the individual mode, shown as dashed curves. The blue curve shows the sum of the individual modes. The size range over which the fitting is effective is listed. The fitted size range was not necessarily equivalent to the size range of the measurement. The estimated surface area, volume, and mass PSDs derived from the fitted number PSD are presented in the remaining plots. Size-integrated concentrations are also provided in the figure.

Figure 2.5 is representative of urban aerosol number PSDs spanning the accumulation and coarse modes measured with aerodynamic-based techniques that are included in the Appendix A. The black dotted curve in the number PSD represents the measured data. The dotted line in the D_a-based volume PSD was converted from the measured D_a-based number PSD. The solid black lines in the volume and mass PSDs are D_{em}-based PSDs converted from the measured D_a-based number PSD. The rainbow color lines are the converted D_{em}-based volume and mass PSDs for a range of ρ_{eff} to account for the uncertainties of ρ_{eff} in the coarse regime. The relationship between the color and ρ_{eff} is shown in the color bar. The dashed color lines are the lognormal fitting curves for each mode. The dashed black lines in the volume and mass PSDs are the sum of the fitted sub-modes. The fitted volume PSD was converted back to number and surface area PSDs, which are shown as the dashed black lines. The effective size range for the lognormal fitting is shown. A D_{em}-based mass PSD was also determined assuming a uniform apparent particle density of 1.65 g cm^{-3} as the dotted black line.[73] It should be noted that three modes were applied in this example; however, four modes might be used in the lognormal fitting for the volume or mass PSDs. The size-resolved ρ_{eff} function (A, B, or C) for the conversion is listed and the vertical dashed green lines correspond to the different size ranges for the ρ_{eff} functions (denoted in Figure 2.9).

Figure 2.6 is representative of urban aerosol mass PSDs measured by gravimetric methods with inertial impactors. The black dotted curve in the mass PSD indicates the measured data. The solid black lines in the volume and mass PSDs are D_{em}-based PSDs converted from the measured

D_a-based mass PSD by using ρ^B_{eff}. The rainbow color lines are the converted D_{em}-based volume and mass PSDs for a range of ρ_{eff} to account for the uncertainties of ρ_{eff} in the coarse regime. The relationship between the color and ρ_{eff} is shown in the color bar. The dotted color lines are the lognormal fitting curves for each mode. The dashed black lines in the volume and mass PSDs are the sum of the fitted sub-modes. The fitted volume PSD was converted back to number and surface area PSDs, which are shown as the dashed black lines. The effective size range for the lognormal fitting is shown.

2.6 Methodology for determining size-resolved urban aerosol respiratory tract deposited dose rates

The compilation of urban aerosol number and mass PSDs from around the globe offers a basis to evaluate the implications of geographical variations in the shape and magnitude of PSDs on human inhalation exposure. The respiratory tract deposited dose rate (RTDDR), or inhaled deposited dose rate, is a valuable, yet underused, exposure metric that combines an aerosol PSD with size-resolved respiratory tract deposition fractions to predict the number and mass of particles deposited in each region of the human respiratory tract per unit time. Despite the utility of this metric in offering a useful link between air pollution and human health outcomes, only a few studies have determined RTDDRs for outdoor or indoor aerosols (e.g. Hussein et al.[116]; Löndahl et al.[117,118]; Wu et al.[119]). Here, the RTDDR is evaluated in the form of a lognormal size distribution, $dRTDDR_{N/M}/dLogD_{em}$, to be consistent with the presentation of the urban aerosol PSDs. The subscripts *N* and *M* denote the number and mass dose rate, respectively.

The $dRTDDR_N/dLogD_{em}$ (h^{-1}) and $dRTDDR_M/dLogD_{em}$ ($\mu g\ h^{-1}$) were calculated for an adult engaged in light physical activity (e.g. walking) in the urban outdoor environment as follows:

$$dRTDDR_N/dLogD_{em} = dN/dLogD_{em} \times V_T \times f \times DF(D_p) \quad (2\text{-}13)$$

$$dRTDDR_M/dLogD_{em} = dM/dLogD_{em} \times V_T \times f \times DF(D_p) \quad (2\text{-}14)$$

where $dN/dLogD_{em}$ and $dM/dLogD_{em}$ are the urban aerosol number and mass PSDs, respectively; V_T is the tidal volume (mL); f is the breathing frequency (min^{-1}); and $DF(D_p)$ is the size-resolved particle deposition fraction in the human respiratory tract (–). The V_T and f were taken as the average for an adult female and male engaged in light activity: V_T = 1083 mL and f = 18 min^{-1} (U.S. EPA, 2011). Total and regional (head airways, tracheobronchial region, and pulmonary region) size-resolved particle deposition fractions for an adult were obtained using the

age-specific symmetric single-path model from the open-source Multiple-Path Particle Dosimetry (MPPD) Model (v3.04, Applied Research Associates, Inc., Albuquerque, NM, USA)[120], as illustrated in Figure 2.7. The model considers impaction, diffusion, and sedimentation as relevant deposition mechanisms. The input parameters to the MPPD Model include: the tidal volume, breathing frequency, breathing route, age, functional residual capacity, and geometry type of respiratory tract. We applied the preset values for an adult with an upright upper body and a nasal breathing route. Uncertainties may exist for each of the input parameters due to discrepancies between the preset values and the realistic geometry of the human respiratory tract, which may vary to some extent from person to person. However, since the focus of the modeling is to probe the geographical variations in urban aerosol PSDs on human inhalation exposure, a fixed deposition curve, even with some uncertainties, has a minor influence on comparisons in the $dRTDDR_{N/M}/dLogD_{em}$ in each region.

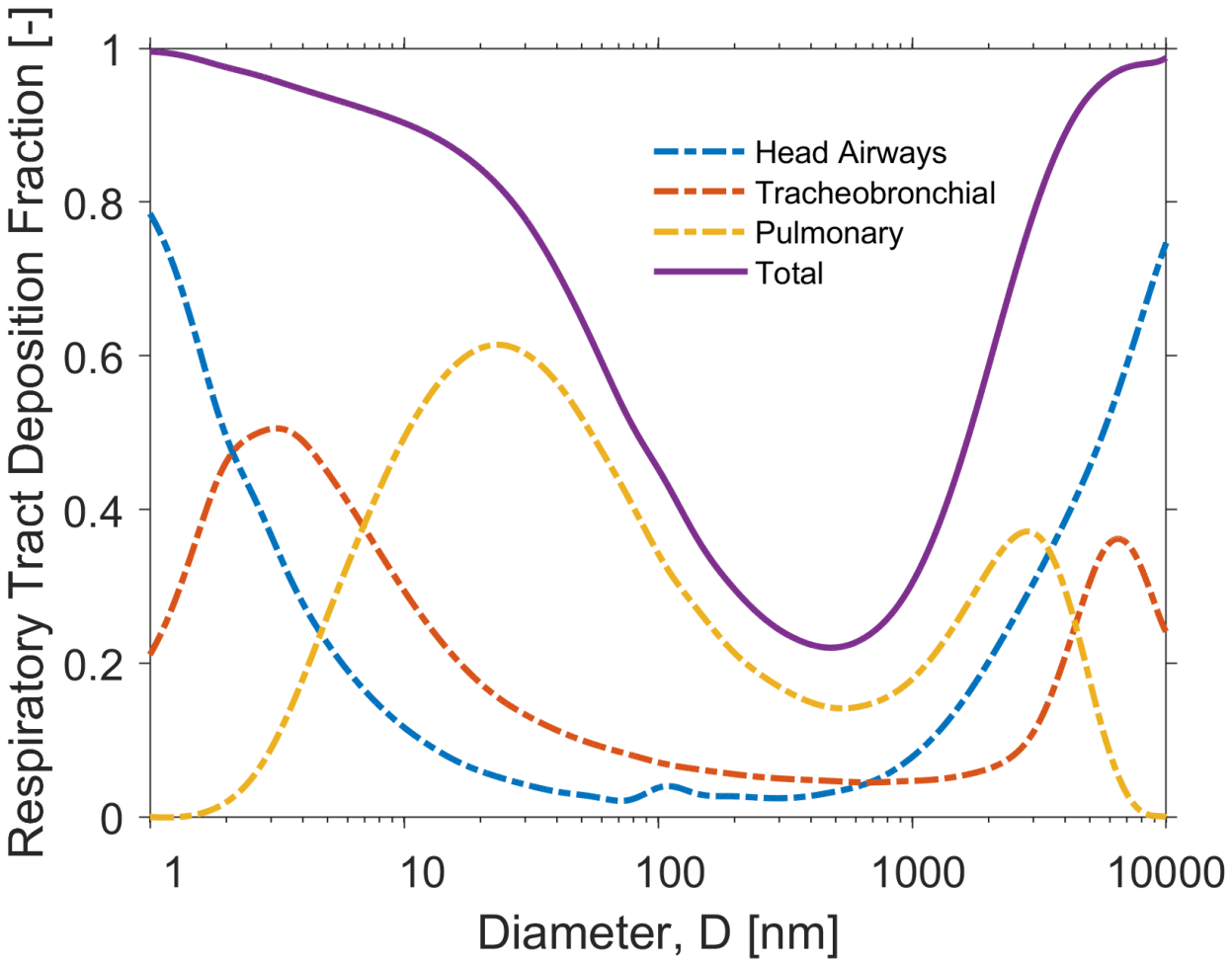

Figure 2.7 Size-resolved particle deposition fractions in the human respiratory tract, estimated by using the symmetric single-path model from the open-source Multiple-Path Particle Dosimetry (MPPD) Model (v3.04, Applied Research Associates, Inc., Albuquerque, NM, USA)[120] for an adult with an upright upper body.

Hygroscopic growth of the inhaled urban aerosol is not considered given the broad collection of PSDs analyzed in this study and the unknown chemical composition, mixing state, and hygroscopic growth factors associated with the aerosol populations. Hygroscopic growth of the inhaled aerosol can shift the size-resolved deposition fractions, and in turn, the estimated $dRTDDR_N/dLogD_{em}$ and $dRTDDR_M/dLogD_{em}$ (e.g. Löndahl et al.[117]). An inhaled dose study by Kodros et al.[121] found that the deposited mass concentration of aerosols in urban areas are lower than those in rural areas due to the higher hydrophobic content of urban aerosols. As aerosols are transported from an urban to rural area, the hydrophobic content becomes hydrophilic under atmospheric ageing, and the SO_2 converts to particle-phase sulfate. Relatively hydrophilic

particles can undergo hygroscopic growth under the high relative humidity conditions of the human respiratory tract. Hygroscopic growth of the inhaled urban aerosol may increase the RTDDR of accumulation mode particles as the growth shifts the mass PSD out of the minimum of the particle deposition fraction curve at approximately D_{em} = 400 nm.

The $\mathrm{dRTDDR_N/dLogD_{em}}$ were only determined for urban aerosol number PSDs measured with electrical mobility-based techniques involving the UFP regime. The $\mathrm{dRTDDR_M/dLogD_{em}}$ were determined for urban aerosol mass PSDs converted from number PSDs measured via one or more measurement techniques, including electrical mobility- and aerodynamic-/optical-based techniques, as well as mass PSDs measured directly via gravimetric methods with inertial impactors.

2.7 Methodology for evaluating the urban aerosol PSD that penetrates through a building ventilation system filter

The compilation of urban aerosol number and mass PSDs from around the globe offers a basis to evaluate the implications of geographical variations in the shape and magnitude of PSDs on indoor air quality and aerosol filtration in buildings. One of the pathways by which urban aerosols can enter the indoor environment, where people spend approximately 90% of their time[122], is through the ventilation system of a commercial or residential building[7]. Heating, ventilation, and air conditioning (HVAC) filters are installed in building ventilation sytems to filter outdoor air and recirculated indoor air. Thus, HVAC filters serve as an important interface between the outdoor and indoor atmospheres.

The relationship between the urban aerosol number PSD and a HVAC filter's size-resolved filtration efficiency determines the PSD of the urban aerosol that penetrates through the filter. The filter-transformed PSD is a useful indicator of the urban aerosol PSD to which occupants will be exposed to in buildings where the majority of outdoor air is provided via the ventilation system. Furthermore, the shape of the urban aerosol PSD that passes through the HVAC filter plays an important role in influencing the loading kinetics of the filter.[32] PSD-driven changes in the loading behavior can affect the evolution of the filter's pressue drop over time and the associated HVAC blower energy consumption required to overcome this airflow resistance.[25]

The urban aerosol PSD that penetrates through a HVAC filter installed in a single-pass building ventilation system was calculated as:

$$Penetrated\ (dN/dLogD_{em}) = dN/dLogD_{em} \times (1 - Filtration\ Efficiency) \quad (2\text{-}15)$$

Penetrated urban aerosol PSDs were determined for filters with the Minimum Efficiency Reporting Value (MERV) rating of 8 and 14. Size-resolved filtration efficiencies for the MERV 8 and 14 filters were estimated from Hecker and Hofacre[123], as illustrated in Figure 2.8. The impact of aerosol hygroscopicity and electrostatic charge, filter ageing, filter bypass, and ventilation airflow parameters (e.g. face velocity) on changes in the size-resolved filtration efficiency were not considered. The transformation of the urban aerosol PSD due to penetration through the building envelope (e.g. infiltration) was not evaluated.

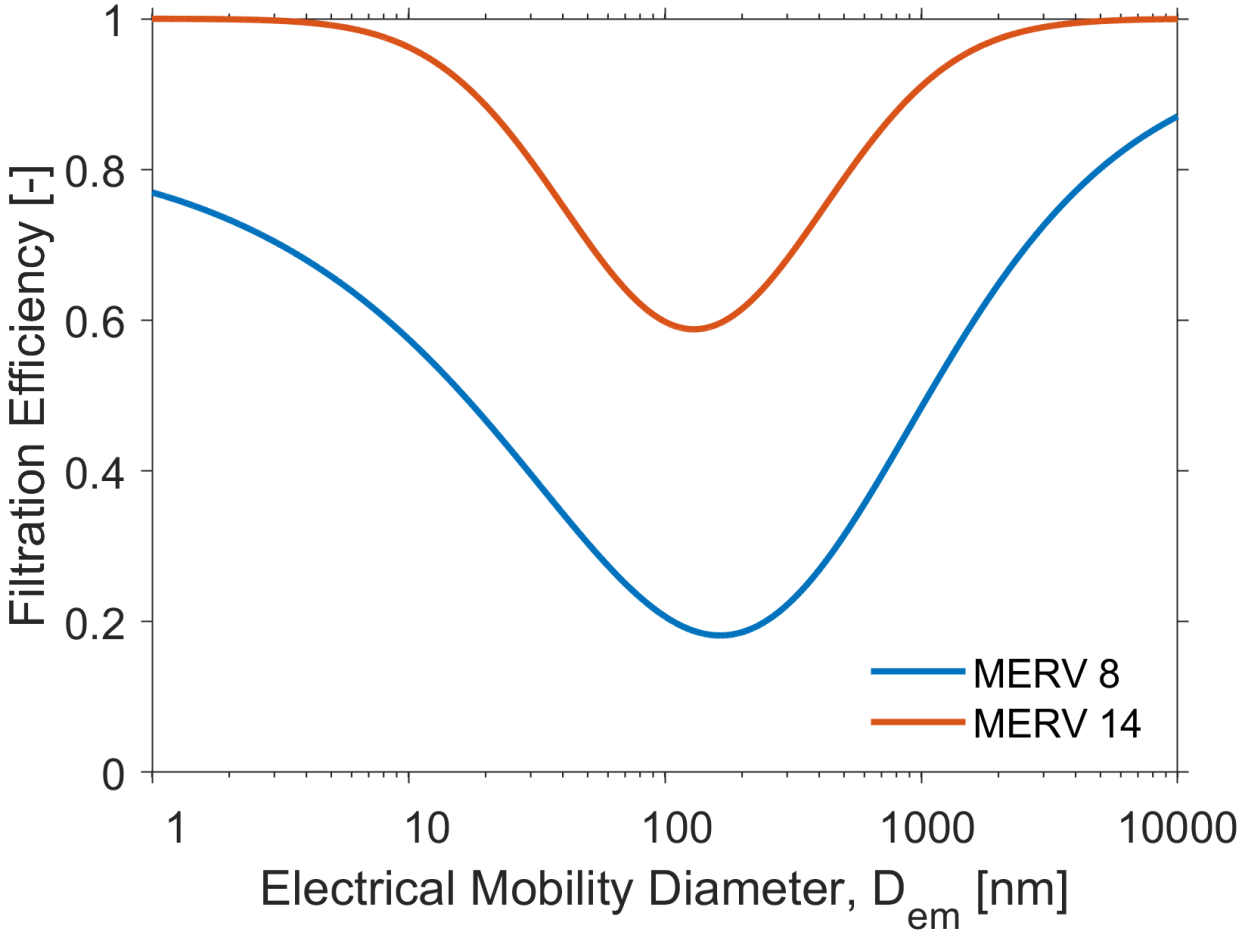

Figure 2.8 Size-resolved filtration efficiency curves for MERV 8 and MERV 14 filters for estimating the number PSDs of the penetrated urban aerosol.[123]

2.8 Summary of size-resolved urban aerosol effective densities

The size-resolved ρ_{eff} functions for Groups A, B, and C are illustrated in Figure 2.9. The blue lines indicate the mean ρ_{eff} values derived from direct measurements of ρ_{eff}, such as through evaluation of the mass-mobility relationship of an aerosol population. The grey areas represent the maximum and minimum values of the directly measured ρ_{eff} for each group. The associated measurement techniques for ρ_{eff} are noted. The directly measured ρ_{eff} in Groups A and B, both of which are in the 'urban' environment, present similar values and do not show much variation among the different studies conducted in China and the United States (Table 2.2). Furthermore, across the size range covered by direct ρ_{eff} measurements in Groups A and B, there is no clear size-dependency of ρ_{eff}, in part because organics and secondary inorganic ions are dominant in this size range.

The directly measured ρ_{eff} values collected from cities in the United States (Group B) are between 1.1 to 1.6 g cm^{-3}, while those measured in China (Group A) are slightly greater, with values between 1.3 to 1.9 g cm^{-3}, possibly due to a greater abundance of secondary inorganic species. The directly measured ρ_{eff} in the 'traffic' environment (Group C) presents a decreasing trend with the increase in particle size for 50 nm < D_{em} < 400 nm. This is largely due to primary emissions of soot particles from vehicle exhaust, which typically adopt a loose, chain-like agglomerated morphology with a fractal dimension (mass-mobility exponent) less than 3.[62,101,102,124,125]

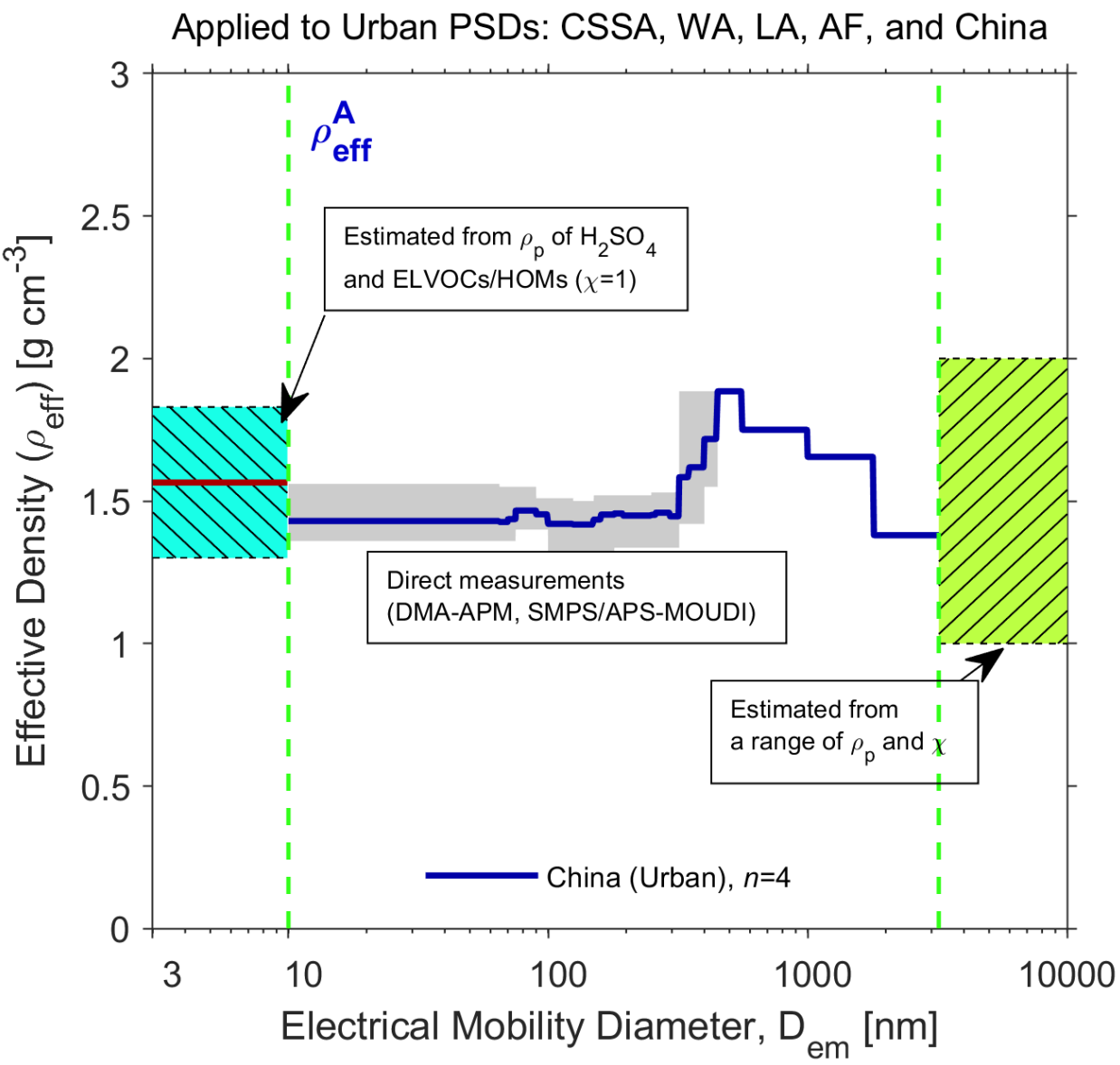

Figure 2.9 Size-resolved urban aerosol effective density functions (ρ_{eff}) for Group A ('urban'; obtained from measurements in China), Group B ('urban'; obtained from measurements in the United States), and Group C ('traffic'; obtained from measurements in the United States, Finland, and Denmark). Details of the ρ_{eff} measurements are summarized in Table 2. ρ_{eff} values for different combinations of χ and ρ_p are illustrated in Figure 2.4. Measurement technique nomenclature: DMA: Differential Mobility Analyzer, APM: Aerosol Particle Mass Analyzer, SMPS: Scanning Mobility Particle Sizer, APS: Aerodynamic Particle Sizer, MOUDI: Micro-Orifice Uniform Deposit Impactor.

Figure 2.9 continued.

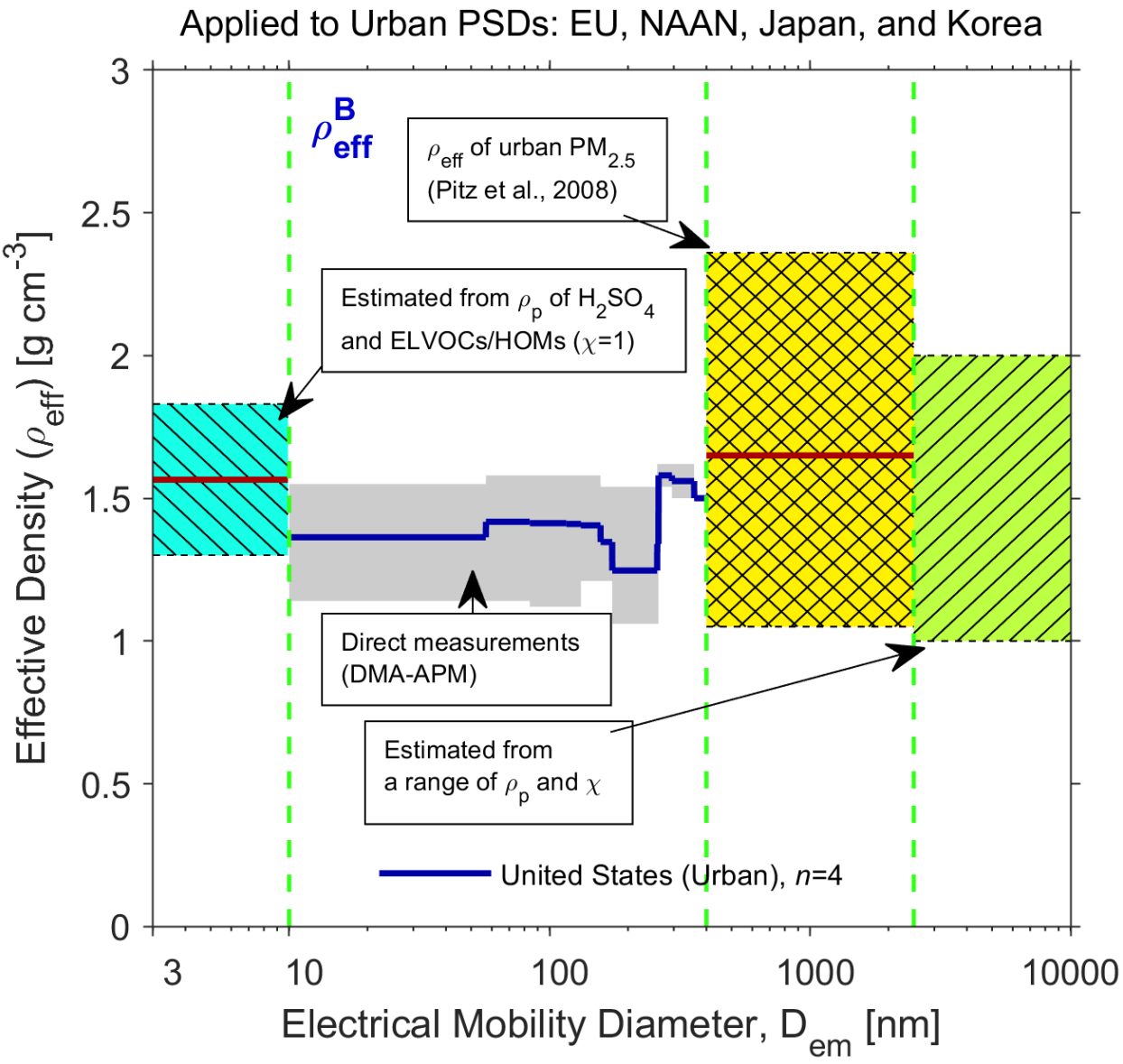

Figure 2.9 continued.

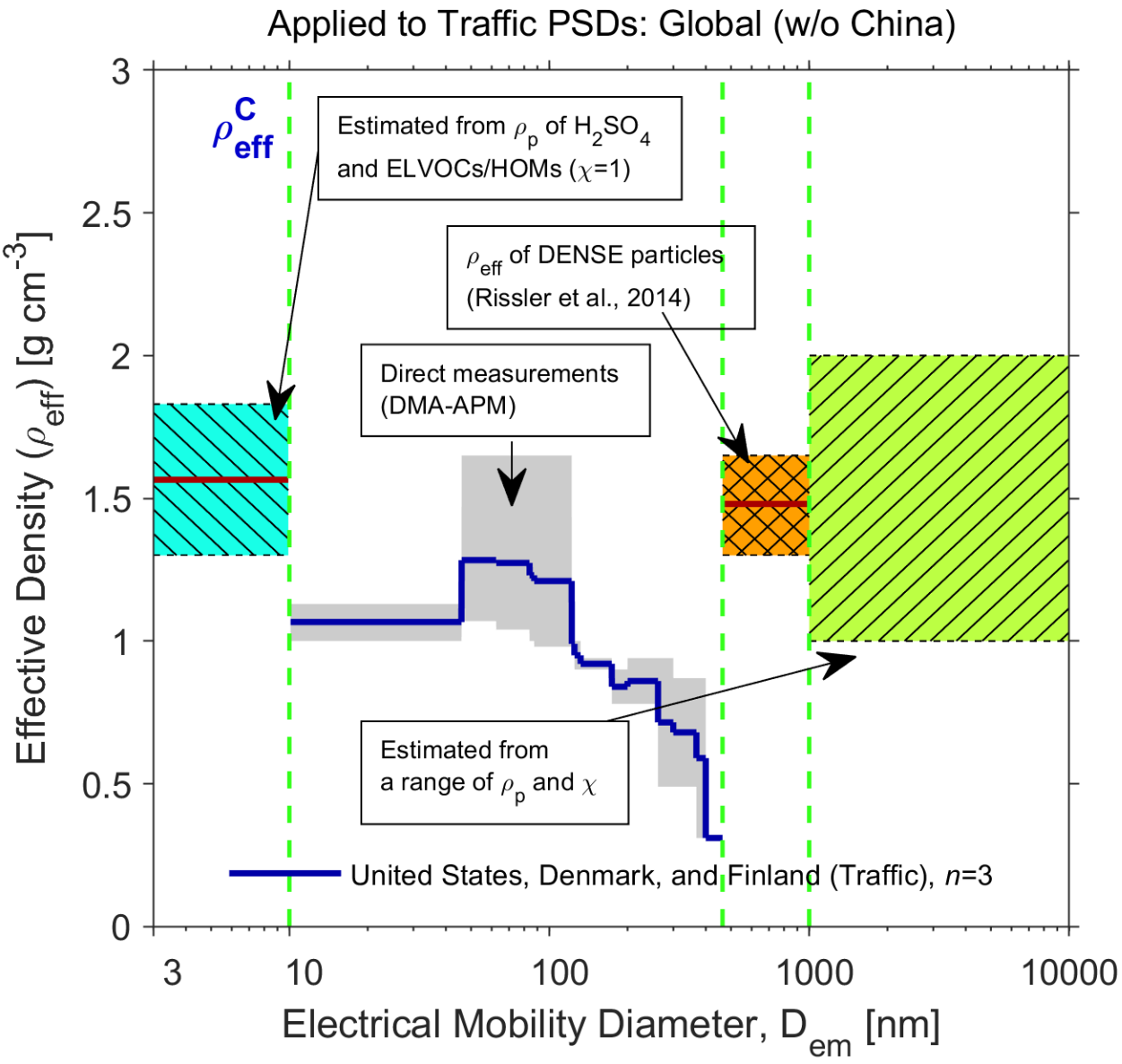

Numerous studies have revealed the decrease of ρ_{eff} with the increase in particle size for vehicle exhaust aerosol.[67,102,124,126–128] For size ranges where direct measurement of ρ_{eff} are unavailable, various assumptions were made to estimate a range of ρ_{eff} values, as discussed in Section 2.3. The light blue, yellow, and light green areas in Figure 2.9 represent the range of possible ρ_{eff} values for the three size fractions, and the red lines represent the mean values. The light green area in the coarse regime shows estimated ρ_{eff} values derived from a combination of

different χ and ρ_p (e.g. Figure 2.2), which take a variety of particle morphologies and chemical compositions into consideration. The wide variation in ρ_{eff} for coarse mode particles has important implications for estimating urban aerosol mass PSDs from number PSDs measured via commonly deployed instruments (e.g. APS, OPS, OPC).

ρ_{eff} is dependent on the chemical composition and morphological features (χ and ρ_p) of an urban aerosol population. Typically, direct ρ_{eff} measurements are conducted between D_{em} = 30 to 400 nm. Particles in this size range often consist of organics, secondary inorganic material, and black carbon. As discussed in Section 2.3.5, studies have found SOA to have ρ_{eff} values between 1 to 1.65 g cm^{-3} and secondary inorganic material, such as H_2SO_4, $(NH_4)_2SO_4$, and NH_4NO_3 to have ρ_{eff} values between 1.7 and 1.83 g cm^{-3}.[72,85–92] The ρ_{eff} of soot particles can fall below 1 g cm^{-3}, with a decreasing trend with the increase in particle size. The relative fraction of various species in an urban air mass, such as organics, secondary inorganic materials, and loosely agglomerated soot particles, among others, will determine the size dependency of the ρ_{eff} for the externally and internally mixed aerosol population. For example, previous direct ρ_{eff} measurements conducted in Los Angeles, Copenhagen, and Beijing found ρ_{eff} to be inversely proportional to particle size when the fraction of soot particles from vehicle emissions were relatively abundant due to elevated traffic intensity.[57,62,63] Conversely, a study in Shanghai observed an increase in ρ_{eff} with particle size (Table 2.2), which was attributed to an abundance of hygroscopic species, such as $(NH_4)_2SO_4$ and NH_4NO_3.[64,129]

Urban aerosol ρ_{eff} is expected to be temporally variant at a given sampling location due to the transient nature of emission sources. For example, in the urban environment, diurnal patterns in traffic density can drive time-dependent shifts in ρ_{eff} as the relative fraction of soot particles changes throughout the day. A low fraction of soot particles was observed in Copenhagen during the nighttime due to the low traffic density.[62] Two minima in ρ_{eff} were found in Houston in the morning at 07:00 and in the evening at 19:00 to 20:00, likely due to increased emissions of soot particles during rush hours.[66] In Beijing, one study found ρ_{eff} to decrease during the nighttime due to an increase in the abundance of soot particles.[55] This temporal shift in the urban aerosol ρ_{eff} was found to be due to the emissions of heavy trucks, which are only allowed to enter the fifth ring road in Beijing during the night, as well as more intense coal burning for domestic heating in the night during the heating season.

Urban aerosol ρ_{eff} is also influenced by air pollution events and air mass origins. Direct ρ_{eff} measurements in Beijing observed higher ρ_{eff} values during clean air quality episodes compared to polluted air quality episodes.[55] This finding was attributed to the greater relative fraction of mineral dust during the clean episodes and abundance of organics and secondary inorganic ions in the particle-phase during the polluted episodes.[55] The ρ_{eff} can shift during atmospheric NPF events, depending on the dominant condensable vapor during the particle growth period. Qiao et al.[57] found ρ_{eff} to decrease during a NPF event in Beijing, indicating that the condensable vapors were dominated by organics, which corresponded to the increase in the fraction of organic material in sub-micron particle mass concentrations. In contrast, ρ_{eff} measurements in Shanghai observed an increase in ρ_{eff} during NPF events, suggesting that relatively heavier secondary inorganic materials were the primary driver for particle condensational growth.[64,65] Wind direction can affect ρ_{eff} by changing the air mass origin. Direct ρ_{eff} measurements in a street canyon in central Copenhagen showed higher fractions of dense mode particles when the air mass traveled over more polluted regions than when the air mass come from clean sea/ocean areas.[62]

While the studies summarized in Figure 2.9 and Table 2.2 provide valuable insights into variations of ρ_{eff} with particle size, geographical location, and intra-city environments (urban vs. traffic), more measurements are clearly needed in many cities around the world to develop a more comprehensive understanding of the nature of urban aerosol morphology and the factors that drive changes in size-resolved ρ_{eff}. In particular, direct ρ_{eff} measurements are needed in the accumulation and coarse modes given the variability identified in this study and the contribution of both modes to urban aerosol mass PSDs (Section 2.9). Doing so will provide a basis to better translate measured number PSDs to mass PSDs and D_a-based PSDs to D_{em}-based PSDs.

2.9 Urban aerosol PSD observations around the globe: an overview of existing data

Urban aerosol PSD observations made between 1998 and 2017 were collected and analyzed to evaluate geographical variations in the shape and magnitude of number and mass PSDs and to identify gaps in PSD measurements. In total, *n*=793 PSDs from *n*=125 cities in *n*=51 countries were collected. The measured PSDs were fit to the multi-modal lognormal distribution function and translated across number, surface area, volume, and mass domains following the methodologies outlined in Section 2.4. The PSD observations are summarized and categorized in the Appendix A and are grouped by geographical region: AF, CSSA, EA, EU, LA, NAAN, and WA. Table 2.1 lists the number of PSDs in each city and country partitioned among the seven geographical regions. It is important to note that the sampling duration of the PSD observations presented in Table 2.1 are variable. Among all PSDs, 14.3% were long-term measurements (LT: > 6 months) and 33.3% were moderate-term measurements (MT: 1 – 6 months). The remaining PSDs represent observations made over periods less than one month through short-term field measurement campaigns.

Figure 2.1 illustrates the temporal and geographical distribution by year between 1998 and 2017 of the urban aerosol PSD references analyzed in this study. Between 1998 and 2007, there is a clear increase in the number of published studies reporting urban aerosol PSD observations. During this period, the majority of PSD measurements were conducted in cities in EU and NAAN. However, beginning in 2006 and continuing through 2017, a greater fraction of published PSD observations were collected in cities in EA and CSSA. Studies reporting PSD observations in NAAN cities appear to have declined between 2009 and 2017. Urban aerosol PSD observations in LA, WA, and AF remain sparse across the examined time period, however, the frequency of publications reporting PSD measurements in LA has been fairly stable between 2009 and 2017. Based upon the criteria employed in the literature search (Section 2.2), the year with the greatest number of published studies reporting urban aerosol PSD measurements was 2009 (*n*=17), followed by 2014 (*n*=15). 1998 and 1999 were associated with the fewest number of published PSD measurements (*n*=1).

Figure 2.10 presents the global distribution of urban aerosol PSD measurement locations included in this study. It is apparent that there are regions were numerous observations have been made (e.g. EU) and others were measurements are scarce (e.g. WA, LA, AF). Among the *n*=793 urban aerosol PSD observations collected in this study, 39.8% of them are from EU, 15.2% are

from North America, and 18.1% are from EA. Conversely, only 7.2% are from WA, 5.9% from LA, and 3.6% from AF. The three countries that contribute the most to the collection of urban aerosol PSD observations in this study are the United States (13.3%), China (12.2%), and Germany (8.8%).

The majority of PSD observations in EU have been collected in Germany (n=68), Finland (n=52), the United Kingdom (n=37), Italy (n=31), and Denmark (n=26). The top five EU cities with the greatest number of urban aerosol PSD observations include Helsinki, Finland (n=52), Leipzig, Germany (n=27), Copenhagen, Denmark (n=25), London, United Kingdom (n=16), and Milan, Italy (n=15). The n=101 PSD observations compiled from the United States represent n=16 cities, including Los Angeles, California (n=34), Riverside, California (n=8), Pittsburgh, Pennsylvania (n=7), and Buffalo, New York (n=6). A growing number of PSD measurements have been made in China (n=93), in cities such as Beijing (n=38), Guangzhou (n=14), and Shanghai (n=12). In India, n=48 PSD observations were analyzed from Kanpur (n=23) and New Delhi (n=13), among other cities.

A paucity of urban aerosol PSD measurements is clear throughout the entirety of AF, LA, and WA; CSSA excluding India; Canada, although a few measurements have been conducted in the Greater Toronto and Hamilton Area (total of n=15); Russia (n=1 from Tiksi); Australia (n=10 across Launceston, Brisbane, and Wollongong); and New Zealand (n=8 from Auckland). The few published PSD measurements in AF, CSSA excluding India, and WA were primarily reported as columnar volume PSDs by using sun/sky radiometers. Urban aerosol PSD observations have only been made in n=8 countries in AF, including Egypt (n=12), South Africa (n=6), Zambia (n=4), Botswana (n=3), Kenya (n=1), Cape Verde (n=1), Mali (n=1), and Senegal (n=1). Similarly, in LA, PSD measurements have been made in a few countries, the majority of which have been reported in Brazil (n=38, with n=35 from São Paulo), Chile (n=6), Mexico (n=3), and Cuba (n=1). n=58 urban aerosol PSD measurements have been reported in WA, many of which were made in Zanjan, Iran (n=23), followed by Istanbul, Turkey (n=13), Fahaheel, Kuwait (n=12), and Yanbu, Saudi Arabia (n=9). 68.6% of the PSD observations in CSSA have been reported in India, with comparatively less measurements coming from other countries in the region, including Pakistan (n=8), Singapore (n=6), Nepal (n=4), Thailand (n=2), and Vietnam (n=2).

Table 2.2 List of the number of urban PSDs that have been extracted and analyzed in each region, country, and city.

Region	**Country**	**City**
Africa (*n*=29)	Botswana (3)	Gaborone (3)
	Cape Verde (1)	Praia City (1)
	Egypt (12)	Cairo (12)
	Kenya (1)	Nairobi (1)
	Mali (1)	Bamako (1)
	Senegal (1)	Dakar (1)
	South Africa (6)	Johannesburg (2)
		Pretoria (4)
	Zambia (4)	Mongu (4)
Central, South, and Southeast Asia (*n*=70)	India (48)	Durg (4)
		Kanpur (23)
		Mumbai (2)
		New Delhi (13)
		Pune (2)
		Trivandrum (4)
	Nepal (4)	Lalitpur (1)
		Dhulikhel (3)
	Pakistan (8)	Karachi (3)
		Lahore (3)
		Peshawar (1)
		Rawalpindi (1)
	Singapore (6)	Singapore City (6)
	Thailand (2)	Chiang Mai (1)
		Silpakorn (1)
	Vietnam (2)	Ho Chi Minh (2)
East Asia (*n*=138)	China (93)	Beijing (38)
		Guangzhou (14)
		Hong Kong (6)
		Jinan (1)
		Jinhua (1)
		Lanzhou (11)
		Nanjing (2)
		Shanghai (12)
		Shenzhen (3)
		Zhengzhou (2)
		Urumchi (1)
		Wuxi (2)

Table 2.2 continued.

East Asia (*n*=138)	Japan (17)	Kawasaki (10)
		Sapporo (6)
		Tokyo (1)
	South Korea (24)	Gwangju (16)
		Seoul (4)
		Ulsan (4)
	China: Taiwan (4)	Taipei (3)
		Taichung (1)
Europe (*n*=316)	Austria (7)	Vienna (7)
	Belgium (1)	Gent (1)
	Switzerland (4)	Zurich (4)
	Czech Republic (4)	Prague (4)
	Germany (68)	Aachen (1)
		Augsburg (2)
		Braunschweig (12)
		Dresden (4)
		Duisburg (1)
		Erfurt (9)
		Essen (5)
		Heidelberg (2)
		Karlsruhe (5)
		Leipzig (27)
	Denmark (26)	Copenhagen (25)
		Odense (1)
	Spain (17)	Barcelona (7)
		Ciudad Real (2)
		Madrid （8）
	Finland (52)	Helsinki (52)
	France (10)	Marseilles (5)
		Paris (3)
		Dunkirk (2)
	United Kingdom (37)	Birmingham (1)
		Cambridge (7)
		Leeds (3)
		Leicester (2)
		London (19)
		Manchester (5)
	Greece (7)	Athens (3)
		Chania (4)

Table 2.2 continued.

Europe (*n*=316)	Hungary (9)	Budapest (9)
	Italy (31)	Bologna (2)
		Cagliari (1)
		Cassino (2)
		Ispra (4)
		Milan (15)
		Rome (7)
	Lithuania (9)	Vilnius (9)
	Netherland (6)	Amsterdam (4)
		Rotterdam (2)
	Norway (3)	Oslo (3)
	Portugal (12)	Oporto (10)
		Lisbon (2)
	Russia (1)	Tiksi (1)
	Sweden (11)	Gothenburg (3)
		Stockholm (8)
	Moldova (1)	Chisinau (1)
Latin America (*n*=48)	Brazil (38)	Porto Alegre (3)
		São Paulo (35)
	Chile (6)	Santiago (6)
	Mexico (3)	Mexico City (3)
	Cuba (1)	Camagüey (1)
North America, Australia and New Zealand (*n*=134)	Australia (10)	Brisbane (2)
		Launceston (7)
		Wollongong (1)
	New Zealand (8)	Auckland (8)
	Canada (15)	Hamilton (2)
		Toronto (13)

Table 2.2 continued.

North America, Australia and New Zealand (*n*=134)	United States (U.S.) (101)	Atlanta (4)
		Boulder (1)
		Buffalo (6)
		Claremont (5)
		Corpus Christi (4)
		Detroit (6)
		Downey (4)
		Fresno (12)
		Houston (1)
		Los Angeles (34)
		New York (5)
		Newark (2)
		Pittsburgh (7)
		Raleigh (1)
		Riverside (8)
		Rochester (1)
West Asia (*n*=58)	Iran (23)	Zanjan (23)
	Jordan (1)	NA
	Kuwait (12)	Fahaheel (12)
	Saudi Arabia (9)	Yanbu (9)
	Turkey (13)	Istanbul (13)

The vast majority of urban aerosol PSD measurements analyzed in this study were made via electrical mobility-based techniques, as summarized in Table A.1. Comparatively less direct measurements of mass PSDs were made via gravimetric methods employing inertial impactors (Table A.4). In total, 76.8% of the urban aerosol PSDs reported number PSDs down to the UFP fraction of the sub-micron regime. However, only six of the urban aerosol number PSDs involving the UFP regime are from Southeast Asia; only thirteen are from WA, and none are from AF. The lack of urban aerosol PSD measurements down to the UFP regime in many regions of the world makes it very challenging to accurately estimate urban aerosol inhalation exposures. This is of concern given the inhalation toxicity and adverse health effects associated with UFPs.[12,14,15,17,130–133]

Figure 2.10 Global distribution of urban aerosol PSD measurement locations included in this study.

2.10 Urban Aerosol PSDs: From Number to Mass

2.10.1 Geographical variations in the magnitude and shape of sub-micron urban aerosol number PSDs

Geographical variations in sub-micron urban aerosol number PSD measurements ($dN/dLogD_{em}$, cm^{-3}) are presented in Figure 2.11. Each log-log plot incorporates number PSDs measured with electrical mobility-based techniques that cover the sub-micron regime (n=624, Section 2.4.1.1, Table A.1). Each line represents an individual PSD and the color indicates the occurrence frequency of the number PSDs at a given particle size (D_{em}) with a certain particle number concentration. Red, orange, and yellow curves indicate the number PSDs where the occurrence frequency is high among the analyzed studies. All number PSD observations are included in the 'Global' plot (top-left). Number PSDs for EA, CSSA, EU, LA, and NAAN are presented in the remaining plots; however, AF and WA are not included due to the lack of PSD measurements in the sub-micron regime in the two regions. The solid black lines indicate the median number PSDs for each group, which are also presented in Figure 2.12 on a linear y-axis scale. It can be seen that among the geographical regions, the greatest amount of sub-micron number PSDs have been reported for cities in EU, NAAN, and EA; comparatively less have been reported in CSSA and LA.

The visualization of the global distribution in sub-micron urban aerosol number PSDs (Figure 2.11, top-left) demonstrates that there exist significant variations in both the magnitude and shape of number PSDs measured across urban environments around the world. For a given particle size (D_{em}), there can exist over two orders of magnitude variation in the particle number concentration. This variation in the amplitude of the number PSDs is persistent across the considered size range, from D_{em} = 3 to 1000 nm, which includes the nucleation, Aitken, and accumulation modes. The red-yellow region of the global plot surrounds the median number PSD (black line). Wide variability in the magnitude of the number PSDs above and below the median PSD is apparent. Thus, defining a globally representative urban aerosol number PSD is challenging given the vast array of factors that can influence the shape of a PSD at a particular sampling location within in a city. However, the red region suggests that on a global-basis, some trends do exist in regard to the shape and magnitude of urban aerosol number PSDs. Notably, number PSDs are often dominated by particles between D_{em} = 10 to 100 nm, with varying

contributions from the sub-10 nm fraction and accumulation mode, depending on the conditions that exist at the measurement site. Across this size fraction, there is a high occurrence frequency of number PSDs with an amplitude between 1000 to 10000 cm^{-3}. In some cases, the amplitude can reach or exceed 50000 cm^{-3}, most commonly in the nucleation and Aitken modes. The global median number PSD demonstrates that number PSDs often drop off in magnitude by nearly a factor of a hundred across the width of the accumulation mode, from approximately 1000 cm^{-3} at D_{em} = 100 nm to 10 cm^{-3} as D_{em} approaches 1000 nm.

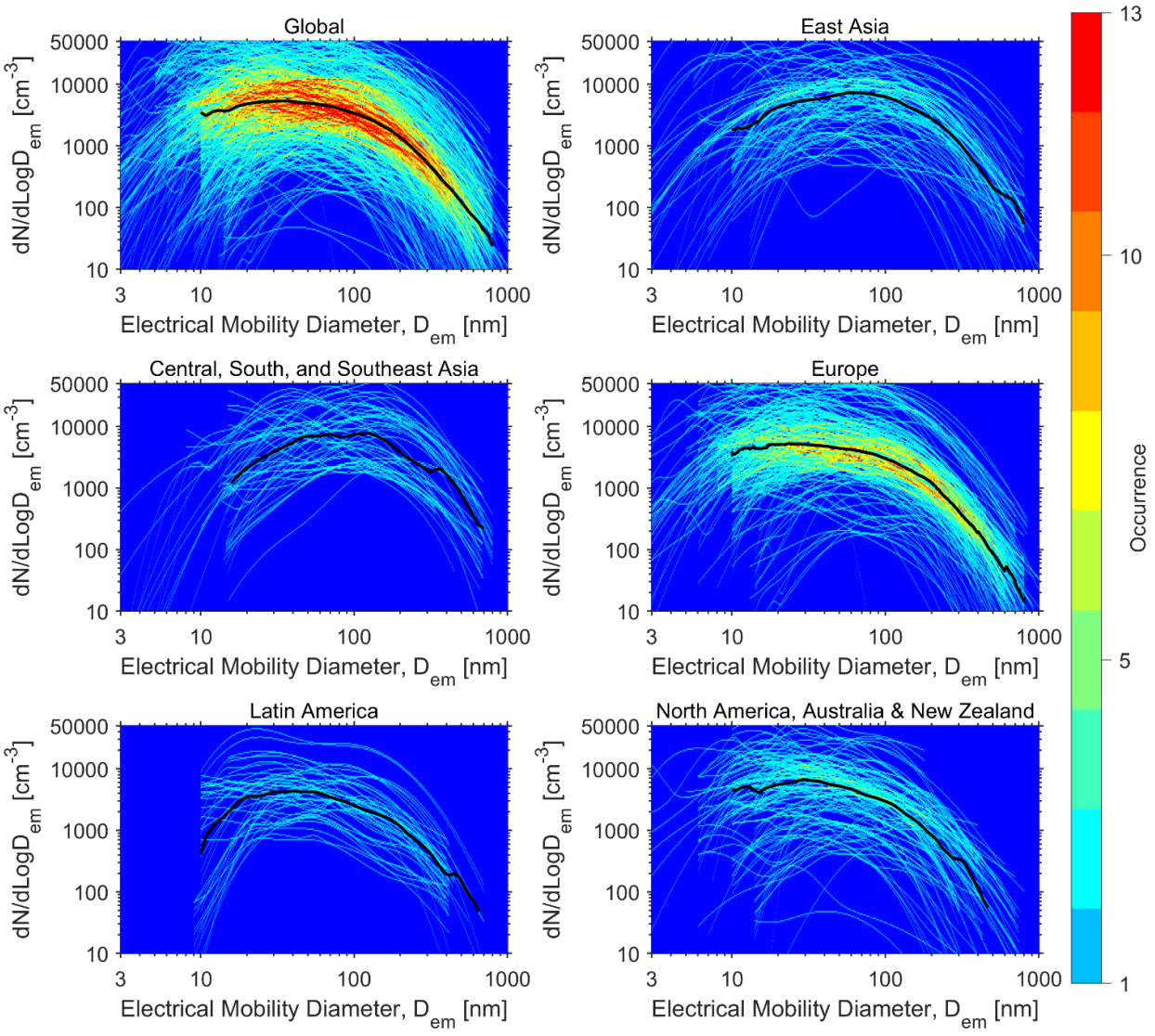

Figure 2.11 Urban aerosol number PSDs analyzed in this study, grouped by geographical region. The figure incorporates all sub-micron number PSDs measured by electrical mobility-based techniques (n=624). The color represents the occurrence frequency of the number PSDs at a given particle size with a certain concentration. The black lines indicate the median number PSDs in each group.

The geographically-resolved collections of urban aerosol number PSDs presented in Figure 2.11 and 2.12 indicate that there exists inter-region variability in the shape and magnitude of number PSDs. Number PSDs in NAAN and EU present similar structural characteristics; similarly, number PSDs in EA and CSSA are alike in both shape and magnitude. Number PSDs measured in cities in NAAN and EU tend to skew to the left and are often dominated by nucleation and Aitken mode particles, whereas number PSDs measured in cities in EA and CSSA tend to skew to the right and are often dominated by Aitken and accumulation mode particles. The magnitude of the number PSDs in the accumulation mode in EA and CSSA tends to be higher than that in NAAN and EU. This is apparent in the collection of individual PSDs in each of the geographical regions in Figure 2.11, as well as in the median number PSDs presented in Figure 2.12. Conversely, the magnitude of the number PSDs in the sub-50 nm fraction of the UFP regime in EA and CSSA tends to be lower than those measured in NAAN and EU. This is especially true for the nucleation mode, which is often much more pronounced in the urban atmospheres of NAAN and EU cities. The median number PSD for LA more closely resembles number PSDs measured in NAAN and EU as compared to those in EA and CSSA. However, the lack of PSD observations in LA makes it difficult to draw conclusions about the shape of PSDs in this region. The D_{em} associated with the prominent peak for each of the median number PSDs presented in Figure 2.12 are: $D_{em} \sim 20$ nm for EU, $D_{em} \sim 30$ nm for NAAN, $D_{em} \sim 35$ nm for LA, and $D_{em} \sim 60$ to 100 nm for EA and CSSA.

The variation in the magnitude of the number PSDs for EA, CSSA, EU, LA, and NAAN is generally consistent with that observed in the global distribution of PSDs presented in Figure 2.11. The abundance of number PSD observations in EU provides a basis to more reliably identify a representative PSD for the region. The red-yellow-light green band for EU demonstrates that a large fraction of PSD measurements in EU cities tend to cluster around the median number PSD. Between $D_{em} = 10$ to 100 nm, the amplitude of this PSD band varies between 1000 and 10000 cm^{-3}. Less frequently, number PSDs with magnitudes exceeding 10000 cm^{-3}, or as low as 100 cm^{-3}, have been reported in EU cities. A faint band of moderate occurrence frequency can be observed in both EA and NAAN, however, the comparatively few PSD observations in CSSA and LA make it difficult to identify such trends in these two regions.

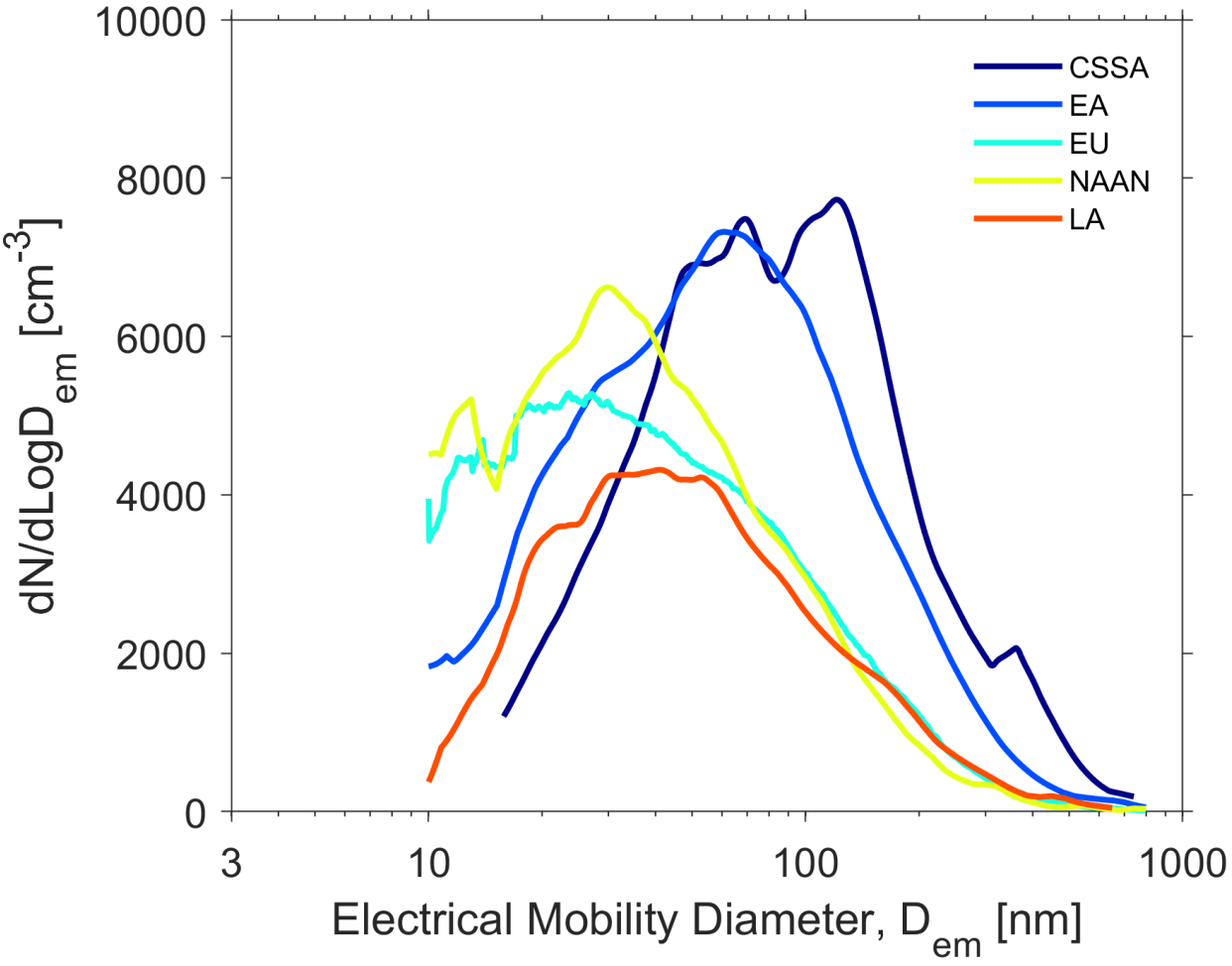

Figure 2.12 Median number PSDs for each geographical region.

To better visualize differences in the shape of the urban aerosol number PSDs and to probe the relative fraction of particles in different modes, each number PSD was normalized by its maximum concentration such that variations in the magnitude of the number PSDs can be neglected (Figure 2.13). The normalized urban aerosol number PSDs presented in Figure 2.13 are grouped by country and geographical region (from top to bottom): WA, NAAN, LA, EU, EA, and CSSA. Many of the normalized number PSDs in EA and CSSA tend to show a peak (red-orange color) at around D_{em} = 100 nm and few show peaks at or near the nucleation mode. Some of the normalized number PSDs measured in China and India present prominent peaks in the accumulation mode, between D_{em} = 100 to 200 nm. However, it can be seen that particles greater than D_{em} = 300 nm contribute negligibly to normalized number PSDs in EA and CSSA. Normalized number PSDs in NAAN and EU generally exhibit peaks at smaller particle sizes (D_{em}

= 10 to 50 nm), while a few observations made in Germany, Italy, and the United States present peaks near D_{em} = 100 nm. The normalized number PSDs measured in LA, predominately in São Paulo, Brazil, closely resemble observations reported in NAAN and EU. The prominent nucleation mode in the WA normalized number PSDs is in part due to the few PSD observations collected from the region, which were made at a 'traffic' site in Fahaheel, Kuwait.

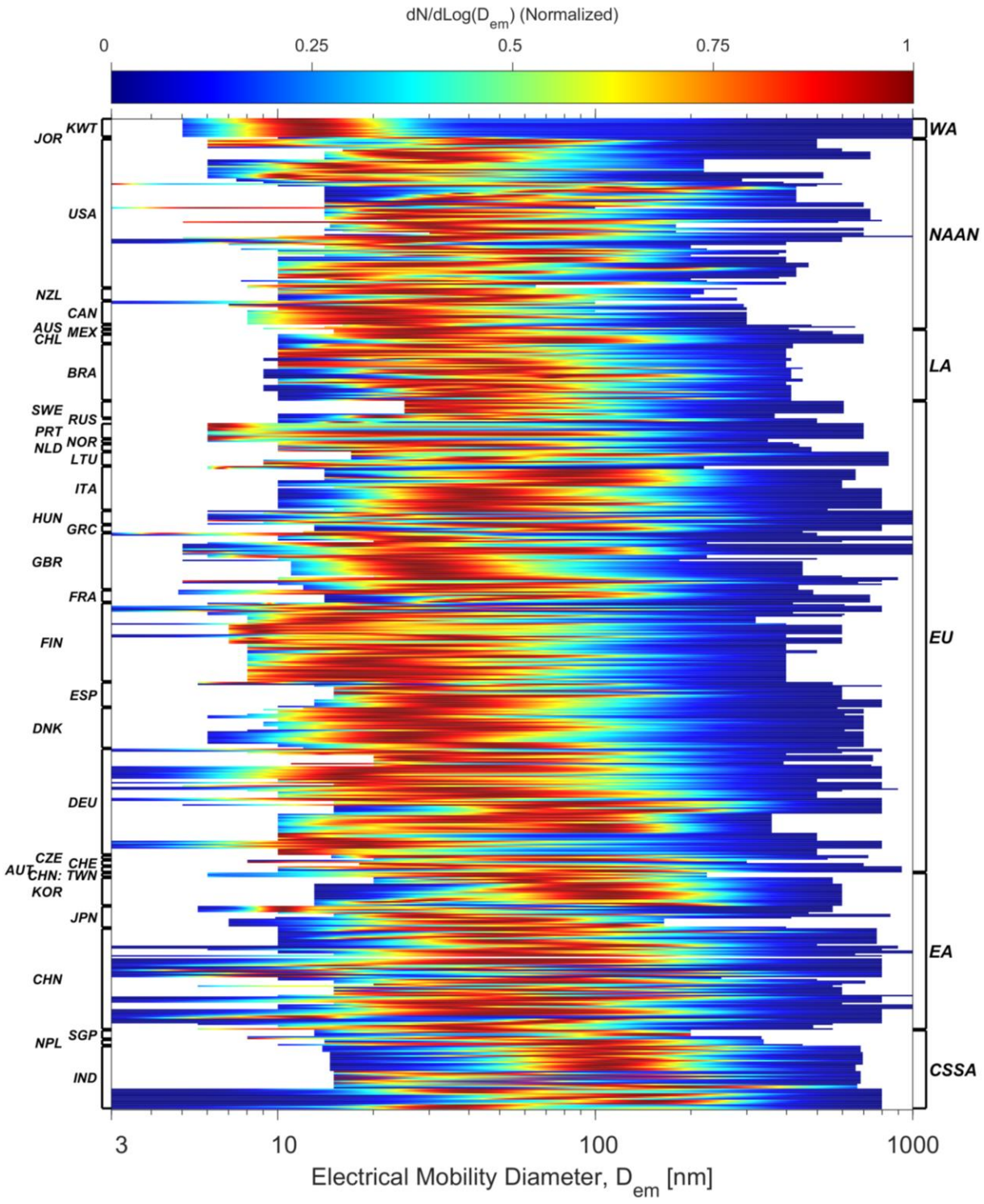

Figure 2.13 Normalized urban aerosol number PSDs analyzed in this study from around the globe. The country codes are listed on the left and the region codes are listed on the right.

There are clear distinctions between urban aerosol number PSDs measured in NAAN/EU and EA/CSSA. Figure 2.14 presents the relationship between total particle number concentration, integrated over the measured size range of a PSD measurement, and the count median diameter (CMD) for each of the sub-micron number PSDs presented in Figure 2.11. Number PSDs in EA and CSSA tend to cluster to the right, from CMD = 50 to 100 nm, whereas number PSDs in NAAN and EU tend to cluster toward the left, from CMD = 20 to 60 nm. There are, however, outliers in each region, such as number PSDs in EA with prominent nucleation modes and CMDs of approximately 10 nm, and number PSDs in NAAN with prominent accumulation modes and CMDs approaching 100 nm. There are only a few number PSDs in CSSA that exhibit CMDs below 50 nm. In all geographical regions, there exists nearly two orders of magnitude variation in total particle number concentrations, which are often bounded by 1000 cm^{-3} at the lower end and 100000 cm^{-3} at the upper end. Number PSDs in EU, NAAN, and EA that have CMDs < 20 nm are associated with total particle number concentrations exceeding 10000 cm^{-3}. A clear inverse relationship between total particle number concentration and CMD does not appear to exist. Interestingly, numerous number PSDs in EA and CSSA with CMDs of approximately 100 nm have concentrations > 10000 cm^{-3}. The wide variation in the total particle number concentrations presented in Figure 2.14 is consistent with the trends reported in a review of geographical variations in total particle number concentrations across forty urban roadside measurement sites around the world.[134]

It should be noted that many factors can influence the magnitude and shape of urban aerosol number PSDs, beyond geographical region, which is the focus of the global-scale analysis presented in Figure 2.11-2.14. Country-wide PSD measurement campaigns have identified significant variations in number PSDs among different cities within the same country[5,135] and at different measurement sites within the same city[136–141]. Regarding the latter, several studies conducted in EU cities have shown that total particle number concentrations can vary as high as a factor of roughly nine within the same city.[138,142–144] Localized spatial variations in urban aerosol PSDs and number concentrations are due in part to the nature of local emission sources near the measurement site and meteorological conditions, including wind speed and direction, temperature, and relative humidity.[145–156] Physiochemical processes that can transform an aerosol population over space and time are also very important, such as particle growth due to coagulation and

condensation, particle shrinkage due to evaporation, reactive uptake, and wet and dry deposition, among others.[157–165]

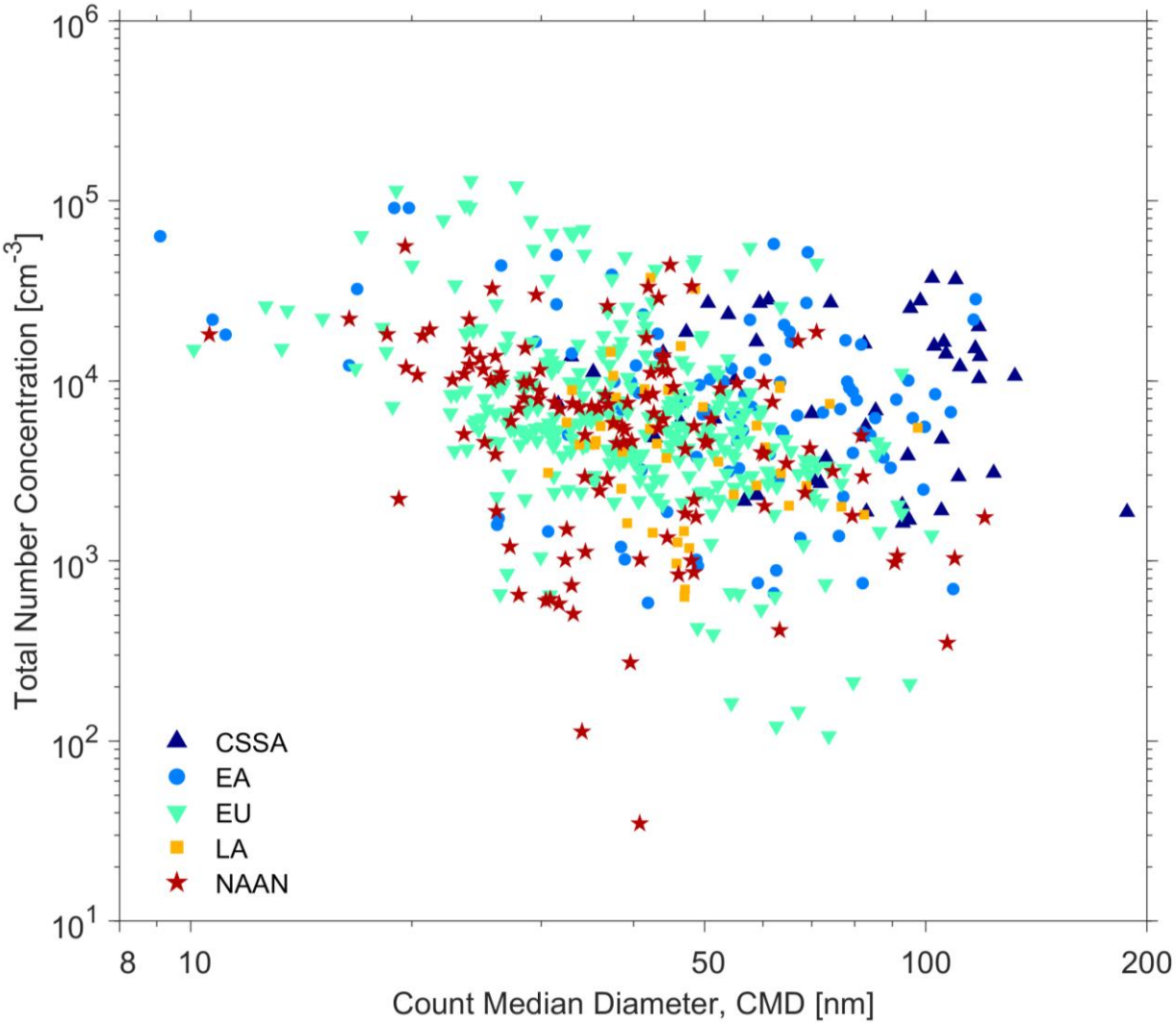

Figure 2.14 Relationship between the total particle number concentration, integrated over the measured size range, and the count median diameter (CMD), determined for each sub-micron number PSD measured by electrical mobility-based techniques (*n*=624) and grouped by geographical region.

2.10.2 Geographical Variations in the Magnitude and Shape of Urban Aerosol Mass PSDs

Global variations in urban aerosol mass PSD measurements ($dM/dLogD_{em}$, $\mu g\ m^{-3}$) are presented in Figure 2.15. The log-log plot incorporates mass PSDs measured by gravimetric methods with inertial impactors and measurements made with electrical mobility- and aerodynamic-/optical-based techniques that cover both the sub-micron and coarse modes (n=122, Section 2.4.1.2-2.4.1.3, Tables A.2-A.4). As discussed in Section 2.4, the size-resolved ρ_{eff} functions for Groups A, B, and C (Figure 2.9) were used in converting D_a-based PSDs to D_{em}-based PSDs and translating measured number PSDs to mass PSDs. Similar to Figure 2.11, each line represents an individual PSD observation compiled in Appendix A and the color indicates the occurrence frequency of the mass PSDs at a given particle size (D_{em}) with a certain particle mass concentration. The solid black line indicates the median mass PSD among the global compilation of observations. In comparing Figure 2.11 and 2.15, it is evident that sub-micron urban aerosol number PSDs are more commonly reported in the literature compared to mass PSDs or number PSDs spanning the sub-micron and coarse regimes.

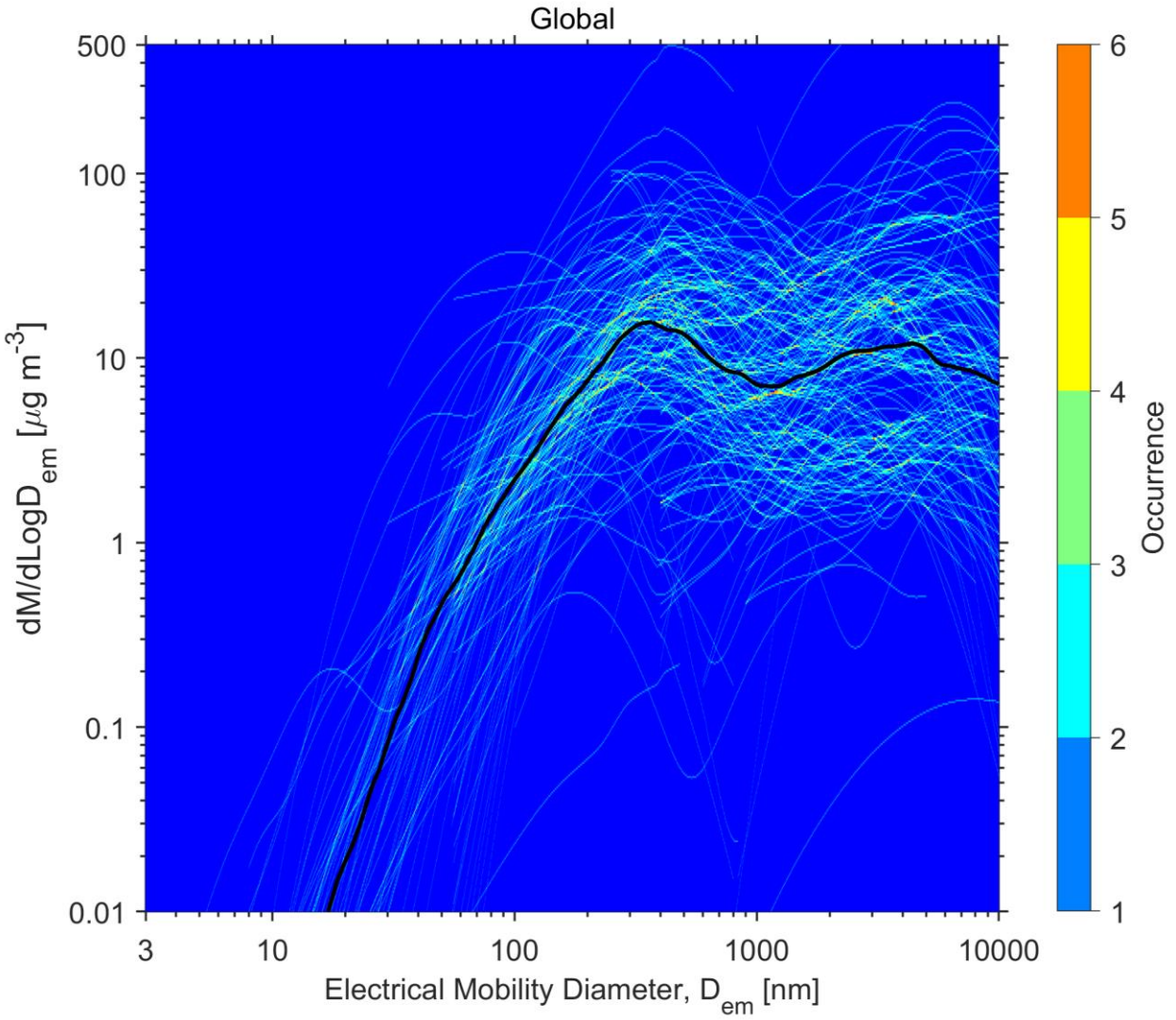

Figure 2.15 Urban aerosol mass PSDs analyzed in this study from around the globe (n=122). The figure incorporates mass PSDs measured by gravimetric methods with inertial impactors and measurements made with electrical mobility-based and aerodynamic-/optical-based techniques that cover both the sub-micron and coarse modes. The color represents the occurrence frequency of the mass PSDs at a given particle size with a certain concentration. The black line indicates the median mass PSD.

The visualization of the global distribution in urban aerosol mass PSDs in Figure 2.15 demonstrates that there exist significant variations in both the magnitude and shape of mass PSDs measured across urban environments around the world. While the limited amount of mass PSD observations makes it difficult to discern clear trends in the structure of mass PSDs, some trends are evident. Notably, urban aerosol mass PSDs are dominated by particles with D_{em} > 100 nm and

are typically bi-modal, exhibiting peaks in both the accumulation and coarse modes, as indicated by the median mass PSD. The relative contribution of the two modes is variable among the PSD observations. In some cases, urban aerosol mass PSDs are dominated by accumulation mode particles, while other PSDs present a prominent coarse mode. Within the accumulation mode, the amplitude of the mass PSDs spans two orders of magnitude, from 1 μg m^{-3} to 100 μg m^{-3}. The D_{em} associated with the prominent peak in the accumulation mode is variable. The spread in the magnitude of the mass PSD in the coarse mode is consistent with that observed in the accumulation mode. Some mass PSDs exhibit amplitudes that exceed 100 μg m^{-3}, however, their occurrence frequency is very low. The magnitude of mass PSDs in the UFP regime is relatively insignificant and ranges from 0.01 to 1 μg m^{-3}. Unlike for the number PSDs in Figure 2.11, a band of high occurrence frequency is not evident in Figure 2.15. Some degree of clustering of mass PSDs around the median PSD is evident, however, there is clearly more variation in the structure of mass PSDs as compared to number PSDs. This may be due to the variety of measurement techniques employed and uncertainties in translating number PSDs to mass PSDs using the size-resolved ρ_{eff} functions for Groups A, B, and C.

As with the sub-micron urban aerosol number PSDs, the mass PSDs were normalized by their maximum concentrations such that variations in the magnitude of the mass PSDs can be neglected (Figure 2.16). The normalized urban aerosol mass PSDs presented in Figure 2.16 are grouped by country and geographical region (from top to bottom): WA, NAAN, LA, EU, EA, CSSA, and AF. The normalized mass PSDs demonstrate that a significant fraction of particle mass exists below D_{em} = 1000 nm in numerous cities in NAAN, EU, EA, and CSSA. For measurements that included the UFP regime, it is clear that sub-100 nm particles contribute little to urban aerosol mass PSDs. The majority of the normalized mass PSDs in NAAN and EU show a peak in the accumulation mode (red-orange color) between D_{em} = 200 to 600 nm, while some show peaks in both the accumulation and coarse modes. Most of the normalized mass PSDs in EA (predominately from China) are bi-modal with accumulation mode peaks that span D_{em} = 300 to 1000 nm and coarse mode peaks that span D_{em} = 3000 to 8000 nm. A few mass PSDs in EA (measured in Korea) are uni-modal with a prominent coarse mode that extend beyond D_{em} = 10000 nm. The normalized mass PSDs in CSSA are more variable in shape, with varying contributions from both modes. The D_{em} = 100 to 200 nm fraction of the accumulation mode in both EA and

CSSA, which contributed meaningfully to number PSDs in the two regions, represents a minor component of sub-micron aerosol mass.

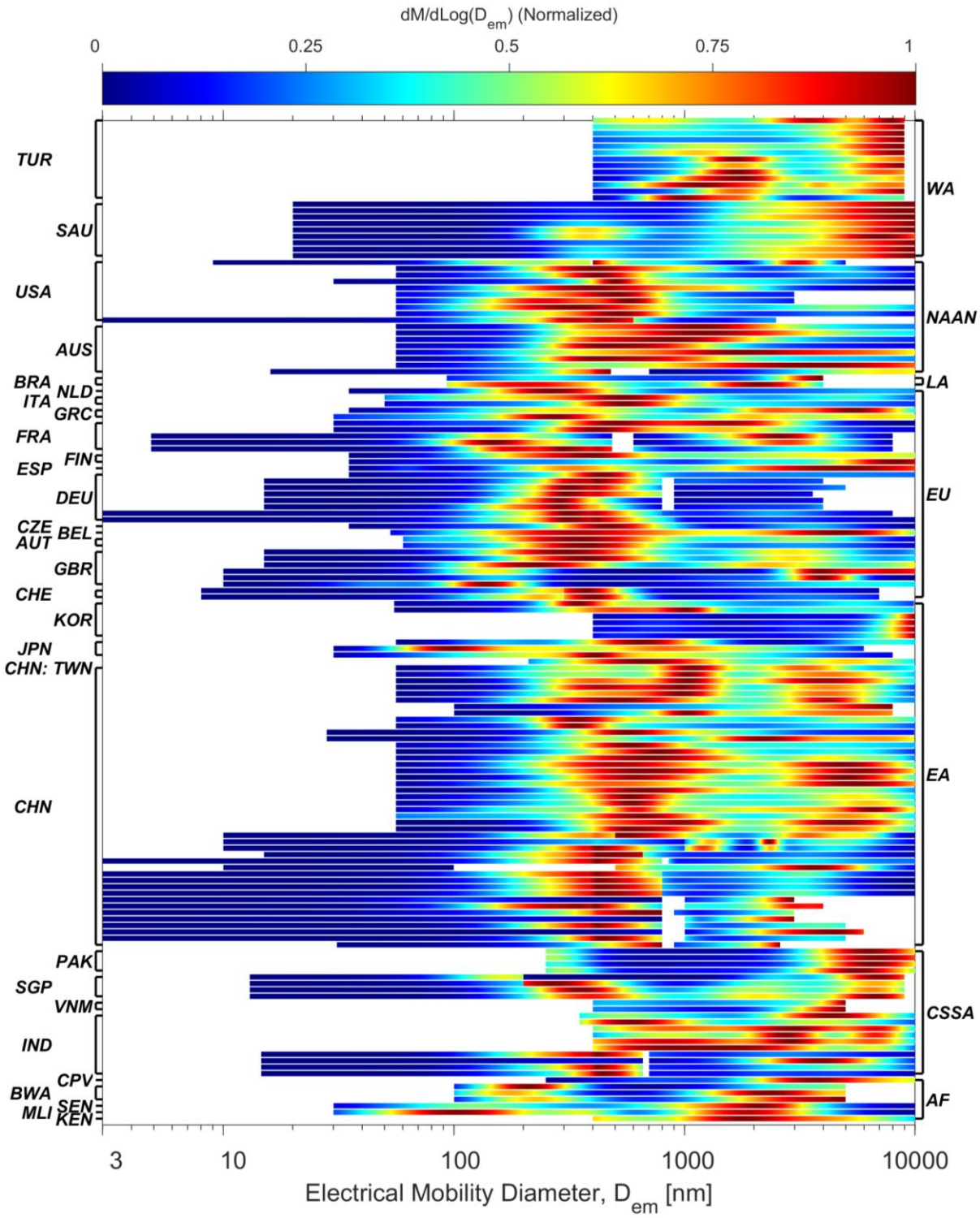

Figure 2.16 Normalized urban aerosol mass PSDs analyzed in this study from around the globe. The country codes are listed on the left and the region codes are listed on the right.

The shape of normalized urban aerosol mass PSDs in WA and AF are uniquely different from the other geographical regions. In WA, the normalized mass PSDs are clearly dominated by coarse mode particles. Measurements made in Istanbul, Turkey show a prominent peak between D_{em} = 6000 to 10000 nm, with some displaying a second coarse mode peak between D_{em} = 1000 to 2000 nm. Normalized mass PSDs from Yanbu, Saudi Arabia show a strong peak near D_{em} = 10000 nm, with either a very weak or non-existent peak in the accumulation mode. The prominent coarse modes in WA cities are likely due to frequent dust events and enhanced dust resuspension in WA cities and the relatively large size of mineral dust particles.[166] The few PSD observations from AF display a dominant coarse mode, with peaks spanning D_{em} = 1000 to 5000 nm.

2.10.3 Intra-city Variations in Urban Aerosol Number PSDs between Urban Background and Traffic-influenced Sites

Urban aerosol PSDs can exhibit intra-city spatial variations depending on the measurement location and its proximity to local emission sources, such as traffic. The urban aerosol PSD observations were categorized by intra-city sampling location, as documented in Appendix A. This provides a basis to compare the shape of PSDs collected at urban background (UB) and traffic-influenced (TR) sites from cities across the globe. Figure 2.17 presents normalized sub-micron urban aerosol number PSDs divided into UB (top) and TR (bottom) sites. UB represents urban areas that are far from direct emission sources and are not meaningfully affected by local traffic emissions, while TR indicates an environment that is strongly influenced by traffic emissions, such as an urban street canyon or roadside.[138] The aerosol populations measured at UB sites are typically transported from other urban microenvironments, undergoing various transformation and ageing processes during transport. The PSDs at UB and TR sites are grouped by country in Figure 2.17. Only PSD observations with a measurement period greater than one week are presented. The majority of the measurements presented in Figure 2.17 are from NAAN and EU cities, with only a few from EA, WA, and LA.

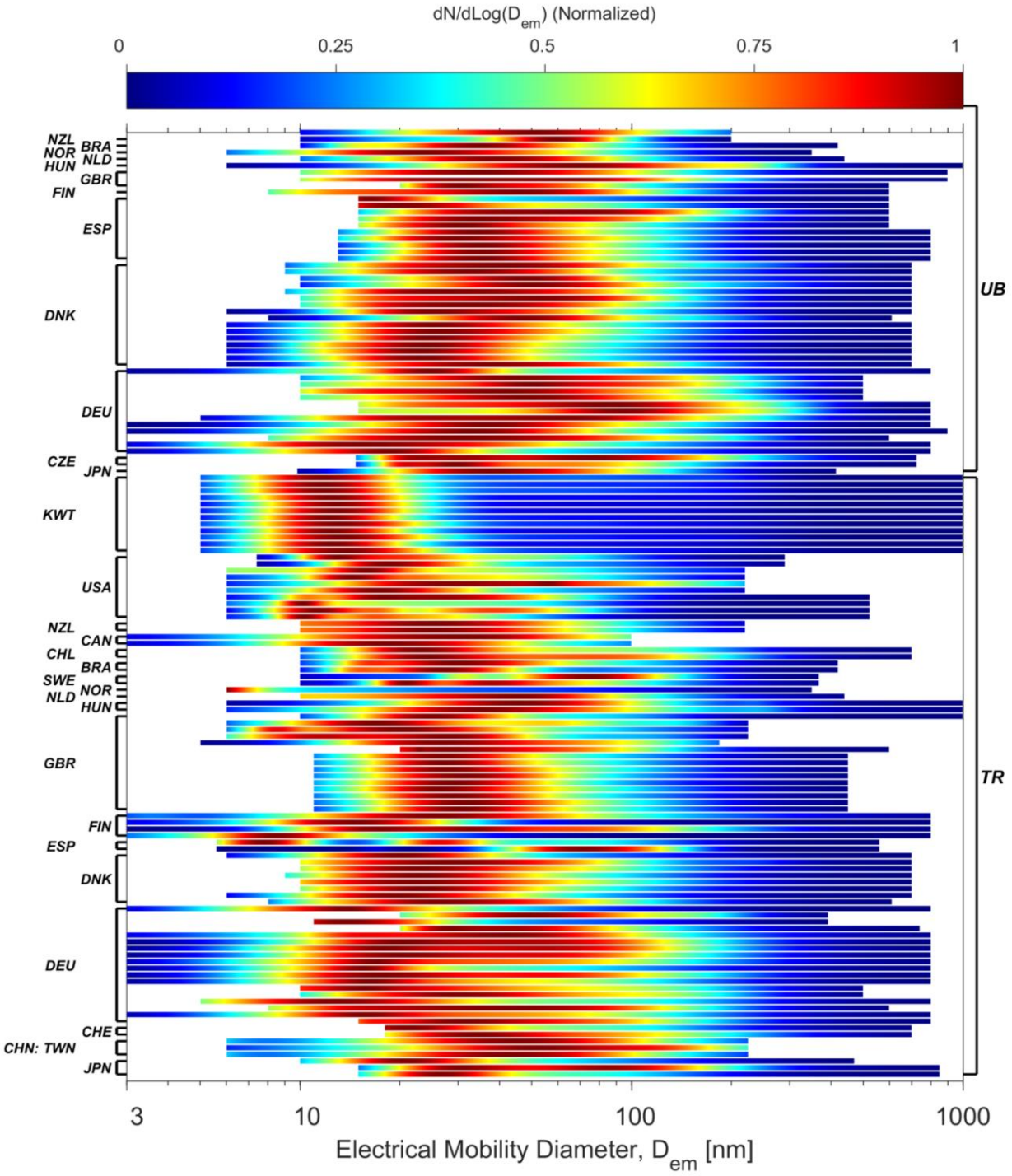

Figure 2.17 Comparison between normalized urban aerosol number PSDs measured at urban background (UB) and traffic-influenced (TR) sites. Only the number PSDs with a measurement period greater than one week are presented. The country codes are listed on the left and the site type is listed on the right.

Normalized number PSDs measured at UB sites often show prominent peaks at larger particle sizes compared to those measured at TR sites. UB measurements are typically dominated by Aitken mode particles, with peaks ranging from D_{em} = 20 to 90 nm. In contrast, many of the TR measurements exhibit prominent nucleation modes with peaks falling below D_{em} = 30 nm, and in some cases, below D_{em} = 10 nm. For both UB and TR, there exists variability in the shape of the PSDs among the cities and countries. In some cases, the structure of the normalized number PSDs are similar at UB and TR sites as some TR sites exhibit prominent Aitken mode. The larger particles observed at UB sites are due in part to various aerosol transformation processes, such as particle growth due to coagulation and the uptake of condensable organic and inorganic vapors during short- and long-range transport.[136,167] A few of the normalized number PSDs at UB sites show meaningful contributions from the accumulation mode, between D_{em} = 100 to 200 nm; such particles tend to persist in the urban atmosphere for longer periods of time due to their lower rates of coagulation compared to nucleation and Aitken mode particles and lower deposition rates compared to coarse mode particles.[18,19]

Urban aerosol number PSD observations made at TR sites are strongly influenced by traffic emissions. Vehicle emissions are a major source of UFPs in the urban atmospheric environment.[134,168,169] Several studies have reviewed the characteristics of aerosol emissions from traffic, including urban SOA formation associated with vehicle exhaust.[168–171] Traffic emissions can be broadly classified as exhaust- and non-exhaust-related. Exhaust-related vehicle emissions include soot particles from incomplete combustion and particles formed via the nucleation and condensation of H_2SO_4 and hydrocarbons as the hot exhaust is cooled and diluted in the ambient atmosphere.[136,157,168,172–175]

Vehicle exhaust aerosol PSDs are influenced by many factors, including vehicle type[176–178], vehicle/engine operational mode[157,179,180], fuel type[181–184], and use of aftertreatment technologies[185,186]. As illustrated in Figure 2.18, which presents normalized number PSDs for selected urban aerosol sources, vehicle exhaust PSDs are typically dominated by UFPs. Freshly nucleated particles in vehicle exhaust are relatively small, with D_{em} < 30 nm. Near-road measurements at TR sites commonly present peaks in the sub-30 nm size fraction (Figure 2.17), and some TR sites can be dominated by sub-10 nm particles (Pedata et al., 2015; Rönkkö et al., 2017).[115,187] This indicates that the freshly nucleated particles can contribute significantly to number PSDs at TR sites.[10,78,158,188,189] However, with the increase of distance from the road, either

horizontally or vertically, these particles can grow by coagulation and condensation during transport[158,159,190–192], while some can shrink due to evaporation[193–195]. Non-exhaust-related traffic emissions include brake wear, road-tire interactions, and road dust resuspension; the former is an important source of sub-micron particles. Brake wear aerosol PSDs are influenced by the material and operational temperature of the brake pad.[196–200] As shown in Figure 2.18, normalized sub-micron number PSDs of brake wear aerosol can span from the nucleation mode to the accumulation mode.

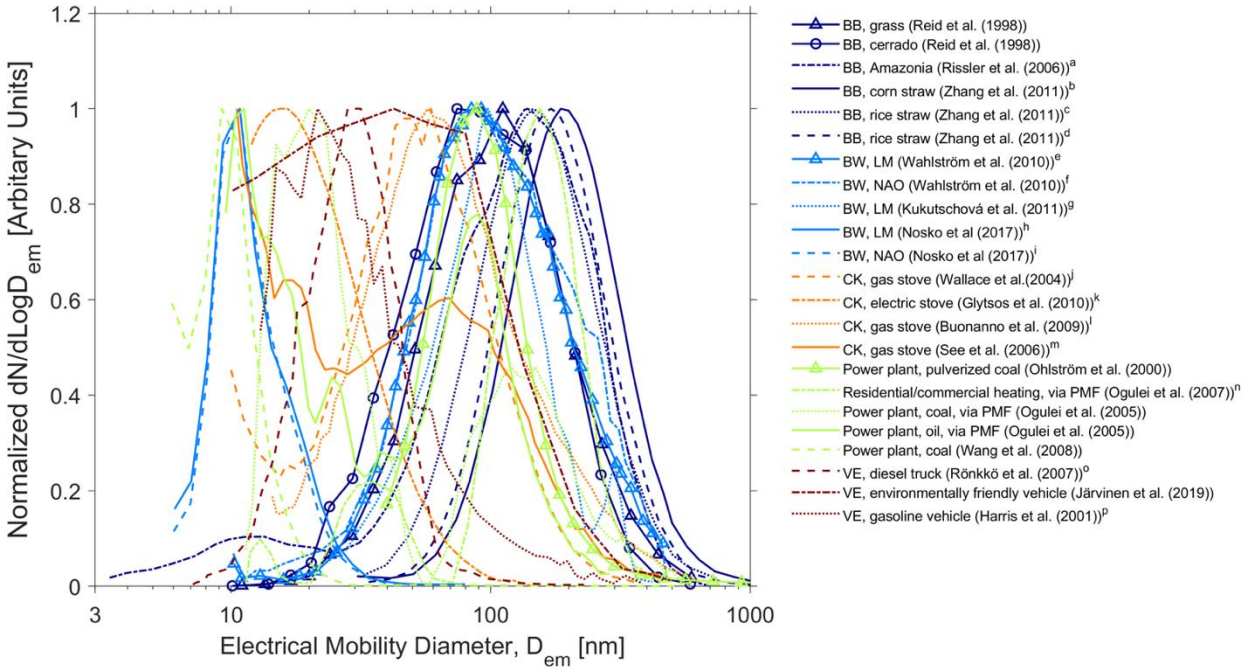

[a]Dry period in Fig. 4a in Rissler et al.[201].
[bcd]PSD after ageing of 30 min in Fig. 6 in Zhang et al.[202].
[e]LM1 in Fig. 7 in Wahlström et al.[200]. Brake pad material: low metallic (LM).
[f]NAO1 in Fig. 7 in Wahlström et al.[200]. Brake pad material: non-asbestos organic (NAO).
[g]t0+30 min in Fig. 6a in Kukutschová et al.[198]. Brake pad material: LM.
[h]LM 175 °C in Fig. 7 in Nosko et al.[197]. Brake pad material: LM.
[i]NAO 175 °C in Fig. 7 in Nosko et al.[197]. Brake pad material: NAO.
[j]DMA-CPC measurement in Fig. 4 in Wallace et al.[203].
[k]Frying onion, t=7 min in Fig. 13 in Glytsos et al.[204].
[l]Grilling bacon with maximum power in Fig. 6a in Buonanno et al.[205].
[m]Boiling in Fig. 2a in See and Balasubramanian[206].
[n]Residential/commercial heating in winter in Fig. 6 in Ogulei et al.[207].
[o]Test condition 8 without thermodenuder in Fig. 2a in Rönkkö et al.[208].
[p]Gasoline engine #2 at 96 km h^{-1} in Fig. 4 in Harris and Maricq[178].

Figure 2.18 Normalized number PSDs of selected urban aerosol sources, including biomass burning (BB), brake wear (BW), cooking (CK), coal and oil burning for energy and heating, and vehicle exhaust (VE). Each number PSD is normalized by its maximum concentration.

2.10.4 Sub-micron urban aerosol number PSDs in Asia: factors contributing to the prominent accumulation mode

The results presented in Figure 2.11-2.14 indicate that urban aerosol number PSDs in EA and CSSA are more commonly associated with a significant fraction of accumulation mode particles and CMDs of approximately 100 nm compared to those reported in NAAN and EU. This indicates that sub-micron urban aerosol populations in EA and CSSA, and particularly in China and India, are relatively larger in size than those reported in other geographical regions. A multitude of factors are responsible for governing the shape of number PSDs in urban environments in EA and CSSA. The pronounced accumulation mode can be driven by the direct emissions of accumulation mode particles in both the urban area, as well as regional transport of such particles from rural and industrialized areas. Biomass burning is an important emission source in a number of countries in EA and CSSA. The PSDs of biomass burning aerosol depend on a variety of factors, including: the type of biomass, the condition of the flame, and atmospheric ageing processes.[201,202,209–211] As shown in Figure 2.18, the burning of grass, corn straw, and rice straw produces normalized number PSDs with a significant fraction of accumulation mode particles and CMDs of approximately 100 nm.[209,210,212] It has been observed that residential biomass burning, possibly for cooking and heating, can contribute to high particle number concentrations of accumulation mode particles in the evening in New Delhi, India.[213] A recent study using the GEOS-Chem-TOMAS model identified significant aerosol emissions from biomass burning in India and Indonesia from residential, agricultural, and wildfire sources.[121] Direct burning has been reported to be a common technique to eliminate agricultural residuals in both China and India.[214] The contribution of biomass burning to urban aerosols was confirmed by the high content of water-soluble potassium in the particle-phase.[215,216] In addition to biomass burning, other urban sources may directly emit accumulation mode particles, such as vehicle exhaust, power plants, and industrial activities.[3]

Another factor contributing to the abundance of accumulation mode particles in EA and CSSA are ageing processes that can grow nucleation and Aitken mode particles through coagulation and condensation of organic or inorganic vapors.[217,218] Back trajectories indicate that aerosols transported from industrialized regions south and west of Beijing, China can grow into larger sizes by condensation within slowly moving air masses, thereby contributing to the pronounced accumulation mode in urban areas.[4] The abundance of condensable organic and

inorganic vapors (e.g. NO_x, SO_2, and VOCs) in polluted areas can aid particle growth to larger sizes. It has been reported that the concentrations of condensable vapors are higher in urban areas in China and India compared to those in NAAN and EU due to heavier air pollution in the former.[121,213,219–226] High levels of gas-phase precursors in China can result in significant SOA formation, which can contribute to severe haze events that are often dominated by accumulation mode particles.[226] The elevated number concentrations of accumulation mode particles in EA and CSSA have a substantial surface area that can serve as a coagulation sink for nucleation and Aitken mode particles. This suppression of UFPs can cause the number PSDs in EA and CSSA to further skew to larger particle sizes.

2.11 Urban aerosol PSDs: implications of human inhalation exposure assessment

2.11.1 Geographical variations in size-resolved urban aerosol number respiratory tract deposited dose rates

Geographical variations in size-resolved urban aerosol number respiratory tract deposited dose rates (RTDDRs), expressed in the form of lognormal size distributions ($dRTDDR_N/dLogD_{em}$, h^{-1}), are presented in Figure 2.19. Urban aerosol PSD measurements are a valuable tool for human inhalation exposure assessment given the strong size dependency of particle deposition in the respiratory system. RTDDRs provide a basis to understand how variations in the shape and magnitude of urban aerosol number PSDs affect the rate at which particles deposit in each region of the human respiratory tract.[116–118] As described in Section 2.5, number RTDDRs were estimated by integrating the urban aerosol number PSDs complied for each geographical region (Figure 2.11) with size-resolved particle deposition fractions in the human respiratory tract (Figure 2.7) and selected breathing parameters.

The urban aerosol number RTDDRs are presented in the form of a grid, with each row corresponding to a geographical region (CSSA, EA, EU, NAAN, and LA) and each column corresponding to a region (or summation across regions as the total) of the human respiratory tract (total, head airways, tracheobronchial, and pulmonary). In a given number RTDDR log-log plot, each line represents a RTDDR (as $dRTDDR_N/dLogD_{em}$, used interchangeably herein) estimated from a sub-micron urban aerosol number PSD presented in Figure 2.11 and the color indicates the occurrence frequency of the number RTDDRs at a given particle size (D_{em}) with a certain RTDDR

value. The solid black lines indicate the median number RTDDR for each geographical and respiratory tract region pair, which are illustrated in Figure 2.20 on a linear y-axis scale. It should be noted that the RTDDRs presented in Figure 2.19 are estimates derived for an adult engaged in light physical activity (e.g. walking) in the urban outdoor environment. As noted in Section 2.5, hygroscopic growth of the inhaled urban aerosol is not considered given the broad collection of PSDs analyzed in this study and the unknown chemical composition and hygroscopic growth factors associated with the aerosol populations. Thus, care should be used in interpreting the number RTDDRs presented herein. However, valuable insight can still be gleaned by the vast collection of urban aerosol number PSDs, and associated RTDDRs, analyzed in this study.

There exists significant geographical variation in number RTDDRs for each respiratory tract region, as shown in Figure 2.19 and 2.20. Similar to the urban aerosol number PSDs, there can exist over two orders of magnitude variation in the number RTDDR for a given particle size (D_{em}). The amplitude of the total $\mathrm{dRTDDR_N/dLogD_{em}}$ (left column) is typically between 10^8 and 10^{10} h^{-1} in the UFP regime, with values exceeding 10^{11} h^{-1} in the nucleation mode and as low as 10^6 h^{-1} in the accumulation mode. Despite the variability in the magnitude, a clear red-orange-yellow band is present around the median number RTDDRs in EA, EU, and NAAN, suggesting a general trend exists in each geographical region. Total number RTDDRs are dominated by sub-micron particles across all geographical regions. The pronounced differences observed between NAAN/EU and EA/CSSA urban aerosol number PSDs in Figure 2.11 and 2.12 are evident in the total number RTDDRs. Similar to the median number PSDs presented in Figure 2.12, the median total number RTDDRs in NAAN/EU (and LA) and EA/CSSA are similar in both shape and magnitude. In NAAN, EU, and LA cities, nucleation and Aitken mode particles contribute significantly to total number RTDDRs, whereas in EA and CSSA cities, total number RTDDRs receive significant contributions from both Aitken and accumulation mode particles (Figure 2.19 and 2.20). A prominent mode in the median total $\mathrm{dRTDDR_N/dLogD_{em}}$ in NAAN/EU/LA is evident between D_{em} = 20 to 30 nm, with a partial second mode occurring at D_{em} < 10 nm for NAAN/EU. EA/CSSA exhibit a prominent mode between D_{em} = 50 to 70 nm, with CSSA presenting a second mode beyond D_{em} = 100 nm. The magnitude of the prominent modes of the median total $\mathrm{dRTDDR_N/dLogD_{em}}$ in all geographical regions are on the order of 10^9 h^{-1}, and vary between 3 and 6 x 10^9 h^{-1}.

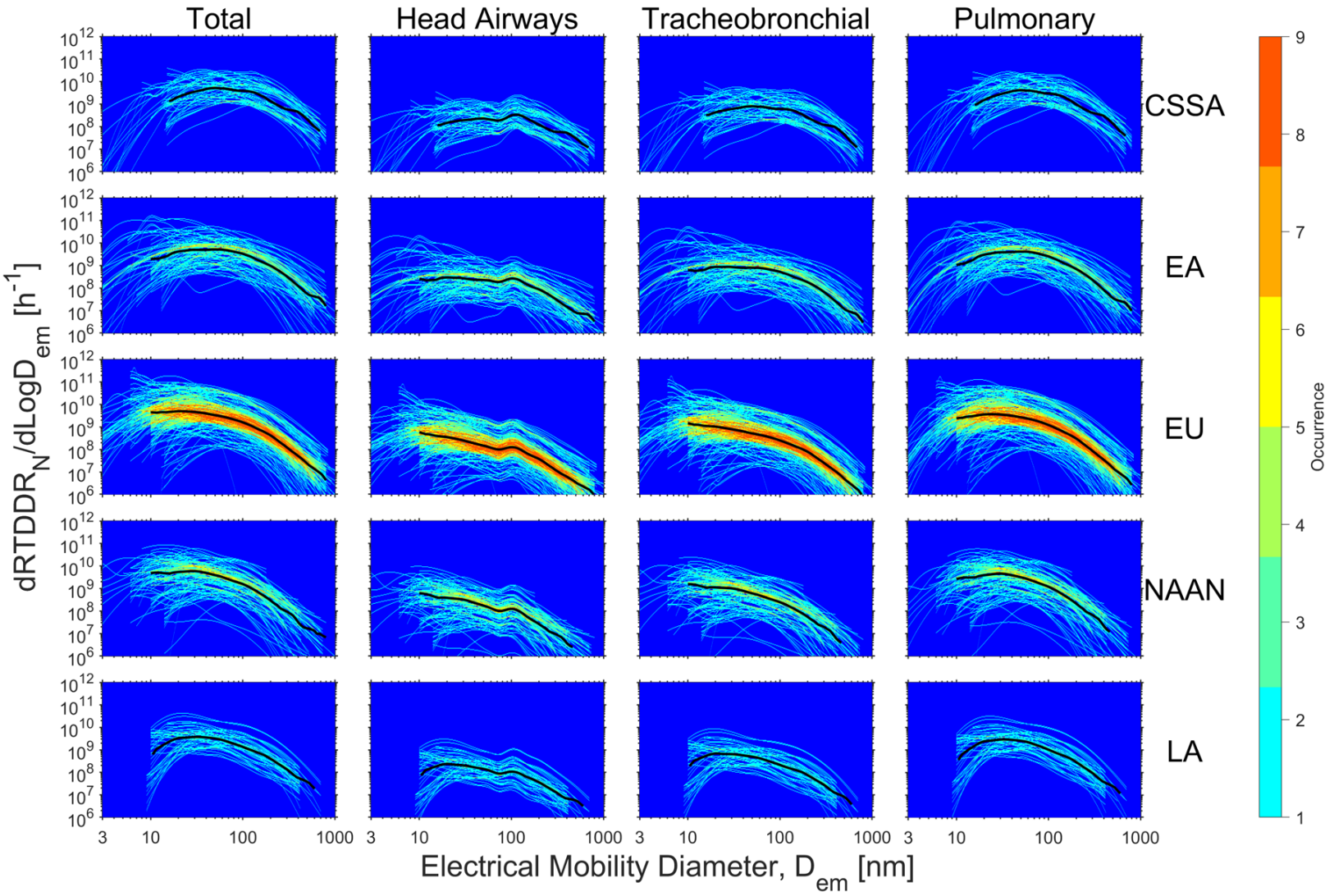

Figure 2.19 The total and regional $dRTDDR_N/dLogD_{em}$ in the respiratory tract in different geographical regions determined using the urban number PSDs analyzed in this study. The color represents the occurrence frequency of the $dRTDDR_N/dLogD_{em}$ at a given particle size with a certain dose rate. The black lines indicate the median $dRTDDR_N/dLogD_{em}$ in each group.

High number RTDDRs occur for size fractions where prominent modes of the urban aerosol number PSDs coincide with high deposition fractions. The deposition fraction curve for the pulmonary region exhibits a maximum at approximately D_{em} = 30 nm (Figure 2.7). In the UFP regime, the deposition fraction curve for the tracheobronchial region increases with decreasing particle size from D_{em} = 100 nm to approximately D_{em} = 2 nm, where it obtains its maximum. Similarly, the head airways deposition curve increases with decreasing particle size from D_{em} = 70 to 1 nm in the UFP regime. As a result, the sub-micron total deposition fraction curve increases with decreasing particle size from a minimum at approximately D_{em} = 400 nm to nearly unity at D_{em} = 1 nm (Figure 2.7). Thus, particles in the UFP regime more efficiently deposit in the human respiratory tract compared to particles in the accumulation mode.

NAAN/EU number PSDs are often dominated by nucleation and Aitken mode particles, with CMDs between 20 and 60 nm, whereas EA/CSSA number PSDs are often dominated by Aitken and accumulation mode particles, with CMDs between 50 and 100 nm (Figure 2.13 and 2.14). The strong contribution of the nucleation mode in NAAN/EU number PSDs, as compared to EA/CSSA cities, results in comparatively higher number RTDDRs for D_{em} < 30 nm in both the tracheobronchial region and head airways (Figure 2.19 and 2.20). For NAAN/EU, the median $\mathrm{dRTDDR_N/dLogD_{em}}$ for the tracheobronchial region and head airways reaches a peak at D_{em} = 10 nm (Figure 2.20), with some individual PSDs exhibiting a peak at D_{em} < 10 nm (Figure 2.19). In the pulmonary region, the prominent peak of the median $\mathrm{dRTDDR_N/dLogD_{em}}$ for NAAN/EU is present near D_{em} = 20 nm, which is the approximate location of the prominent mode of the median number PSDs in NAAN/EU and the maximum of the pulmonary deposition fraction curve. Median number RTDDRs in the sub-30 nm fraction are greater in NAAN/EU compared to EA/CSSA for each of the three respiratory tract regions. Conversely, greater number RTDDRs are observed for particles with D_{em} > 50 nm for all respiratory tract regions in EA/CSSA as compared to NAAN/EU. The magnitude of the median $\mathrm{dRTDDR_N/dLogD_{em}}$ for particles with D_{em} > 50 nm are about a factor of two greater in EA/CSSA compared to NAAN/EU/LA. In both the tracheobronchial and pulmonary regions, the median number RTDDRs for EA/CSSA exhibit a prominent mode at approximately D_{em} = 50 nm, while in the head airways, a peak is present near D_{em} = 100 nm.

For a given geographical region, variations in the dose rate are observed among the three respiratory tract regions. As can be seen in both Figure 2.19 and 2.20, the magnitude of the

$dRTDDR_N/dLogD_{em}$ is greatest for the pulmonary region across all geographical regions, followed by the tracheobronchial region and head airways. For all geographical regions, the median $dRTDDR_N/dLogD_{em}$ in the pulmonary region is nearly one order of magnitude higher than that in the head airways, and two to three times higher than in the tracheobronchial region. This is due to the significant contribution of Aitken mode particles to urban aerosol number PSDs in most cities and the high deposition fractions observed in the Aitken mode for the pulmonary region. Thus, the pulmonary region experiences the greatest dose burden in regard to the number of particles that deposit per unit time.

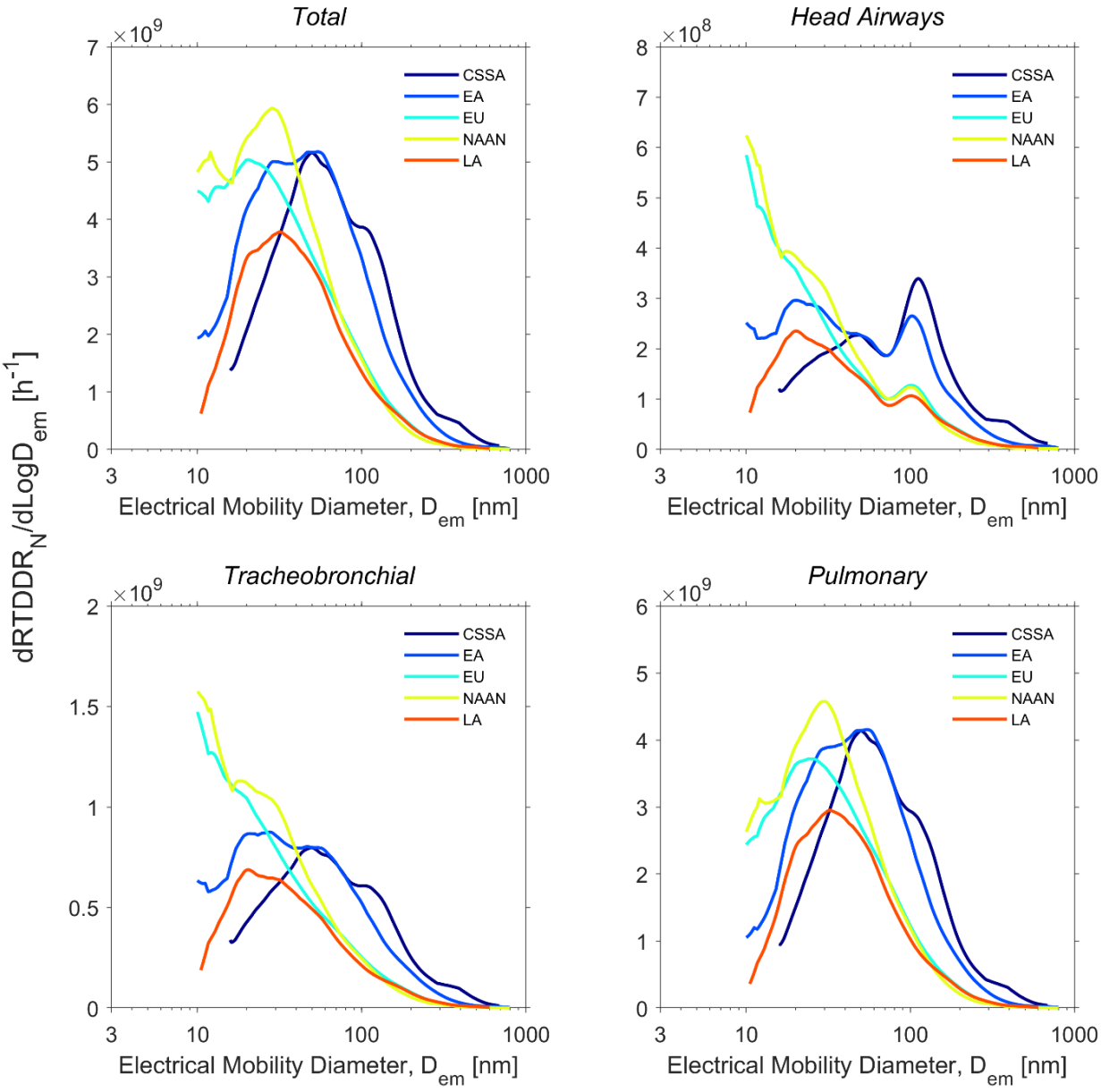

Figure 2.20 Median $dRTDDR_N/dLogD_{em}$ in each geographical region (black lines in Figure 2.19).

2.11.2 Geographical variations in size-resolved urban aerosol mass respiratory tract deposited dose rates

Geographical variations in size-resolved urban aerosol mass RTDDRs, expressed in the form of lognormal size distributions ($dRTDDR_M/dLogD_{em}$, μg h^{-1}), are presented in Figure 2.21. Mass RTDDRs were estimated for CSSA, EA, EU, NAAN, LA, and WA. In a given mass RTDDR log-log plot, each line represents a RTDDR (as $dRTDDR_M/dLogD_{em}$, used interchangeably herein) estimated from urban aerosol mass PSDs presented in Figure 2.15 and the color indicates the occurrence frequency of the mass RTDDRs at a given particle size (D_{em}) with a certain RTDDR value. The solid black lines indicate the median mass RTDDR for each geographical and respiratory tract region pair, which are illustrated in Figure 2.22 on a linear y-axis scale.

Similar to the urban aerosol number RTDDRs, there can exist over two orders of magnitude variation in the mass RTDDR for a given particle size (D_{em}). The amplitude of the total $dRTDDR_M/dLogD_{em}$ (left column) is typically between 10^{-1} and 10^{1}μg h^{-1} in the accumulation and coarse modes, with values as low as 10^{-2} μg h^{-1} in the UFP regime. Despite the variability in the magnitude, a clear red-orange-yellow band is present around the median mass RTDDRs in EA, EU, and NAAN, suggesting a general trend exists in each geographical region. In contrast to the number RTDDRs, most mass RTDDRs are bimodal and dominated by accumulation and coarse mode particles across all geographical and respiratory tract regions (Figure 2.21 and 2.22). However, the relative contribution of the two modes to the mass RTDDRs varies among the urban aerosol mass PSD observations. As illustrated in Figure 2.19 and 2.21, UFPs tend to dominate number RTDDRs in most urban environments, but contribute negligibly to mass RTDDRs. The magnitude of $dRTDDR_M/dLogD_{em}$ is greatest for cities in CSSA, followed by EA, for all respiratory tract regions. This is consistent with the findings of Kodros et al.[121], which reported high aerosol mass deposited concentrations in the human respiratory tract for India and Eastern China. Cities in NAAN and EU are associated with $dRTDDR_M/dLogD_{em}$ lower in magnitude compared to the other geographical regions. LA and WA lie in between mass RTDDRs for EA/CSSA and NAAN/EU. The magnitude of $dRTDDR_M/dLogD_{em}$ are fairly consistent across all respiratory tract regions.

Similar to the number RTDDRs, high mass RTDDRs occur for size fractions where prominent modes of the urban aerosol mass PSDs coincide with high deposition fractions. From D_{em} = 100 to 10000 nm, the head airways deposition curve increases with increasing particle size,

with local maxima observed for the pulmonary region at approximately D_{em} = 3000 nm and for the tracheobronchial region at around D_{em} = 7000 nm (Figure 2.7). As a result, the total deposition fraction curve increases with increasing particle size from a minimum at approximately D_{em} = 400 nm to nearly unity at D_{em} = 10000 nm (Figure 2.7). Thus, coarse mode particles more efficiently deposit in the human respiratory tract compared to particles in the accumulation mode.

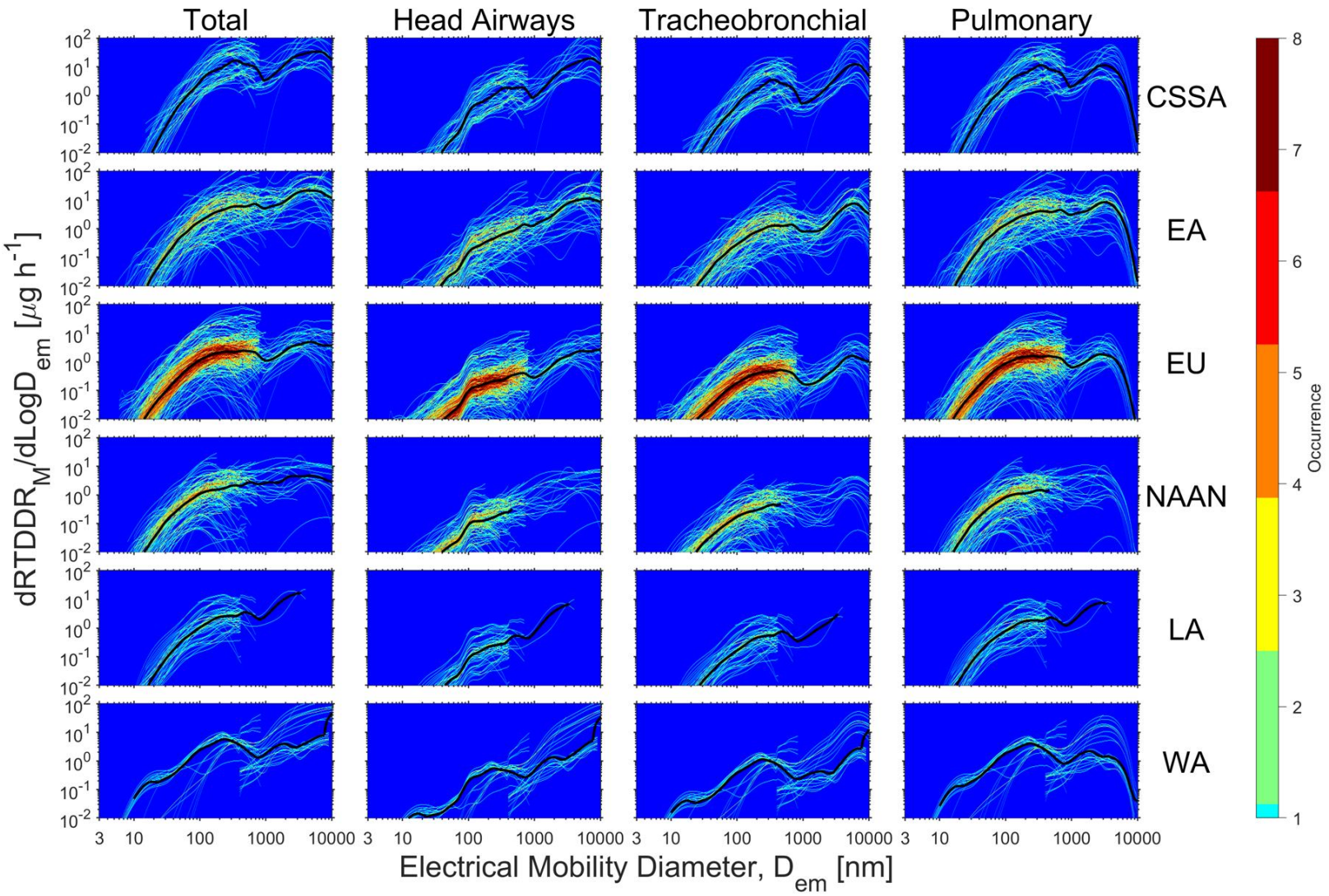

Figure 2.21 The total and regional $dRTDDR_M/dLogD_{em}$ in the respiratory tract in different geographical regions determined using the urban mass PSDs analyzed in this study. The color represents the occurrence frequency of the $dRTDDR_M/dLogD_{em}$ at a given particle size with a certain dose rate. The black lines indicate the median $dRTDDR_M/dLogD_{em}$ in each group.

Coarse mode particles tend dominate the total, tracheobronchial, and head airways $dRTDDR_M/dLogD_{em}$ for each geographical region (Figure 2.21 and 2.22). This is due to high deposition fractions coinciding with coarse modes that exceed, or are nearly equal to, the accumulation mode in most cities (Figure 2.16). The dominance of the coarse mode to the mass RTDDRs is especially strong in both the head airways and the tracheobronchial regions. In CSSA and EA, the prominent mode of the mass RTDDR in the coarse mode is located at approximately D_{em} = 6000 nm for the head airways and the tracheobronchial regions, while in the pulmonary region it is located near D_{em} = 3000 nm. For both the tracheobronchial and pulmonary regions, this peak occurs near the local maximum in the deposition curves for both regions (Figure 2.7). Mass RTDDRs in NAAN and EU are similar in shape to those in CSSA and EA in the tracheobronchial region, however, in the head airways, a partial second mode is observed at around D_{em} = 10000 nm. Mass RTDDRs in LA and WA exhibit a prominent coarse mode for the head airways and tracheobronchial region. However, the full extent of the mass RTDDRs for LA and WA in the coarse mode cannot be reliably characterized due to the lack of mass PSD observations in the two regions. As shown in Kodros et al.[121], desert regions of WA and AF are associated with very high deposited mass concentrations in the human respiratory tract.

In contrast to the head airways and the tracheobronchial regions, mass RTDDRs in the pulmonary region receive near equal contributions from the accumulation and coarse modes in CSSA, EU, and NAAN. The location of the prominent mode of the mass RTDDRs in the accumulation mode varies among the geographical regions, but is typically between D_{em} = 200 to 500 nm. As illustrated in Figure 2.7, the highest deposition fractions in the accumulation mode are found in the pulmonary region. Thus, cities with mass PSDs with prominent accumulation modes can be associated with high mass dose rates in this size fraction for the deepest region of the human respiratory tract. Across all geographical regions, the pulmonary region contributes significantly to the total mass RTDDRs from D_{em} = 100 to 1000 nm.

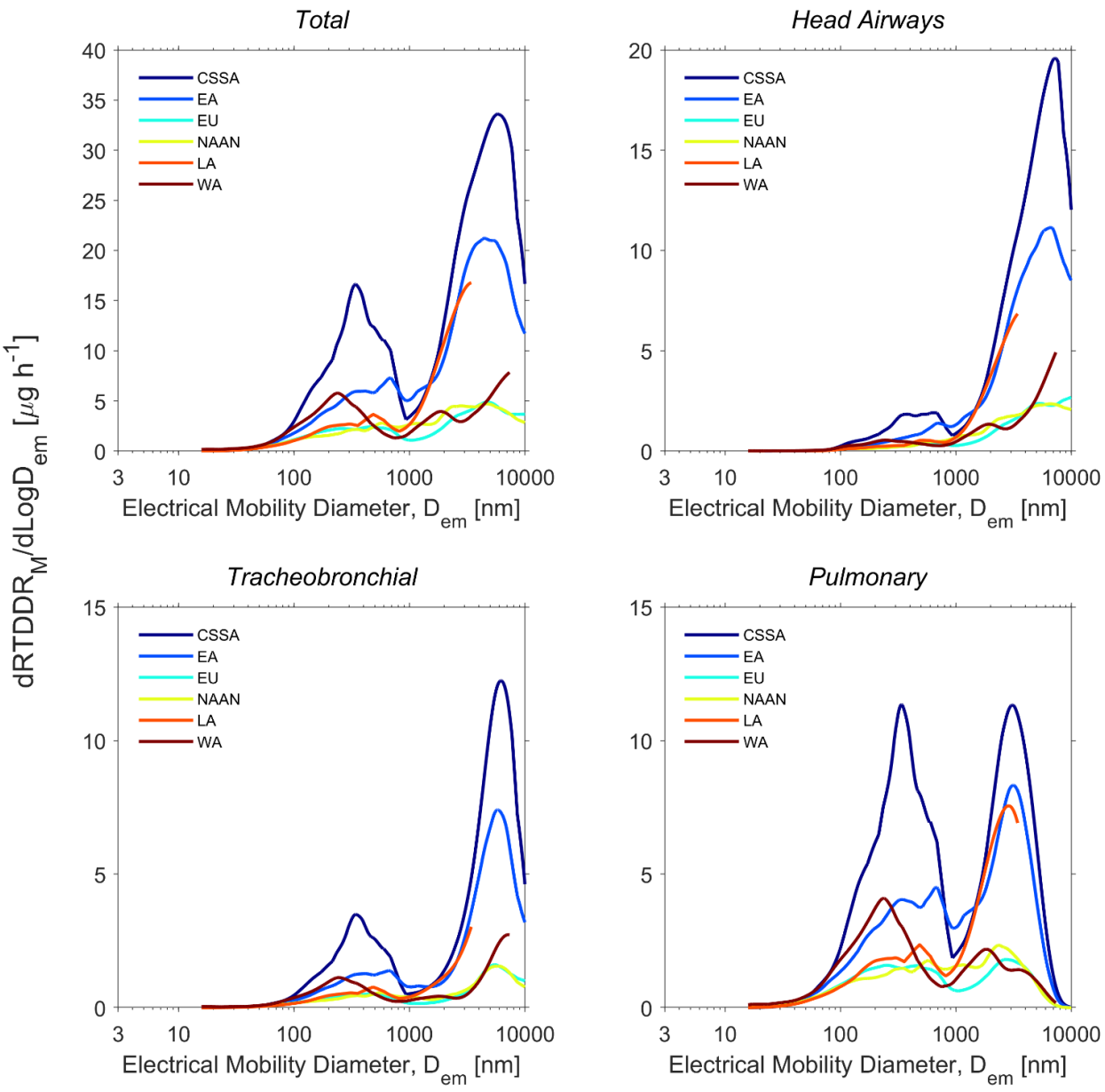

Figure 2.22 Median $dRTDDR_M/dLogD_{em}$ in each geographical region (black lines in Figure 2.21).

2.12 Urban aerosol PSDs: implications for indoor air quality & aerosol filtration in building ventilation systems

The compilation of urban aerosol PSDs from around the globe offers a basis to evaluate the implications of geographical variations in the shape and magnitude of PSDs on indoor air quality and aerosol filtration in buildings. Urban aerosols can be transported into the indoor environment though mechanical and natural ventilation or through infiltration via cracks and gaps in the building envelope. HVAC filters in mechanical ventilation systems of commercial or residential buildings can influence the transport of urban aerosols into the indoor atmosphere. Thus, understanding how HVAC filters modulate an urban aerosol PSD can provide insights on evaluation of human inhalation exposure to aerosols of outdoor origin.

Geographical variations in urban aerosol number PSDs that penetrate through a HVAC filter installed in a single-pass building ventilation system are presented in Figure 2.23. The penetrated urban aerosol number PSDs are presented in the form of a grid, with each row corresponding to a geographical region (CSSA, EA, EU, NAAN, and LA) and the two columns corresponding to MERV 8 and 14 filters. The solid black lines indicate the median penetrated urban aerosol number PSD for each geographical region and MERV filter, which are illustrated in Figure 2.24 on a linear y-axis scale. Similar to the urban aerosol number PSDs presented in Figure 2.11, there are significant geographical variations in both the shape and magnitude of the filter-transformed PSDs. The sub-micron penetrated PSDs are unimodal for all geographical regions and for both filters. The magnitude of the penetrated PSDs are greater in CSSA and EA as compared to NAAN, EU, and LA for both the MERV 8 and 14 filters. However, the nucleation mode of the penetrated PSDs for a MERV 8 filter in NAAN/EU are slightly greater than those for EA/CSSA. The PSDs of the penetrated urban aerosol in NAAN, EU, and LA present a peak at approximately D_{em} = 30 to 50 nm for the MERV 8 filter, while those in CSSA and EA show a peak between D_{em} = 70 to 120 nm. The magnitude of the penetrated PSDs is lower for the MERV 14 filter given its higher filtration efficiency compared to the MERV 8 filter (Figure 2.8). For NAAN, EU, and LA, the penetrated PSDs shift to the right when transitioning from a MERV 8 to 14 filter, while this shift is not as pronounced for CSSA and EA. The latter is due in part to the overlap between the minimum filtration efficiency at D_{em} = 100 to 200 nm (Figure 2.8) and the strong accumulation mode of the number PSDs in CSSA and EA (Figure 2.12).

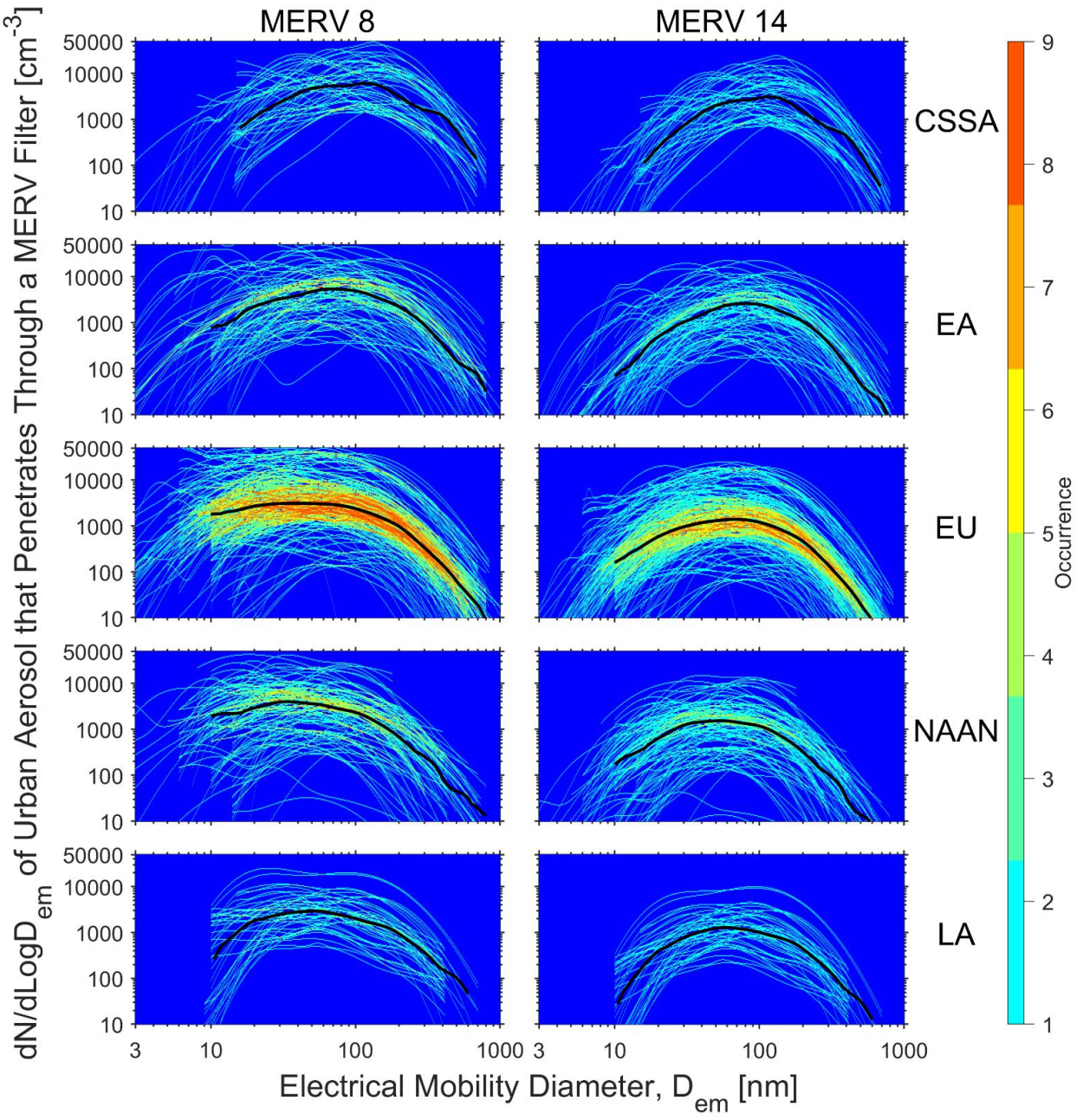

Figure 2.23 Urban aerosol number PSDs that penetrate through a MERV 8 and 14 filter in a building ventilation system for each geographical region, estimated using the number PSDs collected in this study (Figure 2.11) and assuming single-pass MERV 8 and MERV 14 filters. The color represents the occurrence frequency of the penetrated number PSDs at a given particle size with a certain concentration. The black lines indicate the median penetrated number PSDs in each group.

To further characterize the impact of geographical variations in the shape of urban aerosol number PSDs on indoor air quality and aerosol filtration in buildings, the relative fraction of

particles that penetrate or deposit onto the filter were determined (Figure 2.25). The total penetration and deposition fractions were determined as the ratio of the total number of particles that penetrate through the filter or deposit onto the filter to the total number of incoming particles (urban aerosol concentration). In doing so, this negates the impact of variations in the magnitude of the urban aerosol PSDs on filtration. The total penetration and deposition fractions were calculated for each urban aerosol number PSD in each geographical region (Figure 2.11), with the mean and standard deviation for each geographical region shown in Figure 2.25. Notably, a significant decrease of approximately 40% in the total penetration fraction is apparent for all geographical regions when switching from a MERV 8 to 14 filter.

Differences in the total penetration fractions among the five geographical regions with the same MERV-rated filter suggests that the shape of the urban aerosol number PSDs influences the overall filter performance in different regions. For both filters, the total penetration fractions are higher in EA/CSSA as compared to NAAN/EU by 5 to 9%. This is due to the prominent accumulation modes of the number PSDs in EA/CSSA, which coincide with the particle size range (D_{em} = 100 to 200 nm) where the filtration efficiency is at a minimum since the particles are too large to deposit by diffusion and too small to deposit by interception and inertial impaction (Figure 2.8). Thus, the results presented in Figure 2.25 suggests that the same filter may perform less effectively in EA/CSSA as compared to NAAN/EU due to variations in the shape of the number PSDs between the regions.

It is important to note that the analysis of the urban aerosol number PSDs that penetrate through HVAC filters is intended to serve as an illustrative example of how geographical variations in the shape and magnitude of urban PSDs can influence indoor air quality in mechanically ventilated buildings. The modeling approach simply integrates the urban aerosol PSDs and fixed HVAC filtration efficiency curves; thus, it may not represent actual filtration processes occurring in real HVAC installations. The actual filtration efficiency can vary from filter to filter, even among those with the same MERV rating. In addition, the filtration efficiency of a filter is not fixed during its service life and will evolve over time with the formation of solid dendrites and liquid films within the filter fiber matrix [227]. A multitude of factors can affect the actual penetrated urban aerosol PSD downstream of a filter, including: the type of filter (e.g. electret filter) [228], relative humidity [227], the filter installation method (which influences the bypass

of particles around the filter), face velocity [229], morphological features of the particles [230], and the mechanical ventilation recirculation ratio.

In addition, different geographical locations may result in different environmental factors, which can influence the performance of a filter. For example, the dendrites of the deposited particles may experience more frequent collapse in geographical regions with annual rainy seasons when the relative humidity increases significantly. The dendrites may restructure to adopt a compact morphology under elevated humidity due to the capillary effect of condensed water, which will lower the filtration efficiency and pressure drop across the filter.[227] In addition, the hygroscopic content of the dendrites may transition to form a liquid film on the filter fiber, and decrease the filtration efficiency before eventually reaching an equilibrium.[231,232] This is attributes to the low viscosity of the liquid film, which allows the liquid particles to coalesce, relocate, and drain along the filter fiber.

Beyond filtration of the urban aerosol as it enters the indoor environment, other physiochemical transformations can occur due to heating and cooling processes in mechanical ventilation systems. Heating of outdoor air can cause the volatile component of the urban aerosol population to evaporate from the particles, as well as to reduce the aerosol liquid water content and possibly transfer water-soluble species into the gas phase.[233–235] Such evaporation processes can shift the urban aerosol PSDs to smaller sizes. Sudden elevations in relative humidity due to humidification in mechanical ventilation systems may induce hygroscopic growth of the urban aerosol as it enters the indoor environment, as well as increase the aerosol liquid water content, which could enhance the uptake of water-soluble species indoors.

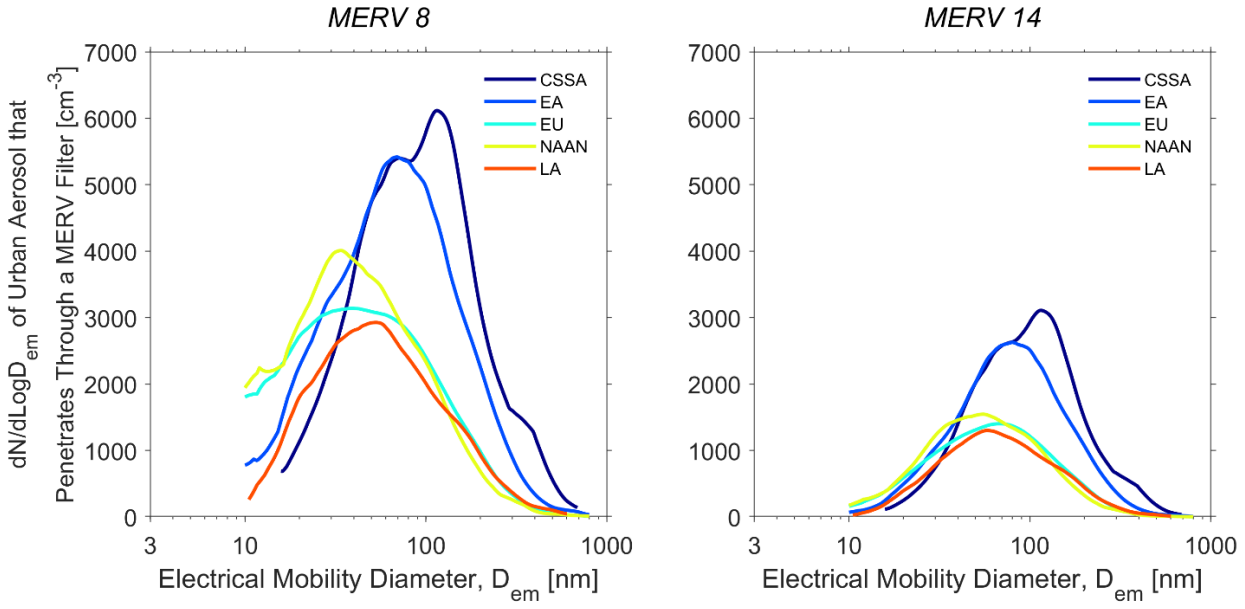

Figure 2.24 Median urban aerosol number PSDs that penetrate through a MERV 8 (left) and a MERV 14 (right) filter in a building ventilation system for each geographical region (black lines in Figure 2.23).

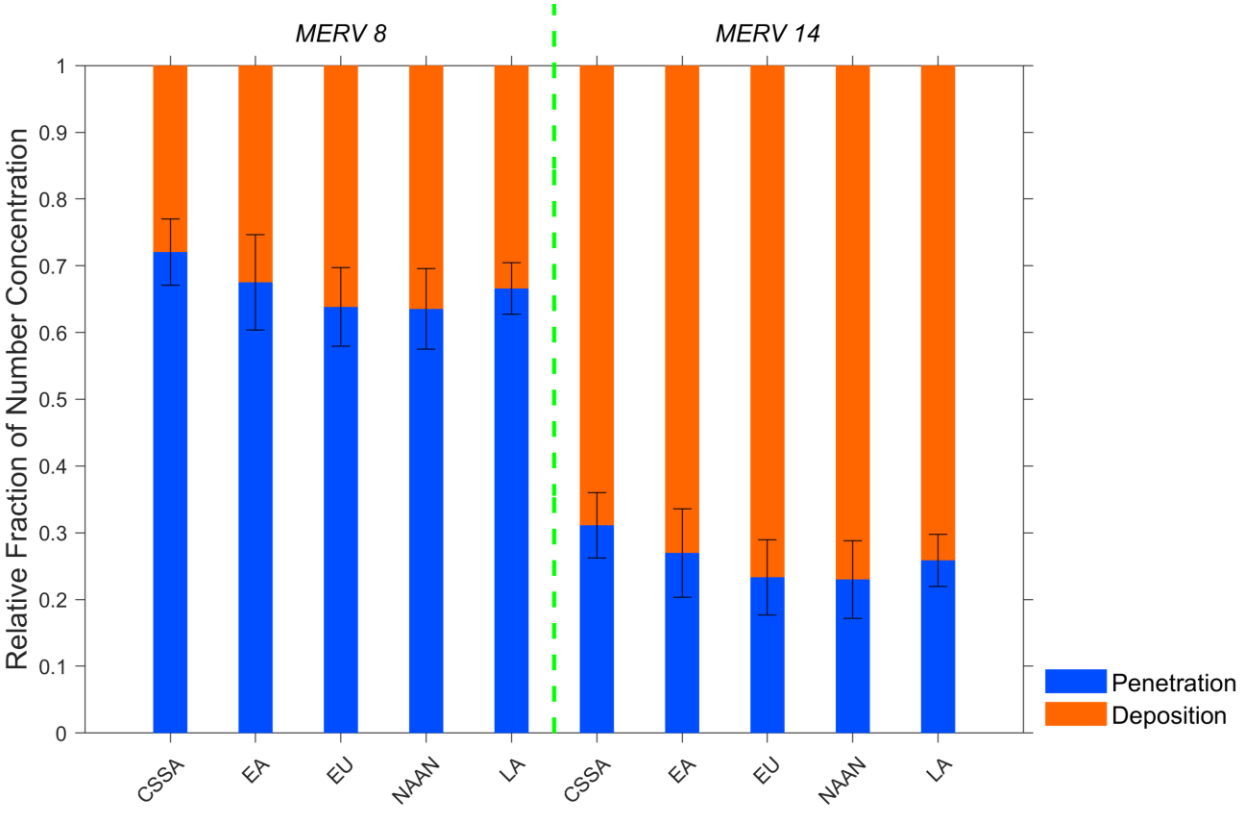

Figure 2.25 Mean HVAC filter penetration and deposition fractions for each geographical region, assuming single-pass MERV 8 and MERV 14 filters.

2.13 Framing future research directions for urban aerosol PSD observations at a global-scale

This critical review has provided a comprehensive overview of urban aerosol number and mass PSD observations made in cities around the globe. Critical gaps in urban aerosol PSD observations were identified in many geographical regions and countries, with a severe lack of ground-based PSD data for cities in AF, LA, WA, and parts of CSSA (Figure 2.1 and 2.10). Available PSD measurement data is often short in duration, with only 14.3% of the analyzed observations extending beyond 6 months. Similarly, there have been few direct measurements of size-resolved urban aerosol effective densities, and existing data is limited for many size fractions (Figure 2.9, Table 2.2). A greater number of direct measurements of urban aerosol effective densities will enable for accurate translation of urban aerosol number PSDs to mass PSDs in a given urban environment.

There exist significant geographical variations in the shape and magnitude of urban aerosol PSDs due to differences in primary and secondary aerosol sources and meteorological conditions (Figure 2.11 and 2.15). Such differences have important implications for human exposure and health as they drive large changes in the rate at which particles deposit in each region of the human respiratory tract (Figure 2.19 and 2.21). The important contribution of sub-200 nm particles to urban aerosol number PSDs in all regions reinforces the need for routine monitoring of the smallest particles in the urban atmosphere. Urban aerosol PSD observations that span the UFP to coarse regimes are especially lacking, with only 14% of the analyzed PSDs measuring particles across this wide size range. Coordinated global efforts are needed to build a continuous, long-term, wide size range, and ground-based urban PSD observation network in cities across the world. Such a network is necessary for improving our ability to link urban air pollution with human health and toxicological outcomes, understanding the atmospheric transformations of urban aerosol populations, and supporting air quality legislation and policy decisions that address particles both big and small.[236]

Existing ground-based air quality monitoring stations are largely focused on measurements of size-integrated $PM_{2.5}$ mass concentrations. Expansive observational datasets of $PM_{2.5}$ mass concentrations are now available. This has significantly advanced knowledge of the impact of $PM_{2.5}$ on urban air pollution and human health in the past two decades.[237–243] $PM_{2.5}$ measurement gaps do exist, with 141 of 243 countries lacking ground-based $PM_{2.5}$ monitoring stations.[244] The

ubiquity of low-cost aerosol sensors (e.g. OPCs) are providing a foundation for large-scale deployment of $PM_{2.5}$ monitoring networks.[245] However, given the nature of urban aerosol number and mass PSDs, as illustrated in Figure 2.11 and 2.15, observations of $PM_{2.5}$ mass concentrations are insufficient to accurately characterize an urban aerosol population. Of particular importance is the measurement of PSDs that include the UFP regime, given their significant contribution to particle number concentrations (Figure 2.11, 2.12, and 2.13). This is especially important given that UFP number concentrations and $PM_{2.5}$ mass concentrations are not representative of each other, as particles that contribute to the two size-integrated metrics often originate from different sources.[242]

The compilation of urban aerosol PSD observations in this review demonstrates the need for a transition from size-integrated $PM_{2.5}$ mass concentration measurement to broader size range PSD measurements that include the nucleation, Aitken, accumulation, and coarse modes. CMDs of urban aerosol number PSDs often fall between D_{em} = 10 to 100 nm (Figure 2.14); such particles contribute negligibly to urban aerosol mass PSDs (Figure 2.15 and 2.16). Many urban aerosol sources, such as biomass burning, traffic emissions (exhaust and non-exhaust), industrial and domestic combustion, cooking, and atmospheric new particle formation events, produce particles in the UFP regime (Figure 2.18).[3,134,246,247] Urban aerosol PSDs provide more detailed information of emission sources than do size-integrated concentrations. Several PSD-based models have been developed using characteristic emission profiles of different sources to identify and apportion the emission sources.[207,248–259] A detailed review of such models was given by Vu et al.[3].

$PM_{2.5}$ measurements are motivated in part by existing air quality legislation and exposure guideline values, whereas there are no existing nationwide regulations based on UFP or total particle number concentrations.[134] However, emission standards in the European Union now regulate particle number emissions for diesel passenger cars and light commercial vehicles in Euro 5, and for both gasoline and diesel passenger cars, light commercial vehicles, and heavy-duty diesel engines in Euro 6.[260] A transition from $PM_{2.5}$ measurement to routine urban aerosol PSD monitoring down the UFP regime can help support new legislation based upon UFP or total particle number concentrations.[261]

Future urban aerosol PSD measurements should span the entire UFP regime, including sub-3 nm nanocluster aerosol. The nanocluster aerosol mode is especially prominent during atmospheric new particle formation events and has been shown to dominate number PSDs

measured at both urban background and traffic sites.[115,262–264] Number concentrations of nanocluster aerosol can exceed 10000 cm^{-3} in polluted megacities, such as Shanghai and Nanjing, China[262]; while roadside measurements have reported concentrations in excess of 100000 cm^{-3} [115]. Achieving continuous urban aerosol number PSD observations from 1 to 10000 nm at the global-scale remains a challenge given the cost of sensitive aerosol instrumentation required for the detection of UFPs down to 1 nm and the collection of different measurement techniques needed to detect particles across such a wide size range. While advancements in low-cost optical particle sensing for detection of aerosols down to approximately D_{em} = 300 to 500 nm have been made in recent years, efforts are still needed to develop low-cost condensation particle counters, differential mobility analyzers, and diffusion chargers for measurement of PSDs down to the UFP regime.

A future urban aerosol PSD observation network will improve our ability to more fully understand the health implications of urban aerosols. Measurement of PSDs incorporating the UFP regime are needed given the importance of UFPs on human health and the size-dependency of deposition in the human respiratory tract (Figure 2.7). The health effects of UFPs are increasingly receiving more attention due to their high number concentrations in the urban environment, high surface area to mass ratio, and higher oxidative stress compared to larger particles.[11,14–17,130–133,265] Human exposure to UFPs has been associated with the development of cardiopulmonary and cardiovascular diseases, lung cancer, and asthma.[13–15,17,131,133,266–268] As illustrated in Figure 2.19 and 2.20, inhaled deposited dose rates (RTDDRs) on a number-basis are dominated by UFPs in nearly all geographical and respiratory tract regions. The deposition fraction in the pulmonary region, which is often assumed to be more relevant for respiratory diseases, shows a maximum at approximately D_{em} = 30 nm (Figure 2.7), which overlaps with the prominent modes of many urban aerosol number PSDs in NAAN, EU, and LA (Figure 2.11 and 2.12). UFPs can penetrate deep into the lung, can be transported into the bloodstream, and can translocate to different organs.[132,269]

3. CHARACTERIZATION OF A THERMAL AEROSOL GENERATOR FOR HVAC FILTRATION EXPERIMENTS (RP-1734)

3.1 Overview

This chapter presents the results of an in-depth characterization of a novel thermal aerosol generator for HVAC filtration experiments, with a focus on the physical characteristics of the synthesized aerosol. The impact of the generator operational conditions on the particle size distribution (PSD) output was investigated. The results indicate that the thermal aerosol generator is a cost-effective technique for rapid ageing of HVAC filters with a PSD that more accurately represents, compared to conventional loading dusts, what filters encounter in real HVAC installations.

3.2 Introduction

HVAC filters used in commercial and residential buildings encounter a complex mixture of aerosols of outdoor and indoor origin during their service life. Aerosols can span in size from a few nanometers to tens of micrometers.[18] Outdoor and indoor aerosols exhibit diverse characteristics, including morphological features, such as their PSD, shape, and density; chemical and biological composition; whether they exist as a liquid, solid, or a phase state between the two; their tendency to uptake moisture (hygroscopicity); and the electrostatic charge that they carry (number of charges, polarity).[270] These properties influence the size-resolved particle removal efficiency and dust loading behavior of HVAC filters.[32,271–278] As aerosols are captured by HVAC filters, they will begin to form complex deposits of solid dendrites and liquid films within the filter fiber matrix.[20–22] A combination of depth filtration and cake formation across the filter restricts airflow and imposes a pressure drop that must be overcome by the blower in the air handling unit (AHU).[23–25] It is necessary to characterize the loading kinetics of HVAC filters aged with an aerosol representative of that found in outdoor (urban) and indoor environments in order to better predict the trend in airflow resistance, and associated AHU blower power draw to overcome this pressure drop, during a filter's service life.

Loading aerosols typically used to age HVAC filters include ISO-12103-1-A2 Fine Test Dust, ISO-12103-1-A4 Coarse Test Dust, and ASHRAE Test Dust per ANSI/ASHRAE Standard

52.2-2017.[26,27] Such aerosols are primarily composed of coarse mode particles (1,000 to 100,000 nm). While useful for providing insights into differences in loading kinetics among filter media, coarse mode loading aerosols have a particle number and mass PSD unlike that found in outdoor (urban) and indoor environments.[7,18,26,28–30] Thus, the HVAC filter will undergo a much different loading process than what it will encounter in real HVAC installations.[26,31,32]

Outdoor (urban) and indoor aerosol number PSDs are often dominated by particles smaller than 100 nm size, while mass PSDs include significant contributions from both the accumulation mode (100 to 2,500 nm) and a fraction of the coarse mode (1,000 to 10,000 nm)[7,18,26,28–30] From the perspective of HVAC filter loading, it is of primary interest to reproduce outdoor (urban) and indoor aerosol mass PSDs as loading data is often expressed on a gravimetric basis (loaded particle mass per unit filter area). Filters aged with sub-micron particles (≤ 1,000 nm) obtain significantly higher pressure drops at a given loaded mass compared to those aged with coarse mode particles.[32,279] It is expected that the evolution in the pressure drop of filters installed in commercial and residential AHUs will differ from loading curves obtained from coarse mode test dust.

Cost-effective, high mass output (≥ 10 g/h) aerosol generators are needed to more accurately reproduce sub-micron mass PSDs of outdoor (urban) and indoor aerosols during HVAC filter loading experiments in full-scale experimental test facilities. Doing so will enable for a more realistic simulation of how filters are aged in real environments. Such generators are to be used in the proposed ASHRAE Guideline 35: Method for Determining the Energy Consumption Caused by Air-Cleaning and Filtration Devices. ASHRAE Guideline 35 will establish a consistent experimental methodology to determine the AHU blower energy consumption induced by HVAC filters as they are loaded with a sub-micron aerosol with a mass PSD representative of that found in actual HVAC systems in commercial buildings located in urban areas.

Numerous aerosol generation techniques are capable of producing sub-micron particles, including evaporation-condensation of metallic and organic vapors in tube furnaces, soot generation via diffusion flames, atomization of salts, spark-discharge generation, glowing hot-wire generation, electrospray generation, cold plasma via dielectric barrier discharge, and nanopowder dispersion.[280] While such generation techniques can produce sub-micron aerosols with varied PSDs and other physiochemical properties, their mass production rates are often insufficient (≤ 1 g/h) for conducting rapid (≤ 8 hours) HVAC filter loading experiments as will be required in the

proposed ASHRAE Guideline 35. One viable technique is thermal aerosol generation in which high mass concentrations of sub-micron salt particles are generated via evaporation-condensation of salt vapor.[281–283] Thermal aerosol generators can produce mass PSDs with mass median diameters of approximately 200 to 400 nm, however, characteristics of the salt aerosol have not yet been systematically assessed.[281,283]

The objective of this study is to evaluate the number and mass PSDs and morphological features of sodium chloride (NaCl) and potassium chloride (KCl) particles produced by a newly designed commercially available thermal aerosol generator under different operational conditions. The results will inform the suitability of such a generation technique for reproducing the sub-micron fraction of outdoor (urban) and indoor aerosol mass PSDs at high mass production rates for rapid HVAC loading experiments as per the proposed ASHRAE Guideline 35.

3.3 Materials and methods

3.3.1 Thermal aerosol generator

The thermal aerosol generator (Series 6000, SFP Services Ltd., Christchurch, UK) produces salt particles via evaporation-condensation by burning salt sticks in a high temperature oxygen-propane flame (Figure 3.1). The generator consists of a conventional blowtorch fitted with an annular burner, a battery-powered feeder for the salt stick, and two rotameters for controlling the flow rates of oxygen (O_2) and propane (C_3H_8). The O_2 and C_3H_8 flows are premixed and then ignited. A flame cone is formed in front of the annular burner. The salt stick passes through the nozzle of the annular burner from the rear and then enters the flame. The stick is gripped between a serrated drive roller connected to a variable speed motor and a smooth idler roller that is mounted on a sprung guide arm. The arm guide is fully opened when inserting the salt stick and then gently released to prevent damaging the salt stick prior to burning. The salt stick feed rate is calibrated by the manufacturer and can be controlled through a dial. The nominal flow rates of O_2 and C_3H_8 for generating the salt particles are 17 L/min and 4 L/min, respectively. The primary content of the salt sticks is NaCl or KCl, with a trace amount of magnesium oxide (MgO) added to serve as a binding agent for the stick. The MgO will not vaporize in the flame and will fall as hot ash. For each batch of salt sticks, the effective content (abundance of NaCl or KCl) is provided as a mass

per unit length of the stick by the manufacturer. The effective content of the salt sticks analyzed in this study ranged from 99 to 144 mg/mm.

3.3.2 Experimental Design

In this study, the number ($1/cm^3$) and mass ($\mu g/m^3$) PSDs of the salt aerosol synthesized by the thermal aerosol generator at different operational conditions were examined. Three operational factors were considered: the type of salt (NaCl and KCl), the feed rate of the salt stick (3, 5, 10, 18, and 25 mm/min), and the diameter of the stick (10 mm and 12 mm). Salt particles were generated for both salt types at each feed rate and for both stick diameters, thus a total of twenty operating conditions were examined. During the experiments, the thermal aerosol generator was placed in a fume hood. The duration of each PSD experiment varied with the feed rate. For tests with a feed rate of 3, 5, and 10 mm/min, the test duration was 20 to 30 minutes. For tests with a feed rate of 18 and 25 mm/min, the test duration was 15 to 20 minutes due to the high consumption rate of the salt sticks. Morphological features of the salt particles were characterized in a sub-set of experiments for 10 mm sticks of both salt types at a feed rate of 5 mm/min.

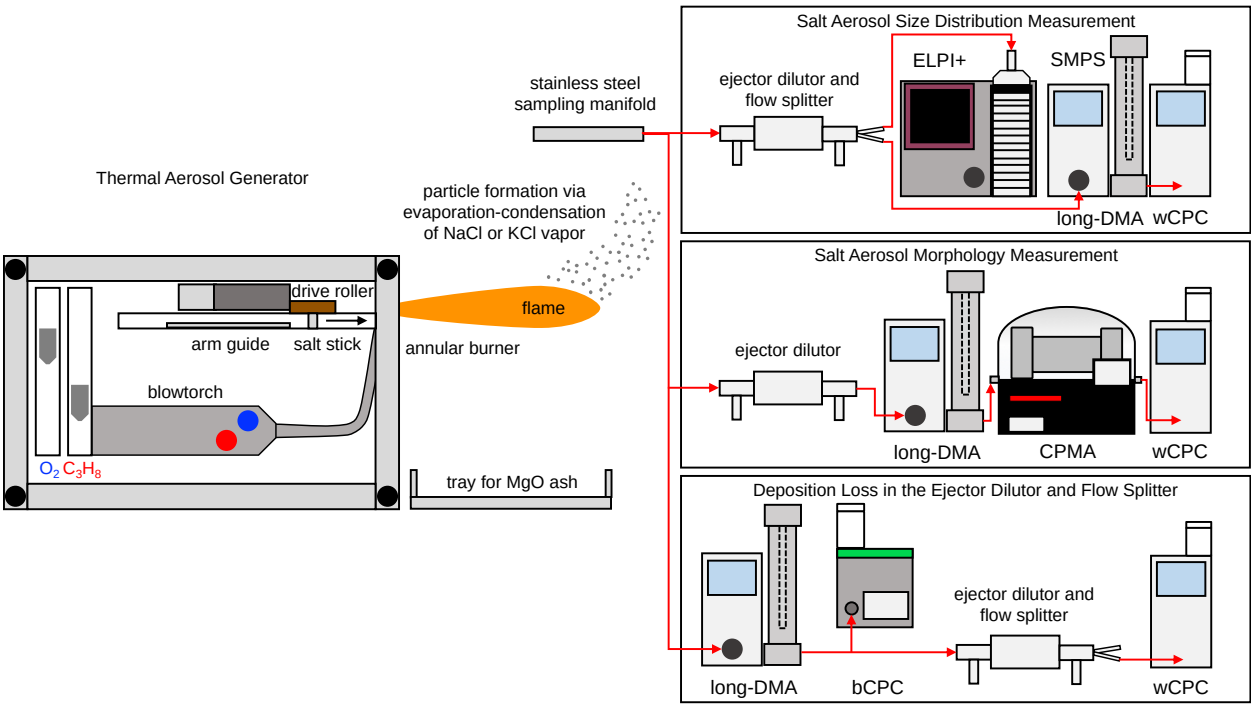

Figure 3.1 Setup for thermal aerosol generator experiments: (top) measurement of salt aerosol particle size distributions, (middle) measurement of salt aerosol morphological features, and (bottom) evaluation of particle deposition loss in the ejector dilutor and flow splitter assembly.

3.3.3 Measurement of Salt Aerosol Size Distributions

The salt aerosol was extracted at 50 cm above the flame of the thermal generator via a stainless steel sampling manifold. The aerosol sample was diluted by an ejector dilutor (DI-1000, Dekati Ltd., Kangasala, Finland) and then entered a flow splitter (Model 1104, Brechtel Manufacturing Inc., Hayward, CA, USA) prior to measurement of the PSD. A differential pressure gauge monitored the pressure difference between the inlet and outlet of the ejector dilutor, which was used to estimate the dilution factor according to the calibration curve provided by the manufacturer. Electrical mobility diameter (D_{em})-based number PSDs of the salt aerosol were measured with a Scanning Mobility Particle Sizer (SMPS, Model 3938NL88, TSI Inc., Shoreview, MN, USA), consisting of a Kr-85 bi-polar charger (370 MBq, Model 3077A, TSI Inc., Shoreview, MN, USA), a long Differential Mobility Analyzer (long-DMA, Model 3081, TSI Inc., Shoreview, MN, USA), and a water-based Condensation Particle Counter (wCPC, Model 3788, TSI Inc., Shoreview, MN, USA). Aerodynamic diameter (D_a)-based number PSDs were measured with a High Resolution Electrical Low-Pressure Impactor (HR-ELPI+, Dekati Ltd., Kangasala, Finland). Sintered collection plates were used to eliminate particle bounce and impactor overloading. The HR-ELPI+ was operated in normal resolution mode with fourteen size fractions from 6 to 10,000 nm in D_a (henceforth referred to as ELPI+).

3.3.4 Measurement of salt aerosol morphological features

Morphological features of the NaCl and KCl particles, including size-resolved effective densities (ρ_{eff}), size-resolved dynamic shape factors (χ), and mass-mobility exponents (ε_m), were determined by combining a long-DMA with a Centrifugal Particle Mass Analyzer (CPMA, Cambustion Ltd., Cambridge, UK) and a wCPC (Figure 3.1). The DMA-CPMA-CPC technique is used to evaluate the mass-mobility relationship of an aerosol population.[284] Here, the effective density (ρ_{eff}) is defined as the ratio of the particle mass (m_p) to the volume assuming a sphere with a diameter of D_{em} (Equation 3-1).[54] The dynamic shape factor (χ) is defined as the ratio of the actual drag force on the particle to the drag force on a sphere with a diameter equal to the volume equivalent diameter (D_{ve}).[19] χ is used to characterize the irregular, non-spherical shape of the particle.[19] χ is unity for a sphere, often greater than 1 for an irregular particle, and can approach and exceed 2 for agglomerates.[54,285] The mass-mobility exponent (ε_m) is used to describe the

fractal nature of the particles. ε_m approaches 3 for a sphere and becomes less than 2 for fractal agglomerates formed by diffusion-limited processes. The combination of ρ_{eff}, χ, and ε_m enable for a quantitative assessment of the morphology of the NaCl and KCl particles produced by the thermal generator. Such parameters are useful in interpreting number and mass PSDs and in understanding how the morphological features of the salt aerosol may impact the filtration mechanisms and loading behavior of HVAC filters.

As with the PSD measurements, the salt aerosol was extracted at 50 cm above the flame and diluted with an ejector dilutor. The aerosol sample passed through a Kr-85 bi-polar charger to achieve a Boltzmann equilibrium charge distribution. The salt particles then entered the long-DMA, which operated in stepping mode to select particles with a certain D_{em}. The sample and sheath flow rates of the long-DMA were set at 1.5 L/min and 7.5 L/min, respectively.

Following mobility classification with the long-DMA, the particles were further classified by their mass-to-charge ratio with the CPMA. As the particles pass through the gap between the inner and outer coaxial rotating electrodes of the CPMA, they experience opposing centrifugal and electrostatic forces. Particles can penetrate the CPMA only when the two forces are in balance. By adjusting the rotation speed and the voltage potential between the inner and outer electrodes, the mass-to-charge setpoint can be controlled, thereby selecting particles with a certain mass. At each D_{em} setpoint, the CPMA scanned over a wide mass range with a fixed mass resolution (R_m = 5). At the downstream location of the CPMA, a wCPC measured the number concentration of the mobility- and mass-classified particles. The concentration at each mass setpoint was averaged over 4 seconds with a delay of 3 seconds between two measurement points.

The DMA-CPMA-CPC measurements were used to estimate variations in the ρ_{eff} for a given D_{em}, termed the ρ_{eff} distribution, through the following equation[54]:

$$\rho_{eff} = \frac{6m_p}{\pi D_{em}^3} \tag{3-1}$$

Many of the ρ_{eff} distributions presented a dominant peak and a shoulder (Figure 3.2), the latter of which is due to doubly-charged particles. Thus, each ρ_{eff} distribution was fitted with two normal distributions that represent the singly- and doubly-charged particles, respectively. The mean ρ_{eff} of the fitting for the singly-charged particles was adopted as the ρ_{eff} for a given D_{em} setpoint, and the standard deviation was adopted as the uncertainty of the measurement. Thus, size-resolved effective density functions, $\rho_{eff}(D_{em})$, were determined for both NaCl and KCl.

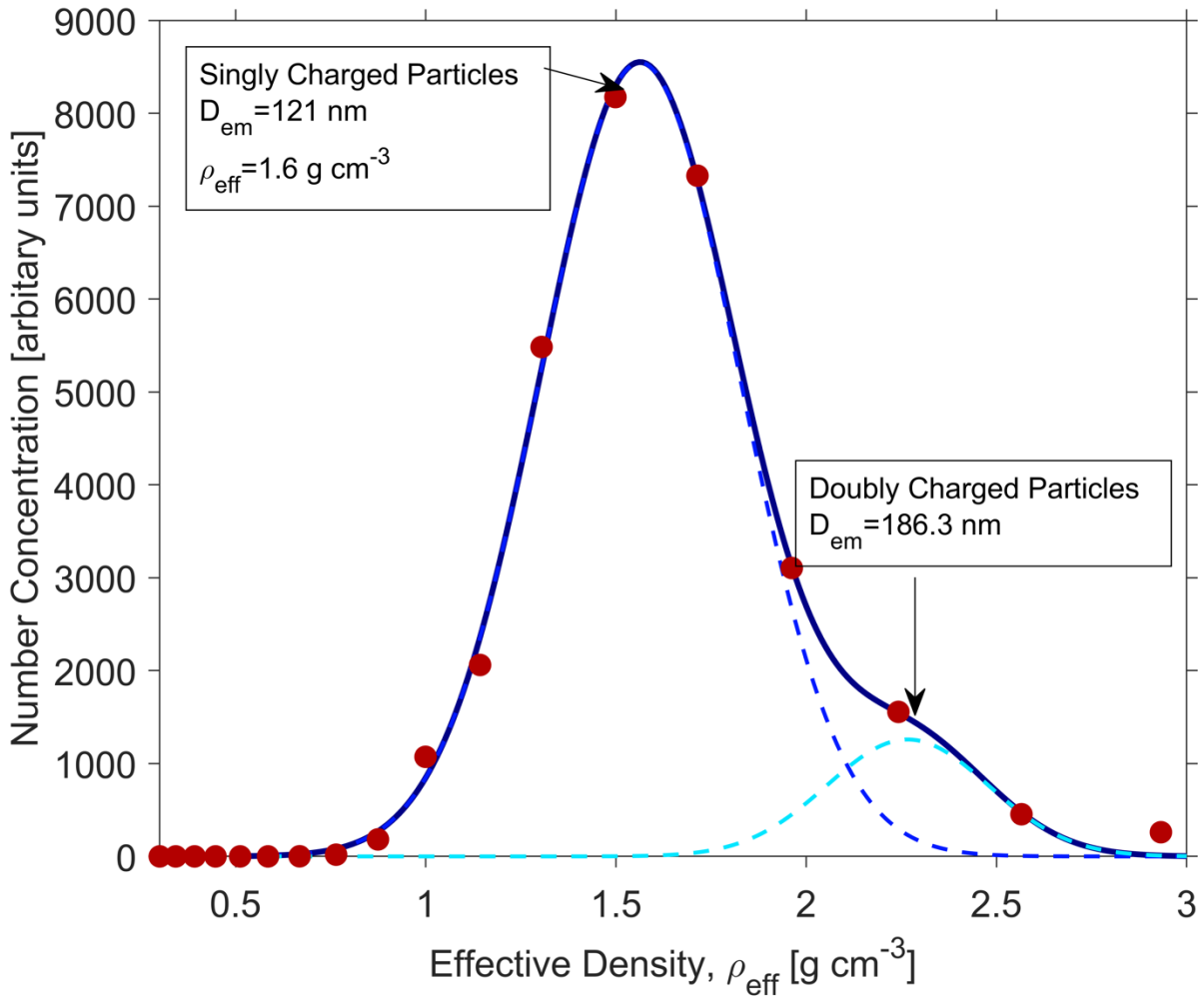

Figure 3.2 An example of the two-mode fitting for the effective density (ρ_{eff}) distribution with a DMA setting of D_{em} = 121 nm. The red circles represent the measured data points via the DMA-CPMA-CPC setup. The two dashed lines represent the fitted ρ_{eff} distributions for the singly (dark blue) and doubly (light blue) charged particles. The solid blue line represents the sum of the two fitted ρ_{eff} distributions.

An example fitting of a ρ_{eff} distribution for a D_{em} setpoint of 121 nm is illustrated in Figure 3.2. The red circles represent the measured data points. The dark blue dashed line on the left represents the singly-charged particles with a nominal diameter of 121 nm, while the light blue dashed line on the right represents the doubly-charged particles with a nominal diameter of 186.3 nm. This fitting method is used simply to differentiate the singly- and doubly-charged particles and does not take the transfer functions of DMA and CPMA into consideration. Therefore, the width of the reported ρ_{eff} distribution is relatively wide compared to the actual distribution, which can be obtained by a data inversion routine that accounts for the charging efficiency of the bi-polar

charger, transfer functions of the long-DMA and CPMA, and the wCPC detection efficiency (Buckley et al. 2017; Rawat et al. 2016). However, due to temporal fluctuations of the salt aerosol PSDs during the operation of the thermal aerosol generator, the inversion of the measured data was not successful.

Dynamic shape factors of the NaCl and KCl particles were estimated as a function of D_{em}. First, the D_{ve} corresponding to each D_{em} setpoint was calculated from the ρ_{eff} and the bulk density of the salt (ρ_m) via Equation (3-2), assuming no internal voids within the particles such that the bulk density and particle density (ρ_p) are equivalent[54]:

$$D_{ve} = \sqrt[3]{\frac{6m_p}{\pi\rho_m}} = \sqrt[3]{\frac{\rho_{eff}{D_{em}}^3}{\rho_m}} \quad (3\text{-}2)$$

The dynamic shape factor at a given D_{em} can be estimated by Equation (3-3), which defines the relationship between D_{em} and D_{ve}[54]:

$$\chi = \frac{D_{em}}{D_{ve}} \frac{C_c(D_{ve})}{C_c(D_{em})} \quad (3\text{-}3)$$

where C_c is the Cunningham Slip Correction Factor[19].

The mass-mobility exponent (ε_m) was determined for the NaCl and KCl particles to characterize their fractal-like nature. The mass-mobility relationship of particles formed via diffusion-limited processes, such as soot particles and metal agglomerates, can be described by a power law function[101,102,126,127,286–290]:

$$m_p = KD_{em}^{\varepsilon_m} \quad (3\text{-}4)$$

where K is a constant. Combining Equations (3-1) and (3-4), we obtain the following equation relating ρ_{eff}, D_{em}, and ε_m:

$$\rho_{eff} = \frac{6K{D_{em}}^{\varepsilon_m - 3}}{\pi} \quad (3\text{-}5)$$

The size-resolved effective density functions, ρ_{eff} (D_{em}), were fit with Equation (3-5) to estimate ε_m for each salt type.

3.3.5 Particle deposition loss in the ejector dilutor and flow splitter

The size-resolved particle deposition loss fraction in the dilutor-flow splitter assembly was measured by the setup shown in Figure 3.1. The salt particles were first mobility classified by the long-DMA. Particle number concentrations were then measured at the upstream and downstream locations of the dilutor-flow splitter assembly with a butanol-based CPC (bCPC, Model A20, Airmodus Ltd., Helsinki, Finland) and a wCPC, respectively. The deposition loss fraction for particles with a diameter *i* (L_i) can be calculated as:

$$L_i = 1 - \frac{C_{2,i} \times DF}{C_{1,i}} \quad (3\text{-}6)$$

where *DF* is the nominal dilution factor, which can be inferred by the difference in pressure between the inlet and outlet of the ejector dilutor; $C_{2,i}$ is the particle number concentration at the downstream location of the dilutor-flow splitter assembly; and $C_{1,i}$ is the particle number concentration at the upstream location of the dilutor-flow splitter assembly. The correction factor for the deposition loss of particles with a diameter *i* (α_i) in the assembly can be expressed as:

$$\alpha_i = \frac{1}{L_i} \quad (3\text{-}7)$$

3.3.6 Calculation of particle deposition in the tubing of the sampling manifold

The number PSDs of the salt particles as measured by the SMPS and ELPI+ were corrected for particle deposition in the dilutor-flow splitter assembly using α_i and the tubing of the sampling manifold using empirical relationships. The overall penetration efficiency of particles transported through the tubing of the sampling manifold, $\eta_{overall}$, is the product of the transmission efficiencies of each sampling element. The overall penetration efficiency can be calculated as[291]:

$$\eta_{overall} = \eta_{tube,grav}\eta_{tube,diff}\eta_{bend,inert} \quad (3\text{-}8)$$

where $\eta_{tube,grav}$ represents the transmission efficiency for gravitational deposition in the sampling tubes, $\eta_{tube,diff}$ represents the transmission efficiency for diffusive deposition in the sampling tubes, and $\eta_{bend,inert}$ represents the transmission efficiency for inertial impaction in the bends of the tubing.

The transmission efficiency for gravitational deposition due to laminar flow in a circular tube can be expressed as[291,292]:

$$\eta_{tube,grav} = 1 - \frac{2}{\pi}[2\kappa\sqrt{1 - \kappa^{2/3}} - \kappa^{1/3}\sqrt{1 - \kappa^{2/3}} + arcsin(\kappa^{1/3})] \quad (3\text{-}9)$$

$$\kappa = \frac{3}{4}\frac{L}{d}\frac{V_{ts}}{U}cos\theta \quad (3\text{-}10)$$

where d = inside diameter of the tube, L = length of the tube, V_{ts} = particle terminal settling velocity, U = flow velocity in the tube, and θ = angle with respect to the horizontal.

The transmission efficiency for diffusive deposition in a tube can be expressed as[293]:

$$\eta_{tube,diff} = 1 - 2.56\xi^{2/3} + 1.2\xi + 0.177\xi^{4/3}, for\ \xi < 0.02 \quad (3\text{-}11)$$

$$\eta_{tube,diff} = 0.819\,exp(-3.657\xi) + 0.097\,exp(-22.3\xi) + 0.032\,exp(-57\xi), for\ \xi > 0.02 \quad (3\text{-}12)$$

$$\xi = \frac{\pi DL}{Q} \quad (3\text{-}13)$$

where D = particle diffusion coefficient and Q = volumetric flow rate.

The transmission efficiency for inertial deposition due to laminar flow in a 90° bend can be expressed as[294]:

$$\eta_{bend,inert} = 1 - Stk\varphi \quad (3\text{-}14)$$

where Stk = Stokes number and φ = angle of the bend in radians.

3.3.7 Analysis of Salt Aerosol Size Distributions

The number PSDs measured by the SMPS and ELPI+ were reported as a function of D_{em} and D_a, respectively. Mass PSDs were only determined from the ELPI+ measurements given the wider operational size range of the instrument, which covered the full accumulation mode (100 to 2,500 nm). To convert the measured number PSDs of the ELPI+ to mass PSDs, the D_a impactor cut-offs for each stage of the ELPI+ were first transformed to D_{em}. This was done as the relationship between particle mass and ρ_{eff} is defined through D_{em}, not D_a (Equation 3-1). To relate D_a to D_{em}, Equations (3-2) and (3-3) are combined to derive:

$$\rho_{eff} = \frac{\rho_m}{\chi^3}\frac{C_c(D_{ve})^3}{C_c(D_{em})^3} \quad (3\text{-}15)$$

D_{ve} can be converted to D_a according to DeCarlo et al.[54] and assuming no internal voids such that ρ_m and ρ_p are equivalent:

$$D_a = D_{ve}\sqrt{\frac{1}{\chi}\frac{\rho_m}{\rho_0}\frac{C_c(D_{ve})}{C_c(D_a)}} \quad (3\text{-}16)$$

where ρ_0 is standard density (1 g/cm^3). Combining Equations (3-3) and (3-16), we can define the relationship between D_{em} and D_a:

$$\frac{D_a}{D_{em}} = \frac{1}{\chi^{3/2}} \sqrt{\frac{\rho_m}{\rho_0 C_c(D_a)}} \frac{C_c(D_{ve})^{3/2}}{C_c(D_{em})} \quad (3\text{-}17)$$

Substituting Equation (3-15) into Equation (3-17), D_a can be converted to D_{em} using ρ_{eff}:

$$\frac{\rho_{eff}}{\rho_0} = \left(\frac{D_a}{D_{em}}\right)^2 \frac{C_c(D_a)}{C_c(D_{em})} \quad (3\text{-}18)$$

After converting D_a to D_{em}, the number PSDs measured by the ELPI+ were converted to D_{em}-based mass PSDs using $\rho_{eff}(D_{em})$ via Equation (3-1). The mean number and mass PSDs for each thermal generator operational condition were normalized by the maximum value in each PSD to better visualize the PSD shape and the prominent mode(s). The normalized PSDs were then fit to the multi-lognormal distribution function.[18] Time-series plots of the number and mass PSDs were used to characterize the stability of the thermal generator output.

3.4 Results and Discussion

The following sections present the results of the experimental investigation into the characteristics of salt particles produced by the thermal aerosol generator. First, size-resolved morphological features of the NaCl and KCl particles are discussed. Number and mass size distributions are then presented, followed by mass production rates. The results explain how operational conditions of the thermal generator influence the physical properties of the synthesized aerosol, thereby informing the utility of such a generation technique for HVAC filter loading experiments as per ASHRAE Guideline 35.

3.4.1 Morphological Features of Salt Aerosol Produced by the Thermal Aerosol Generator

Figure 3.3 presents the measured effective densities (ρ_{eff}) of the NaCl and KCl particles produced by the thermal generator as a function of electrical mobility diameter, D_{em}. The measured effective densities (denoted as markers) are compared with theoretical ρ_{eff} values calculated by Equation (3-15) using the bulk density of NaCl (ρ_m = 2.165 g/cm^3) and KCl (ρ_m = 1.98 g/cm^3) and assuming the particles adopt either a spherical (χ = 1, dotted lines) or cubic structure (χ = 1.08, dashed lines).

The effective densities of both NaCl and KCl particles varied with particle size. This size-dependency was most pronounced for D_{em} > 100 nm. For D_{em} < 100 nm, the salt aerosol was more morphologically consistent. Across the electrical mobility span of D_{em} = 30 to 100 nm, ρ_{eff}

exhibited a small variation with particle size, with an average ρ_{eff} of 1.79±0.11 g/cm^3 (mean±SD) for NaCl particles and 1.67±0.12 g/cm^3 for KCl particles. Between D_{em} = 100 and 400 nm, the effective densities for NaCl and KCl particles decreased with increasing particle size. For NaCl particles, ρ_{eff} decreased from 1.72±0.26 at D_{em} = 99.2 nm to 0.84±0.17 at D_{em} = 350 nm. For KCl particles, ρ_{eff} decreased from 1.52±0.36 at D_{em} = 99.2 nm to 0.82±0.15 at D_{em} = 328 nm.

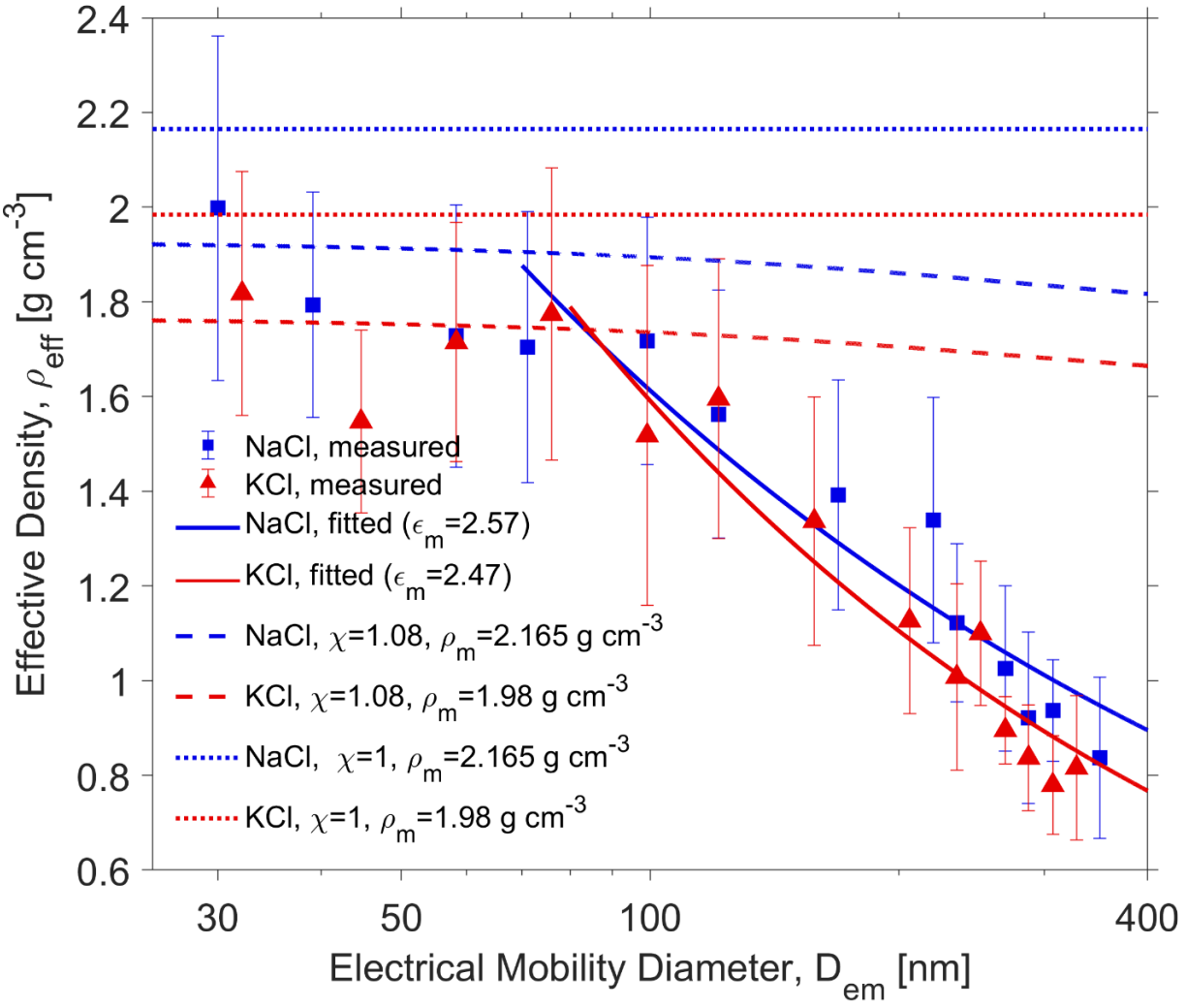

Figure 3.3 Measured size-resolved effective densities (ρ_{eff}) for NaCl (blue squares) and KCl (red triangles) particles. The error bars represent the standard deviation of the fitting for the ρ_{eff} distribution for resolving the singly and doubly charged particles for each D_{em}. Theoretical ρ_{eff} values calculated by Equation (3-8) using the bulk density of NaCl (ρ_m = 2.165 g/cm^3) and KCl (ρ_m = 1.98 g/cm^3) are shown assuming the particles adopt either a cubic structure (χ = 1.08, dashed lines) or spherical structure (χ = 1, dotted lines). The power law function (Equation 3-4) was fit to the measured ρ_{eff} data to determine the mass-mobility exponent (ε_m) for NaCl (solid blue line) and KCl (solid red line) particles.

The effective densities for each salt were nearest to their respective bulk densities at D_{em} = 30 nm for NaCl (ρ_{eff} = 2.00±0.36 g/cm^3) and D_{em} = 32.1 nm for KCl (ρ_{eff} = 1.82±0.26 g/cm^3). From D_{em} = 30 to 100 nm, the measured ρ_{eff} were within 8-23% of the theoretical ρ_{eff} calculated for spherical particles (χ = 1) with the bulk density of each salt. Above D_{em} = 100 nm, the measured ρ_{eff} deviated significantly from that for a sphere.

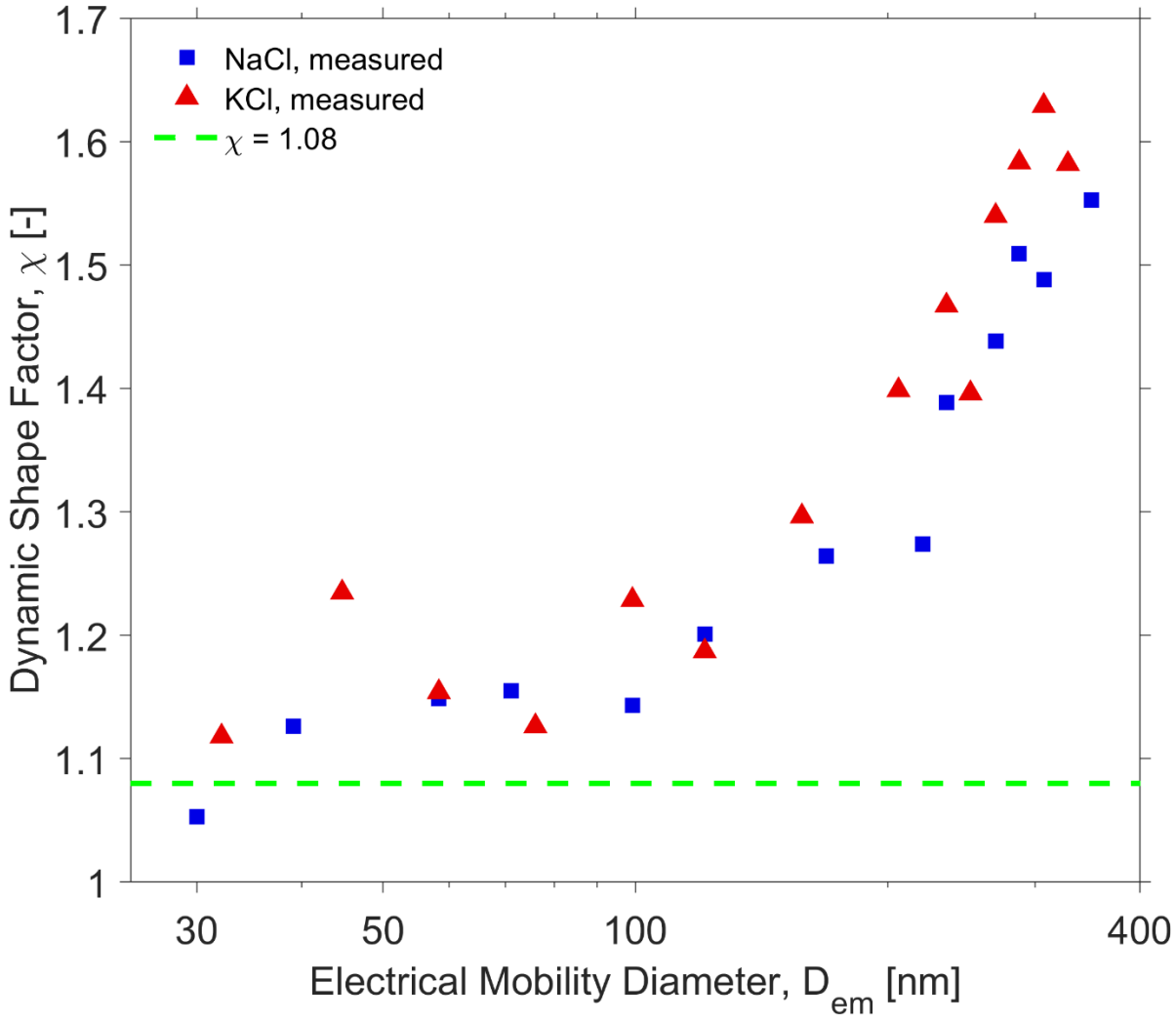

Figure 3.4 The measured size-resolved dynamic shape factors (χ) for NaCl (blue squares) and KCl (red triangles) particles. The χ for particles adopting a cubic structure (χ = 1.08) is provided as a reference (dashed green line)

Intuitively, it may be assumed that NaCl and KCl particles adopt a cubic structure with a χ = 1.08[19] (for an ideal cube) as the crystal structure of both salts are cubic. The cubic assumption results in theoretical ρ_{eff} values of approximately 1.7 to 1.9 g/cm^3 across the measured size range.

The measured ρ_{eff} was closest to that for a cube for particles less than D_{em} = 80 nm. For particles larger than D_{em} = 100 nm, the measured ρ_{eff} was much less than that for a cube.

The morphologies of the NaCl and KCl particles synthesized by the thermal generator can be further interpreted through size-resolved dynamic shape factors (χ), which are presented in Figure 3.4. χ increased with particle size for both salt types from D_{em} = 30 to 400 nm. A sharp increase in χ was observed for particles larger than D_{em} = 100 nm. For NaCl particles, χ increased from 1.05 at D_{em} = 30 nm to 1.55 at D_{em} = 350 nm. Similarly, for KCl particles, χ increased from 1.12 at D_{em} = 32.1 nm to 1.58 at D_{em} = 328 nm. From D_{em} = 30 to 100 nm, the dynamic shape factors are similar to that for compact clusters of three (χ = 1.15) or four (χ = 1.17) spheres.[19]

NaCl and KCl particles exhibited similar trends in their size-resolved morphologies across the measured size range. Effective densities for KCl particles were generally 5 to 10% lower than that for the NaCl particles. Conversely, the dynamic shape factors for KCl particles were generally 2 to 9% greater than that of the NaCl particles.

The morphological features of the thermal generator aerosol can be compared with NaCl and KCl particles generated by other techniques. Zelenyuk et al.[295] demonstrated that NaCl particles generated via nebulizing aqueous NaCl solutions could adopt three types of morphologies depending upon particle size and drying conditions, including: nearly spherical ($\chi \sim 1.02$), cubic ($\chi \sim 1.065$ to 1.17), and agglomerates ($\chi \sim 1.3$ to 1.4). The effective densities of the spherical particles were found to be close to the bulk density of NaCl, while the effective densities of the agglomerates were between 1.2 to 1.4 g/m^2. Wang et al.[296] found that the drying rate can influence χ while generating NaCl particles from aqueous solutions. For a given particle size, χ decreases with an increase in drying rate. NaCl particles formed by evaporation-condensation, as is the case for the thermal generator, tend to form agglomerates. Through electron microscopy, Craig and McIntosh[297] revealed that chain-like cubic NaCl particles are formed by through evaporation-condensation of NaCl in a tube furnace. Similarly, Krämer et al.[298] found NaCl agglomerates formed by evaporation-condensation to have a branched-chain structure with $\chi \sim 5$. In contrast to NaCl particles, there is comparatively less information on the morphology of KCl particles. Chindapan et al.[299] used scanning electron microscopy to show that KCl particles generated by a spray dryer have a highly agglomerated structure. The morphologies of KCl particles formed by evaporation-condensation have not been investigated to date in the literature.

The measured ρ_{eff} and χ, and their comparison with theoretical values and results from previous experimental studies, suggests that NaCl and KCl particles smaller than D_{em} = 100 nm adopt spherical or cubic structures or compact clusters thereof, while those larger than D_{em} = 100 nm adopt irregular morphologies suggestive of agglomerates. As particle size increases from D_{em} = 100 nm to 400 nm, the NaCl and KCl particles become progressively more chain-like and agglomerated with a decrease in ρ_{eff} and an increase in χ. However, electron microscopy analysis of the salt particles is needed to verify the results of the DMA-CPMA-CPC measurements.

The fractal-like nature of the NaCl and KCl agglomerates can be further characterized by the mass-mobility exponent (ε_m) in the power law function (Equation (3-4)), which describes the relationship between particle mass (m_p) and electrical mobility diameter (D_{em}). The power law function was fit to the measured effective density data from D_{em} = 71.1 to 350 nm for NaCl and from D_{em} = 76 to 328 nm for KCl (solid lines in Figure 3.3). A coefficient of determination (R^2) of 0.89 and 0.92 for NaCl and KCl, respectively, indicates that the mass-mobility relationship for both salt types can be described well by the power law function.

The ε_m for NaCl and KCl were found to be 2.57 and 2.47, respectively. These values are within the range of mass-mobility exponents reported for agglomerates synthesized through different techniques, further demonstrating that the NaCl and KCl particles adopt an irregular, agglomerated structure beyond D_{em} = 100 nm. Previous studies indicate that the ε_m of soot particles generated from heavy-duty diesel engines, light-duty vehicles, premixed charge compression ignition combustion, and flame soot generators can vary from 2.2 to 2.56.[102,124,126,127,300,301] Leskinen et al.[289] found the ε_m of particles generated from small-scale combustion of different solid wood fuels to be in the range of 2.22 to 2.46. Shin et al.[287] reported a ε_m of 2.126 for silver agglomerates from D_{em} = 80 to 300 nm generated via evaporation-condensation of silver in a tube furnace. Charvet et al.[290] (2014) used a spark discharge generator to generate metal agglomerates with constantan, copper, graphite, iron, silver, and titanium, and found ε_m for these agglomerates to be the range from 1.98 to 2.329.

The size-resolved ρ_{eff} of NaCl and KCl particles generated by the thermal generator show a slightly different pattern from those measured in urban atmospheric environments. The average ρ_{eff} of NaCl and KCl particles between D_{em} = 30 to 100 nm are greater than those reported for urban aerosols in the same size range, which are typically between 1.14 to 1.58 g/cm^3.[56,57,63–66] The average ρ_{eff} for NaCl and KCl particles in this size range are similar to that of H_2SO_4, $(NH_4)_2SO_4$,

and NH_4NO_3 (approximately 1.7 to 1.83 g/cm^3), which are common inorganic components of urban aerosols.[72,89–92] However, they are greater than those measured for organic aerosols and soot particles from vehicle exhaust.[85–88,124,128]

NaCl and KCl particles between D_{em} = 100 to 220 nm exhibit ρ_{eff} values close to that reported for urban aerosols, while those greater than D_{em} = 250 nm present lower ρ_{eff} values than urban aerosols. The decrease in NaCl and KCl ρ_{eff} with increasing particle size is similar to the pattern observed for urban aerosol ρ_{eff} measured in near-traffic environments due to the existence of soot particles, which adopt a fractal-like morphology for D_{em} > 100 nm.[62] Geller et al.[63] found the urban aerosol ρ_{eff} measured at a freeway to be 1.13 g/cm^3 at D_{em} = 50 nm and 0.31 g/cm^3 at D_{em} = 414 nm, with a mass-mobility exponent of 2.54, which is similar to the mass-mobility exponents of NaCl and KCl particles produced by the thermal generator.

A comparison of size-resolved ρ_{eff} of NaCl and KCl particles with those reported for indoor aerosols is constrained by the limited number of direct ρ_{eff} measurements for indoor aerosols. The ρ_{eff} of cigarette smoke can vary between 1.18 to 1.51 g/cm^3, which can be influenced by smoke mass, cigarette format, filter type, and mouth hold period.[302,303] It is suggested that the ρ_{eff} is independent of particle size, indicating that cigarette smoke particles likely adopt a spherical shape. The aerosol from secondhand smoke of waterpipe tobacco was reported to adopt a mass-mobility exponent of 2.85 with a ρ_{eff} of 1.25 g/cm^3 at D_{em} = 80 nm and 0.98 g/cm^3 at D_{em} = 400 nm.[304] The ρ_{eff} of several indoor aerosol sources were calculated by Vu et al.[305]. Vacuum cleaning, kitchen cleaning, and tobacco smoking were found to generate aerosols with ρ_{eff} values of 1.16, 0.88, and 1.56 g/cm^3, respectively.

3.4.2 Number and Mass Size Distributions of Salt Aerosol Produced by the Thermal Aerosol Generator

Figures 3.5-3.8 present the normalized mean number and mass PSDs of NaCl and KCl particles produced by the thermal aerosol generator for different salt stick feed rates (3, 5, 10, 18, and 25 mm/min) and diameters (10 and 12 mm). Number PSDs as measured by the SMPS (D_{em}-based) and ELPI+ (D_a-based) are presented, along with D_{em}-based mass PSDs estimated from the ELPI+ number PSDs (D_a transformed to D_{em}) and size-resolved effective densities. The measured PSDs are fitted to the multi-lognormal distribution function and function parameters are included for each mode: $Mode_i$ = modal diameter (nm), σ_i = geometric standard deviation (–), and N_i or M_i = normalized number or mass amplitude, respectively (–).

The shape of the normalized mean number PSDs as measured by the SMPS (D_{em}-based) and ELPI+ (D_a-based) agree well across all experimental conditions. In general, the number PSDs for NaCl and KCl particles are unimodal and exhibit a single prominent peak is the sub-micron size fraction (≤ 1,000 nm), with a significant number of particles in the ultrafine particle (UFP) size fraction (≤ 100 nm). The shape of the NaCl and KCl number PSDs at a feed rate of 3 mm/min is similar to those reported in outdoor (urban) environments in European and North American cities, as well as number PSDs reported indoors under a variety of conditions.[7,28–30] The shape of the number PSDs at feed rates from 5 to 25 mm/min are similar to those reported in cities in China and India, where the number PSDs include a significant contribution from the accumulation mode.[213,231] The width of the prominent peaks of the number PSDs are relatively narrow, with geometric standard deviations of individual modes often between 1.4 and 1.7. A partial secondary peak tends to appear below D_{em} ~ 20 nm. This peak is unlikely to be associated with salt particles formed via evaporation-condensation, but rather particles formed by the O_2-C_3H_8 flame itself. The mixing ratio of the pre-mixed O_2-C_3H_8 is near, but does not reach, the fuel-lean condition. Particles in this secondary peak could include soot precursors or organic carbon. Previous studies suggest that under high temperature, small hydrocarbons (e.g. C_3H_8) can undergo a series of chemical reactions, including dehydrogenation, polymerization, cyclization, and radical chain reactions, to form larger polycyclic aromatic hydrocarbons (PAHs) or even soot nuclei within the flame.[306–310]

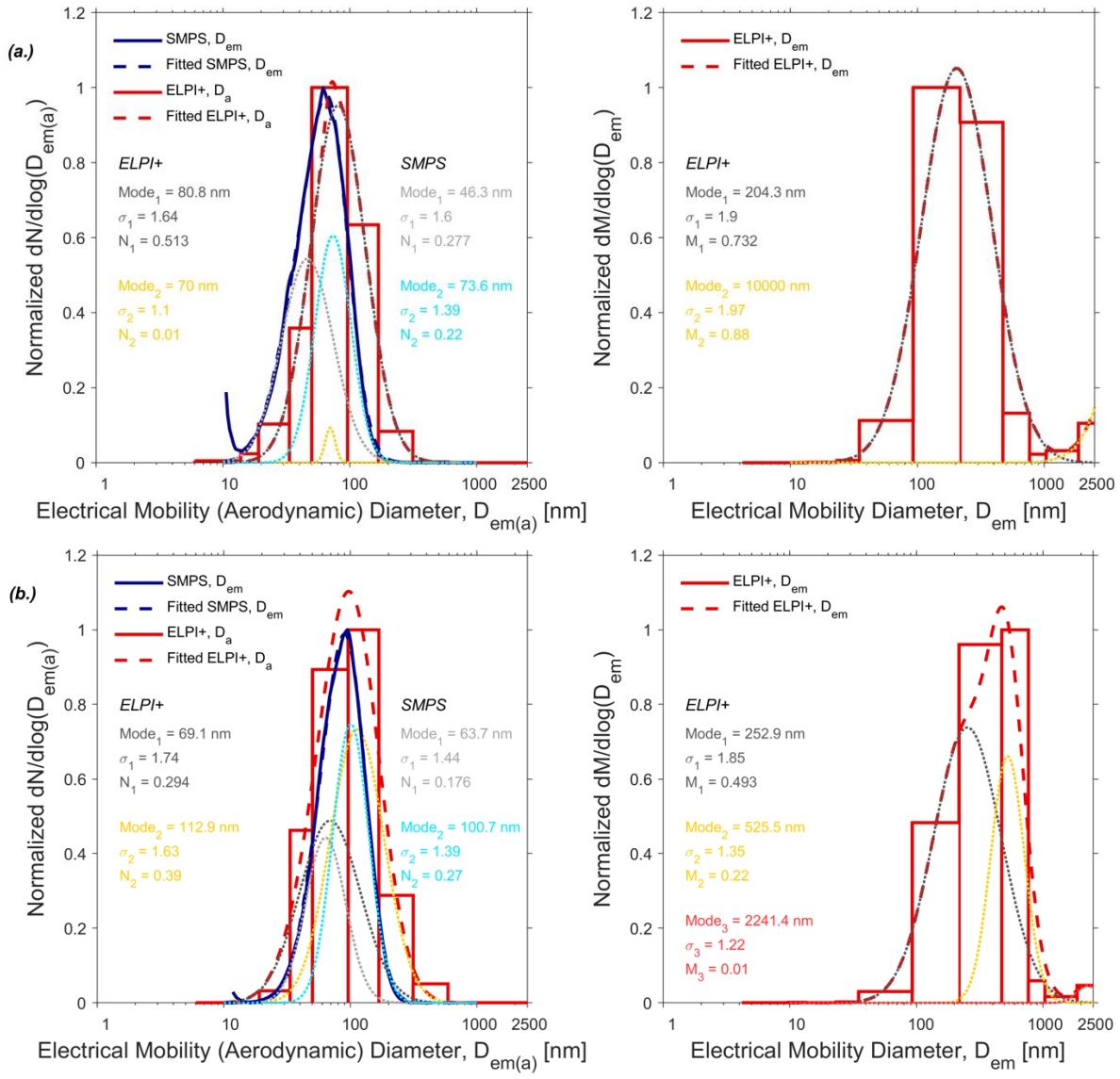

Figure 3.5 Normalized mean number (left) and mass (right) particle size distributions (PSDs) of NaCl particles generated by salt sticks with a diameter of 10 mm at feed rates of: (a.) 3 mm/min, (b.) 5 mm/min, (c.) 10 mm/min, and (d.) 18 mm/min. The solid blue lines represent the PSDs measured by the SMPS (number: D_{em}-based) and the red bar plots represent those measured by the ELPI+ (number: D_a-based, mass: D_{em}-based). The dashed lines represent the fitted multi-lognormal distribution functions (blue: SMPS, red: ELPI+) and the dotted lines represent the individual modes. The multi-lognormal distribution function parameters for each mode are listed on the side: $Mode_i$ = modal diameter (nm), σ_i = geometric standard deviation (–), and N_i or M_i = normalized number or mass amplitude, respectively (–). The NaCl PSDs for the feed rate of 25 mm/min are not presented since the salt stick clogged the nozzle of the thermal aerosol generation during the experiment.

Figure 3.5 continued.

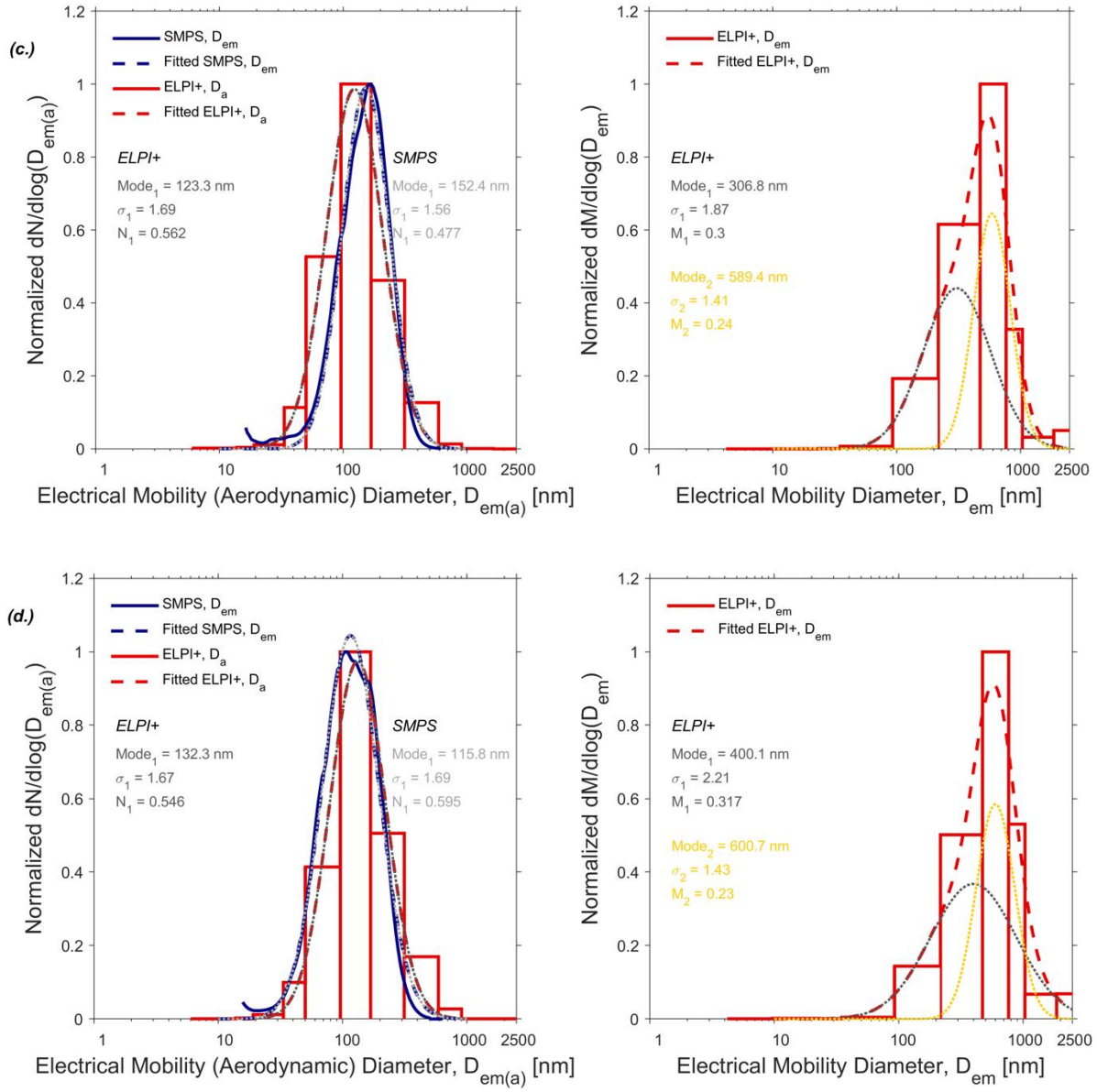

The normalized mean mass PSDs are typically unimodal and present a dominant peak in the accumulation mode (100 to 2,500 nm) across all operating conditions of the thermal aerosol generator. The mass PSDs in the sub-micron fraction are representative of those found in outdoor (urban) and indoor environments (Tronville and Rivers 2005; Seinfeld and Pandis 2012; Azimi et al. 2014; Stephens 2018; Fazli et al. 2019). The mass PSDs tend to be wider compared to the number PSDs. This can be discerned through the geometric standard deviations of individual modes, which often exceed 1.7 for the mass PSDs. A partial secondary peak in the mass PSDs can be found at approximately 2,500 nm. This peak may be associated with residual MgO ash

particles blown off the salt stick by the high-velocity O_2-C_3H_8 flow. Collection of the synthesized particles on filter substrates and subsequent electron microscopy analysis can verify the existence of the MgO ash particles.

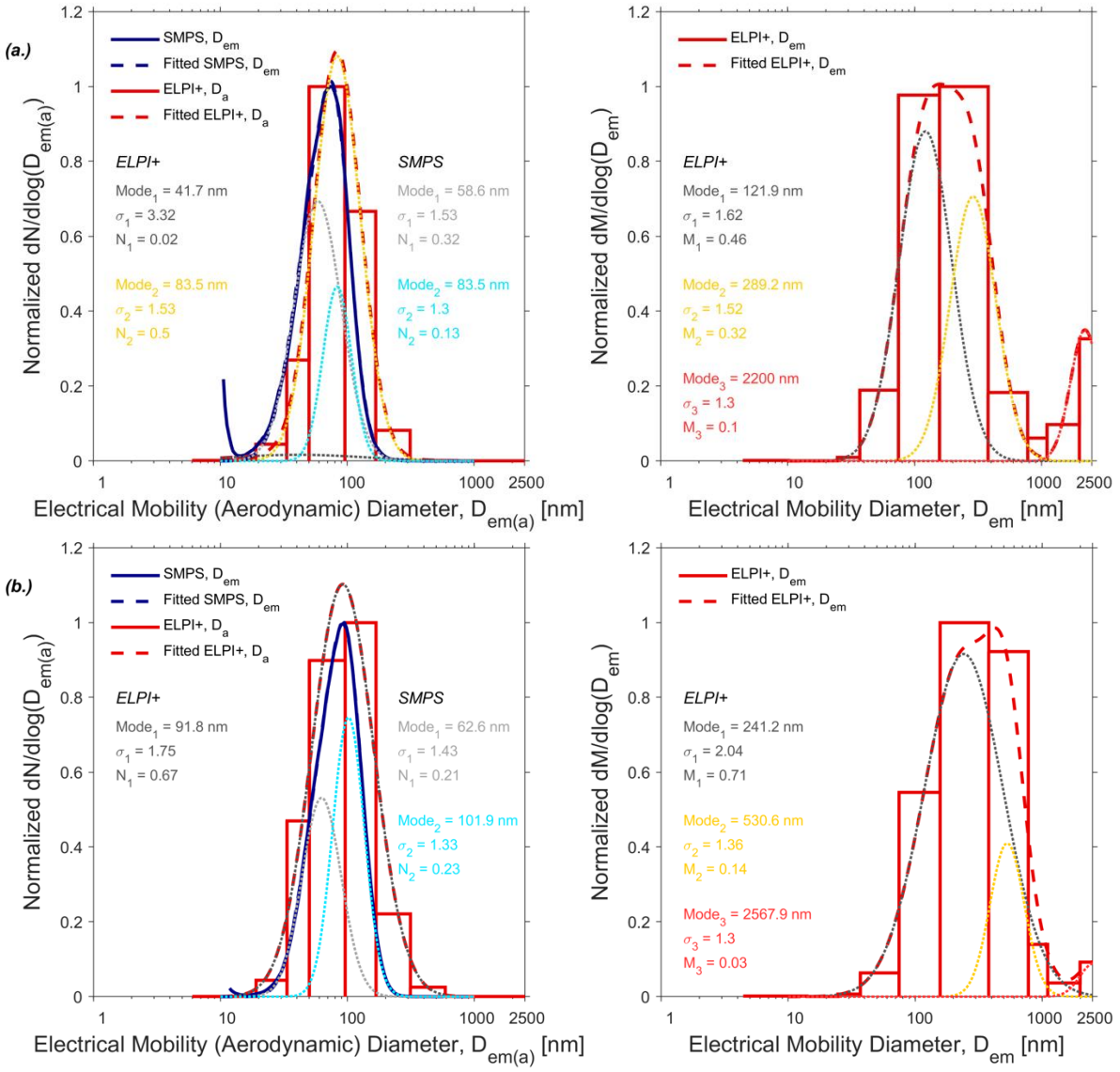

Figure 3.6 Normalized mean number (left) and mass (right) particle size distributions (PSDs) of KCl particles generated by salt sticks with a diameter of 10 mm at feed rates of: (a.) 3 mm/min, (b.) 5 mm/min, (c.) 10 mm/min, (d.) 18 mm/min, and (e.) 25 mm/min. The solid blue lines represent the PSDs measured by the SMPS (number: D_{em}-based) and the red bar plots represent those measured by the ELPI+ (number: D_a-based, mass: D_{em}-based). The dashed lines represent the fitted multi-lognormal distribution functions (blue: SMPS, red: ELPI+) and the dotted lines represent the individual modes. The multi-lognormal distribution function parameters for each mode are listed on the side: $Mode_i$ = modal diameter (nm), σ_i = geometric standard deviation (–), and N_i or M_i = normalized number or mass amplitude, respectively (–).

Figure 3.6 continued.

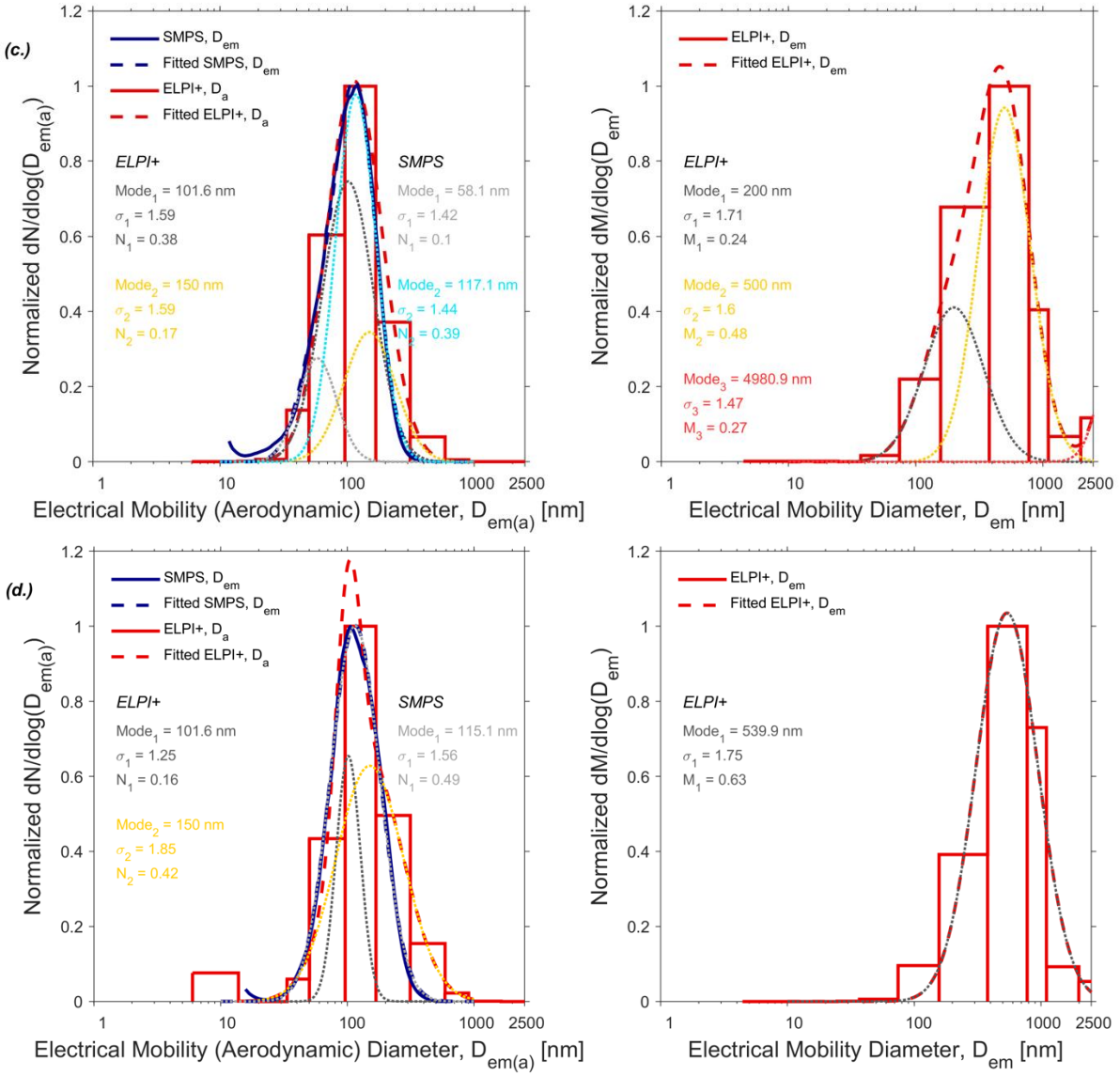

Figure 3.6 continued.

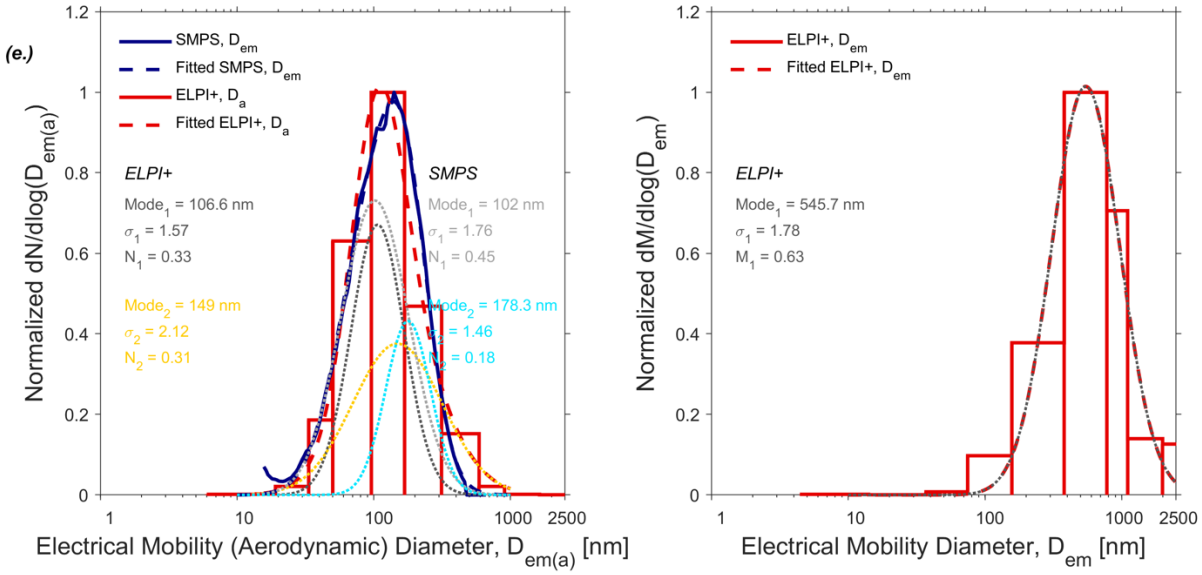

The salt stick feed rate has the most significant influence on the shape of the PSDs among the three thermal aerosol generator operational factors that were evaluated (salt type, feed rate, and stick diameter). For both salt types and stick diameters, the prominent peaks of the number PSDs shift to larger particle sizes as the salt stick feed rate increases. For example, the diameter of the prominent peak of the normalized mean number PSDs of KCl particles generated by the 10 mm sticks is ~80 nm for a feed rate of 3 mm/min, ~90 nm for a feed rate of 5 mm/min, ~115 nm for feed rates of 10 and 18 mm/min, and ~140 nm for a feed rate of 25 mm/min (Figure 3.6). A gradual shift in the normalized mass PSDs with increasing feed rate is also observed for both salt types and stick diameters. For example, for KCl particles generated with 10 mm sticks, the prominent peak of the normalized mass PSDs shifts from ~200 nm to ~550 nm as the feed rate increases from 3 to 25 mm/min (Figure 3.6). The multi-lognormal fitting of each mass PSD demonstrates that the modal diameters of each individual mode also increase with the feed rate. The shift of the number and mass PSDs to larger particle size fractions with the increase in feed rate indicates that the salt particles are generally larger at higher feed rates. A possible explanation for this shift is that greater quantities of salt vapor are produced at higher feed rates which can aid condensational growth of the particles to larger sizes.

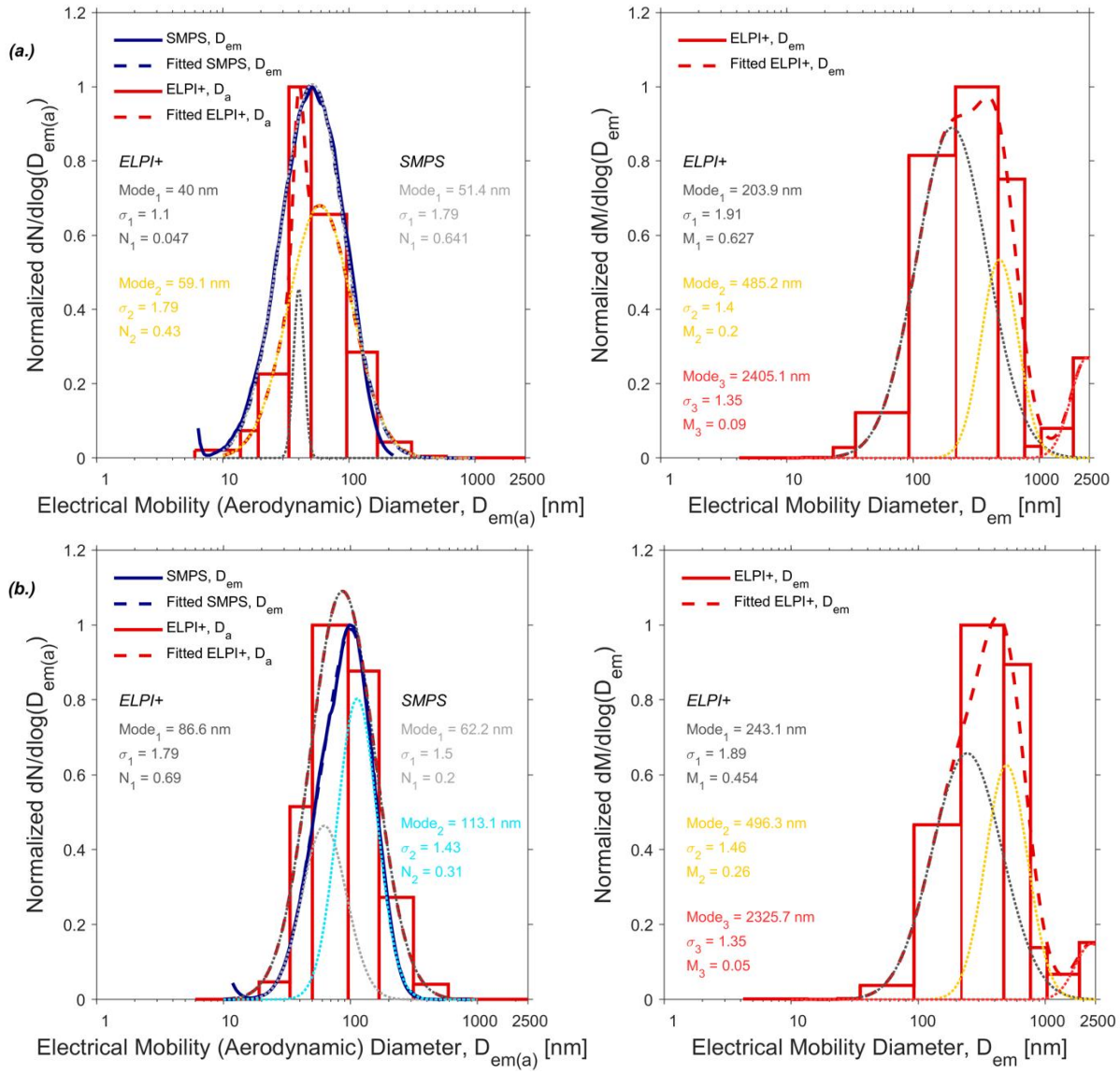

Figure 3.7 Normalized mean number (left) and mass (right) particle size distributions (PSDs) of NaCl particles generated by salt sticks with a diameter of 12 mm at feed rates of: (a.) 3 mm/min, (b.) 5 mm/min, (c.) 10 mm/min, (d.) 18 mm/min, and (e.) 25 mm/min. The solid blue lines represent the PSDs measured by the SMPS (number: D_{em}-based) and the red bar plots represent those measured by the ELPI+ (number: D_a-based, mass: D_{em}-based). The dashed lines represent the fitted multi-lognormal distribution functions (blue: SMPS, red: ELPI+) and the dotted lines represent the individual modes. The multi-lognormal distribution function parameters for each mode are listed on the side: $Mode_i$ = modal diameter (nm), σ_i = geometric standard deviation (–), and N_i or M_i = normalized number or mass amplitude, respectively (–).

Figure 3.7 continued.

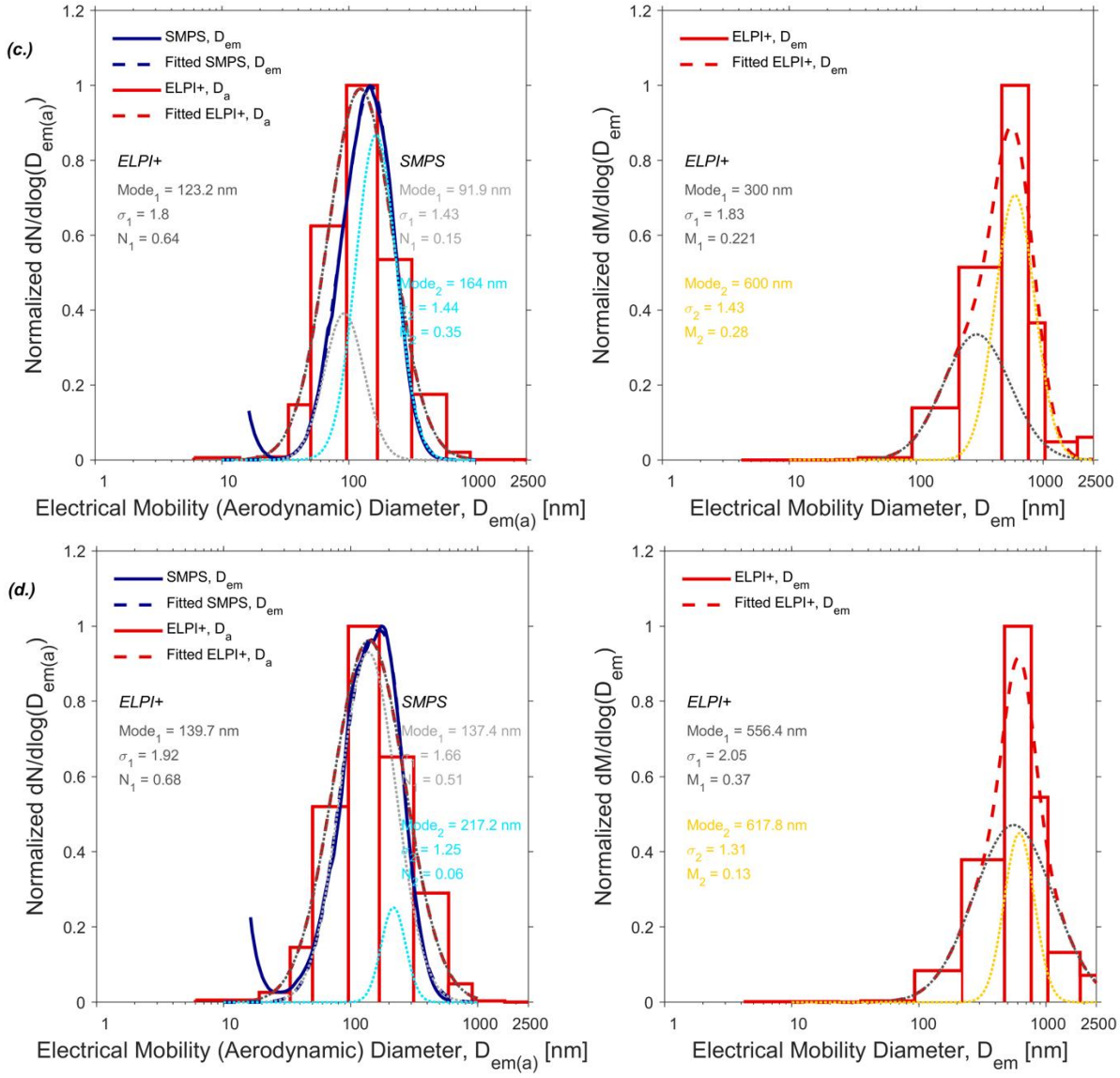

Figure 3.7 continued.

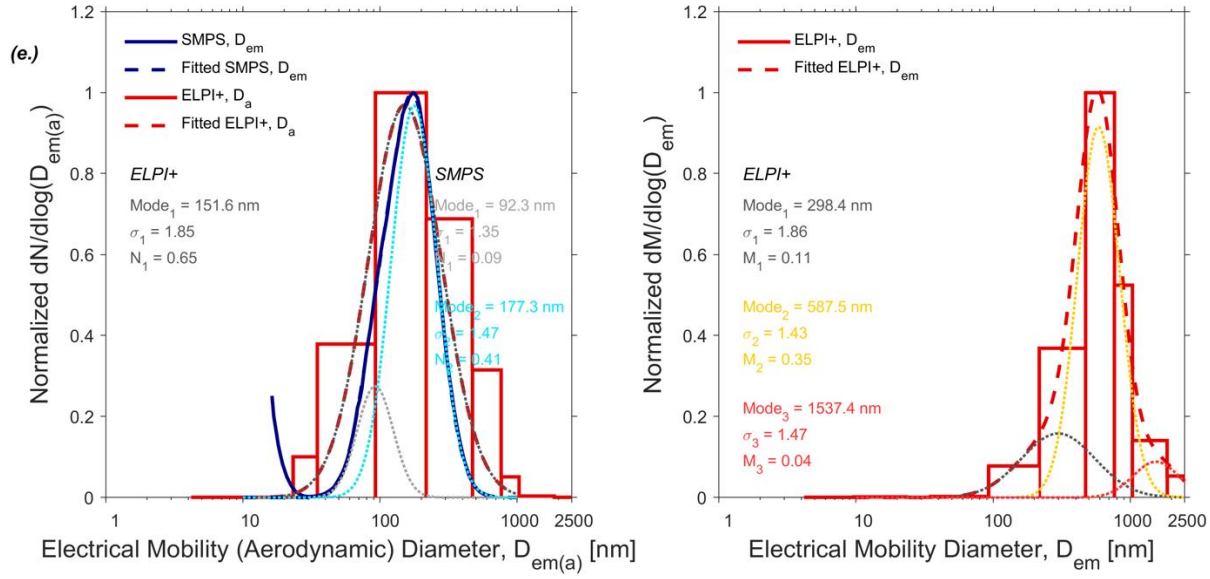

The shape of the number and mass PSD output of the thermal aerosol generator is not strongly influenced by the salt stick diameter and salt type. The 10 and 12 mm sticks produce similar normalized mean number and mass PSDs for both NaCl and KCl, with only small variations observed in the location of the prominent peak and the modal diameters of individual modes for a given feed rate. For the same salt stick diameter and feed rate, the normalized mean number PSDs of NaCl and KCl particles are very similar. However, the KCl mass PSDs exhibit a larger shift with increasing feed rate compared to the NaCl particles. For example, the prominent peak of the normalized mass PSDs for KCl particles (12 mm sticks) increases from ~170 nm at 3 mm/min to ~700 nm at 25 mm/min (Figure 3.8), whereas for NaCl (12 mm sticks), the peak increases from ~350 nm at 3 mm/min to ~590 nm at 25 mm/min (Figure 3.7).

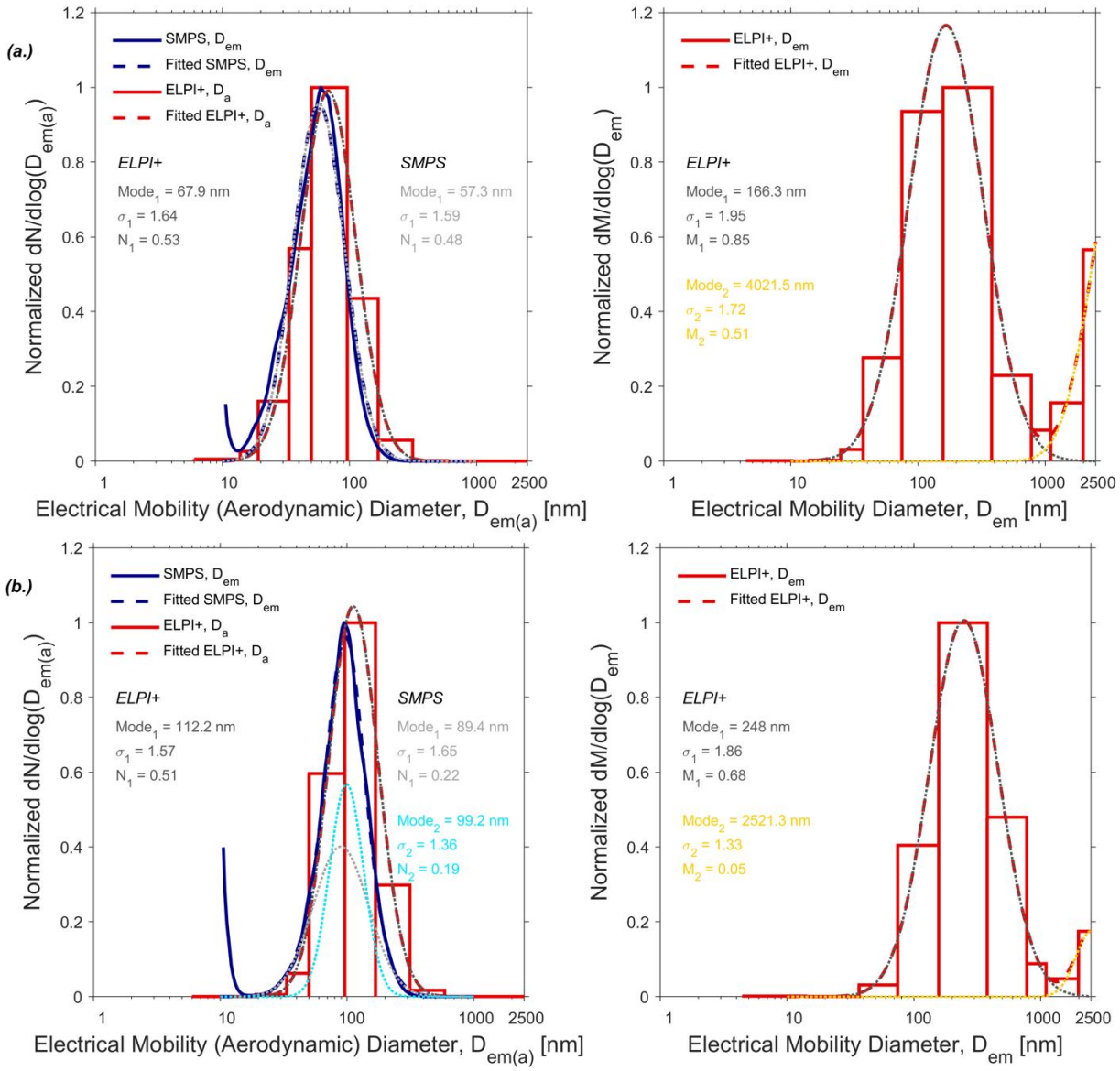

Figure 3.8 Normalized mean number (left) and mass (right) particle size distributions (PSDs) of KCl particles generated by salt sticks with a diameter of 12 mm at feed rates of: (a.) 3 mm/min, (b.) 5 mm/min, (c.) 10 mm/min, (d.) 18 mm/min, and (e.) 25 mm/min. The solid blue lines represent the PSDs measured by the SMPS (number: D_{em}-based) and the red bar plots represent those measured by the ELPI+ (number: D_a-based, mass: D_{em}-based). The dashed lines represent the fitted multi-lognormal distribution functions (blue: SMPS, red: ELPI+) and the dotted lines represent the individual modes. The multi-lognormal distribution function parameters for each mode are listed on the side: $Mode_i$ = modal diameter (nm), σ_i = geometric standard deviation (–), and N_i or M_i = normalized number or mass amplitude, respectively (–).

Figure 3.8 continued.

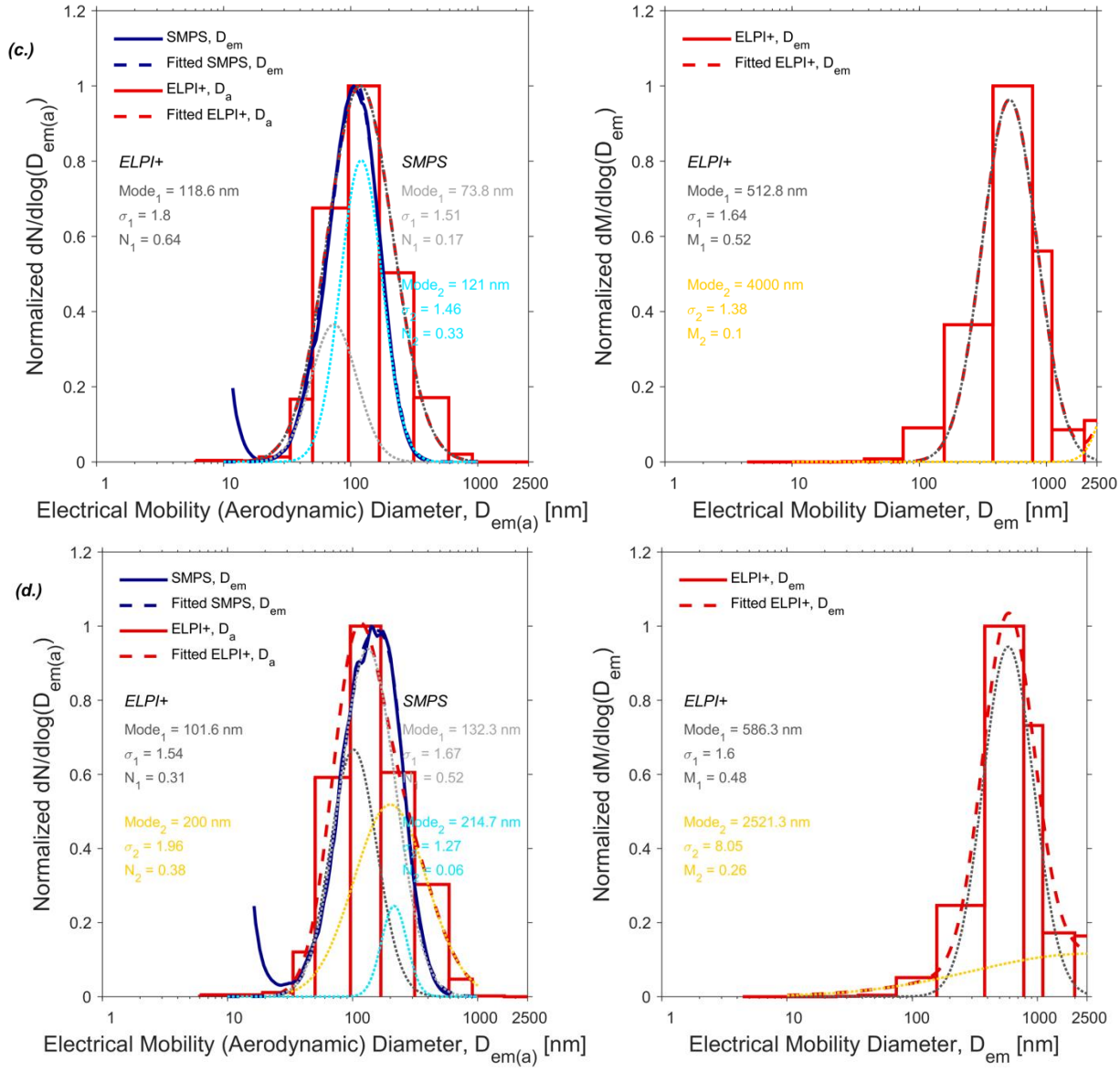

Figure 3.8 continued.

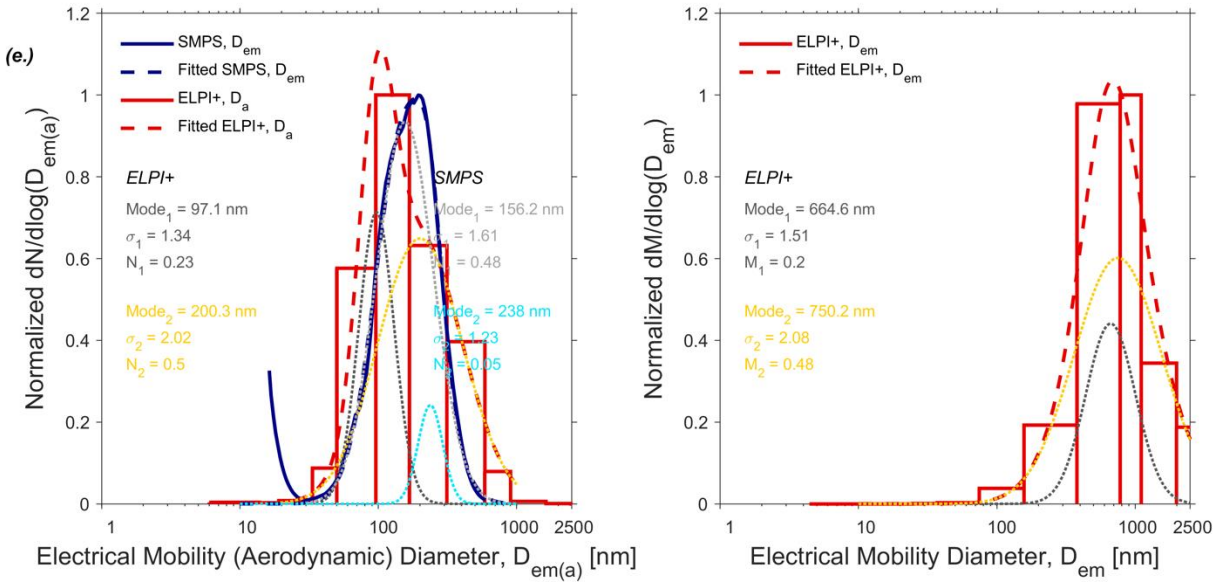

The thermal aerosol generator produces a stable PSD output of sub-micron NaCl and KCl particles. Figure 3.9 shows example time-series plots of D_a-based number PSDs as measured by the ELPI+ with a sampling interval of 1 second and D_{em}-based number PSDs as measured by the SMPS with a scan period of 70 seconds, both for NaCl particles generated by a salt stick with a diameter of 10 mm at a feed rate of 5 mm/min. The number PSDs are relatively stable over the measurement period of 30 minutes. This is especially true for the PSD measurements made with the ELPI+. More pronounced temporal variations are observed in the SMPS measurements as an artifact of the longer scan period. A high concentration of NaCl particles can be found across the size range from ~30 to ~300 nm, which is consistent with the normalized mean number PSDs (Figure 3.5b). A clear peak is observed at ~100 nm in the number PSDs measured by both the ELPI+ and SMPS.

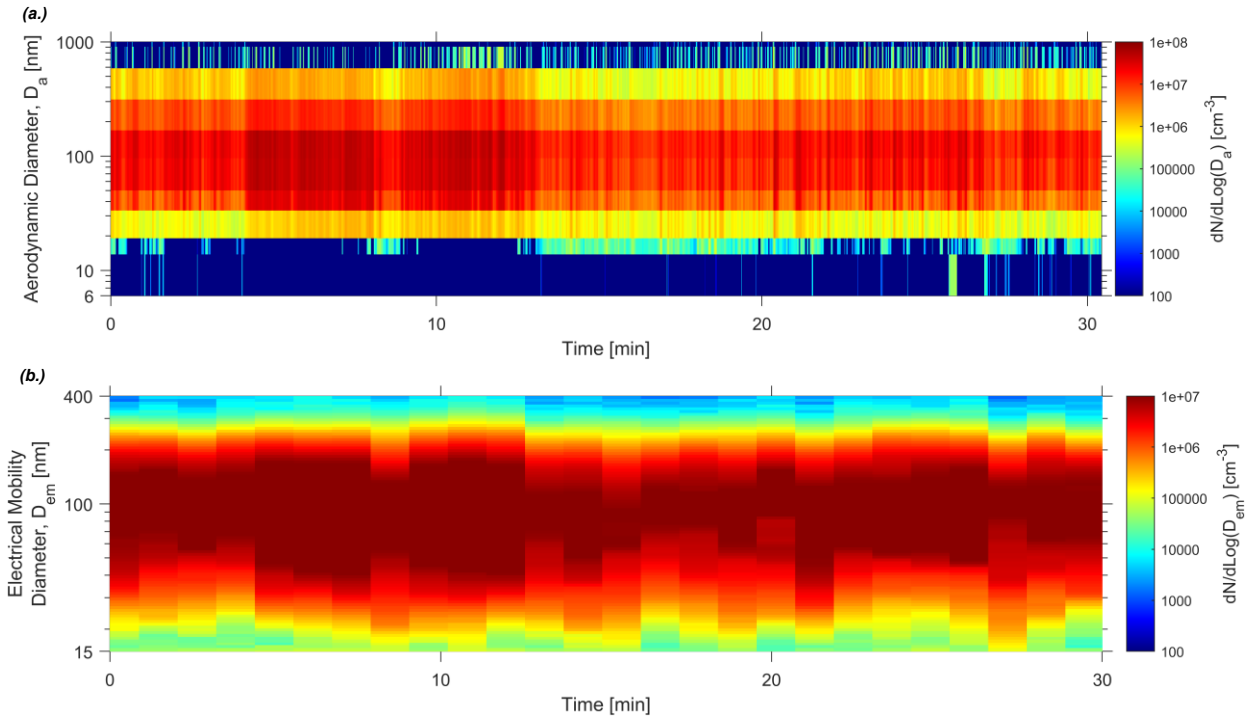

Figure 3.9 Time-series plots of (a.) D_a-based (ELPI+: sampling interval of 1 second) and (b.) D_{em}-based (SMPS: scan period of 70 seconds) number particle size distributions of NaCl particles generated by a salt stick with a diameter of 10 mm at a feed rate of 5 mm/min.

3.4.3 Mass Production Rates of Salt Aerosol Produced by the Thermal Aerosol Generator

The thermal aerosol generator is intended to be used for HVAC filtration experiments to evaluate filter mass loading curves, defined as the relationship between the filter pressure drop and loaded particle mass per unit filter area. As such, the mass production rate of the thermal aerosol generator at different operational conditions is an important parameter to be characterized. Figure 3.10 presents estimated nominal mass production rates as the product of the salt stick feed rate and the effective content (salt mass per unit length), assuming the entirety of the salt is vaporized and condensed to form particles. Nominal mass production rates ranged from 18 to 207 g/h, depending on the salt type, feed rate, and stick diameter. The production rate is most sensitive to the feed rate.

The nominal mass production rates are likely to be overestimates of the actual production rates. The entirety of the salt mass may not get fully vaporized in the O_2-C_3H_8 flame and some of the non-vaporized salts may fall with MgO as ash. Actual production rates derived from the PSD measurements and a material balance model could not be determined due to uncertainties in

characterization of the airflow regime within the fume hood where the thermal aerosol generator was housed. Delivery of the salt particles into a HVAC filtration test facility necessitates the design of a precisely controlled carrier flow system and evaluation of how the carrier flow system affects the transformation of the salt particles through coagulation and deposition. Such a system will enable accurate determination of the mass production rate.

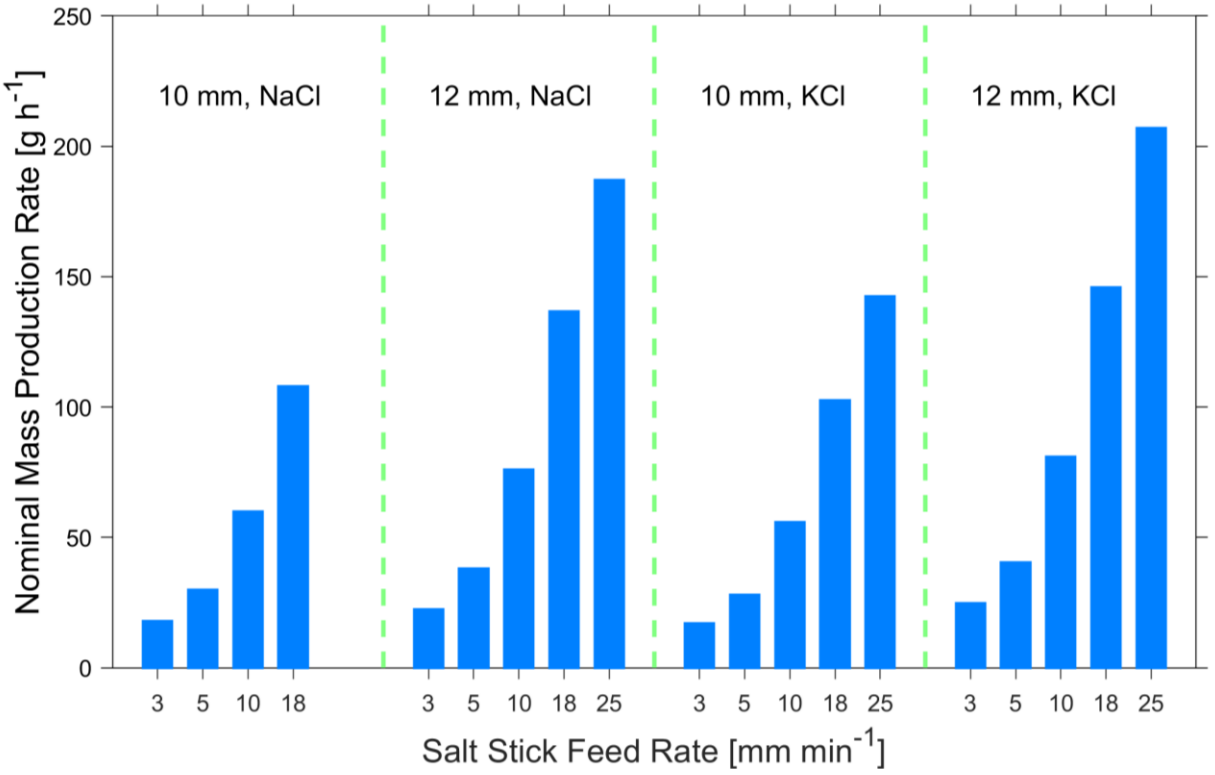

Figure 3.10 Nominal mass production rates of NaCl and KCl particles for both salt stick diameters (10 and 12 mm) as a function of the salt stick feed rate (3, 5, 10, 18, and 25 mm/min). The nominal mass production rates were calculated as the product of the salt stick feed rate and the effective content (salt mass per unit length), assuming the entirety of the salt is vaporized and condensed to form particles.

3.4.4 Measurement Uncertainties Due to Unipolar and Bi-Polar Charging of the Salt Aerosol

The morphological characterization of the salt aerosol demonstrated that NaCl and KCl particles larger than D_{em} = 100 nm adopt irregular morphologies suggestive of agglomerates. This may induce uncertainties in the unipolar charging of the particles in the ELPI+ (via a unipolar corona charger) and bi-polar charging of the particles in the SMPS (via a Kr-85 bi-polar charger).

The charging efficiency of the unipolar corona charger of the ELPI+ was calibrated with particles of a compact morphology. Previous studies indicate that agglomerates can carry more charges per particle than a sphere with the same D_{em} when passing through a unipolar corona charger. Thus, the particle number concentration measured by the ELPI+ may be overestimated. Shin et al.[311] found that the mean charge per particle for loose silver agglomerates is higher than that for coalesced spheres with the same D_{em} by 24% after unipolar corona charging. Ouf and Sillon[312] suggested that the corona charger of the ELPI could induce a higher charging efficiency for fractal soot particles compared to compact spherical or cubic particles by up to 25%. Oh et al.[313] indicated that titanium dioxide agglomerates could have about 30% more charges than sintered spherical particles using an indirect photoelectric charger. During the thermal aerosol generator PSD measurements, the concentrations of salt particles in the accumulation mode were likely overestimated relative to the UFPs as the particles became more agglomerated with the increase in size (Figure 3.3). Conversely, the concentrations of salt particles in the accumulation mode as measured by the SMPS may be underestimated. The SMPS employs a Kr-85 bi-polar diffusion charger. Maricq[314] found that the single positive and negative charging fraction of soot agglomerates is 15% and 10% lower, respectively, than oil droplets at a D_{em} = 400 nm. Since the salt particles are very likely agglomerates in the accumulation mode, the SMPS may underestimate the particle concentration due to low charging efficiency.

4. INFANT AND ADULT INHALATION EXPOSURE TO RESUSPENDED BIOLOGICAL PARTICULATE MATTER

4.1 Overview

This chapter presents a chamber study to evaluate infant and adult inhalation exposure and respiratory tract deposited dose rates (RTDDRs) of resuspended biological particulate matter (*bio*PM) from carpets. Locomotion in the form of crawling and walking were performed by a robotic infant and an adult volunteer, respectively. The transient breathing zone size distribution of fluorescent *bio*PM was monitored with a high time-resolution laser-induced fluorescence instrument to estimate the regional RTDDR for an infant and adult.

4.2 Introduction

Indoor dust is a large reservoir for microbial content. Indoor dust in urban homes includes an amazing diversity of bacteria and fungi, often dominated by gram-positive bacterial taxa and yeasts associated with the human skin and oral flora, such *Staphylococcus*, *Micrococcus*, *Streptococcus*, *Lactococcus*, *Corynebacterium*, and *Malassezia*, and fungi that are predominantly of outdoor origin.[315–318] Mite and animal allergen-carrying particles and pollen grains are also found in house dusts.[319,320] Dust collected from homes on small farms is different in its composition and typically more diverse compared to that in urban and rural residences. It can be heavily enriched with environmental bacteria, including *Acinetobacter sp.*, *Clostridium*, *Lactobacillus spp.*, and *Staphylococcus sciuri*, and animal allergens derived from livestock, fodder, and soil.[43,51] While these microbes come from the farm and animal sheds, much of the exposure is occurring indoors, where the *bio*PM is transported via building ventilation and tracked-in on clothing and shoes.[321,322]

Exposure to microbes and allergens can cause various adverse health effects. Exposure to bacterial endotoxin (lipopolysaccharides) is associated with increased asthma prevalence and wheezing.[41] Reponen et al.[323] identified specific fungal species as being strongly associated with the development of asthma and Dannemiller et al.[40] found increased asthma severity among atopic children to be associated with elevated concentrations of fungi in dust. High concentrations of airborne fungal spores have been positively correlated with frequency of asthmatic attacks and

certain fungal spores, such as those of *Aspergillus fumigatus*, and their allergenic proteins can damage epithelia cells and lead to respiratory infections.[37,39,324] Mite allergens, at certain dust concentrations, can lead to the development of mite sensitization, asthma, and allergic rhinitis[35,36,38]. Pollen grains of various plant species, such as ragweed and birch, are coated in allergenic proteins, inhalation of which can cause allergic reactions in a significant fraction asthmatic children and adults.[325–327]

On the other hand, protective health effects ("farm effect," "hygiene hypothesis") were found to be associated with exposure to environmental microbes and specific allergens have been identified in numerous studies. Early-life exposures to increased bacterial and fungal diversity and high indoor dust concentrations of bacterial and fungal cells; bacterial lipopolysaccharides and muramic acid; polysaccharides of fungi, pollen, and plants; and allergenic proteins of dust mites and animal dander have been linked to a reduced prevalence of asthma, atopy, wheeze, hay fever, and allergies later in life.[42–52] It has been hypothesized that a balanced population of beneficial microbes in the lower and upper airways may provide colonization resistance against pathogenic bacteria and fungi and that exposure to beneficial microbes during infancy may play a key role in shaping the evolution of the respiratory microbiota.[51,52,328–330]

Release of house dust into the air due to human movement-induced resuspension may represent a significant pathway by which we are exposed to the embedded *bio*PM. Resuspension is a major indoor source of coarse-mode (> 1 μm) abiotic and biological particulate matter (or *bio*PM), such as bacterial cells and fungal spores.[315,331–335] Simply walking across a carpet can release on the order of 10 to 100 million particles per minute.[53] Despite the health and environmental significance of indoor dust, which is widely used as a long-term inhalation exposure surrogate, we have a limited understanding of the relationship between particle resuspension induced by age-dependent forms of locomotion, such as crawling and walking, with the transient exposures and respiratory tract deposited doses of *bio*PM that are received by infants, children, and adults.

Resuspension is influenced by different forms of physical activity.[53,336] Evolution of human locomotion during the first year of life involves an array of complex near-floor movements that transition towards various forms of crawling at around 6 months and eventually to walking between 12 and 14 months.[337] Very little is known as to how the crawling motion of an infant

resuspends indoor dust and the resulting size distributions of resuspended *bio*PM an infant is exposed to in their near-floor microenvironment.[40,44,338]

Recent advances in DNA-based methods and laser-induced fluorescence (LIF) techniques for *bio*PM identification and quantification allow for improved *bio*PM exposure assessment beyond what can be achieved with traditional culture-based methods.[327] LIF-based aerosol instrumentation can be used to study the transport of resuspended *bio*PM to the infant and adult breathing zone (BZ) at the short time-scales of relevance to resuspension (e.g. seconds to minutes) and at high size-resolution. LIF techniques target the intrinsic biological fluorophores of bacterial cells, fungal spores, and pollen grains, such as amino acids (e.g. tryptophan, phenylalanine, and tyrosine), flavins, and co-enzymes (e.g. nicotinamide adenine dinucleotide (NADH)).[339] LIF can reliably detect and discriminate super-micron *bio*PM from abiotic particles and is generally viewed as a lower limit of total *bio*PM, or primary biological aerosol particles (PBAPs), as some *bio*PM exhibit little to no fluorescence.[339,340] Abiotic particles can fluoresce; however, non-biological interference is generally of concern for sub-micron particles.[339,341], as discussed in detail in Table 4.1. Particles whose fluorescence properties are within the excitation-emission operational range of a LIF-based instrument are registered as fluorescent biological aerosol particles, or FBAPs (Table 4.2). When integrated in tandem with quantitative PCR (qPCR) and next-generation sequencing (NGS), LIF is a valuable tool to advance knowledge on exposures to *bio*PM released from inherently episodic indoor emission sources, such as resuspension.

Table 4.1 List of possible non-microbial fluorescent interferents in the present study

Non-Microbial Fluorescent Interferents	Possible Origin in Carpet Dust of the Present Study	λ_{ex} (nm)	λ_{em} (nm)	Relevance to the Present Study
Polycyclic aromatic hydrocarbon-(PAH)-containing particles[339]	Combustion-generated aerosols, both indoors and outdoors of residence in which carpet was located.	230-390[339]	310-540[339]	While fluorescent, interference is primarily of concern for particles in the sub-micron range. We observed minimal concentrations of resuspended FBAPs < 1 μm, thus, this was not a relevant interferent.
Soot[339,342]	Combustion-generated aerosols from engines and biomass burning, can be transported from outdoors to indoors.	Unknown	Unknown	Previously detected by the WIBS as FBAPs[342], they are possibly present in the dust, but are unlikely to contribute significantly to coarse-mode resuspended FBAPs.
Secondary organic aerosol (SOA)[339]	Oxidation of volatile organic compounds (VOCs), both indoors and outdoors of residence in which carpet was located.	280-425[339]	360-490[339]	While fluorescent, interference is primarily of concern for particles in the sub-micron range. We observed minimal concentrations of resuspended FBAPs < 1 μm, thus, this was not a relevant interferent.
Humic-like substances (HULIS) associated with soil particles[339,342]	Tracked-in from outdoors on shoes and transferred to carpet via contact transfer.	230-500[339]	350-600[339]	Most HULIS and mineral dust exhibit low fluorescence intensity and may not cause significant interference with fluorescent *bio*PM[339], while certain types of mineral dusts and HULIS present high fluorescence intensity[342]. They are likely present in indoor dust to varying extents and may contribute to the resuspended FBAPs reported in the present study. It is also possible that resuspended soil and mineral particles may act as carriers for *bio*PM, making them fluorescent.
Mineral dust[339,342]				

Table 4.1 continued.

Squames (skin cells and cell fragments)[343]	Desquamation by humans and pets living in residence in which carpet was located.	Range, depending on protein, co-enzyme, or skin pigment[343]	Range, depending on protein, co-enzyme, or skin pigment[343]	Squames are the most likely non-microbial interferent that may bias the resuspended FBAP data reported in the present study. Skin cells can contain fluorescing proteins, co-enzymes, and skin pigments.[343] However, as >90% of skin fragments are larger than 10 μm in size[344], the interference will predominately affect concentrations of the super-10 μm FBAPs. Squames can also serve as carriers of skin-associated bacteria[338] and may agglomerate with *bio*PM in dust deposits, making them fluorescent.
Particles from clothing fabrics[342]	Clothing and carpet fibers that have accumulated in dust deposit.	Unknown	Unknown	Particles from clothing fabric have been detected by the WIBS as FBAPs in previous measurements.[342] These particles and carpet/fabric fibers containing fluorescent whitening agents may exist in indoor dust and resuspend. However, given the high fraction of bacterial and fungal cells detected in our carpet dust samples (Table 4.3, Figure 4.11), it is likely they did not significantly bias the FBAP data.
Coloring and fluorescent whitening agents in fabric fibers and detergent residue[342,345–347]				
Dust mite and animal allergen-carrying particles	Mites in carpet dust and animal dander.	Unknown	Unknown	Both can be associated with sub-10 μm particles[319] and may have been detected as FBAPs, but their fluorescent properties are presently unknown.

Table 4.2 Comparison of operational parameters of three LIF-based aerosol instruments

LIF-Based Aerosol Instrument	Particle Size Range	Excitation Wavelength (λ_{ex}, nm)	Emission Wavelength (λ_{em}, nm)
BioScout, Environics Ltd.[340] (used in present study)	0.4-15.4 μm	405	> 442
WIBS-NEO, DMT Inc.	0.5-50 μm	280, 370	310-400, 420-650
UV-APS, TSI Inc.[340]	0.5-20 μm	355	430-580

Inhalation exposure to resuspended *bio*PM can be better linked to cellular response in the lungs and respiratory and allergic health outcomes in infants and adults through size-resolved respiratory tract deposited dose rate (RTDDR) analysis.[348] The number, surface area, and mass of particles deposited in each region of the respiratory system per unit time are determined through integration of respiratory tract deposition fractions and BZ particle size distributions. Few studies have reported RTDDRs[116,117,349–354] and it has yet to be used for *bio*PM measurements made *in situ* in the infant and adult BZ or for assessing exposure to indoor dust. This is in part due to the difficulty of measuring BZ particle size distributions with heavy aerosol instrumentation, especially for infants and young children. More broadly, empirically-based doses and uptake rates for environmental stressors as determined for infant-specific physiologies, in this case, the respiratory system and crawling posture, are needed to elucidate the key factors affecting health during the most critical stages of human development.[355]

The primary aim of this study is to mechanistically link infant crawling-induced and adult walking-induced resuspension of carpet dust with transient *bio*PM exposure and regional deposited dose rate analysis via application of real-time (1 Hz) LIF monitoring of FBAPs in the infant and adult BZ in controlled chamber experiments. This study makes unique use of a custom-built simplified mechanical crawling infant to measure resuspended FBAP size distributions in the infant BZ during crawling. Here, FBAPs are viewed as a proxy for total *bio*PM, supplemented with off-line qPCR and NGS analysis.

4.3 Materials and Methods

4.3.1 Experimental design

Resuspension experiments were conducted in an environmentally controlled chamber with a volume of 81.4 m^3 (Figures 4.2-4.4) at the Finnish Institute of Occupational Health (FIOH) in Helsinki, Finland from January to March 2015. The walls and floor of the chamber were made of stainless steel and glass. The supply air was filtered with both HEPA and activated carbon filters (Camfil Farr) and the chamber was maintained at a slight positive pressure. Two fans, positioned in opposite corners of the chamber, were used to aid in the mixing of the bulk air (a Philips type HR 3270/B 28W and a Domesto Mod. Gliding Grille, Art.-Nr.: 16401 80). The chamber air exchange rate was 0.66 h^{-1}, as determined by a sulfur hexafluoride (SF_6) tracer gas decay with a multi-gas monitor (Type 1302, Brüel and Kjær). Chamber air temperature and relative humidity (RH) were measured with a HOBO sensor and data logger (HOBO U12-012, Onset Computer Corp., Bourne, MA, USA) and were 23.11±0.77°C and 23.89±4.77% (mean ± s.d.) during the entire measurement campaign.

Five carpets borrowed from residents in Helsinki, Finland were used in the resuspension experiments and tested as-is (Table 4.3, Figure 4.1). The residents were asked to refrain from vacuuming their carpets for two weeks. Carpets were carefully folded at the residence, maintaining contact among the upward facing surface, and then carefully transported to FIOH.

Each carpet was divided into five paths across its width, with each path being 34 cm wide. Depending on the overall width of the carpet, there was some overlap among the paths. For each path on each carpet, one crawling and one walking resuspension experiment, 45-minutes in duration, were conducted, for a total of fifty individual experiments. Each resuspension experiment consisted of three periods: (1.) a 10-minute background period in which the chamber was vacant, (2.) a 20-minute crawling- or walking-induced resuspension period, and (3.) a 15-minute decay period in which the chamber was vacant (Figure 4.7).

Table 4.3 Summary of tested carpets and dust deposits

Carpet ID	Residence & Location	Location of Carpet in Residence	Carpet *l* x *w* (m)	Carpet Material	Carpet Type	No. Occup.	No. Pets	Dust Load (g/m^2)*	Total Surface Number Concen. > 1 μm ($\#/m^2$)**	Gram + Bacterial Concen. in Dust (CE/m^2)***	Gram - Bacterial Concen. in Dust (CE/m^2)***	Total Fungal Concen. in Dust (CE/m^2)****	Total Bacterial & Fungal Concen. in Dust (CE/m^2)***
1	R1, Helsinki	Bedroom	2.32x 1.73	Wool	Finnish Woven	2	1, cat	2.79	2.28×10^9	1.01×10^9	1.85×10^8	8.55×10^6	1.20×10^9
2	R2, Helsinki	Living Room	2 x 1.4	50% Wool, 50% Sisal	Jute	4	0	16.72	7.30×10^9	1.91×10^9	1.16×10^9	3.87×10^7	3.11×10^9
3	R1, Helsinki	Corridor	1.95 x 1.33	Worsted Wool	Knotted, Pile-Woven	2	1, cat	5.26	5.34×10^9	7.00×10^8	1.99×10^8	3.88×10^6	9.03×10^8
4	R3, Helsinki	Living Room	1.44 x 1.3	Cotton	Jute	2	0	2.63	1.06×10^9	3.40×10^8	1.49×10^8	2.54×10^7	5.15×10^8
5	R4, Helsinki	Living Room	2.33 x 1.6	Wool	Knotted, Pile-Woven	1	0	4.52	2.53×10^{10}	2.17×10^8	2.00×10^8	1.94×10^7	4.37×10^8

A simplified robotic infant performing a modified belly crawl was used to simulate the crawling locomotion of an infant in a repeatable manner (mass: 4 kg, contact area: 25 cm^2 per hand + 325 cm^2 for lower torso, hand contact frequency: 200 min^{-1}). The robot utilized two high torque servo motors controlled by a microcontroller to simulate the crawling motion of the arms and for forward propulsion. The exterior of the robot was lined with grounded aluminum tape to minimize the accumulation of electrostatic surface charge and was wiped with isopropyl alcohol after each experiment. The walking experiments were conducted by an adult male volunteer wearing a full clean suit outfit with booties and a hood (DuPont™, Tyvek Pro-Tech Suit Classic), nitrile gloves, and a filter mask to minimize particle emissions from the human envelope (mass: 80 kg, height: 188 cm, contact area: 160 cm^2 per foot, footfall contact frequency: 70 min^{-1}). The chamber floor was vacuumed and wiped with isopropyl alcohol after each set of experiments with a given carpet.

Figure 4.1 Photos of the five tested carpets, 1-5.

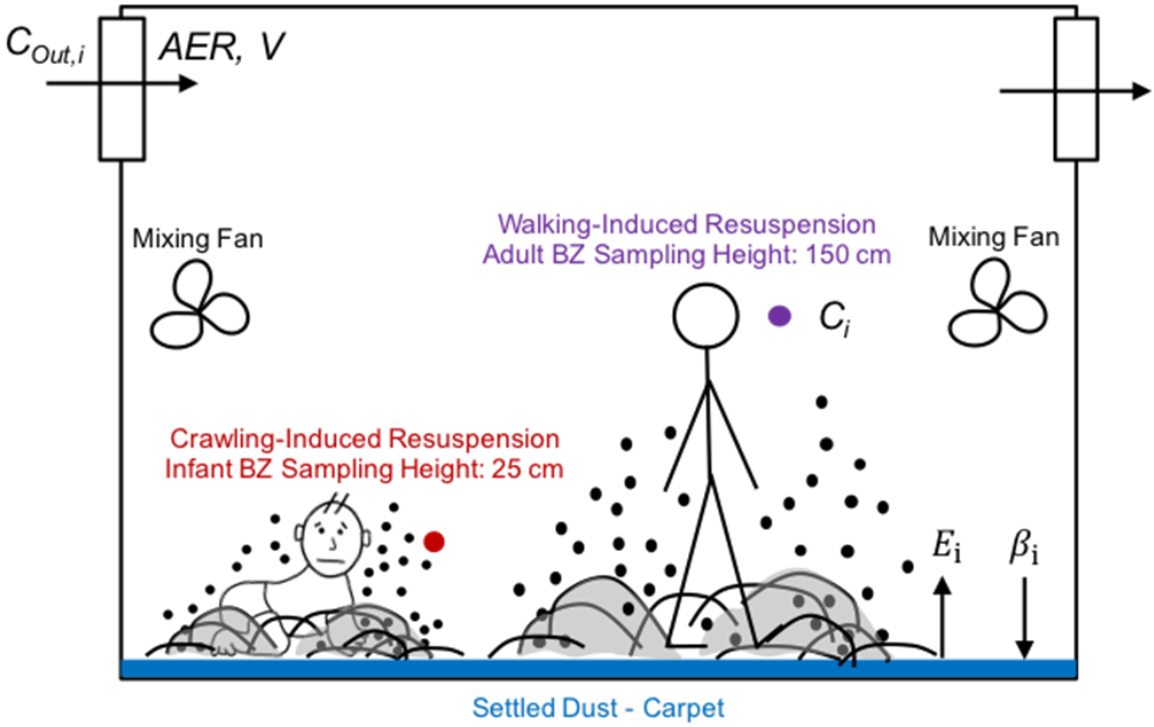

Figure 4.2 Schematic of chamber setup and material balance model parameters for estimating the size-resolved FBAP emission rates during adult walking resuspension events.

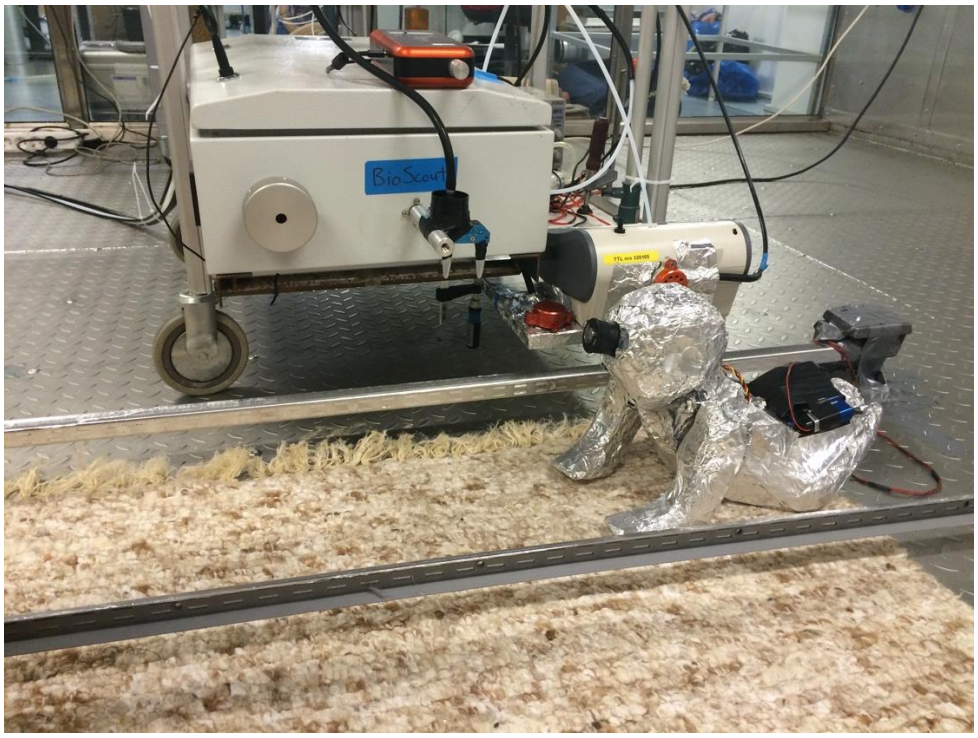

Figure 4.3 Photo of simplified mechanical crawling infant with mobile aerosol sampling (BioScout and OPS) on a mobile trolley in the infant breathing zone. Note: the OPS inlet was recessed 10 cm back from the crawling path.

Figure 4.4 Photo of chamber setup with aerosol sampling (BioScout and OPS) in the adult breathing zone.

4.3.2 Aerosol instrumentation

FBAP (N_F) and total (N_T) particle number size distributions (cm^{-3}) were monitored throughout each resuspension sequence with a LIF-based instrument – the BioScout (1 Hz sampling frequency, nominal sample flow: 2 L min^{-1}) (ENVI BioScout^{TM}, Environics Ltd., Mikkeli, Finland).[340,356,357] The BioScout uses a 200-mW laser diode that emits excitation light at a wavelength of 405 nm (Table 4.2). After the excitation light impinges on the particle, the scattered light is collected via a photomultiplier tube (PMT) to determine the particle size. The fluorescence emitted by the biological fluorophores in the particle are captured with another PMT and sorted into 16 fluorescence intensity channels. The particles recorded in fluorescence channels 2-16 were classified as FBAPs, with particles in channel 1 considered as non-fluorescent.[340,356,357] The operative size range was optimized between 0.4 and 15.4 μm based on laboratory calibration (16 size fractions). Total (N_T) particle number size distributions were also monitored with an optical particle sizer (nominal sample flow: 1.001 L min^{-1}) (OPS, model 3330, TSI Inc., Shoreview, MN, USA). The measurement size range was 0.314 to 11.2 μm (16 size fractions). As the BioScout data indicated that a significant fraction of the particles was likely of biological origin, a refractive index of 1.4 - 0.003i, representative of general *bio*PM, was used to correct the raw data.[19,343,358,359] In the following sections of the paper, all references to measured particle size or diameter are based on the optical diameters reported by both instruments. Additional small-chamber experiments with aerosolized dust collected from the five carpets were used to estimate the effective density (ρ_{eff}) of the resuspended particles (1.204 g cm^{-3}) to convert BioScout and OPS particle number concentrations to mass (following Application Note OPS-001 (TSI, 2012), assuming particles to be spherical). All BioScout and OPS data were time-averaged to one minute prior to data analysis. Additionally, an IOM (Institute of Medicine) sampler with 25 mm 0.8 μm pore size MCE (mixed cellulose ester) filters (nominal sample flow: 10 L min^{-1}, cut-off ~100 μm) (SKC Inc., Eighty Four, PA, USA) was used to collect resuspended particles for gravimetric analysis; qPCR analysis for quantification of gram-positive and gram-negative bacteria, selected fungal groups; and bacterial 16S rRNA gene sequencing, as reported in our parallel study, Hyytiäinen et al.[360]

A horizontally oriented aluminum tube of length 12 cm was used upstream of the BioScout inlet. The BioScout data was corrected for size-resolved sampling inlet efficiencies and deposition losses in the sample tube.[292,361] No sample tubes were used for the OPS. The OPS data was

corrected for size-resolved sampling inlet efficiencies (vertically oriented inlet). Settled dust from each carpet was collected at the end of the resuspension experiments using a 37 mm MCE filter cassette and nylon sock for gravimetric, optical particle counting (via PAMAS SVSS, PAMAS GmbH, Rutesheim, Germany), and microbial analysis.

For the crawling experiments, the BioScout and OPS were placed on a mobile trolley that followed in parallel to the robot, with sampling inlets at the approximate breathing zone (BZ) height of an infant performing a belly crawl (25 cm).[321] For the walking experiments, the instruments were placed on a stand in the middle of the carpet, with the sampling inlets at the adult BZ height (150 cm).

4.3.3 Analysis of FBAP Size Distributions, Respiratory Tract Deposited Dose Rates, and Emission Rates

All BioScout and OPS data were processed and analyzed with custom-written scripts in MATLAB (The MathWorks, Inc., Natick, MA, USA). For each resuspension experiment (crawling or walking path), the mean FBAP (N_F) and total (N_T) particle number size distributions were fitted with a unimodal lognormal distribution (Equation 4-1).[18] The geometric mean diameter ($\overline{D_{pg,i}}$), geometric standard deviation ($\sigma_{g,i}$), and particle number concentration or amplitude (A) in each mode were determined by the least squares method.

$$\frac{dN}{dlogD_p} = \frac{A}{(2\pi)^{1/2}\log(\sigma_g)} \exp[-\frac{(\log D_p - \log \overline{D_{pg}})^2}{2log^2(\sigma_g)}] \quad (4\text{-}1)$$

To evaluate the amount of resuspended FBAPs (*bio*PM proxy) that deposit in the infant and adult respiratory system, the total and regional FBAP number and surface area respiratory tract deposited doses (# or μm^2 of deposited FBAPs) were estimated using Equations (4-2) and (4-3). We assume that during the crawling or walking periods, the infant and adult are exposed to a constant FBAP concentration, which is defined by the carpet-averaged mean N_F size distributions measured on each carpet in the BZ during the resuspension periods ($dN_F/dlogD_p$ (cm^{-3})). In Equations (4-2) and (4-3), the subscripts *i* and *j* denote the particle size fraction (D_{p1} to D_{p2}) and the region of respiratory tract (head airways, tracheobronchial region, and pulmonary region), respectively. The doses are then expressed as FBAP respiratory tract deposited dose rates ($RTDDR_F$s) (# or μm^2 of FBAPs deposited per minute) by normalizing by an exposure period (t_1 to t_2) of one minute of crawling or walking. To convert from number to surface area concentration,

the geometric midpoint diameter of each size fraction was used and the FBAPs were assumed to be spherical.

$$Number\ Respiratory\ Tract\ Deposited\ Dose_{i,j} = \int_{t1}^{t2} \int_{D_{p1}}^{D_{p2}} \frac{dN_F}{dlogD_p} \times \dot{V}_E \times DF_{i,j} \times dlogD_p \times dt \quad (4\text{-}2)$$

$$Surface\ Area\ Respiratory\ Tract\ Deposited\ Dose_{i,j} = \int_{t1}^{t2} \int_{D_{p1}}^{D_{p2}} \frac{dN_F}{dlogD_p} \times \dot{V}_E \times DF_{i,j} \times \pi D_p^2 \times dlogD_p \times dt \quad (4\text{-}3)$$

Size-resolved deposition fractions ($DF_{i,j}$) as a function of particle aerodynamic diameter for the infant and adult respiratory tract were obtained from the open-source Multiple-Path Particle Dosimetry (MPPD) Model (v3.04, Applied Research Associates, Inc., Albuquerque, NM, USA) (Figure 4.5). The MPPD model accounts for the inhalable fraction of particles for a given breathing route. The MPPD model conditions that were selected to best represent the exposure scenario are as follows: the age of the infant and the adult are 3 months and 21 years, respectively; the upper body of the infant is leaning forward while crawling, while the body of the adult is upright; nasal breathing route for the adult; and nasal and oral breathing routes for the infant. The respiratory minute volume ($\dot{V}_E = f \times V_T$), breathing frequency (*f*), and tidal volume (V_T) for an infant under 1 year of age in light activity were assumed to be (from Hofmann et al.[362]): 0.00598 $m^3\ min^{-1}$, 32 min^{-1}, and 187 mL, respectively, and for an adult in light activity (average of male and female[363]): 0.0195 $m^3\ min^{-1}$, 18 min^{-1}, and 1083 mL, respectively. Weight-normalized $RTDDR_F$s ($min^{-1}\ kg^{-1}$) were also calculated, assuming infant and adult body masses of 9.2 kg (6-12 months) and 80 kg, respectively.[363]

Hygroscopic growth of inhaled *bio*PM in the respiratory tract, where the air approaches saturation (RH ~ 99.5%), is likely.[116,117,364–366] The impact of hygroscopic growth was evaluated by comparing $RTDDR_F$s for two cases: (1.) no particle growth and (2.) correcting the inhaled BZ FBAP size distributions with a hygroscopic growth factor (GF) of 1.12, which represents the median of maximum GFs reported for various bacterial and fungal species at 98% RH.[34]

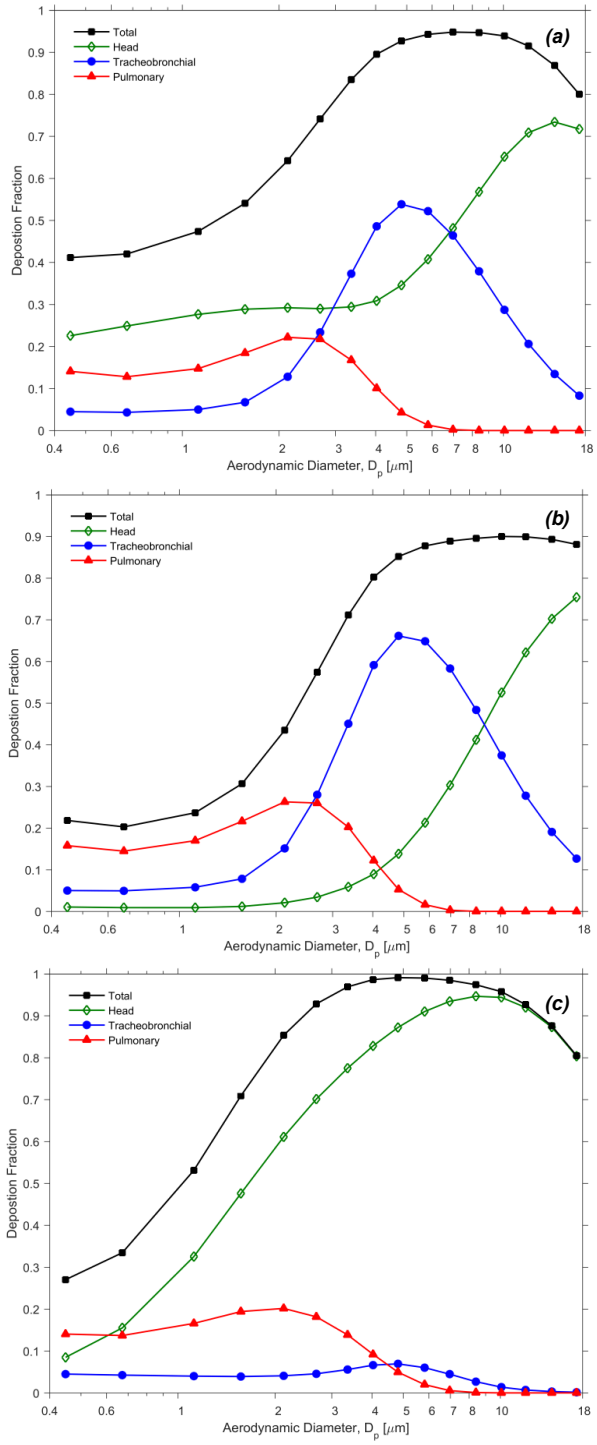

Figure 4.5 Size-resolved total and regional deposition fractions in the respiratory system for an extended size range up to 18 μm to match the hygroscopic-growth shifted FBAP size distributions in the infant and adult BZ: (a.) a 3-month old infant, nasal breathing route, (b.) a 3-month old infant, oral breathing route, and (c.) a 21-year old adult, nasal breathing route, obtained from the Multiple-Path Particle Dosimetry (MPPD) Model for breathing parameters stated in Section 4.3.

Size-resolved FBAP emission rates (E_i^W, # of FBAPs emitted per hour) for the adult walking-induced resuspension experiments, where the chamber air was reasonably well-mixed given the intensity of human movement and use of two mixing fans, were determined through application of a single-zone material balance model:

$$V\frac{dC_i}{dt} = AER \cdot V \cdot C_{Out,i} - AER \cdot V \cdot C_i - \beta_i \cdot V \cdot C_i + E_i \quad (4\text{-}4)$$

where, V is the volume of the chamber (cm^3); C_i is the FBAP number concentration in the chamber for a given particle size fraction *i*, measured at the adult BZ height (cm^{-3}); AER is the air exchange rate of the chamber (h^{-1}); $C_{Out,i}$ is the FBAP number concentration in the chamber supply air (cm^{-3}); β_i is the first-order deposition loss rate coefficient (h^{-1}); and E_i is the FBAP emission rate during adult walking (# of FBAPs emitted per hour). E_i^W was then estimated using Equation (4-5) for a given particle size fraction *i* (from Zhou et al.[367]):

$$E_i^W = V \times \left[\frac{\Delta C_i^W}{t_W} + (\beta_i + AER) \times \overline{C_i^W}\right] - V \times \left[\frac{\Delta C_i^B}{t_B} + (\beta_i + AER) \times \overline{C_i^B}\right] \quad (4\text{-}5)$$

ΔC_i^W and ΔC_i^B (cm^{-3}) represent the difference in FBAP concentration between the beginning and end of a 20-minute walking resuspension period (W, t_W) and the 10-minute background period (B, t_B) in the walking tests, respectively. $\overline{C_i^W}$ and $\overline{C_i^B}$ (cm^{-3}) represent the mean FBAP concentration measured during the resuspension period and background periods in the walking tests, respectively. Size-resolved first-order deposition loss rate coefficients (β_i) were estimated from the 15 minute decay period (Figure 4.6) and are in agreement with previously published empirical estimates.[345,368–370]

It should be noted that the emission rate analysis presented in this study is influenced by mixing conditions of the bulk chamber air as the adult volunteer walked across the carpet, which were deliberately enhanced through use of two mixing fans positioned in opposing corners of the chamber, as well as variations in relative humidity among the experiments (23.89±4.77%), the latter of which can affect the adhesion forces (e.g. capillary and electrostatic forces) acting on the settled *bio*PM (e.g. Qian et al.[371]).

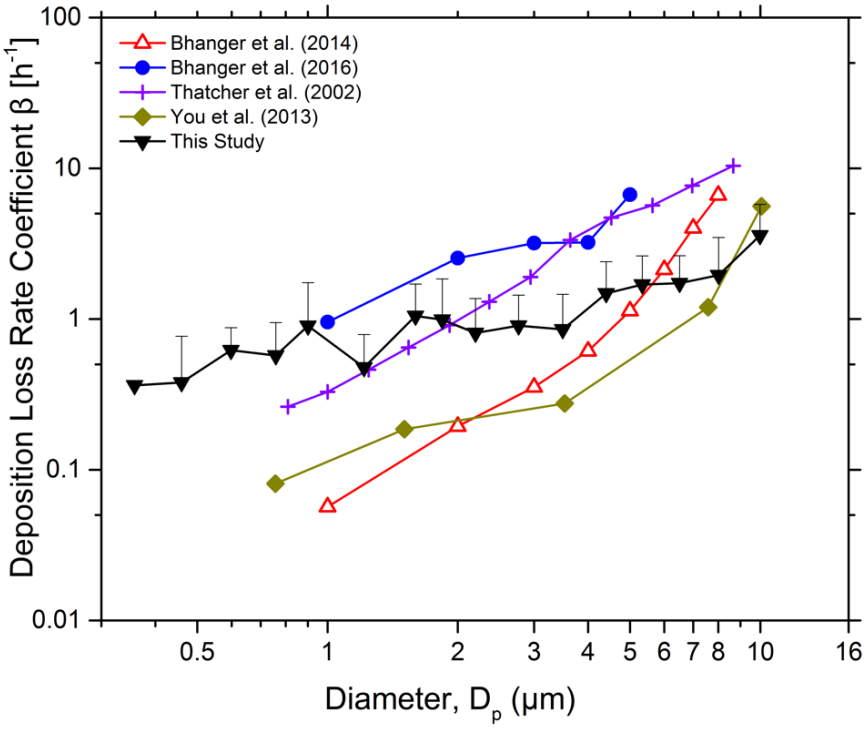

Figure 4.6 FBAP first-order deposition loss rate coefficients (β_i, h^{-1}) measured during the 10 minute decay periods of the adult walking experiments. FBAP deposition loss rate coefficients from Bhangar et al.[368] and Bhangar et al.[345] and total particle deposition loss rate coefficients from Thatcher et al.[369] (72) and You et al. (85) are shown for comparison

4.3.4 Statistical analysis

The Mann-Whitney test was used to evaluate the impact of activity patterns (crawling and walking) and differences in carpets on the exposure to resuspended FBAPs and $RTDDR_F$, as well as the impact of breathing routes on the infant $RTDDR_F$s. *p*-values below 0.05 were considered statistically significant. To compare the carpet-averaged resuspended N_F and N_T with the total bacterial and fungal concentrations (via qPCR) in the air and carpet dust, dust load, and total particle number concentration (>1 μm) in carpet dust (via PAMAS), *p*-values (Wilcoxon signed rank test) and Pearson correlation coefficients were calculated in MATLAB. The total particle number concentration (>1 μm) in carpet dust was also compared with the total bacterial and fungal concentration in carpet dust. Results are presented in Tables 4.4 and 4.5.

4.4 Results and discussion

A detailed summary of the fifty resuspension experiments is presented in Table B.1, including FBAP and total particle number concentrations, modal lognormal fitting parameters of mean FBAP and total particle number size distributions, and total particle mass concentrations.

4.4.1 Crawling and walking resuspension sequence & transient exposure to resuspended *bio*PM (FBAPs)

Figure 4.7 illustrates the transient nature, on a time scale on the order of a minute, of human movement-induced resuspension of FBAPs from carpet dust and the infant and adult inhalation exposures that occur both during and after a resuspension event. The characteristic time-series plots of FBAP and total particle number size distributions and size-integrated (0.4-15.4 μm) FBAP number concentrations that are shown in Figure 4.7 for crawling and walking on carpet 3 are representative of what was observed across all fifty resuspension experiments (Figure B1). The temporal dynamics of *bio*PM resuspension due to the crawling motion of an infant are presented in this paper for the first time, to the authors' knowledge, enabled by the high sampling rate of a LIF-based aerosol instrument.

There are distinct differences in the time-evolution of resuspended FBAP concentrations between crawling and walking. For infants, an abrupt burst of resuspended FBAPs in the infant BZ can be observed at the onset of crawling (Figure 4.7a), after which the FBAP concentration fluctuated with respect to time during the remainder of the resuspension period and decreased rapidly during the decay period. The initial, short-term peak in FBAPs in the air around the infant was observed in nearly every resuspension experiment, with concentrations often in the range of 2 to 4 cm^{-3}, far exceeding concentrations of FBAPs in the adult BZ during walking. The accelerated decay in FBAP concentrations post-crawling suggests that an infant will receive much of their exposure to self-induced resuspended *bio*PM during periods where they are actively engaged in movement. This was found to be especially true for FBAPs larger than 7 μm in size. Given the idiosyncratic behavior patterns and movements of infants during their first year of life[337], one would expect the concentrations of *bio*PM in the infant BZ to vary from minute to minute, as the child crawls, stops to sit and play with toys, then continues crawling.

An adult walking across a carpet will be exposed to a gradual rise in concentrations of resuspended *bio*PM throughout the duration of their movement (Figure 4.7b). After 10 to 15

minutes of walking, FBAP concentrations approach a near steady-state condition, followed by a slow decay as activity ceases. The enhanced mixing of the chamber air associated with the walking motion of an adult aids in the dispersion of FBAPs, prolonging exposure to biological material in floor dust well beyond the duration of the resuspension event itself.

The sporadic and time variant nature of crawling-induced FBAP resuspension appears to be distinctly unique to a crawling infant. Incomplete mixing of air around the infant may be one of the drivers for this phenomenon, along with the high deposition rates for the coarse-mode particles (Figure 4.6), random contact locations of the small stomping hands of the robotic platform, and spatial variability in the dust deposits along the crawling path. The latter two may give rise to periods of high and low FBAP concentrations during the resuspension period, depending on the magnitude of the surface loading of the settled particles that are agitated at each point of contact.

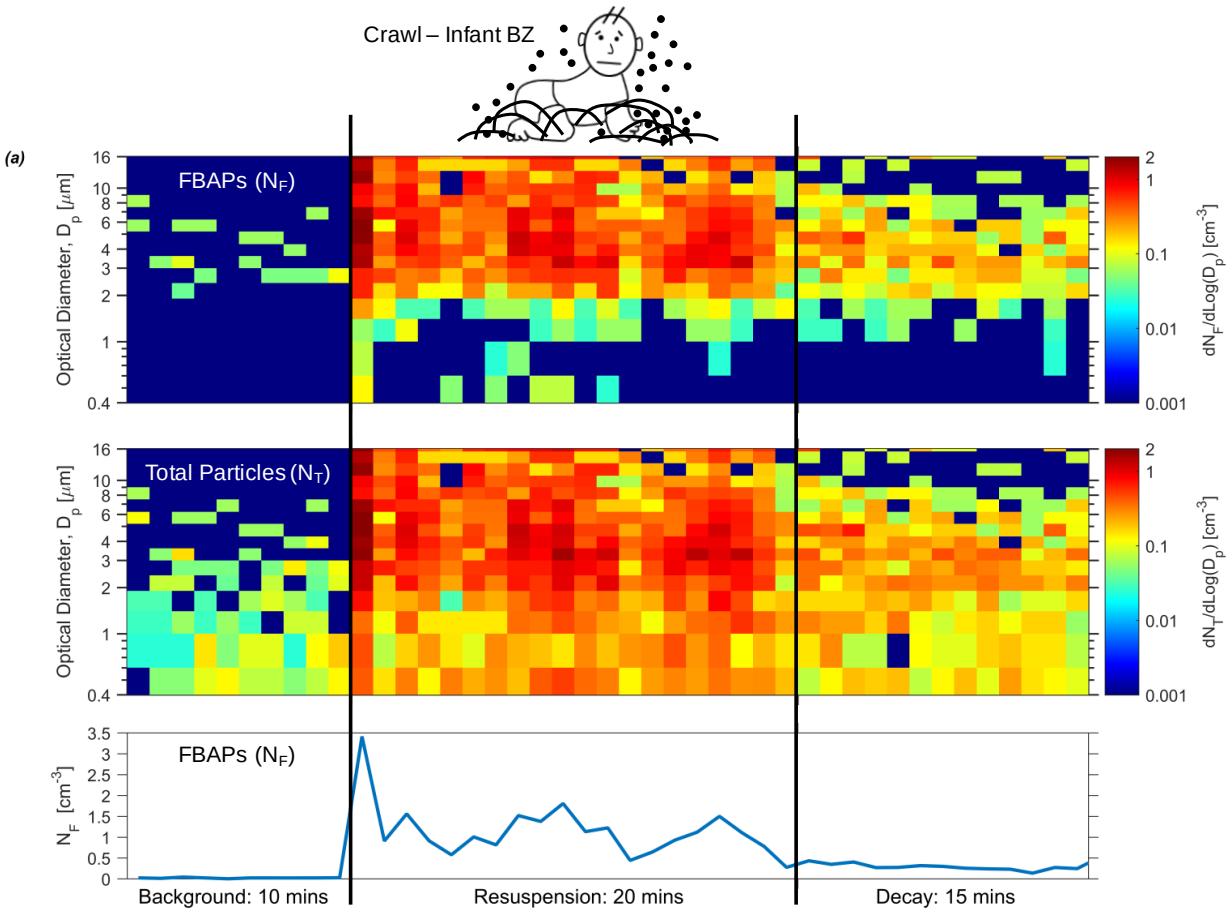

Figure 4.7 Time-series plots of FBAP number size distributions ($dN_F/dlogD_p$, upper), total particle number size distributions ($dN_T/dlogD_p$, middle), and size-integrated (0.4-15.4 μm) FBAP number concentrations (N_F, lower) for (a.) an infant crawling resuspension experiment and (b.) adult walking resuspension experiment on carpet 3.

Figure 4.7 continued.

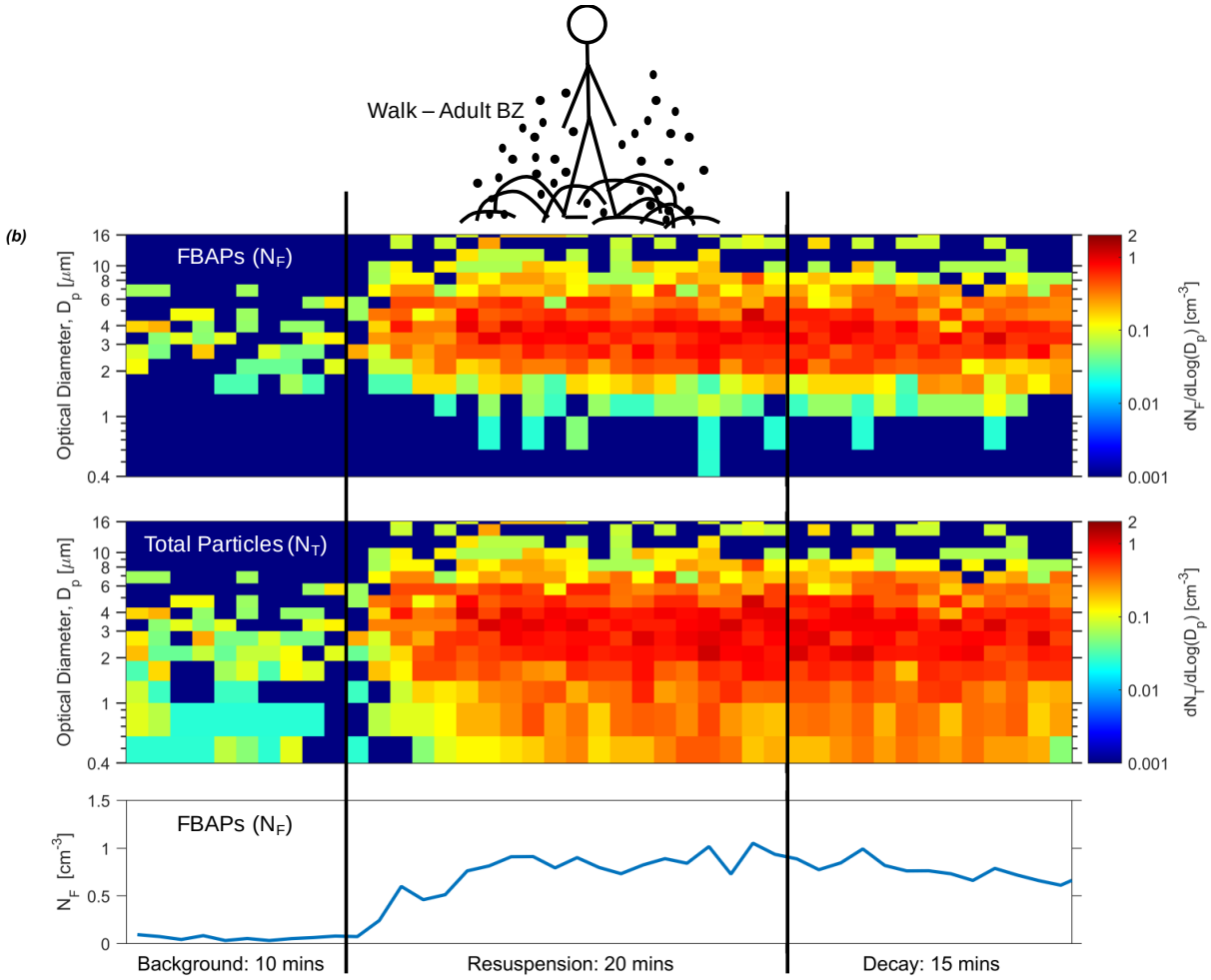

4.4.2 Resuspended FBAP number size distributions and concentrations in the infant and adult breathing zones

Size distributions of resuspended FBAPs in the infant and adult BZs displayed a unimodal lognormal distribution, exhibiting a prominent mode between 3 and 5 µm, while a partial second mode was observed for super-10 µm FBAPs in the infant BZ (Figure 4.8). This is illustrated in Figure 4.8 for the crawling and walking resuspension experiments on carpet 5. Size distributions for the remaining carpets are provided in Figure B2. Modal diameters of the FBAP size distributions among the five carpets ranged from 3.43 to 4.42 µm for the infant BZ and from 3.23 to 3.78 µm for the adult BZ. The total particle size distributions (Figure 4.8b,e) displayed a broader mode with modal diameters that were generally 0.5 to 1 µm smaller than those of the FBAP distributions. The geometric standard deviations of the dominant 3 to 5 µm FBAP mode varied

from 1.54 to 1.80, indicating that the mode is associated with different types of *bio*PM.[372] While the focus of this paper is on *bio*PM, the results and analysis for total particle size distributions are useful in evaluating human inhalation exposure to chemical contaminants in indoor dust, such as particle-bound semi-volatile organic compounds (SVOCs).

Most of the coarse-mode resuspended particles were fluorescent. Figure 4.8c,f shows the size-resolved ratios of FBAPs to total particles (N_F/N_T). Above 1 μm, N_F/N_T increased sharply with size, reaching approximately 0.8 for 3 μm particles and nearly unity for particles larger than 8 μm. Very few of the sub-1 μm particles fluoresced. The high N_F/N_T ratios for particles larger than 1 μm in size suggest that a significant fraction of the resuspended coarse mode particles is comprised of *bio*PM; abiotic particles with surface adhered biological material, such as clusters of skin fragments and skin-associated bacteria; and non-microbial fluorescent interferents (Table 4.1). It is also possible that some of the high intensity scattered light from these large particles leaks to the fluorescence detector, causing a positive artefact to fluorescent particle detection. The N_F/N_T trend presented here is consistent with a previous indoor FBAP study[345], but greater than those reported in outdoor FBAP measurements.[372–374]

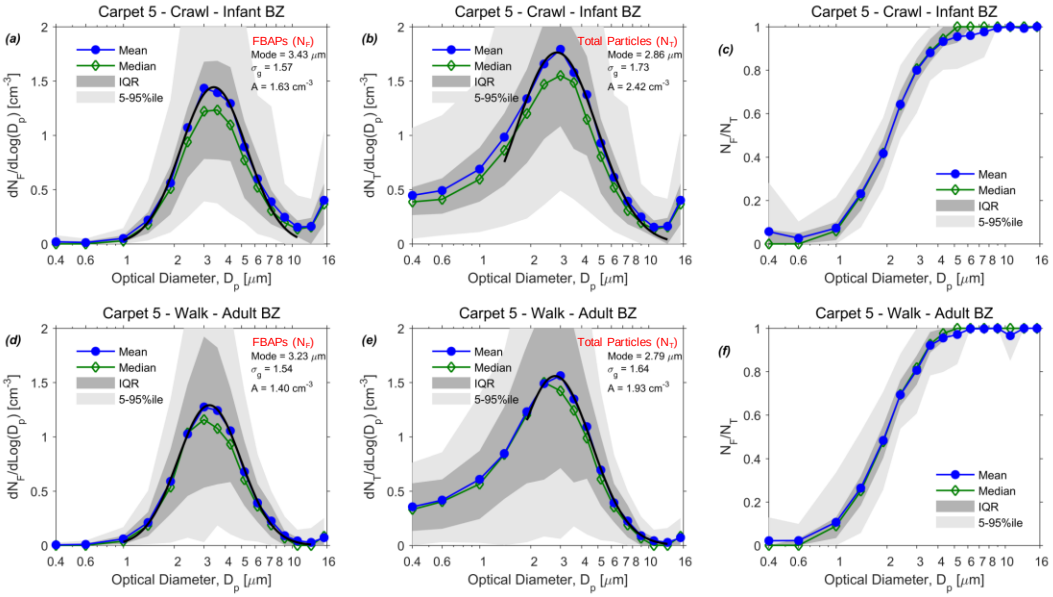

Figure 4.8 Carpet-averaged $dN_F/dlogD_p$ (left), $dN_T/dlogD_p$ (middle), and size-resolved N_F/N_T ratios (right) measured during the crawling (a.-c.) and walking (d.-e.) periods on carpet 5. Blue curves represent mean values, green curves represent median values, dark gray regions represent the interquartile range (IQR), and light gray regions represent the 5-95th percentile range among five crawling or walking paths on the same carpet (100 minutes in total). Black curves show the lognormal fitting of the dominant peaks. The mode, geometric standard deviation (σ_g), and amplitude (A) are presented.

The results of the qPCR analysis and bacterial 16S rRNA gene sequencing of the resuspended particles collected with filter samplers offer some clues on the origin of the highly fluorescent resuspended particles in the dominate 3 and 5 μm mode.[360] The most abundant identified bacterial phyla and genera included: Proteobacteria (50-55% (percentage of relative abundance), genera: *Oxalobacteraceae gen., Acinetobacter, Paracoccus*); Actinobacteria (20-25%, genera: *Corynebacterium*, *Micrococcus*, *Propionibacterium*); Firmicutes (~15%, genera: *Staphylococcus*, *Streptococcus*, *Clostridium*); and Bacteroidetes (< 10%, genera: *Sediminibacterium*). Quantified fungal groups included: *Penicillium* spp., *Aspergillus* spp., *Paecilomyces variotii*, and *Cladosporium herbarum.* The concentration of bacterial cell equivalents (CEs) in both the carpet dust and infant and adult BZ were more than one order of magnitude greater than that for fungal CEs. Thus, bacteria likely contribute much more to the resuspended FBAP concentrations reported here than do fungi.

Single cells of many bacterial species are approximately 1 μm or smaller in size[360], including species of genera identified in this study: *Micrococcus luteus* (equivalent optical diameter (EOD): 0.9 μm), *Staphylococcus aureus* (EOD: 0.7 μm), and *Acinetobacter baumannii* (EOD: 1.1 μm).[375] However, very few resuspended FBAPs 1 μm or smaller were observed in the infant and adult BZ. As documented in numerous studies, this finding suggests that the bacterial cells preferentially exist in the form of cellular agglomerates larger than 2 μm or carried on larger non-microbial particles.[34,338,345,372,376–381] Spores of the four quantified fungal groups are typically 2 to 4 μm in both EOD and aerodynamic diameter.[349,366,375,382,383] Thus, the dominant 3 and 5 μm FBAP mode was likely comprised of bacterial cell agglomerates and, to a lesser extent, fungal spores. However, sub-10 μm fluorescing mite and animal allergen-carrying particles, squames, and pollen grains may also contribute to this mode.[344,375,384,385]

FBAP number concentrations were greater in the infant BZ during crawling compared to the adult BZ during walking for four out of five carpets (1, 3, 4, 5), with infant BZ FBAP mass concentrations (M_F) greater than those in the adult BZ for all five carpets (Figure 4.9e). For carpets 1 and 4, an infant's exposure to resuspended FBAPs was 2.4-fold and 2-fold greater than that of an adult, respectively. The average total number concentration of FBAPs from 1 to 15.4 μm across all crawling paths on the five carpets was 1.281±0.793 cm^{-3} (mean ± s.d.) and 0.827±0.468 cm^{-3} for the walking paths (Table B.1). This results in average inhalation intakes (N_F x breathing rate)

of 7.66×10^3 and 1.61×10^4 inhaled FBAPs per minute for infants and adults, respectively. To put these values in perspective, the daily average FBAP number concentration reported for an occupied classroom was 0.039 cm^{-3} (UV-APS[345]) and the average FBAP concentrations in an adult's and children's hospital were 0.06 and 0.03 cm^{-3}, respectively (UV-APS[386]). It is important to note that these two studies were not aimed at FBAP exposure assessment, sampled in the bulk room air, and account for a wide variation in occupancy and activity patterns. Intermittent and short-term exposures to elevated concentrations of FBAPs, on the order of 1 cm^{-3}, during active periods of locomotion, as evaluated in this study (Figures 4.7, 4.9), may contribute significantly to the daily cumulative FBAP exposures of infants and adults. However, personal exposures to resuspended *bio*PM at the high time resolution afforded by LIF have yet to be measured in field conditions.

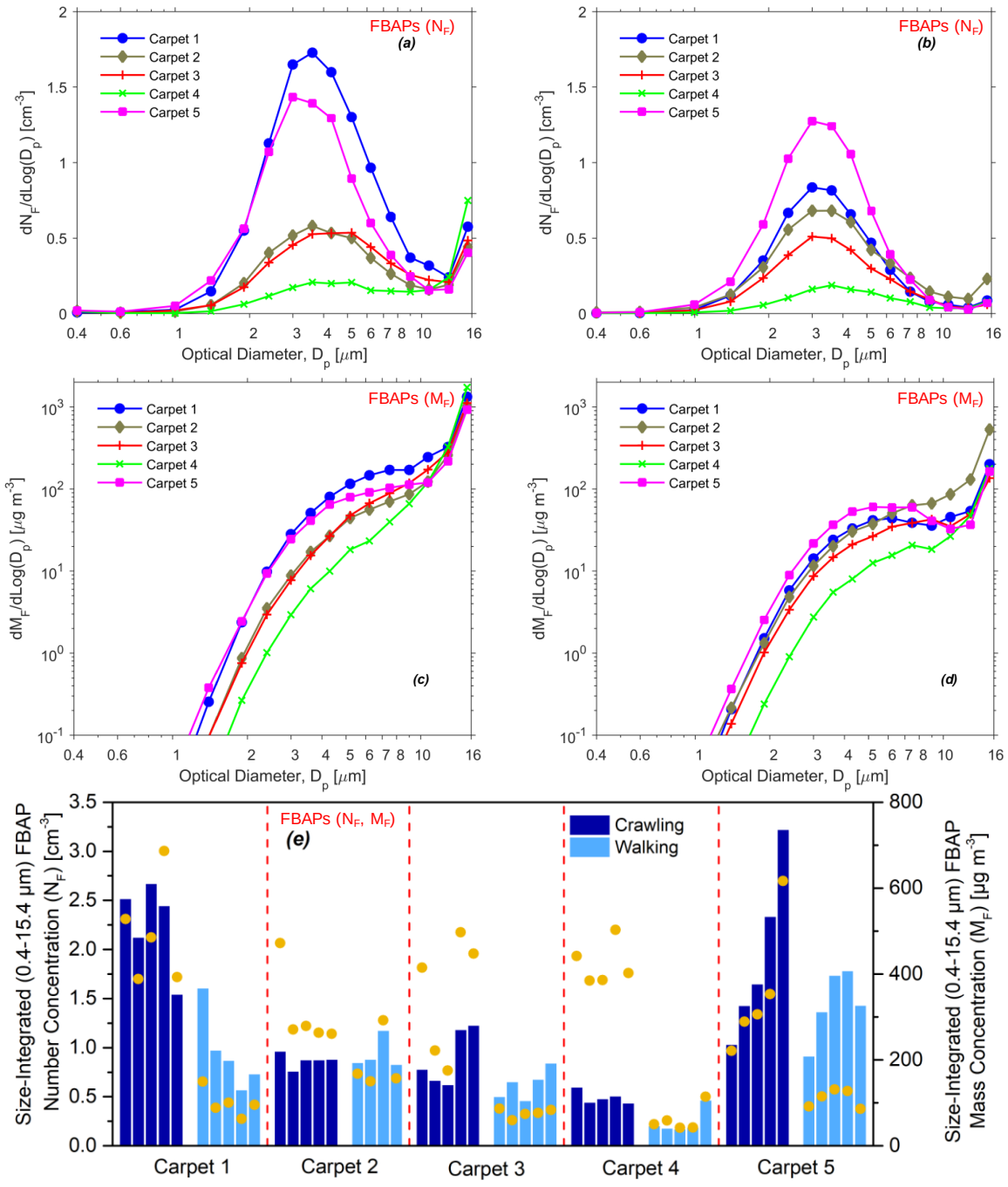

Figure 4.9 Carpet-averaged mean FBAP number ($dN_F/dlogD_p$) and mass ($dM_F/dlogD_p$) size distributions measured during resuspension periods on five carpets for both crawling (a., c.) and walking (b., d.) experiments; (e.) mean size-integrated (0.4-15.4 µm) FBAP number concentrations (N_F, blue bars) and size-integrated (0.4-15.4 µm) FBAP mass concentrations (M_F, yellow dots) measured in each sequential path on each carpet during the resuspension periods. Note: when computing M_F, FBAPs are assumed to be spherical with a ρ of 1.204 g cm^{-3} from OPS calibration (Section 4.22) and particles below ~1 µm are not shown in the $dM_F/dlogD_p$ plots to improve visibility of the partial super-10 µm mode.

The inhalation height of a crawling infant (25 cm) was associated with greater numbers of FBAPs larger than 3 μm compared to that of an adult (1.5 m) (Figures 4.7, 4.8, B.1, B.2). This trend can be observed by noticing that the geometric mean diameter of the dominant FBAP mode was larger during crawling than while walking, ranging from a fraction of a micrometer for carpet 5 to as much as 1.03 μm for carpet 3. The fraction of total FBAP number concentrations attributed to particles in the size range of 7.5-15.4 μm were (from carpets 1 to 5): 0.12, 0.20, 0.23, 0.47, 0.10 for the crawling experiments, and 0.05, 0.11, 0.07, 0.14, 0.03 for the walking experiments. Furthermore, the development of a second, larger mode in the 10 to 15.4 μm range was identified in the infant BZ. This partial mode was particularly strong for carpets 2, 3, and 4 and dominates the FBAP mass size distributions (Figure 4.9c,d). While this mode could not be fully captured given the upper size-limit of the BioScout, it suggests that infants will be exposed to a greater number of super-10 μm resuspended *bio*PM compared to adults. *bio*PM in this size range include multicellular fungal spores, pollen grains, and abiotic *bio*PM carrier particles.[34,380] Fluorescing squames and clothing fabric fibers may also contribute to the observed super-10 μm FBAPs (Table 4.1).

Crawling- and walking-induced resuspension contributed minimally to concentrations of sub-1 μm FBAPs in the BZ ($N_F < 0.01$ cm^{-3}), but were associated with a meaningful elevation of non-fluorescent sub-1 μm particles, especially for carpets 1 and 2 (Figures 4.7, 4.8, B.1, B.2). This suggests that sub-1 μm *bio*PM, such as some single bacterial cells, fungal fragments, and subpollen particles[387,388], are either preferentially carried on larger particles or in an agglomerated state, are very weakly fluorescent, or are sparsely present in the dust deposits of the five carpets. The former two are most likely, given the tendency of *bio*PM to exist as agglomerates and previous reports of weakly fluorescent *bio*PM in the 0.5 to 1 μm range.[379] The resuspension of sub-1 μm non-fluorescent particles as small as 0.4 μm is consistent with previous resuspension studies on adult footfalls.[389]

Infant and adult exposure to resuspended FBAPs is influenced by the carpet and dust deposit over which the activity is occurring (Figure 4.9). Carpet-to-carpet variability is shown in Figure 4.9 for FBAP number and mass size distributions and concentrations. Although the shape of the FBAP size distributions were similar, their lognormally-fitted modal number concentrations spanned nearly an order of magnitude, from 0.29 cm^{-3} for crawling on carpet 4 to 2.11 cm^{-3} for crawling on carpet 1. The highest FBAP number concentrations occurred for crawling and walking

on carpets 1 and 5 (Figure 4.9e), with N_F exceeding 1 cm^{-3} for most of the resuspension events. Wool carpets from the same Helsinki residence (carpet 1: bedroom, carpet 3: corridor, two occupants, one indoor cat) exhibited markedly different FBAP size distributions during crawling, with the lognormally-fitted modal amplitude of carpet 1 (2.11 cm^{-3}) 2.6-fold greater than that of carpet 3 (0.80 cm^{-3}) (Figures 4.9, B.2). BZ mass concentrations of total particles (BioScout, 0.4-15.4 μm) varied among the five carpets (Figure 4.9e) and were typically in the range of 50 to 600 $\mu g/m^3$, exceeding 600 $\mu g/m^3$ for one crawling path on carpet 1 and 5. Despite differences in FBAP size distributions, the size-resolved N_F/N_T ratio curves were similar among all five carpets and for both crawling and walking (Figure 4.10).

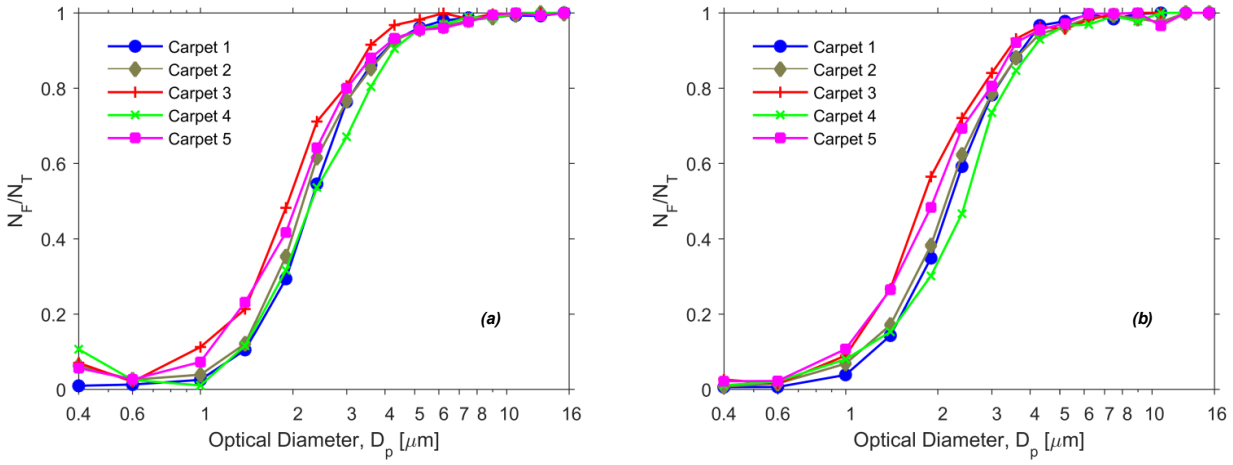

Figure 4.10 Carpet-averaged size-resolved N_F/N_T ratios measured during resuspension periods on five carpets for both crawling (a.) and walking (b.) experiments.

The five carpets exhibited variations in dust mass loading (2.63 to 16.72 g/m^2), total particle number concentrations in the settled dust (~10^9 to 10^{10} $\#/m^2$), and bacterial and fungal cell concentrations in the settled dust (Table 4.3, Figure 4.11). While crawling on carpets 2 and 3 contributed similar levels of FBAPs to the infant BZ, 0.858 and 0.882 cm^{-3}, respectively, carpet 2 had a dust load 3.17-fold greater than carpet 3 with 3.44 times as many bacterial and fungal CEs. Carpet 1 was associated with the highest FBAP concentration in the infant BZ (2.257 cm^{-3}), but had the fourth lowest loadings of particle mass (2.79 g/m^2) and number (2.28 x 10^9 $\#/m^2$) among the four carpets. Interestingly, while carpet 5 had the highest particle number concentrations in the dust (2.53 x 10^{10} $\#/m^2$), it had the lowest microbial loading (4.37 x 10^8 CE/m^2). Previous research has demonstrated that carpet type, fiber structure and polymer, usage, and structure of the

dust deposit can affect resuspension[389–391] and biological particle adhesion[392]. Our results suggest that the magnitude of a person's inhalation exposure to resuspended *bio*PM can change from carpet to carpet, even within the same home, due to the complexity of the carpet and the *bio*PM which is embedded into it.

Resuspended FBAP concentrations and size distributions generally did not decrease with repeated crawling or walking paths on the same carpet (Figures 4.9e, B.1). In total, each carpet experienced 200 minutes of crawling and walking across its exposed upward facing surface area. This suggests that resuspension of carpet dust can act as a near-continuous supply of *bio*PM to the BZ over time-scales of several hours, especially if particles have time to re-deposit and re-accumulate on the carpet during periods of limited to no human locomotion. While resuspension can lead to significant elevations in coarse-mode FBAP and total particle number and mass concentrations (Figure 4.9e), the fraction of settled particles that resuspend (resuspension fraction) per physical disturbance is quite small, on the order of 10^{-5} to 10^{-2}.[53] Given the high number concentrations of total particles (10^9 to 10^{10} #/m^2, > 1 μm, Table 4.3) and bacterial and fungal CEs (10^8 to 10^9 CE/m^2, Table 4.3) in the dust, along with high particle deposition loss rates due to gravitational settling (1 to 10 μm: ~1 to 3 h^{-1}, Figure 4.3), it would take considerable time to deplete the carpet dust *bio*PM reservoir due to resuspension alone.

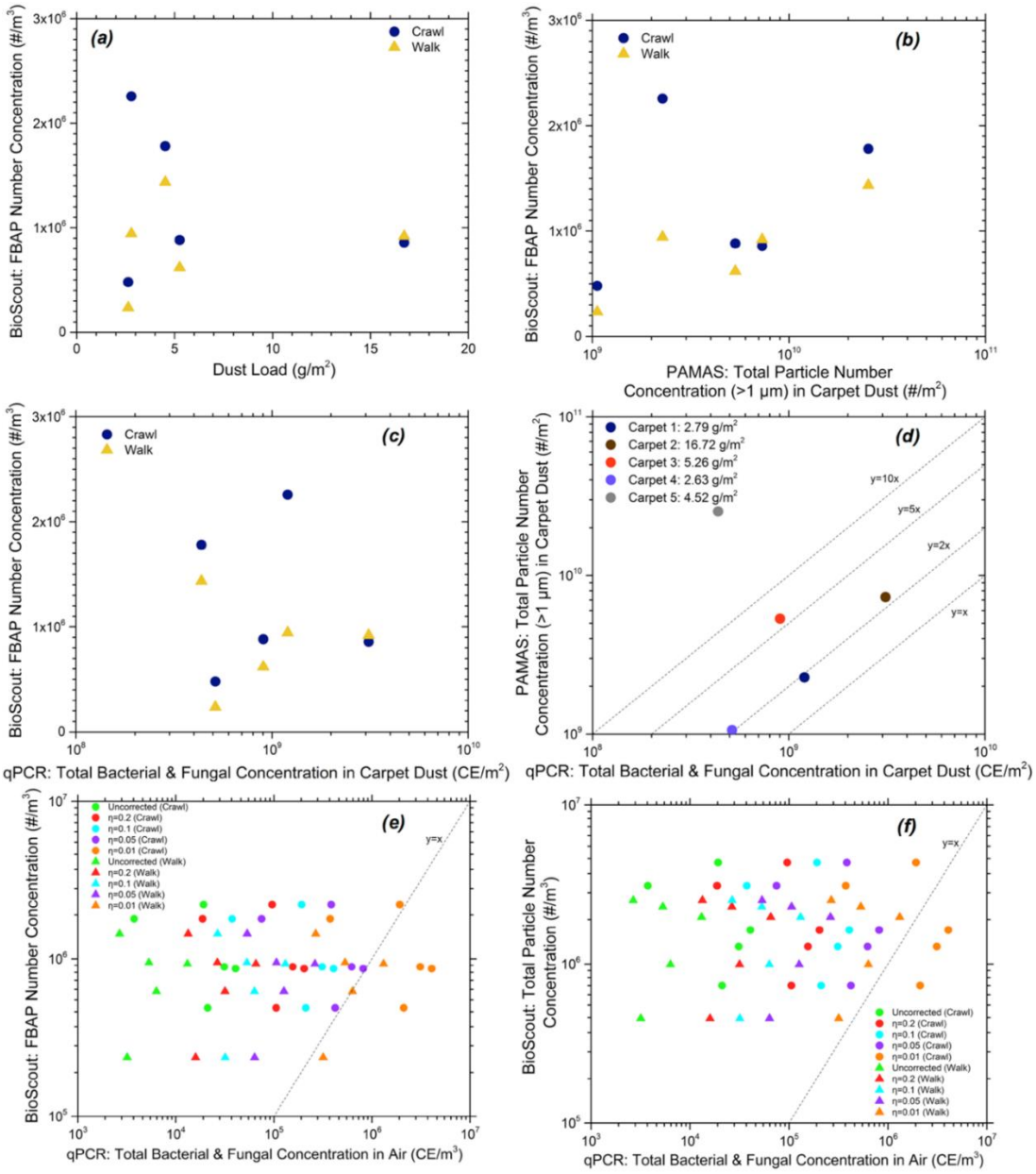

Figure 4.11 Comparison between size-integrated (1-15.4 µm) FBAP number concentrations, as measured by the BioScout during both crawling and walking, with: (a.) sieved gravimetric carpet dust loads (pore size 1 mm x 1 mm), (b.) total particle number concentrations in carpet dust (> 1 µm) via PAMAS, and (c.) total bacterial and fungal concentrations in carpet dust via qPCR (Hyytiäinen et al.[360])); (d.) comparison between total particle number concentrations in carpet dust (> 1 µm) via PAMAS with total bacterial and fungal concentrations in carpet dust via qPCR; comparison between (e.) size-integrated (1-15.4 µm) FBAP and (f.) total particle number concentrations, as measured by the BioScout, with total bacterial and fungal concentrations in the infant and adult BZ via qPCR (Hyytiäinen et al.[360]), for a range of possible overall DNA and filter extraction efficiencies (η), informed by Hospodsky et al.[381]. Note: 1 µm is used here as the lower size-cutoff for the BioScout data to match the PAMAS data.

4.4.3 Comparison between BioScout and OPS total particle number size distributions

The magnitude and shape of the mean total particle size distributions ($dN_T/dlogD_p$ (cm^{-3})) measured by both the BioScout and OPS agreed very well during the walking experiments (adult BZ sampling) for each of the five carpets, as shown in Figure B2. In contrast, distinct differences in the magnitude of the total particle size distributions were observed in the crawling experiments (Figure B2). We hypothesize that this is due to spatial variability in concentrations of resuspended particles within and around the infant personal cloud. Due to the layout of the mobile trolley, the sampling inlets of the two instruments were not identical within a plane at infant BZ height (see Figure 4.3), with the OPS inlet recessed 10 cm further back from the edge of the crawling path compared to the BioScout inlet. The total particle size distributions for the BioScout were roughly a factor of two greater than those reported by the OPS, for all particle sizes > 0.8 μm. This may suggest that the resuspended particle cloud around the robot was highly spatially variant at a length scale on the order of 10 cm, with particle concentrations decreasing radially outward from the crawling path. In the above, we assume nearly identical counting statistics for both instruments (> 1 μm) and have corrected the raw data for sampling inlet efficiencies and deposition losses in the BioScout sample tube.

4.4.4 Size-resolved emission rates of resuspended *bio*PM (FBAPs) during walking

Figure 4.12 presents the size-resolved lognormalized emission rates of resuspended FBAPs during the adult walking experiments on each of the five carpets ($dE_F/dlogD_p$, # of FBAPs emitted per hour). For comparison, per-person FBAP emission rates from Bhangar et al.[345] (transition periods in a classroom) and Bhangar et al.[368] (walking on carpeted flooring in a chamber) are also shown, assuming a CO_2 emission rate during walking of 38 g/min.[345] The lognormalized FBAP emission rate distributions exhibited a primary mode between 2 and 5 μm, with a shoulder from 6 to 9 μm and a second, weaker mode developing for particles > 9 μm. The dominant peak between 2 and 5 μm is consistent with the FBAP emission rates reported by Bhangar et al.[345,368] qPCR-based emission rates follow a similar trend, with Qian et al.[380] reporting a predominant peak between 3 and 5 μm (aerodynamic diameter) for bacteria in an occupied classroom and Hospodsky et al.[381] reporting dominant peaks in bacterial and fungal emission rates in the range of 4.7 and 9 μm (aerodynamic diameter).

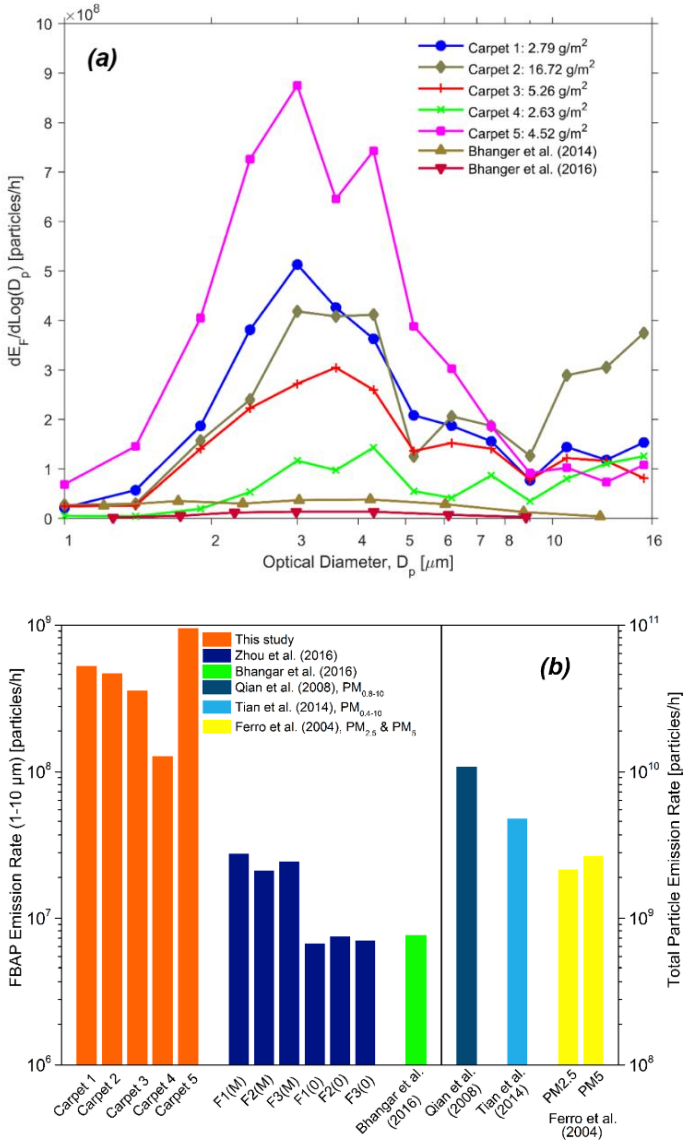

Figure 4.12 (a.) Size-resolved log-normalized emission rates of resuspended FBAPs during the adult walking experiments on each of the five carpets, per-person FBAP emission rates during the transition periods in a university classroom (Bhangar et al.[345] 2014), and per-person FBAP emission rates for walking on carpet in a controlled chamber (Bhangar et al.[368]), assuming that the CO_2 emission rate during walking is 38 g/min (Bhangar et al.[368]), and (b.) carpet-averaged size-integrated (1-10 μm) emission rates of resuspended FBAPs during the adult walking experiments on each of the five carpets (this study), size-integrated FBAP emission rates of three volunteers (F1, F2, F3) measured during walking on vinyl flooring in a chamber (Zhou et al.[367]) ('M' and '0' represent with and without the application of moisturizer, respectively), size-integrated FBAP emission rates for walking on carpet in a controlled chamber (Bhangar et al., and size-integrated total particle emission rates for walking-induced resuspension from Qian et al.[371], Tian et al.[389], and Ferro et al., the latter three of which are presented on a re-scaled secondary y-axis. Note: the particle size reported in this study, Zhou et al., Qian et al., and Tian et al.is an optical diameter, whereas the particle size measured by Bhangar et al. is aerodynamic.

Figure 4.12b summarizes size-integrated (1-10 μm) mean FBAP emission rates during walking on each of the five carpets, along with FBAP emission rates reported by Bhangar et al.[368] and Zhou et al.[367] (FBAP emissions from three volunteers with and without applying skin moisturizer) and total particle emission rates for walking induced resuspension.[53,371,389,393] Walking on carpet was found to release on the order of 10^8 to 10^9 FBAPs per hour. Thus, in only one minute of walking, one would resuspend 1 to 10 million FBAPs. Carpet dust offers a plentiful supply of *bio*PM, with total bacterial and fungal loads ranging from 10^8 to 10^9 CE/m^2 (Table 4.3). There was nearly an order of magnitude difference in total FBAP emissions between carpets 4 (cotton) and 5 (wool), despite containing a similar number of settled bacterial and fungal cell equivalents, 5.15 x 10^8 and 4.37 x 10^8 CE/m^2, respectively. This demonstrates that the structure of the dust deposit along the depth of the carpet fibers, interaction between the fibers and human foot during contact, and impact of carpet fiber material on particle adhesion forces likely all play a role in affecting the number of FBAPs that resuspend

The FBAP emission rates reported in this study are greater than those reported by Bhangar et al.[345,368] and Zhou et al.[367], but lower than those reported for total particles for walking-induced resuspension as summarized in Qian et al.[53]. This may be due in part to the magnitude of available *bio*PM in the carpet dust for resuspension. In this study, the carpets were not cleaned for at least two weeks prior to the measurements, with dust loads in the range of 2.6 to 5.3 g/m^2 (carpets 1, 3, 4, 5) and 16.7 g/m^2 (carpet 2). In Bhangar et al.[345], custodial cleaning was conducted daily in the classroom, and in Bhangar et al. the carpeted floor was vacuumed daily. Qian et al.[371] evaluated resuspension for a dust load of 20 g/m^2 and Tian et al.[389] studied 2 and 8 g/m^2. The lower FBAP emission rates reported in the present study, as compared to the total particle emission rates summarized in Qian et al.[53], may be due in part to the low N_F/N_T ratios for sub-2 μm particles, which do resuspend in meaningful quantities (Figures 4.8, B.1). As the net number of particles that resuspend from a surface (not necessarily the resuspension fraction) generally increases with dust loading[336,391], this may explain the difference in FBAP emission rates, but other factors, such as the footfall contact frequency, carpet fiber material, chamber relative humidity, and chamber bulk air mixing conditions will likely affect the emission rates reported in Figure 4.12. The FBAP emission rates in this study are one to two orders of magnitude greater than those reported for particle release from the human envelope by Zhou et al.[367] Thus, walking-induced resuspension may play a more dominant role in elevating indoor concentrations of *bio*PM compared to direct

skin shedding, which is consistent with the results reported in Hospodsky et al.[381] and Adams et al.[335]

Table 4.4 Statistical analysis (p-values) of the comparisons of N_F, M_F, and $RTDDR_F$ between different activity patterns, carpets, and breathing routes.

			Activity Patterns: Crawling and walking		
BioScout: N_F (*N*=25)			**0.039**		
BioScout: M_F (*N*=25)			**<0.001**		
$RTDDR_F$ – Total (*N*=5)			0.095		
$RTDDR_F$ – Head (*N*=5)			**0.032**		
$RTDDR_F$ – Tracheobronchial (*N*=5)			0.056		
$RTDDR_F$ – Pulmonary (*N*=5)			0.095		
Weight-Normalized $RTDDR_F$ – Total (*N*=5)			**0.016**		
Weight-Normalized $RTDDR_F$ – Head (*N*=5)			0.151		
Weight-Normalized $RTDDR_F$ – Tracheobronchial (*N*=5)			**0.008**		
Weight-Normalized $RTDDR_F$ – Pulmonary (*N*=5)			0.095		
			Breathing Routes: Nasal & Oral		
$RTDDR_F$-Total (*N*=5)			0.548		
$RTDDR_F$-Head (*N*=5)			0.095		
$RTDDR_F$-Tracheobronchial (*N*=5)			0.548		
$RTDDR_F$-Pulmonary (*N*=5)			0.421		
N_F – Crawling (for each *p*-value, *N*=5)					
	Carpet 1	Carpet 2	Carpet 3	Carpet 4	Carpet 5
Carpet 1	--	**0.008**	**0.008**	**0.008**	0.421
Carpet 2	--	--	0.841	**0.008**	**0.008**
Carpet 3	--	--	--	**0.008**	**0.032**
Carpet 4	--	--	--	--	**0.008**
N_F – Walking (for each *p*-value, *N*=5)					
	Carpet 1	Carpet 2	Carpet 3	Carpet 4	Carpet 5
Carpet 1	--	0.841	0.095	**0.008**	0.095
Carpet 2	--	--	0.222	0.151	**0.016**
Carpet 3	--	--	--	**0.016**	**0.008**
Carpet 4	--	--	--	--	**0.008**
M_F – Crawling (for each *p*-value, *N*=5)					
	Carpet 1	Carpet 2	Carpet 3	Carpet 4	Carpet 5
Carpet 1	--	**0.032**	0.310	0.310	0.095
Carpet 2	--	--	1	0.095	0.421
Carpet 3	--	--	--	0.841	1
Carpet 4	--	--	--	--	0.151
M_F – Walking (for each *p*-value, *N*=5)					
	Carpet 1	Carpet 2	Carpet 3	Carpet 4	Carpet 5
Carpet 1	--	0.151	0.095	0.095	0.690
Carpet 2	--	--	0.151	0.151	0.151
Carpet 3	--	--	--	0.151	**0.016**
Carpet 4	--	--	--	--	**0.032**

Table 4.5 Statistical analysis of the comparisons between LIF and qPCR.

	BioScout: FBAP Number Concentration*			
	Crawling		Walking	
	Correlation Coefficient	*p*-value	Correlation Coefficient	*p*-value
qPCR: Total Bacterial & Fungal Concentration in Air	-0.550	**0.021**	0.021	**0.014**
qPCR: Total Bacterial & Fungal Concentration in Carpet Dust	-0.160	0.065	0.093	0.065
PAMAS: Total Particle Number Concentration (>1 μm) in Carpet Dust	0.344	0.134	0.828	0.134
Dust Load	-0.308	**0.019**	0.179	**0.014**
	BioScout: Total Particle Number Concentration			
	Crawling		Walking	
	Correlation Coefficient	*p*-value	Correlation Coefficient	*p*-value
qPCR: Total Bacterial & Fungal Concentration in Air	-0.492	**0.030**	0.142	**0.014**
	PAMAS: Total Particle Number Concentration (>1 μm) in Carpet Dust			
	Correlation Coefficient		*p*-value	
qPCR: Total Bacterial & Fungal Concentration in Carpet Dust	-0.210		0.196	

4.4.6 Infant Crawling-Induced and Adult Walking-Induced Resuspension Mechanisms

Both the belly crawling of an infant and walking (footfalls) of an adult contribute to appreciable resuspension of *bio*PM from carpet dust. While the latter is well characterized for abiotic particles[53], the former has received little attention, with only several studies attempting to investigate near-floor exposures of infants and children.[394–396] In this study, it is likely that differences in body mass, contact area, and contact frequency between the adult volunteer (mass: 80 kg, height: 188 cm, contact area: 160 cm^2 per foot, footfall contact frequency: 70 min^{-1}) and the simplified robotic infant (mass: 4 kg, contact area: 25 cm^2 per hand + 325 cm^2 for lower torso, hand contact frequency: 200 min^{-1}) influenced the resuspension process and resulting number of resuspended FBAPs. The differences in the nature of contact and applied surface pressure likely induce different airflow patterns and surface vibrations at and near the point of contact of the body with the carpet, which were not characterized in this study. Gomes et al.[397] demonstrated that the dominant mechanism of walking-induced resuspension is the highly impulsive airflow generated at and near the point of contact between the foot and the floor. It is unknown if this holds true for crawling. Contact electrification likely plays a significant role in affecting the directionality of electrostatic adhesion forces for crawling-induced resuspension, given the repetitive nature of contact and separation between the body and carpet fibers, along with the large surface area in contact with, and sliding against, the carpet fibers (e.g. lower torso for belly crawling).[398–400]

4.4.7 Respiratory tract deposited dose rates of resuspended *bio*PM (FBAPs) in infant and adult respiratory system

In one minute of crawling or walking across a carpet, on the order of 10^3 to 10^4 resuspended FBAPs, with an associated surface area of 10^5 to 10^6 μm^2, will deposit in the human respiratory system (Figure 4.13). For an infant, the mean total $RTDDR_F$s across five carpets were 6.3±3.3 x 10^3 and 5.7±2.8 x 10^3 deposited FBAPs per minute crawling for nasal and oral breathing, respectively (Figure 4.13a,e) (mean ± s.d.). The mean total $RTDDR_F$ for an adult was 1.5±0.72 x 10^4 deposited FBAPs per minute walking (Figure 4.13b), 2.4-fold greater than that of an infant. This difference can be primarily attributed to the adult breathing rate (0.0195 m^3 min^{-1}), which is 3.3-fold greater than that of the infant (0.00598 m^3 min^{-1}) for light activity. Furthermore, for each minute of walking, approximately 1.6 x 10^3 FBAPs will deposit in the airways of an adult for every million FBAPs that resuspend (based on emission rate analysis).

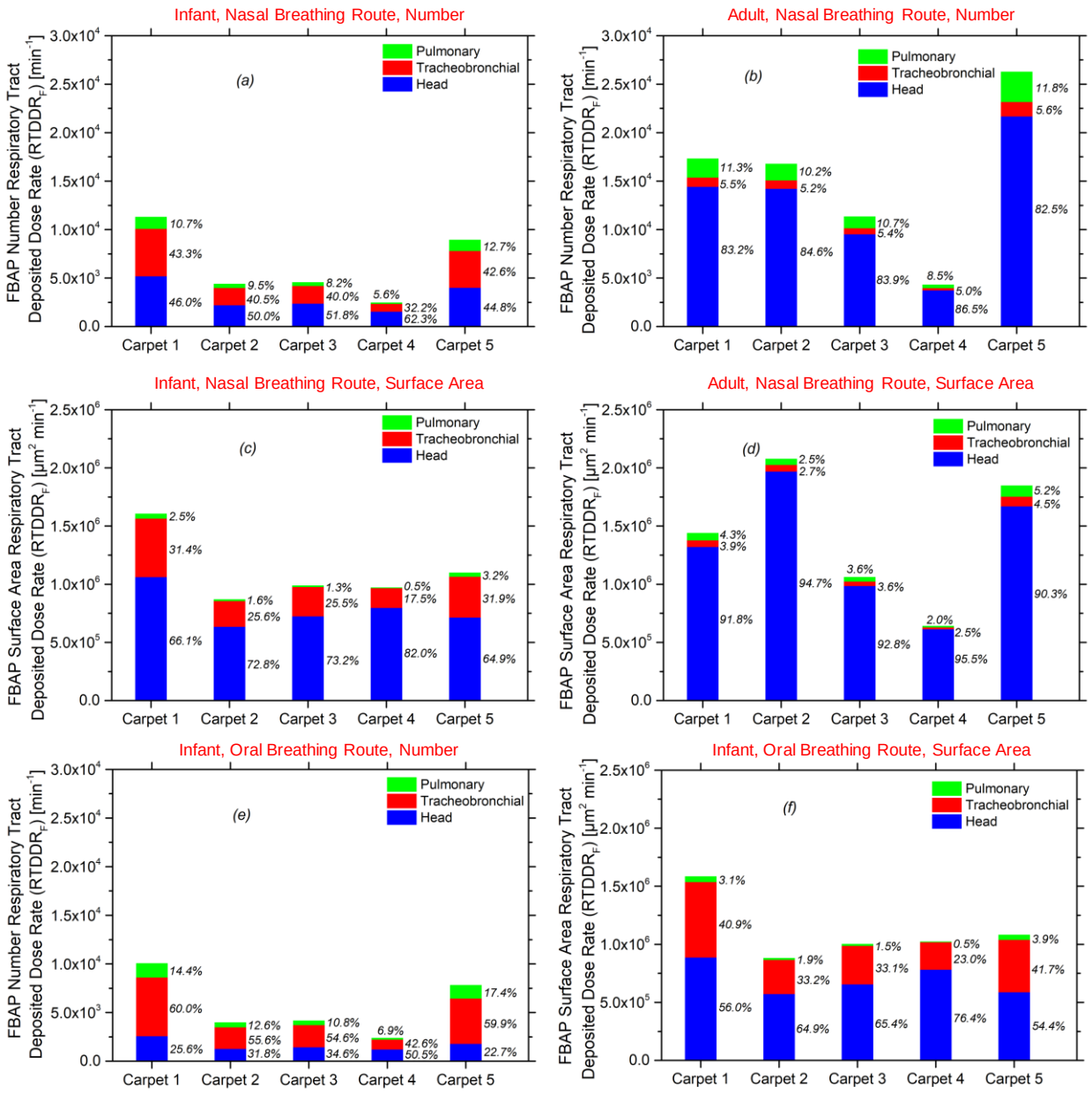

Figure 4.13 Total and regional size-integrated (0.4-15.4 μm) FBAP respiratory tract deposited dose rates ($RTDDR_{FS}$) (per minute crawling or walking) for each of the five carpets: (a.) infant, nasal breathing route, number, (b.) adult, nasal breathing route, number, (c.) infant, nasal breathing route, surface area, (d.) adult, nasal breathing route, surface area, (e.) infant, oral breathing route, number, and (f.) infant, oral breathing route, surface area. The fractional dose in each region, expressed as a percentage, is shown to the right of each bar. Note: a hygroscopic growth factor of 1.12 was applied to the BZ FBAP size distributions.

The magnitude of the $RTDDR_F$ for each carpet naturally follows the total FBAP number concentrations shown in Figure 4.9e, with the greatest $RTDDR_F$s found for carpets 1 and 5. Direct comparisons with previous estimates of RTDDRs for *bio*PM are difficult, as they relied on either bulk air measurement of culturable bacteria or fungi, such as ~0.1 to 5 CFU/min for indoor culturable fungi by Reponen et al.[349] and ~6 to 33 CFU/min for culturable bacteria and fungi by Gao et al.[353], or evaluated exposure to fungal spore release directly from an agar plate under high speed jets (1.5×10^3 and 10^4 spores per minute for infants and adults, respectively, by Cho et al.[351]). Regarding the latter, the magnitude of $RTDDR_F$s reported here are similar as what one would receive inhaling air directly above a moldy material agitated by high air velocities.[351]

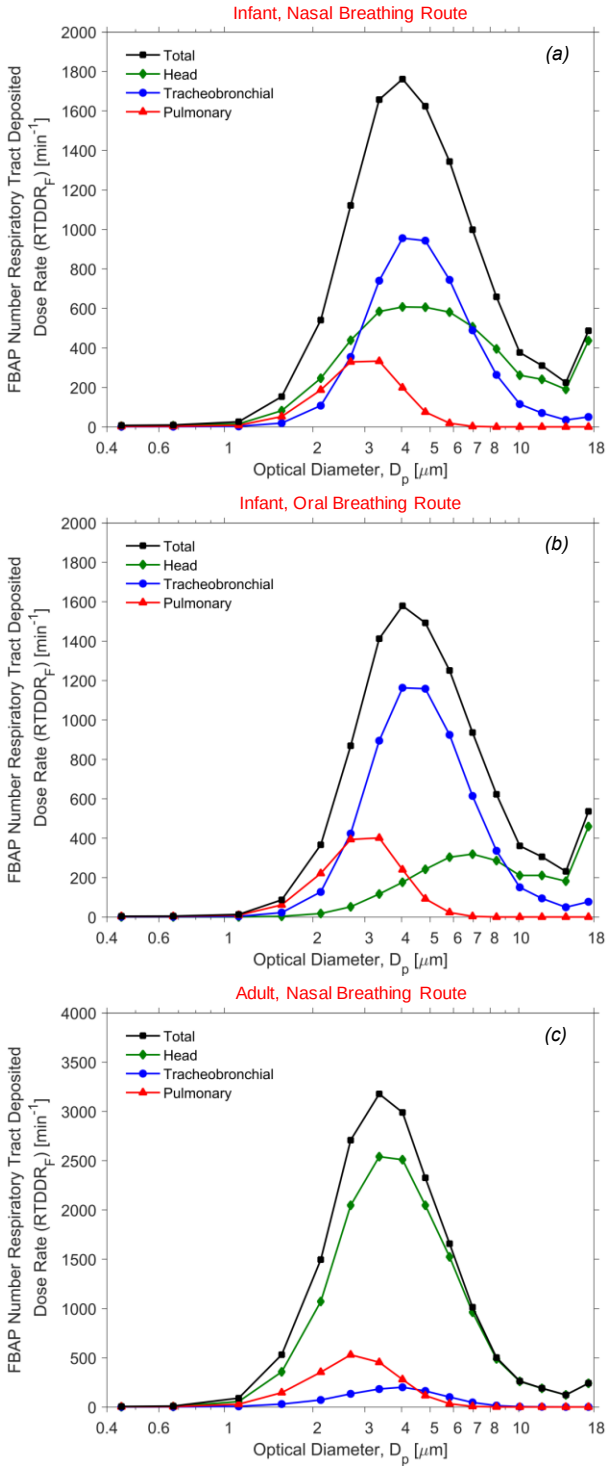

Figure 4.14 Total and regional size-resolved FBAP number respiratory tract deposited dose rates ($RTDDR_{FS}$) (per minute crawling or walking) on carpet 1, for (a.) infant crawling, nasal breathing route, (b.) infant crawling, oral breathing route, and (c.) adult walking, nasal breathing route. Note: a hygroscopic growth factor of 1.12 was applied to the BZ FBAP size distributions.

The tracheobronchial regional $RTDDR_F$ was much greater for infants (41% of total, 2.6±1.5 x 10^3 min^{-1}, nasal) compared to adults (5.4% of total, 8.3±4.2 x 10^2 min^{-1}, nasal) (Figures 4.13a,b and 4.14). The opposite was true for the head airways, which was the predominant deposition region for adults (84% of total, 1.3±0.59 x 10^4 min^{-1}, nasal). Accounting for hygroscopic growth of inhaled FBAPs resulted in a small increase in the overall total $RTDDR_F$ for both infants and adults, but a reduction in the pulmonary regional $RTDDR_F$ by 15% for infants and 13% for adults (Figure 4.13, 4.16). This is consistent with the regional deposition analysis of fungal spores in Reponen et al.[365]

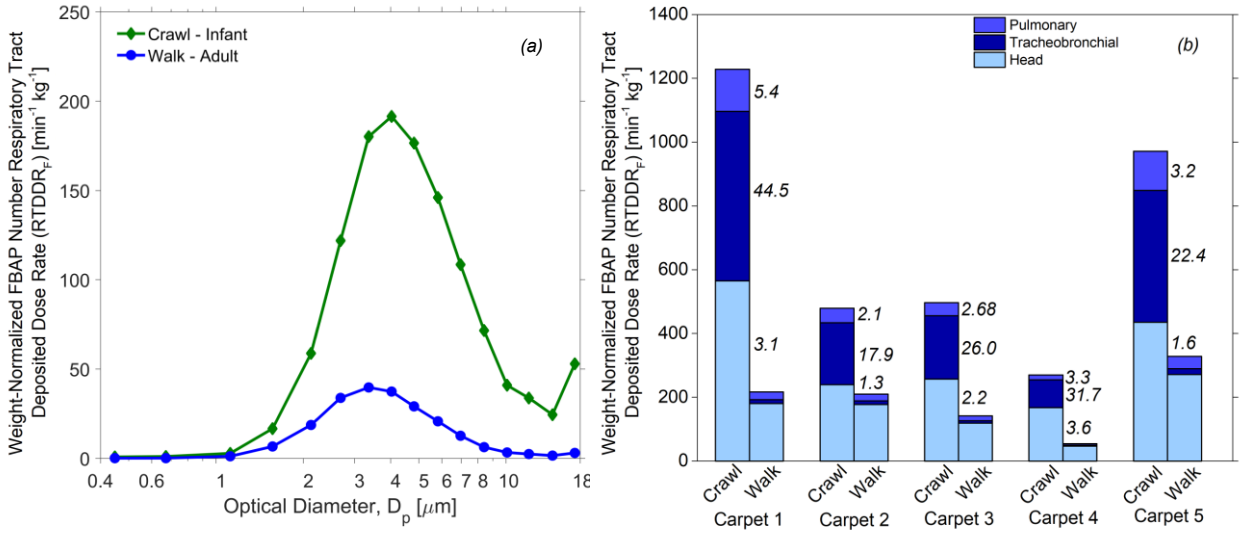

Figure 4.15 (a.) Weight-normalized total size-resolved FBAP number respiratory tract deposited dose rates ($RTDDR_F$s) for infant crawling and adult walking on carpet 1 (both nasal breathing route) and (b.) weight-normalized regional size-integrated (0.4-15.4 μm) FBAP number $RTDDR_F$s for infant crawling and adult walking on each of the five carpets (both nasal breathing route). Note in (b.), a log-scale is used for the y-axis to improve visualization of the difference in weight-normalized doses between an infant and adult. The ratio of the infant to adult weight-normalized FBAP $RTDDR_F$ in each region is shown to the right of each infant bar. Note: a hygroscopic growth factor of 1.12 was applied to the BZ FBAP size distributions.

A significant shift in infant respiratory tract deposition patterns can occur if nasal breathing transitions to oral breathing during a crawling period (Figure 4.17). Upon oral breathing, a reduction in the head airways regional $RTDDR_F$ is associated with both an absolute and relative increase in $RTDDR_F$s for the lower airways. For example, on carpet 1, the pulmonary regional $RTDDR_F$ increased from 1.21 x 10^3 min^{-1} for nasal (10.7% of total) to 1.45 x 10^3 min^{-1} for oral

(14.4% of total) and the tracheobronchial $RTDDR_F$ increased from 4.89 x 10^3 min^{-1} for nasal (43.3% of total) to 6.04 x 10^3 min^{-1} for oral (60% of total). The greater number of resuspended FBAPs that will deposit in the lower respiratory system for oral breathing is important, given the greater prevalence of this breathing route among infants and children compared to adults[401,402] and the resulting change in potential colonization locations of inhaled bacterial cells and fungal spores.

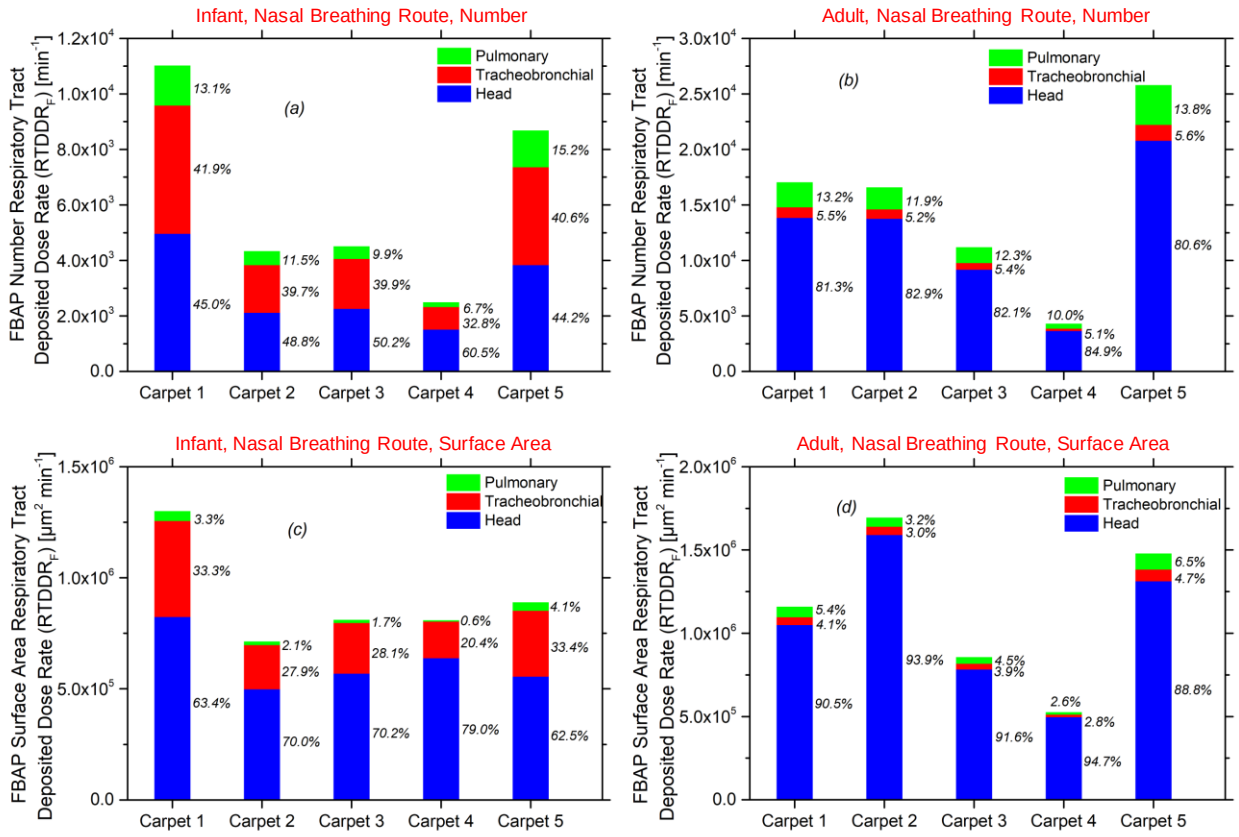

Figure 4.16 Total and regional size-integrated (0.4-15.4 μm) FBAP respiratory tract deposited dose rates ($RTDDR_F$s) (per minute crawling or walking) for each of the five carpets (a.) infant, nasal breathing route, number, (b.) adult, nasal breathing route, number, (c.) infant, nasal breathing route, surface area, and (d.) adult, nasal breathing route, surface area. The fractional dose in each region, expressed as a percentage, is shown to the right of each bar. Note: the hygroscopic growth factor was **not** applied.

The size-resolved total $RTDDR_F$s exhibit a prominent mode between 2.5 and 8 μm (Figure 4.14). For infants, the development of the $RTDDR_F$ mode is the result of the dominant mode of the BZ FBAP size distributions coinciding with the local maxima in depositions fractions for the pulmonary (2 to 4 μm) and tracheobronchial (3 to 7 μm) regions, whereas for adults, the mode develops due to the high deposition fractions (> 0.7) in the head airways for particles above 3 μm

(Figure 4.17). Thus, for infants, a significant fraction of 3 to 6 μm agglomerated bacterial cells and fungal spores can penetrate the head airways and deposit and possibly colonize the lower respiratory microbiota. As shown for carpet 1 in Figure 4.14b, the modal peak in the size-resolved tracheobronchial regional $RTDDR_F$ at roughly 4 μm for an infant under oral breathing is approximately 1.15×10^3 min^{-1}, 73% of the corresponding modal peak in the total $RTDDR_F$ curve (1.58×10^3 min^{-1}). Furthermore, the partial second mode in the infant BZ FBAP size distributions above 10 μm (Figures 4.8, 4.9) occurs at the local maxima for deposition fractions in the head airways (Figure 4.17). Super-10 μm *bio*PM and abiotic particles will preferentially deposit in this region, with size-resolved head airways regional $RTDDR_F$s for carpet 1 peaking at around 4.3×10^2 min^{-1} near 18 μm. Lastly, adults will receive much of their dose to 2.5 to 7 μm *bio*PM in their upper airways, which can be of concern for those with asthma and allergic rhinitis (e.g. Baldacci et al.[403]).

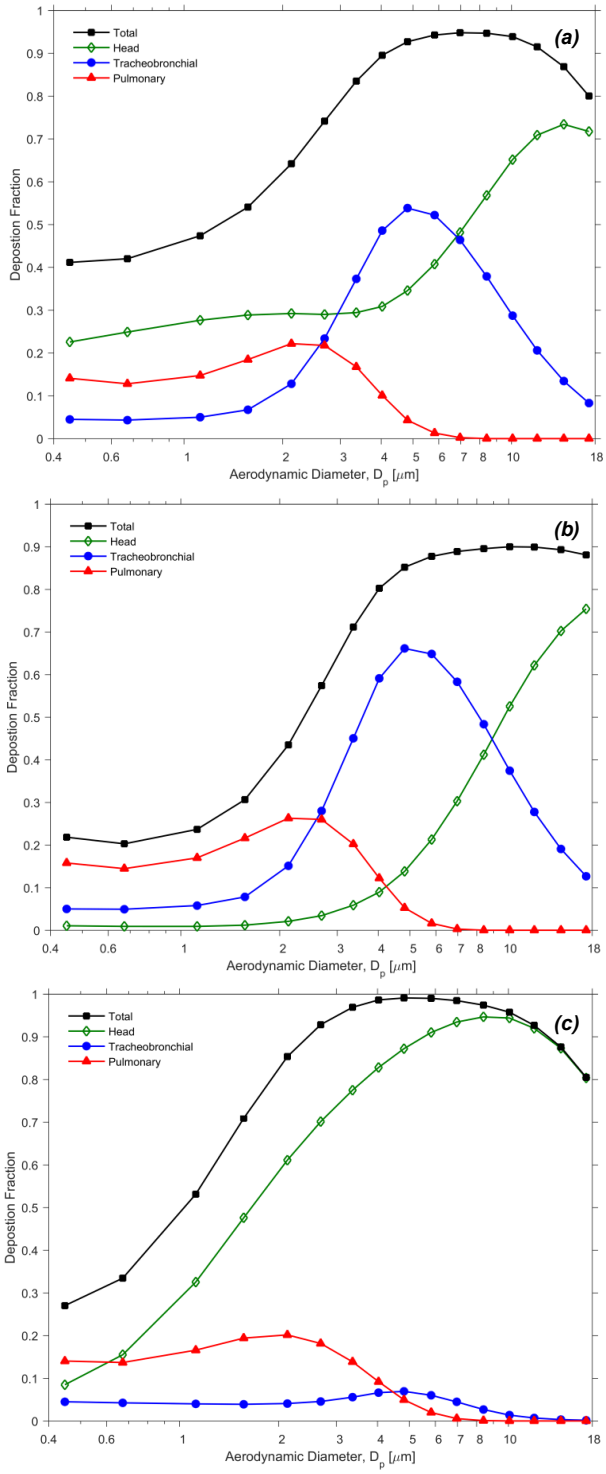

Figure 4.17 Size-resolved total and regional deposition fractions in the respiratory system for an extended size range up to 18 μm to match the hygroscopic-growth shifted FBAP size distributions in the infant and adult BZ (Figure 4.18): (a.) a 3-month old infant, nasal breathing route, (b.) a 3-month old infant, oral breathing route, and (c.) a 21-year old adult, nasal breathing route, obtained from the Multiple-Path Particle Dosimetry (MPPD) Model for breathing parameters stated in Section 4.3.

Infants inhale considerably more air per kg body mass (650 cm^3/kg-min) than do adults (244 cm^3/kg-min). The effect was captured through the analysis of weight-normalized $RTDDR_F$s. As shown in Figure 4.15, an infant receives a 3.88±1.26-fold greater dose of respiratory tract deposited FBAPs per kg body mass compared to an adult (mean ± s.d.). The difference in age-specific weight-normalized $RTDDR_F$s was particularly pronounced in the tracheobronchial region, where they were 22.4- to 44.5-fold greater for an infant compared to an adult. This was also true for FBAPs between 3 and 5 μm (Figure 4.15a). As suggested in Phalen and Phalen[404], weight-normalized RTDDRs may provide a useful basis to compare the resulting biological effects of exposure to inhaled particles between young children and adults. Alternatively, RTDDRs can be normalized by lung mass or surface area.[401] The $RTDDR_F$s reported in this study not only account for infant physiology (respiratory and breathing parameters, body mass), but also a form of human locomotion in belly crawling that is unique to humans under the age of one. The *in situ* BZ measurement of resuspended FBAPs with a robotic crawling platform allows for a much more accurate determination of early-life exposures and RTDDRs to *bio*PM than what can achieved with bulk indoor air sampling (e.g. 1-2 m above infant BZ) or settled house dust analysis.

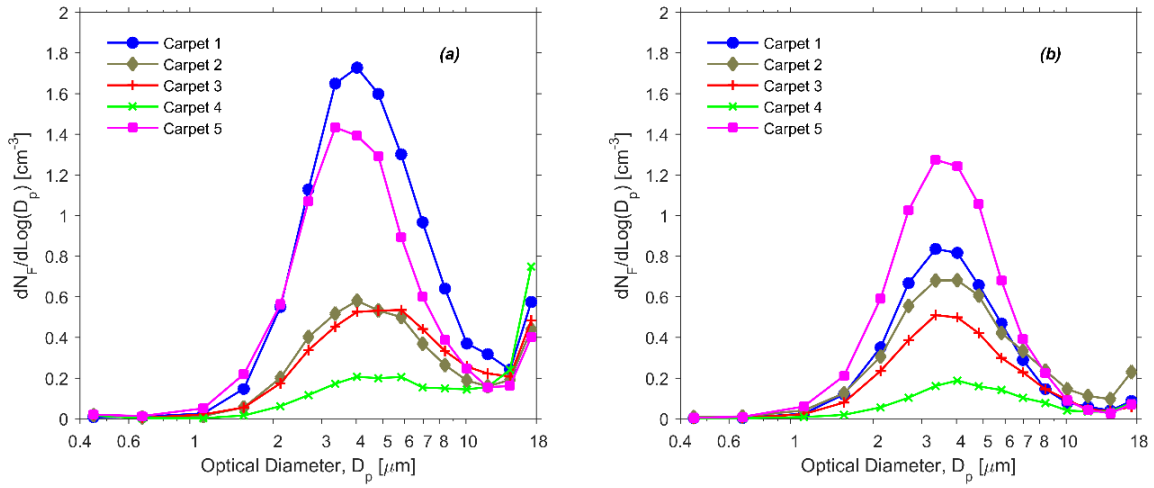

Figure 4.18 Carpet-averaged mean $dN_F/dlogD_p$ (corrected by the hygroscopic growth factor of 1.12) measured during the resuspension periods on five carpets for both crawling (a.) and walking (b.) experiments. Note: the size distributions are slightly shifted to the right, with an upper-limit of 18 μm, compared to Figure 4.9, due to hygroscopic particle growth.

4.4.8 Study limitations

An important limitation of this study is the crawling motion of the simplified robotic infant, which only represents a single crawling style at a given contact frequency (modified belly crawl) and cannot capture the true complexity of the locomotion of an infant. It is likely that resuspension would vary with a particular crawling style, such as hands-and-feet crawling compared to creeping[405], and with age, as the infant learns to walk. Advanced anatomically-correct robotic platforms could be developed to simulate these movements, and their associated contact frequencies, more accurately and evaluate their impact on the resuspension of *bio*PM. Differences in room airflow distribution and mixing conditions between this chamber study and real-world conditions will affect the measured *bio*PM concentrations in the BZ. In addition, the tested carpets were collected from residences in Finland, where it is not common to wear shoes indoors. It is likely the dust loading and microbial composition would be different for homes in other countries where shoes are worn indoors (e.g. track-in effect). The $RTDDR_F$ analysis can be improved by accounting for the non-sphericity of *bio*PM through size-resolved dynamic shape factors specific to different *bio*PM types, measurement of FBAP aerodynamic diameter-based size distributions, and application of actual GFs.[366,406] Lastly, the utility of LIF for $RTDDR_F$ analysis of resuspended *bio*PM can be further assessed through comparison with size-resolved qPCR analysis of bacteria and fungi and application of known DNA and filter extraction efficiencies for the given sampling and analysis protocol.

5. CONCLUSIONS

Particle size is the most basic, yet important, property for an aerosol since it governs the motion of a single particle, which significantly affects its fate. The size-resolved aerosol concentration provides more information of an aerosol population, which may not be reflected by size-integrated measurement metrics. This dissertation presents studies on the size distributions of urban aerosols, resuspended indoor *bio*PM, and synthesized salt particles used for HVAC filter testing. The analysis in the dissertation reveals the importance of PSD measurements on pollutant source identification, aerosol inhalation exposure assessment, and understanding aerosol transport and transformation processes.

The critical review on urban aerosol PSDs identifies geographical variations in the shape and magnitude of PSDs from cities around the globe. The number PSDs in EA and CSSA tend to present peaks at larger diameters, with a meaningful contribution from the accumulation mode particles to the total concentration, while those in EU and NAAN present peaks at smaller diameters. Mass PSDs typically exhibit one peak in the accumulation mode and another in the coarse mode, while those in WA tend to show only one dominant peak in the coarse mode. The median mass PSDs in CSSA present the highest magnitude among all geographical regions, followed by the one in EA. Geographical variations of urban aerosol PSDs suggest differences in emission sources and air pollution levels, and drive large differences in the urban aerosol inhaled deposited dose rate received in each region of the human respiratory system. Similarly, inter-region variations in the shape of PSDs impact the penetration of urban aerosols through filters in building ventilation systems, which were investigated by using a simplified single-pass filtration model. For the same rated HVAC filter, the total penetration fractions of the urban aerosol might be greater in CSSA and EA compared to other regions, since the prominent modes of the number PSDs coincide with the size range where the filtration efficiency is at a minimum. Three urban aerosol effective density functions were constructed, based on a literature review of size-resolved urban aerosol effective densities, to help in converting between number and mass PSDs.

The review of urban aerosol PSD observations identifies current measurement gaps and helps frame future research directions. Building a global network of urban aerosol observation stations to continuously monitor PSDs with a wide size range is helpful to further understand the implications of urban aerosols on human exposure, health effects, and urban air pollution levels.

Currently, only ~20% of the cities in the urban aerosol PSD database include measurements greater than 6 months, and only 14% of the PSD observations spanned from the UFP to coarse regime. A severe lack of data in Africa, Latin America, West Asia, Central and Southeast Asia suggests the urgent need for additional PSD measurements. In addition, more direct measurements of urban aerosol effective densities are needed for accurate translation of urban aerosol number PSDs to mass PSDs in a given urban environment.

As shown in the literature review of urban aerosol PSDs, most of the urban emission sources result in particles dominant in the UFP regime, which validates the needs to develop a new particle generation method to reproduce PSDs similar to the typical urban aerosols PSDs for rapid HVAC filter ageing testing and to replace traditionally used test dusts that are too large to mimic the loading kinetics for realistic scenarios, where the filters are mostly exposed to the urban aerosol. In this dissertation, a newly designed commercially available thermal aerosol generator was introduced, and the physical characteristics of synthesized salt aerosol under variable operational conditions were evaluated. The thermal aerosol generator produces a stable, high mass output of sub-micron NaCl and KCl particles by burning a stick of salt in an O_2-C_3H_8 flame. The generator is capable of creating salt aerosol with sub-micron number and mass PSDs similar in shape to those reported in urban and indoor environments. The salt stick feed rate has a pronounced impact on the PSD output, with increasing feed rate shifting the PSDs to larger sizes. The type of salt (NaCl, KCl) and salt stick diameter have a small influence on the shape of the PSD. The feed rate can be varied from < 3 mm/min to 25 mm/min, providing a basis to modulate the PSD shape as per the requirements of the HVAC filtration experiment. The morphological features of the salt aerosol suggest that NaCl and KCl particles smaller than 100 nm adopt compact spherical or cubic structures, while those larger than 100 nm transition to agglomerates.

The detailed evaluation of the synthesized salt aerosol, including multi-lognormal distribution function parameters for number and mass PSDs, size-resolved effective densities and dynamic shape factors, and mass-mobility exponents provide a basis to understand how the aerosol characteristics can impact HVAC filtration performance during full-scale experiments. The thermal aerosol generator represents a cost-effective tool for rapid loading of HVAC filters with a sub-micron mass PSD similar to that found in real HVAC installations, and thus, is appropriate for use in the proposed ASHRAE Guideline 35 for evaluating the AHU blower energy implications of aged HVAC filters.

The thermal flame generator is capable to produce salt particles with the number and mass PSDs similar to the urban aerosol in shape. Figure 5.1 shows an example of the comparisons among the normalized mass PSDs of the synthesized NaCl salt particle with 12 mm stick diameter at variant feed rates, normalized median mass PSDs in each geographical region, and normalized mass PSDs of particles produced from the traditional filter loading methods. The normalized NaCl salt particles mass PSDs generated at the feed rates of 10, 18, and 25 mm/min match well with the peaks in the accumulation mode of the normalized median mass PSDs in CSSA, EA, EU, and NA, while the normalized mass PSDs of the fine and coarse Arizona road dust only present peaks in the coarse mode. In addition, the KCl particles generated as per ASHRAE 52.2 and the dioctyl phthalate (DOP) particles generated as per Mil-Std-282 also have the normalized mass PSDs similar to the normalized median mass PSDs in the critical review.

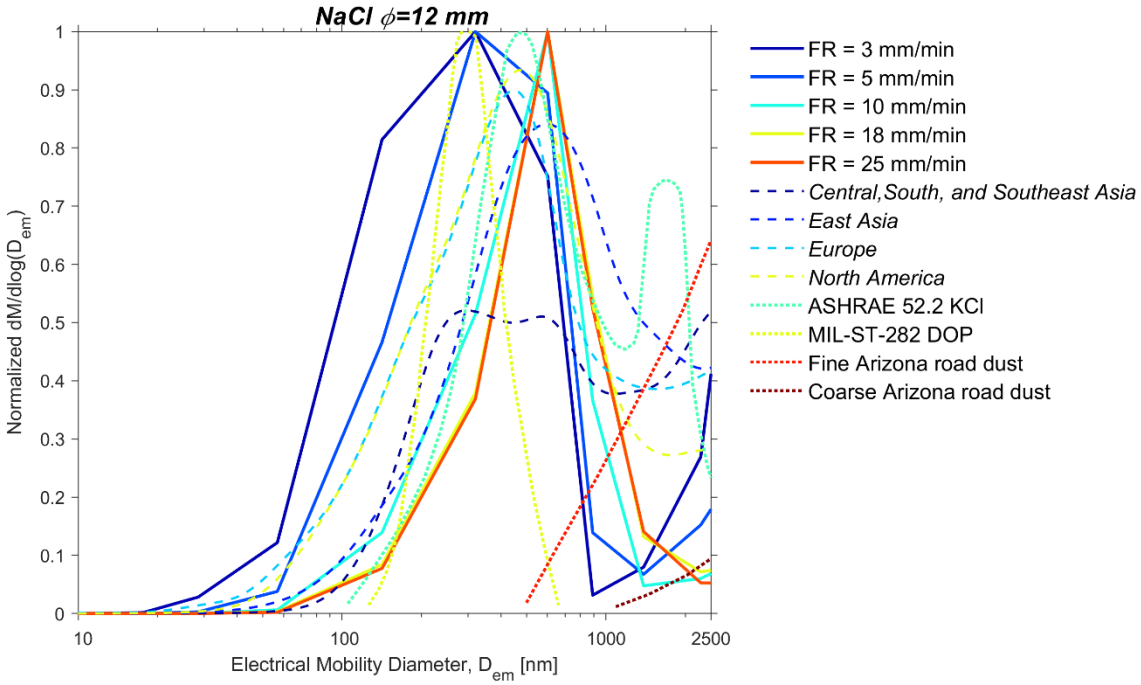

Figure 5.1 Comparisons of the shapes between the normalized mass PSDs of the synthesized particles from different generation techniques with the normalized median agglomerated mass PSDs in different geographical regions. The synthesized particles include the salt particles from the thermal aerosol generator with 12 mm NaCl stick at different feed rates, ASHRAE 52.2 KCl particles, MIL-ST-282 DOP, fine Arizona road dust, and coarse Arizona road dust.

In the indoor environment, human-induced resuspension of the settled dusts is the main source of airborne coarse particles. Since the settled dust is enriched with *bio*PM, this mechanism

becomes the main exposure pathway for occupants to inhale *bio*PM. This dissertation presents a chamber study to characterize infant and adult inhalation exposures and respiratory tract deposited dose rates of resuspended *bio*PM from carpets. The results show the highly transient exposure to the resuspended airborne *bio*PM in both the crawling and walking experiments. The infants are exposed to the self-induced airborne *bio*PM only during the period of active movements, with the concentrations in the near-floor microenvironment higher than those in the adult breathing zone in the walking experiments. The adult may be exposed to self-induced resuspended *bio*PM during post-walking periods due to the enhanced mixing of the walking. The measured concentration of the airborne *bio*PM exhibited no or minimum drop over 200 minutes resuspension experiments, which indicates that the carpet can serve as a continuous reservoir for the airborne *bio*PM in the indoor environment.

In just one minute of crawling or walking, 10^3-10^4 resuspended FBAPs can deposit in the respiratory tract, with an infant receiving much of their number respiratory tract deposited dose in their lower airways. Per kg body mass, an infant will receive nearly four times greater number respiratory tract deposited dose of resuspended FBAPs compared to an adult.

The hourly mass respiratory tract deposited dose rates of the resuspended *bio*PM from the carpets received by the infants and adults could be much greater than those of the urban aerosol in the urban outdoor environments. Figure 5.2 presents the comparisons of the mean size-integrated mass FBAP $RTDDR_F$ in the crawling and walking tests on five carpets with the median mass RTDDR in each geographical region calculated by using the urban aerosol PSD database, for the particles from 400 to 10000 nm. The mean size-integrated mass FBAP $RTDDR_F$ in the crawling and walking tests are up to ~18 times higher than the median mass RTDDR in NAAN and EU, and those on carpet 1, 2, 3, and 5 are up to ~3 times higher than the median mass RTDDR in CSSA, indicating that the walking and crawling on a carpet indoor could results in much greater mass deposited dose rate than walking in the urban outdoor environment in the heavily polluted area in CSSA.

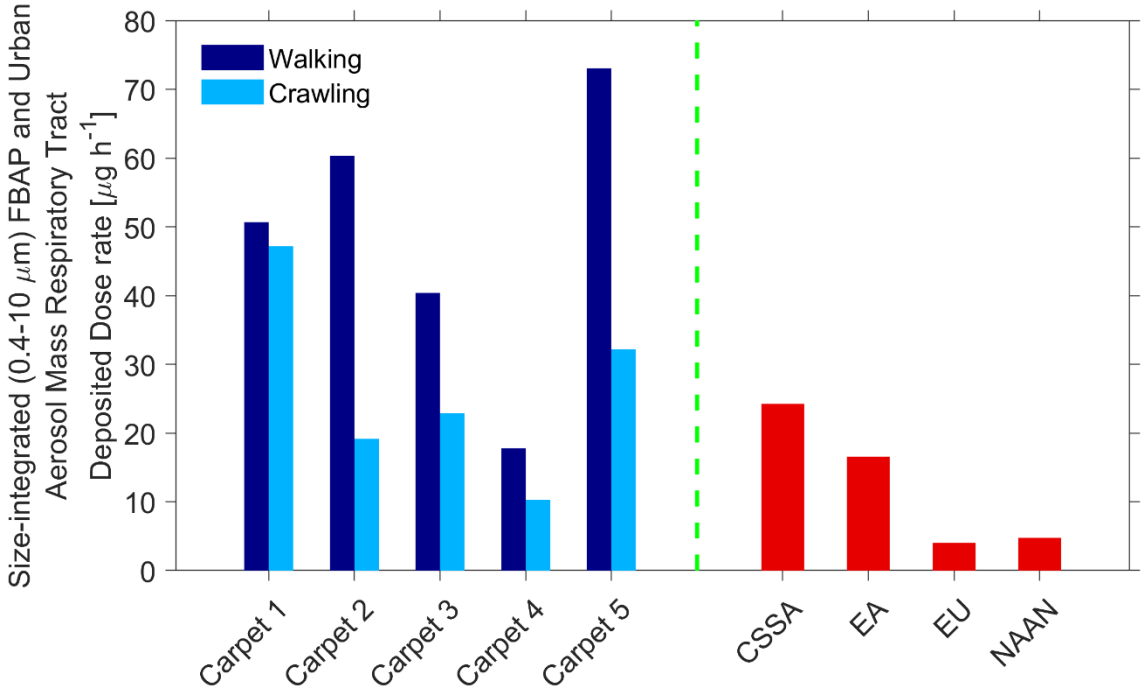

Figure 5.2 Comparisons between the mean size-integrated (400 to 10000 nm) mass $RTDDR_F$ for each carpet in the crawling and walking experiments and the median size-integrated mass RTDDR in each geographical region calculated by using the urban aerosol PSD database.

APPENDIX A. SUPPLEMENTAL MATERIALS FOR URBAN AEROSOL SIZE DISTRIBUTION: A GLOBAL PERSPECTIVE

Table A.1 Urban aerosol size distribution measurements made with electrical mobility-based techniques covering only the sub-micron regime

Region	Country	City	Sampling location	Sampling duration	Time of day	Event identification	Target aerosol population	Measurement type	Prominent mode	Lognormal fitting size range	Mode 1			Mode 2			Mode 3			Reference
											N (cm^{-3})	$\overline{D_p}$ (nm)	σ	N (cm^{-3})	$\overline{D_p}$ (nm)	σ	N (cm^{-3})	$\overline{D_p}$ (nm)	σ	
CSSA	IND	New Delhi	NU	VVST	A	NS	UFP+F	EM	AIT	3-800	500	9.5	1.1	48712	38.5	1.62	13125	148.5	1.73	Mönkkönen et al. (2005)
CSSA	IND	New Delhi	NU	VVST	A	NS	UFP+F	EM	AIT	3-800	10216	18.1	2.24	14375	36	1.61	8550	169.7	1.67	Mönkkönen et al. (2005)
CSSA	IND	New Delhi	NU	VVST	A	NS	UFP+F	EM	AIT	3-800	500	9.5	1.1	48711	38.5	1.62	13126	148.5	1.73	Mönkkönen et al. (2005)
CSSA	IND	New Delhi	NU	VVST	E	NS	UFP+F	EM	ACC	3-800	26728	54.6	1.76	37507	149.4	1.6	--	--	--	Mönkkönen et al. (2005)
CSSA	IND	New Delhi	NU	VVST	E	NS	UFP+F	EM	ACC	3-800	10937	47.2	1.77	35288	156.9	1.63	--	--	--	Mönkkönen et al. (2005)
CSSA	IND	New Delhi	NU	VVST	E	NS	UFP+F	EM	ACC	3-800	7444	44.5	1.93	24102	160.5	1.66	--	--	--	Mönkkönen et al. (2005)
CSSA	IND	New Delhi	NU	VVST	E	NS	UFP+F	EM	AIT	3-800	17291	65.6	1.37	45330	78	2.11	--	--	--	Mönkkönen et al. (2005)
CSSA	IND	New Delhi	NU	VVST	E	NS	UFP+F	EM	AIT-ACC	3-800	1132	25.7	1.29	56675	96.7	1.82	557	315	1.19	Mönkkönen et al. (2005)
CSSA	IND	New Delhi	NU	VVST	E	NS	UFP+F	EM	ACC	3-800	65339	95.6	2.01	6942	139.2	1.26	12090	205	1.39	Mönkkönen et al. (2005)
CSSA	IND	New Delhi	NU	VVST	M	NS	UFP+F	EM	ACC	3-800	21263	47.6	2.29	15841	173	1.66	--	--	--	Mönkkönen et al. (2005)
CSSA	IND	New Delhi	NU	VVST	M	NS	UFP+F	EM	AIT	3-800	40586	40.1	1.8	4082	40.9	1.23	17679	160.8	1.72	Mönkkönen et al. (2005)
CSSA	IND	New Delhi	NU	VVST	M	NS	UFP+F	EM	AIT	3-800	800	9	1.16	36555	37	1.62	16596	134.8	1.8	Mönkkönen et al. (2005)
CSSA	IND	New Delhi	NU	MT	ME	NS	UPF+F	EM	AIT	3-800	4433	11.9	1.36	29858	38	1.67	30735	123.1	1.87	Laasko et al. (2006)
CSSA	IND	Kanpur	NU	ST	ME	NS	UPF+F	EM	ACC	15-670	199	47	1.69	787	141.3	1.6	3451	229.5	1.83	Bhattu et al. (2014)
CSSA	IND	Kanpur	NU	ST	ME	NS	UPF+F	EM	ACC	15-670	2101	11	2.5	2031	105.6	2.47	4684	190.1	2.24	Bhattu et al. (2014)
CSSA	IND	Kanpur	NU	ST	ME	NS	UPF+F	EM	AIT-ACC	15-670	3279	35.9	1.77	1546	92.6	1.44	1838	154.9	1.81	Bhattu et al. (2014)
CSSA	IND	Kanpur	NU	VVST	ME	background aerosol	UPF+F	EM	NUC	15-685	76348	7.7	1.95	42102	12.7	4.26	--	--	--	Misra et al. (2014)
CSSA	IND	Kanpur	NU	VVST	ME	background aerosol	UPF+F	EM	AIT	15-685	2239	20.5	1.27	15377	46	1.73	988	202.2	1.46	Misra et al. (2014)
CSSA	IND	Kanpur	NU	VVST	ME	mixed aerosol	UPF+F	EM	NUC	15-685	12486	15.1	1.62	1532	46.2	1.43	3369	150.9	2.05	Misra et al. (2014)
CSSA	IND	Kanpur	NU	VVST	ME	mixed aerosol	UPF+F	EM	AIT	15-685	1200	40.1	1.45	314	75.3	1.26	3215	130.1	1.83	Misra et al. (2014)

CSSA	IND	Kanpur	NU	VVST	ME	dust dominated aerosol	UPF+F	EM	NUC	15-685	120805	4.4	4.63	259	21.6	1.07	311	45.4	1.19	Misra et al. (2014)
CSSA	IND	Kanpur	NU	VVST	ME	dust dominated aerosol	UPF+F	EM	AIT	15-685	443	28.1	1.29	3988	92.5	2.36	--	--	--	Misra et al. (2014)
CSSA	IND	Kanpur	NU	VVST	ME	pollution dominated aerosol	UPF+F	EM	AIT	15-685	3073	19.2	1.41	9945	44	1.62	1578	174.7	1.67	Misra et al. (2014)
CSSA	IND	Kanpur	NU	VVST	ME	pollution dominated aerosol	UPF+F	EM	NUC	15-685	33873	13.4	2.01	1064	94.5	1.41	2756	195.3	1.64	Misra et al. (2014)
CSSA	IND	Kanpur	SUB	VVST	E	NS	UFP+F	EM	AIT-ACC	14.6-697	945	28.4	1.35	33361	108.6	1.7	3572	116.6	1.28	Baxla et al. (2009)
CSSA	IND	Kanpur	SUB	VVST	E	NS	UFP+F	EM	AIT-ACC	14.6-697	3505	35.4	1.54	5037	76.1	1.45	7286	138.9	1.52	Baxla et al. (2009)
CSSA	IND	Kanpur	SUB	VVST	E	NS	UFP+F	EM	AIT-ACC	14.6-697	1619	20.2	1.36	163	106.8	1.06	33725	127.3	2.08	Baxla et al. (2009)
CSSA	IND	Kanpur	SUB	VVST	E	NS	UFP+F	EM	ACC	14.6-697	79484	99.5	1.95	6568	137.5	1.17	--	--	--	Baxla et al. (2009)
CSSA	IND	Kanpur	SUB	VVST	M	NS	UFP+F	EM	AIT	14.6-697	4344	87.7	1.31	28279	109.9	1.81	--	--	--	Baxla et al. (2009)
CSSA	IND	Kanpur	SUB	VVST	M	NS	UFP+F	EM	AIT-ACC	14.6-697	6176	49.8	1.81	4354	79.6	1.96	4824	91.3	1.93	Baxla et al. (2009)
CSSA	IND	Kanpur	SUB	VVST	M	NS	UFP+F	EM	AIT-ACC	14.6-697	770	30	1.29	35265	105.5	1.82	--	--	--	Baxla et al. (2009)
CSSA	IND	Kanpur	SUB	VVST	M	NS	UFP+F	EM	AIT-ACC	14.6-697	98	109.8	1.11	24210	115.2	1.94	--	--	--	Baxla et al. (2009)
CSSA	IND	Kanpur	SUB	LT	ME	NS	UFP+F	EM	AIT	13.8-685	4417	44.6	2.06	3288	88.7	1.55	1109	199.8	1.61	Kanawade et al. (2014)
CSSA	IND	Kanpur	SUB	LT	ME	NS	UFP+F	EM	ACC	13.8-685	20287	94.8	2.39	7370	157.6	1.63	521	318.5	1.29	Kanawade et al. (2014)
CSSA	IND	Kanpur	SUB	LT	ME	NS	UFP+F	EM	AIT-ACC	13.8-685	300	12	1.24	7166	89.2	2.09	1686	128.1	1.67	Kanawade et al. (2014)
CSSA	IND	Kanpur	SUB	LT	ME	NS	UFP+F	EM	ACC	13.8-685	510	14	1.2	873	36.4	1.54	23561	143.7	1.89	Kanawade et al. (2014)
CSSA	NPL	Lalitpur	NU	ST	ME	NS	UPF+F	EM	AIT	10-450	2192	27.9	1.67	2433	85.2	1.64	389	193.8	1.47	Shrestha et al. (2016)
CSSA	NPL	Dhulikhel	SUB	MT	D	NS	UPF+F	EM	AIT	14-340	6210	31	3.73	863	101.8	1.51	182	191.7	1.36	Shrestha et al. (2010)
CSSA	NPL	Dhulikhel	SUB	MT	E	NS	UPF+F	EM	AIT-ACC	14-340	149	25.2	1.54	3860	103	1.85	--	--	--	Shrestha et al. (2010)
CSSA	NPL	Dhulikhel	SUB	MT	ME	NS	UPF+F	EM	AIT	14-340	3815	27.2	3.95	3639	91.3	1.79	156	219.1	1.38	Shrestha et al. (2010)
CSSA	SGP	Singapore	NU	ST	ME	NS	UPF+F	EM	AIT	8-334	5114	6.6	1.34	15987	26.6	3.16	2442	35.3	1.47	See et al. (2006)
CSSA	SGP	Singapore	NU	ST	ME	HZ	UPF+F	EM	NUC	8-334	5339	6.6	1.67	38502	50.7	2.07	2972	46	1.31	See et al. (2006)
EA	CHN	Beijing	NU	ST	D	NS	UFP+F	EM	AIT	5.6-560	2172	10.3	1.84	821	35.9	1.45	1323	61.8	1.71	Shi et al. (2007)
EA	CHN	Shanghai	NU	VST	D	NS	UFP+F	EM	AIT	10-487	93422	22	2.94	9856	39.3	1.29	8061	93.4	1.3	Li et al. (2007)
EA	CHN	Shanghai	NU	VST	D	NS	UFP+F	EM	AIT	10-487	45248	28	1.94	11387	132.3	1.77	--	--	--	Li et al. (2007)
EA	CHN	Beijing	NU	ST	E	NS	UFP+F	EM	AIT	5.6-560	458	12.3	1.42	2074	43.7	1.67	230	112.8	1.42	Shi et al. (2007)

EA	CHN	Beijing	NU	VVST	E	NPF	UFP+F	EM	AIT	3-800	16888	44.6	2.5	5019	67.9	1.41	--	--	--	Wang et al. (2013)
EA	CHN	Beijing	NU	VVST	E	NS	UFP+F	EM	AIT	3-800	7436	61.4	2.96	8830	71.6	1.32	3841	172	1.41	Wiedensohler et al. (2009)
EA	CHN	Beijing	NU	VVST	E	NS	UFP+F	EM	AIT-ACC	3-800	5157	33.3	2.05	9311	88.8	1.36	8691	188.4	1.57	Wiedensohler et al. (2009)
EA	CHN	Beijing	NU	VVST	M	NPF	UFP+F	EM	NUC	3-800	29803	7.1	1.5	10649	13	1.19	10422	26.6	1.87	Wang et al. (2013)
EA	CHN	Beijing	NU	VVST	A	NPF	UFP+F	EM	NUC-AIT	3-800	36292	13.8	2.13	7416	23.2	1.2	--	--	--	Wang et al. (2013)
EA	CHN	Beijing	NU	VVST	A	NPF	UFP+F	EM	AIT	3-800	3000	2.6	1.2	24270	27.1	2.47	9304	37.9	1.33	Wang et al. (2013)
EA	CHN	Beijing	NU	VVST	M	NS	UFP+F	EM	NUC	3-800	18173	10.2	1.64	4806	11.9	1.27	5225	111.2	1.76	Wiedensohler et al. (2009)
EA	CHN	Beijing	NU	VVST	A	NS	UFP+F	EM	AIT	3-800	4086	29	1.26	12877	52.8	1.34	4566	143	1.48	Wiedensohler et al. (2009)
EA	CHN	Shanghai	NU	LT	ME	HZ	UFP+F	EM	AIT	10-1000	1321	22.3	1.26	2359	35.5	1.38	12940	68.8	2.24	Wang et al. (2014)
EA	CHN	Shanghai	NU	LT	ME	NS	UFP+F	EM	AIT	10-1000	1116	18.6	1.25	1827	32.7	1.32	4637	50.6	2.53	Wang et al. (2014)
EA	CHN	Shanghai	NU	LT	ME	photochemical smog	UFP+F	EM	AIT	10-1000	2136	24	1.32	947	85.9	1.17	20566	52.9	1.99	Wang et al. (2014)
EA	CHN	Shanghai	NU	MT	ME	NS	UFP+F	EM	AIT	15-600	4449	25	1.55	5863	71	1.7	917	218	1.49	Peng et al. (2014)
EA	CHN	Beijing	NU	MT	ME	NS	UFP+F	EM	AIT	3-800	615	5.7	1.33	31702	32.8	2.61	614	114.4	1.55	Massling et al. (2009)
EA	CHN	Beijing	NU	MT	ME	NS	UFP+F	EM	AIT	3-800	12536	17.2	1.98	8605	50.5	1.79	11445	105.5	1.98	Massling et al. (2009)
EA	CHN	Beijing	NU	MT	ME	NS	UFP+F	EM	AIT-ACC	3-800	2190	14	1.53	23816	60.8	2.66	4346	128.4	1.73	Massling et al. (2009)
EA	CHN	Beijing	NU	MT	ME	NS	UFP+F	EM	AIT-ACC	3-800	3206	15.7	1.72	30012	76.4	2.21	5575	222.7	1.69	Massling et al. (2009)
EA	CHN	Jinan	NU	ST	ME	NS	UFP+F	EM	AIT	10-1000	15533	31.7	2	1200	175.7	1.57	--	--	--	Gao et al. (2007)
EA	CHN	Guangzhou	NU	ST	ME	NS	UFP+F	EM	AIT	15-600	5621	17	1.82	5404	65	1.72	3078	166	1.6	Peng et al. (2014)
EA	CHN	Urumchi	NU	ST	ME	NS	UFP+F	EM	AIT	15-600	18910	24	1.73	7122	59	1.83	555	146	1.89	Peng et al. (2014)
EA	CHN	Wuxi	NU	ST	ME	NS	UFP+F	EM	AIT	15-600	1250	29	1.33	9878	63	1.67	4972	142	1.6	Peng et al. (2014)
EA	CHN	Wuxi	NU	ST	ME	NS	UFP+F	EM	AIT	15-600	7473	23	1.59	7844	61	1.6	2092	154	1.61	Peng et al. (2014)
EA	CHN	Jinhua	NU	ST	ME	NS	UFP+F	EM	ACC	15-600	1892	36	1.52	10753	116	1.71	206	329	1.23	Peng et al. (2014)
EA	CHN	Beijing	NU	ST	ME	NS	UFP+F	EM	AIT	5.6-560	1355	11.4	1.73	1206	38.4	1.49	929	73.3	1.63	Shi et al. (2007)
EA	CHN	Hong Kong	NU	VST	ME	NS	UFP+F	EM	NUC	20-600	1102	18.3	1.48	1155	82.2	2.46	--	--	--	Ning et al. (2013)
EA	CHN	Nanjing	SUB	LT	ME	NS	UFP+F	EM	AIT	6-800	1054	17.6	1.48	11825	40.1	2.66	6692	112.2	1.95	Qi et al. (2015)
EA	CHN	Guangzhou	SUB	ST	ME	NS	UFP+F	EM	AIT	3-900	11016	65	2.13	3791	72.6	1.56	--	--	--	Rose et al. (2011)
EA	CHN	Guangzhou	SUB	ST	ME	BB	UFP+F	EM	ACC	3-900	173	30.6	1.18	10294	84.7	2.2	3865	142.2	1.54	Rose et al. (2011)
EA	CHN	Beijing	NU	MT	ME	NS	UPF+F	EM	AIT-ACC	15-710.5	13379	44.6	2.08	7931	145.4	1.81	743	304.1	1.43	Liu et al. (2016)
EA	CHN	Beijing	NU	MT	ME	NS	UPF+F	EM	AIT-ACC	15-710.5	708	24.8	1.4	12205	60.6	2.08	2862	158.5	1.66	Liu et al. (2016)
EA	CHN	Beijing	NU	MT	ME	NS	UPF+F	EM	AIT	10-500	2281	30.1	1.53	4141	91.6	1.95	113	279.9	1.13	Gao et al. (2012)
EA	CHN	Hongkong	NU	MT	ME	NS	UPF+F	EM	AIT	10-250	70	23.8	1.29	644	72.7	1.45	1089	57.2	2.32	Meng et al. (2014)
EA	CHN	Lanzhou	NU	VVST	E	NS	UPF+F	EM	AIT	10-770	52131	70.1	2.47	11313	56.4	1.61	--	--	--	Zhao et al. (2014)

EA	CHN	Lanzhou	NU	VVST	E	NS	UPF+F	EM	AIT	10-770	4503	24	1.37	9097	44	1.35	33604	80.9	2	Zhao et al. (2014)
EA	CHN	Lanzhou	NU	VVST	E	NS	UPF+F	EM	AIT	10-770	12134	30.3	1.33	45272	51	1.47	62442	102.6	2.3	Zhao et al. (2014)
EA	CHN	Lanzhou	NU	VVST	E	NS	UPF+F	EM	AIT	10-770	4704	19.1	1.33	3417	32.4	1.51	3512	65.6	1.89	Zhao et al. (2014)
EA	CHN	Lanzhou	NU	VVST	E	NS	UPF+F	EM	AIT	10-770	1013	18.5	1.25	8920	36.9	1.67	5202	99.8	2.21	Zhao et al. (2014)
EA	CHN	Lanzhou	NU	VVST	E	NS	UPF+F	EM	AIT	10-770	467	16.5	1.19	39153	57.4	2.02	3803	255.8	1.5	Zhao et al. (2014)
EA	CHN	Lanzhou	NU	VVST	E	NS	UPF+F	EM	AIT	10-770	530	22	1.23	6528	41.2	1.35	31198	73	2.17	Zhao et al. (2014)
EA	CHN	Lanzhou	NU	VVST	E	NS	UPF+F	EM	ACC	10-770	48781	96.1	2.26	17263	210.3	1.76	--	--	--	Zhao et al. (2014)
EA	CHN	Lanzhou	NU	VVST	E	NS	UPF+F	EM	AIT	10-770	654	19.4	1.28	3716	50.1	2.1	--	--	--	Zhao et al. (2014)
EA	CHN	Lanzhou	NU	VVST	E	NS	UPF+F	EM	AIT	10-770	10339	52.4	1.88	2252	20.9	1.39	1988	220	1.66	Zhao et al. (2014)
EA	JPN	Tokyo	NU	ST	ME	NS	UFP+F	EM	AIT	10-400	3841	29.9	1.77	3376	94.7	1.69	123	287.5	1.26	Mochida et al. (2006)
EA	JPN	Kawasaki	TR	ST	M	NS	UFP+F	EM	AIT	15-850	24173	25.4	1.46	20013	71.8	1.94	--	--	--	Hasegawa et al. (2004)
EA	JPN	Kawasaki	TR	ST	M	NS	UFP+F	EM	AIT	15-850	42393	27.1	1.45	92945	86.7	1.91	--	--	--	Hasegawa et al. (2004)
EA	JPN	Kawasaki	TR	ST	ME	NS	UFP+F	EM	NUC-AIT	10-470	15809	19.5	1.45	37303	24	1.9	11980	88.1	1.78	Fushimi et al. (2008)
EA	JPN	Kawasaki	UB	ST	ME	NS	UFP+F	EM	AIT	9.8-414	1032	20.2	1.34	7570	31.4	1.59	8605	71.8	1.79	Fushimi et al. (2008)
EA	JPN	Sapporo	NU	VST	ME	NS	UPF+F	EM	AIT-ACC	7-165	123	17.6	1.48	1799	70.5	2.05	377	125.7	1.25	Jung et al. (2013)
EA	JPN	Sapporo	NU	VST	ME	NS	UPF+F	EM	AIT-ACC	7-165	1491	35.3	1.94	822	112.6	1.54	30	117.3	1.07	Jung et al. (2013)
EA	JPN	Sapporo	NU	VST	ME	NPF	UPF+F	EM	AIT	7-165	12	14.9	1.12	2184	39.1	2.06	225	49.3	1.39	Jung et al. (2013)
EA	JPN	Sapporo	NU	VST	ME	NPF	UPF+F	EM	AIT	7-165	1293	40.5	2.09	57	69.4	1.19	61	142.6	1.23	Jung et al. (2013)
EA	JPN	Sapporo	NU	VST	ME	NPF	UPF+F	EM	AIT	7-165	1894	44.6	1.94	442	71.2	1.33	68	146.3	1.14	Jung et al. (2013)
EA	JPN	Kawasaki	TR	VST	ME	NS	UPF+F	EM	NUC	5.6-560	30806	10.9	1.54	59420	48.3	1.88	12382	10.2	1.15	Fujitani et al. (2012)
EA	JPN	Kawasaki	TR	VST	ME	NS	UPF+F	EM	NUC	5.6-560	21986	10.1	1.13	191401	20.9	1.85	--	--	--	Fujitani et al. (2012)
EA	JPN	Kawasaki	TR	VST	ME	NS	UPF+F	EM	NUC	5.6-560	22091	10.3	1.18	10045	16	1.2	83047	45.9	1.85	Fujitani et al. (2012)
EA	JPN	Kawasaki	TR	VST	ME	NS	UPF+F	EM	NUC	5.6-560	35150	10	1.16	42720	15.6	1.43	135510	22.9	2.03	Fujitani et al. (2012)
EA	KOR	Kwangju	NU	VVST	A	PC	UFP+F	EM	ACC	13-600	289	16.8	1.32	367	96.3	1.83	1006	173.7	1.45	Park et al. (2009)
EA	KOR	Kwangju	NU	VVST	A	PC	UFP+F	EM	ACC	13-600	1091	19.7	1.27	2316	77.1	1.69	1877	163.8	1.52	Park et al. (2009)
EA	KOR	Kwangju	NU	VVST	A	PC	UFP+F	EM	NUC	13-600	3349	22.1	1.35	739	62.1	1.34	3578	122.6	1.69	Park et al. (2009)
EA	KOR	Kwangju	NU	VVST	A	PC	UFP+F	EM	AIT	13-600	1032	28.6	1.19	4178	33.7	1.98	4174	116.4	1.79	Park et al. (2009)
EA	KOR	Kwangju	NU	VVST	E	PC	UFP+F	EM	AIT-ACC	13-600	2129	31.7	1.3	7057	105.5	1.85	--	--	--	Park et al. (2009)
EA	KOR	Kwangju	NU	VVST	E	PC	UFP+F	EM	AIT-ACC	13-600	118	17.3	1.17	1291	33.4	1.28	7255	107	1.82	Park et al. (2009)
EA	KOR	Kwangju	NU	VVST	E	PC	UFP+F	EM	AIT-ACC	13-600	1919	36.7	1.43	1376	79.9	1.37	4297	138.5	1.63	Park et al. (2009)
EA	KOR	Kwangju	NU	VVST	E	PC	UFP+F	EM	AIT-ACC	13-600	603	31.3	1.36	4313	101.6	1.74	829	204.8	1.47	Park et al. (2009)
EA	KOR	Kwangju	NU	VVST	E	CB	UFP+F	EM	AIT-ACC	13-600	69	40.3	1.09	4447	41	1.62	7445	124	1.68	Park et al. (2009)
EA	KOR	Kwangju	NU	VVST	E	CB	UFP+F	EM	AIT-ACC	13-600	1079	32	1.54	704	50.9	1.29	12571	95.4	1.83	Park et al. (2009)

EA	KOR	Kwangju	NU	VVST	E	CB	UFP+F	EM	AIT	13-600	210	20.1	1.26	1539	53.6	1.26	16280	85.1	1.79	Park et al. (2009)
EA	KOR	Kwangju	NU	VVST	E	CB	UFP+F	EM	AIT	13-600	2380	49.9	2.11	252	61.8	1.16	15632	99.6	1.85	Park et al. (2009)
EA	KOR	Kwangju	NU	VVST	E	CB	UFP+F	EM	AIT-ACC	13-600	15253	87	1.65	4191	191.6	1.54	--	--	--	Park et al. (2009)
EA	KOR	Kwangju	NU	VVST	E	CB	UFP+F	EM	AIT-ACC	13-600	638	70.2	1.26	14835	110.5	1.79	--	--	--	Park et al. (2009)
EA	KOR	Seoul	NU	VST	A	NS	UPF+F	EM	AIT	20-560	934	32.6	1.52	215	54.4	1.23	2143	105.2	1.79	Hung et al. (2010)
EA	KOR	Seoul	NU	VST	E	NS	UPF+F	EM	AIT	20-560	243	61.7	1.19	1720	74.3	2.86	--	--	--	Hung et al. (2010)
EA	KOR	Seoul	NU	VST	E	NS	UPF+F	EM	AIT	20-560	375	32.6	1.28	118	57.3	1.19	2760	69.5	2.15	Hung et al. (2010)
EA	KOR	Seoul	NU	VST	M	NS	UPF+F	EM	AIT-ACC	20-560	11753	81.8	1.97	--	--	--	--	--	--	Hung et al. (2010)
EA	CHN: TWN	Taipei	TR	ST	D	NS	UFP+F	EM	AIT	6-225	10000	3	1.53	23243	42.7	2.45	21	64.9	1.11	Cheng et al. (2013)
EA	CHN: TWN	Taipei	TR	ST	M	NS	UFP+F	EM	AIT	6-225	1404	51.7	1.68	8097	53.1	3.54	595	132	1.35	Cheng et al. (2013)
EA	CHN: TWN	Taipei	TR	ST	ME	NS	UFP+F	EM	AIT	6-225	8000	3	1.55	20408	44.3	2.51	--	--	--	Cheng et al. (2013)
EU	AUT	Vienna	NU	VST	E	NS	UFP+F	EM	ACC	10-925	3319	28	3.84	170	41	1.32	2061	132.8	1.7	Burkart et al. (2010)
EU	AUT	Vienna	NU	VVST	E	NS	UFP+F	EM	AIT-ACC	10-925	3390	46.1	2.63	3616	84	1.5	3103	159	1.51	Burkart et al. (2010)
EU	AUT	Vienna	NU	VST	M	NS	UFP+F	EM	AIT	10-925	4731	22.7	1.66	4411	80.8	2.11	190	88.7	1.18	Burkart et al. (2010)
EU	AUT	Vienna	NU	VST	ME	NS	UFP+F	EM	AIT-ACC	10-925	907	13	2.26	19	35.3	1.09	945	96	2	Burkart et al. (2010)
EU	AUT	Vienna	NU	VVST	E	NS	UFP+F	EM	AIT-ACC	10-925	3390	46.1	2.63	3616	84	1.5	3103	159	1.51	Burkart et al. (2010)
EU	CHE	Zurich	TR	MT	E	NS	UFP+F	EM	AIT	18-700	4559	28	1.67	6211	87.2	2.17	--	--	--	Imhof et al. (2005)
EU	CHE	Zurich	TR	MT	M	NS	UFP+F	EM	AIT	18-700	26240	19.6	1.62	25533	62.9	2.33	499	114	1.31	Imhof et al. (2005)
EU	CZE	Prague	SUB	MT	ME	NS	UPF+F	EM	AIT-ACC	20-540	1733	0.04	103.5	3439	81.8	2.34	--	--	--	Lazaridis et al. (2017)
EU	CZE	Prague	UB	ST	ME	NS	UPF+F	EM	AIT	14.7-724	366	19.5	1.13	1167	27.5	1.3	4031	63.7	2.07	Talbot et al. (2017)
EU	CZE	Prague	UB	ST	ME	NS	UPF+F	EM	AIT	14.7-724	406	19.7	1.18	803	27.6	1.33	4896	76	2.25	Talbot et al. (2017)
EU	DEU	Erfurt	NU	LT	ME	NS	UFP+F	EM	NUC	10-500	1562	11	1.26	12959	14.8	2.57	1878	148.1	1.59	Tuch et al. (2003)
EU	DEU	Erfurt	NU	LT	ME	NS	UFP+F	EM	NUC	10-500	1795	10.3	1.32	7473	23.5	2.94	1159	161.6	1.52	Tuch et al. (2003)
EU	DEU	Erfurt	NU	LT	ME	NS	UFP+F	EM	NUC	10-500	130836	1.5	6.04	1514	154.4	1.39	--	--	--	Tuch et al. (2003)
EU	DEU	Erfurt	NU	LT	ME	NS	UFP+F	EM	NUC	10-500	2343	11	1.26	13105	15.8	2.7	1846	149.1	1.57	Tuch et al. (2003)
EU	DEU	Leipzig	NU	LT	ME	NS	UFP+F	EM	NUC	3-800	9311	15.5	1.98	522	17.8	1.23	3523	79.9	2.31	Tuch et al. (2003)
EU	DEU	Leipzig	NU	LT	ME	NS	UFP+F	EM	NUC-AIT	3-800	1915	8.7	1.64	458	20.4	1.4	8431	31.7	2.96	Tuch et al. (2003)
EU	DEU	Leipzig	NU	LT	ME	NS	UFP+F	EM	NUC	3-800	14919	16.5	1.9	130	18.8	1.07	4270	66.6	2.35	Tuch et al. (2003)
EU	DEU	Leipzig	NU	LT	ME	NS	UFP+F	EM	NUC	3-800	195	3.2	1.13	6435	12.5	1.99	8910	33.8	2.87	Tuch et al. (2003)
EU	DEU	Leipzig	NU	LT	ME	NS	UFP+F	EM	NUC	3-800	7382	15.8	1.96	435	40.2	1.3	5640	70.6	2.3	Tuch et al. (2006)
EU	DEU	Erfurt	NU	LT	ME	NS	UFP+F	EM	NUC	10-500	15482	12.5	2.29	2439	135.6	1.85	--	--	--	Wichmann et al. (2000)

EU	DEU	Erfurt	NU	LT	ME	NS	UPF+F	EM	NUC	10-500	141	13.1	1.18	2437	17	2.08	420	132.4	1.71	Kreyling et al. (2003)
EU	DEU	Erfurt	NU	LT	ME	NS	UPF+F	EM	NUC	10-500	763	9.6	1.31	2202	13.3	2.56	258	150.9	1.58	Kreyling et al. (2003)
EU	DEU	Erfurt	NU	LT	ME	NS	UPF+F	EM	NUC	10-500	976	8.7	1.38	1274	17.1	2.15	217	141.3	1.64	Kreyling et al. (2003)
EU	DEU	Erfurt	NU	LT	ME	NS	UPF+F	EM	NUC	10-500	3581	6.4	3.96	56	145.4	1.22	100	162.1	1.85	Kreyling et al. (2003)
EU	DEU	Braunschweig	NU	ST	ME	NS	UPF+F	EM	AIT-ACC	10-360	316	14.9	1.19	9313	32.5	2.34	3819	110.5	1.5	Ghassoun et al. (2015)
EU	DEU	Braunschweig	NU	ST	ME	NS	UPF+F	EM	AIT-ACC	10-360	930	14.8	1.34	5194	35.6	2.02	3741	113.6	1.58	Ghassoun et al. (2015)
EU	DEU	Braunschweig	NU	ST	ME	NS	UPF+F	EM	AIT	10-360	2228	14.9	1.69	4681	38.9	1.61	4690	106.2	1.6	Ghassoun et al. (2015)
EU	DEU	Braunschweig	NU	ST	ME	NS	UPF+F	EM	BIM (AIT, ACC)	10-360	351	12.6	1.25	5148	30.3	1.68	4959	111	1.56	Ghassoun et al. (2015)
EU	DEU	Braunschweig	NU	ST	ME	NS	UPF+F	EM	AIT-ACC	10-360	832	14.6	1.27	6132	32.3	2.1	4070	107.8	1.54	Ghassoun et al. (2015)
EU	DEU	Braunschweig	NU	ST	ME	NS	UPF+F	EM	BIM (NUC, ACC)	10-360	1278	14.7	1.32	4550	34.9	2.3	3564	107.9	1.59	Ghassoun et al. (2015)
EU	DEU	Braunschweig	NU	ST	ME	NS	UPF+F	EM	AIT	10-360	880	15.7	1.22	19959	34.1	2.23	1686	113.7	1.43	Ghassoun et al. (2015)
EU	DEU	Braunschweig	NU	ST	ME	NS	UPF+F	EM	AIT	10-360	1412	16	1.34	7564	37	1.93	3599	107.4	1.5	Ghassoun et al. (2015)
EU	DEU	Braunschweig	NU	ST	ME	NS	UPF+F	EM	AIT	10-360	4131	15.7	1.47	7690	36.5	1.56	6552	99.5	1.57	Ghassoun et al. (2015)
EU	DEU	Braunschweig	NU	ST	ME	NS	UPF+F	EM	AIT	10-360	512	14.4	1.3	7370	39.9	1.96	3173	110	1.51	Ghassoun et al. (2015)
EU	DEU	Braunschweig	NU	ST	ME	NS	UPF+F	EM	AIT	10-360	551	14.8	1.23	12405	33.8	2.1	3399	106.4	1.52	Ghassoun et al. (2015)
EU	DEU	Braunschweig	NU	ST	ME	NS	UPF+F	EM	AIT	10-360	3441	21.5	1.74	6931	67.1	1.61	1933	122.4	1.4	Ghassoun et al. (2015)
EU	DEU	Dresden	UB	MT	M	NS	UFP+F	EM	AIT	5-800	2836	17	1.77	5329	71.8	2.22	225	245.6	1.35	Birmili et al. (2013)
EU	DEU	Dresden	UB	MT	M	NS	UFP+F	EM	AIT	15-800	6059	21.4	3.61	3047	103.7	1.67	760	257.4	1.36	Birmili et al. (2013)
EU	DEU	Dresden	UB	MT	M	NS	UFP+F	EM	AIT	15-800	2167	22.6	1.83	3560	94.6	1.99	248	255.5	1.35	Birmili et al. (2013)
EU	DEU	Leipzig	UB	LT	ME	NS	UFP+F	EM	NUC-ACC	3-800	14560	15.7	1.99	732	20.6	1.27	5116	74	2.3	Wehner et al. (2003)
EU	DEU	Leipzig	UB	LT	ME	NS	UFP+F	EM	NUC	3-800	4510	10.1	1.79	8405	30.4	2.24	1100	139.9	1.83	Wehner et al. (2003)
EU	DEU	Leipzig	UB	MT	ME	NS	UFP+F	EM	AIT	10-500	1977	13	2.75	3587	57.7	2.25	340	199.3	1.49	Costabile et al. (2009)
EU	DEU	Leipzig	UB	MT	ME	NS	UFP+F	EM	AIT	10-500	1610	12.9	1.5	10065	41.8	2.42	890	156.9	1.48	Costabile et al. (2009)
EU	DEU	Leipzig	UB	MT	ME	NS	UFP+F	EM	AIT	10-500	3539	27.3	2.81	215	48.8	1.28	1643	115.6	1.93	Costabile et al. (2009)
EU	DEU	Leipzig	UB	MT	ME	NS	UFP+F	EM	AIT	10-500	6426	41.4	2.42	982	148.2	1.65	--	--	--	Costabile et al. (2009)
EU	DEU	Leipzig	UB	LT	ME	NS	UPF+F	EM	AIT	8-600	3687	20.1	2.22	2394	77.8	2.01	219	194.9	1.4	Von Bismarck-Osten et al. (2013)
EU	DEU	Dresden	TR	MT	M	NS	UFP+F	EM	NUC	5-800	16935	12.6	2.2	4891	76.3	2.04	1706	140.7	1.85	Birmili et al. (2013)
EU	DEU	Leipzig	TR	LT	ME	NS	UFP+F	EM	AIT	15-800	129	15.5	1.16	1245	24.3	1.68	1797	72.8	2.08	Franck et al. (2006)

EU	DEU	Leipzig	TR	LT	ME	NS	UFP+F	EM	NUC	3-800	8255	12.4	1.86	682	15.4	1.26	13083	51.2	2.49	Tuch et al. (2006)
EU	DEU	Leipzig	TR	MT	ME	NS	UFP+F	EM	AIT	10-500	139	14.5	1.18	10251	29	2.15	2789	130.8	1.66	Costabile et al. (2009)
EU	DEU	Leipzig	TR	MT	ME	NS	UFP+F	EM	NUC	10-500	176	15.5	1.16	18223	17.1	3.12	2914	118.8	1.76	Costabile et al. (2009)
EU	DEU	Leipzig	TR	MT	ME	NS	UFP+F	EM	NUC	3-800	10444	13.3	1.82	859	16.3	1.24	13229	53	2.39	Voigtlander et al. (2006)
EU	DEU	Leipzig	TR	MT	ME	NS	UFP+F	EM	NUC	3-800	7528	16.8	1.97	1848	56.8	1.54	3444	105	1.9	Voigtlander et al. (2006)
EU	DEU	Leipzig	TR	MT	ME	NS	UFP+F	EM	NUC	3-800	5190	12.3	1.72	1029	16	1.23	8161	40.8	2.82	Voigtlander et al. (2006)
EU	DEU	Leipzig	TR	MT	ME	NS	UFP+F	EM	NUC	3-800	3956	12.8	1.96	282	16.6	1.2	5874	57.2	2.47	Voigtlander et al. (2006)
EU	DEU	Leipzig	TR	MT	ME	NS	UFP+F	EM	NUC	3-800	8741	18.6	1.95	2060	59.3	1.56	4300	101.9	1.95	Voigtlander et al. (2006)
EU	DEU	Leipzig	TR	MT	ME	NS	UFP+F	EM	NUC	3-800	6532	13.6	1.8	362	17.6	1.25	12595	61.7	2.29	Voigtlander et al. (2006)
EU	DEU	Leipzig	TR	MT	ME	NS	UFP+F	EM	NUC-AIT	3-800	3457	15.7	1.86	278	18	1.29	6622	62.9	2.27	Voigtlander et al. (2006)
EU	DEU	Leipzig	TR	MT	ME	NS	UFP+F	EM	AIT	3-800	436	14	1.26	8704	32.4	3.18	987	53.6	1.72	Voigtlander et al. (2006)
EU	DEU	Essen	TR	MT	ME	NS	UFP+F	EM	AIT	20-740	1271	24.9	1.22	6001	38.2	1.65	5706	78.5	2	Weber et al. (2013)
EU	DEU	Heidelberg	TR	ST	ME	NS	UFP+F	EM	AIT	11-392	28514	13.6	1.8	6616	64.1	1.97	--	--	--	Rosenbohm et al. (2005)
EU	DEU	Heidelberg	TR	ST	ME	NS	UFP+F	EM	NUC	20-392	4290	49.6	2.06	333	165.9	1.32	--	--	--	Rosenbohm et al. (2005)
EU	DEU	Essen	TR	VVST	ME	NS	UFP+F	EM	AIT	20-750	5005	24.3	1.35	16921	61.4	2.06	187	291	1.23	Weber et al. (2009)
EU	DEU	Essen	TR	VVST	ME	NS	UFP+F	EM	AIT	20-750	1383	25	1.21	16346	53.7	2.24	111	302.5	1.19	Weber et al. (2009)
EU	DEU	Essen	TR	VVST	ME	NS	UFP+F	EM	AIT	20-750	11281	22.4	1.62	9001	70.4	1.87	301	296.8	1.45	Weber et al. (2009)
EU	DEU	Essen	TR	VVST	ME	NS	UFP+F	EM	AIT	20-750	4639	24.7	1.34	1570	46.4	1.32	11015	63.7	2.11	Weber et al. (2009)
EU	DEU	Aachen	TR	VVST	ME	NS	UFP+F	EM	AIT	10-400	6862	12.8	2.3	123	13.9	1.05	8581	69.2	2.06	Wehner et al. (2004a)
EU	DEU	Leipzig	TR	LT	ME	NS	UPF+F	EM	AIT	8-600	148	13.6	1.22	7164	20.7	2.56	3322	83.8	1.95	Von Bismarck-Osten et al. (2013)
EU	DEU	Leipzig	UB	MT	ME	NS	UFP+F	EM	AIT	3-800	3168	10.8	1.45	7021	24.7	1.41	15839	41.9	3.04	Wehner et al. (2002)
EU	DEU	Leipzig	TR	MT	ME	NS	UFP+F	EM	NUC	3-800	86356	11.4	1.89	3628	14.4	1.19	59252	29.1	2.53	Wehner et al. (2002)
EU	DNK	Copenhagen	NU	VST	ME	NS	UPF+F	EM	AIT	12-580	1754	21	1.55	3493	57.4	1.65	521	200	1.54	Löndahl et al. (2009)
EU	DNK	Copenhagen	UB	ST	D	NS	UFP+F	EM	AIT	10-700	343	16.3	1.39	5228	50.9	2.11	431	238.7	1.58	Wang et al. (2010a)
EU	DNK	Copenhagen	UB	ST	E	NS	UFP+F	EM	AIT	10-700	3202	29.8	2.07	1850	58.5	1.62	662	193	1.81	Wang et al. (2010a)
EU	DNK	Copenhagen	UB	LT	ME	NS	UFP+F	EM	AIT	6-700	545	14.6	1.37	1454	25.2	1.64	5451	54.4	2.25	Anderson et al. (2007)
EU	DNK	Copenhagen	UB	LT	ME	NS	UFP+F	EM	AIT	6-700	20719	21.4	1.8	9373	66.1	2.07	--	--	--	Wåhlin et al. (2009)
EU	DNK	Copenhagen	UB	LT	ME	NS	UFP+F	EM	AIT	6-700	574	11.3	1.16	10920	20.6	1.61	21776	36.6	2.57	Wåhlin et al. (2009)
EU	DNK	Copenhagen	UB	LT	ME	NS	UFP+F	EM	AIT	6-700	1480	11.4	1.25	13611	21.4	1.67	13150	52.2	2.22	Wåhlin et al. (2009)
EU	DNK	Copenhagen	UB	LT	ME	NS	UFP+F	EM	AIT	6-700	14649	21.6	1.83	642	23.7	1.32	10488	61.5	2.11	Wåhlin et al. (2009)
EU	DNK	Copenhagen	UB	LT	ME	NS	UFP+F	EM	AIT	6-700	5254	17.4	1.81	4282	24.2	1.68	13481	50.3	2.3	Wåhlin et al. (2009)
EU	DNK	Copenhagen	UB	LT	ME	NS	UFP+F	EM	AIT	6-700	3160	17.4	1.67	2517	24.7	1.56	13544	40.9	2.44	Wåhlin et al. (2009)
EU	DNK	Copenhagen	UB	MT	ME	NS	UFP+F	EM	AIT	6-700	4948	19.2	1.52	8738	44.3	1.81	1282	137.3	1.59	Wåhlin et al. (2009)

EU	DNK	Copenhagen	UB	LT	ME	NS	UPF+F	EM	AIT	8-610	212	17.6	1.4	3578	47	1.91	421	170.8	1.51	Von Bismarck-Osten et al. (2013)
EU	DNK	Copenhagen	UB	MT	ME	NS	UPF+F	EM	AIT	10-700	376	17.9	1.34	9192	36.2	2.56	--	--	--	Ketzel et al. (2003)
EU	DNK	Copenhagen	UB	MT	ME	NS	UPF+F	EM	AIT	10-700	2261	17.1	1.69	4654	60.1	2	--	--	--	Ketzel et al. (2003)
EU	DNK	Copenhagen	UB	MT	ME	NS	UPF+F	EM	AIT	9-700	907	17.8	1.45	8419	39.7	2.46	--	--	--	Ketzel et al. (2004)
EU	DNK	Copenhagen	UB	ST	ME	NS	UPF+F	EM	AIT	9-700	8106	32.8	2.29	474	197.3	1.58	--	--	--	Ketzel et al. (2004)
EU	DNK	Copenhagen	UB	ST	ME	NS	UPF+F	EM	AIT	9-700	642	16.9	1.52	3982	45.7	2.2	331	219.8	1.55	Ketzel et al. (2004)
EU	DNK	Copenhagen	TR	ST	D	NS	UFP+F	EM	AIT	10-700	17134	18.8	1.9	338	74.8	1.23	13861	59.5	2.28	Wang et al. (2010a)
EU	DNK	Copenhagen	TR	ST	E	NS	UFP+F	EM	AIT	10-700	20453	28.1	2.76	209	70.3	1.33	243.4	243.4	1.21	Wang et al. (2010a)
EU	DNK	Copenhagen	TR	MT	ME	NS	UFP+F	EM	NUC-AIT	6-700	9140	13.4	1.55	17919	22.7	1.74	14151	50.2	2.17	Wåhlin et al. (2001)
EU	DNK	Odense	TR	ST	ME	NS	UFP+F	EM	NUC-AIT	6-700	49734	19.5	1.77	12601	71.7	2.04	--	--	--	Wåhlin et al. (2001)
EU	DNK	Copenhagen	TR	LT	ME	NS	UPF+F	EM	AIT	8-610	523	10.5	1.25	2895	18.8	1.59	10747	41.4	2.26	Von Bismarck-Osten et al. (2013)
EU	DNK	Copenhagen	TR	MT	ME	NS	UPF+F	EM	AIT	10-700	21668	23.7	2.08	917	79.1	1.41	2116	129	1.64	Ketzel et al. (2003)
EU	DNK	Copenhagen	TR	MT	ME	NS	UPF+F	EM	AIT	10-700	14210	21.5	2.39	2485	98	1.88	--	--	--	Ketzel et al. (2003)
EU	DNK	Copenhagen	TR	MT	ME	NS	UPF+F	EM	AIT	9-700	18661	21.6	1.92	5699	80.6	1.92	--	--	--	Ketzel et al. (2004)
EU	DNK	Copenhagen	TR	VST	ME	NS	UPF+F	EM	NUC-AIT	12-580	13299	19.7	1.85	2695	57.4	1.49	4169	81.9	2.02	Löndahl et al. (2009)
EU	ESP	Barcelona	NU	LT	ME	NS	UFP+F	EM	AIT	10-800	3844	20.9	1.43	4796	36.4	1.44	8447	70	1.88	Rodríguez et al. (2007)
EU	ESP	Barcelona	UB	MT	ME	NS	UFP+F	EM	AIT	13-800	10427	30.8	1.62	7932	77.7	1.83	--	--	--	Dall'Osto et al. (2012)
EU	ESP	Barcelona	UB	MT	ME	NS	UFP+F	EM	AIT	13-800	6204	29.7	1.59	7012	64.6	1.93	--	--	--	Dall'Osto et al. (2012)
EU	ESP	Barcelona	UB	MT	ME	NS	UFP+F	EM	AIT	13-800	4636	23.6	1.55	11531	54.4	2.14	--	--	--	Dall'Osto et al. (2012)
EU	ESP	Barcelona	UB	MT	ME	NS	UFP+F	EM	AIT	13-800	15398	32.8	1.76	4879	105.6	1.7	--	--	--	Dall'Osto et al. (2012)
EU	ESP	Madrid	UB	ST	ME	NS	UFP+F	EM	AIT	15-600	5294	20.1	1.48	2319	32.4	1.32	25630	47	2.34	Gómez-Moreno et al. (2011)
EU	ESP	Madrid	UB	ST	ME	NS	UFP+F	EM	AIT	15-600	14538	26.4	1.7	18080	79.3	1.94	--	--	--	Gómez-Moreno et al. (2011)
EU	ESP	Madrid	UB	ST	ME	NS	UFP+F	EM	AIT	15-600	4961	28.5	1.64	8267	88	1.88	--	--	--	Gómez-Moreno et al. (2011)
EU	ESP	Madrid	UB	ST	ME	NS	UFP+F	EM	NUC-AIT	15-600	4531	16.2	1.47	703	28.2	1.28	9107	46.2	2.3	Gómez-Moreno et al. (2011)
EU	ESP	Madrid	UB	ST	ME	NS	UFP+F	EM	NUC	15-600	504	14.9	1.2	4603	17.1	1.48	3976	49	2.24	Gómez-Moreno et al. (2011)
EU	ESP	Madrid	UB	VST	ME	NS	UFP+F	EM	AIT	15-600	2246	26	1.58	32	63.7	1.15	5263	80.3	1.92	Gómez-Moreno et al. (2011)
EU	ESP	Madrid	UB	VST	ME	NS	UFP+F	EM	NUC-AIT	15-600	11461	20.3	1.8	169	31	1.27	6142	54.6	2.27	Gómez-Moreno et al. (2011)
EU	ESP	Madrid	UB	VST	ME	NS	UFP+F	EM	AIT	15-600	778	22.2	1.29	9652	24.7	2.99	139	31	1.18	Gómez-Moreno et al. (2011)
EU	ESP	Barcelona	UB	LT	ME	NS	UPF+F	EM	AIT	13-800	4268	21.6	1.46	5471	37.7	1.48	7152	77.9	1.84	Pey et al. (2008)

EU	ESP	Ciudad Real	TR	LT	A	NS	UPF+F	EM	AIT	5.6-560	26	16.8	1.09	1146	62.1	1.44	542	110.3	1.36	Aranda et al. (2015)
EU	ESP	Ciudad Real	TR	LT	A	NS	UPF+F	EM	NUC	5.6-560	3977	7.8	1.34	2843	25.6	1.31	3289	67.1	1.82	Aranda et al. (2015)
EU	FIN	Helsinki	NU	MT	ME	NS	UFP+F	EM	NUC	8-400	14915	10.4	1.69	16359	25.4	1.83	9816	59.4	2.87	Hussein et al. (2005a)
EU	FIN	Helsinki	NU	MT	ME	NS	UFP+F	EM	AIT	8-400	4720	8	1.65	10184	36.9	2.13	626	119	1.58	Hussein et al. (2005a)
EU	FIN	Helsinki	NU	ST	ME	NS	UFP+F	EM	NUC-AIT	8-400	11126	11	1.9	11690	30.8	1.9	1246	135	1.79	Hussein et al. (2004)
EU	FIN	Helsinki	NU	ST	ME	NS	UFP+F	EM	NUC	8-400	14360	11.4	1.9	10358	35.2	1.9	1717	115	1.9	Hussein et al. (2004)
EU	FIN	Helsinki	NU	ST	ME	NS	UFP+F	EM	NUC-AIT	8-400	6059	11.4	1.69	8584	37.6	1.9	1486	118	1.83	Hussein et al. (2004)
EU	FIN	Helsinki	NU	ST	ME	NS	UFP+F	EM	NUC	8-400	5391	11.7	1.62	10339	31.6	1.9	1812	109	1.9	Hussein et al. (2004)
EU	FIN	Helsinki	NU	ST	ME	NS	UFP+F	EM	NUC	8-400	7255	10.9	1.9	6545	35.7	1.9	878	155	1.72	Hussein et al. (2004)
EU	FIN	Helsinki	NU	ST	ME	NS	UFP+F	EM	NUC	8-400	9750	9.7	1.9	7642	33.8	1.9	2189	104	1.9	Hussein et al. (2004)
EU	FIN	Helsinki	NU	ST	ME	NS	UFP+F	EM	AIT	8-400	4196	11.1	1.77	6158	42	1.9	1173	110	1.84	Hussein et al. (2004)
EU	FIN	Helsinki	NU	ST	ME	NS	UFP+F	EM	AIT	8-400	5588	12.5	1.87	6098	45.2	1.9	749	158	1.65	Hussein et al. (2004)
EU	FIN	Helsinki	NU	ST	ME	NS	UFP+F	EM	NUC-AIT	8-400	10128	19.5	1.8	2124	50.2	1.8	801	150	1.8	Hussein et al. (2004)
EU	FIN	Helsinki	NU	ST	ME	NS	UFP+F	EM	NUC	8-400	8999	17	1.8	3554	58.5	1.8	900	101	1.8	Hussein et al. (2004)
EU	FIN	Helsinki	NU	ST	ME	NS	UFP+F	EM	NUC	8-400	5847	14.5	1.8	4000	55.4	1.8	1300	126	1.8	Hussein et al. (2004)
EU	FIN	Helsinki	NU	ST	ME	NS	UFP+F	EM	NUC	8-400	7100	17	1.65	2701	50	1.65	901	130	1.8	Hussein et al. (2004)
EU	FIN	Helsinki	NU	ST	ME	NS	UFP+F	EM	NUC	8-400	3581	17.5	1.65	1705	55	1.65	457	191	1.53	Hussein et al. (2004)
EU	FIN	Helsinki	NU	ST	ME	NS	UFP+F	EM	AIT	8-400	3900	17.5	1.75	3950	55.5	1.75	543	172	1.57	Hussein et al. (2004)
EU	FIN	Helsinki	NU	ST	ME	NS	UFP+F	EM	AIT	8-400	2600	15.5	1.8	3000	55	1.7	1200	125	1.75	Hussein et al. (2004)
EU	FIN	Helsinki	NU	ST	ME	NS	UFP+F	EM	NUC	8-400	3700	17	1.8	1801	55	1.65	600	140	1.65	Hussein et al. (2004)
EU	FIN	Helsinki	NU	ST	ME	NS	UFP+F	EM	AIT	8-500	5663	21.4	1.64	7130	38.1	1.92	2445	86.5	2.97	Hussein et al. (2005a)
EU	FIN	Helsinki	NU	ST	ME	NS	UFP+F	EM	AIT	8-500	6049	25.6	1.85	3738	54.9	1.87	311	213.9	1.47	Hussein et al. (2005a)
EU	FIN	Helsinki	NU	ST	ME	NS	UFP+F	EM	NUC	8-400	6477	10.4	1.69	7106	25.4	1.83	4261	59.4	2.86	Hussein et al. (2005a)
EU	FIN	Helsinki	NU	ST	ME	NS	UFP+F	EM	NUC	8-400	4443	9.7	1.78	8664	27.4	2.68	--	--	--	Hussein et al. (2005a)
EU	FIN	Helsinki	NU	ST	ME	NS	UFP+F	EM	AIT	8-400	1369	8.6	1.41	623	13	1.29	29043	29.7	2.15	Hussein et al. (2005a)
EU	FIN	Helsinki	NU	ST	ME	NS	UFP+F	EM	AIT	8-400	911	7.4	1.5	596	11.8	1.34	15814	26.8	2.3	Hussein et al. (2005a)
EU	FIN	Helsinki	SUB	MT	E	NS	UFP+F	EM	NUC	7-600	1347	8	1.2	3653	11.1	1.6	8753	46.3	2.27	Hussein et al. (2004a)
EU	FIN	Helsinki	SUB	MT	E	NS	UFP+F	EM	NUC	7-600	2433	8	1.2	6269	10.5	1.6	9207	46.2	2.22	Hussein et al. (2004a)
EU	FIN	Helsinki	SUB	MT	E	NS	UFP+F	EM	AIT	7-600	3942	8.9	1.7	7950	42.7	2.12	--	--	--	Hussein et al. (2004a)

EU	FIN	Helsinki	SUB	MT	E	NS	UFP+F	EM	BIM (NUC, AIT)	7-600	295	8.4	1.07	9196	23.5	3.36	825	41.4	1.27	Hussein et al. (2004a)
EU	FIN	Helsinki	SUB	VVST	E	NS	UFP+F	EM	AIT	3-400	2755	11.6	1.6	702	31.6	1.27	6168	63.7	2.03	Hussein et al. (2005)
EU	FIN	Helsinki	SUB	VVST	E	NS	UFP+F	EM	AIT	3-400	571	12.1	1.26	2236	27.6	1.55	3770	54.3	3.31	Hussein et al. (2005)
EU	FIN	Helsinki	SUB	MT	M	NS	UFP+F	EM	NUC	7-600	3281	8.1	1.23	5371	15	1.4	10739	39.7	2.4	Hussein et al. (2004a)
EU	FIN	Helsinki	SUB	MT	M	NS	UFP+F	EM	NUC	7-600	347	8.8	1.1	7019	11.7	2.34	4044	83.4	1.87	Hussein et al. (2004a)
EU	FIN	Helsinki	SUB	MT	M	NS	UFP+F	EM	NUC	7-600	3326	8.5	1.29	3028	14.9	1.4	9675	39.5	2.23	Hussein et al. (2004a)
EU	FIN	Helsinki	SUB	MT	M	NS	UFP+F	EM	NUC	7-600	1907	7.5	1.22	2984	13	1.44	7410	46.4	2.2	Hussein et al. (2004a)
EU	FIN	Helsinki	SUB	MT	ME	NS	UFP+F	EM	NUC	7-600	1845	8	1.23	4069	13.1	1.51	8211	43.5	2.26	Hussein et al. (2004a)
EU	FIN	Helsinki	SUB	MT	ME	NS	UFP+F	EM	NUC	7-600	1247	7.8	1.19	2524	11.7	1.5	7688	43	2.34	Hussein et al. (2004a)
EU	FIN	Helsinki	SUB	VVST	ME	NS	UFP+F	EM	BIM (NUC, AIT)	3-400	1855	11	1.51	3319	51.5	2.03	452	278.2	1.51	Hussein et al. (2005)
EU	FIN	Helsinki	UB	MT	ME	NS	UFP+F	EM	NUC	8-320	2048	12.7	1.4	2190	24.5	1.86	1425	89.9	2.95	Hussein et al. (2007)
EU	FIN	Helsinki	UB	MT	ME	NS	UFP+F	EM	NUC	8-320	5228	17.2	1.77	13415	19.8	3.65	--	--	--	Hussein et al. (2007)
EU	FIN	Helsinki	UB	MT	ME	NS	UFP+F	EM	NUC	8-320	4734	14	1.44	5074	31.5	2.12	--	--	--	Hussein et al. (2007)
EU	FIN	Helsinki	UB	MT	ME	NS	UFP+F	EM	NUC	8-320	2927	13.7	1.44	4894	34.5	1.89	2097	127.7	2.52	Hussein et al. (2007)
EU	FIN	Helsinki	UB	LT	ME	NS	UPF+F	EM	AIT	8-600	1267	11.8	1.63	3923	47.4	2.19	--	--	--	Von Bismarck-Osten et al. (2013)
EU	FIN	Helsinki	UB	VST	ME	NS	UPF+F	EM	NUC	6-610	332	10.2	1.2	1361	15.6	1.37	5475	30.9	2.49	Karl et al. (2016)
EU	FIN	Helsinki	UB	VST	ME	NS	UPF+F	EM	AIT	6-420	133	16.5	1.1	20308	22.4	1.93	3024	104.1	1.78	Karl et al. (2016)
EU	FIN	Helsinki	TR	MT	ME	NS	UFP+F	EM	NUC	3-800	6243	8.3	1.32	30523	9.3	2.22	--	--	--	Hussein et al. (2007)
EU	FIN	Helsinki	TR	MT	ME	NS	UFP+F	EM	NUC	3-800	2716	15.3	1.56	403	34	1.25	5195	64.1	2.31	Hussein et al. (2007)
EU	FIN	Helsinki	TR	MT	ME	NS	UFP+F	EM	NUC	3-800	465	10.7	1.12	18250	11.9	3.13	34480	15.1	1.7	Hussein et al. (2007)
EU	FIN	Helsinki	TR	MT	ME	NS	UFP+F	EM	NUC-AIT	3-800	263	3.4	1.25	2860	57.3	3.11	3830	22	2.22	Hussein et al. (2007)
EU	FIN	Helsinki	TR	VST	ME	NS	UPF+F	EM	NUC	6-610	105294	2.1	4.36	6168	9.3	1.18	3583	15.2	1.18	Karl et al. (2016)
EU	FIN	Helsinki	TR	VST	ME	NS	UPF+F	EM	NUC	6-420.	3364	9.4	1.03	36516	21.3	1.27	67282	17.3	2.24	Karl et al. (2016)
EU	FRA	Marseilles	NU	VVST	A	NS	UFP+F	EM	AIT	14-735	294	32.8	1.17	558	48.2	1.66	132	121.3	1.48	Cachier et al. (2005)
EU	FRA	Marseilles	NU	VVST	A	NS	UFP+F	EM	AIT	14-735	375	38.9	1.28	535	61.3	1.93	--	--	--	Cachier et al. (2005)
EU	FRA	Marseilles	NU	VVST	E	NS	UFP+F	EM	AIT	14-735	199	49.6	1.51	78	113.6	1.51	--	--	--	Cachier et al. (2005)
EU	FRA	Marseilles	NU	VVST	E	NS	UFP+F	EM	AIT	14-735	246	73.6	1.74	--	--	--	--	--	--	Cachier et al. (2005)
EU	FRA	Marseilles	NU	VVST	M	NS	UFP+F	EM	AIT	14-735	224	34.2	1.42	1254	67.9	2.02	--	--	--	Cachier et al. (2005)
EU	GBR	Bloomsbury	NU	LT	A	NS	UFP+F	EM	AIT	12-437	721	20.9	1.36	2520	30.5	1.44	7188	54	2.23	Dingenena et al. (2004)
EU	GBR	Bloomsbury	NU	LT	E	NS	UFP+F	EM	AIT	12-437	338	25	1.34	5875	52.3	2.12	--	--	--	Dingenena et al. (2004)
EU	GBR	Bloomsbury	NU	LT	M	NS	UFP+F	EM	AIT	12-437	2074	24.5	1.37	8680	51.7	2.09	--	--	--	Dingenena et al. (2004)

EU	GBR	London	NU	LT	ME	NS	UFP+F	EM	AIT	10-800	833	29.9	1.77	6326	31.6	1.87	4552	93.1	1.81	Rodríguez et al. (2007)
EU	GBR	London	NU	MT	ME	NS	UFP+F	EM	AIT	5-673	150	5	1.16	2484	19.6	1.55	8345	94.6	2.06	Dall'Osto et al. (2011)
EU	GBR	London	NU	MT	ME	NS	UFP+F	EM	NUC	5-800	37316	8.1	2.44	2611	53	1.49	4448	98.4	1.93	Dall'Osto et al. (2011)
EU	GBR	Leicester	UB	MT	ME	NS	UFP+F	EM	AIT	10-900	3103	18.1	1.95	4200	73	2.19	111	80.9	1.33	Hama et al. (2017)
EU	GBR	Leicester	UB	MT	ME	NS	UFP+F	EM	AIT	10-900	4996	33.3	2.69	307	111.4	1.86	--	--	--	Hama et al. (2017)
EU	GBR	London	UB	LT	ME	NS	UPF+F	EM	AIT	20-600	1445	26.1	1.33	2015	46.6	1.54	1797	85.4	1.89	Von Bismarck-Osten et al. (2013)
EU	GBR	London	TR	LT	A	NS	UFP+F	EM	AIT	11-450	38141	28.7	1.71	30	50	1.9	15910	87	1.82	Charron and Harrison (2003)
EU	GBR	London	TR	LT	A	NS	UFP+F	EM	AIT	11-450	11592	27.9	1.56	36542	42.6	2.32	327	136.3	1.29	Charron and Harrison (2003)
EU	GBR	London	TR	LT	A	NS	UFP+F	EM	AIT	11-450	34236	29.5	1.77	13379	85.8	1.86	--	--	--	Charron and Harrison (2003)
EU	GBR	London	TR	LT	E	NS	UFP+F	EM	AIT	11-450	3314	23.8	1.37	4986	105.6	1.79	28687	30.2	2.03	Charron and Harrison (2003)
EU	GBR	London	TR	LT	E	NS	UFP+F	EM	AIT	11-450	8516	3.6	7.21	24950	26.2	1.69	15156	55.2	2.1	Charron and Harrison (2003)
EU	GBR	London	TR	LT	E	NS	UFP+F	EM	AIT	11-450	33779	30.3	1.83	5747	107.3	1.76	--	--	--	Charron and Harrison (2003)
EU	GBR	London	TR	LT	M	NS	UFP+F	EM	AIT	11-450	34691	25	1.66	26229	64.2	2.05	--	--	--	Charron and Harrison (2003)
EU	GBR	London	TR	LT	M	NS	UFP+F	EM	AIT	11-450	12876	25.6	1.46	37698	38.6	2.48	--	--	--	Charron and Harrison (2003)
EU	GBR	London	TR	LT	M	NS	UFP+F	EM	AIT	11-450	25434	25.5	1.68	9747	77.9	1.86	--	--	--	Charron and Harrison (2003)
EU	GBR	London	TR	ME	ME	NS	UFP+F +C	EM+A	AIT	15-10000	45000	9	1.25	15393	24	1.51	64135	73.4	2.1	Harrison et al. (2012)
EU	GBR	London	TR	MT	ME	NS	UFP+F	EM	AIT	5-184	3868	15.1	1.44	30373	25.5	1.72	23582	79.5	1.81	Dall'Osto et al. (2011)
EU	GBR	Birmingham	TR	VST	ME	NS	UFP+F	EM	NUC-AIT	10-500	8222	19.2	1.16	158605	27.4	2.18	--	--	--	Shi et al. (1999)
EU	GBR	Leeds	TR	ST	A	NS	UPF+F	EM	BIM (NUC, AIT)	6-225	17375	10	1.53	23329	29.8	1.64	5140	108.7	1.48	Lingard et al. (2006)
EU	GBR	Leeds	TR	ST	A	NS	UPF+F	EM	NUC	6-225	3642	8.2	1.16	31429	18.9	1.9	11626	71.5	2.09	Lingard et al. (2006)
EU	GBR	Cambridge	TR	VVST	D	NS	UPF+F	EM	AIT	5-1000	5093	7.2	1.58	21513	28.9	1.64	15828	100	1.59	Kumar et al. (2008)
EU	GBR	Cambridge	TR	VVST	D	NS	UPF+F	EM	BIM (NUC, AIT)	5-1000	5264	5.7	1.24	9863	19.7	1.74	18403	72	1.9	Kumar et al. (2008)
EU	GBR	Cambridge	TR	VVST	D	NS	UPF+F	EM	AIT	5-1000	19605	30.3	1.96	8517	99.1	1.42	--	--	--	Kumar et al. (2008)
EU	GBR	Cambridge	TR	VVST	D	NS	UPF+F	EM	AIT	5-1000	6073	5.9	1.23	51712	26.8	2.08	28881	87.1	1.62	Kumar et al. (2008)
EU	GBR	Cambridge	TR	VVST	D	NS	UPF+F	EM	AIT	5-1000	6660	10.6	1.45	40193	36.5	1.78	16434	105.5	1.43	Kumar et al. (2008)
EU	GBR	Cambridge	TR	VVST	D	NS	UPF+F	EM	NUC	5-1000	3046	15.5	1.26	11701	25.2	1.78	2828	95.2	1.36	Kumar et al. (2008)
EU	GBR	Cambridge	TR	VVST	D	NS	UPF+F	EM	NUC	5-1000	14078	16.5	1.58	1134	32.7	1.17	6096	75.5	1.71	Kumar et al. (2008)
EU	GBR	Leeds	TR	ST	M	NS	UPF+F	EM	NUC	6-225	25990	16.8	1.81	9463	62	1.47	3559	138	1.31	Lingard et al. (2006)

EU	GBR	London	TR	LT	ME	NS	UPF+F	EM	AIT	20-600	22	22.9	1.02	9831	22.6	1.65	11394	65.8	1.89	Von Bismarck-Osten et al. (2013)
EU	GBR	Manchester	NU	MT	ME	NS	UFP+F	EM	NUC	3-500	23759	14.2	1.85	1290	36	1.16	2119	65.3	2.83	Williams et al. (2000)
EU	GBR	Manchester	NU	MT	ME	NS	UFP+F	EM	NUC	3-500	9846	4.3	1.2	45626	13.2	1.82	4959	61.3	1.59	Williams et al. (2000)
EU	GRC	Athens	CC	MT	ME	NS	UPF+F	EM	AIT	12-450	11340	7.3	1.49	26590	30.2	1.97	6546	107.9	1.75	Lazaridis et al. (2017)
EU	GRC	Chania	NU	MT	ME	NS	UPF+F	EM	AIT-ACC	13-800	3	16.5	1.14	26	27.9	1.4	461	85.2	1.71	Kopanakis et al. (2013)
EU	GRC	Chania	NU	MT	ME	NS	UPF+F	EM	AIT-ACC	13-800	1	18.6	1.06	36	45.7	1.66	442	101.2	1.68	Kopanakis et al. (2013)
EU	GRC	Chania	NU	MT	ME	NS	UPF+F	EM	AIT	13-800	9	9.7	1.55	300	61.3	1.88	36	138.4	1.35	Kopanakis et al. (2013)
EU	GRC	Chania	NU	ST	ME	NS	UPF+F	EM	AIT	13-800	109	21.3	1.89	178	49.1	1.58	112	108	1.54	Kopanakis et al. (2013)
EU	HUN	Budapest	CC	LT	ME	NS	UFP+F	EM	AIT	6-1000	7380	40.1	2.62	454	107.5	1.34	446	245.7	1.31	Salma et al. (2014)
EU	HUN	Budapest	CC	VVST	NS	NPF	UFP+F	EM	NUC	9-1000	9375	15.4	1.47	1794	58.6	1.44	1981	123.1	1.77	Salma et al. (2014)
EU	HUN	Budapest	NU	VVST	M	NPF	UFP+F	EM	NUC	6-1000	7576	8.1	1.56	6202	49.3	1.76	449	208.4	1.35	Salma et al. (2011)
EU	HUN	Budapest	NU	VVST	ME	NS	UFP+F	EM	AIT	6-1000	6044	26.4	2.02	4828	83.1	2.06	163	261.4	1.2	Salma et al. (2011)
EU	HUN	Budapest	UB	MT	ME	NS	UFP+F	EM	AIT	6-1000	2285	56	2.28	393	122.3	1.8	165	230.3	1.26	Salma et al. (2014)
EU	HUN	Budapest	UB	VVST	NS	NPF	UFP+F	EM	NUC-AIT	6-1000	704	21.3	1.15	5948	19.7	1.41	5753	52.5	2.77	Salma et al. (2014)
EU	HUN	Budapest	TR/CC	MT	ME	NS	UFP+F	EM	AIT	6-1000	13993	39.5	2.74	502	29.9	1.44	274	248.9	1.17	Salma et al. (2014)
EU	HUN	Budapest	TR/CC	VVST	NS	NPF	UFP+F	EM	NUC	9-1000	16594	14	1.53	4704	56.3	1.55	540	197.8	1.36	Salma et al. (2014)
EU	HUN	Budapest	TR	ST	ME	NS	UFP+F	EM	AIT	6-1000	99805	45.8	2.19	1040	234.8	1.11	1364	314.1	1.21	Salma et al. (2014)
EU	ITA	Milan	CC	MT	ME	NS	UPF+F	EM	AIT	15-540	193	15.1	1.21	12656	39.2	1.95	3527	146.4	1.68	Lazaridis et al. (2017)
EU	ITA	Milan	NU	LT	A	NS	UFP+F	EM	AIT	10-800	838	21.1	1.22	1967	31.2	1.37	19461	47.9	2.48	Lonati et al. (2011)
EU	ITA	Milan	NU	LT	A	NS	UFP+F	EM	AIT	10-800	224	18.4	1.21	4645	32.9	1.46	6154	72.7	2.06	Lonati et al. (2011)
EU	ITA	Milan	NU	LT	E	NS	UFP+F	EM	AIT	10-800	7405	28.3	1.66	10378	91.1	1.8	--	--	--	Lonati et al. (2011)
EU	ITA	Milan	NU	LT	E	NS	UFP+F	EM	AIT	10-800	7521	32	1.76	7391	106.7	1.71	--	--	--	Lonati et al. (2011)
EU	ITA	Milan	NU	LT	E	NS	UFP+F	EM	AIT	10-800	907	21.5	1.22	2226	32.6	1.36	25383	46.6	2.44	Lonati et al. (2011)
EU	ITA	Milan	NU	LT	E	NS	UFP+F	EM	AIT	10-800	11325	27.8	1.72	13985	83.2	1.88	--	--	--	Lonati et al. (2011)
EU	ITA	Milan	NU	LT	E	NS	UFP+F	EM	AIT	10-800	4781	33.6	1.59	8734	72.8	1.98	--	--	--	Lonati et al. (2011)
EU	ITA	Milan	NU	LT	E	NS	UFP+F	EM	AIT	10-800	1298	26	1.49	6010	46.4	1.7	3423	110.8	1.76	Lonati et al. (2011)
EU	ITA	Milan	NU	LT	E	NS	UFP+F	EM	AIT	10-800	1574	22.1	1.35	5672	40	1.49	4815	87.4	1.87	Lonati et al. (2011)
EU	ITA	Milan	NU	LT	E	NS	UFP+F	EM	AIT	10-800	3678	24.5	1.39	5972	43.3	1.43	9172	80.7	1.89	Lonati et al. (2011)
EU	ITA	Milan	NU	LT	M	NS	UFP+F	EM	AIT	10-800	9543	31.6	1.58	31971	55.2	2.17	--	--	--	Lonati et al. (2011)
EU	ITA	Milan	NU	LT	M	NS	UFP+F	EM	AIT	10-800	1213	22.7	1.37	5900	37.2	1.52	9620	77.2	1.96	Lonati et al. (2011)
EU	ITA	Milan	NU	LT	ME	NS	UFP+F	EM	AIT	10-800	3737	19.3	1.47	5319	36.2	1.4	17541	69.3	2.06	Rodríguez et al. (2007)
EU	ITA	Milan	NU	ST	ME	NS	UFP+F	EM	AIT	15-600	2251	26.7	1.33	32763	31.6	2.53	--	--	--	Baltensperger et al. (2002)
EU	ITA	Ispra	SUB	MT	ME	NS	UFP+F	EM	AIT	10-600	630	16.6	1.74	4000	51.1	1.95	1694	126	1.66	Asmi et al. (2011)

EU	ITA	Ispra	SUB	MT	ME	NS	UFP+F	EM	AIT	10-600	1370	19.9	2.1	2573	50.1	2	2027	106.9	1.94	Asmi et al. (2011)
EU	ITA	Ispra	SUB	MT	ME	NS	UFP+F	EM	AIT	10-600	60	14.2	1.21	2264	31.4	1.79	6002	94.9	1.76	Asmi et al. (2011)
EU	ITA	Ispra	SUB	MT	ME	NS	UFP+F	EM	AIT-ACC	10-600	1022	22.1	1.59	469	36.4	1.36	9108	103.5	1.75	Asmi et al. (2011)
EU	ITA	Rome	SUB	MT	D	NS	UPF+F	EM	AIT-ACC	14-661	1912	24.4	1.49	872	51.2	1.36	4395	103.3	1.68	Costabile et al. (2010)
EU	ITA	Rome	SUB	MT	D	NS	UPF+F	EM	AIT	14-661	4887	22.3	1.74	1755	60.1	1.46	2995	130.9	1.59	Costabile et al. (2010)
EU	ITA	Rome	SUB	MT	D	NS	UPF+F	EM	AIT	14-661	489	27.4	1.24	1906	50.6	1.55	3817	107.8	1.76	Costabile et al. (2010)
EU	ITA	Rome	SUB	MT	D	NS	UPF+F	EM	AIT	14-661	1026	27.7	1.3	2687	56.4	1.6	3243	109.5	1.68	Costabile et al. (2010)
EU	ITA	Rome	SUB	MT	E	NS	UPF+F	EM	AIT-ACC	14-661	3151	32.1	1.73	5466	99.1	1.74	--	--	--	Costabile et al. (2010)
EU	ITA	Rome	SUB	MT	E	NS	UPF+F	EM	AIT	14-661	3497	28.3	2.28	3991	63	1.86	2647	123.1	1.61	Costabile et al. (2010)
EU	ITA	Rome	SUB	MT	E	NS	UPF+F	EM	AIT-ACC	14-661	362	30.1	1.29	8604	89.4	1.78	--	--	--	Costabile et al. (2010)
EU	ITA	Cassino	TR/CC	VST	ME	NS	UFP+F	EM	NUC	6-220	22094	6.6	1.04	145559	7.4	1.36	40097	21.7	1.35	Buonanno et al. (2009)
EU	ITA	Cassino	TR/CC	VST	ME	NS	UFP+F	EM	NUC	6-220	3200	7.1	1.1	31421	9.7	1.41	26221	18.6	2.04	Buonanno et al. (2009)
EU	LTU	Vilnius	NU	VVST	A	NS	UFP+F	EM	NUC	9-840	227191	16.5	1.63	32550	58.7	1.32	42208	116.2	1.7	Byčenkienė et al. (2014)
EU	LTU	Vilnius	NU	VVST	E	NS	UFP+F	EM	NUC	9-840	57763	9.5	1.45	133621	40	2.51	--	--	--	Byčenkienė et al. (2014)
EU	LTU	Vilnius	NU	VVST	E	NS	UFP+F	EM	AIT	9-840	33374	9.3	1.46	90658	62.8	2.17	--	--	--	Byčenkienė et al. (2014)
EU	LTU	Vilnius	NU	VVST	E	NS	UFP+F	EM	AIT	9-840	9000	10.5	1.25	65132	33.2	1.59	23882	124	1.62	Byčenkienė et al. (2014)
EU	LTU	Vilnius	NU	VVST	E	NS	UFP+F	EM	AIT	17-840	73817	42.2	1.52	17369	147	1.47	--	--	--	Byčenkienė et al. (2014)
EU	LTU	Vilnius	NU	VVST	E	NS	UFP+F	EM	AIT	17-840	16064	43.7	1.32	37970	56.7	2.22	7816	140.6	1.37	Byčenkienė et al. (2014)
EU	LTU	Vilnius	NU	VVST	E	NS	UFP+F	EM	NUC	17-840	84709	12.7	1.76	77974	100.6	1.94	--	--	--	Byčenkienė et al. (2014)
EU	LTU	Vilnius	NU	VVST	E	NS	UFP+F	EM	ACC	17-840	2778	9.1	1.7	32806	5.4	4.91	17416	134.6	1.89	Byčenkienė et al. (2014)
EU	LTU	Vilnius	NU	VVST	M	NS	UFP+F	EM	NUC	17-840	213206	8.7	1.95	27689	54.2	2.05	67532	86.8	2.08	Byčenkienė et al. (2014)
EU	NLD	Amsterdam	NU	MT	D	NS	UPF+F	EM	NUC	10-480	2239	12.9	1.42	14319	29.8	2.78	153	67.9	1.15	Keuken et al. (2015)
EU	NLD	Amsterdam	NU	MT	E	NS	UPF+F	EM	AIT	10-480	9058	41.9	2.34	1085	68.3	1.56	--	--	--	Keuken et al. (2015)
EU	NLD	Amsterdam	NU	MT	ME	NS	UPF+F	EM	NUC	10-480	46937	14.9	1.82	6978	62.9	1.75	203	236.4	1.2	Keuken et al. (2015)
EU	NLD	Rotterdam	UB	ST	ME	NS	UPF+F	EM	AIT	10-440	2836	38.6	2.27	12347	39.7	2.18	--	--	--	Karl et al. (2016)
EU	NLD	Rotterdam	TR/ SUB	ST	ME	NS	UPF+F	EM	AIT	10-440	282628	0.1	8.74	878	53.3	1.33	19195	42.2	2.29	Karl et al. (2016)
EU	NOR	Oslo	SUB	MT	ME	NS	UPF+F	EM	NUC-AIT	10-420	19	10.7	1.07	2226	17.1	1.7	3170	63.4	2.44	Lazaridis et al. (2017)
EU	NOR	Oslo	UB	MT	ME	NS	UPF+F	EM	AIT	6-350	4479	22.1	2.14	789	76.7	1.68	--	--	--	Karl et al. (2016)
EU	NOR	Oslo	TR	MT	ME	NS	UPF+F	EM	NUC	6-350	15580	4.8	1.36	8016	11.6	1.82	6044	50.2	2.22	Karl et al. (2016)
EU	PRT	Oporto	UB	VVST	A	NS	UFP+F	EM	NUC	6-700	118638	5.3	1.42	104734	15.4	1.88	70977	78.3	1.95	Oliveira et al. (2009)
EU	PRT	Oporto	UB	VVST	A	NS	UFP+F	EM	NUC	6-700	21030	6.2	1.24	45948	13.7	1.62	67876	59.2	2.14	Oliveira et al. (2009)
EU	PRT	Oporto	UB	VVST	E	NS	UFP+F	EM	AIT	6-700	156	6.6	1.06	99898	30.1	2.71	17636	87.3	1.53	Oliveira et al. (2009)

EU	PRT	Oporto	UB	VVST	E	NS	UFP+F	EM	AIT	6-700	148491	23.4	3.05	17400	78.6	1.47	--	--	--	Oliveira et al. (2009)
EU	PRT	Oporto	UB	VVST	M	NS	UFP+F	EM	NUC	6-700	2304	6.9	1.36	64879	16.7	1.94	53495	73.9	2.08	Oliveira et al. (2009)
EU	PRT	Oporto	TR	VVST	A	NS	UFP+F	EM	NUC	6-700	4335	6.3	1.07	386241	4.5	1.71	149496	34.9	2.53	Oliveira et al. (2009)
EU	PRT	Oporto	TR	VVST	A	NS	UFP+F	EM	NUC	6-700	1868669	0.8	3.19	104371	40	2.33	--	--	--	Oliveira et al. (2009)
EU	PRT	Oporto	TR	VVST	E	NS	UFP+F	EM	NUC	6-700	26873	6.5	1.21	53337	12.9	1.83	113566	48	2.21	Oliveira et al. (2009)
EU	PRT	Oporto	TR	VVST	E	NS	UFP+F	EM	NUC	6-700	63831	6.3	1.24	78637	13	1.69	107200	50.8	2.13	Oliveira et al. (2009)
EU	PRT	Oporto	TR	VVST	M	NS	UFP+F	EM	NUC	6-700	48824	6.4	1.18	165165	9.5	2.28	148979	47.2	2.28	Oliveira et al. (2009)
EU	PRT	Lisbon	TR	VVST	ME	NS	UFP+F	EM	NUC	10-500	32441	16.3	1.16	15146	20.4	1.92	--	--	--	Albuquerque et al. (2012)
EU	PRT	Lisbon	TR	VVST	ME	NS	UFP+F	EM	AIT-ACC	10-500	2358	25.8	1.8	60	31.7	1.11	5292	102.6	1.76	Albuquerque et al. (2012)
EU	RUS	Tiksi	SUB	LT	ME	NS	UFP+F	EM	AIT	10-500	267	25.8	2.24	282	52.1	1.54	139	172.8	1.49	Asmi et al. (2016)
EU	SWE	Gothenburg	NU	ST	ME	NS	UFP+F	EM	NUC-AIT	10-368	2574	20.9	1.27	1816	40.8	1.26	2084	93.4	1.6	Molnár et al. (2002)
EU	SWE	Gothenburg	TR	ST	ME	NS	UFP+F	EM	NUC-AIT	10-368	778	20.2	1.18	576	35.8	1.28	3869	50.8	2.12	Molnár et al. (2002)
EU	SWE	Gothenburg	TR	ST	ME	NS	UFP+F	EM	NUC-AIT	10-368	162	18.7	1.55	88	30.5	1.14	1002	74.6	1.61	Molnár et al. (2002)
EU	SWE	Stockholm	TR	MT	A	NS	UPF+F	EM	AIT	25-606	15159	44.9	2.17	72987	2.8	3.34	--	--	--	Krecl et al. (2015)
EU	SWE	Stockholm	TR	MT	A	NS	UPF+F	EM	AIT	25-606	10041	30.3	1.55	4542	71.5	1.81	--	--	--	Krecl et al. (2015)
EU	SWE	Stockholm	TR	MT	E	NS	UPF+F	EM	AIT	25-606	15286	25.1	2.33	1446	93.9	1.73	--	--	--	Krecl et al. (2015)
EU	SWE	Stockholm	TR	MT	E	NS	UPF+F	EM	AIT	25-606	5695	25.3	2.07	6936	64.6	1.88	--	--	--	Krecl et al. (2015)
EU	SWE	Stockholm	TR	MT	M	NS	UPF+F	EM	AIT	25-606	33313	3.9	4.43	3600	60.8	1.87	--	--	--	Krecl et al. (2015)
EU	SWE	Stockholm	TR	MT	M	NS	UPF+F	EM	AIT	25-606	36564	19.4	2.31	5675	81.2	1.8	--	--	--	Krecl et al. (2015)
EU	SWE	Stockholm	TR	MT	M	NS	UPF+F	EM	AIT	25-606	9083	39	2.37	677	77.8	1.39	--	--	--	Krecl et al. (2015)
EU	SWE	Stockholm	TR	MT	M	NS	UPF+F	EM	AIT	25-606	71751	1.5	5.15	3916	56.9	1.89	--	--	--	Krecl et al. (2015)
LA	BRA	São Paulo	NU	ST	E	NS	UFP+F	EM	AIT	10-414	474	20.7	1.36	1457	45.3	1.75	322	171.8	1.77	Martins et al. (2010)
LA	BRA	São Paulo	NU	ST	E	NS	UFP+F	EM	ACC	10-414	4764	56.1	1.72	52	130.1	1.17	7976	138.7	1.66	Martins et al. (2010)
LA	BRA	São Paulo	NU	ST	E	NS	UFP+F	EM	AIT	10-414	2377	25.2	1.43	5207	45.9	1.64	1063	141.6	1.82	Martins et al. (2010)
LA	BRA	São Paulo	NU	ST	E	NS	UFP+F	EM	AIT	10-414	6150	40	1.5	395	76.7	1.23	3320	127.8	1.59	Martins et al. (2010)
LA	BRA	São Paulo	NU	ST	M	NS	UFP+F	EM	AIT	10-414	3410	25.9	1.47	5536	44.5	1.63	1448	129.3	1.78	Martins et al. (2010)
LA	BRA	São Paulo	NU	ST	M	NS	UFP+F	EM	AIT	10-414	8124	42.5	1.58	9216	123.3	1.72	--	--	--	Martins et al. (2010)
LA	BRA	São Paulo	NU	MT	A	NS	UPF+F	EM	AIT	9-414	1624	30.9	1.27	596	58.6	1.21	3198	73.2	2.01	de Almeida Albuquerque et al. (2012)
LA	BRA	São Paulo	NU	MT	A	NS	UPF+F	EM	AIT	9-414	3186	36.4	1.43	480	77.1	1.16	2364	107.1	1.63	de Almeida Albuquerque et al. (2012)
LA	BRA	São Paulo	NU	MT	A	NS	UPF+F	EM	AIT	9-414	766	22.4	1.26	1619	55.6	1.54	774	99.3	5.83	de Almeida Albuquerque et al. (2012)
LA	BRA	São Paulo	NU	MT	A	NS	UPF+F	EM	AIT	9-414	764	24.2	1.31	300	52.9	1.23	2330	57.2	2.14	de Almeida Albuquerque et al. (2012)

LA	BRA	São Paulo	NU	VVST	A	NS	UPF+F	EM	AIT	10-400	15860	30.7	3.74	4736	31.7	1.51	3434	71.9	1.59	Almeida et al. (2014)
LA	BRA	São Paulo	NU	VVST	A	NS	UPF+F	EM	NUC	10-400	100	15.1	1.07	18341	19.3	3.59	210	200.7	1.28	Almeida et al. (2014)
LA	BRA	São Paulo	NU	ST	D	NS	UPF+F	EM	AIT	10-450	5922	31.9	2.22	2739	113.3	1.82	--	--	--	Eduardo Souto-Oliveira et al. (2016)
LA	BRA	São Paulo	NU	ST	D	NPF	UPF+F	EM	AIT	10-450	5884	23.3	1.73	7067	63.4	2.21	--	--	--	Eduardo Souto-Oliveira et al. (2016)
LA	BRA	São Paulo	NU	MT	E	NS	UPF+F	EM	AIT	9-414	1136	37.5	1.51	151	72.5	1.07	3370	100.1	1.86	de Almeida Albuquerque et al. (2012)
LA	BRA	São Paulo	NU	MT	E	NS	UPF+F	EM	AIT	9-414	1646	44	1.65	168	75.8	1.18	2388	132.8	1.76	de Almeida Albuquerque et al. (2012)
LA	BRA	São Paulo	NU	MT	E	NS	UPF+F	EM	AIT-ACC	9-414	2367	34	1.42	547	71.6	1.23	3097	117.5	1.56	de Almeida Albuquerque et al. (2012)
LA	BRA	São Paulo	NU	MT	E	NS	UPF+F	EM	AIT	9-414	314	21.7	1.33	1017	49.1	1.78	154	222.7	1.7	de Almeida Albuquerque et al. (2012)
LA	BRA	São Paulo	NU	MT	E	NS	UPF+F	EM	AIT	9-414	316	26.7	1.37	41	54.8	1.11	1265	53.3	2.2	de Almeida Albuquerque et al. (2012)
LA	BRA	São Paulo	NU	MT	E	NS	UPF+F	EM	AIT	9-414	362	22	1.27	2246	49.4	1.89	136	283.3	1.5	de Almeida Albuquerque et al. (2012)
LA	BRA	São Paulo	NU	ST	E	NS	UPF+F	EM	AIT	10-450	67	9.1	1.2	1634	14.6	2.94	3668	85.4	2.05	Eduardo Souto-Oliveira et al. (2016)
LA	BRA	São Paulo	NU	VVST	E	NS	UPF+F	EM	AIT	10-400	10895	14.8	3.58	2456	60.4	1.63	163	198.6	1.27	Almeida et al. (2014)
LA	BRA	São Paulo	NU	VVST	E	NS	UPF+F	EM	NUC	10-400	18980	7	3.77	2534	64.5	1.5	668	174	1.47	Almeida et al. (2014)
LA	BRA	São Paulo	NU	VVST	E	NS	UPF+F	EM	AIT	10-400	3731	11.4	1.87	2917	48.7	1.61	788	189.6	1.77	Almeida et al. (2014)
LA	BRA	São Paulo	NU	VVST	E	NS	UPF+F	EM	NUC	10-400	6944	5	4.41	1128	54.3	1.52	398	171.1	1.55	Almeida et al. (2014)
LA	BRA	São Paulo	NU	MT	M	NS	UPF+F	EM	AIT	9-414	22.6	1.11	1.3	2263	37.4	1.38	4846	83.5	2.06	de Almeida Albuquerque et al. (2012)
LA	BRA	São Paulo	NU	MT	M	NS	UPF+F	EM	AIT	9-414	424	23.3	1.22	2710	41.5	1.81	203	201.8	1.49	de Almeida Albuquerque et al. (2012)
LA	BRA	São Paulo	NU	VVST	M	NS	UPF+F	EM	NUC	10-400	6527	10.7	1.72	6685	55.5	2.4	840	7.6	1.3	Almeida et al. (2014)
LA	BRA	São Paulo	NU	VVST	M	NS	UPF+F	EM	NUC	10-400	8010	13.8	1.87	7039	60.1	2.44	900	74.7	1.27	Almeida et al. (2014)
LA	BRA	São Paulo	NU	VVST	M	NS	UPF+F	EM	NUC	10-400	15713	6.3	4.04	1099	52.3	1.66	218	199.9	1.35	Almeida et al. (2014)
LA	BRA	São Paulo	NU	VVST	M	NS	UPF+F	EM	NUC	10-400	10985	16.6	2.59	1850	55.6	1.42	652	161.1	1.65	Almeida et al. (2014)
LA	BRA	São Paulo	NU	VVST	E	NS	UPF+F	EM	AIT	10-400	9394	18.6	2.18	11973	41.6	2.97	670	86.1	1.24	Almeida et al. (2014)
LA	BRA	São Paulo	NU	VVST	E	NS	UPF+F	EM	NUC	10-400	42859	2.6	4.69	5162	49.9	2	261	250	1.37	Almeida et al. (2014)
LA	BRA	Porto Alegre	TR	MT	E	NS	UPF+F	EM	AIT	10-420	1500	14.3	1.15	16205	27.1	1.63	3157	117.1	1.45	Schneider et al. (2015)
LA	BRA	Porto Alegre	TR	MT	E	NS	UPF+F	EM	AIT	10-420	1700	15.3	1.15	25500	28.9	1.78	6999	98.1	1.72	Schneider et al. (2015)
LA	BRA	Porto Alegre	UB	MT	E	NS	UPF+F	EM	AIT	10-420	900	14.3	1.18	10386	33.4	1.73	2123	88.9	1.54	Schneider et al. (2015)
LA	CHL	Santiago	NU	ST	E	NS	UPF+F	EM	AIT	10-700	5586	26.9	1.6	15478	80.9	1.7	602	229	1.41	Gramsch et al. (2009)
LA	CHL	Santiago	NU	ST	M	NS	UPF+F	EM	AIT	10-700	1031	26.5	1.28	7795	36.6	1.74	12229	95.6	1.82	Gramsch et al. (2009)
LA	CHL	Santiago	TR	ST	E	NS	UPF+F	EM	AIT	10-700	30232	21.5	1.57	10438	42.7	1.8	35733	93.7	1.89	Gramsch et al. (2009)

LA	CHL	Santiago	TR	ST	M	NS	UPF+F	EM	AIT	10-700	29975	19.5	1.5	26975	33	1.66	30976	100.9	1.81	Gramsch et al. (2009)
LA	CHL	Santiago	UB	VST	E	NS	UPF+F	EM	AIT	10-700	4231	24.7	1.63	8692	83.7	1.74	243	234.9	1.19	Gramsch et al. (2009)
LA	CHL	Santiago	UB	VST	M	NS	UPF+F	EM	AIT	10-700	3081	21.1	1.44	12070	53.1	2.22	1613	115.8	1.6	Gramsch et al. (2009)
LA	MEX	Mexico City	NU	ST	D	NS	UFP+F	EM	AIT	15-560	24086	31.4	2.32	1404	173.5	1.44	--	--	--	Wang et al. (2010b)
LA	MEX	Mexico City	NU	ST	M	NS	UFP+F	EM	AIT	15-560	36332	25.2	2.12	1941	87.8	1.34	6488	136.5	1.63	Wang et al. (2010b)
LA	MEX	Mexico City	NU	ST	ME	NS	UFP+F	EM	AIT	15-440	20454	18.7	1.85	8617	40.8	1.53	2953	131	1.64	Kleinman et al. (2009)
NAAN	AUS	Brisbane	NU	ST	D	NS	UFP+F	EM	AIT	9-407	6132	13	1.49	7921	28.9	1.53	13496	85	1.86	Holmes et al. (2005)
NAAN	AUS	Wollongong	NU	MT	ME	NS	UPF+F	EM	AIT	14-660	24	11.3	1.44	77	41.4	1.89	--	--	--	Dominick et al. (2018)
NAAN	CAN	Toronto	TR	ST	ME	NS	UFP	EM	NUC	3-100	1878	11.2	1.42	14351	30	3.56	11600	20.4	1.87	Jeong and Evans (2009)
NAAN	CAN	Toronto	TR	ST	ME	NS	UFP	EM	AIT	3-100	167	12.7	1.33	13005	28.2	2.79	75	40.7	1.19	Jeong and Evans (2009)
NAAN	CAN	Toronto	NU	LT	A	NS	UFP+F	EM	NUC-AIT	8-300	34320	18.9	1.92	440	49	1.24	2654	83.1	1.53	Sabaliauskas et al. (2012)
NAAN	CAN	Toronto	NU	LT	A	NS	UFP+F	EM	NUC-AIT	8-300	21246	20.5	2.11	721	45.2	1.31	2656	88.4	1.53	Sabaliauskas et al. (2012)
NAAN	CAN	Toronto	NU	LT	E	NS	UFP+F	EM	NUC-AIT	8-300	14404	19.2	2	926	47.9	1.34	2312	84.3	1.59	Sabaliauskas et al. (2012)
NAAN	CAN	Toronto	NU	LT	E	NS	UFP+F	EM	NUC-AIT	8-300	23485	19.9	2.04	567	49.3	1.29	2214	87.2	1.59	Sabaliauskas et al. (2012)
NAAN	CAN	Toronto	NU	LT	E	NS	UFP+F	EM	AIT	8-300	6205	16.5	1.86	5405	53.7	1.71	667	119	1.42	Sabaliauskas et al. (2012)
NAAN	CAN	Toronto	NU	LT	E	NS	UFP+F	EM	AIT	8-300	8143	15.1	1.79	7790	44.2	1.68	1290	111.1	1.45	Sabaliauskas et al. (2012)
NAAN	CAN	Toronto	NU	LT	M	NS	UFP+F	EM	NUC-AIT	8-300	30118	19.5	1.92	431	50.9	1.26	2660	82.2	1.59	Sabaliauskas et al. (2012)
NAAN	CAN	Toronto	NU	LT	M	NS	UFP+F	EM	NUC	8-300	11775	15.7	1.78	6727	52.2	1.71	1088	113.2	1.45	Sabaliauskas et al. (2012)
NAAN	CAN	Toronto	NU	VST	ME	NS	UFP+F	EM	NUC-AIT	8-100	1205	10.9	1.32	2604	20	1.45	6188	39	2.18	Zimmerman et al. (2014)
NAAN	CAN	Toronto	NU	LT	ME	NS	UPF+F	EM	AIT	10-300	27898	17.8	2.14	4836	81.8	1.53	--	--	--	Jun et al. (2014)
NAAN	CAN	Toronto	NU	LT	ME	NS	UPF+F	EM	NUC	10-300	31408	15.1	2.02	562	48.5	1.25	1927	75.9	1.53	Jun et al. (2014)
NAAN	CAN	Hamilton	NU	MT	ME	NS	UPF+F	EM	NUC	7-294	26087	0.2	36.14	2994	11.6	1.52	4244	33.9	1.92	Chan and Mozurkewich (2007)
NAAN	CAN	Hamilton	NU	ST	ME	NS	UPF+F	EM	AIT	7-294	273	17.6	1.32	2448	41.6	1.79	1400	87.4	2.13	Chan and Mozurkewich (2007)
NAAN	NZL	Auckland	NU	MT	D	NS	UPF+F	EM	AIT	10-280	639	19.2	1.49	1140	38.6	1.53	612	96.1	1.69	Coulson et al. (2016)
NAAN	NZL	Auckland	NU	MT	E	NS	UPF+F	EM	AIT	10-280	109	15.5	1.32	1690	40	1.71	547	107.1	1.67	Coulson et al. (2016)
NAAN	NZL	Auckland	TR	ST	D	NS	UPF+F	EM	AIT	10-220	292	9.1	1.28	1563	18.4	1.9	2191	41.9	2.29	Coulson et al. (2016)

NAAN	NZL	Auckland	TR	VST	D	NS	UPF+F	EM	AIT	10-220	2443	17.9	1.68	4174	37.7	1.94	597	119.2	1.6	Coulson et al. (2016)
NAAN	NZL	Auckland	TR	ST	E	NS	UPF+F	EM	AIT	10-220	292	9.1	1.28	1563	18.4	1.9	2191	41.9	2.29	Coulson et al. (2016)
NAAN	NZL	Auckland	TR	VST	E	NS	UPF+F	EM	AIT	10-280	1176	15.4	1.41	4303	34.3	1.67	1220	95.8	1.7	Coulson et al. (2016)
NAAN	NZL	Auckland	UB	MT	D	NS	UPF+F	EM	AIT	10-200	18	12.1	1.15	1008	21.3	1.48	3232	59.9	1.48	Coulson et al. (2016)
NAAN	NZL	Auckland	UB	MT	E	NS	UPF+F	EM	AIT	10-200	69	20.1	1.25	618	50.4	1.77	1461	53.2	2.47	Coulson et al. (2016)
NAAN	USA	New York City	NU	MT	ME	NS	UFP	EM	NUC	8-65	19582	13.2	1.52	31505	33.2	2.27	--	--	--	Bae et al. (2010)
NAAN	USA	New York City	NU	ST	ME	NS	UFP	EM	NUC	8-65	77480	12.3	1.8	84470	25.2	2.16	--	--	--	Bae et al. (2010)
NAAN	USA	Fresno	NU	MT	A	NS	UFP+F	EM	AIT	10-400	2305	6.7	1.42	5684	25.5	2.12	4266	91.6	1.89	Hering et al. (2007)
NAAN	USA	Fresno	NU	MT	A	NS	UFP+F	EM	AIT	10-400	1347	11	1.54	485	23.1	1.29	8000	73.5	1.96	Hering et al. (2007)
NAAN	USA	Los Angeles	NU	MT	A	NS	UFP+F	EM	AIT	7.64-225	1911	27.3	1.3	12297	32.5	2.1	--	--	--	Verma et al. (2009)
NAAN	USA	Downey	NU	VVST	A	NS	UFP+F	EM	NUC	14-200	190	16.3	1.12	1540	26	1.78	229	127.2	1.58	Kim et al. (2002)
NAAN	USA	Fresno	NU	VVST	A	NS	UFP+F	EM	NUC	10-379	56880	5.9	3.23	2680	37.9	1.17	1823	85.8	1.5	Watson et al. (2011)
NAAN	USA	Detroit	NU	VVST	A	NS	UFP+F	EM	NUC	10-430	66119	14.2	1.57	8243	47.2	1.3	15060	79.2	1.59	Young et al. (2012)
NAAN	USA	Detroit	NU	VVST	A	NS	UFP+F	EM	NUC	10-430	54527	13.7	1.69	15355	46.9	1.44	14157	78.4	1.8	Young et al. (2012)
NAAN	USA	Detroit	NU	VVST	A	NS	UFP+F	EM	AIT	10-430	29311	17.3	1.57	23611	51.4	1.43	10295	93	1.83	Young et al. (2012)
NAAN	USA	Detroit	NU	VVST	A	NS	UFP+F	EM	AIT	10-430	20468	23.3	2.13	9129	55.6	1.38	4984	143.1	1.55	Young et al. (2012)
NAAN	USA	Detroit	NU	VVST	A	NS	UFP+F	EM	NUC	10-430	1653	12.3	1.3	11560	23	2.6	3450	167.5	1.42	Young et al. (2012)
NAAN	USA	Detroit	NU	VVST	A	NS	UFP+F	EM	ACC	10-430	6322	19.5	2.5	3220	140.3	1.65	1010	173.4	1.33	Young et al. (2012)
NAAN	USA	New York City	NU	ST	D	NS	UFP+F	EM	NUC-AIT	10-470	54	15.4	1.34	92	20.4	1.36	1391	27.3	2.23	Hogrefe et al. (2006)
NAAN	USA	New York City	NU	ST	D	NS	UFP+F	EM	AIT	10-470	952	20.8	1.84	148	41.7	1.72	423	46.4	1.73	Hogrefe et al. (2006)
NAAN	USA	New York City	NU	ST	D	NS	UFP+F	EM	AIT	10-470	748	19.4	1.68	661	47.1	1.65	--	--	--	Hogrefe et al. (2006)
NAAN	USA	Fresno	NU	MT	E	NS	UFP+F	EM	AIT	10-400	5434	11.3	1.62	2136	23.9	1.34	15903	61.7	1.86	Hering et al. (2007)
NAAN	USA	Fresno	NU	MT	E	NS	UFP+F	EM	AIT	10-400	2821	13.5	1.62	2124	27.2	1.32	34157	77.1	1.62	Hering et al. (2007)
NAAN	USA	Fresno	NU	MT	E	NS	UFP+F	EM	AIT	10-400	3343	11.5	1.62	1713	24.8	1.33	18621	68.6	1.68	Hering et al. (2007)

NAAN	USA	Fresno	NU	MT	E	NS	UFP+F	EM	AIT	10-400	2002	15	1.57	1184	28.5	1.3	40163	77.3	1.61	Hering et al. (2007)
NAAN	USA	Downey	NU	VVST	E	NS	UFP+F	EM	AIT	14-200	500	28.8	1.2	3218	43.6	2.7	--	--	--	Kim et al. (2002)
NAAN	USA	Fresno	NU	VVST	E	NS	UFP+F	EM	AIT	10-379	23002	1.8	3.81	1534	31.9	1.47	6575	79.3	1.64	Watson et al. (2011)
NAAN	USA	Fresno	NU	MT	M	NS	UFP+F	EM	AIT	10-400	13520	6.6	2.53	2554	26.3	1.42	18780	54.3	2.1	Hering et al. (2007)
NAAN	USA	Fresno	NU	MT	M	NS	UFP+F	EM	AIT	10-400	3552	9.9	2.19	1932	27.1	1.41	13948	81.4	1.85	Hering et al. (2007)
NAAN	USA	Los Angeles	NU	MT	M	NS	UFP+F	EM	AIT	7.64-225	10599	36.3	2.59	885	69.1	1.47	--	--	--	Verma et al. (2009)
NAAN	USA	Downey	NU	VVST	M	NS	UFP+F	EM	AIT	14-200	5858	24.4	3.25	1901	28.2	1.36	--	--	--	Kim et al. (2002)
NAAN	USA	Downey	NU	VVST	M	NS	UFP+F	EM	AIT	14-200	2479	24.6	1.66	165	74.4	1.2	305	124.4	1.48	Kim et al. (2002)
NAAN	USA	Atlanta	NU	VVST	M	NS	UFP+F	EM	NUC	7-400	8193	17.2	1.24	29954	13.7	1.73	7582	36.6	3.15	Stolzenburg et al. (2005)
NAAN	USA	Atlanta	NU	VVST	M	NS	UFP+F	EM	NUC	3-400	22721	9.3	1.4	15785	23.2	1.31	16188	24.3	7.67	Stolzenburg et al. (2005)
NAAN	USA	Atlanta	NU	VVST	M	NS	UFP+F	EM	AIT	3-600	10680	22.7	2.17	9567	27.4	1.49	2609	90.8	1.62	Woo et al. (2001)
NAAN	USA	Atlanta	NU	VVST	M	NS	UFP+F	EM	AIT	3-600	970	11.9	1.2	11065	24.1	1.84	7274	83.8	2.43	Woo et al. (2001)
NAAN	USA	Pittsburgh	NU	LT	ME	NS	UFP+F	EM	NCA	10-1000	2854	9.3	1.72	16300	32.2	2.37	866	115.7	1.52	Stanier et al. (2004)
NAAN	USA	Los Angeles	NU	MT	ME	NS	UFP+F	EM	AIT	14-700	796	34.1	1.29	2920	56.8	1.53	3544	112.2	1.96	Singh et al. (2006)
NAAN	USA	Houston	NU	MT	ME	NS	UFP+F	EM	AIT	30-700	3909	23.9	1.56	9445	66.7	1.86	--	--	--	Gasparini et al. (2004)
NAAN	USA	Los Angeles	NU	MT	ME	NS	UFP+F	EM	AIT	16-180	10573	26	1.54	4673	73.8	1.94	--	--	--	Ntziachristos et al. (2007)
NAAN	USA	Riverside	NU	MT	ME	NS	UFP+F	EM	AIT	14-700	243	21.8	1.28	1471	34.5	1.55	6433	75.5	2.13	Singh et al. (2006)
NAAN	USA	Los Angeles	NU	MT	ME	NS	UFP+F	EM	AIT	14-700	7745	26.7	1.73	6962	78.9	1.78	384	207.8	1.56	Singh et al. (2006)
NAAN	USA	Los Angeles	NU	MT	ME	NS	UFP+F	EM	AIT	14.6-180	43499	30.3	1.45	51304	49.7	2.58	18366	89.2	1.57	Verma et al. (2011)
NAAN	USA	Los Angeles	NU	MT	ME	NS	UFP+F	EM	AIT	14.6-180	18942	27.2	1.36	53543	49.5	2.33	1838	99.1	1.33	Verma et al. (2011)
NAAN	USA	Los Angeles	NU	MT	ME	NS	UFP+F	EM	AIT	14.6-180	22790	16.8	1.54	10401	30.1	1.35	65224	81.3	2.34	Verma et al. (2011)
NAAN	USA	Pittsburgh	NU	MT	ME	NS	UFP+F	EM	NUC	3-583	13853	2.6	1.25	16975	12.4	3.74	4762	88.2	1.98	Zhou et al. (2004)
NAAN	USA	Riverside	NU	ST	ME	NS	UFP+F	EM	AIT	22-800	36	62.2	1.13	7544	67.1	2.57	131	97.9	1.37	Pratt and Prather (2009)
NAAN	USA	Los Angeles	NU	VST	ME	NS	UFP+F	EM	NUC-AIT	14-736	1342	19.1	1.18	2327	24.1	1.37	17736	24.4	2.56	Krudysz et al. (2009)

NAAN	USA	Los Angeles	NU	VST	ME	NS	UFP+F	EM	NUC-AIT	14-736	398	19.7	1.14	932	25.9	1.36	21144	32.6	2.48	Krudysz et al. (2009)
NAAN	USA	Los Angeles	NU	VST	ME	NS	UFP+F	EM	AIT	14-736	2071	22.2	1.32	6327	37.2	1.91	7646	49	2.07	Krudysz et al. (2009)
NAAN	USA	Los Angeles	NU	VST	ME	NS	UFP+F	EM	NUC-AIT	14-736	1590	19.4	1.21	3543	24.7	1.46	7811	49.7	2.11	Krudysz et al. (2009)
NAAN	USA	Los Angeles	NU	VST	ME	NS	UFP+F	EM	AIT	14-736	1060	22.4	1.25	3567	32.6	1.47	16713	58.7	2.07	Krudysz et al. (2009)
NAAN	USA	Los Angeles	NU	VST	ME	NS	UFP+F	EM	AIT	14-736	554	19.3	1.13	1556	25.3	1.28	11381	43	2.21	Krudysz et al. (2009)
NAAN	USA	Los Angeles	NU	VST	ME	NS	UFP+F	EM	AIT	14-736	1424	19.9	1.18	2916	26.3	1.33	16461	44.2	2.21	Krudysz et al. (2009)
NAAN	USA	Boulder	NU	VVST	ME	NPF	UFP+F	EM	NUC	3-100	17850	5.2	1.49	14724	12.3	1.56	11060	24.8	2.2	Iida et al. (2006)
NAAN	USA	Los Angeles	NU	VVST	ME	NS	UFP+F	EM	AIT	14-700	1133	35.4	1.28	3901	63.6	1.56	6423	110.3	1.83	Singh et al. (2006)
NAAN	USA	Riverside	NU	VVST	ME	NS	UFP+F	EM	AIT	14-700	1405	21.9	1.38	9996	49.9	2.31	--	--	--	Singh et al. (2006)
NAAN	USA	Los Angeles	NU	VVST	ME	NS	UFP+F	EM	AIT	14-700	15514	19	4.15	1969	27	1.58	2103	81.1	1.58	Singh et al. (2006)
NAAN	USA	Claremont	NU	VVST	E	NS	UPF+F	EM	AIT-ACC	14-430	685	98.9	1.63	216	351.3	3	--	--	--	Fine et al. (2004)
NAAN	USA	Claremont	NU	VVST	E	NS	UPF+F	EM	AIT	14-430	499	27.1	1.25	1015	43.9	1.43	428	98.3	1.92	Fine et al. (2004)
NAAN	USA	Claremont	NU	VVST	E	NS	UPF+F	EM	AIT	14-430	167	32.2	1.24	806	72.2	2.19	--	--	--	Fine et al. (2004)
NAAN	USA	Riverside	NU	VVST	E	NS	UPF+F	EM	AIT	14-430	1639	40.6	1.4	2539	130.2	1.91	--	--	--	Fine et al. (2004)
NAAN	USA	Riverside	NU	VVST	E	NS	UPF+F	EM	AIT	14-430	1348	31.4	1.18	2433	56.5	1.26	1737	167.2	1.49	Fine et al. (2004)
NAAN	USA	Riverside	NU	VVST	E	NS	UPF+F	EM	AIT	14-430	578	37.9	1.08	3319	49.6	1.71	793	184.1	1.43	Fine et al. (2004)
NAAN	USA	Claremont	NU	VVST	M	NS	UPF+F	EM	AIT-ACC	14-430	153	61.8	1.15	1723	84.8	2.26	446	141.6	1.36	Fine et al. (2004)
NAAN	USA	Claremont	NU	VVST	M	NS	UPF+F	EM	AIT-ACC	14-430	1631	83.4	2.06	382	75.1	1.23	474	150.5	1.31	Fine et al. (2004)
NAAN	USA	Riverside	NU	VVST	M	NS	UPF+F	EM	ACC	14-430	720	43.5	1.75	1774	170.3	1.78	--	--	--	Fine et al. (2004)
NAAN	USA	Riverside	NU	VVST	M	NS	UPF+F	EM	ACC	14-430	1442	53.4	1.97	705	109.6	1.16	1955	224.4	1.39	Fine et al. (2004)
NAAN	USA	Rochester	NU	LT	ME	NS	UPF+F	EM	AIT	10-500	366	19.7	1.28	2412	32	1.65	2288	85.1	1.85	Wang et al. (2010c)
NAAN	USA	Los Angeles	TR	ST	E	NS	UFP+F	EM	NUC	7.4-290	5108	15.4	1.33	7467	23.7	1.46	5965	61.3	1.98	Zhu et al. (2006)
NAAN	USA	Los Angeles	TR	ST	E	NS	UFP+F	EM	NUC	7.4-290	879	12	1.22	1461	19	1.41	2020	45.6	1.82	Zhu et al. (2006)
NAAN	USA	Los Angeles	TR	MT	ME	NS	UFP+F	EM	NUC	6-523	3811	10.1	1.15	852	16.3	1.15	23563	20.8	2.02	Ning et al. (2010)

NAAN	USA	Los Angeles	TR	MT	ME	NS	UFP+F	EM	NUC	6-523	10399	11	1.34	893	17.8	1.12	17216	38.2	1.74	Ning et al. (2010)
NAAN	USA	Los Angeles	TR	MT	ME	NS	UFP+F	EM	NUC	6-523	4208	10.1	1.12	20419	11.4	1.65	21768	37.8	1.85	Ning et al. (2010)
NAAN	USA	Los Angeles	TR	MT	ME	NS	UFP+F	EM	NUC	6-523	1528	10.1	1.13	1463	15.9	1.2	29289	26.9	2.11	Ning et al. (2010)
NAAN	USA	Corpus Christi	TR	MT	ME	NS	UFP+F	EM	NUC	6-220	15881	17	1.46	39825	22.4	3.29	1145	31.3	1.23	Wang et al. (2010c)
NAAN	USA	Corpus Christi	TR	MT	ME	NS	UFP+F	EM	AIT	6-220	1183	19.5	1.54	10164	45.9	2.91	92	56.8	1.09	Wang et al. (2010c)
NAAN	USA	Corpus Christi	TR	MT	ME	NS	UFP+F	EM	NUC	6-220	2226	13.9	1.26	195	23.5	1.13	12170	29.4	2.63	Wang et al. (2010c)
NAAN	USA	Corpus Christi	TR	MT	ME	NS	UFP+F	EM	NUC	6-220	34970	11.1	5.82	3368	15.9	1.24	2543	37.5	1.73	Wang et al. (2010c)
NAAN	USA	Los Angeles	TR	VST	ME	NS	UFP+F	EM	NUC	6-220	15330	14.3	1.4	12001	33.9	1.58	8154	87.9	1.71	Barone and Zhu (2008)
NAAN	USA	Los Angeles	TR	VST	ME	NS	UFP+F	EM	NUC	6-220	11418	12.8	1.4	8505	31.6	1.37	5734	87	1.58	Barone and Zhu (2008)
NAAN	USA	Los Angeles	TR	VST	ME	NS	UFP+F	EM	AIT	6-220	14192	26.6	1.76	862	52.1	1.14	2398	110.5	1.56	Barone and Zhu (2008)
NAAN	USA	Los Angeles	TR	VST	ME	NS	UFP+F	EM	AIT	6-220	4458	14.1	1.4	9459	39	1.43	2788	109.1	1.43	Barone and Zhu (2008)
NAAN	USA	Los Angeles	TR	VST	ME	NS	UFP+F	EM	AIT	14-736	2111	21.7	1.27	14959	35.8	1.59	9649	67.5	2.21	Krudysz et al. (2009)
NAAN	USA	Los Angeles	TR	VST	ME	NS	UFP+F	EM	AIT	14-736	2401	22.5	1.38	15531	37.5	1.86	494	157.8	1.39	Krudysz et al. (2009)
NAAN	USA	Los Angeles	TR	VST	ME	NS	UFP+F	EM	AIT	14-736	2342	21.1	1.31	7766	38.6	1.73	652	124.2	1.47	Krudysz et al. (2009)
NAAN	USA	Los Angeles	TR	VST	ME	NS	UFP+F	EM	AIT	14-736	877	19.7	1.19	5720	27.6	1.63	7237	45.6	2.24	Krudysz et al. (2009)
NAAN	USA	Los Angeles	TR	VST	ME	NS	UFP+F	EM	AIT	14-736	1458	20.9	1.23	23371	30	1.89	8766	86.4	1.98	Krudysz et al. (2009)
NAAN	USA	Los Angeles	TR	VVST	ME	NS	UFP+F	EM	NUC-AIT	16-600	22051	17.6	1.29	8119	21	1.36	61492	46.7	2.25	Westerdahl et al. (2005)
NAAN	USA	Los Angeles	TR	VVST	ME	NS	UFP+F	EM	AIT	16-600	7108	28.4	1.31	36318	34.9	2.14	1440	77.3	2.81	Westerdahl et al. (2005)
NAAN	USA	Buffalo	TR	VVST	ME	NS	UFP+F	EM	NUC	6-500	7092	9.1	3.11	167	10.1	1.13	356	81.7	1.41	Ogulei et al. (2007)
NAAN	USA	Buffalo	TR	VVST	ME	NS	UFP+F	EM	AIT	6-500	1620	7.2	1.7	1008	36.1	1.43	728	76.7	1.5	Ogulei et al. (2007)
NAAN	USA	Buffalo	TR	VVST	ME	NS	UFP+F	EM	AIT	6-500	976	8.1	1.59	817	40.6	1.45	795	75	1.49	Ogulei et al. (2007)
NAAN	USA	Buffalo	TR	VVST	ME	NS	UFP+F	EM	AIT	6-500	496	7.2	1.57	499	39	1.67	345	87.3	1.48	Ogulei et al. (2007)
NAAN	USA	Buffalo	TR	VVST	ME	NS	UFP+F	EM	AIT	6-500	1767	2.8	5.47	194	10.6	1.32	726	50.8	1.53	Ogulei et al. (2007)
NAAN	USA	Buffalo	UB	VVST	ME	NS	UFP+F	EM	AIT	6-500	218	19.3	1.93	18	41.8	1.2	400	56	1.54	Ogulei et al. (2007)

WA	JOR	Multiple cities	NU	VST	ME	NS	UFP+F +C	EM+ O	AIT	10-1000	20000	30	1.6	500	150	1.7	6	2500	1.6	Hussein et al. (2017)
WA	KWT	Fahaheel	TR	ST	E	NS	UFP+F	EM	NUC	5-1000	100433	13.4	1.7	25444	70.3	2.37	--	--	--	Al-Dabbous and Kumar (2014)
WA	KWT	Fahaheel	TR	ST	E	NS	UFP+F	EM	NUC	5-1000	115174	12.4	1.57	18822	52.7	2.02	5487	161.1	1.53	Al-Dabbous and Kumar (2014)
WA	KWT	Fahaheel	TR	ST	E	NS	UFP+F	EM	NUC	5-1000	82110	13.4	1.71	13546	71.6	1.88	2114	190.3	1.33	Al-Dabbous and Kumar (2014)
WA	KWT	Fahaheel	TR	ST	E	NS	UFP+F	EM	NUC	5-1000	56929	12.1	1.5	37972	14.2	1.79	13782	95.3	2.03	Al-Dabbous and Kumar (2014)
WA	KWT	Fahaheel	TR	ST	E	NS	UFP+F	EM	NUC	5-1000	74882	13.1	1.69	12314	69.3	1.77	2691	200.3	1.39	Al-Dabbous and Kumar (2014)
WA	KWT	Fahaheel	TR	ST	E	NS	UFP+F	EM	NUC	5-1000	75180	12.1	1.53	30645	38.3	3.18	--	--	--	Al-Dabbous and Kumar (2014)
WA	KWT	Fahaheel	TR	ST	M	NS	UFP+F	EM	NUC	5-1000	160348	12.9	1.61	11772	55.0	1.56	11284	142.7	1.54	Al-Dabbous and Kumar (2014)
WA	KWT	Fahaheel	TR	ST	M	NS	UFP+F	EM	NUC	5-1000	127942	12.9	1.59	8969	48.5	1.58	9832	131.5	1.57	Al-Dabbous and Kumar (2014)
WA	KWT	Fahaheel	TR	ST	M	NS	UFP+F	EM	NUC	5-1000	104919	12.5	1.62	15965	72.7	1.91	2709	188.6	1.31	Al-Dabbous and Kumar (2014)
WA	KWT	Fahaheel	TR	ST	ME	NS	UFP+F	EM	NUC	5-1000	70353	11.7	1.62	24544	62.8	2.31	1641	180.9	1.3	Al-Dabbous and Kumar (2014)
WA	KWT	Fahaheel	TR	ST	ME	NS	UFP+F	EM	NUC	5-1000	54414	11.5	1.59	15619	38.9	2.18	6418	140.2	1.63	Al-Dabbous and Kumar (2014)
WA	KWT	Fahaheel	TR	ST	ME	NS	UFP+F	EM	NUC	5-1000	53665	11.6	1.61	17789	67.7	2	2884	186.3	1.32	Al-Dabbous and Kumar (2014)

Table A.2 Urban aerosol size distribution measurements made with both electrical mobility-based techniques and aerodynamic-based techniques covering the sub-micron and coarse regime.

Region	Country	City	Sampling location	Sampling duration	Time of day	Event identification	Target aerosol population	Measurement type	Prominent mode	Electrical Mobility-Based Techniques										Aerodynamic-Based Techniques														Reference
										Lognormal fitting size range	Mode 1			Mode 2			Mode 3			Lognormal fitting size range	Mode 1			Mode 2			Mode 3			Mode 1			Mode 2			Mode 3			
											N (cm^{-3})	$\overline{D_p}$ (nm)	σ	N (cm^{-3})	$\overline{D_p}$ (nm)	σ	N (cm^{-3})	$\overline{D_p}$ (nm)	σ		V (μm^3 cm^{-3})	$\overline{D_p}$ (nm)	σ	V (μm^3 cm^{-3})	$\overline{D_p}$ (nm)	σ	V (μm^3 cm^{-3})	$\overline{D_p}$ (nm)	σ	M (μg m^{-3})	$\overline{D_p}$ (nm)	σ	M (μg m^{-3})	$\overline{D_p}$ (nm)	σ	M (μg m^{-3})	$\overline{D_p}$ (nm)	σ	
CSSA	IND	Trivandrum	NU	MT	ME	NS	UFP+F+C	EM+A	AIT-ACC	14.6-661.2	458	30.4	1.57	5934	111.8	1.7	424	368.2	1.34	700-10000	302.9	6.2	7.65	3.5	2082.5	1.38	7.8	4716.4	1.65	266	0.7	62.37	4	2206.9	1.32	6.2	4858.5	1.44	Babu et al. (2016)
CSSA	IND	Trivandrum	NU	MT	ME	NS	UFP+F+C	EM+A	AIT-ACC	14.6-661.2	1750	71.2	2.11	2424	121.1	1.64	253	319.5	1.4	700-10000	1737.5	0.1	20.92	1.3	2301.2	1.29	12.5	5228.7	1.87	172.2	0.4	86.16	3.7	2409.8	1.34	11	5468.4	1.51	Babu et al. (2016)
CSSA	IND	Trivandrum	NU	MT	ME	NS	UFP+F+C	EM+A	AIT-ACC	14.6-661.2	114	22.3	1.44	275	95.5	1.28	3380	96.6	1.89	700-10000	15.1	2611.4	1.25	65.9	3826.5	2.18	34.5	4543.5	1.36	29.7	1945.7	2.15	130.9	3966.3	1.63	--	--	--	Babu et al. (2016)
CSSA	IND	Trivandrum	NU	MT	ME	NS	UFP+F+C	EM+A	AIT-ACC	14.6-661.2	227	24.4	1.42	1762	96.9	1.44	9030	110.7	1.87	700-10000	450.8	2	12.79	4.2	2424.2	1.34	4.5	4964.2	1.45	1501.5	2.6	8.27	5.9	2362.8	1.48	8.4	4610.4	1.73	Babu et al. (2016)
EA	CHN	Beijing	NU	VVST	A	DS	UFP+F+C	EM+A	NUC	31-800	36107	9.6	1.6	5728	23.4	3.6	297	34.4	1.21	900-2600	0.9	1085.5	1.26	86.7	3430.5	2.13	--	--	--	2687.9	18799.2	1.79	122.1	18200.6	3.97	--	--	--	Wehner et al. (2004b)
EA	CHN	Beijing	NU	VVST	E	DS	UFP+F+C	EM+A	AIT-ACC	3-800	40363	103.7	2.08	4329	110.7	1.36	5841	275.4	1.48	1000-5000	61669.3	135.9	1.78	214.1	3978.1	1.93	--	--	--	133819.9	74.3	2.11	282.9	3979.3	1.86	--	--	--	Wehner et al. (2004b)
EA	CHN	Beijing	NU	VVST	E	DS	UFP+F+C	EM+A	NUC	3-800	1789	11	1.58	1910	69.8	5.35	160	42.5	1.28	1000-6000	415.2	2723.2	1.51	236	5023.3	1.26	--	--	--	1081.6	3694.5	1.85	58.9	5249.4	1.23	--	--	--	Wehner et al. (2004b)
EA	CHN	Beijing	NU	VVST	E	high vol. conc.	UFP+F+C	EM+A	ACC	3-800	4310	17.3	1.37	8186	42.1	1.42	24195	135.1	1.79	1000-5000	178827.3	194	1.48	70.3	2601.8	4.02	42.1	3680.7	1.58	43522769	2.2	3.41	124.3	3823	1.86	--	--	--	Wehner et al. (2004b)
EA	CHN	Beijing	NU	VVST	E	NPF	UFP+F+C	EM+A	NUC	3-800	88923	6.3	1.48	53066	13.2	1.37	7020	35.5	2.06	1000-3000	0.3	1020	1.05	4.6	2000	1.81	6.6	3000.1	1.39	0.8	1000	1.08	2.2	2000	1.49	31.7	5000	2.05	Wehner et al. (2004b)
EA	CHN	Beijing	NU	VVST	E	NPF	UFP+F+C	EM+A	AIT	3-800	6116	17	1.24	12154	36.2	1.46	19996	29.7	2.86	900-3000	0.9	889.4	1.15	33.3	6000	2.09	--	--	--	1	900	1.11	42	6000	2.37	--	--	--	Wehner et al. (2004b)
EA	CHN	Beijing	NU	VVST	M	high vol. conc.	UFP+F+C	EM+A	AIT	3-800	8514	16	1.42	41775	74.9	1.94	--	--	--	1000-4000	332.5	5	914.14	18.9	3143.1	1.34	--	--	--	11.3	912.5	1.33	2.2	2838.5	1.12	118.4	4997.2	2.35	Wehner et al. (2004b)
EA	CHN	Beijing	NU	VVST	M	NPF	UFP+F+C	EM+A	NUC	3-800	28176	8.1	1.62	14936	15.5	1.26	31980	32.3	1.86	1000-3000	40.8	5872.8	2.23	--	--	--	--	--	--	7.5	2000	3.27	7.8	2700.1	1.49	2.8	3059.6	1.18	Wehner et al. (2004b)
EA	CHN	Beijing	NU	LT	ME	NS	UFP+F	EM	AIT	3-800	12122	18.6	2.18	361	39.2	1.26	15689	72.1	2.19	800-10000	92378	3.6	3.73	18.2	3029.9	1.6	--	--	--	46852.6	7.9	3.37	25.3	2981.3	1.61	--	--	--	Wu et al. (2008)
EA	CHN	Beijing	NU	LT	ME	NS	UFP+F	EM	AIT	3-800	3288	13.4	1.79	6095	31	1.69	13619	94.2	2.04	800-10000	1231.8	13.5	4.89	16.2	3100.5	1.52	--	--	--	6845.6	7.4	4.78	23.1	3039.2	1.54	--	--	--	Wu et al. (2008)
EA	CHN	Beijing	NU	LT	ME	NS	UFP+F	EM	AIT	3-800	3525	14.9	1.72	6604	34.4	1.62	15456	97.9	2	800-10000	59	246.5	3.22	15.6	3019	1.46	1.6	4212.4	1.6	47.5	527.4	1.25	12	1216.2	1.5	25.9	3075.2	1.49	Wu et al. (2008)
EA	CHN	Beijing	NU	LT	ME	NS	UFP+F	EM	AIT	3-800	6907	21	2	846	34.4	1.37	19252	78	2.02	800-10000	128	71.8	3.62	6.5	2301.7	1.65	10.5	3785.6	1.47	15645.2	6.3	4.09	23.5	2943.5	1.8	2.6	3442.6	1.23	Wu et al. (2008)
EA	CHN	Lanzhou	NU	MT	ME	NS	F+C	A	--	10-100	--	--	--	--	--	--	--	--	--	500-10000	3.3	497.8	1.3	12.4	1203	2.79	14.3	3777	1.58	5.1	505.6	1.25	23.9	1228.5	2.92	16.7	3847.8	1.51	Yu et al. (2017b)
EA	CHN	Beijing	NU	MT	ME	NS	UFP+F+C	EM+A	AIT	3-800	1589	9.9	1.72	9660	49.2	2.25	3702	143.5	1.77	850-10000	1.708E+13	5.7	1.95	8.3	2840.2	1.87	12.8	5049.1	2.2	2.5	804.4	1.06	6.5	3196.1	1.51	51.6	8832.7	8.69	Yue et al. (2009)
EA	CHN	Guangzhou	NU	VVST	ME	NS	UFP+F+C	EM+A	AIT	15-660	21532	52	2.4	2848	99.4	1.59	--	--	--	660-10000	17	444.9	1.39	12.4	2736.3	2.68	2.8	3543.4	1.37	79.1	311.1	1.65	1.6	1284.2	1.25	15.8	3389.9	1.76	Yue et al. (2010)
EU	DEU	Augsburg	UB	LT	ME	NS	UFP+F+C	EM+A	AIT	3-900	66772	16.1	1.92	52675	38.9	1.67	35274	96	1.89	900-10000	95082.9	29.8	2.31	17.5	2746.7	1.77	1.1	7775.4	1.28	274621602.3	28.7	1.84	27.1	2433.8	1.83	2.8	6730.6	1.6	Pitz et al. (2008)
EU	DEU	Augsburg	UB	LT	ME	NS	UFP+F+C	EM+A	AIT	3-800	469	10.2	1.47	7144	35.6	2.08	1411	135.8	1.73	300-8000	19.1	169.5	2.04	1.6	2661.9	1.59	5.6	135389.7	137.19	510.7	31.5	2.88	1.2	2377.4	1.42	2.6	2982.8	2.21	Birmili et al. (2010)
EU	DEU	Karlsruhe	SUB	VVST	ME	NS	UFP+F+C	EM+A	AIT-ACC	15-800	2017	27.2	1.92	290	53.1	1.15	3154	106.8	1.7	900-4000	0.02	1114.5	1.06	0.1	3622.9	1.14	2.7	3641.6	2.99	3.1	2527.8	2.39	0.9	4971.9	1.24	--	--	--	Bäumer et al. (2008)

EU	DEU	Karlsruhe	SUB	VVST	ME	NS	UFP+F+C	EM+A	ACC	15-800	2245	59.9	2.09	456	69.6	1.38	1608	169.5	1.46	900-4000	0.16	993.4	1.19	0.2	1704.5	1.25	10.2	14318.4	2.37	0.3	1298.9	1.89	1.7	2715.6	2.1	1.8	5942.2	1.42	Bäumer et al. (2008)
EU	DEU	Karlsruhe	SUB	VVST	ME	NS	UFP+F+C	EM+A	ACC	15-800	2654	87.3	2.1	573	193.1	1.41	--	--	--	900-3600	0.02	993.2	1.16	0.7	1716.1	1.97	0.7	3914.1	1.33	0.7	1174.9	1.79	30.9	27384.8	2.75	--	--	--	Bäumer et al. (2008)
EU	DEU	Karlsruhe	SUB	VVST	ME	NS	UFP+F+C	EM+A	AIT	15-800	1237	27.9	1.36	3593	57.7	1.34	2846	137.9	1.71	900-5000	0.1	886.7	1.61	2.5	2553.9	2.46	4.9	8325.7	1.74	0.7	1202	1.76	2.6	2351.1	1.95	4.1	6050.3	1.53	Bäumer et al. (2008)
EU	DEU	Karlsruhe	SUB	VVST	ME	NS	UFP+F+C	EM+A	AIT	15-800	39	18.8	1.11	2712	60.7	1.7	1957	166.2	1.69	900-4000	0.39	967.6	1.14	4.2	1611.3	2.15	24	18669.1	2.17	4.2	909.4	1.83	3.3	1482.2	2	6.1	6027.1	1.76	Bäumer et al. (2008)
EU	FRA	Paris	SUB	ST	ME	NS	UFP+F+C	EM+A	NUC	4.86-486	8089	14.4	1.74	5198	82	1.97	1617	125.5	1.34	600-8000	4.8	375.8	1.44	3.1	3050.1	2.46	1.6	3372.5	1.44	8.7	362.4	1.53	2.1	2164.1	1.8	4.2	3533.8	1.64	Freutel et al. (2013)
EU	FRA	Paris	SUB	ST	ME	NS	UFP+F+C	EM+A	AIT	4.86-486	10711	23.5	2.44	420	55.2	1.27	2699	93.3	1.49	600-8000	1.5	1954.2	1.56	1.4	3361.9	1.35	0.2	5900	1.14	1.6	1657.1	1.66	2.9	2969.4	1.46	0.23	5900	1.2	Freutel et al. (2013)
EU	FRA	Paris	SUB	ST	ME	NS	UFP+F+C	EM+A	NUC	4.86-486	7458	16.5	1.78	923	38.8	1.35	3528	77.5	1.66	600-8000	2.8	2263.3	1.72	0.7	3109.3	1.26	--	--	--	4.6	2257.5	1.64	0.08	6512.3	1.2	--	--	--	Freutel et al. (2013)
NAAN	AUS	Brisbane	NU	LT	ME	NS	UFP+F+C	EM+A	AIT	16-480	160	24.4	1.36	159	29.9	2.98	--	--	--	700-10000	0.2	3744.7	2.26	--	--	--	--	--	--	0.3	8000	2.33	--	--	--	--	--	--	Morawska et al. (1998)
NAAN	USA	Pittsburgh	NU	LT	ME	NS	UFP+F+C	EM+A	AIT	3-600	8000	2.5	1.28	10925	11.9	2.53	11291	49.3	2.29	600-2500	5.9	436.4	1.5	0.2	1230.5	1.2	1.9	2489.4	1.4	9	436.4	1.5	0.3	1230.5	1.2	2.88	2489.4	1.4	Stanier et al. (2004)

Table A.3 Urban aerosol size distribution measurements made with electrical mobility-based techniques and/or optical-based techniques covering the sub-micron and coarse regimes

Region	Country	City	Sampling location	Sampling duration	Time [illegible]	Event identification	Target aerosol population	Measurement type	Prominent mode	Electrical Mobility-Based Techniques										Optical-Based Techniques										Reference
										Lognormal fitting size range	Mode 1			Mode 2			Mode 3			Lognormal fitting size range	Mode 1			Mode 2			Mode 3			
											N (cm^{-3})	$\overline{D_p}$ (nm)	σ	N (cm^{-3})	$\overline{D_p}$ (nm)	σ	N (cm^{-3})	$\overline{D_p}$ (nm)	σ		M (μg m^{-3})	$\overline{D_p}$ (nm)	σ	M (μg m^{-3})	$\overline{D_p}$ (nm)	σ	M (μg m^{-3})	$\overline{D_p}$ (nm)	σ	
CSSA	SGP	Singapore	NU	ST	ME	HZ	UPF+F+C	EM+O	ACC	13-200	3778	28.6	1.78	13465	153.2	1.68	--	--	--	200-9000	149	388.8	1.67	108.2	2078.4	1.65	109.7	6791.9	1.4	Chen et al. (2016)
CSSA	SGP	Singapore	NU	ST	ME	HZ	UPF+F+C	EM+O	ACC	13-200	153	31.8	1.11	3451	33.9	1.8	11085	152.5	1.64	200-9000	102.7	354.9	1.51	76.9	1999.9	1.75	57	6749.7	1.39	Chen et al. (2016)
CSSA	SGP	Singapore	NU	ST	ME	HZ	UPF+F+C	EM+O	AIT	13-200	810	17.4	1.19	5847	31.3	1.48	8818	96.8	1.91	200-9000	58.9	271.1	1.7	22.3	2232.4	1.53	28.5	6888.4	1.45	Chen et al. (2016)
CSSA	SGP	Singapore	NU	ST	ME	NS	UPF+F+C	EM+O	AIT	13-200	1159	16.7	1.2	14406	42.3	1.74	8709	102.9	1.54	200-9000	0.04	8639.5	38.55	6	2415.6	1.33	24.2	6917.1	1.45	Chen et al. (2016)
EA	CHN	Shanghai	NU	MT	ME	NS	UFP+F+C	EM+O	AIT	10-1000	297	22.2	1.24	8641	44.8	1.78	3247	174	1.69	1000-10000	16.1	1203.8	1.2	5.4	2349.6	1.09	16.2	4386.6	1.5	Du et al. (2012)
EA	CHN	Shanghai	NU	MT	ME	NS	UFP+F+C	EM+O	AIT	10-1000	346	22.4	1.22	6165	34.2	1.64	5784	100.3	1.92	1000-10000	19.9	1289.3	1.19	10.7	2320.7	1.08	36	4494.3	1.59	Du et al. (2012)
EA	CHN	Nanjing	SUB	ST	ME	NS	UPF+F+C	EM+O	AIT-ACC	10-500	4419	26.7	1.57	1740	42.3	1.33	16841	111	1.84	500-10000	147.4	543.8	1.88	56	3415.5	1.37	21.6	6187.2	1.22	Kang et al. (2013)
EU	CHE	Zürich	TR	VVST	D	NS	UFP+F+C	EM+O	NUC	8-300	13281	8.2	1.2	65654	15.9	1.85	14403	89.3	1.84	300-7000	18.6	396.8	1.4	9	3449.5	1.96	--	--	--	Bukowiecki et al. (2002)
EU	CHE	Zürich	TR	VVST	E	NS	UFP+F+C	EM+O	AIT-ACC	8-300	1206	27.7	1.46	7073	99.3	2.17	--	--	--	300-7000	15	370.3	1.38	4.6	2462.6	1.92	--	--	--	Bukowiecki et al. (2002)
EU	GBR	Manchester	TR	VVST	A	NS	UFP+F+C	EM+O	AIT	10-10000	78495	27.6	1.51	6044	103.8	1.36	--	--	--	10-10000	3.2	47.9	1.57	9.6	144.8	1.38	21	6000	3.1	Longley et al. (2003)
EU	GBR	Manchester	TR	VVST	E	NS	UFP+F+C	EM+O	AIT	10-10000	8793	30.1	2.03	906	126.1	1.36	--	--	--	10-10000	3.8	158.1	1.47	5.8	1600	1.9	11	3993.8	1.29	Longley et al. (2003)
EU	GBR	Manchester	TR	ST	ME	NS	UFP+F+C	EM+O	AIT	10-10000	29862	25	1.65	7786	88	1.56	--	--	--	10-10000	10.3	145.7	1.49	9	3600	1.26	35	8000	1.8	Longley et al. (2003)
NAAN	USA	Fresno	NU	LT	ME	NS	UFP+F+C	EM	AIT	9-392	11810	37.8	2.7	11769	82.4	1.58	--	--	--	400-5000	28.6	300	1.37	11.6	777.2	1.56	14.8	3122.4	1.27	Watson et al. (2002)
AF	BWA	Gaborone	NU	VVST	E	smoke-filled air	F+C	O	--	--	--	--	--	--	--	--	--	--	--	100-5000	44.6	227.4	1.6	106.4	3617.2	2.24	2.4	5107.9	1.14	Jayaratne et al. (2001)
AF	BWA	Gaborone	NU	VVST	A	NS	F+C	O	--	--	--	--	--	--	--	--	--	--	--	100-5000	0.6	176.7	1.56	1.1	2337.2	1.78	0.1	5576.2	1.19	Jayaratne et al. (2001)
AF	BWA	Gaborone	NU	VVST	ME	residual smoke	F+C	O	--	--	--	--	--	--	--	--	--	--	--	100-5000	7.8	210.1	1.46	5.6	3110.2	1.83	0.7	5270.7	1.2	Jayaratne et al. (2001)
AF	CPV	Praia City	SUB	LT	ME	NS	F+C	O	--	--	--	--	--	--	--	--	--	--	--	250-10000	6.9	737.3	1.56	30.1	3276.2	1.6	37.1	10110.5	2.26	Pio et al. (2014)
CSSA	PAK	Lahore	SUB	VST	ME	NS	F+C	O	--	--	--	--	--	--	--	--	--	--	--	250-10000	29.1	298.5	1.32	79.3	5668.3	1.54	109.7	15682.9	14.81	Majid et al. (2013)
CSSA	PAK	Karachi	TR	VST	ME	NS	F+C	O	--	--	--	--	--	--	--	--	--	--	--	250-10000	76	280.3	1.34	62.5	3555	2.49	239.3	6588.4	1.54	Majid et al. (2013)
CSSA	PAK	Rawalpindi	NU	VST	ME	NS	F+C	O	--	--	--	--	--	--	--	--	--	--	--	250-10000	63.3	266.9	1.33	189.8	6679.5	1.67	1362.9	7574020	42.33	Majid et al. (2013)
CSSA	PAK	Peshawar	TR	VST	ME	NS	F+C	O	--	--	--	--	--	--	--	--	--	--	--	250-10000	83.3	250.6	1.4	141.9	0.8	287.83	246.6	6317.6	1.63	Majid et al. (2013)

Table A.4 Urban aerosol size distribution measurements made with gravimetric methods employing inertial impactors

Region	Country	City	Sampling location	Sampling duration	Time of day	Event identification	Target aerosol population	Measurement type	Lognormal fitting size range	Mode 1			Mode 2			Mode 3			Mode 4			Mode 1			Mode 2			Mode 3			Mode 4			Reference
										V (μm^3 cm^{-3})	$\overline{D_p}$ (nm)	σ	V (μm^3 cm^{-3})	$\overline{D_p}$ (nm)	σ	V (μm^3 cm^{-3})	$\overline{D_p}$ (nm)	σ	V (μm^3 cm^{-3})	$\overline{D_p}$ (nm)	σ	M (μg m^{-3})	$\overline{D_p}$ (nm)	σ	M (μg m^{-3})	$\overline{D_p}$ (nm)	σ	M (μg m^{-3})	$\overline{D_p}$ (nm)	σ	M (μg m^{-3})	$\overline{D_p}$ (nm)	σ	
AF	KEN	Nairobi	UB	MT	ME	NS	F+C	A-G	400-10000	2.7	216.4	2.27	1.7	1826.4	1.7	1.8	5349.3	2.13	--	--	--	4.4	243.9	2.54	1.5	1589.8	1.52	3.2	4069	2.09	--	--	--	Gaita et al. (2016)
AF	MLI	Bamako	TR/CC	VST	ME	NS	UFP+F+C	A	30-10000	67.9	130.3	219	4.2	331.8	1.12	36	1916.5	1.76	--	--	--	63	102.5	1.95	9.6	376.1	1.29	53	1862.7	1.82	--	--	--	Val et al. (2013)
AF	SEN	Dakar	TR/CC	VST	ME	NS	UFP+F+C	A	30-10000	39.4	166.6	2.32	2	358.6	1.2	37.6	1957.4	1.82	--	--	--	35.2	125.6	2.11	53.5	1603.8	2.08	7.8	2326.5	1.31	--	--	--	Val et al. (2013)
CSSA	IND	Durg	NU	MT	ME	NS	F+C	A-G	400-10000	31.9	948.9	2.28	5.7	2332.5	1.27	12.2	7418.1	1.64	--	--	--	23.6	588.7	1.68	39.8	1950	1.97	7	7078.4	1.29	--	--	--	Deshmukh et al. (2012)
CSSA	IND	Durg	NU	MT	ME	NS	F+C	A-G	400-10000	22.9	834.2	2.6	2.6	2628.2	1.23	14.7	6925.3	2.02	--	--	--	19.3	606	2.67	19.7	1000	2.27	7.6	2999.9	1.3	10.7	6650.7	1.38	Deshmukh et al. (2012)
CSSA	IND	Durg	NU	MT	ME	NS	F+C	A-G	400-10000	10.2	914.3	1.99	5	2595.2	1.27	10.4	6654.3	1.63	--	--	--	16.2	865.4	1.91	10.7	2814	1.33	9.2	6793.1	1.29	--	--	--	Deshmukh et al. (2012)
CSSA	IND	Durg	NU	MT	ME	NS	F+C	A-G	400-10000	4	676.5	1.87	1.4	2582.4	1.27	24.6	7139.7	4.83	--	--	--	16	859.3	2.14	9	3240.4	1.51	5.1	7262.1	1.29	--	--	--	Deshmukh et al. (2012)
CSSA	IND	Mumbai	UB	MT	ME	NS	F+C	A-G	350-10000	46	601.2	1.66	42.5	3990.9	1.9	--	--	--	--	--	--	11.3	454.9	1.35	67.1	661.8	1.62	59.4	3977.9	1.88	--	--	--	Venkataraman et al. (2002)
CSSA	IND	Mumbai	UB	MT	ME	NS	F+C	A-G	350-10000	17.5	457.2	1.61	5.7	973.6	1.38	53.1	4385.1	1.74	--	--	--	35.7	533.5	1.66	4.7	1186	1.31	72.2	4370.7	1.7	--	--	--	Venkataraman et al. (2002)
CSSA	VNM	Ho Chi Minh	NU	ST	ME	NS	F+C	A-G	400-5000	59.3	385.3	2.26	218.9	6270.2	1.81	--	--	--	--	--	--	93.1	421.9	2.11	261.8	5427.2	1.69	--	--	--	--	--	--	Hien et al. (2007)
CSSA	VNM	Ho Chi Minh	NU	ST	ME	NS	F+C	A-G	400-5000	10.6	426.6	2.73	12.7	4039.69	1.88	21.4	8118.3	1.36	--	--	--	9.3	462.7	1.7	15.6	2659.3	2.14	33.4	7726.1	1.49	--	--	--	Hien et al. (2007)
EA	CHN	Beijing	NU	ST	A	NS	UFP+F+C	A-G	56-10000	64.6	701.7	1.89	17	3585.9	1.35	48.5	6829.4	2.01	--	--	--	2.9	519	1.14	98.6	684.9	1.76	90.3	4785.8	1.89	--	--	--	Guo et al. (2010)
EA	CHN	Beijing	NU	ST	E	NS	UFP+F+C	A-G	56-10000	13	189.4	3.51	51	805.7	1.94	55.5	5136.4	1.68	--	--	--	68.8	601.1	1.78	17.7	1124.6	1.33	86.3	4807.3	1.81	--	--	--	Guo et al. (2010)
EA	CHN	Beijing	NU	ST	M	NS	UFP+F+C	A-G	56-10000	65.2	153.5	4.05	49.4	686.9	1.7	64.4	5004.8	1.8	--	--	--	184.8	431.5	13.02	65.5	645.9	1.59	51.6	5248.2	1.6	--	--	--	Guo et al. (2010)
EA	CHN	Shanghai	NU	MT	ME	NS	UFP+F+C	A-G	56-10000	15.5	238.4	2	3.5	610	1.22	33.5	2960.7	2.6	6.5	6700	1.3	20	230	2	6.5	620	1.22	63.2	3416.6	3.7	6.5	6700	1.25	Ding et al. (2017)
EA	CHN	Shanghai	NU	MT	ME	NS	UFP+F+C	A-G	56-10000	14	465	2.4	3.2	590	1.3	14.5	4060.7	2.4	3.6	6700	1.47	25.4	537.2	2.54	6	595	1.28	6.5	2501.3	1.71	14	6700	1.55	Ding et al. (2017)
EA	CHN	Shanghai	NU	MT	ME	NS	UFP+F+C	A-G	56-10000	3.2	565.7	1.28	20.6	728	3.29	6122.1	1.62	10.1	--	--	--	6.7	580	1.32	28.9	643.3	2.86	15.6	5736.3	1.69	--	--	--	Ding et al. (2017)
EA	CHN	Shanghai	NU	MT	ME	NS	UFP+F+C	A-G	56-10000	3.6	560	1.27	54	938.4	3.04	10.3	6337.7	1.46	--	--	--	61.5	624.4	1.9	39.5	3939.4	2.27	2.5	6420.2	1.25	--	--	--	Ding et al. (2017)
EA	CHN	Guangzhou	NU	MT	ME	NS	UFP+F+C	A-G	56-10000	26	439	2.33	25.2	4726.8	1.72	--	--	--	--	--	--	98.2	499.9	2.36	91.1	5531.2	1.93	1365.2	9372261.8	11.74	--	--	--	Duan et al. (2007)
EA	CHN	Guangzhou	NU	MT	ME	NS	UFP+F+C	A-G	56-10000	24.1	598.1	2	16.3	4578.7	1.5	380.1	36304359	71	--	--	--	43.2	609.8	1.92	36.2	5014.8	1.71	--	--	--	--	--	--	Duan et al. (2007)
EA	CHN	Guangzhou	NU	MT	ME	NS	UFP+F+C	A-G	56-10000	26.9	446.5	2	6	1100	1.32	35.3	4918.1	2.03	--	--	--	63.9	671.9	2.39	38.9	6028.6	1.76	--	--	--	--	--	--	Duan et al. (2007)
EA	CHN	Guangzhou	NU	MT	ME	NS	UFP+F+C	A-G	56-10000	29.7	501	2.33	24.2	4690.7	1.71	--	--	--	--	--	--	47.7	525.1	2.24	34.3	4937.9	1.76	--	--	--	--	--	--	Duan et al. (2007)

EA	CHN	Shenzhen	NU	MT	ME	NS	UFP+F+C	A-G	56-10000	3.9	712.9	3.05	0.3	829.1	1.5	1	5242.2	1.5	--	--	--	6.1	705.5	2.45	1	4300	1.36	0.6	7909	1.28	--	--	--	Huang et al. (2006)
EA	CHN	Shenzhen	NU	MT	ME	NS	UFP+F+C	A-G	56-10000	4.1	565	2.29	1	900	1.4	2.8	4687.1	2.12	--	--	--	8.2	752.9	2.24	0.9	792.4	1.36	2.3	5398.4	1.6	--	--	--	Huang et al. (2006)
EA	CHN	Shenzhen	NU	MT	ME	NS	UFP+F+C	A-G	56-10000	2.2	542.4	1.62	0.5	2643.7	1.8	8.4	8328.9	22.01	--	--	--	0.9	299.8	1.69	2.7	588	1.44	8.9	2431.8	6.49	--	--	--	Lan et al. (2011)
EA	CHN	Beijing	NU	VST	ME	NS	UFP+F+C	A-G	28-9920	13.7	375.7	1.68	28.5	2489.6	1.71	20	10000	1.6	--	--	--	22.5	400.8	1.67	35.3	2129.1	1.61	27.7	7600.2	1.68	--	--	--	Duan et al. (2012)
EA	CHN	Beijing	NU	VST	ME	NS	UFP+F+C	A-G	28-9920	21.9	507.5	1.43	84.7	903.7	2.64	12	9000	1.85	--	--	--	37.9	533.5	1.37	134.9	849.6	2.39	20	9000	1.87	--	--	--	Duan et al. (2012)
EA	CHN	Beijing	NU	VST	ME	NS	UFP+F+C	A-G	56-10000	6.3	315.9	1.26	13.6	457.7	2.4	12.4	5115.7	2.17	--	--	--	10.5	329	1.28	22.9	520.8	2.49	14.2	5158	1.89	--	--	--	Hu et al. (2012)
EA	CHN	Beijing	NU	VST	ME	NS	UFP+F+C	A-G	56-10000	1.2	307.1	1.27	5.9	498.3	3.08	3.9	7267.6	2.01	--	--	--	2.1	333.6	1.32	9.5	577.6	3.25	3.9	6710.8	1.7	--	--	--	Hu et al. (2012)
EA	CHN	Zhengzhou	NU	VST	ME	HZ	UFP+F+C	A	100-8000	13.2	757.3	1.75	8	950	1.25	187.3	11081.1	4.91	--	--	--	19.9	562.6	1.53	28.2	1026.1	1.26	164	5402.7	3.04	--	--	--	Yu et al. (2017)
EA	CHN	Zhengzhou	NU	VST	ME	NS	UFP+F+C	A	100-8000	13.6	1641.4	3.99	2.5	2400	1.2	24.2	9814.2	1.79	--	--	--	9.7	635.2	2.49	55.7	9620.2	2.96	--	--	--	--	--	--	--	Yu et al. (2017)
EA	CHN	Guangzhou	SUB	VVST	ME	NS	UFP+F+C	A-G	56-10000	43.3	454.5	2.2	20.1	3586.3	1.36	8	7543.7	1.32	--	--	--	56.4	477.9	2.04	43.4	3640.3	4.56	17	4200	1.35	--	--	--	Liu et al. (2008)
EA	CHN	Guangzhou	SUB	VVST	ME	NS	UFP+F+C	A-G	56-10000	23.4	419.7	1.85	8.5	1100.3	1.3	22.4	3860.3	1.72	--	--	--	43.5	500	2.1	10.9	1050	1.3	32.6	4219	1.7	--	--	--	Liu et al. (2008)
EA	CHN	Guangzhou	SUB	VVST	ME	NS	UFP+F+C	A-G	56-10000	19.7	419.6	1.61	10	1100.3	1.35	20	4600	1.8	--	--	--	29.4	416.7	1.59	18.2	1050	1.38	26.9	4200	1.7	--	--	--	Liu et al. (2008)
EA	CHN	Guangzhou	SUB	VVST	ME	NS	UFP+F+C	A-G	56-10000	14	370.2	1.55	9	1050	1.29	17	3900.3	1.6	49	6000	8.75	36.5	408	1.68	17.4	1050	1.3	56.4	4026.8	1.91	--	--	--	Liu et al. (2008)
EA	CHN	Guangzhou	SUB	VVST	ME	NS	UFP+F+C	A-G	56-10000	23.6	340.6	2.16	9	1050.3	1.25	34.7	3790.4	1.85	--	--	--	37.2	360.7	2.1	15.6	1050	1.26	46.6	4155.8	1.93	--	--	--	Liu et al. (2008)
EA	CHN	Guangzhou	SUB	VVST	ME	NS	UFP+F+C	A-G	56-10000	16.3	323.1	1.67	14.8	1150	1.37	18.5	3251.3	1.55	6.9	11000	1.4	28.1	363.1	1.81	20	1100	1.33	28	3251.3	1.55	10	11000	1.4	Liu et al. (2008)
EA	CHN:TWN	Taichung	NU	MT	ME	NS	F+C	A-G	210-9900	14.6	343.5	1.52	22.2	820	1.55	29.8	4597	1.95	--	--	--	68.2	667.3	2.02	35.5	5357.6	1.75	--	--	--	--	--	--	--	Cheng et al. (2000)
EA	JPN	Kawasaki	UB	MT	ME	NS	UFP+F+C	A-G	30-8000	7.6	231.2	2.46	0.7	410	1.16	7.4	1590.6	3.95	--	--	--	4	165.7	2.19	1.3	410	1.19	16.7	695	3.54	--	--	--	Fushimi et al. (2008)
EA	JPN	Kawasaki	TR	MT	ME	NS	UFP+F+C	A-G	30-6000	12.9	115.2	1.75	7.1	360.4	1.36	14.1	1081	2.8	--	--	--	12.9	94.6	1.53	5	250	1.43	9.4	695	1.7	10.2	2000.8	2.09	Fushimi et al. (2008)
EA	JPN	Sapporo	NU	VST	ME	NS	UFP+F+C	A-G	56-10000	1.2	180	1.52	4.1	641.5	1.68	2	7865.1	1.54	--	--	--	1.4	150	1.45	6.6	646.4	1.66	2.5	7484.3	1.58	--	--	--	Agarwal et al. (2010)
EA	KOR	Ulsan	NU	MT	ME	NS	F+C	A-G	400-10000	13	532	1.57	216.8	42160.4	4.64	1346.2	25550.5	1.51	--	--	--	18	515	1.5	31	2700	2.6	15152.7	250852.9	3.28	--	--	--	Ny et al. (2011)
EA	KOR	Ulsan	NU	MT	ME	NS	F+C	A-G	400-10000	13.9	733.6	1.74	10.9	3213.9	1.39	137.9	15000.1	1.59	--	--	--	23	734.1	1.74	17	3400	1.46	139	13000	1.53	--	--	--	Ny et al. (2011)
EA	KOR	Ulsan	NU	MT	ME	NS	F+C	A-G	400-10000	14.2	742.3	1.52	14.2	3499	1.53	135.8	13000	1.41	--	--	--	24.2	752.8	1.54	18	3141.3	1.43	180.2	13000	1.51	--	--	--	Ny et al. (2011)
EA	KOR	Ulsan	NU	MT	ME	NS	F+C	A-G	400-10000	14.5	701.3	1.86	24.2	5005.2	2.02	309.8	15000	1.39	--	--	--	22.9	688.4	1.62	34.7	4560.9	2.13	222.7	13080.6	1.4	--	--	--	Ny et al. (2011)
EA	KOR	Gwangju	NU	MT	ME	NS	UFP+F+C	A-G	55-9900	27.1	457.9	1.78	6.7	1055.8	1.22	26.8	4727	2.6	--	--	--	44.3	491.7	1.8	10	1050	1.22	39.9	4771.6	2.62	--	--	--	Yu et al. (2017)
EA	KOR	Gwangju	NU	MT	ME	NS	UFP+F+C	A-G	55-9900	2.7	332	1.25	9.5	585.3	2.32	4.7	5428.3	1.74	--	--	--	4.9	335.1	1.24	5	621.1	1.66	13.3	1186.8	4.36	2.9	5809.8	1.45	Yu et al. (2017)
EU	AUT	Vienna	NU	ST	D	NS	UFP+F+C	A-G	60-10000	6.6	274.3	2.89	3.7	384	1.6	2.5	3871.9	1.83	--	--	--	1.4	80	1.45	13.7	366.5	1.85	4.3	3183.7	1.99	--	--	--	Berner et al. (2004)
EU	AUT	Vienna	NU	ST	D	NS	UFP+F+C	A-G	60-10000	8.3	330.6	2.26	3.2	3202.3	1.62	--	--	--	--	--	--	0.8	70	1.3	12.7	351.5	2.18	4.7	3250.8	1.77	--	--	--	Berner et al. (2004)
EU	BEL	Gent	NU	MT	ME	NS	UFP+F+C	A-G	53-10000	4.7	224.7	1.89	1.8	739.2	1.6	5.8	4434.3	2.04	--	--	--	7.2	272.7	2.27	5.3	1198.4	2.89	5.7	5144.1	1.83	--	--	--	Maenhaut et al. (2002)
EU	CZE	Prague	UB	MT	ME	NS	UFP+F+C	A-G	35-10000	20.7	389.5	2.44	7.5	482.7	1.37	6.2	4385	1.7	--	--	--	6.3	127.6	1.6	34.3	469.7	1.59	11	3385	1.6	--	--	--	Pennanen et al. (2007)

EU	DEU	Duisburg	UB	MT	ME	NS	UFP+F+C	A-G	35-10000	4.3	246.5	2.29	4.6	450.5	1.42	3.8	3335.9	2.08	--	--	--	3.3	206.9	1.9	6.5	445.1	1.36	13.9	3648.1	7.3	--	--	--	Pennanen et al. (2007)
EU	ESP	Barcelona	UB	MT	ME	NS	UFP+F+C	A-G	35-10000	0.8	60	1.25	8.8	296.7	1.83	19.8	4395.4	2.46	--	--	--	1	62	1.23	10.7	309.9	1.69	35.2	4797.6	3.21	--	--	--	Pennanen et al. (2007)
EU	FIN	Helsinki	TR	LT	ME	NS	UFP+F+C	A-G	35-10000	6.1	278.7	2.27	0.7	375	1.15	2.7	2389.9	1.59	7.3	8680.6	1.6	4.2	181.3	2.07	2.3	529.8	1.42	4.1	2114.5	1.61	11.1	8246.4	1.63	Pakkanen et al. (2001)
EU	FIN	Helsinki	UB	MT	ME	NS	UFP+F+C	A-G	35-10000	6.6	289.3	2.1	4.7	3779.3	1.97	--	--	--	--	--	--	6.3	257.1	1.91	1.1	444.5	1.33	13.2	4856.9	4.68	--	--	--	Pennanen et al. (2007)
EU	FRA	Dunkirk	SUB	MT	ME	NS	UFP+F+C	A-G	30-10000	5.5	393.4	1.51	9.5	964.7	4.12	4.5	1720.2	1.89	--	--	--	10.4	401.4	1.5	10.3	1104.8	5.57	10.1	1519.8	1.86	--	--	--	Mbengue et al. (2014)
EU	FRA	Dunkirk	SUB	MT	ME	NS	UFP+F+C	A-G	30-10000	2.9	194.8	3.4	2.6	402.9	1.5	6.6	1502.8	1.95	--	--	--	3	140.4	2.33	5.9	463.1	1.51	10.1	1578.4	1.81	--	--	--	Mbengue et al. (2014)
EU	GRC	Athens	NU	MT	ME	NS	UFP+F+C	A-G	30-10000	3.8	125.5	4.19	3.7	254.7	1.41	181.9	22455345	143.95	--	--	--	4.5	267.8	1.47	14.3	327.3	5.71	2.6	1900	1.43	7.3	7300	1.9	Karanasiou et al. (2007)
EU	GRC	Athens	UB	MT	ME	NS	UFP+F+C	A-G	35-10000	12.2	300.7	2.29	0.7	1900	1.21	16.4	4870.1	1.92	--	--	--	18.8	319.6	2.39	5.7	2221.6	1.34	14.6	5500	1.56	--	--	--	Pennanen et al. (2007)
EU	ITA	Bologna	NU	MT	ME	NS	UFP+F+C	A-G	50-10000	22.5	552.2	1.8	40.6	2499.7	44.91	2.5	3000	1.75	--	--	--	18.5	540.4	1.45	55.6	1000.3	5.58	--	--	--	--	--	--	Matta et al. (2003)
EU	ITA	Bologna	NU	MT	ME	NS	UFP+F+C	A-G	50-10000	10.6	200	2.81	6.1	600	1.94	5.1	10000	1.91	--	--	--	21.4	299.9	3.57	3.9	600	1.5	4.7	5500.6	1.7	--	--	--	Matta et al. (2003)
EU	NLD	Amsterdam	UB	MT	ME	NS	UFP+F+C	A-G	35-10000	34.9	242.1	1.76	10.7	2945.5	2.21	5	7500	1.5	--	--	--	41.6	260	1.69	33.7	2931.5	7.68	6	7500	1.7	--	--	--	Pennanen et al. (2007)
LA	BRA	Sao Paulo	NU	MT	ME	NS	UFP+F+C	A-G	93-4000	31.1	193.8	2.17	16.8	2000	1.52	3.8	2500	1.61	--	--	--	47.3	205.2	2.24	29.9	2095.4	1.59	--	--	--	--	--	--	Miranda et al. (2002)
LA	BRA	Sao Paulo	NU	MT	ME	NS	UFP+F+C	A-G	93-4000	8	216.3	1.8	6.5	2000	2.56	17.6	5000	1.52	--	--	--	5.2	237	1.53	27.3	840.3	16.52	15.6	4000.1	1.4	--	--	--	Miranda et al. (2002)
NAAN	AUS	Launceston	NU	VVST	ME	NS	UFP+F+C	A-G	56-10000	6.2	304.9	2.05	1.1	1129.2	1.42	21.5	4473.5	2.87	--	--	--	3.4	229.1	2.11	0.8	317.6	1.22	41.9	3547	4.3	--	--	--	Keywood et al. (2000)
NAAN	AUS	Launceston	NU	VVST	ME	NS	UFP+F+C	A-G	56-10000	4.4	298.3	1.42	16.2	595.4	1.9	33.4	2411.6	8.08	--	--	--	3.7	348.2	1.29	51.6	613	2.29	18.2	6261.5	2.52	--	--	--	Keywood et al. (2000)
NAAN	AUS	Launceston	NU	VVST	ME	NS	UFP+F+C	A-G	56-10000	2.4	233.6	1.76	29.3	2590.1	4.86	--	--	--	--	--	--	18.1	484.2	2.59	4.8	1661	1.62	22.1	5221.8	2.67	--	--	--	Keywood et al. (2000)
NAAN	AUS	Launceston	NU	VVST	ME	NS	UFP+F+C	A-G	56-10000	2.6	317.6	1.33	20.9	578.4	1.96	13.1	1952.9	8.64	--	--	--	5.3	345.3	1.34	29.9	643.3	1.86	22.2	1265	9.12	--	--	--	Keywood et al. (2000)
NAAN	AUS	Launceston	NU	VVST	ME	NS	UFP+F+C	A-G	56-10000	10.4	375.2	1.47	16.8	935.5	1.66	50.9	1214.3	4.6	--	--	--	11.8	360.6	1.42	56.9	895.9	1.95	56.1	1575.4	6.69	--	--	--	Keywood et al. (2000)
NAAN	AUS	Launceston	NU	VVST	ME	NS	UFP+F+C	A-G	56-10000	3.7	322.4	1.43	5.3	980.5	1.68	37.6	1952.3	3.89	--	--	--	3	330	1.3	39.6	1104.3	2.4	41	7240.5	8.37	--	--	--	Keywood et al. (2000)
NAAN	AUS	Launceston	NU	VVST	ME	NS	UFP+F+C	A-G	56-10000	4.6	366.7	1.49	7.9	1130.2	1.75	21.1	1929.3	4.75	--	--	--	6.8	365.4	1.47	19.9	1134.6	1.89	27.2	2608.1	6.4	--	--	--	Keywood et al. (2000)
NAAN	USA	Pittsburgh	NU	MT	ME	NS	UFP+F+C	A-G	56-10000	10.7	308.7	2.1	1.7	630	1.3	4.5	4998.9	2.84	--	--	--	17.3	385.5	2.41	3.2	550.1	1.35	3.5	4982.8	1.68	--	--	--	Cabada et al. (2004)
NAAN	USA	Pittsburgh	NU	MT	ME	NS	UFP+F+C	A-G	56-10000	0.5	196	1.27	7.5	315.4	2.41	2.9	4500	1.76	--	--	--	11.7	328.6	2.37	4.6	4927.2	1.98	--	--	--	--	--	--	Cabada et al. (2004)
NAAN	USA	Pittsburgh	NU	MT	ME	NS	UFP+F+C	A-G	56-3000	3.3	214.1	1.54	1.6	603.8	1.34	7.8	9999.9	60.06	--	--	--	3.6	230.2	1.67	6.2	514.1	3.42	1.4	603.1	1.25	--	--	--	Cabada et al. (2004)
NAAN	USA	Pittsburgh	NU	MT	ME	NS	UFP+F+C	A-G	56-3000	5.9	274	1.67	2.6	613.5	1.31	9	799.1	26.04	--	--	--	9.6	324	1.87	3.4	560	1.35	11.7	895.2	15.19	--	--	--	Cabada et al. (2004)
NAAN	USA	Fresno	NU	MT	ME	NS	UFP+F+C	A-G	56-10000	4.1	247.2	1.38	39.3	509.8	2.96	--	--	--	--	--	--	52.9	391.4	2.25	10	1600	1.48	1.9	3999.9	1.41	--	--	--	Chow et al. (2008)
NAAN	USA	Raleigh	TR	ST	ME	NS	UFP+F+C	A-G	30-10000	4.6	380.8	1.23	14.5	622.8	2.62	3.3	4200	1.94	--	--	--	2.2	495	1.16	3.5	525	1.45	21.1	1094.6	3.76	--	--	--	Hays et al. (2011)
NAAN	USA	Newark	NU	VST	ME	NS	F+C	A-G	56-10000	14.8	422.9	1.94	4.6	4754.3	1.74	--	--	--	--	--	--	6.6	418.4	1.37	18	453.2	2.56	5.3	5300	1.6	--	--	--	Zhao et al. (2008)
NAAN	USA	Newark	NU	VST	ME	NS	F+C	A-G	56-10000	5.9	395.4	1.94	2.2	1000.5	2.73	1.2	5000	1.45	--	--	--	8.7	387.4	1.72	2.7	1118.4	1.49	2.4	4400	1.5	--	--	--	Zhao et al. (2008)

WA	SAU	Yanbu	TR	MT	ME	land breeze	F+C	A	20-10000	15.43	358.1	1.98	9.9	355.8	1.16	35.7	2170.9	1.9	71	10000	1.7	13.5	379.3	1.41	143.9	6014.6	3.81	15.7	11000	1.4	--	--	--	Al-Mahmodi (2011)
WA	SAU	Yanbu	TR	MT	ME	transition period	F+C	A	20-10000	22.98	368.9	1.99	4.2	354.3	1.11	16.1	1680.1	1.52	170	13044.3	2.5	13.5	379.3	1.41	143.9	6014.6	3.81	15.7	11000	1.4	--	--	--	Al-Mahmodi (2011)
WA	SAU	Yanbu	TR	MT	ME	sea breeze	F+C	A	20-10000	11.61	299.6	1.74	7	365.7	1.22	50.4	2599	2.1	67	10044.3	1.6	9.5	375.2	1.47	4.4	1930.3	1.31	582.6	73576.8	9.86	--	--	--	Al-Mahmodi (2011)
WA	SAU	Yanbu	UB	MT	ME	land breeze	F+C	A	20-10000	9.3	348	1.61	1	352.4	1.16	12.5	2462.4	1.91	34	11044.3	1.8	16.2	369	1.52	11.7	1731.5	1.64	30.7	7102	1.69	--	--	--	Al-Mahmodi (2011)
WA	SAU	Yanbu	UB	MT	ME	transition period	F+C	A	20-10000	12.4	395.2	1.78	2.1	334.8	1.21	14.6	2601.3	1.72	39.9	11044.3	1.8	19.7	372.2	1.54	29.8	2610	2.15	35.6	11000	1.75	--	--	--	Al-Mahmodi (2011)
WA	SAU	Yanbu	UB	MT	ME	sea breeze	F+C	A	20-10000	10.1	346.1	1.5	24.1	2591.3	2.06	89.1	14125.4	1.99	--	--	--	14.3	363.1	1.49	2.7	1540.1	1.25	231.6	26021.8	5.28	--	--	--	Al-Mahmodi (2011)
WA	SAU	Yanbu	NU	ST	ME	land breeze	F+C	A	20-10000	7.4	345.1	1.63	25.1	2417.4	1.67	3091.4	379906.7	5.74	--	--	--	11.7	363.8	1.62	18.8	1956.4	1.55	173.2	10127.8	2.95	--	--	--	Al-Mahmodi (2011)
WA	SAU	Yanbu	NU	ST	ME	transition period	F+C	A	20-10000	14.6	345.4	1.82	56.9	2686.9	1.68	101	8388.9	1.52	--	--	--	22.6	361.4	1.8	24.2	1948.5	1.48	247.1	9228.3	2.61	--	--	--	Al-Mahmodi (2011)
WA	SAU	Yanbu	NU	ST	ME	sea breeze	F+C	A	20-10000	13.8	321.6	1.71	76.6	2718.4	1.77	312.5	14735.7	1.95	--	--	--	21	333.2	1.7	36.9	1979.1	1.59	343.4	10194.9	2.75	--	--	--	Al-Mahmodi (2011)
WA	TUR	Istanbul	NU	MT	ME	NS	F+C	A	400-9000	3.9	996.2	1.43	1.4	1931.2	1.22	140.7	330222.9	5.36	--	--	--	6	942.3	1.38	3	1820.6	1.29	5.2	8663.1	1.78	--	--	--	Onat et al. (2012)
WA	TUR	Istanbul	NU	MT	ME	NS	F+C	A	400-9000	0.9	1133.5	2.28	1.2	1744.3	1.38	272	982266.8	8.13	--	--	--	1.8	1102.1	2.67	1.9	1613.3	1.35	21.8	25485.9	3.57	--	--	--	Onat et al. (2012)
WA	TUR	Istanbul	NU	ST	ME	NS	F+C	A	400-9000	6.8	1356.7	2	0.8	4351.1	1.21	4	9452.6	1.42	--	--	--	9.8	1182.1	1.83	0.2	2058.2	1.13	0.7	3762.3	1.15	6.1	8085.1	1.65	Onat et al. (2012)
WA	TUR	Istanbul	NU	ST	ME	NS	F+C	A	400-9000	6	1631.3	1.77	0.3	1980	1.12	77.6	73724.3	3.07	--	--	--	7.6	1405	1.66	0.5	1982.6	1.19	18.9	20688.4	3.29	--	--	--	Onat et al. (2012)
WA	TUR	Istanbul	NU	ST	ME	NS	F+C	A	400-9000	0.9	993	1.87	1.9	1815.5	1.39	3.4	8723.2	1.68	--	--	--	1.1	785.5	1.86	3.2	1726.5	1.41	3.7	7365	1.58	--	--	--	Onat et al. (2012)
WA	TUR	Istanbul	NU	ST	ME	NS	F+C	A	400-9000	2.5	1248	2.31	1.4	1768	1.34	315.2	251644.5	4.33	--	--	--	3.6	1124.3	2.2	2.4	1676.8	1.35	11.9	10423.4	1.97	--	--	--	Onat et al. (2012)
WA	TUR	Istanbul	NU	ST	ME	NS	F+C	A	400-9000	2.5	1720.7	1.34	2.2	868.2	2.91	546.7	1150100.6	6.83	--	--	--	3.4	719.1	2.64	4.1	1668.7	1.35	10.5	11188.4	2.18	--	--	--	Onat et al. (2012)
WA	TUR	Istanbul	NU	ST	ME	NS	F+C	A	400-9000	4.5	1181.9	2.18	0.4	4107.3	1.16	5.8	10158.6	1.53	--	--	--	2.5	339.4	2.44	5	1195.4	1.75	8.9	9228.2	1.82	--	--	--	Onat et al. (2012)
WA	TUR	Istanbul	NU	ST	ME	NS	F+C	A	400-9000	6	1667.4	2.69	0.3	4050.1	1.17	8	11523.7	1.56	--	--	--	3	401.1	2.87	4.7	1309.2	1.78	12	9442.2	2.01	--	--	--	Onat et al. (2012)
WA	TUR	Istanbul	NU	ST	ME	NS	F+C	A	400-9000	3	697.1	2.89	4.9	6681.9	2.27	6.3	11029.5	1.45	--	--	--	6.8	1004.8	3.51	12.9	10508.7	1.88	--	--	--	--	--	--	Onat et al. (2012)
WA	TUR	Istanbul	NU	ST	ME	NS	F+C	A	400-9000	5	1019.5	3.27	4.1	6226.7	1.67	2.6	9859.6	1.26	--	--	--	5.9	706.9	2.89	1	1023.7	1.67	15.2	10253.8	2.17	--	--	--	Onat et al. (2012)
WA	TUR	Istanbul	NU	ST	ME	NS	F+C	A	400-9000	3.1	704.5	2.66	1.9	4703.7	1.6	2	9472.5	1.29	--	--	--	2.8	550.9	1.86	0.4	1019.9	1.58	44.4	87243	6.49	--	--	--	Onat et al. (2012)
WA	TUR	Istanbul	NU	ST	ME	NS	F+C	A	400-9000	2.4	651.6	2.35	2	3581.6	1.51	2.4	10162.5	1.38	--	--	--	4	677.1	2.17	2.7	3616.3	1.46	1.7	8147.8	1.26	--	--	--	Onat et al. (2012)

Table A.5 Urban aerosol columnar volume size distribution measurements made with sun/sky radiometers

Region	Country	City	Sampling location	Sampling duration	Time of day	Event identification	Target aerosol population	Measurement technique	Lognormal fitting size range	Mode 1			Mode 2			Mode 3			Reference
										V (arbitrary units)	$\overline{D_p}$ (nm)	σ	V (arbitrary units)	$\overline{D_p}$ (nm)	σ	V (arbitrary units)	$\overline{D_p}$ (nm)	σ	
AF	EGY	Cairo	NU	MT	ME	NS	F+C	RS	100-10000	11.8	250.7	1.47	9.7	527.4	1.95	16.1	5697.3	1.87	El-Metwally et al. (2011)
AF	EGY	Cairo	NU	MT	ME	NS	F+C	RS	100-10000	11.7	271.6	1.56	1.7	889	1.27	24.1	4288.2	1.89	El-Metwally et al. (2011)
AF	EGY	Cairo	NU	MT	ME	NS	F+C	RS	100-10000	8.2	223.5	1.43	4	450.4	1.68	26.9	4140.1	1.97	El-Metwally et al. (2011)
AF	EGY	Cairo	NU	MT	ME	NS	F+C	RS	100-10000	16.1	239.4	1.48	5.3	875.5	1.58	38.5	4189.5	1.76	El-Metwally et al. (2011)
AF	EGY	Cairo	NU	MT	ME	NS	F+C	RS	100-10000	12.2	207	1.4	5.1	680.6	1.62	45.8	3873.6	1.83	El-Metwally et al. (2011)
AF	EGY	Cairo	NU	MT	ME	NS	F+C	RS	100-10000	15.6	255.9	1.48	27.7	4731.2	2.09	4.7	7709.7	1.22	El-Metwally et al. (2011)
AF	EGY	Cairo	NU	MT	ME	NS	F+C	RS	100-10000	20.2	249.1	1.51	1.8	927.8	1.26	46.2	4919.2	1.98	El-Metwally et al. (2011)
AF	EGY	Cairo	NU	MT	ME	NS	F+C	RS	100-10000	28.4	265.6	1.41	19.8	5104.5	2.09	4.8	8094.6	1.25	El-Metwally et al. (2011)
AF	EGY	Cairo	NU	MT	ME	NS	F+C	RS	100-10000	17.1	263.9	1.39	8.8	719.6	2.25	22.6	6317.1	1.75	El-Metwally et al. (2011)
AF	EGY	Cairo	NU	MT	ME	NS	F+C	RS	100-10000	13.4	222.2	1.36	8.1	499.5	1.98	37.4	5247.3	1.93	El-Metwally et al. (2011)
AF	EGY	Cairo	NU	MT	ME	NS	F+C	RS	100-10000	26.4	246.7	1.41	26.1	3885.4	2.23	17	7481.4	1.42	El-Metwally et al. (2011)
AF	EGY	Cairo	NU	MT	ME	NS	F+C	RS	100-10000	13.7	238.8	1.39	9.9	1025.7	2.81	18.4	6530.8	1.77	El-Metwally et al. (2011)
AF	ZAF	Johannesburg	NU	MT	ME	NS	F+C	RS	100-10000	0.6	247.8	1.48	0.3	8267.1	1.34	1.7	9219.2	2.55	Adesina et al. (2014b)
AF	ZAF	Johannesburg	NU	MT	ME	NS	F+C	RS	100-10000	1.3	280	1.46	1.8	11264.1	2.64	--	--	--	Adesina et al. (2014b)
AF	ZAF	Pretoria	NU	MT	ME	NS	F+C	RS	100-10000	1.3	336.1	1.49	0.4	590.6	2.48	1.3	8877.3	2.2	Adesina et al. (2014a)
AF	ZAF	Pretoria	NU	MT	ME	NS	F+C	RS	100-10000	1	289.2	1.47	0.6	3350.8	3.41	1	8620.8	1.77	Adesina et al. (2014a)
AF	ZAF	Pretoria	NU	MT	ME	NS	F+C	RS	100-10000	1.1	275.9	1.44	0.8	8997.9	1.65	1.9	11619.1	3.9	Adesina et al. (2014a)
AF	ZAF	Pretoria	NU	MT	ME	NS	F+C	RS	100-10000	1.5	274.4	1..48	0.3	8516.6	1.34	2	9079.5	2.94	Adesina et al. (2014a)
AF	ZMB	Mongu	NU	LT	ME	BB	F+C	RS	100-10000	0.9	295.2	1.45	0.9	5546.4	4.01	0.3	9564.7	1.45	Queface et al. (2011)
AF	ZMB	Mongu	NU	LT	ME	BB	F+C	RS	100-10000	0.2	379.7	1.39	0.5	241.7	1.34	6.2	252738.9	10.62	Queface et al. (2011)
AF	ZMB	Mongu	NU	LT	ME	BB	F+C	RS	100-10000	1.7	268.2	1.43	0.3	1031.3	2.47	1.2	9428	1.86	Queface et al. (2011)
AF	ZMB	Mongu	NU	LT	ME	BB	F+C	RS	100-10000	2.9	274.1	1.42	0.4	582.3	1.82	2.8	10612.2	2.39	Queface et al. (2011)
EA	CHN	Hong Kong	NU	LT	ME	NS	UFP+F+C	RS	25-10000	24.9	402.1	1.63	7.7	2333.9	1.57	13.8	7380.4	1.83	Yang et al. (2009)

EA	CHN	Hong Kong	NU	LT	ME	NS	UFP+F+C	RS	25-10000	24.4	362.3	1.65	5.9	2239.7	1.55	14.7	7129.1	1.83	Yang et al. (2009)
EA	CHN	Hong Kong	NU	LT	ME	NS	UFP+F+C	RS	25-10000	33	392.3	1.63	8.8	2513.9	1.55	15.5	8166.7	1.73	Yang et al. (2009)
EA	CHN	Hong Kong	NU	LT	ME	NS	UFP+F+C	RS	25-10000	29.2	393.9	1.65	9.7	2614.7	1.61	10.7	9007.4	1.77	Yang et al. (2009)
CSSA	IND	Pune	NU	MT	ME	NS	F+C	RS	100-10000	2.5	318.9	1.64	1.4	3866.1	2.22	1.8	8444.4	1.51	More et al. (2013)
CSSA	IND	Pune	NU	MT	ME	NS	F+C	RS	100-10000	1.9	269.3	1.48	4.9	4101.4	2.11	1.8	8566	1.43	More et al. (2013)
CSSA	PAK	Lahore	NU	MT	ME	NS	F+C	RS	50-10000	1.7	122.8	1.6	6.6	2578.7	2.28	10.8	5010.1	1.8	Alam et al. (2012)
CSSA	PAK	Lahore	NU	MT	ME	NS	F+C	RS	50-10000	3.6	196.7	1.72	2.3	2199	2.54	3.5	5783.3	1.63	Alam et al. (2012)
CSSA	PAK	Karachi	NU	MT	ME	NS	F+C	RS	50-10000	1	125.9	1.58	0.5	561.5	1.53	13.5	3522.9	1.93	Alam et al. (2012)
CSSA	PAK	Karachi	NU	MT	ME	NS	F+C	RS	50-10000	1.5	171.9	1.66	5.2	3965.6	2.23	0.5	6101.6	1.37	Alam et al. (2012)
CSSA	THA	Chiang Mai	NU	LT	ME	NS	F+C	RS	100-10000	4.7	286.4	1.5	1.2	524	1.82	3.3	6497.3	2.11	Gautam et al. (2013)
CSSA	THA	Silpakorn	NU	LT	ME	NS	F+C	RS	100-10000	3.7	315.5	1.55	1.4	1535.9	2.81	2.4	7849.4	1.73	Gautam et al. (2013)
EU	ITA	Cagliari	NU	MT	ME	NS	F+C	RS	100-10000	0.7	254.1	1.54	0.4	669	2.19	2.2	5818.9	2.26	Mallet et al. (2015)
EU	MDA	Chisinau	NU	ST	ME	NS	F+C	RS	100-10000	91.5	503	1.39	36.2	1343.4	2.17	167.1	219174.3	5.24	Eck et al. (2003)
LA	CUB	Camagüey	NU	ME	ME	NS	F+C	RS	100-10000	62.2	307.6	1.55	186.5	5655.7	2.45	29.3	9245.1	1.44	Estevan et al. (2011)
WA	IRN	Zanjan	NU	MT	ME	NS	F+C	RS	100-10000	1.2	287.6	1.53	0.1	1038.6	2.21	2.8	5772.5	2.01	Masoumi et al. (2013)
WA	IRN	Zanjan	NU	MT	ME	NS	F+C	RS	100-10000	0.7	322.3	1.58	1.4	4795.7	1.91	--	--	--	Masoumi et al. (2013)
WA	IRN	Zanjan	NU	MT	ME	NS	F+C	RS	100-10000	0.7	309	1.55	0.4	5990.5	1.95	--	--	--	Masoumi et al. (2013)
WA	IRN	Zanjan	NU	MT	ME	NS	F+C	RS	100-10000	1.1	298.7	1.56	0.4	4984.6	1.61	1.8	181617.9	11.77	Masoumi et al. (2013)
WA	IRN	Zanjan	NU	MT	ME	NS	F+C	RS	100-10000	0.7	332.2	1.72	2.8	4712.9	1.86	--	--	--	Masoumi et al. (2013)
WA	IRN	Zanjan	NU	MT	ME	NS	F+C	RS	100-10000	1.6	338.2	1.63	0.3	5008.7	1.47	2.5	4901.5	1.83	Masoumi et al. (2013)
WA	IRN	Zanjan	NU	MT	ME	NS	F+C	RS	100-10000	1.2	278	1.54	3.9	4979.4	1.91	1.6	12523.4	4.4	Masoumi et al. (2013)
WA	IRN	Zanjan	NU	MT	ME	NS	F+C	RS	100-10000	1.6	287.5	1.45	1.5	2936.2	1.72	6.7	5263	1.92	Masoumi et al. (2013)
WA	IRN	Zanjan	NU	MT	ME	NS	F+C	RS	100-10000	1.1	288.4	1.56	3.5	4532.7	1.88	1.9	6874.3	1.69	Masoumi et al. (2013)
WA	IRN	Zanjan	NU	MT	ME	NS	F+C	RS	100-10000	1.5	273.7	1.55	4.7	5237.5	2.01	--	--	--	Masoumi et al. (2013)
WA	IRN	Zanjan	NU	MT	ME	NS	F+C	RS	100-10000	0.8	376.4	1.61	1	4927.9	1.92	--	--	--	Masoumi et al. (2013)
WA	IRN	Zanjan	NU	MT	ME	NS	F+C	RS	100-10000	0.6	407.6	1.61	1.2	4028.9	1.82	0.1	5274.6	1.77	Masoumi et al. (2013)
WA	IRN	Zanjan	NU	MT	ME	NS	F+C	RS	100-10000	0.9	358.9	1.63	0.2	2068.6	1.45	3.8	4907.5	1.93	Masoumi et al. (2013)
WA	IRN	Zanjan	NU	MT	ME	NS	F+C	RS	100-10000	1.3	307.4	1.65	5.9	4848.3	1.94	--	--	--	Masoumi et al. (2013)
WA	IRN	Zanjan	NU	MT	ME	NS	F+C	RS	100-10000	0.9	285.9	1.6	0.1	1916.4	1.07	7.2	5046.5	1.87	Masoumi et al. (2013)
WA	IRN	Zanjan	NU	MT	ME	NS	F+C	RS	100-10000	0.8	283.1	1.48	6	5040.1	1.82	16.6	591897.4	18.13	Masoumi et al. (2013)

WA	IRN	Zanjan	NU	MT	ME	NS	F+C	RS	100-10000	1.2	329.9	1.63	0.3	1907.4	1.52	5.3	5215	1.84	Masoumi et al. (2013)
WA	IRN	Zanjan	NU	MT	ME	NS	F+C	RS	100-10000	1.1	285.8	1.42	0.9	438	1.58	2.9	5750.6	1.82	Masoumi et al. (2013)
WA	IRN	Zanjan	NU	MT	ME	NS	F+C	RS	100-10000	1.2	328.4	1.68	3.1	4993.5	1.84	--	--	--	Masoumi et al. (2013)
WA	IRN	Zanjan	NU	LT	ME	NS	F+C	RS	100-10000	0.7	290.1	2.02	0.1	3237.6	1.09	4.6	4258.6	2.05	Gharibzadeh et al. (2017)
WA	IRN	Zanjan	NU	LT	ME	NS	F+C	RS	100-10000	0.8	258.2	3.9	3.9	5145.8	2.08	0.6	8183.5	1.39	Gharibzadeh et al. (2017)
WA	IRN	Zanjan	NU	LT	ME	NS	F+C	RS	100-10000	0.6	281.6	1.63	3.3	5526.2	2.16	0.2	7827.2	1.26	Gharibzadeh et al. (2017)
WA	IRN	Zanjan	NU	LT	ME	NS	F+C	RS	100-10000	0.4	337.9	1.58	1.8	4012.7	2.22	0.1	4244.2	1.32	Gharibzadeh et al. (2017)

APPENDIX B. SUPPLEMENTAL MATERIALS FOR INFANT AND ADULT INHALATION EXPOSURE TO RESUSPENDED BIOLOGICAL PARTICULATE MATTER

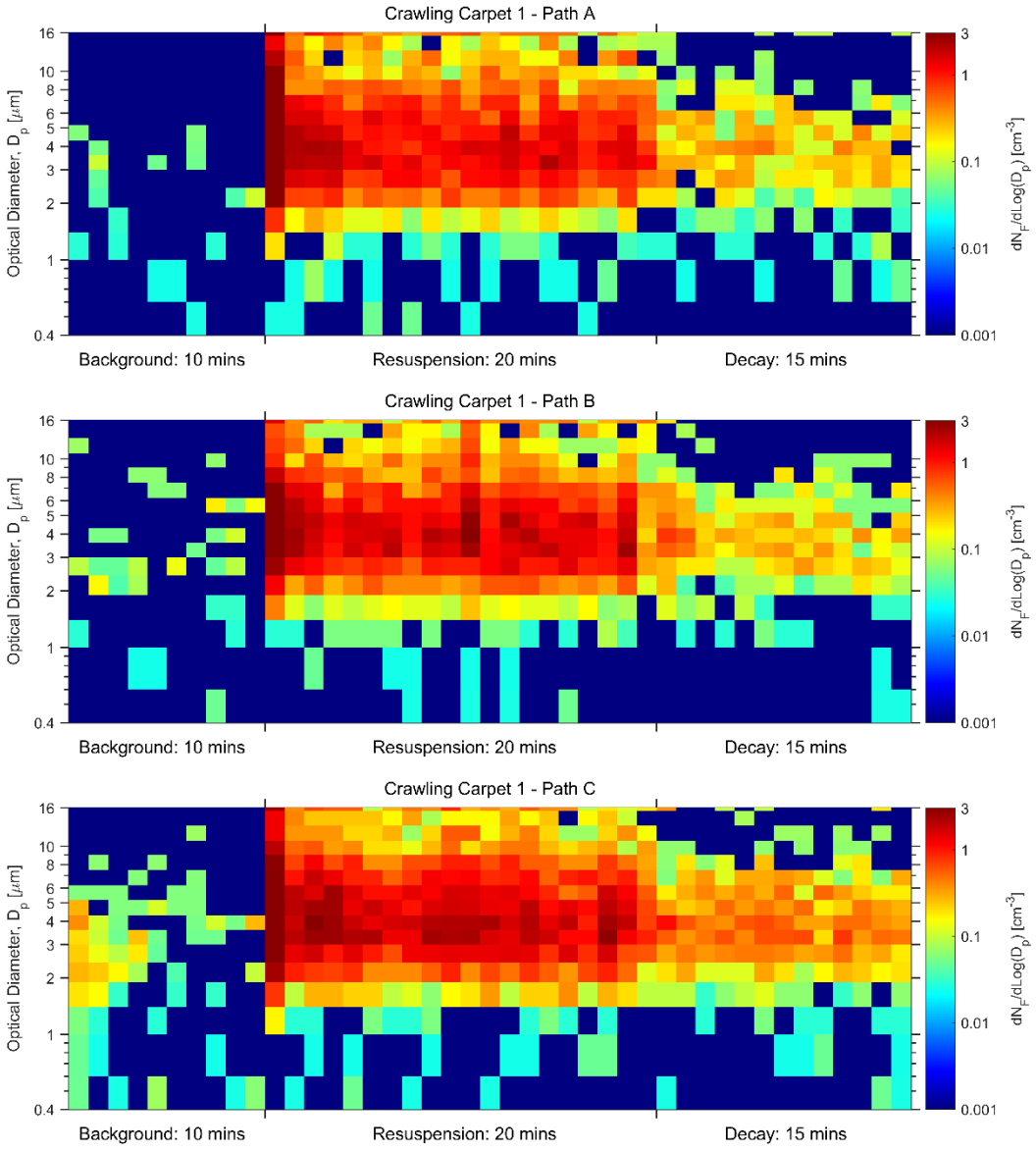

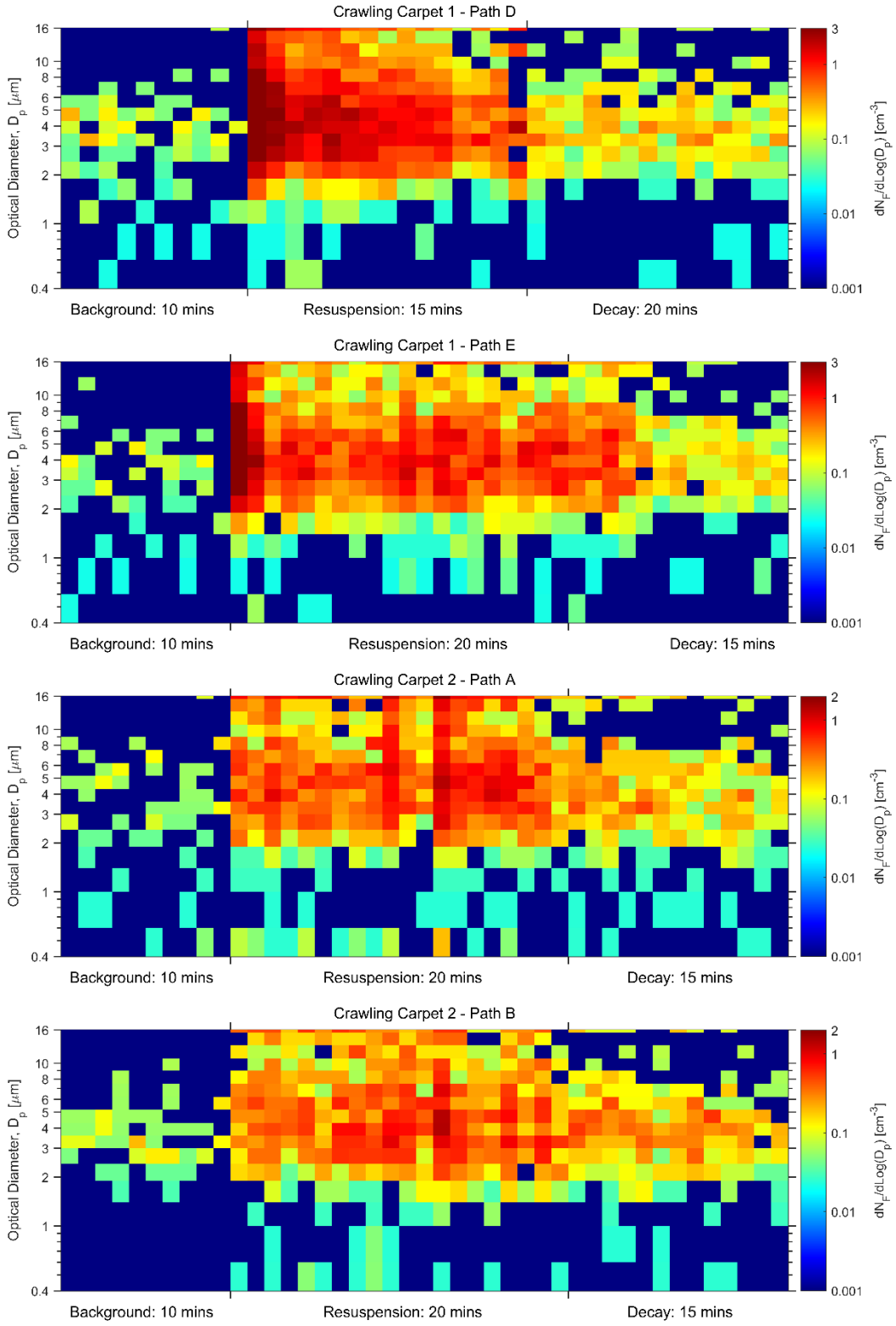
Crawling Carpet 1 - Path D
Optical Diameter, D_p [μm]
16
10
8
6
5
4
3
2
1
0.4
Background: 10 mins
Resuspension: 15 mins
Decay: 20 mins
3
1
0.1
0.01
0.001
$dN_F/dLog(D_p)$ [cm^{-3}]
Crawling Carpet 1 - Path E
Optical Diameter, D_p [μm]
Background: 10 mins
Resuspension: 20 mins
Decay: 15 mins
$dN_F/dLog(D_p)$ [cm^{-3}]
Crawling Carpet 2 - Path A
Optical Diameter, D_p [μm]
Background: 10 mins
Resuspension: 20 mins
Decay: 15 mins
2
1
0.1
0.01
0.001
$dN_F/dLog(D_p)$ [cm^{-3}]
Crawling Carpet 2 - Path B
Optical Diameter, D_p [μm]
Background: 10 mins
Resuspension: 20 mins
Decay: 15 mins
$dN_F/dLog(D_p)$ [cm^{-3}]

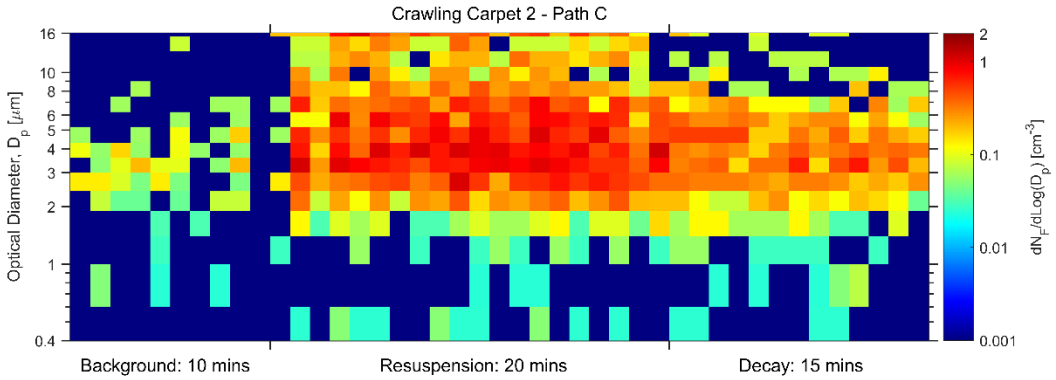
Crawling Carpet 2 - Path C
Optical Diameter, D_p [μm]
16
10
8
6
5
4
3
2
1
0.4
Background: 10 mins
Resuspension: 20 mins
Decay: 15 mins
2
1
0.1
0.01
0.001
$dN_F/dLog(D_p)$ [cm^{-3}]

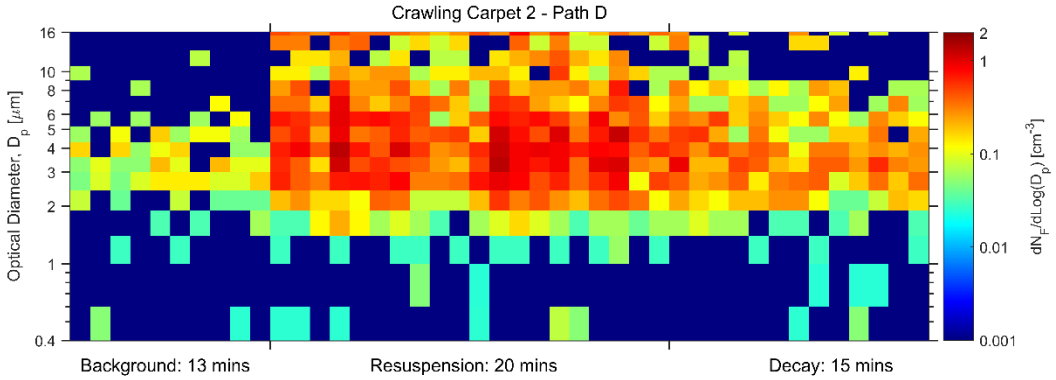
Crawling Carpet 2 - Path D
Optical Diameter, D_p [μm]
16
10
8
6
5
4
3
2
1
0.4
Background: 13 mins
Resuspension: 20 mins
Decay: 15 mins
2
1
0.1
0.01
0.001
$dN_F/dLog(D_p)$ [cm^{-3}]

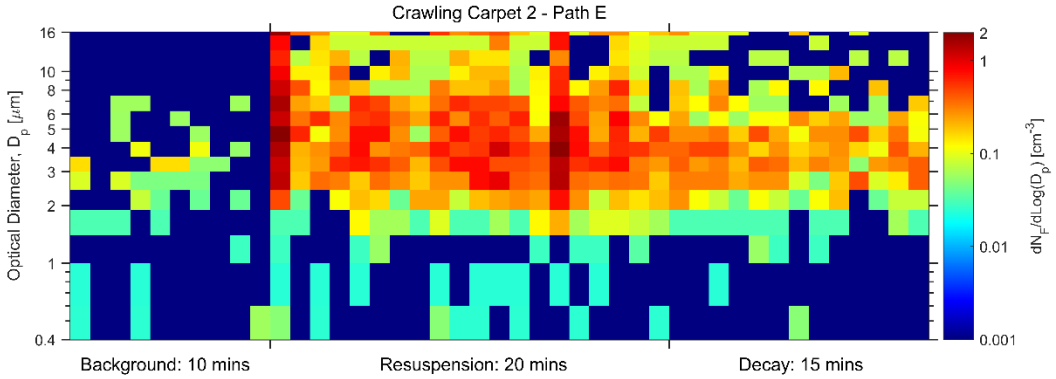
Crawling Carpet 2 - Path E
Optical Diameter, D_p [μm]
16
10
8
6
5
4
3
2
1
0.4
Background: 10 mins
Resuspension: 20 mins
Decay: 15 mins
2
1
0.1
0.01
0.001
$dN_F/dLog(D_p)$ [cm^{-3}]

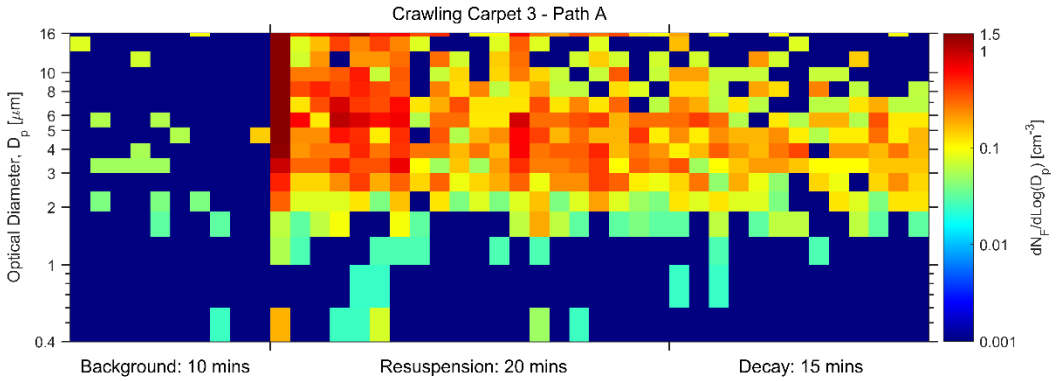
Crawling Carpet 3 - Path A
Optical Diameter, D_p [μm]
16
10
8
6
5
4
3
2
1
0.4
Background: 10 mins
Resuspension: 20 mins
Decay: 15 mins
1.5
1
0.1
0.01
0.001
$dN_F/dLog(D_p)$ [cm^{-3}]

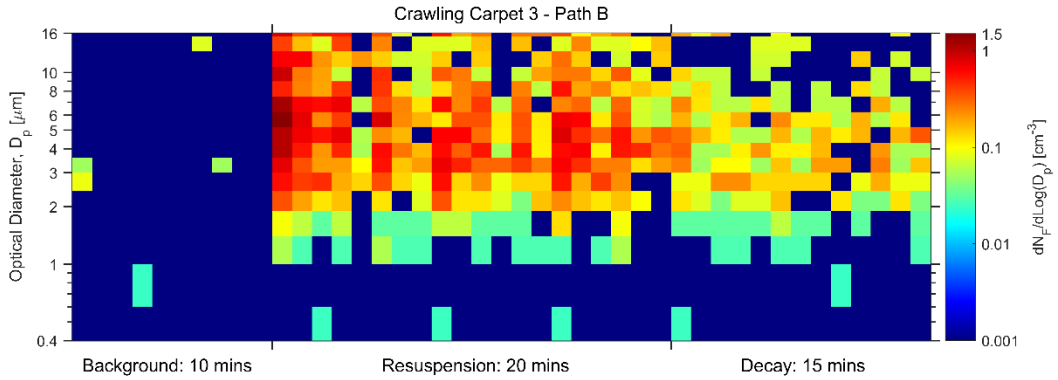
Crawling Carpet 3 - Path B
Optical Diameter, D_p [μm]
16
10
8
6
5
4
3
2
1
0.4
Background: 10 mins
Resuspension: 20 mins
Decay: 15 mins
1.5
1
0.1
0.01
0.001
$dN_F/dLog(D_p)$ [cm^{-3}]

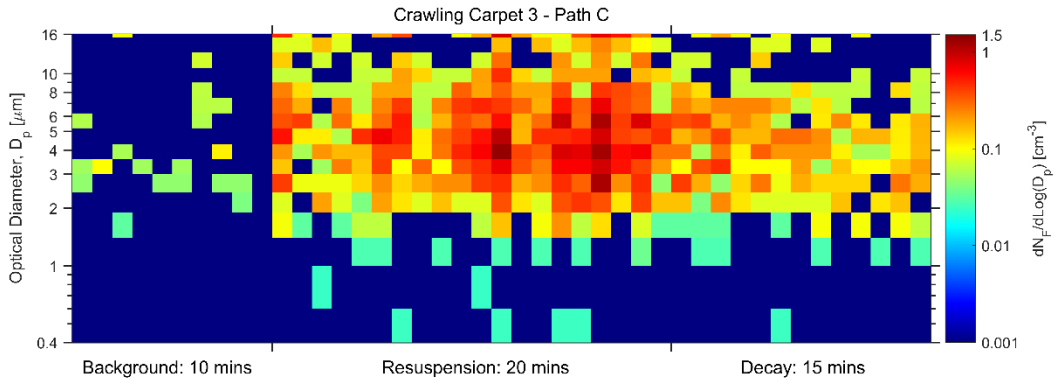
Crawling Carpet 3 - Path C
Optical Diameter, D_p [μm]
16
10
8
6
5
4
3
2
1
0.4
Background: 10 mins
Resuspension: 20 mins
Decay: 15 mins
1.5
1
0.1
0.01
0.001
$dN_F/dLog(D_p)$ [cm^{-3}]

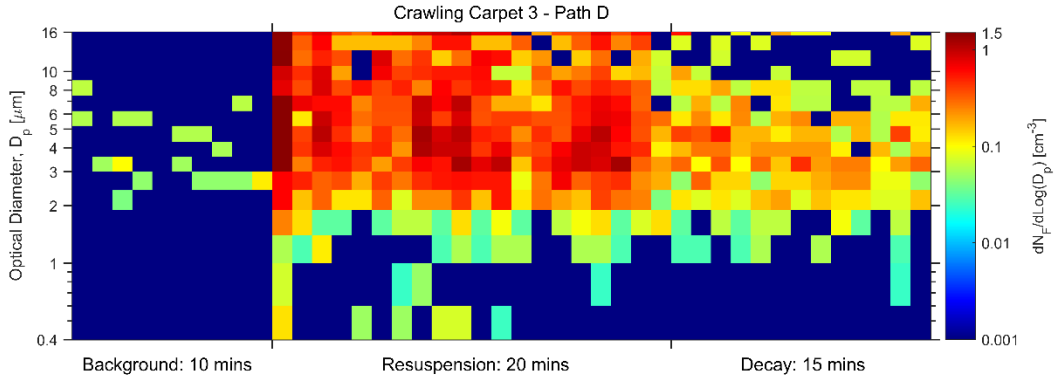
Crawling Carpet 3 - Path D
Optical Diameter, D_p [μm]
16
10
8
6
5
4
3
2
1
0.4
Background: 10 mins
Resuspension: 20 mins
Decay: 15 mins
1.5
1
0.1
0.01
0.001
$dN_F/dLog(D_p)$ [cm^{-3}]

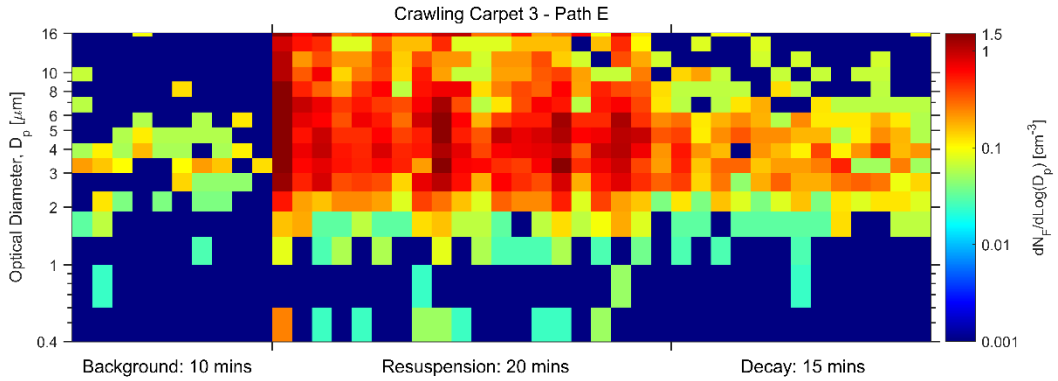
Crawling Carpet 3 - Path E
Optical Diameter, D_p [μm]
16
10
8
6
5
4
3
2
1
0.4
Background: 10 mins
Resuspension: 20 mins
Decay: 15 mins
1.5
1
0.1
0.01
0.001
$dN_F/dLog(D_p)$ [cm^{-3}]

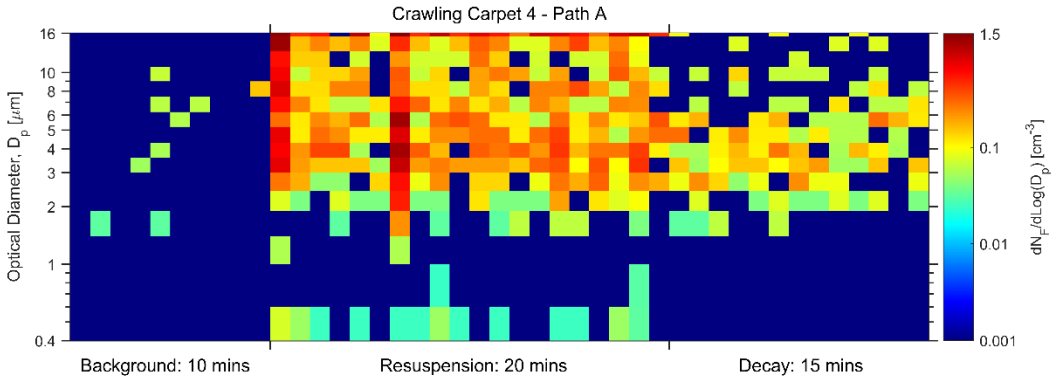
Crawling Carpet 4 - Path A
Optical Diameter, D_p [μm]
16
10
8
6
5
4
3
2
1
0.4
Background: 10 mins
Resuspension: 20 mins
Decay: 15 mins
1.5
0.1
0.01
0.001
$dN_F/dLog(D_p)$ [cm^{-3}]

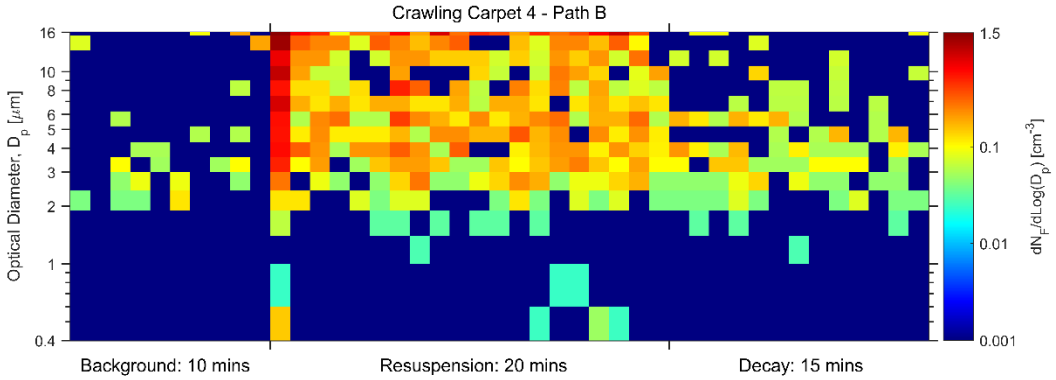
Crawling Carpet 4 - Path B
Optical Diameter, D_p [μm]
16
10
8
6
5
4
3
2
1
0.4
Background: 10 mins
Resuspension: 20 mins
Decay: 15 mins
1.5
0.1
0.01
0.001
$dN_F/dLog(D_p)$ [cm^{-3}]

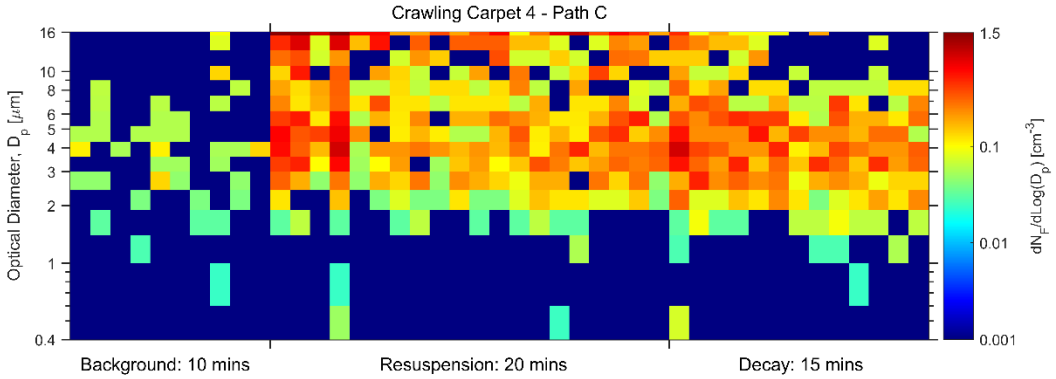
Crawling Carpet 4 - Path C
Optical Diameter, D_p [μm]
16
10
8
6
5
4
3
2
1
0.4
Background: 10 mins
Resuspension: 20 mins
Decay: 15 mins
1.5
0.1
0.01
0.001
$dN_F/dLog(D_p)$ [cm^{-3}]

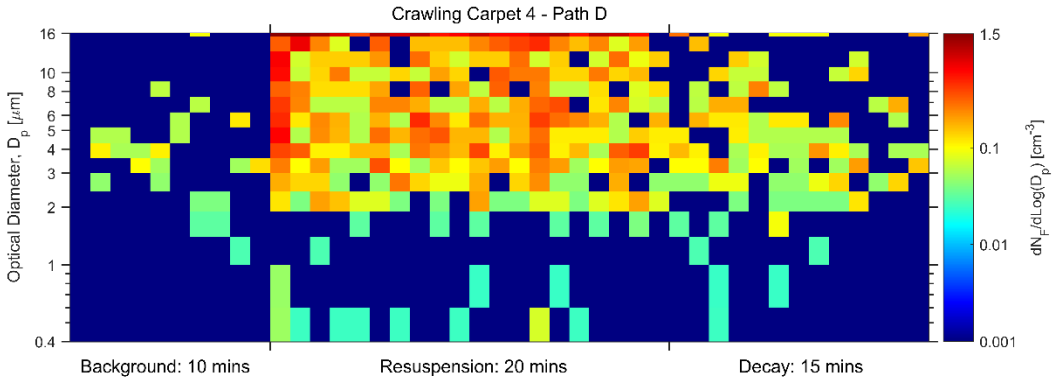
Crawling Carpet 4 - Path D
Optical Diameter, D_p [μm]
16
10
8
6
5
4
3
2
1
0.4
Background: 10 mins
Resuspension: 20 mins
Decay: 15 mins
1.5
0.1
0.01
0.001
$dN_F/dLog(D_p)$ [cm^{-3}]

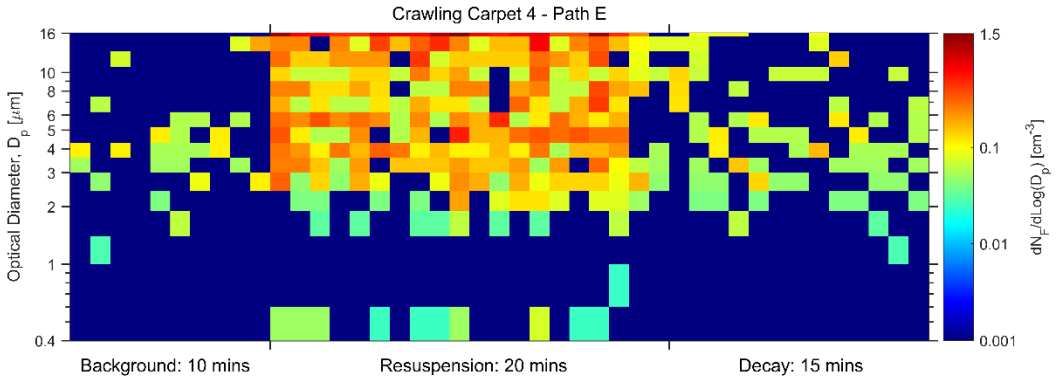
Crawling Carpet 4 - Path E
Optical Diameter, D_p [μm]
16
10
8
6
5
4
3
2
1
0.4
Background: 10 mins
Resuspension: 20 mins
Decay: 15 mins
1.5
0.1
0.01
0.001
$dN_F/dLog(D_p)$ [cm^{-3}]

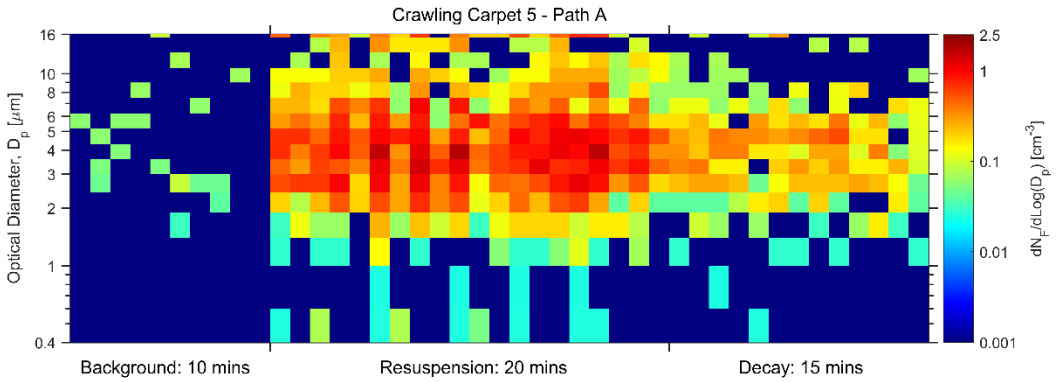
Crawling Carpet 5 - Path A
Optical Diameter, D_p [μm]
16
10
8
6
5
4
3
2
1
0.4
Background: 10 mins
Resuspension: 20 mins
Decay: 15 mins
2.5
1
0.1
0.01
0.001
$dN_F/dLog(D_p)$ [cm^{-3}]

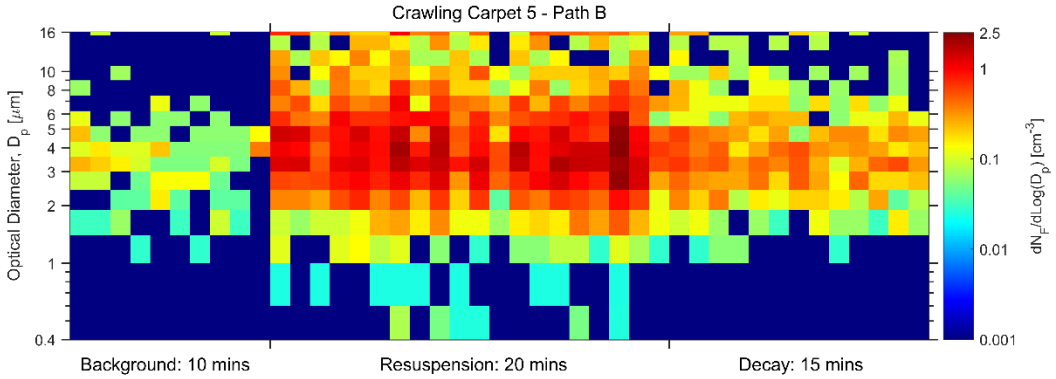
Crawling Carpet 5 - Path B
Optical Diameter, D_p [μm]
16
10
8
6
5
4
3
2
1
0.4
Background: 10 mins
Resuspension: 20 mins
Decay: 15 mins
2.5
1
0.1
0.01
0.001
$dN_F/dLog(D_p)$ [cm^{-3}]

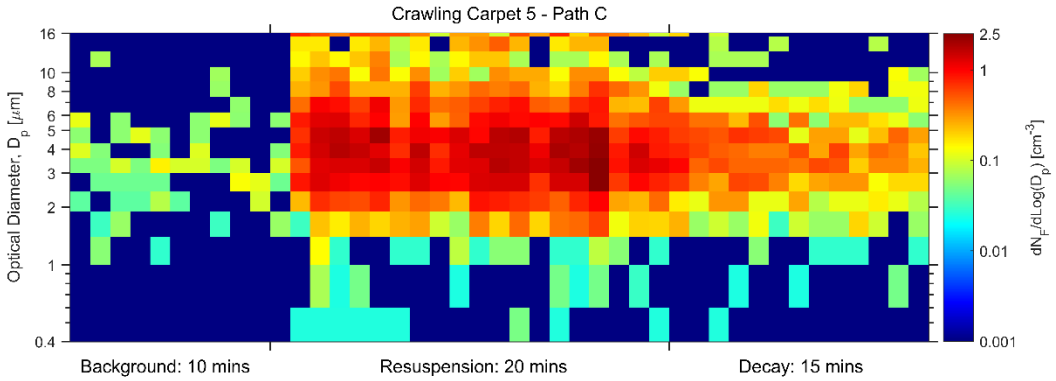
Crawling Carpet 5 - Path C
Optical Diameter, D_p [μm]
16
10
8
6
5
4
3
2
1
0.4
Background: 10 mins
Resuspension: 20 mins
Decay: 15 mins
2.5
1
0.1
0.01
0.001
$dN_F/dLog(D_p)$ [cm^{-3}]

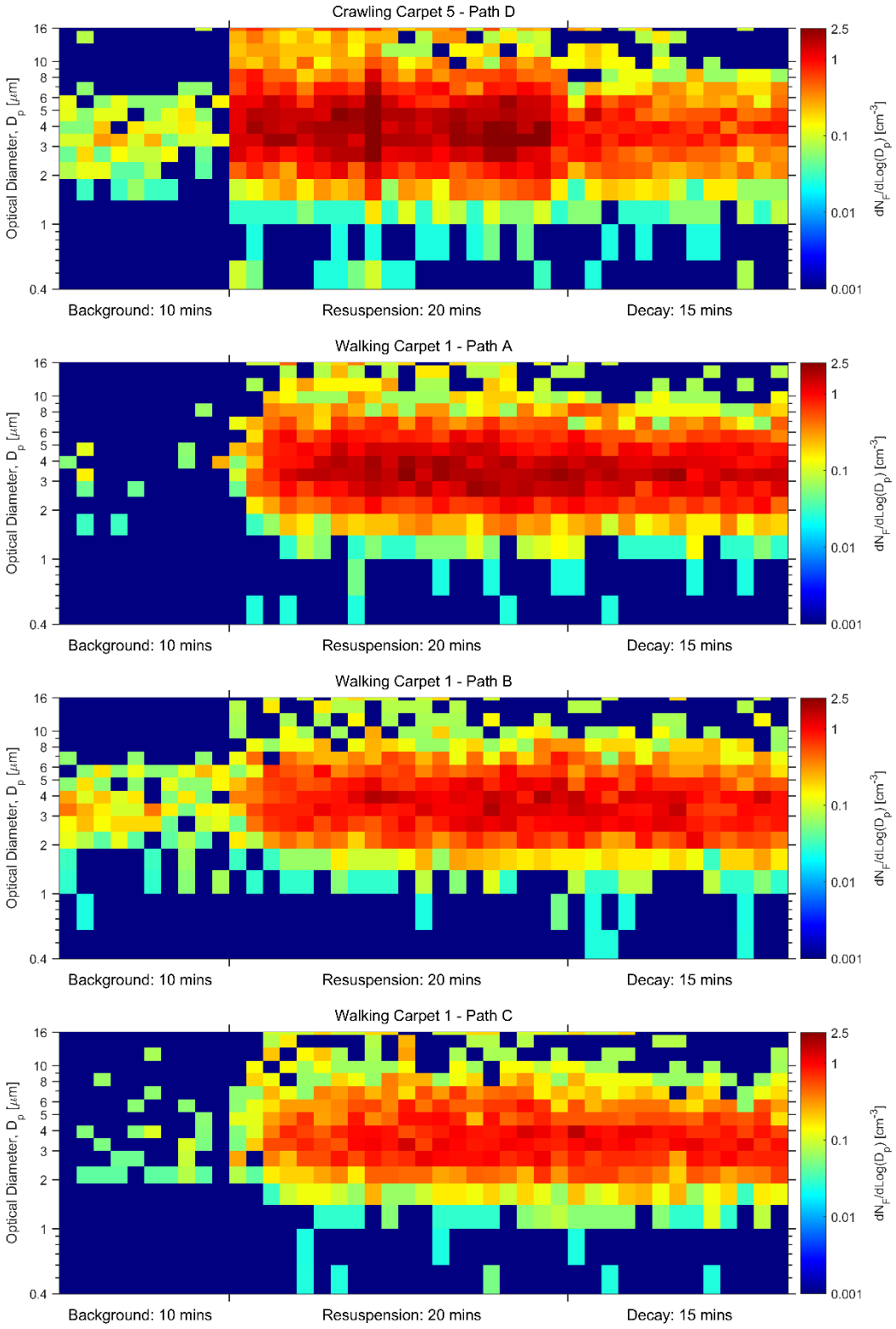
Crawling Carpet 5 - Path D
Walking Carpet 1 - Path A
Walking Carpet 1 - Path B
Walking Carpet 1 - Path C
Optical Diameter, D_p [μm]
16
10
8
6
5
4
3
2
1
0.4
Background: 10 mins
Resuspension: 20 mins
Decay: 15 mins
$dN_F/dLog(D_p)$ [cm^{-3}]
2.5
1
0.1
0.01
0.001

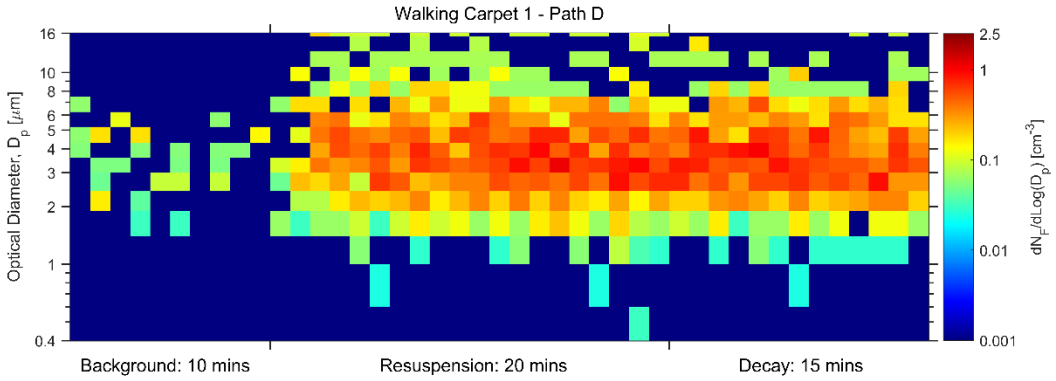
Walking Carpet 1 - Path D
Optical Diameter, D_p [μm]
16
10
8
6
5
4
3
2
1
0.4
2.5
1
0.1
0.01
0.001
$dN_F/dLog(D_p)$ [cm^{-3}]
Background: 10 mins
Resuspension: 20 mins
Decay: 15 mins


Walking Carpet 1 - Path E
Optical Diameter, D_p [μm]
16
10
8
6
5
4
3
2
1
0.4
2.5
1
0.1
0.01
0.001
$dN_F/dLog(D_p)$ [cm^{-3}]
Background: 10 mins
Resuspension: 20 mins
Decay: 15 mins

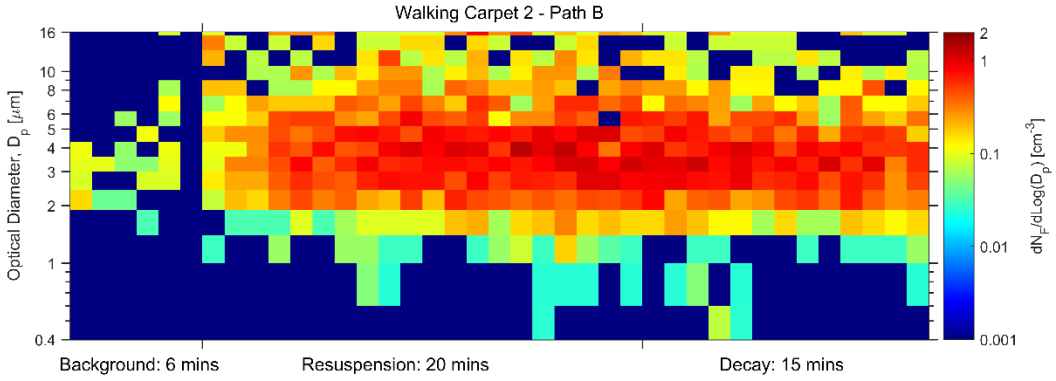
Walking Carpet 2 - Path B
Optical Diameter, D_p [μm]
16
10
8
6
5
4
3
2
1
0.4
2
1
0.1
0.01
0.001
$dN_F/dLog(D_p)$ [cm^{-3}]
Background: 6 mins
Resuspension: 20 mins
Decay: 15 mins

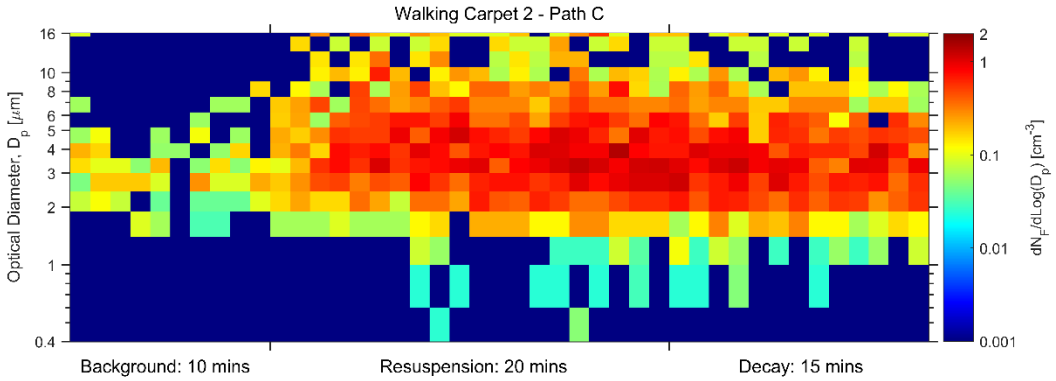
Walking Carpet 2 - Path C
Optical Diameter, D_p [μm]
16
10
8
6
5
4
3
2
1
0.4
2
1
0.1
0.01
0.001
$dN_F/dLog(D_p)$ [cm^{-3}]
Background: 10 mins
Resuspension: 20 mins
Decay: 15 mins

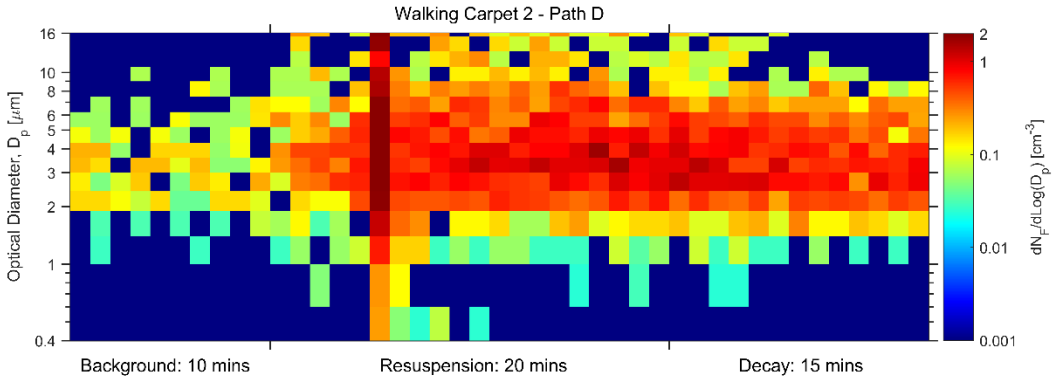
Walking Carpet 2 - Path D
Optical Diameter, D_p [μm]
16
10
8
6
5
4
3
2
1
0.4
Background: 10 mins
Resuspension: 20 mins
Decay: 15 mins
2
1
0.1
0.01
0.001
$dN_F/dLog(D_p)$ [cm^{-3}]

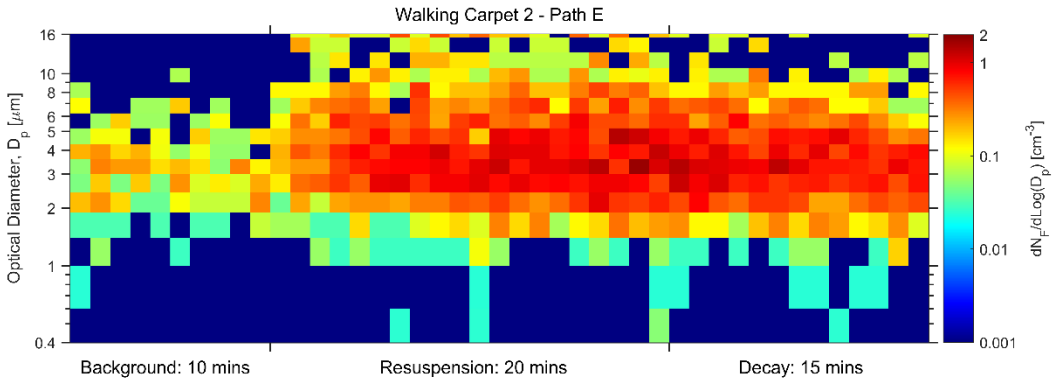
Walking Carpet 2 - Path E
Optical Diameter, D_p [μm]
16
10
8
6
5
4
3
2
1
0.4
Background: 10 mins
Resuspension: 20 mins
Decay: 15 mins
2
1
0.1
0.01
0.001
$dN_F/dLog(D_p)$ [cm^{-3}]

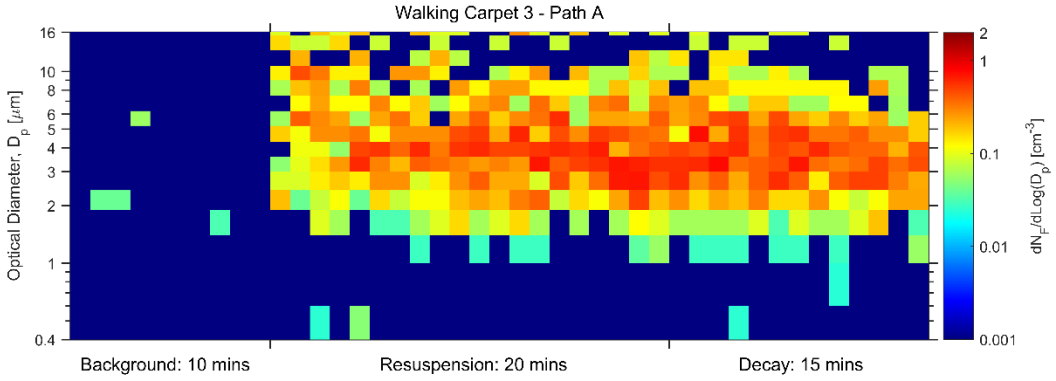
Walking Carpet 3 - Path A
Optical Diameter, D_p [μm]
16
10
8
6
5
4
3
2
1
0.4
Background: 10 mins
Resuspension: 20 mins
Decay: 15 mins
2
1
0.1
0.01
0.001
$dN_F/dLog(D_p)$ [cm^{-3}]

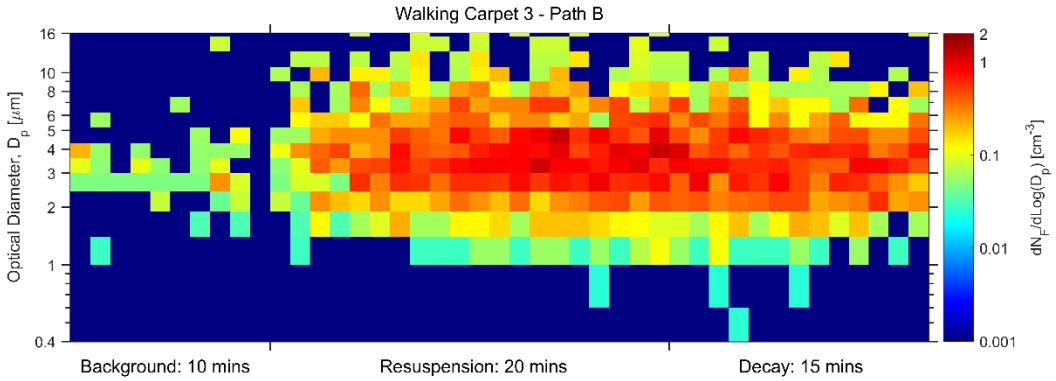
Walking Carpet 3 - Path B
Optical Diameter, D_p [μm]
16
10
8
6
5
4
3
2
1
0.4
Background: 10 mins
Resuspension: 20 mins
Decay: 15 mins
2
1
0.1
0.01
0.001
$dN_F/dLog(D_p)$ [cm^{-3}]

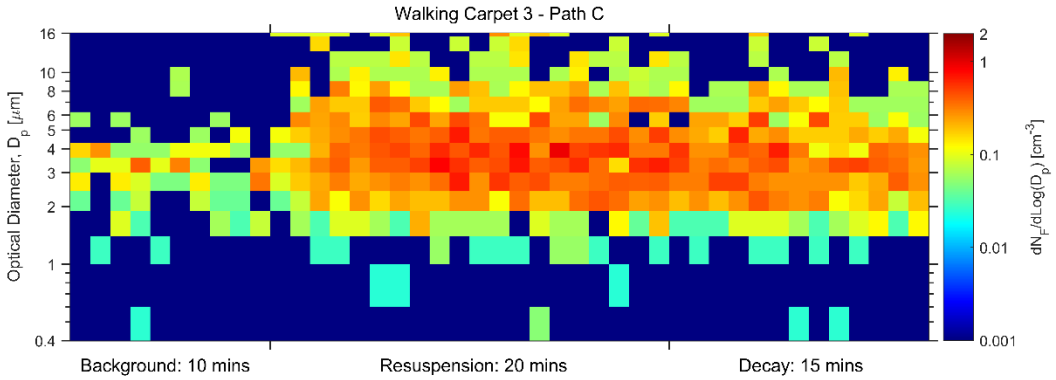
Walking Carpet 3 - Path C
Optical Diameter, D_p [μm]
16
10
8
6
5
4
3
2
1
0.4
2
1
0.1
0.01
0.001
$dN_F/dLog(D_p)$ [cm^{-3}]
Background: 10 mins
Resuspension: 20 mins
Decay: 15 mins

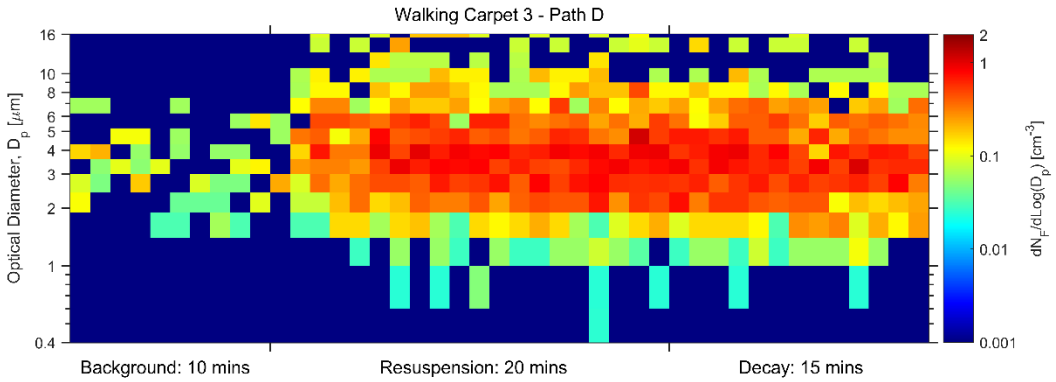
Walking Carpet 3 - Path D
Optical Diameter, D_p [μm]
16
10
8
6
5
4
3
2
1
0.4
2
1
0.1
0.01
0.001
$dN_F/dLog(D_p)$ [cm^{-3}]
Background: 10 mins
Resuspension: 20 mins
Decay: 15 mins

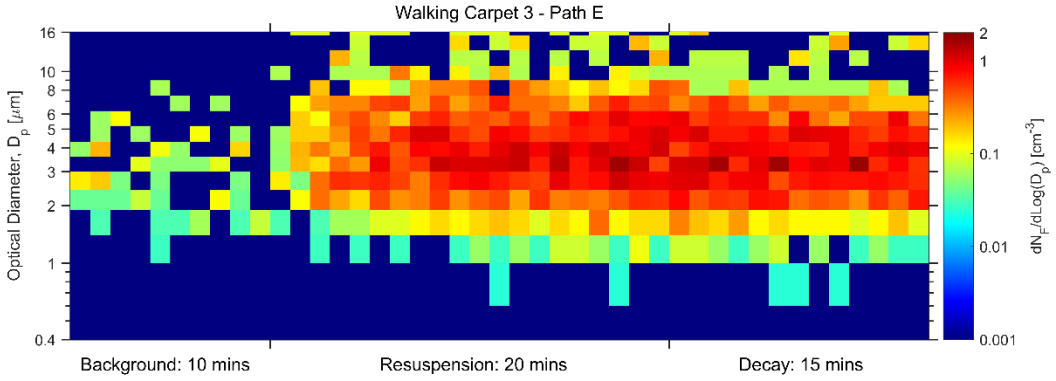
Walking Carpet 3 - Path E
Optical Diameter, D_p [μm]
16
10
8
6
5
4
3
2
1
0.4
2
1
0.1
0.01
0.001
$dN_F/dLog(D_p)$ [cm^{-3}]
Background: 10 mins
Resuspension: 20 mins
Decay: 15 mins

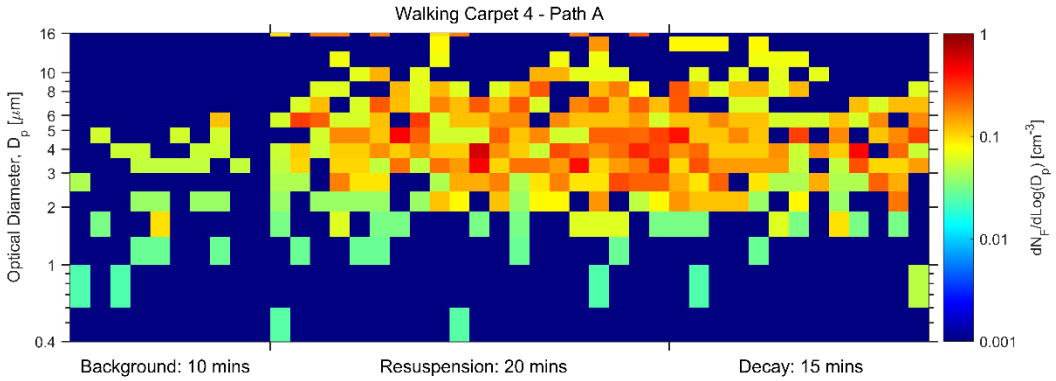
Walking Carpet 4 - Path A
Optical Diameter, D_p [μm]
16
10
8
6
5
4
3
2
1
0.4
1
0.1
0.01
0.001
$dN_F/dLog(D_p)$ [cm^{-3}]
Background: 10 mins
Resuspension: 20 mins
Decay: 15 mins

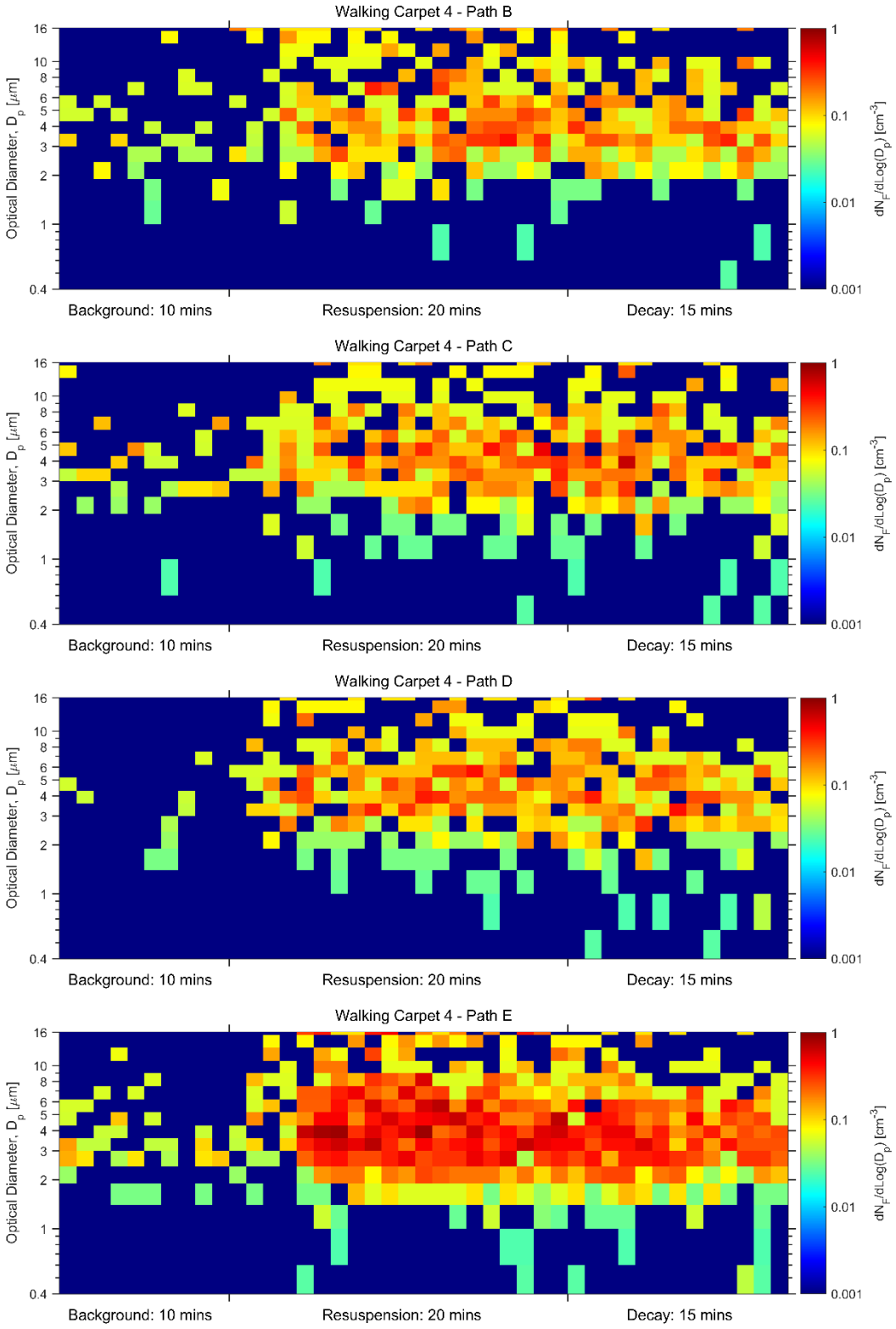
Walking Carpet 4 - Path B
Optical Diameter, D_p [μm]
16
10
8
6
5
4
3
2
1
0.4
Background: 10 mins
Resuspension: 20 mins
Decay: 15 mins
1
0.1
0.01
0.001
$dN_F/dLog(D_p)$ [cm^{-3}]
Walking Carpet 4 - Path C
Optical Diameter, D_p [μm]
Background: 10 mins
Resuspension: 20 mins
Decay: 15 mins
$dN_F/dLog(D_p)$ [cm^{-3}]
Walking Carpet 4 - Path D
Optical Diameter, D_p [μm]
Background: 10 mins
Resuspension: 20 mins
Decay: 15 mins
$dN_F/dLog(D_p)$ [cm^{-3}]
Walking Carpet 4 - Path E
Optical Diameter, D_p [μm]
Background: 10 mins
Resuspension: 20 mins
Decay: 15 mins
$dN_F/dLog(D_p)$ [cm^{-3}]

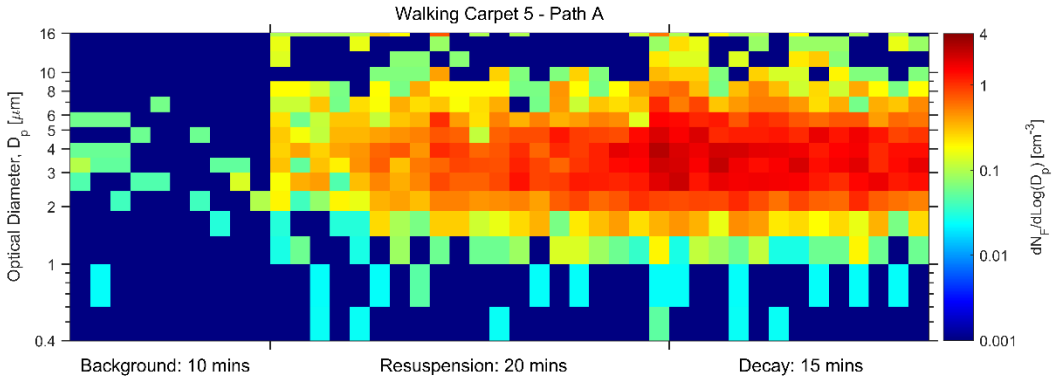
Walking Carpet 5 - Path A
Optical Diameter, D_p [μm]
16
10
8
6
5
4
3
2
1
0.4
Background: 10 mins
Resuspension: 20 mins
Decay: 15 mins
4
1
0.1
0.01
0.001
$dN_F/dLog(D_p)$ [cm^{-3}]

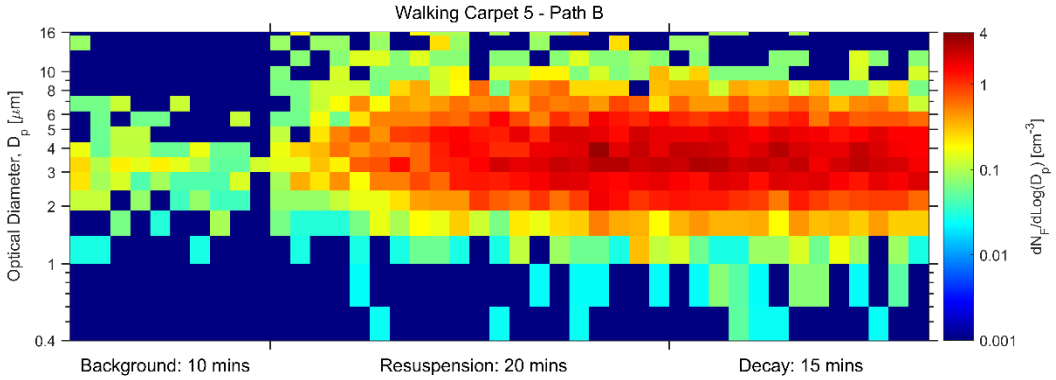
Walking Carpet 5 - Path B
Optical Diameter, D_p [μm]
16
10
8
6
5
4
3
2
1
0.4
Background: 10 mins
Resuspension: 20 mins
Decay: 15 mins
4
1
0.1
0.01
0.001
$dN_F/dLog(D_p)$ [cm^{-3}]

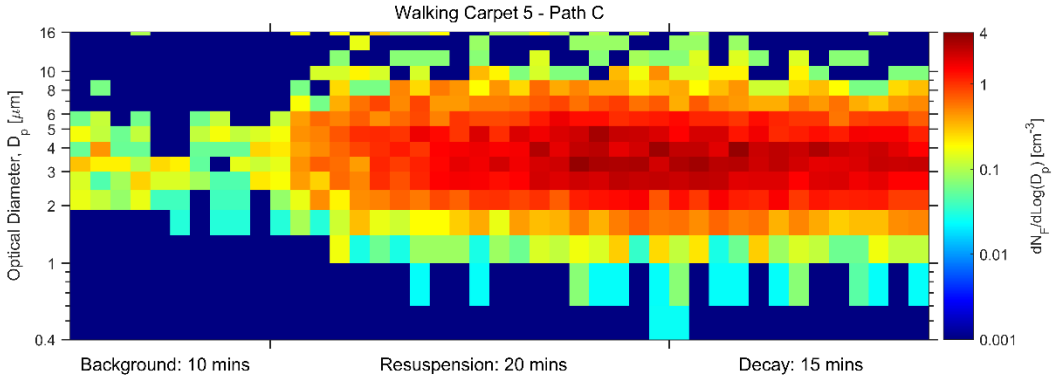
Walking Carpet 5 - Path C
Optical Diameter, D_p [μm]
16
10
8
6
5
4
3
2
1
0.4
Background: 10 mins
Resuspension: 20 mins
Decay: 15 mins
4
1
0.1
0.01
0.001
$dN_F/dLog(D_p)$ [cm^{-3}]

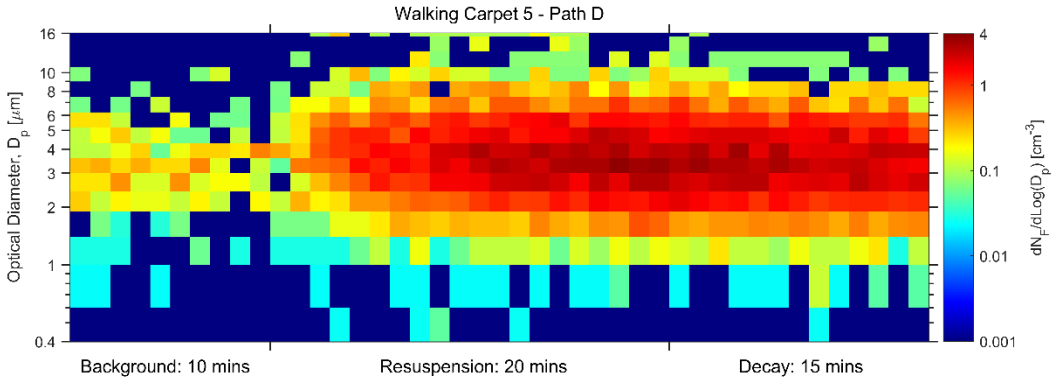
Walking Carpet 5 - Path D
Optical Diameter, D_p [μm]
16
10
8
6
5
4
3
2
1
0.4
Background: 10 mins
Resuspension: 20 mins
Decay: 15 mins
4
1
0.1
0.01
0.001
$dN_F/dLog(D_p)$ [cm^{-3}]

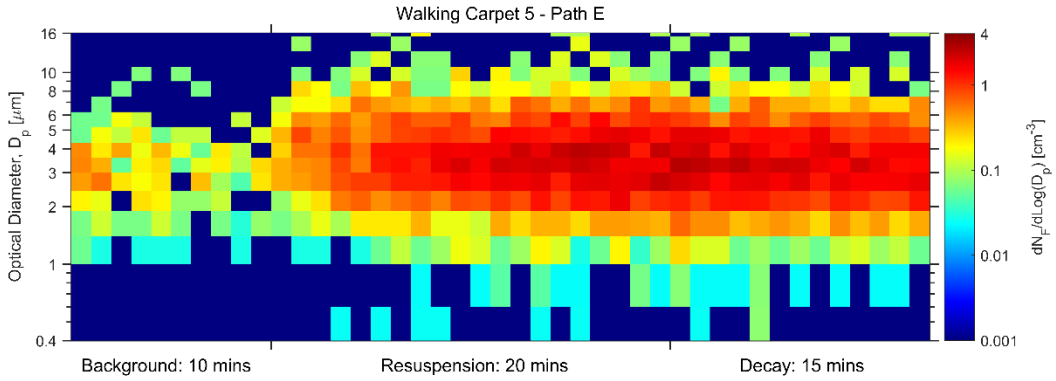

Figure B.1 Time-series plots of FBAP number size distributions ($dN_F/dlogD_p$) for all fifty crawling (infant breathing zone) and walking (adult breathing zone) resuspension experiments.

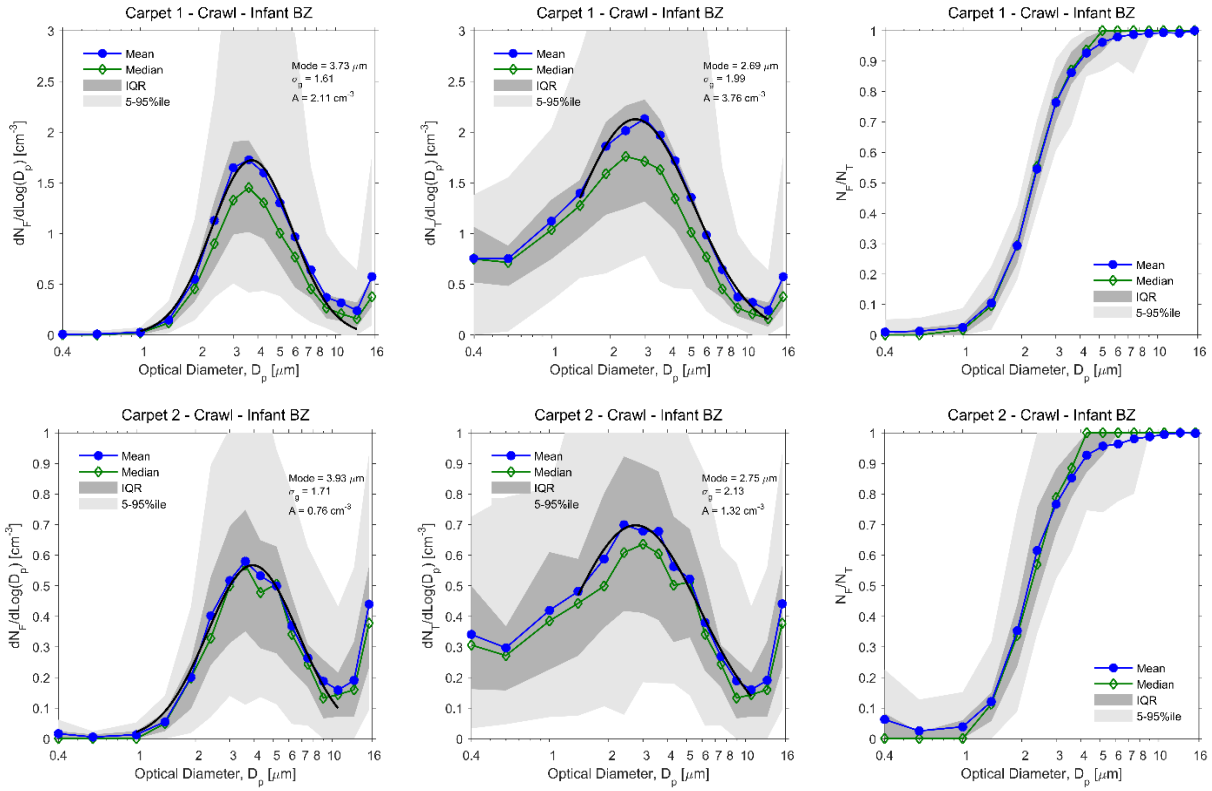

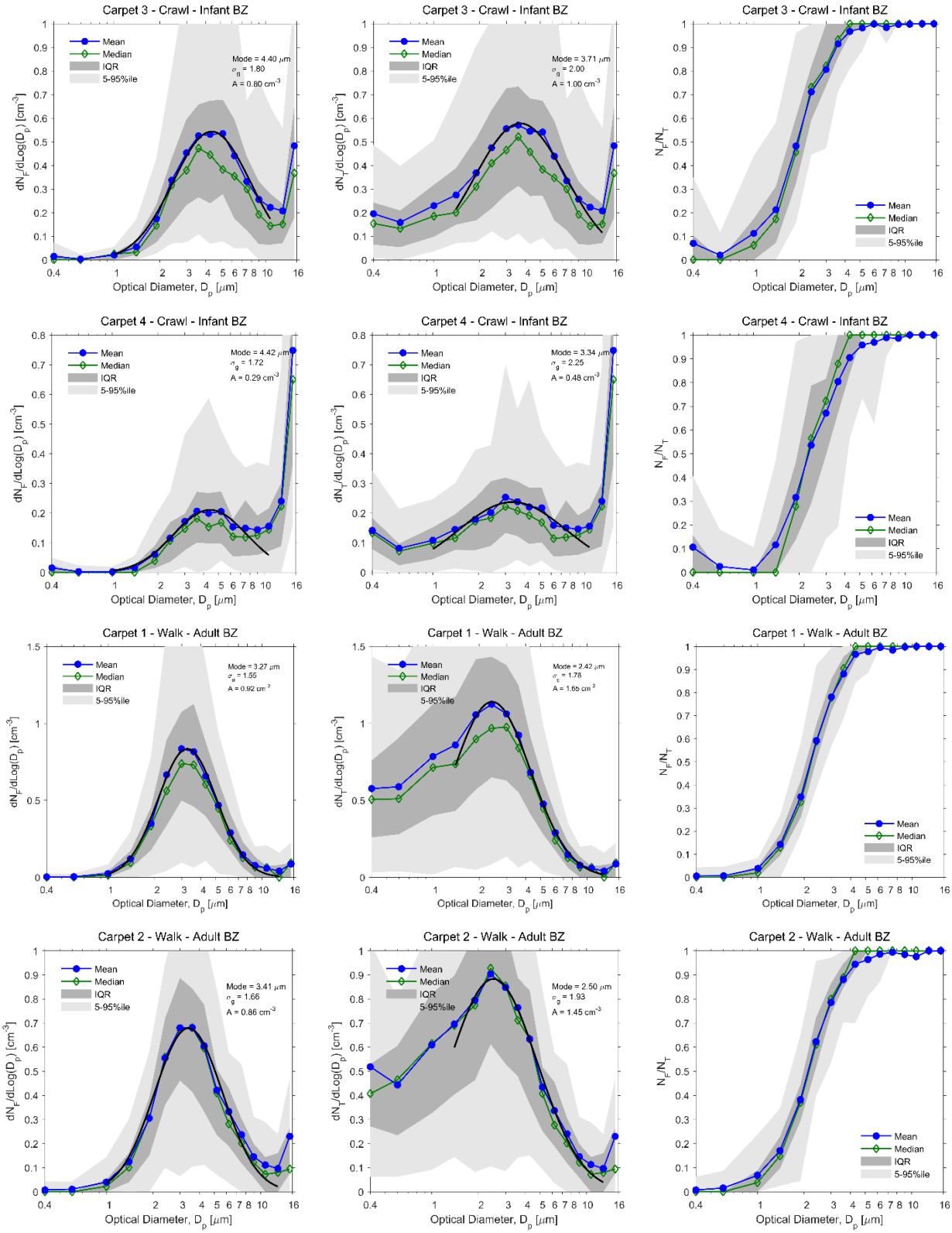
Carpet 3 - Crawl - Infant BZ
Mean
Median
IQR
5-95%ile
Mode = 4.40 μm
σg = 1.80
A = 0.80 cm-3
dNF/dLog(Dp) [cm-3]
Optical Diameter, Dp [μm]
Carpet 3 - Crawl - Infant BZ
Mean
Median
IQR
5-95%ile
Mode = 3.71 μm
σg = 2.00
A = 1.00 cm-3
dNT/dLog(Dp) [cm-3]
Optical Diameter, Dp [μm]
Carpet 3 - Crawl - Infant BZ
Mean
Median
IQR
5-95%ile
NF/NT
Optical Diameter, Dp [μm]
Carpet 4 - Crawl - Infant BZ
Mean
Median
IQR
5-95%ile
Mode = 4.42 μm
σg = 1.72
A = 0.29 cm-3
dNF/dLog(Dp) [cm-3]
Optical Diameter, Dp [μm]
Carpet 4 - Crawl - Infant BZ
Mean
Median
IQR
5-95%ile
Mode = 3.34 μm
σg = 2.25
A = 0.48 cm-3
dNT/dLog(Dp) [cm-3]
Optical Diameter, Dp [μm]
Carpet 4 - Crawl - Infant BZ
Mean
Median
IQR
5-95%ile
NF/NT
Optical Diameter, Dp [μm]
Carpet 1 - Walk - Adult BZ
Mean
Median
IQR
5-95%ile
Mode = 3.27 μm
σg = 1.55
A = 0.92 cm-3
dNF/dLog(Dp) [cm-3]
Optical Diameter, Dp [μm]
Carpet 1 - Walk - Adult BZ
Mean
Median
IQR
5-95%ile
Mode = 2.42 μm
σg = 1.78
A = 1.65 cm-3
dNT/dLog(Dp) [cm-3]
Optical Diameter, Dp [μm]
Carpet 1 - Walk - Adult BZ
Mean
Median
IQR
5-95%ile
NF/NT
Optical Diameter, Dp [μm]
Carpet 2 - Walk - Adult BZ
Mean
Median
IQR
5-95%ile
Mode = 3.41 μm
σg = 1.66
A = 0.86 cm-3
dNF/dLog(Dp) [cm-3]
Optical Diameter, Dp [μm]
Carpet 2 - Walk - Adult BZ
Mean
Median
IQR
5-95%ile
Mode = 2.50 μm
σg = 1.93
A = 1.45 cm-3
dNT/dLog(Dp) [cm-3]
Optical Diameter, Dp [μm]
Carpet 2 - Walk - Adult BZ
Mean
Median
IQR
5-95%ile
NF/NT
Optical Diameter, Dp [μm]

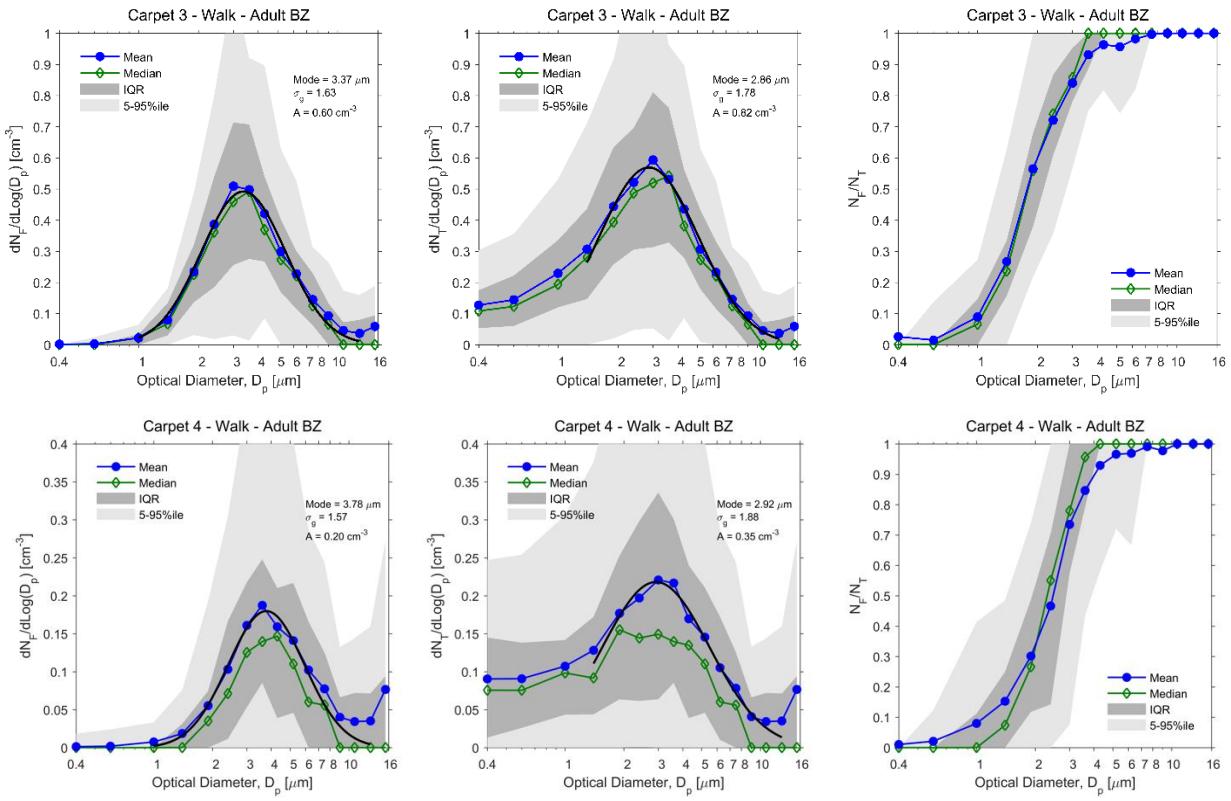

Figure B.2 Carpet-averaged $dN_F/dlogD_p$ (left), $dN_T/dlogD_p$ (middle), and size-resolved N_F/N_T ratios (right) measured during the crawling and walking periods on carpets 1-4 (carpet 5 presented in the main body of the text). Blue curves represent mean values, green curves represent median values, dark gray regions represent the interquartile range (IQR), and light gray regions represent the 5-95th percentile range among five crawling or walking paths on the same carpet (100 minutes in total). Black curves show the lognormal fitting of the dominant peaks. The mode, geometric standard deviation (σ_g), and amplitude (A) are presented.

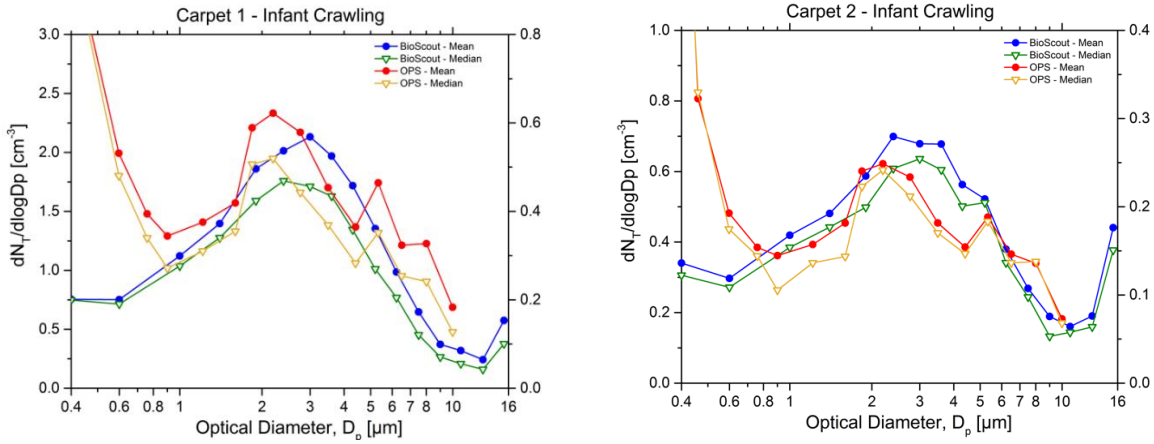

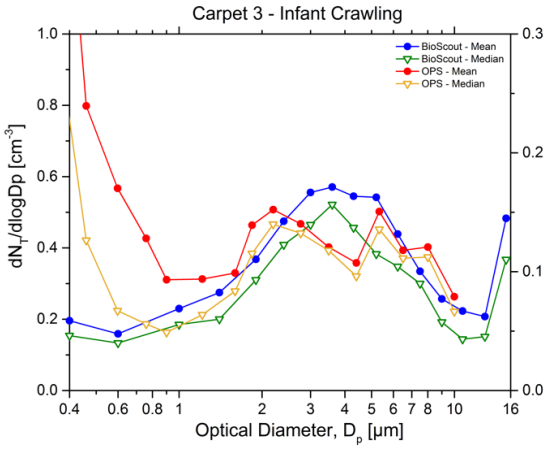
Carpet 3 - Infant Crawling
BioScout - Mean
BioScout - Median
OPS - Mean
OPS - Median
dN_T/dlogDp [cm^-3]
Optical Diameter, D_p [µm]

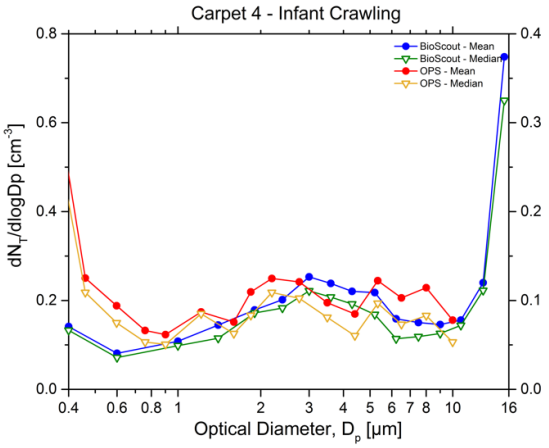
Carpet 4 - Infant Crawling
BioScout - Mean
BioScout - Median
OPS - Mean
OPS - Median
dN_T/dlogDp [cm^-3]
Optical Diameter, D_p [µm]

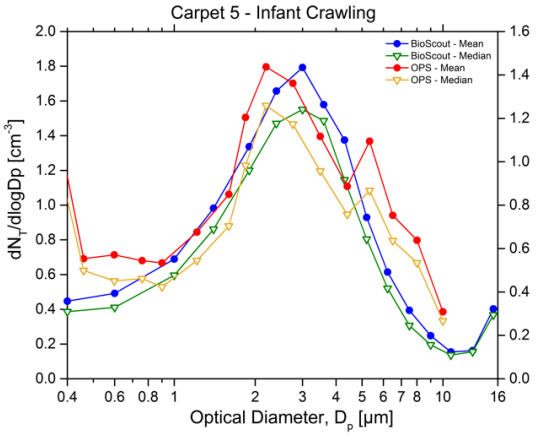
Carpet 5 - Infant Crawling
BioScout - Mean
BioScout - Median
OPS - Mean
OPS - Median
dN_T/dlogDp [cm^-3]
Optical Diameter, D_p [µm]

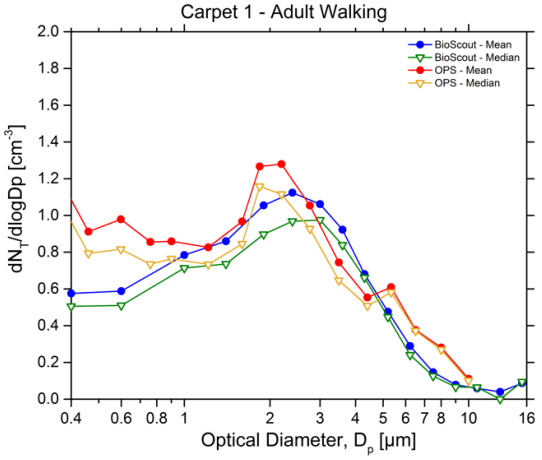
Carpet 1 - Adult Walking
BioScout - Mean
BioScout - Median
OPS - Mean
OPS - Median
dN_T/dlogDp [cm^-3]
Optical Diameter, D_p [µm]

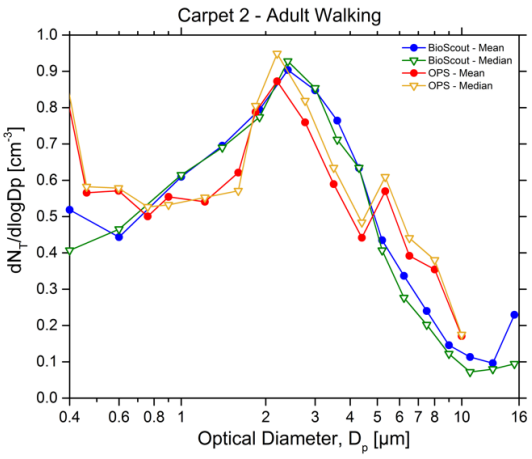
Carpet 2 - Adult Walking
BioScout - Mean
BioScout - Median
OPS - Mean
OPS - Median
dN_T/dlogDp [cm^-3]
Optical Diameter, D_p [µm]

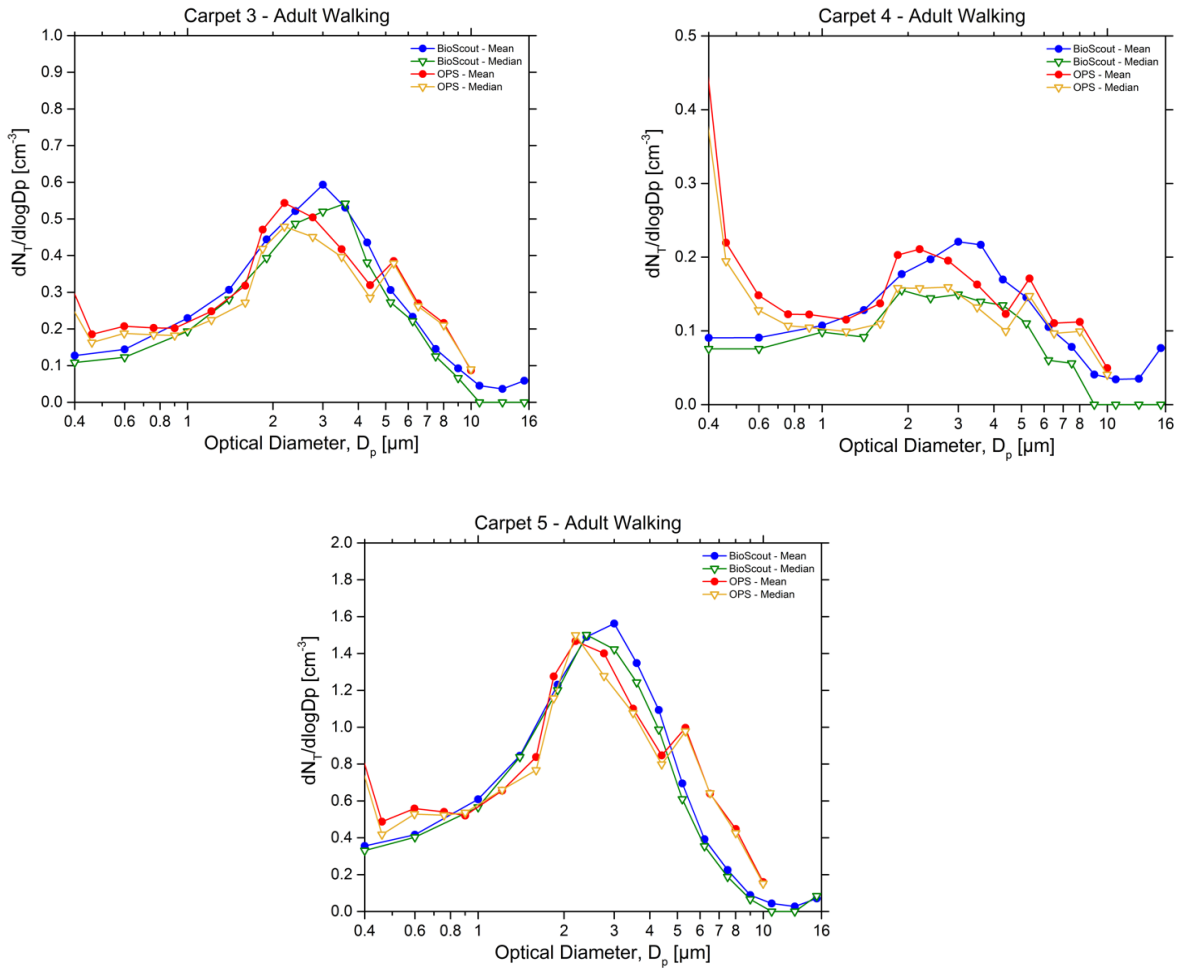

Figure B.3 Median and mean total particle size distributions as measured by the BioScout and OPS during the resuspension periods in the crawling and walking experiments on all five carpets. The size distributions measured by the OPS in the crawling experiments were re-scaled on a secondary y-axis.

Table B.1 Summary tables for the fifty crawling and walking resuspension experiments.

Carpet	Movement	Test	Path	Temperature (°C) (mean ± standard deviation)	Relative Humidity (%) (mean ± standard deviation)	BioScout											
						N_F (cm^{-3})	$N_{F,bgd}$ (cm^{-3})	N_T (cm^{-3})	$N_{T,bgd}$ (cm^{-3})	$dN_F/dlogDp$			$dN_T/dlogDp$			M_F ($\mu g\ m^{-3}$)	M_T ($\mu g\ m^{-3}$)
										$Mode_{FBAP}$			$Mode_{Total}$				
										A (cm^{-3})	D_{pg} (μm)	σ_g	A (cm^{-3})	D_{pg} (μm)	σ_g		
1	Crawling	n = 1	A	23.34 ± 0.11	25.98 ± 0.93	2.513	0.017	5.014	0.082	2.33	3.64	1.62	4.05	2.64	1.97	527.70	538.24
		n = 2	B	23.66 ± 0.08	27.18 ± 0.86	2.119	0.044	4.484	0.128	1.92	3.71	1.52	3.24	2.87	1.81	388.08	399.48
		n = 3	C	23.85 ± 0.07	27.31 ± 0.52	2.666	0.116	4.685	0.685	2.53	3.69	1.59	4.33	2.73	1.89	484.90	500.80
		n = 4	D	23.94 ± 0.05	27.46 ± 0.71	2.440	0.095	4.704	0.233	2.24	3.85	1.67	3.64	2.91	1.96	686.45	701.92
		n = 5	E	24.07 ± 0.07	26.63 ± 0.91	1.539	0.057	3.170	0.123	1.50	3.78	1.61	2.54	2.80	1.92	392.59	400.33
		Mean		23.76 ± 0.26	26.90 ± 1.52	2.255	0.066	4.411	0.250	2.11	3.73	1.61	3.76	2.69	1.99	495.94	508.16
2	Crawling	n = 6	A	23.97 ± 0.09	25.59 ± 0.57	0.958	0.048	1.466	0.181	0.75	4.06	1.68	1.06	3.42	1.95	472.00	476.50
		n = 7	B	24.14 ± 0.07	26.08 ± 0.37	0.755	0.059	1.363	0.139	0.66	3.84	1.75	1.08	2.85	2.17	270.92	276.79
		n = 8	C	24.22 ± 0.05	26.33 ± 0.31	0.871	0.075	1.742	0.197	0.77	3.75	1.65	1.31	2.74	1.97	278.72	283.25
		n = 9	D	24.29 ± 0.06	26.61 ± 0.60	0.871	0.095	1.963	0.219	0.79	3.73	1.68	1.55	2.46	2.07	263.31	269.98
		n = 10	E	24.30 ± 0.09	25.75 ± 0.24	0.877	0.045	1.630	0.142	0.78	3.90	1.66	1.27	2.97	1.98	261.00	265.38
		Mean		24.2 ± 0.14	26.17 ± 0.61	0.866	0.065	1.633	0.176	0.76	3.93	1.71	1.32	2.75	2.13	309.19	314.38
3	Crawling	n = 11	A	22.96 ± 0.01	23.23 ± 0.06	0.773	0.020	1.015	0.053	0.63	5.01	1.75	0.82	4.58	2.06	414.69	416.49
		n = 12	B	22.95 ± 0.01	23.77 ± 0.13	0.661	0.006	0.934	0.019	0.58	4.22	1.71	0.79	3.62	2.02	221.79	223.05
		n = 13	C	22.93 ± 0.01	24.24 ± 0.09	0.617	0.025	1.145	0.082	0.56	3.96	1.66	0.71	3.42	1.84	174.96	176.33
		n = 14	D	23.82 ± 0.08	28.18 ± 0.53	1.178	0.020	1.660	0.065	1.00	4.21	1.81	1.44	3.46	2.20	497.43	501.33
		n = 15	E	24.00 ± 0.08	28.35 ± 0.38	1.221	0.071	1.683	0.129	1.09	4.23	1.73	1.32	3.74	1.90	447.56	449.75
		Mean		23.3 ± 0.48	25.40 ± 2.25	0.890	0.028	1.288	0.070	0.80	4.40	1.80	1.00	3.71	2.00	351.29	353.39
4	Crawling	n = 16	A	24.13 ± 0.07	26.78 ± 0.68	0.592	0.010	0.918	0.028	0.39	4.08	1.72	0.63	3.27	2.13	441.52	443.58
		n = 17	B	24.26 ± 0.05	27.68 ± 0.48	0.439	0.035	0.655	0.089	0.27	4.97	1.72	0.43	4.16	2.34	384.86	386.97
		n = 18	C	24.36 ± 0.04	28.75 ± 0.69	0.474	0.048	0.737	0.088	0.28	3.95	1.60	0.48	3.18	1.98	385.68	387.85
		n = 19	D	24.41 ± 0.06	28.77 ± 0.37	0.502	0.030	0.696	0.075	0.28	4.67	1.87	0.57	3.94	3.23	503.03	504.83
		n = 20	E	24.50 ± 0.03	29.01 ± 0.24	0.430	0.037	0.647	0.075	0.26	4.70	1.89	0.45	3.64	2.64	402.42	404.30
		Mean		24.32 ± 0.14	28.10 ± 1.03	0.488	0.032	0.731	0.071	0.29	4.42	1.72	0.48	3.34	2.25	423.50	425.51
5	Crawling	n = 21	A	24.29 ± 0.08	26.51 ± 0.33	1.026	0.022	1.640	0.114	0.91	3.46	1.56	1.31	2.96	1.71	220.95	226.42
		n = 22	B	24.46 ± 0.05	27.37 ± 0.54	1.422	0.110	2.547	0.207	1.27	3.37	1.57	1.97	2.77	1.73	288.81	295.39
		n = 23	C	24.56 ± 0.05	28.05 ± 0.49	1.644	0.066	2.961	0.137	1.50	3.42	1.57	2.30	2.80	1.74	305.74	314.62

		n = 24	D	24.66 ± 0.05	28.37 ± 0.23	2.329	0.124	4.038	0.260	2.15	3.46	1.55	3.17	2.89	1.72	353.03	363.65
		n = 25	E	24.73 ± 0.04	27.93 ± 0.04	3.216	0.149	5.450	0.276	2.93	3.43	1.59	4.22	2.87	1.76	616.70	627.59
		Mean		24.52 ± 0.16	27.61 ± 0.79	1.928	0.094	3.327	0.199	1.63	3.43	1.57	2.24	2.86	1.73	357.04	365.53

Carpet	Movement	Test	Path	OPS										IOM Data		
								dN/dlogDp						Avg. PM_{100} (µg/m^3)		
								Mode 1			Mode 2					
				N_T (cm^{-3})	$N_{T,bgd}$ (cm^{-3})	Avg. $PM_{2.5}$ (µg/m^3)	Avg. PM_{10} (µg/m3)	A (cm^{-3})	D_{pg} (µm)	σ_g	A (cm^{-3})	D_{pg} (µm)	σ_g	Infant BZ	Adult BZ	Infant BZ/ Adult BZ
1	Crawling	n = 1	A	0.983	0.035	0.963	43.355	2.56	2.90	1.60	1.18	5.90	1.20	187.76	57.95	3.24
		n = 2	B	1.026	0.049	0.807	36.823	2.15	2.90	1.60	1.03	5.80	1.20			
		n = 3	C	0.891	0.050	0.739	28.241	1.87	2.80	1.60	0.80	5.80	1.20			
		n = 4	D	0.896	0.099	0.637	42.517	2.06	3.20	1.70	0.90	6.20	1.20			
		n = 5	E	0.801	0.054	0.470	24.872	1.36	3.00	1.60	0.64	5.90	1.20			
		Mean		0.919	0.057	0.715	34.279	1.87	2.87	1.57	0.96	5.89	1.20			
2	Crawling	n = 6	A	0.118	0.073	0.154	10.810	0.57	3.30	1.70	0.18	5.80	1.10	259.03	--	--
		n = 7	B	0.365	0.054	0.250	13.071	0.47	2.50	1.40	0.58	5.80	1.30			
		n = 8	C	0.559	0.062	0.425	19.773	1.06	2.70	1.60	0.84	6.40	1.30			
		n = 9	D	0.496	0.104	0.369	12.927	0.74	2.50	1.50	0.74	6.60	1.40			
		n = 10	E	0.348	0.061	0.256	14.323	1.08	3.80	1.80	0.21	5.90	1.10			
		Mean		0.377	0.071	0.291	14.181	0.77	2.87	1.60	0.43	6.02	1.22			
3	Crawling	n = 11	A	0.147	0.022	0.111	12.009	0.37	3.20	1.50	0.31	6.10	1.20	207.57	17.73	11.7
		n = 12	B	0.142	0.009	0.123	9.925	0.31	2.90	1.50	0.27	6.10	1.20			
		n = 13	C	0.548	0.034	0.290	10.609	0.38	2.20	1.40	0.71	6.10	1.40			
		n = 14	D	0.179	0.030	0.161	13.512	0.47	3.00	1.50	0.30	5.90	1.20			
		n = 15	E	0.216	0.060	0.193	17.840	0.86	3.70	1.80	0.28	5.90	1.10			
		Mean		0.247	0.031	0.175	12.779	0.47	2.96	1.60	0.36	6.03	1.22			
4	Crawling	n = 16	A	0.226	0.013	0.200	12.837	0.59	3.00	1.60	0.34	6.00	1.20	306.63	149.93	2.05
		n = 17	B	0.089	0.035	0.067	4.630	0.14	2.70	1.40	0.14	5.90	1.20			
		n = 18	C	0.136	0.033	0.110	7.829	0.34	3.00	1.70	0.15	6.20	1.20			
		n = 19	D	0.234	0.037	0.170	19.901	0.51	3.20	1.60	0.44	6.10	1.20			

		n = 20	E	0.199	0.039	0.158	14.011	0.42	3.10	1.60	0.34	6.10	1.20			
		Mean		0.177	0.031	0.141	11.842	0.37	2.92	1.53	0.32	6.10	1.22			
5	Crawling	n = 21	A	0.688	0.051	0.783	43.342	2.27	3.00	1.50	1.38	5.80	1.20	86.76	67.79	1.28
		n = 22	B	0.935	0.076	1.100	47.959	2.99	2.90	1.50	1.59	5.80	1.20			
		n = 23	C	1.399	0.060	1.578	72.060	4.20	2.90	1.50	2.38	5.80	1.20			
		n = 24	D	1.754	0.113	2.014	90.030	5.09	2.80	1.50	4.39	6.20	1.30			
		n = 25	E	2.212	0.113	2.623	114.169	7.08	2.90	1.50	3.98	5.90	1.20			
		Mean		1.398	0.082	1.508	68.995	3.76	2.80	1.48	3.06	5.97	1.27			

Carpet	Movement	Test	Path	Temperature (°C) (mean ± standard deviation)	Relative Humidity (%) (mean ± standard deviation)	BioScout											
						N_F (cm^{-3})	$N_{F,bgd}$ (cm^{-3})	N_T (cm^{-3})	$N_{T,bgd}$ (cm^{-3})	$dN_F/dlogDp$			$dN_T/dlogDp$			M_F ($\mu g\ m^{-3}$)	M_T ($\mu g\ m^{-3}$)
										$Mode_{FBAP}$			$Mode_{Total}$				
										A (cm^{-3})	D_{pg} (μm)	σ_g	A (cm^{-3})	D_{pg} (μm)	σ_g		
1	Walking	n = 26	A	24.26 ± 0.04	21.43 ± 0.33	1.601	0.016	3.952	0.037	1.53	3.18	1.52	2.79	2.38	1.73	149.36	156.47
		n = 27	B	24.43 ± 0.04	22.05 ± 0.44	0.970	0.150	2.592	0.375	0.93	3.29	1.51	1.88	2.30	1.80	88.44	94.67
		n = 28	C	24.45 ± 0.02	21.64 ± 0.38	0.864	0.030	2.036	0.096	0.84	3.23	1.56	1.39	2.49	1.75	100.59	103.99
		n = 29	D	24.59 ± 0.02	21.76 ± 0.34	0.564	0.038	1.227	0.125	0.52	3.30	1.51	0.84	2.65	1.69	62.84	65.27
		n = 30	E	24.61 ± 0.03	21.49 ± 0.27	0.726	0.070	1.629	0.166	0.71	3.51	1.60	1.27	2.52	1.87	95.40	99.09
		Mean		24.47 ± 0.13	21.67 ± 0.41	0.945	0.061	2.287	0.160	0.92	3.27	1.55	1.65	2.42	1.78	99.33	103.90
2	Walking	n = 31	A	23.95 ± 0.07	16.02 ± 0.38	--	--	--	--	--	--	--	--	--	--	--	
		n = 32	B	24.07 ± 0.2	16.46 ± 0.60	0.841	0.071	1.876	0.146	0.75	3.35	1.60	1.31	2.50	1.87	167.53	171.06
		n = 33	C	24.14 ± 0.02	16.43 ± 0.46	0.876	0.099	1.784	0.239	0.83	3.50	1.64	1.38	2.61	1.93	150.09	153.81
		n = 34	D	24.20 ± 0.03	16.38 ± 0.34	1.169	0.142	2.564	0.306	1.02	3.43	1.66	1.82	2.42	2.00	292.15	297.38
		n = 35	E	24.31 ± 0.03	16.23 ± 0.12	0.824	0.171	1.639	0.386	0.78	3.32	1.65	1.30	2.49	1.88	156.94	162.19
		Mean		24.13 ± 0.13	16.30 ± 0.43	0.927	0.121	1.966	0.269	0.86	3.41	1.66	1.45	2.50	1.93	191.68	196.11
3	Walking	n = 36	A	24.32 ± 0.07	30.26 ± 0.70	0.496	0.004	0.746	0.014	0.45	3.47	1.61	0.61	3.04	1.74	86.79	88.65
		n = 37	B	24.51 ± 0.05	30.92 ± 0.48	0.647	0.052	1.056	0.093	0.60	3.31	1.54	0.81	2.89	1.71	59.54	61.20
		n = 38	C	24.62 ± 0.07	30.79 ± 0.27	0.454	0.095	0.659	0.165	0.46	3.50	1.77	0.58	3.02	1.86	73.95	75.05
		n = 39	D	24.66 ± 0.03	30.84 ± 0.39	0.673	0.058	1.110	0.095	0.65	3.25	1.61	0.89	2.76	1.78	76.25	77.94
		n = 40	E	24.72 ± 0.03	31.16 ± 0.44	0.836	0.062	1.384	0.114	0.83	3.33	1.60	1.15	2.80	1.73	83.64	86.10
		Mean		24.57 ± 0.15	30.79 ± 0.54	0.621	0.054	0.991	0.096	0.60	3.37	1.63	0.82	2.86	1.78	76.03	77.79
4	Walking	n = 41	A	24.09 ± 0.05	19.07 ± 0.20	0.199	0.028	0.346	0.078	0.19	4.05	1.72	0.30	3.03	1.98	49.83	50.85

		n = 42	B	24.26 ± 0.05	19.11 ± 0.50	0.175	0.031	0.353	0.077	0.14	3.67	1.58	0.27	2.68	1.94	59.17	60.65
		n = 43	C	24.31 ± 0.04	18.93 ± 0.47	0.166	0.036	0.337	0.085	0.14	3.94	1.54	0.23	3.10	1.92	41.70	42.68
		n = 44	D	24.44 ± 0.02	18.92 ± 0.73	0.181	0.010	0.386	0.023	0.16	4.06	1.54	0.28	3.02	1.92	42.32	43.39
		n = 45	E	24.54 ± 0.02	20.23 ± 0.62	0.461	0.043	0.850	0.098	0.42	3.70	1.62	0.65	2.91	1.78	113.95	116.26
		Mean		24.33 ± 0.16	19.25 ± 0.71	0.236	0.030	0.454	0.072	0.20	3.78	1.57	0.35	2.92	1.88	61.40	62.77
5	Walking	n = 46	A	24.48 ± 0.06	28.21 ± 0.39	0.909	0.027	1.699	0.086	0.88	3.07	1.58	1.36	2.52	1.73	91.55	95.27
		n = 47	B	24.55 ± 0.03	28.21 ± 0.53	1.359	0.109	2.223	0.214	1.30	3.31	1.52	1.86	2.81	1.65	115.01	119.42
		n = 48	C	24.55 ± 0.04	28.82 ± 0.18	1.732	0.126	2.945	0.215	1.69	3.26	1.57	2.41	2.74	1.69	131.04	136.89
		n = 49	D	24.67 ± 0.04	28.30 ± 0.16	1.778	0.244	3.071	0.434	1.68	3.27	1.49	2.30	2.86	1.58	127.24	134.05
		n = 50	E	24.80 ± 0.01	28.62 ± 0.28	1.424	0.229	2.617	0.376	1.42	3.17	1.55	2.06	2.64	1.67	86.10	90.86
		Mean		24.61 ± 0.12	28.67 ± 0.54	1.440	0.147	2.511	0.265	1.40	3.23	1.54	1.93	2.79	1.64	110.19	115.30

Carpet	Movement	Test	Path	OPS										IOM Data		
								dN/dlogDp						Avg. PM_{100} ($\mu g/m^3$)		
								Mode 1			Mode 2					
				N_T (cm^{-3})	$N_{T,bgd}$ (cm^{-3})	Avg. $PM_{2.5}$ ($\mu g/m^3$)	Avg. PM_{10} ($\mu g/m^3$)	A (cm^{-3})	D_{pg} (μm)	σ_g	A (cm^{-3})	D_{pg} (μm)	σ_g	Infant BZ	Adult BZ	Infant BZ/ Adult BZ
1	Walking	n = 26	A	2.119	0.057	2.589	54.665	5.30	2.50	1.50	2.97	5.80	1.30	21.96	52.50	0.42
		n = 27	B	1.450	0.316	1.771	34.254	4.06	2.60	1.60	1.16	5.80	1.20			
		n = 28	C	1.103	0.130	1.315	30.170	2.65	2.50	1.50	1.54	5.90	1.30			
		n = 29	D	0.646	0.157	0.761	20.760	1.62	2.60	1.50	0.71	5.70	1.20			
		n = 30	E	0.888	0.164	1.058	26.842	2.57	2.70	1.60	0.89	5.80	1.20			
		Mean		1.241	0.165	1.499	33.338	3.24	2.58	1.53	1.34	5.73	1.22			
2	Walking	n = 31	A	0.673	0.288	0.737	32.449	1.82	2.80	1.50	1.08	5.90	1.20	52.04	37.90	1.37
		n = 32	B	0.989	0.241	1.113	37.335	2.67	2.70	1.60	1.19	5.90	1.20			
		n = 33	C	0.984	0.271	1.077	39.565	2.76	2.80	1.60	1.18	5.90	1.20			
		n = 34	D	0.959	0.362	1.072	38.676	2.68	2.80	1.60	1.25	5.80	1.20			
		n = 35	E	0.850	0.413	0.951	38.862	2.12	2.70	1.50	1.36	5.80	1.20			
		Mean		0.891	0.315	0.990	37.377	2.54	2.83	1.59	1.07	5.87	1.18			
3	Walking	n = 36	A	0.324	0.212	0.393	17.628	1.07	2.90	1.50	0.65	5.90	1.20	68.52	35.80	1.91
		n = 37	B	0.501	0.103	0.614	23.078	1.55	2.80	1.50	0.85	5.80	1.20			

		n = 38	C	0.266	0.178	0.304	17.783	1.12	3.30	1.60	0.50	6.10	1.20			
		n = 39	D	0.538	0.120	0.647	23.198	1.67	2.80	1.50	0.91	5.80	1.20			
		n = 40	E	0.716	0.131	0.896	32.782	2.36	2.90	1.50	1.15	5.90	1.20			
		Mean		0.469	0.149	0.571	22.894	1.55	2.90	1.52	0.86	5.92	1.22			
4	Walking	n = 41	A	0.174	0.028	0.188	9.484	0.47	2.80	1.50	0.33	5.80	1.20	27.03	17.03	1.59
		n = 42	B	0.180	0.039	0.158	6.552	0.42	2.80	1.60	0.22	5.70	1.20			
		n = 43	C	0.210	0.036	0.161	8.049	0.44	2.90	1.60	0.25	5.90	1.20			
		n = 44	D	0.317	0.008	0.183	9.543	0.51	3.00	1.60	0.29	5.90	1.20			
		n = 45	E	0.487	0.045	0.500	21.081	1.22	2.80	1.50	0.68	5.80	1.20			
		Mean		0.274	0.031	0.238	10.942	0.67	2.95	1.59	1.09	5.82	1.17			
5	Walking	n = 46	A	0.739	0.040	1.055	28.942	2.66	2.80	1.50	1.11	5.80	1.20	78.56	69.95	1.12
		n = 47	B	1.050	0.089	1.233	50.745	3.67	3.00	1.50	1.99	5.90	1.20			
		n = 48	C	1.459	0.094	1.719	64.747	4.81	2.90	1.50	2.48	5.80	1.20			
		n = 49	D	1.521	0.169	1.965	62.614	4.11	2.60	1.40	3.95	5.70	1.30			
		n = 50	E	1.374	0.150	1.699	49.064	4.26	2.80	1.50	2.06	5.70	1.20			
		Mean		0.916	0.109	1.534	51.223	3.35	2.64	1.42	3.17	5.79	1.31			

Notes:

N_F: Averaged size-integrated (0.4-15.4 μm) FBAP number concentration measured during the 20-minute resuspension periods.

N_T: Averaged size-integrated (0.4-15.4 μm for the BioScout, 1-11.2 μm for the OPS) total particle number concentration measured during the 20-minute resuspension periods.

$N_{F,bgd}$: Averaged size-integrated (0.4-15.4 μm) FBAP number concentration measured during the 10 minute background periods.

$N_{T,bgd}$: Averaged size-integrated (0.4-15.4 μm for the BioScout, 1-11.2 μm for the OPS) total particle number concentration measured during the 10 minute background periods.

M_F: Averaged size-integrated (0.4-15.4 μm) FBAP mass concentration measured during the 20-minute resuspension periods.

M_T: Averaged size-integrated (0.4-15.4 μm for the BioScout) total particle mass concentration measured during the 20-minute resuspension periods.

$dN/dlogD_p$: Lognormal fitting parameters of the mean number concentration size distribution measured during the resuspension periods, including amplitude (A), modal diameter (D_{pg}), and standard deviation (σ_g).

Avg. $PM_{2.5}$: Averaged particle mass concentration (< 2.5 μm) measured during the 20-minute resuspension periods, from OPS (ρ_{eff}=1.204 g cm^{-3}).

Avg. PM_{10}: Averaged particle mass concentration (< 10 μm) measured during the 20-minute resuspension periods, from OPS (ρ_{eff}=1.204 g cm^{-3}).

Avg. PM100: Averaged particle mass concentration (< 100 μm) over all five paths on each carpet measured during the resuspension periods (100 minute in total), from IOM.

REFERENCES

(1) Hussein, T.; Puustinen, A.; Aalto, P. P.; Mäkelä, J. M.; Hämeri, K.; Kulmala, M. Urban Aerosol Number Size Distributions. *Atmos. Chem. Phys. Discuss.* **2003**, *3* (5), 5139–5184. https://doi.org/10.5194/acpd-3-5139-2003.

(2) Harrison, R. M.; Beddows, D. C. S.; Dall'Osto, M. PMF Analysis of Wide-Range Particle Size Spectra Collected on a Major Highway. *Environ. Sci. Technol.* **2011**, *45* (13), 5522–5528.

(3) Vu, T. V.; Delgado-Saborit, J. M.; Harrison, R. M. Review: Particle Number Size Distributions from Seven Major Sources and Implications for Source Apportionment Studies. *Atmos. Environ.* **2015**, *122*, 114–132. https://doi.org/10.1016/j.atmosenv.2015.09.027.

(4) Wu, Z.; Hu, M.; Lin, P.; Liu, S.; Wehner, B.; Wiedensohler, A. Particle Number Size Distribution in the Urban Atmosphere of Beijing, China. *Atmos. Environ.* **2008**, *42* (34), 7967–7980. https://doi.org/10.1016/j.atmosenv.2008.06.022.

(5) Peng, J. F.; Hu, M.; Wang, Z. B.; Huang, X. F.; Kumar, P.; Wu, Z. J.; Guo, S.; Yue, D. L.; Shang, D. J.; Zheng, Z.; et al. Submicron Aerosols at Thirteen Diversified Sites in China: Size Distribution, New Particle Formation and Corresponding Contribution to Cloud Condensation Nuclei Production. *Atmos. Chem. Phys.* **2014**, *14* (18), 10249–10265. https://doi.org/10.5194/acp-14-10249-2014.

(6) Shiraiwa, M.; Ueda, K.; Pozzer, A.; Lammel, G.; Kampf, C. J.; Fushimi, A.; Enami, S.; Arangio, A. M.; Fröhlich-Nowoisky, J.; Fujitani, Y.; et al. Aerosol Health Effects from Molecular to Global Scales. *Environ. Sci. Technol.* **2017**, acs.est.7b04417. https://doi.org/10.1021/acs.est.7b04417.

(7) Azimi, P.; Zhao, D.; Stephens, B. Estimates of HVAC Filtration Efficiency for Fine and Ultrafine Particles of Outdoor Origin. *Atmos. Environ.* **2014**, *98*, 337–346. https://doi.org/10.1016/j.atmosenv.2014.09.007.

(8) Asmi, A.; Wiedensohler, A.; Laj, P.; Fjaeraa, A. M.; Sellegri, K.; Birmili, W.; Weingartner, E.; Baltensperger, U.; Zdimal, V.; Zikova, N.; et al. Number Size Distributions and Seasonality of Submicron Particles in Europe 2008-2009. *Atmos. Chem. Phys.* **2011**, *11* (11), 5505–5538. https://doi.org/10.5194/acp-11-5505-2011.

(9) Morawska, L.; Thomas, S.; Bofinger, N.; Wainwright, D.; Neale, D. Comprehensive Characterization of Aerosols in a Subtropical Urban Atmosphere: Particle Size Distribution and Correlation with Gaseous Pollutants. *Atmos. Environ.* **1998**, *32* (14–15), 2467–2478. https://doi.org/10.1016/S1352-2310(98)00023-5.

(10) Shi, J. P.; Khan, A. A.; Harrison, R. M. Measurements of Ultrafine Particle Concentration and Size Distribution in the Urban Atmosphere. *Sci. Total Environ.* **1999**, *235* (1–3), 51–64. https://doi.org/10.1016/S0048-9697(99)00189-8.

(11) Allen, J. L.; Oberdorster, G.; Morris-Schaffer, K.; Wong, C.; Klocke, C.; Sobolewski, M.; Conrad, K.; Mayer-Proschel, M.; Cory-Slechta, D. A. Developmental Neurotoxicity of Inhaled Ambient Ultrafine Particle Air Pollution: Parallels with Neuropathological and Behavioral Features of Autism and Other Neurodevelopmental Disorders. *Neurotoxicology* **2017**, *59*, 140–154. https://doi.org/10.1016/j.neuro.2015.12.014.

(12) Sioutas, C.; Delfino, R. J.; Singh, M. Exposure Assessment for Atmospheric Ultrafine Particles (UFPs) and Implications in Epidemiologic Research. *Environ. Health Perspect.* **2005**, *113* (8), 947–955. https://doi.org/10.1289/ehp.7939.

(13) Meldrum, K.; Guo, C.; Marczylo, E. L.; Gant, T. W.; Smith, R.; Leonard, M. O. Mechanistic Insight into the Impact of Nanomaterials on Asthma and Allergic Airway Disease. *Part. Fibre Toxicol.* **2017**, *14* (1), 1–35. https://doi.org/10.1186/s12989-017-0228-y.

(14) Oberdörster, G.; Oberdörster, E.; Oberdörster, J. Nanotoxicology: An Emerging Discipline Evolving from Studies of Ultrafine Particles. *Environ. Health Perspect.* **2005**, *113* (7), 823–839. https://doi.org/10.1289/ehp.7339.

(15) Rychlik, K. A.; Secrest, J. R.; Lau, C.; Pulczinski, J.; Zamora, M. L.; Leal, J.; Langley, R.; Myatt, L. G.; Raju, M.; Chang, R. C.-A. In Utero Ultrafine Particulate Matter Exposure Causes Offspring Pulmonary Immunosuppression. *Proc. Natl. Acad. Sci.* **2019**, *116* (9), 3443–3448.

(16) Burnett, R.; Chen, H.; Szyszkowicz, M.; Fann, N.; Hubbell, B.; Pope, C. A.; Apte, J. S.; Brauer, M.; Cohen, A.; Weichenthal, S. Global Estimates of Mortality Associated with Long-Term Exposure to Outdoor Fine Particulate Matter. *Proc. Natl. Acad. Sci.* **2018**, *115* (38), 9592–9597.

(17) Delfino, R. J.; Sioutas, C.; Malik, S. Potential Role of Ultrafine Particles in Associations between Airborne Particle Mass and Cardiovascular Health. *Environ. Health Perspect.* **2005**, *113* (8), 934–946. https://doi.org/10.1289/ehp.7938.

(18) Seinfeld, J. H.; Pandis, S. N. *Atmospheric Chemistry and Physics: From Air Pollution to Climate Change*; John Wiley & Sons, 2012.

(19) Hinds, W. C. *Aerosol Technology: Properties, Behavior, and Measurement of Airborne Particles*; John Wiley & Sons, 2012.

(20) Barros, P. M.; Tanabe, E. H.; Aguiar, M. L. Performance of Fibrous Filters during Nanoparticle Cake Formation. *Sep. Sci. Technol.* **2016**, *51* (6), 1042–1052. https://doi.org/10.1080/01496395.2015.1119845.

(21) Gac, J. M.; Jackiewicz, A.; Werner, Ł.; Jakubiak, S. Consecutive Filtration of Solid Particles and Droplets in Fibrous Filters. *Sep. Purif. Technol.* **2016**, *170*, 234–240. https://doi.org/10.1016/j.seppur.2016.06.057.

(22) Kasper, G.; Schollmeier, S.; Meyer, J. Structure and Density of Deposits Formed on Filter Fibers by Inertial Particle Deposition and Bounce. *J. Aerosol Sci.* **2010**, *41* (12), 1167–1182.

(23) Stephens, B.; Novoselac, A.; Siegel, J. A. The Effects of Filtration on Pressure Drop and Energy Consumption in Residential HVAC Systems (RP-1299). *Hvac&R Res.* **2010**, *16* (3), 273–294.

(24) Zaatari, M.; Novoselac, A.; Siegel, J. The Relationship between Filter Pressure Drop, Indoor Air Quality, and Energy Consumption in Rooftop HVAC Units. *Build. Environ.* **2014**, *73*, 151–161. https://doi.org/10.1016/j.buildenv.2013.12.010.

(25) He, X.; Brem, B. T.; Bahk, Y. K.; Kuo, Y. Y.; Wang, J. Effects of Relative Humidity and Particle Type on the Performance and Service Life of Automobile Cabin Air Filters. *Aerosol Sci. Technol.* **2016**, *50* (6), 542–554. https://doi.org/10.1080/02786826.2016.1167832.

(26) Tronville, P.; Rivers, R. D. International Standards: Filters for Vehicular Applications. *Filtr. Sep.* **2005**, *42* (9), 24–27.

(27) ASHRAE. *ANSI/ASHRAE Standard 52.2-2017: Method of Testing General Ventilation Air-Cleaning Devices for Removal Efficiency by Particle Size*; American Society of Heating, Refrigerating and Air-Conditioning Engineers, Inc.: Atlanta, 2017.

(28) Hussein, T.; Puustinen, A.; Aalto, P. P.; Mäkelä, J. M.; Hämeri, K.; Kulmala, M. Urban Aerosol Number Size Distributions. *Atmos. Chem. Phys.* **2004**, *4* (2), 391–411.

(29) Stephens, B. Evaluating the Sensitivity of the Mass-Based Particle Removal Calculations for HVAC Filters in ISO 16890 to Assumptions for Aerosol Distributions. *Atmosphere (Basel)*. **2018**, *9* (3). https://doi.org/10.3390/atmos9030085.

(30) Fazli, T.; Zeng, Y.; Stephens, B. Fine and Ultrafine Particle Removal Efficiency of New Residential HVAC Filters. *Indoor Air* **2019**, *29* (4), 656–669.

(31) Tronville, P.; Rivers, R. D. Global Standards for Filter Testing. *ASHRAE J.* **2006**, *48* (8), 58.

(32) Valmari, T.; Lehtimäki, M.; Taipale, A. Filter Clogging by Bimodal Aerosol. *Aerosol Sci. Technol.* **2006**, *40* (4), 255–260. https://doi.org/10.1080/02786820500543282.

(33) Fröhlich-Nowoisky, J.; Kampf, C. J.; Weber, B.; Huffman, J. A.; Pöhlker, C.; Andreae, M. O.; Lang-Yona, N.; Burrows, S. M.; Gunthe, S. S.; Elbert, W. Bioaerosols in the Earth System: Climate, Health, and Ecosystem Interactions. *Atmos. Res.* **2016**, *182*, 346–376.

(34) Després, V.; Huffman, J. A.; Burrows, S. M.; Hoose, C.; Safatov, A.; Buryak, G.; Fröhlich-Nowoisky, J.; Elbert, W.; Andreae, M.; Pöschl, U. Primary Biological Aerosol Particles in the Atmosphere: A Review. *Tellus B Chem. Phys. Meteorol.* **2012**, *64* (1), 15598.

(35) Torrent, M.; Sunyer, J.; Muñoz, L.; Cullinan, P.; Iturriaga, M. V.; Figueroa, C.; Vall, O.; Taylor, A. N.; Anto, J. M. Early-Life Domestic Aeroallergen Exposure and IgE Sensitization at Age 4 Years. *J. Allergy Clin. Immunol.* **2006**, *118* (3), 742–748.

(36) Sporik, R.; Holgate, S. T.; Platts-Mills, T. A. E.; Cogswell, J. J. Exposure to House-Dust Mite Allergen (Der p I) and the Development of Asthma in Childhood: A Prospective Study. *N. Engl. J. Med.* **1990**, *323* (8), 502–507.

(37) Méheust, D.; Le Cann, P.; Reboux, G.; Millon, L.; Gangneux, J.-P. Indoor Fungal Contamination: Health Risks and Measurement Methods in Hospitals, Homes and Workplaces. *Crit. Rev. Microbiol.* **2014**, *40* (3), 248–260.

(38) Calderón, M. A.; Linneberg, A.; Kleine-Tebbe, J.; De Blay, F.; de Rojas, D. H. F.; Virchow, J. C.; Demoly, P. Respiratory Allergy Caused by House Dust Mites: What Do We Really Know? *J. Allergy Clin. Immunol.* **2015**, *136* (1), 38–48.

(39) Denning, D. W.; O'driscoll, B. R.; Hogaboam, C. M.; Bowyer, P.; Niven, R. M. The Link between Fungi and Severe Asthma: A Summary of the Evidence. *Eur. Respir. J.* **2006**, *27* (3), 615–626.

(40) Dannemiller, K. C.; Gent, J. F.; Leaderer, B. P.; Peccia, J. Influence of Housing Characteristics on Bacterial and Fungal Communities in Homes of Asthmatic Children. *Indoor Air* **2016**, *26* (2), 179–192.

(41) Thorne, P. S.; Kulhánková, K.; Yin, M.; Cohn, R.; Arbes Jr, S. J.; Zeldin, D. C. Endotoxin Exposure Is a Risk Factor for Asthma: The National Survey of Endotoxin in United States Housing. *Am. J. Respir. Crit. Care Med.* **2005**, *172* (11), 1371–1377.

(42) Von Mutius, E.; Vercelli, D. Farm Living: Effects on Childhood Asthma and Allergy. *Nat. Rev. Immunol.* **2010**, *10* (12), 861–868.

(43) Valkonen, M.; Wouters, I. M.; Täubel, M.; Rintala, H.; Lenters, V.; Vasara, R.; Genuneit, J.; Braun-Fahrländer, C.; Piarroux, R.; Von Mutius, E. Bacterial Exposures and Associations with Atopy and Asthma in Children. *PLoS One* **2015**, *10* (6).

(44) Dannemiller, K. C.; Mendell, M. J.; Macher, J. M.; Kumagai, K.; Bradman, A.; Holland, N.; Harley, K.; Eskenazi, B.; Peccia, J. Next-generation DNA Sequencing Reveals That Low Fungal Diversity in House Dust Is Associated with Childhood Asthma Development. *Indoor Air* **2014**, *24* (3), 236–247.

(45) Tovey, E. R.; Almqvist, C.; Li, Q.; Crisafulli, D.; Marks, G. B. Nonlinear Relationship of Mite Allergen Exposure to Mite Sensitization and Asthma in a Birth Cohort. *J. Allergy Clin. Immunol.* **2008**, *122* (1), 114–118.

(46) Tischer, C.; Weikl, F.; Probst, A. J.; Standl, M.; Heinrich, J.; Pritsch, K. Urban Dust Microbiome: Impact on Later Atopy and Wheezing. *Environ. Health Perspect.* **2016**, *124* (12), 1919–1923.

(47) Stein, M. M.; Hrusch, C. L.; Gozdz, J.; Igartua, C.; Pivniouk, V.; Murray, S. E.; Ledford, J. G.; Marques dos Santos, M.; Anderson, R. L.; Metwali, N. Innate Immunity and Asthma Risk in Amish and Hutterite Farm Children. *N. Engl. J. Med.* **2016**, *375* (5), 411–421.

(48) Peters, M.; Kauth, M.; Scherner, O.; Gehlhar, K.; Steffen, I.; Wentker, P.; von Mutius, E.; Holst, O.; Bufe, A. Arabinogalactan Isolated from Cowshed Dust Extract Protects Mice from Allergic Airway Inflammation and Sensitization. *J. Allergy Clin. Immunol.* **2010**, *126* (3), 648–656.

(49) Lawson, J. A.; Dosman, J. A.; Rennie, D. C.; Beach, J. R.; Newman, S. C.; Crowe, T.; Senthilselvan, A. Endotoxin as a Determinant of Asthma and Wheeze among Rural Dwelling Children and Adolescents: A Case–Control Study. *BMC Pulm. Med.* **2012**, *12* (1), 56.

(50) Lynch, S. V; Wood, R. A.; Boushey, H.; Bacharier, L. B.; Bloomberg, G. R.; Kattan, M.; O'Connor, G. T.; Sandel, M. T.; Calatroni, A.; Matsui, E. Effects of Early-Life Exposure to Allergens and Bacteria on Recurrent Wheeze and Atopy in Urban Children. *J. Allergy Clin. Immunol.* **2014**, *134* (3), 593–601.

(51) Ege, M. J.; Mayer, M.; Schwaiger, K.; Mattes, J.; Pershagen, G.; Van Hage, M.; Scheynius, A.; Bauer, J.; Von Mutius, E. Environmental Bacteria and Childhood Asthma. *Allergy* **2012**, *67* (12), 1565–1571.

(52) Ege, M. J.; Mayer, M.; Normand, A.-C.; Genuneit, J.; Cookson, W. O. C. M.; Braun-Fahrländer, C.; Heederik, D.; Piarroux, R.; von Mutius, E. Exposure to Environmental Microorganisms and Childhood Asthma. *N. Engl. J. Med.* **2011**, *364* (8), 701–709.

(53) Qian, J.; Peccia, J.; Ferro, A. R. Walking-Induced Particle Resuspension in Indoor Environments. *Atmos. Environ.* **2014**, *89*, 464–481.

(54) DeCarlo, P. F.; Slowik, J. G.; Worsnop, D. R.; Davidovits, P.; Jimenez, J. L. Particle Morphology and Density Characterization by Combined Mobility and Aerodynamic Diameter Measurements. Part 1: Theory. *Aerosol Sci. Technol.* **2004**, *38* (12), 1185–1205.

(55) Hu, M.; Peng, J.; Sun, K.; Yue, D.; Guo, S.; Wiedensohler, A.; Wu, Z. Estimation of Size-Resolved Ambient Particle Density Based on the Measurement of Aerosol Number, Mass, and Chemical Size Distributions in the Winter in Beijing. *Environ. Sci. Technol.* **2012**, *46* (18), 9941–9947. https://doi.org/10.1021/es204073t.

(56) McMurry, P. H.; Wang, X.; Park, K.; Ehara, K. The Relationship between Mass and Mobility for Atmospheric Particles: A New Technique for Measuring Particle Density. *Aerosol Sci. Technol.* **2002**, *36* (2), 227–238. https://doi.org/10.1080/027868202753504083.

(57) Qiao, K.; Wu, Z.; Pei, X.; Liu, Q.; Shang, D.; Zheng, J.; Du, Z.; Zhu, W.; Wu, Y.; Lou, S.; et al. Size-Resolved Effective Density of Submicron Particles during Summertime in the Rural Atmosphere of Beijing, China. *J. Environ. Sci. (China)* **2018**, No. February. https://doi.org/10.1016/j.jes.2018.01.012.

(58) Allen, M. D.; Raabe, O. G. Re-Evaluation of Millikan's Oil Drop Data for the Motion of Small Particles in Air. *J. Aerosol Sci.* **1982**, *13* (6), 537–547.

(59) Allen, M. D.; Raabe, O. G. Slip Correction Measurements of Spherical Solid Aerosol Particles in an Improved Millikan Apparatus. *Aerosol Sci. Technol.* **1985**, *4* (3), 269–286.

(60) Guo, S.; Hu, M.; Wang, Z. B.; Slanina, J.; Zhao, Y. L. Size-Resolved Aerosol Water-Soluble Ionic Compositions in the Summer of Beijing: Implication of Regional Secondary Formation. *Atmos. Chem. Phys.* **2010**, *10* (3), 947–959. https://doi.org/10.5194/acp-10-947-2010.

(61) Zhang, W.; Zhuang, G.; Guo, J.; Xu, D.; Wang, W.; Baumgardner, D.; Wu, Z.; Yang, W. Sources of Aerosol as Determined from Elemental Composition and Size Distributions in Beijing. *Atmos. Res.* **2010**, *95* (2–3), 197–209.

(62) Rissler, J.; Nordin, E. Z.; Eriksson, A. C.; Nilsson, P. T.; Frosch, M.; Sporre, M. K.; Wierzbicka, A.; Svenningsson, B.; Löndahl, J.; Messing, M. E.; et al. Effective Density and Mixing State of Aerosol Particles in a Near-Traffic Urban Environment. *Environ. Sci. Technol.* **2014**, *48* (11), 6300–6308. https://doi.org/10.1021/es5000353.

(63) Geller, M.; Biswas, S.; Sioutas, C. Determination of Particle Effective Density in Urban Environments with a Differential Mobility Analyzer and Aerosol Particle Mass Analyzer. *Aerosol Sci. Technol.* **2006**, *40* (9), 709–723. https://doi.org/10.1080/02786820600803925.

(64) Yin, Z.; Ye, X.; Jiang, S.; Tao, Y.; Shi, Y.; Yang, X.; Chen, J. Size-Resolved Effective Density of Urban Aerosols in Shanghai. *Atmos. Environ.* **2015**, *100*, 133–140. https://doi.org/10.1016/j.atmosenv.2014.10.055.

(65) Xie, Y.; Ye, X.; Ma, Z.; Tao, Y.; Wang, R.; Zhang, C.; Yang, X.; Chen, J.; Chen, H. Insight into Winter Haze Formation Mechanisms Based on Aerosol Hygroscopicity and Effective Density Measurements. *Atmos. Chem. Phys.* **2017**, *17* (11), 7277–7290. https://doi.org/10.5194/acp-17-7277-2017.

(66) Levy, M. E.; Zhang, R.; Khalizov, A. F.; Zheng, J.; Collins, D. R.; Glen, C. R.; Wang, Y.; Yu, X. Y.; Luke, W.; Jayne, J. T.; et al. Measurements of Submicron Aerosols in Houston, Texas during the 2009 SHARP Field Campaign. *J. Geophys. Res. Atmos.* **2013**, *118* (18), 10518–10534. https://doi.org/10.1002/jgrd.50785.

(67) Virtanen, A.; Rönkkö, T.; Kannosto, J.; Ristimäki, J.; Mäkelä, J. M.; Keskinen, J.; Pakkanen, T.; Hillamo, R.; Pirjola, L.; Hämeri, K. Winter and Summer Time Size Distributions and Densities of Traffic-Related Aerosol Particles at a Busy Highway in Helsinki. *Atmos. Chem. Phys.* **2006**, *6* (9), 2411–2421. https://doi.org/10.5194/acp-6-2411-2006.

(68) Kulmala, M.; Kontkanen, J.; Junninen, H.; Lehtipalo, K.; Manninen, H. E.; Nieminen, T.; Petaja, T.; Sipila, M.; Schobesberger, S.; Rantala, P.; et al. Direct Observations of Atmospheric Aerosol Nucleation. *Science (80-.).* **2013**, *339* (6122), 943–946. https://doi.org/10.1126/science.1227385.

(69) Wang, L.; Khalizov, A. F.; Zheng, J.; Xu, W.; Ma, Y.; Lal, V.; Zhang, R. Atmospheric Nanoparticles Formed from Heterogeneous Reactions of Organics. *Nat. Geosci.* **2010**, *3* (4), 238.

(70) Ehn, M.; Thornton, J. A.; Kleist, E.; Sipilä, M.; Junninen, H.; Pullinen, I.; Springer, M.; Rubach, F.; Tillmann, R.; Lee, B.; et al. A Large Source of Low-Volatility Secondary Organic Aerosol. *Nature* **2014**, *506* (7489), 476–479. https://doi.org/10.1038/nature13032.

(71) Tröstl, J.; Chuang, W. K.; Gordon, H.; Heinritzi, M.; Yan, C.; Molteni, U.; Ahlm, L.; Frege, C.; Bianchi, F.; Wagner, R. The Role of Low-Volatility Organic Compounds in Initial Particle Growth in the Atmosphere. *Nature* **2016**, *533* (7604), 527.

(72) Xiao, S.; Wang, M. Y.; Yao, L.; Kulmala, M.; Zhou, B.; Yang, X.; Chen, J. M.; Wang, D. F.; Fu, Q. Y.; Worsnop, D. R.; et al. Strong Atmospheric New Particle Formation in Winter in Urban Shanghai, China. *Atmos. Chem. Phys.* **2015**, *15* (4), 1769–1781. https://doi.org/10.5194/acp-15-1769-2015.

(73) Pitz, M.; Schmid, O.; Heinrich, J.; Birmili, W.; Maguhn, J.; Zimmermann, R.; Wichmann, H. E.; Peters, A.; Cyrys, J. Seasonal and Diurnal Variation of PM2.5 Apparent Particle Density in Urban Air in Augsburg, Germany. *Environ. Sci. Technol.* **2008**, *42* (14), 5087–5093.

(74) Daher, N.; Saliba, N. A.; Shihadeh, A. L.; Jaafar, M.; Baalbaki, R.; Sioutas, C. Chemical Composition of Size-Resolved Particulate Matter at near- Freeway and Urban Background Sites in the Greater Beirut Area. **2013**, *80*, 96–106.

(75) Song, S.; Wu, Y.; Jiang, J.; Yang, L.; Cheng, Y.; Hao, J. Chemical Characteristics of Size-Resolved PM2.5at a Roadside Environment in Beijing, China. *Environ. Pollut.* **2012**, *161*, 215–221. https://doi.org/10.1016/j.envpol.2011.10.014.

(76) Brüggemann, E.; Gerwig, H.; Gnauk, T.; Müller, K.; Herrmann, H. Influence of Seasons, Air Mass Origin and Day of the Week on Size-Segregated Chemical Composition of Aerosol Particles at a Kerbside. *Atmos. Environ.* **2009**, *43* (15), 2456–2463. https://doi.org/10.1016/j.atmosenv.2009.01.054.

(77) Massoli, P.; Fortner, E. C.; Canagaratna, M. R.; Williams, L. R.; Zhang, Q.; Sun, Y.; Schwab, J. J.; Trimborn, A.; Onasch, T. B.; Demerjian, K. L.; et al. Pollution Gradients and Chemical Characterization of Particulatematter from Vehicular Traffic near Major Roadways: Results from the 2009 Queens College Air Quality Study in NYC. *Aerosol Sci. Technol.* **2012**, *46* (11), 1201–1218. https://doi.org/10.1080/02786826.2012.701784.

(78) Fushimi, A.; Hasegawa, S.; Takahashi, K.; Fujitani, Y.; Tanabe, K.; Kobayashi, S. Atmospheric Fate of Nuclei-Mode Particles Estimated from the Number Concentrations and Chemical Composition of Particles Measured at Roadside and Background Sites. *Atmos. Environ.* **2008**, *42* (5), 949–959. https://doi.org/10.1016/j.atmosenv.2007.10.019.

(79) Cozic, J.; Verheggen, B.; Wiangartner, E.; Crosier, J.; Bower, K. N.; Flynn, M.; Coe, H.; Henning, S.; Steinbacher, M.; Henne, S.; et al. Chemical Composition of Free Tropospheric Aerosol for PM1 and Coarse Mode at the High Alpine Site Jungfraujoch. *Atmos. Chem. Phys.* **2008**, *8* (2), 407–423. https://doi.org/10.5194/acp-8-407-2008.

(80) Cheung, K.; Daher, N.; Kam, W.; Shafer, M. M.; Ning, Z.; Schauer, J. J.; Sioutas, C. Spatial and Temporal Variation of Chemical Composition and Mass Closure of Ambient Coarse Particulate Matter (PM10-2.5) in the Los Angeles Area. *Atmos. Environ.* **2011**, *45* (16), 2651–2662. https://doi.org/10.1016/j.atmosenv.2011.02.066.

(81) Pakkanen, T. A.; Loukkola, K.; Korhonen, C. H.; Aurela, M.; Mäkelä, T.; Hillamo, R. E.; Aarnio, P.; Koskentalo, T.; Kousa, A.; Maenhaut, W. Sources and Chemical Composition of Atmospheric Fine and Coarse Particles in the Helsinki Area. *Atmos. Environ.* **2001**, *35* (32), 5381–5391. https://doi.org/10.1016/S1352-2310(01)00307-7.

(82) Koçak, M.; Mihalopoulos, N.; Kubilay, N. Chemical Composition of the Fine and Coarse Fraction of Aerosols in the Northeastern Mediterranean. *Atmos. Environ.* **2007**, *41* (34), 7351–7368. https://doi.org/10.1016/j.atmosenv.2007.05.011.

(83) Kim, K. H.; Choi, G. H.; Kang, C. H.; Lee, J. H.; Kim, J. Y.; Youn, Y. H.; Lee, S. R. The Chemical Composition of Fine and Coarse Particles in Relation with the Asian Dust Events. *Atmos. Environ.* **2003**, *37* (6), 753–765. https://doi.org/10.1016/S1352-2310(02)00954-8.

(84) Koulouri, E.; Saarikoski, S.; Theodosi, C.; Markaki, Z.; Gerasopoulos, E.; Kouvarakis, G.; Mäkelä, T.; Hillamo, R.; Mihalopoulos, N. Chemical Composition and Sources of Fine and Coarse Aerosol Particles in the Eastern Mediterranean. *Atmos. Environ.* **2008**, *42* (26), 6542–6550. https://doi.org/10.1016/j.atmosenv.2008.04.010.

(85) Kostenidou, E.; Pandis, S. N.; Pathak, R. K.; Pandis, S. N.; Kostenidou, E.; Pandis, S. N. An Algorithm for the Calculation of Secondary Organic Aerosol Density Combining Ams and Smps Data. *Aerosol Sci. Technol.* **2007**, *41* (11), 1002–1010. https://doi.org/10.1080/02786820701666270.

(86) Malloy, Q. G. J.; Nakao, S.; Qi, L.; Austin, R.; Stothers, C.; Hagino, H.; Cocker, D. R. Real-Time Aerosol Density Determination Utilizing a Modified Scanning Mobility Particle Sizer Aerosol Particle Mass Analyzer System. *Aerosol Sci. Technol.* **2009**, *43* (7), 673–678. https://doi.org/10.1080/02786820902832960.

(87) Nakao, S.; Tang, P.; Tang, X.; Clark, C. H.; Qi, L.; Seo, E.; Asa-Awuku, A.; Cocker III, D. Density and Elemental Ratios of Secondary Organic Aerosol: Application of a Density Prediction Method. *Atmos. Environ.* **2013**, *68*, 273–277.

(88) Zelenyuk, A.; Yang, J.; Song, C.; Zaveri, R. A.; Imre, D. A New Real-Time Method for Determining Particles' Sphericity and Density: Application to Secondary Organic Aerosol Formed by Ozonolysis of α-Pinene. *Environ. Sci. Technol.* **2008**, *42* (21), 8033–8038.

(89) Neusüß, C.; Wex, H.; Birmili, W.; Wiedensohler, A.; Koziar, C.; Busch, B.; Brüggemann, E.; Gnauk, T.; Ebert, M.; Covert, D. S. Characterization and Parameterization of Atmospheric Particle Number-, Mass-, and Chemical-Size Distributions in Central Europe during LACE 98 and MINT. *J. Geophys. Res. Atmos.* **2002**, *107* (21), 1–13. https://doi.org/10.1029/2001JD000514.

(90) Tang, I. N. Chemical and Size Effects of Hygroscopic Aerosols on Light Scattering Coefficients. *J. Geophys. Res. Atmos.* **1996**, *101* (D14), 19245–19250.

(91) Mikhailov, E.; Vlasenko, S.; Rose, D.; Pöschl, U. Mass-Based Hygroscopicity Parameter Interaction Model and Measurement of Atmospheric Aerosol Water Uptake. *Atmos. Chem. Phys.* **2013**, *13* (2), 717–740. https://doi.org/10.5194/acp-13-717-2013.

(92) Lide, D. R. Physical Constant of Inorganic Compound. *Handb. Chem. Phys.* **2005**, *474*.

(93) Reid, J. S.; Jonsson, H. H.; Maring, H. B.; Smirnov, A.; Savoie, D. L.; Cliff, S. S.; Reid, E. A.; Livingston, J. M.; Meier, M. M.; Dubovik, O.; et al. Comparison of Size and Morphological Measurements of Coarse Mode Dust Particles from Africa. *J. Geophys. Res.* **2003**, *108* (D19), 8593. https://doi.org/10.1029/2002JD002485.

(94) Park, K.; Kittelson, D. B.; Zachariah, M. R.; McMurry, P. H. Measurement of Inherent Material Density of Nanoparticle Agglomerates. *J. Nanoparticle Res.* **2004**, *6* (2–3), 267–272. https://doi.org/10.1023/B:NANO.0000034657.71309.e6.

(95) Abramson, E.; Imre, D.; Beránek, J.; Wilson, J.; Zelenyuk, A. Experimental Determination of Chemical Diffusion within Secondary Organic Aerosol Particles. *Phys. Chem. Chem. Phys.* **2013**, *15* (8), 2983–2991. https://doi.org/10.1039/c2cp44013j.

(96) Pajunoja, A.; Malila, J.; Hao, L.; Joutsensaari, J.; Lehtinen, K. E. J.; Virtanen, A. Estimating the Viscosity Range of SOA Particles Based on Their Coalescence Time. *Aerosol Sci. Technol.* **2014**, *48* (2). https://doi.org/10.1080/02786826.2013.870325.

(97) Virtanen, A.; Joutsensaari, J.; Koop, T.; Kannosto, J.; Yli-Pirilä, P.; Leskinen, J.; Mäkelä, J. M.; Holopainen, J. K.; Pöschl, U.; Kulmala, M.; et al. An Amorphous Solid State of Biogenic Secondary Organic Aerosol Particles. *Nature* **2010**, *467* (7317), 824–827. https://doi.org/10.1038/nature09455.

(98) Kaaden, N.; Massling, A.; Schladitz, A.; Müller, T.; Kandler, K.; Schütz, L.; Weinzierl, B.; Petzold, A.; Tesche, M.; Leinert, S.; et al. State of Mixing, Shape Factor, Number Size Distribution, and Hygroscopic Growth of the Saharan Anthropogenic and Mineral Dust Aerosol at Tinfou, Morocco. *Tellus, Ser. B Chem. Phys. Meteorol.* **2009**, *61* (1), 51–63. https://doi.org/10.1111/j.1600-0889.2008.00388.x.

(99) Davies, C. N. Particle-Fluid Interaction. *J. Aerosol Sci.* **1979**, *10* (5), 477–513.

(100) Happonen, M.; Lähde, T.; Messing, M. E.; Sarjovaara, T.; Larmi, M.; Wallenberg, L. R.; Virtanen, A.; Keskinen, J. The Comparison of Particle Oxidation and Surface Structure of Diesel Soot Particles between Fossil Fuel and Novel Renewable Diesel Fuel. *Fuel* **2010**, *89* (12), 4008–4013.

(101) Pagels, J.; Khalizov, A. F.; McMurry, P. H.; Zhang, R. Y. Processing of Soot by Controlled Sulphuric Acid and Water Condensation Mass and Mobility Relationship. *Aerosol Sci. Technol.* **2009**, *43* (7), 629–640. https://doi.org/10.1080/02786820902810685.

(102) Rissler, J.; Messing, M. E.; Malik, A. I.; Nilsson, P. T.; Nordin, E. Z.; Bohgard, M.; Sanati, M.; Pagels, J. H. Effective Density Characterization of Soot Agglomerates from Various Sources and Comparison to Aggregation Theory. *Aerosol Sci. Technol.* **2013**, *47* (7), 792–805. https://doi.org/10.1080/02786826.2013.791381.

(103) Riemer, N.; Ault, A. P.; West, M.; Craig, R. L.; Curtis, J. H. Aerosol Mixing State: Measurements, Modeling, and Impacts. *Rev. Geophys.* **2019**.

(104) Hudson, P. K.; Gibson, E. R.; Young, M. A.; Kleiber, P. D.; Grassian, V. H. A Newly Designed and Constructed Instrument for Coupled Infrared Extinction and Size Distribution Measurements of Aerosols. *Aerosol Sci. Technol.* **2007**, *41* (7), 701–710. https://doi.org/10.1080/02786820701408509.

(105) Hudson, P. K.; Gibson, E. R.; Young, M. A.; Kleiber, P. D.; Grassian, V. H. Coupled Infrared Extinction and Size Distribution Measurements for Several Clay Components of Mineral Dust Aerosol. *J. Geophys. Res. Atmos.* **2008**, *113* (1), 1–11. https://doi.org/10.1029/2007JD008791.

(106) Cao, J.-J.; Zhu, C.-S.; Tie, X.-X.; Geng, F.-H.; Xu, H.-M.; Ho, S. S. H.; Wang, G.-H.; Han, Y.-M.; Ho, K.-F. Characteristics and Sources of Carbonaceous Aerosols from Shanghai, China. *Atmos. Chem. Phys.* **2013**, *13* (2), 803–817.

(107) Feng, Y.; Chen, Y.; Guo, H.; Zhi, G.; Xiong, S.; Li, J.; Sheng, G.; Fu, J. Characteristics of Organic and Elemental Carbon in PM2. 5 Samples in Shanghai, China. *Atmos. Res.* **2009**, *92* (4), 434–442.

(108) Huang, Y.; Li, L.; Li, J.; Wang, X.; Chen, H.; Chen, J.; Yang, X.; Gross, D. S.; Wang, H.; Qiao, L. A Case Study of the Highly Time-Resolved Evolution of Aerosol Chemical and Optical Properties in Urban Shanghai, China. *Atmos. Chem. Phys.* **2013**, *13* (8), 3931–3944.

(109) Pitz, M.; Birmili, W.; Schmid, O.; Peters, A.; Wichmann, H. E.; Cyrys, J. Quality Control and Quality Assurance for Particle Size Distribution Measurements at an Urban Monitoring Station in Augsburg, Germany. *J. Environ. Monit.* **2008**, *10* (9), 1017–1024. https://doi.org/10.1039/b807264g.

(110) Bäumer, D.; Vogel, B.; Versick, S.; Rinke, R.; Möhler, O.; Schnaiter, M. Relationship of Visibility, Aerosol Optical Thickness and Aerosol Size Distribution in an Ageing Air Mass over South-West Germany. *Atmos. Environ.* **2008**, *42* (5), 989–998. https://doi.org/10.1016/j.atmosenv.2007.10.017.

(111) Yue, D.; Hu, M.; Wu, Z.; Wang, Z.; Guo, S.; Wehner, B.; Nowak, A.; Achtert, P.; Wiedensohler, A.; Jung, J.; et al. Characteristics of Aerosol Size Distributions and New Particle Formation in the Summer in Beijing. *J. Geophys. Res. Atmos.* **2009**, *114* (14), 1–13. https://doi.org/10.1029/2008JD010894.

(112) Wehner, B.; Philippin, S.; Wiedensohler, A.; Scheer, V.; Vogt, R. Variability of Non-Volatile Fractions of Atmospheric Aerosol Particles with Traffic Influence. *Atmos. Environ.* **2004**, *38* (36), 6081–6090. https://doi.org/10.1016/j.atmosenv.2004.08.015.

(113) Babu, S. S.; Kompalli, S. K.; Moorthy, K. K. Aerosol Number Size Distributions over a Coastal Semi Urban Location: Seasonal Changes and Ultrafine Particle Bursts. *Sci. Total Environ.* **2016**, *563–564*, 351–365. https://doi.org/10.1016/j.scitotenv.2016.03.246.

(114) Yue, D. L.; Hu, M.; Wu, Z. J.; Guo, S.; Wen, M. T.; Nowak, A.; Wehner, B.; Wiedensohler, A.; Takegawa, N.; Kondo, Y.; et al. Variation of Particle Number Size Distributions and Chemical Compositions at the Urban and Downwind Regional Sites in the Pearl River Delta during Summertime Pollution Episodes. *Atmos. Chem. Phys.* **2010**, *10* (19), 9431–9439. https://doi.org/10.5194/acp-10-9431-2010.

(115) Rönkkö, T.; Kuuluvainen, H.; Karjalainen, P.; Keskinen, J.; Hillamo, R.; Niemi, J. V.; Pirjola, L.; Timonen, H. J.; Saarikoski, S.; Saukko, E.; et al. Traffic Is a Major Source of Atmospheric Nanocluster Aerosol. *Proc. Natl. Acad. Sci.* **2017**, *114* (29), 7549–7554. https://doi.org/10.1073/pnas.1700830114.

(116) Hussein, T.; Löndahl, J.; Paasonen, P.; Koivisto, A. J.; Petäjä, T.; Hämeri, K.; Kulmala, M. Modeling Regional Deposited Dose of Submicron Aerosol Particles. *Sci. Total Environ.* **2013**, *458*, 140–149.

(117) Löndahl, J.; Massling, A.; Pagels, J.; Swietlicki, E.; Vaclavik, E.; Loft, S. Size-Resolved Respiratory-Tract Deposition of Fine and Ultrafine Hydrophobic and Hygroscopic Aerosol Particles during Rest and Exercise. *Inhal. Toxicol.* **2007**, *19* (2), 109–116.

(118) Löndahl, J.; Massling, A.; Swietlicki, E.; Bräuner, E. V.; Ketzel, M.; Pagels, J.; Loft, S. Experimentally Determined Human Respiratory Tract Deposition of Airborne Particles at a Busy Street. *Environ. Sci. Technol.* **2009**, *43* (13), 4659–4664.

(119) Wu, T.; Täubel, M.; Holopainen, R.; Viitanen, A.-K.; Vainiotalo, S.; Tuomi, T.; Keskinen, J.; Hyvärinen, A.; Hämeri, K.; Saari, S. E.; et al. Infant and Adult Inhalation Exposure to Resuspended Biological Particulate Matter. *Environ. Sci. Technol.* **2018**, *52* (1), 237–247. https://doi.org/10.1021/acs.est.7b04183.

(120) Miller, F. J.; Asgharian, B.; Schroeter, J. D.; Price, O. Improvements and Additions to the Multiple Path Particle Dosimetry Model. *J. Aerosol Sci.* **2016**, *99*, 14–26.

(121) Kodros, J. K.; Volckens, J.; Jathar, S. H.; Pierce, J. R. Ambient Particulate Matter Size Distributions Drive Regional and Global Variability in Particle Deposition in the Respiratory Tract. *GeoHealth* **2018**, *2* (10), 298–312.

(122) Klepeis, N. E.; Nelson, W. C.; Ott, W. R.; Robinson, J. P.; Tsang, A. M.; Switzer, P.; Behar, J. V; Hern, S. C.; Engelmann, W. H. The National Human Activity Pattern Survey (NHAPS): A Resource for Assessing Exposure to Environmental Pollutants. *J. Expo. Sci. Environ. Epidemiol.* **2001**, *11* (3), 231.

(123) Hecker, R.; Hofacre, K. C. Development of Performance Data for Common Building Air Cleaning Devices (Final Report No. EPA/600/R-08/013). *US Environ. Prot. Agency, Off. Res. Dev. Homel. Secur. Res. Cent. Res. Triangle Park. NC* **2008**.

(124) Barone, T. L.; Lall, A. A.; Storey, J. M. E.; Mulholland, G. W.; Prikhodko, V. Y.; Frankland, J. H.; Parks, J. E.; Zachariah, M. R. Size-Resolved Density Measurements of Particle Emissions from an Advanced Combustion Diesel Engine: Effect of Aggregate Morphology. *Energy & Fuels* **2011**, *25* (5), 1978–1988.

(125) Rawat, V. K.; Buckley, D. T.; Kimoto, S.; Lee, M. H.; Fukushima, N.; Hogan, C. J. Two Dimensional Size-Mass Distribution Function Inversion from Differential Mobility Analyzer-Aerosol Particle Mass Analyzer (DMA-APM) Measurements. *J. Aerosol Sci.* **2016**, *92*, 70–82. https://doi.org/10.1016/j.jaerosci.2015.11.001.

(126) Park, K.; Cao, F.; Kittelson, D. B.; McMurry, P. H. Relationship between Particle Mass and Mobility for Diesel Exhaust Particles. *Environ. Sci. Technol.* **2003**, *37* (3), 577–583. https://doi.org/10.1021/es025960v.

(127) Olfert, J. S.; Symonds, J. P. R.; Collings, N. The Effective Density and Fractal Dimension of Particles Emitted from a Light-Duty Diesel Vehicle with a Diesel Oxidation Catalyst. *J. Aerosol Sci.* **2007**, *38* (1), 69–82. https://doi.org/10.1016/j.jaerosci.2006.10.002.

(128) Maricq, M. M.; Podsiadlik, D. H.; Chase, R. E. Size Distributions of Motor Vehicle Exhaust PM: A Comparison between ELPI and SMPS Measurements. *Aerosol Sci. Technol.* **2000**, *33* (3), 239–260.

(129) Ye, X.; Ma, Z.; Hu, D.; Yang, X.; Chen, J. Size-Resolved Hygroscopicity of Submicrometer Urban Aerosols in Shanghai during Wintertime. *Atmos. Res.* **2011**, *99* (2), 353–364. https://doi.org/10.1016/j.atmosres.2010.11.008.

(130) Li, R.; Yang, J.; Saffari, A.; Jacobs, J.; Baek, K. I.; Hough, G.; Larauche, M. H.; Ma, J.; Jen, N.; Moussaoui, N.; et al. Ambient Ultrafine Particle Ingestion Alters Gut Microbiota in Association with Increased Atherogenic Lipid Metabolites. *Sci. Rep.* **2017**, *7* (August 2016), 1–12. https://doi.org/10.1038/srep42906.

(131) Li, N.; Georas, S.; Alexis, N.; Fritz, P.; Xia, T.; Williams, M. A.; Horner, E.; Nel, A. A Work Group Report on Ultrafine Particles (American Academy of Allergy, Asthma & Immunology): Why Ambient Ultrafine and Engineered Nanoparticles Should Receive Special Attention for Possible Adverse Health Outcomes in Human Subjects. *J. Allergy Clin. Immunol.* **2016**, *138* (2), 386–396. https://doi.org/10.1016/j.jaci.2016.02.023.

(132) Oberdörster, G.; Sharp, Z.; Atudorei, V.; Elder, A.; Gelein, R.; Kreyling, W.; Cox, C. Translocation of Inhaled Ultrafine Particles to the Brain. *Inhal. Toxicol.* **2004**, *16* (6–7), 437–445. https://doi.org/10.1080/08958370490439597.

(133) Pietropaoli, A. P.; Frampton, M. W.; Hyde, R. W.; Morrow, P. E.; Oberdörster, G.; Cox, C.; Speers, D. M.; Frasier, L. M.; Chalupa, D. C.; Huang, L. S.; et al. Pulmonary Function, Diffusing Capacity, and Inflammation in Healthy and Asthmatic Subjects Exposed to Ultrafine Particles. *Inhal. Toxicol.* **2004**, *16* (SUPPL. 1), 59–72. https://doi.org/10.1080/08958370490443079.

(134) Kumar, P.; Morawska, L.; Birmili, W.; Paasonen, P.; Hu, M.; Kulmala, M.; Harrison, R. M.; Norford, L.; Britter, R. Ultrafine Particles in Cities. *Environ. Int.* **2014**, *66*, 1–10.

(135) Tuch, T. M.; Wehner, B.; Pitz, M.; Cyrys, J.; Heinrich, J.; Kreyling, W. G.; Wichmann, H. E.; Wiedensohler, A. Long-Term Measurements of Size-Segregated Ambient Aerosol in Two German Cities Located 100 Km Apart. *Atmos. Environ.* **2003**, *37* (33), 4687–4700. https://doi.org/10.1016/j.atmosenv.2003.07.010.

(136) Wehner, B.; Birmili, W.; Gnauk, T.; Wiedensohler, A. Particle Number Size Distributions in a Street Canyon and Their Transformation into the Urban Background: Measurements and a Simple Model Study. *Atmos. Environ.* **2002**, *36*, 2215–2223. https://doi.org/10.1016/S1352-2310(02)00174-7.

(137) Costabile, F.; Birmili, W.; Klose, S.; Tuch, T.; Wehner, B.; Wiedensohler, A.; Franck, U.; Konig, K.; Sonntag, A. Spatio-Temporal Variability and Principal Components of the Particle Number Size Distribution in an Urban Atmosphere. *Atmos. Chem. Phys.* **2009**, *9* (9), 3163–3195. https://doi.org/10.5194/acp-9-3163-2009.

(138) Birmili, W.; Tomsche, L.; Sonntag, A.; Opelt, C.; Weinhold, K.; Nordmann, S.; Schmidt, W. Variability of Aerosol Particles in the Urban Atmosphere of Dresden (Germany): Effects of Spatial Scale and Particle Size. *Meteorol. Zeitschrift* **2013**, *22* (2), 195–211. https://doi.org/10.1127/0941-2948/2013/0395.

(139) Ketzel, M. P.; Wåhlin, P.; Kristensson, A.; Swietlicki, E.; Berkowicz, R.; Nielsen, O. J.; Palmgren, F. Particle Size Distribution and Particle Mass Measurements at Urban, near-City and Rural Level in the Copenhagen Area and Southern Sweden. *Atmos. Chem. Phys* **2004**, *4*, 281–292. https://doi.org/10.5194/acp-4-281-2004.

(140) Hussein, T.; Hämeri, K.; Aalto, P. P.; Paatero, P.; Kulmala, M. Modal Structure and Spatial-Temporal Variations of Urban and Suburban Aerosols in Helsinki - Finland. *Atmos. Environ.* **2005**, *39* (9), 1655–1668. https://doi.org/10.1016/j.atmosenv.2004.11.031.

(141) Tuch, T. M.; Herbarth, O.; Franck, U.; Peters, A.; Wehner, B.; Wiedensohler, A.; Heintzenberg, J. Weak Correlation of Ultrafine Aerosol Particle Concentrations <800 Nm between Two Sites within One City. *J. Expo. Sci. Environ. Epidemiol.* **2006**, *16* (6), 486–490. https://doi.org/10.1038/sj.jes.7500469.

(142) Mishra, V. K.; Kumar, P.; Van Poppel, M.; Bleux, N.; Frijns, E.; Reggente, M.; Berghmans, P.; Panis, L. I.; Samson, R. Wintertime Spatio-Temporal Variation of Ultrafine Particles in a Belgian City. *Sci. Total Environ.* **2012**, *431*, 307–313.

(143) Buonanno, G.; Fuoco, F. C.; Stabile, L. Influential Parameters on Particle Exposure of Pedestrians in Urban Microenvironments. *Atmos. Environ.* **2011**, *45* (7), 1434–1443.

(144) Mejía, J. F.; Morawska, L.; Mengersen, K. Spatial Variation in Particle Number Size Distributions in a Large Metropolitan Area. *Atmos. Chem. Phys.* **2008**, *8* (5), 1127–1138.

(145) Wehner, B.; Wiedensohler, A. Long Term Measurements of Submicrometer Urban Aerosols: Statistical Analysis for Correlations with Meteorological Conditions and Trace Gases. *Atmos. Chem. Phys.* **2003**, *3* (3), 867–879. https://doi.org/10.5194/acp-3-867-2003.

(146) Väkevä, M.; Hämeri, K.; Puhakka, T.; Nilsson, E. D.; Hohti, H.; Mäkelä, J. M. Effects of Meteorological Processes on Aerosol Particle Size Distribution in an Urban Background Area. *J. Geophys. Res. Atmos.* **2000**, *105* (D8), 9807–9821. https://doi.org/10.1029/1999JD901143.

(147) Weingartner, E.; Burtscher, H.; Baltensperger, U. Hygroscopic Properties of Carbon and Diesel Soot Particles. *Atmos. Environ.* **1997**, *31* (15), 2311–2327.

(148) Rose, D.; Nowak, A.; Achtert, P.; Wiedensohler, A.; Hu, M.; Shao, M.; Zhang, Y.; Andreae, M. O.; Pöschl, U. Cloud Condensation Nuclei in Polluted Air and Biomass Burning Smoke near the Mega-City Guangzhou, China - Part 1: Size-Resolved Measurements and Implications for the Modeling of Aerosol Particle Hygroscopicity and CCN Activity. *Atmos. Chem. Phys.* **2010**, *10* (7), 3365–3383. https://doi.org/10.5194/acp-10-3365-2010.

(149) Yu, F.; Wang, Q.; Yan, Q.; Jiang, N.; Wei, J.; Wei, Z.; Yin, S. Particle Size Distribution, Chemical Composition and Meteorological Factor Analysis: A Case Study during Wintertime Snow Cover in Zhengzhou, China. *Atmos. Res.* **2018**, *202* (November 2017), 140–147. https://doi.org/10.1016/j.atmosres.2017.11.016.

(150) Stanier, C. O.; Khlystov, A. Y.; Pandis, S. N. Nucleation Events during the Pittsburgh Air Quality Study: Description and Relation to Key Meteorological, Gas Phase, and Aerosol Parameters Special Issue of Aerosol Science and Technology on Findings from the Fine Particulate Matter Supersites Program. *Aerosol Sci. Technol.* **2004**, *38* (S1), 253–264.

(151) Birmili, W.; Wiedensohler, A.; Heintzenberg, J.; Lehmann, K. Atmospheric Particle Number Size Distribution in Central Europe: Statistical Relations to Air Masses and Meteorology. *J. Geophys. Res. Atmos.* **2001**, *106* (D23), 32005–32018.

(152) Charron, A.; Harrison, R. M. Primary Particle Formation from Vehicle Emissions during Exhaust Dilution in the Roadside Atmosphere. *Atmos. Environ.* **2003**, *37* (29), 4109–4119. https://doi.org/10.1016/S1352-2310(03)00510-7.

(153) Nieto, P. J. G.; García, B. A.; Diaz, J. M. F.; Brana, M. A. R. Parametric Study of Selective Removal of Atmospheric Aerosol by Below-Cloud Scavenging. *Atmos. Environ.* **1994**, *28* (14), 2335–2342.

(154) Baxla, S. P.; Roy, A. A.; Gupta, T.; Tripathi, S. N.; Bandyopadhyaya, R. Analysis of Diurnal and Seasonal Variation of Submicron Outdoor Aerosol Mass and Size Distribution in a Northern Indian City and Its Correlation to Black Carbon. *Aerosol Air Qual. Res.* **2009**, *9* (4), 458–469. https://doi.org/10.4209/aaqr.2009.03.0017.

(155) Kaul, D. S.; Gupta, T.; Tripathi, S. N.; Tare, V.; Collett Jr, J. L. Secondary Organic Aerosol: A Comparison between Foggy and Nonfoggy Days. *Environ. Sci. Technol.* **2011**, *45* (17), 7307–7313.

(156) Swietlicki, E.; Hansson, H. C.; Hämeri, K.; Svenningsson, B.; Massling, A.; Mcfiggans, G.; Mcmurry, P. H.; Petäjä, T.; Tunved, P.; Gysel, M.; et al. Hygroscopic Properties of Submicrometer Atmospheric Aerosol Particles Measured with H-TDMA Instruments in Various Environments - A Review. *Tellus, Ser. B Chem. Phys. Meteorol.* **2008**, *60 B* (3), 432–469. https://doi.org/10.1111/j.1600-0889.2008.00350.x.

(157) Shi, J. P.; Harrison, R. M. Investigation of Ultrafine Particle Formation during Diesel Exhaust Dilution. *Environ. Sci. Technol.* **1999**, *33* (21), 3730–3736.

(158) Zhu, Y.; Hinds, W. C.; Kim, S.; Sioutas, C. Concentration and Size Distribution of Ultrafine Particles near a Major Highway. *J. Air Waste Manag. Assoc.* **2002**, *52* (9), 1032–1042. https://doi.org/10.1080/10473289.2002.10470842.

(159) Zhu, Y.; Hinds, W. C.; Kim, S.; Shen, S.; Sioutas, C. Study of Ultrafine Particles near a Major Highway with Heavy-Duty Diesel Traffic. *Atmos. Environ.* **2002**, *36* (27), 4323–4335.

(160) Salma, I.; Borsòs, T.; Weidinger, T.; Aalto, P.; Hussein, T.; Dal Maso, M.; Kulmala, M. Production, Growth and Properties of Ultrafine Atmospheric Aerosol Particles in an Urban Environment. *Atmos. Chem. Phys.* **2011**, *11* (3), 1339–1353. https://doi.org/10.5194/acp-11-1339-2011.

(161) Lin, Y.-H.; Zhang, Z.; Docherty, K. S.; Zhang, H.; Budisulistiorini, S. H.; Rubitschun, C. L.; Shaw, S. L.; Knipping, E. M.; Edgerton, E. S.; Kleindienst, T. E. Isoprene Epoxydiols as Precursors to Secondary Organic Aerosol Formation: Acid-Catalyzed Reactive Uptake Studies with Authentic Compounds. *Environ. Sci. Technol.* **2011**, *46* (1), 250–258.

(162) Moise, T.; Rudich, Y. Reactive Uptake of Ozone by Aerosol-Associated Unsaturated Fatty Acids: Kinetics, Mechanism, and Products. *J. Phys. Chem. A* **2002**, *106* (27), 6469–6476.

(163) Tang, M. J.; Thieser, J.; Schuster, G.; Crowley, J. N. Uptake of NO 3 and N 2 O 5 to Saharan Dust, Ambient Urban Aerosol and Soot: A Relative Rate Study. *Atmos. Chem. Phys.* **2010**, *10* (6), 2965–2974.

(164) Gaston, C. J.; Riedel, T. P.; Zhang, Z.; Gold, A.; Surratt, J. D.; Thornton, J. A. Reactive Uptake of an Isoprene-Derived Epoxydiol to Submicron Aerosol Particles. *Environ. Sci. Technol.* **2014**, *48* (19), 11178–11186.

(165) Limbeck, A.; Kulmala, M.; Puxbaum, H. Secondary Organic Aerosol Formation in the Atmosphere via Heterogeneous Reaction of Gaseous Isoprene on Acidic Particles. *Geophys. Res. Lett.* **2003**, *30* (19).

(166) Al-Mahmodi, J. N. H. Measurements and Prediction of Particulate Number Concentrations and Their Chemical Composition over Yanbu Industrial City, Saudi Arabia. The University of Manchester (United Kingdom) 2011.

(167) Fine, P. M.; Shen, S.; Sioutas, C. Inferring the Sources of Fine and Ultrafine Particulate Matter at Downwind Receptor Sites in the Los Angeles Basin Using Multiple Continuous Measurements. *Aerosol Sci. Technol.* **2004**, *38* (SUPPL. 1), 182–195. https://doi.org/10.1080/02786820390229499.

(168) Morawska, L.; Ristovski, Z.; Jayaratne, E. R.; Keogh, D. U.; Ling, X. Ambient Nano and Ultrafine Particles from Motor Vehicle Emissions: Characteristics, Ambient Processing and Implications on Human Exposure. *Atmos. Environ.* **2008**, *42* (35), 8113–8138. https://doi.org/10.1016/j.atmosenv.2008.07.050.

(169) Pant, P.; Harrison, R. M. Estimation of the Contribution of Road Traffic Emissions to Particulate Matter Concentrations from Field Measurements: A Review. *Atmos. Environ.* **2013**, *77*, 78–97. https://doi.org/10.1016/j.atmosenv.2013.04.028.

(170) Thorpe, A.; Harrison, R. M. Sources and Properties of Non-Exhaust Particulate Matter from Road Traffic: A Review. *Sci. Total Environ.* **2008**, *400* (1–3), 270–282. https://doi.org/10.1016/j.scitotenv.2008.06.007.

(171) Kittelson, D. B.; Watts, W. F.; Johnson, J. P. On-Road and Laboratory Evaluation of Combustion Aerosols-Part1: Summary of Diesel Engine Results. *J. Aerosol Sci.* **2006**, *37* (8), 913–930. https://doi.org/10.1016/j.jaerosci.2005.08.005.

(172) Shi, J. P.; Harrison, R. M.; Evans, D. Comparison of Ambient Particle Surface Area Measurement by Epiphaniometer and SMPS/APS. *Atmos. Environ.* **2001**, *35* (35), 6193–6200. https://doi.org/10.1016/S1352-2310(01)00382-X.

(173) Meyer, N. K.; Ristovski, Z. D. Ternary Nucleation as a Mechanism for the Production of Diesel Nanoparticles: Experimental Analysis of the Volatile and Hygroscopic Properties of Diesel Exhaust Using the Volatilization and Humidification Tandem Differential Mobility Analyzer. *Environ. Sci. Technol.* **2007**, *41* (21), 7309–7314.

(174) Kleeman, M. J.; Schauer, J. J.; Cass, G. R. Size and Composition Distribution of Fine Particulate Matter Emitted from Motor Vehicles. *Environ. Sci. Technol.* **2000**, *34* (7), 1132–1142.

(175) Dallmann, T. R.; Onasch, T. B.; Kirchstetter, T. W.; Worton, D. R.; Fortner, E. C.; Herndon, S. C.; Wood, E. C.; Franklin, J. P.; Worsnop, D. R.; Goldstein, A. H. Characterization of Particulate Matter Emissions from On-Road Gasoline and Diesel Vehicles Using a Soot Particle Aerosol Mass Spectrometer. *Atmos. Chem. Phys.* **2014**, *14* (14), 7585–7599.

(176) Gupta, T.; Kothari, A.; Srivastava, D. K.; Agarwal, A. K. Measurement of Number and Size Distribution of Particles Emitted from a Mid-Sized Transportation Multipoint Port Fuel Injection Gasoline Engine. *Fuel* **2010**, *89* (9), 2230–2233.

(177) Liang, B.; Ge, Y.; Tan, J.; Han, X.; Gao, L.; Hao, L.; Ye, W.; Dai, P. Comparison of PM Emissions from a Gasoline Direct Injected (GDI) Vehicle and a Port Fuel Injected (PFI) Vehicle Measured by Electrical Low Pressure Impactor (ELPI) with Two Fuels: Gasoline and M15 Methanol Gasoline. *J. Aerosol Sci.* **2013**, *57*, 22–31.

(178) Harris, S. J.; Maricq, M. M. Signature Size Distributions for Diesel and Gasoline Engine Exhaust Particulate Matter. *J. Aerosol Sci.* **2001**, *32* (6), 749–764.

(179) Li, T.; Chen, X.; Yan, Z. Comparison of Fine Particles Emissions of Light-Duty Gasoline Vehicles from Chassis Dynamometer Tests and on-Road Measurements. *Atmos. Environ.* **2013**, *68*, 82–91.

(180) Giechaskiel, B.; Ntziachristos, L.; Samaras, Z.; Scheer, V.; Casati, R.; Vogt, R. Formation Potential of Vehicle Exhaust Nucleation Mode Particles On-Road and in the Laboratory. *Atmos. Environ.* **2005**, *39* (18), 3191–3198.

(181) Jones, A. M.; Harrison, R. M.; Barratt, B.; Fuller, G. A Large Reduction in Airborne Particle Number Concentrations at the Time of the Introduction of “Sulphur Free” Diesel and the London Low Emission Zone. *Atmos. Environ.* **2012**, *50*, 129–138.

(182) Kittelson, D.; Watts, W.; Johnson, J. Diesel Aerosol Sampling Methodology–CRC E-43. *Final report, Coord. Res. Counc.* **2002**.

(183) Agarwal, A. K.; Gupta, T.; Dixit, N.; Shukla, P. C. Assessment of Toxic Potential of Primary and Secondary Particulates/Aerosols from Biodiesel Vis-a-Vis Mineral Diesel Fuelled Engine. *Inhal. Toxicol.* **2013**, *25* (6), 325–332.

(184) Armas, O.; Gómez, A.; Mata, C.; Ramos, Á. Particles Emitted during the Stops of an Urban Bus Fuelled with Ethanol–Biodiesel–Diesel Blends. *Urban Clim.* **2012**, *2*, 43–54.

(185) Giechaskiel, B.; Chirico, R.; DeCarlo, P. F.; Clairotte, M.; Adam, T.; Martini, G.; Heringa, M. F.; Richter, R.; Prevot, A. S. H.; Baltensperger, U. Evaluation of the Particle Measurement Programme (PMP) Protocol to Remove the Vehicles’ Exhaust Aerosol Volatile Phase. *Sci. Total Environ.* **2010**, *408* (21), 5106–5116.

(186) Mayer, A.; Czerwinski, J.; Legerer, F.; Wyser, M. *VERT Particulate Trap Verification*; SAE Technical Paper, 2002.

(187) Pedata, P.; Stoeger, T.; Zimmermann, R.; Peters, A.; Oberdï¿½rster, G.; D’Anna, A. “Are We Forgetting the Smallest, Sub 10 Nm Combustion Generated Particles?” *Part. Fibre Toxicol.* **2015**, *12* (1), 10–13. https://doi.org/10.1186/s12989-015-0107-3.

(188) Ketzel, M.; Wåhlin, P.; Berkowicz, R.; Palmgren, F. Particle and Trace Gas Emission Factors under Urban Driving Conditions in Copenhagen Based on Street and Roof-Level Observations. *Atmos. Environ.* **2003**, *37* (20), 2735–2749. https://doi.org/10.1016/S1352-2310(03)00245-0.

(189) Buonanno, G.; Lall, A. A.; Stabile, L. Temporal Size Distribution and Concentration of Particles near a Major Highway. *Atmos. Environ.* **2009**, *43* (5), 1100–1105. https://doi.org/10.1016/j.atmosenv.2008.11.011.

(190) Li, X. L.; Wang, J. S.; Tu, X. D.; Liu, W.; Huang, Z. Vertical Variations of Particle Number Concentration and Size Distribution in a Street Canyon in Shanghai, China. *Sci. Total Environ.* **2007**, *378* (3), 306–316. https://doi.org/10.1016/j.scitotenv.2007.02.040.

(191) Agus, E. L.; Young, D. T.; Lingard, J. J. N.; Smalley, R. J.; Tate, J. E.; Goodman, P. S.; Tomlin, A. S. Factors Influencing Particle Number Concentrations, Size Distributions and Modal Parameters at a Roof-Level and Roadside Site in Leicester, UK. *Sci. Total Environ.* **2007**, *386* (1–3), 65–82.

(192) Hitchins, J.; Morawska, L.; Wolff, R.; Gilbert, D. Concentrations of Submicrometre Particles from Vehicle Emissions near a Major Road. *Atmos. Environ.* **2000**, *34* (1), 51–59.

(193) Zhang, K. M.; Wexler, A. S.; Zhu, Y. F.; Hinds, W. C.; Sioutas, C. Evolution of Particle Number Distribution near Roadways. Part II: The 'Road-to-Ambient'Process. *Atmos. Environ.* **2004**, *38* (38), 6655–6665.

(194) Ning, Z.; Hudda, N.; Daher, N.; Kam, W.; Herner, J.; Kozawa, K.; Mara, S.; Sioutas, C. Impact of Roadside Noise Barriers on Particle Size Distributions and Pollutants Concentrations near Freeways. *Atmos. Environ.* **2010**, *44* (26), 3118–3127. https://doi.org/10.1016/j.atmosenv.2010.05.033.

(195) Dall'Osto, M.; Thorpe, A.; Beddows, D. C. S.; Harrison, R. M.; Barlow, J. F.; Dunbar, T.; Williams, P. I.; Coe, H. Remarkable Dynamics of Nanoparticles in the Urban Atmosphere. *Atmos. Chem. Phys.* **2011**, *11* (13), 6623–6637. https://doi.org/10.5194/acp-11-6623-2011.

(196) Grigoratos, T.; Martini, G. Brake Wear Particle Emissions: A Review. *Environ. Sci. Pollut. Res.* **2015**, *22* (4), 2491–2504. https://doi.org/10.1007/s11356-014-3696-8.

(197) Nosko, O.; Vanhanen, J.; Olofsson, U. Emission of 1.3–10 Nm Airborne Particles from Brake Materials. *Aerosol Sci. Technol.* **2017**, *51* (1), 91–96. https://doi.org/10.1080/02786826.2016.1255713.

(198) Kukutschová, J.; Moravec, P.; Tomášek, V.; Matějka, V.; Smolík, J.; Schwarz, J.; Seidlerová, J.; Šafářová, K.; Filip, P. On Airborne Nano/Micro-Sized Wear Particles Released from Low-Metallic Automotive Brakes. *Environ. Pollut.* **2011**, *159* (4), 998–1006.

(199) Timmers, V. R. J. H.; Achten, P. A. J. Non-Exhaust PM Emissions from Electric Vehicles. *Atmos. Environ.* **2016**, *134*, 10–17. https://doi.org/10.1016/j.atmosenv.2016.03.017.

(200) Wahlström, J.; Söderberg, A.; Olander, L.; Jansson, A.; Olofsson, U. A Pin-on-Disc Simulation of Airborne Wear Particles from Disc Brakes. *Wear* **2010**, *268* (5–6), 763–769.

(201) Rissler, J.; Vestin, A.; Swietlicki, E.; Fisch, G.; Zhou, J.; Artaxo, P.; Andreae, M. O. Size Distribution and Hygroscopic Properties of Aerosol Particles from Dry-Season Biomass Burning in Amazonia. *Atmos. Chem. Phys.* **2006**, *6* (2), 471–491.

(202) Zhang, H.; Hu, D.; Chen, J.; Ye, X.; Wang, S. X.; Hao, J. M.; Wang, L.; Zhang, R.; An, Z. Particle Size Distribution and Polycyclic Aromatic Hydrocarbons Emissions from Agricultural Crop Residue Burning. *Environ. Sci. Technol.* **2011**, *45* (13), 5477–5482.

(203) Wallace, L. A.; Emmerich, S. J.; Howard-Reed, C. Source Strengths of Ultrafine and Fine Particles Due to Cooking with a Gas Stove. *Environ. Sci. Technol.* **2004**, *38* (8), 2304–2311.

(204) Glytsos, T.; Ondráček, J.; Džumbová, L.; Kopanakis, I.; Lazaridis, M. Characterization of Particulate Matter Concentrations during Controlled Indoor Activities. *Atmos. Environ.* **2010**, *44* (12), 1539–1549.

(205) Buonanno, G.; Morawska, L.; Stabile, L. Particle Emission Factors during Cooking Activities. *Atmos. Environ.* **2009**, *43* (20), 3235–3242.

(206) See, S. W.; Balasubramanian, R. Physical Characteristics of Ultrafine Particles Emitted from Different Gas Cooking Methods. *Aerosol Air Qual. Res.* **2006**, *6* (1), 82–92.

(207) Ogulei, D.; Hopke, P. K.; Ferro, A. R.; Jaques, P. A. Factor Analysis of Submicron Particle Size Distributions near a Major United States–Canada Trade Bridge. *J. Air Waste Manag. Assoc.* **2007**, *57* (2), 190–203. https://doi.org/10.1080/10473289.2007.10465316.

(208) RÖnkkÖ, T.; Virtanen, A.; Kannosto, J.; Keskinen, J.; Lappi, M.; Pirjola, L. Nucleation Mode Particles with a Nonvolatile Core in the Exhaust of a Heavy Duty Diesel Vehicle. *Environ. Sci. Technol.* **2007**, *41* (18), 6384–6389.

(209) Janhäll, S.; Andreae, M. O.; Pöschl, U. Biomass Burning Aerosol Emissions from Vegetation Fires: Particle Number and Mass Emission Factors and Size Distributions. *Atmos. Chem. Phys.* **2010**, *10* (3), 1427–1439.

(210) Sakamoto, K. M.; Laing, J. R.; Stevens, R. G.; Jaffe, D. A.; Pierce, J. R. The Evolution of Biomass-Burning Aerosol Size Distributions Due to Coagulation: Dependence on Fire and Meteorological Details and Parameterization. *Atmos. Chem. Phys.* **2016**, *16* (12), 7709–7724.

(211) Reid, J. S.; Hobbs, P. V. Physical and Optical Properties of Young Smoke from Individual Biomass Fires in Brazil. *J. Geophys. Res. Atmos.* **1998**, *103* (D24), 32013–32030.

(212) Reid, J. S.; Koppmann, R.; Eck, T. F.; Eleuterio, D. P. A Review of Biomass Burning Emissions Part II: Intensive Physical Properties of Biomass Burning Particles. *Atmos. Chem. Phys.* **2005**, *5* (3), 799–825.

(213) Mönkkönen, P.; Koponen, I. K.; Lehtinen, K. E. J.; Hämeri, K.; Uma, R.; Kulmala, M. Measurements in a Highly Polluted Asian Mega City: Observations of Aerosol Number Size Distribution, Modal Parameters and Nucleation Events. *Atmos. Chem. Phys.* **2005**, *5* (1), 57–66.

(214) Bi, X.; Dai, Q.; Wu, J.; Zhang, Q.; Zhang, W.; Luo, R.; Cheng, Y.; Zhang, J.; Wang, L.; Yu, Z. Characteristics of the Main Primary Source Profiles of Particulate Matter across China from 1987 to 2017. *Atmos. Chem. Phys.* **2019**, *19* (5), 3223–3243.

(215) Zheng, X.; Liu, X.; Zhao, F.; Duan, F.; Yu, T.; Cachier, H. Seasonal Characteristics of Biomass Burning Contribution to Beijing Aerosol. *Sci. China Ser. B Chem.* **2005**, *48* (5), 481–488.

(216) Qi, X. M.; Ding, A. J.; Nie, W.; Petäjä, T.; Kerminen, V.-M.; Herrmann, E.; Xie, Y. N.; Zheng, L. F.; Manninen, H.; Aalto, P. Aerosol Size Distribution and New Particle Formation in the Western Yangtze River Delta of China: 2 Years of Measurements at the SORPES Station. *Atmos. Chem. Phys.* **2015**, *15* (21), 12445–12464.

(217) Moffet, R. C.; Foy, B. de; Molina, L. T. al; Molina, M. J.; Prather, K. A. Measurement of Ambient Aerosols in Northern Mexico City by Single Particle Mass Spectrometry. *Atmos. Chem. Phys.* **2008**, *8* (16), 4499–4516.

(218) Yang, F.; Chen, H.; Du, J.; Yang, X.; Gao, S.; Chen, J.; Geng, F. Evolution of the Mixing State of Fine Aerosols during Haze Events in Shanghai. *Atmos. Res.* **2012**, *104*, 193–201.

(219) Shen, X. J.; Sun, J. Y.; Zhang, X. Y.; Zhang, Y. M.; Zhang, L.; Fan, R. X.; Zhang, Z. X.; Zhang, X. L.; Zhou, H. G.; Zhou, L. Y. The Influence of Emission Control on Particle Number Size Distribution and New Particle Formation during China's V-Day Parade in 2015. *Sci. Total Environ.* **2016**, *573*, 409–419.

(220) Gao, J.; Wang, T.; Zhou, X.; Wu, W.; Wang, W. Measurement of Aerosol Number Size Distributions in the Yangtze River Delta in China: Formation and Growth of Particles under Polluted Conditions. *Atmos. Environ.* **2009**, *43* (4), 829–836.

(221) Wang, Z. B.; Hu, M.; Sun, J. Y.; Wu, Z. J.; Yue, D. L.; Shen, X. J.; Zhang, Y. M.; Pei, X. Y.; Cheng, Y. F.; Wiedensohler, A. Characteristics of Regional New Particle Formation in Urban and Regional Background Environments in the North China Plain. *Atmos. Chem. Phys.* **2013**, *13* (24), 12495–12506. https://doi.org/10.5194/acp-13-12495-2013.

(222) Shen, X.; Sun, J.; Zhang, X.; Zhang, Y.; Zhang, L.; Fan, R. Key Features of New Particle Formation Events at Background Sites in China and Their Influence on Cloud Condensation Nuclei. *Front. Environ. Sci. Eng.* **2016**, *10* (5), 5.

(223) Misra, A.; Gaur, A.; Bhattu, D.; Ghosh, S.; Dwivedi, A. K.; Dalai, R.; Paul, D.; Gupta, T.; Tare, V.; Mishra, S. K.; et al. An Overview of the Physico-Chemical Characteristics of Dust at Kanpur in the Central Indo-Gangetic Basin. *Atmos. Environ.* **2014**, *97*, 386–396. https://doi.org/10.1016/j.atmosenv.2014.08.043.

(224) Wehner, B.; Wiedensohler, A.; Tuch, T. M.; Wu, Z. J.; Hu, M.; Slanina, J.; Kiang, C. S. Variability of the Aerosol Number Size Distribution in Beijing, China: New Particle Formation, Dust Storms, and High Continental Background. *Geophys. Res. Lett.* **2004**, *31* (22), 1–4. https://doi.org/10.1029/2004GL021596.

(225) Kulmala, M.; Petäjä, T.; Mönkkönen, P.; Koponen, I. K.; Maso, M. D.; Aalto, P. P.; Lehtinen, K. E. J.; Kerminen, V.-M. On the Growth of Nucleation Mode Particles: Source Rates of Condensable Vapor in Polluted and Clean Environments. *Atmos. Chem. Phys.* **2005**, *5* (2), 409–416.

(226) Huang, R.-J.; Zhang, Y.; Bozzetti, C.; Ho, K.-F.; Cao, J.-J.; Han, Y.; Daellenbach, K. R.; Slowik, J. G.; Platt, S. M.; Canonaco, F. High Secondary Aerosol Contribution to Particulate Pollution during Haze Events in China. *Nature* **2014**, *514* (7521), 218.

(227) Pei, C.; Ou, Q.; Pui, D. Y. H. Effect of Relative Humidity on Loading Characteristics of Cellulose Filter Media by Submicrometer Potassium Chloride, Ammonium Sulfate, and Ammonium Nitrate Particles. *Sep. Purif. Technol.* **2019**, *212*, 75–83.

(228) Tang, M.; Chen, S.-C.; Chang, D.-Q.; Xie, X.; Sun, J.; Pui, D. Y. H. Filtration Efficiency and Loading Characteristics of PM2. 5 through Composite Filter Media Consisting of Commercial HVAC Electret Media and Nanofiber Layer. *Sep. Purif. Technol.* **2018**, *198*, 137–145.

(229) Leung, W. W.-F.; Hung, C.-H.; Yuen, P.-T. Effect of Face Velocity, Nanofiber Packing Density and Thickness on Filtration Performance of Filters with Nanofibers Coated on a Substrate. *Sep. Purif. Technol.* **2010**, *71* (1), 30–37.

(230) Wang, J. Effects of Particle Size and Morphology on Filtration of Airborne Nanoparticles. *KONA Powder Part. J.* **2012**, *30* (30), 256–266. https://doi.org/10.14356/kona.2013024.

(231) Li, P.; Wang, C.; Zhang, Y.; Wei, F. Air Filtration in the Free Molecular Flow Regime: A Review of High-Efficiency Particulate Air Filters Based on Carbon Nanotubes. *Small* **2014**, *10* (22), 4553–4561. https://doi.org/10.1002/smll.201401553.

(232) Walsh, D. C.; Stenhouse, J. I. T.; Scurrah, K. L.; Graef, A. Effect of Solid and Liquid Aerosol Particle Loading on Fibrous Filter Material Performance. *J. Aerosol Sci.* **1996**, *27* (Suppl 1), S617–S618. https://doi.org/10.1016/0021-8502(96)00381-3.

(233) Huffman, J. A.; Docherty, K. S.; Mohr, C.; Cubison, M. J.; Ulbrich, I. M.; Ziemann, P. J.; Onasch, T. B.; Jimenez, J. L. Chemically-Resolved Volatility Measurements of Organic Aerosol from Different Sources. *Environ. Sci. Technol.* **2009**, *43* (14), 5351–5357.

(234) Donahue, N. M.; Robinson, A. L.; Stanier, C. O.; Pandis, S. N. Coupled Partitioning, Dilution, and Chemical Aging of Semivolatile Organics. *Environ. Sci. Technol.* **2006**, *40* (8), 2635–2643.

(235) Johnson, A. M.; Waring, M. S.; DeCarlo, P. F. Real-time Transformation of Outdoor Aerosol Components upon Transport Indoors Measured with Aerosol Mass Spectrometry. *Indoor Air* **2017**, *27* (1), 230–240.

(236) Kulmala, M. Build a Global Earth Observatory. *Nature* **2018**, *553*, 21–23.

(237) Gelencsér, A.; May, B.; Simpson, D.; Sánchez-Ochoa, A.; Kasper-Giebl, A.; Puxbaum, H.; Caseiro, A.; Pio, C. A.; Legrand, M. Source Apportionment of PM2.5 Organic Aerosol over Europe: Primary/Secondary, Natural/Anthropogenic, and Fossil/Biogenic Origin. *J. Geophys. Res. Atmos.* **2007**, *112* (23), 1–12. https://doi.org/10.1029/2006JD008094.

(238) Van Donkelaar, A.; Martin, R. V; Brauer, M.; Kahn, R.; Levy, R.; Verduzco, C.; Villeneuve, P. J. Global Estimates of Ambient Fine Particulate Matter Concentrations from Satellite-Based Aerosol Optical Depth: Development and Application. *Environ. Health Perspect.* **2010**, *118* (6), 847–855.

(239) Cheng, Z.; Luo, L.; Wang, S.; Wang, Y.; Sharma, S.; Shimadera, H.; Wang, X.; Bressi, M.; de Miranda, R. M.; Jiang, J.; et al. Status and Characteristics of Ambient PM2.5pollution in Global Megacities. *Environ. Int.* **2016**, *89–90*, 212–221. https://doi.org/10.1016/j.envint.2016.02.003.

(240) Apte, J. S.; Marshall, J. D.; Cohen, A. J.; Brauer, M. Addressing Global Mortality from Ambient PM2. 5. *Environ. Sci. Technol.* **2015**, *49* (13), 8057–8066.

(241) West, J. J.; Cohen, A.; Dentener, F.; Brunekreef, B.; Zhu, T.; Armstrong, B.; Bell, M. L.; Brauer, M.; Carmichael, G.; Costa, D. L. What We Breathe Impacts Our Health: Improving Understanding of the Link between Air Pollution and Health. ACS Publications 2016.

(242) de Jesus, A. L.; Rahman, M. M.; Mazaheri, M.; Thompson, H.; Knibbs, L. D.; Jeong, C.; Evans, G.; Nei, W.; Ding, A.; Qiao, L. Ultrafine Particles and PM2. 5 in the Air of Cities around the World: Are They Representative of Each Other? *Environ. Int.* **2019**, *129*, 118–135.

(243) Thunis, P.; Degraeuwe, B.; Pisoni, E.; Trombetti, M.; Peduzzi, E.; Belis, C. A.; Wilson, J.; Vignati, E. *Urban PM2.5 Atlas - Air Quality in European Cities*; 2017. https://doi.org/10.2760/336669.

(244) Martin, R. V; Brauer, M.; van Donkelaar, A.; Shaddick, G.; Narain, U.; Dey, S. No One Knows Which City Has the Highest Concentration of Fine Particulate Matter. *Atmos. Environ. X* **2019**, 100040.

(245) Motlagh, N. H.; Lagerspetz, E.; Nurmi, P.; Li, X.; Varjonen, S.; Mineraud, J.; Siekkinen, M.; Rebeiro-Hargrave, A.; Hussein, T.; Petaja, T. Toward Massive Scale Air Quality Monitoring. *IEEE Commun. Mag.* **2020**, *58* (2), 54–59.

(246) Venecek, M. A.; Yu, X.; Kleeman, M. J. Predicted Ultrafine Particulate Matter Source Contribution across the Continental United States during Summertime Air Pollution Events. *Atmos. Chem. Phys.* **2019**, *19* (14), 9399–9412.

(247) Brines, M.; Dall'Osto, M.; Beddows, D. C. S.; Harrison, R. M.; Gómez-Moreno, F.; Núñez, L.; Artíñano, B.; Costabile, F.; Gobbi, G. P.; Salimi, F.; et al. Traffic and Nucleation Events as Main Sources of Ultrafine Particles in High-Insolation Developed World Cities. *Atmos. Chem. Phys.* **2015**, *15* (10), 5929–5945. https://doi.org/10.5194/acp-15-5929-2015.

(248) Tunved, P.; Ström, J.; Hansson, H.-C. An Investigation of Processes Controlling the Evolution of the Boundary Layer Aerosol Size Distribution Properties at the Swedish Background Station Aspvreten. *Atmos. Chem. Phys.* **2004**, *4* (11/12), 2581–2592.

(249) Kim, E.; Hopke, P. K.; Larson, T. V; Covert, D. S. Analysis of Ambient Particle Size Distributions Using Unmix and Positive Matrix Factorization. *Environ. Sci. Technol.* **2004**, *38* (1), 202–209.

(250) Harrison, R. M.; Beddows, D. C. S.; Dall'Osto, M. PMF Analysis of Wide-Range Particle Size Spectra Collected on a Major Highway. *Environ. Sci. Technol.* **2011**, *45* (13), 5522–5528. https://doi.org/10.1021/es2006622.

(251) Yue, D. L.; Hu, M.; Wang, Z. B.; Wen, M. T.; Guo, S.; Zhong, L. J.; Wiedensohler, A.; Zhang, Y. H. Comparison of Particle Number Size Distributions and New Particle Formation between the Urban and Rural Sites in the PRD Region, China. *Atmos. Environ.* **2013**, *76*, 181–188. https://doi.org/10.1016/j.atmosenv.2012.11.018.

(252) Beddows, D. C. S.; Dall'Osto, M.; Harrison, R. M.; Dall'Osto, M.; Harrison, R. M.; Dall'Osto, M.; Harrison, R. M. Cluster Analysis of Rural, Urban, and Curbside Atmospheric Particle Size Data. *Environ. Sci. Technol.* **2009**, *43* (13), 4694–4700. https://doi.org/10.1021/es803121t.

(253) Beddows, D. C. S.; Dall'Osto, M.; Harrison, R. M.; Kulmala, M.; Asmi, A.; Wiedensohler, A.; Laj, P.; Fjæraa, A. M.; Sellegri, K.; Birmili, W. Variations in Tropospheric Submicron Particle Size Distributions across the European Continent 2008–2009. *Atmos. Chem. Phys.* **2014**, *14* (8), 4327–4348.

(254) Dall'Osto, M.; Monahan, C.; Greaney, R.; Beddows, D. C. S.; Harrison, R. M.; Ceburnis, D.; O'Dowd, C. D. A Statistical Analysis of North East Atlantic (Submicron) Aerosol Size Distributions. *Atmos. Chem. Phys.* **2011**, *11* (24), 12567–12578.

(255) Charron, A.; Birmili, W.; Harrison, R. M. Fingerprinting Particle Origins According to Their Size Distribution at a UK Rural Site. *J. Geophys. Res. Atmos.* **2008**, *113* (D7).

(256) Thimmaiah, D.; Hovorka, J.; Hopke, P. K. Source Apportionment of Winter Submicron Prague Aerosols from Combined Particle Number Size Distribution and Gaseous Composition Data. *Aerosol Air Qual. Resarch* **2009**, *9* (2), 209–236.

(257) Friend, A. J.; Ayoko, G. A.; Jayaratne, E. R.; Jamriska, M.; Hopke, P. K.; Morawska, L. Source Apportionment of Ultrafine and Fine Particle Concentrations in Brisbane, Australia. *Environ. Sci. Pollut. Res.* **2012**, *19* (7), 2942–2950.

(258) Kasumba, J.; Hopke, P. K.; Chalupa, D. C.; Utell, M. J. Comparison of Sources of Submicron Particle Number Concentrations Measured at Two Sites in Rochester, NY. *Sci. Total Environ.* **2009**, *407* (18), 5071–5084.

(259) Gu, J.; Pitz, M.; Schnelle-Kreis, J.; Diemer, J.; Reller, A.; Zimmermann, R.; Soentgen, J.; Stoelzel, M.; Wichmann, H.-E.; Peters, A. Source Apportionment of Ambient Particles: Comparison of Positive Matrix Factorization Analysis Applied to Particle Size Distribution and Chemical Composition Data. *Atmos. Environ.* **2011**, *45* (10), 1849–1857.

(260) European Parliament and the Council of the European Union. *Regulation (EC) No 715/2007 of the European Parliament and of the Council of 20 June 2007 on Type Approval of Motor Vehicles with Respect to Emissions from Light Passenger and Commercial Vehicles (Euro 5 and Euro 6) and on Access to Vehicle Repair and Mai*; 2007; Vol. 171.

(261) Morawska, L.; Keogh, D. U.; Thomas, S. B.; Mengersen, K. Modality in Ambient Particle Size Distributions and Its Potential as a Basis for Developing Air Quality Regulation. *Atmos. Environ.* **2008**, *42* (7), 1617–1628. https://doi.org/10.1016/j.atmosenv.2007.09.076.

(262) Kontkanen, J.; Lehtipalo, K.; Ahonen, L.; Kangasluoma, J.; Manninen, H. E.; Hakala, J.; Rose, C.; Sellegri, K.; Xiao, S.; Wang, L.; et al. Measurements of Sub-3nm Particles Using a Particle Size Magnifier in Different Environments: From Clean Mountain Top to Polluted Megacities. *Atmos. Chem. Phys.* **2017**, *17* (3), 2163–2187. https://doi.org/10.5194/acp-17-2163-2017.

(263) Kangasniemi, O.; Kuuluvainen, H.; Heikkilä, J.; Pirjola, L.; Niemi, J. V; Timonen, H.; Saarikoski, S.; Rönkkö, T.; Dal Maso, M. Dispersion of a Traffic Related Nanocluster Aerosol near a Major Road. *Atmosphere (Basel).* **2019**, *10* (6), 309.

(264) Olin, M.; Kuuluvainen, H.; Aurela, M.; Kalliokoski, J.; Kuittinen, N.; Isotalo, M.; Timonen, H. J.; Niemi, J. V; Rönkkö, T.; Dal Maso, M. Traffic-Originated Nanocluster Emission Exceeds H2SO4-Driven Photochemical New Particle Formation in an Urban Area. *Atmos. Chem. Phys.* **2020**, *20* (1), 1–13.

(265) Pieters, N.; Koppen, G.; van Poppel, M.; de Prins, S.; Cox, B.; Dons, E.; Nelen, V.; Panis, L. I.; Plusquin, M.; Schoeters, G.; et al. Blood Pressure and Same-Day Exposure to Air Pollution at School: Associations with Nano-Sized to Coarse PM in Children. *Environ. Health Perspect.* **2015**, *123* (7), 737–742. https://doi.org/10.1289/ehp.1408121.

(266) Valavanidis, A.; Fiotakis, K.; Vlachogianni, T. Airborne Particulate Matter and Human Health: Toxicological Assessment and Importance of Size and Composition of Particles for Oxidative Damage and Carcinogenic Mechanisms. *J. Environ. Sci. Heal. - Part C Environ. Carcinog. Ecotoxicol. Rev.* **2008**, *26* (4), 339–362. https://doi.org/10.1080/10590500802494538.

(267) Anderson, J. O.; Thundiyil, J. G.; Stolbach, A. Clearing the Air: A Review of the Effects of Particulate Matter Air Pollution on Human Health. *J. Med. Toxicol.* **2012**, *8* (2), 166–175. https://doi.org/10.1007/s13181-011-0203-1.

(268) Tsiouri, V.; Kakosimos, K. E.; Kumar, P. Concentrations, Sources and Exposure Risks Associated with Particulate Matter in the Middle East Area—a Review. *Air Qual. Atmos. Heal.* **2015**, *8* (1), 67–80. https://doi.org/10.1007/s11869-014-0277-4.

(269) Li, X.-Y.; Hao, L.; Liu, Y.-H.; Chen, C.-Y.; Pai, V. J.; Kang, J. X. Protection against Fine Particle-Induced Pulmonary and Systemic Inflammation by Omega-3 Polyunsaturated Fatty Acids. *Biochim. Biophys. Acta (BBA)-General Subj.* **2017**, *1861* (3), 577–584.

(270) Pöschl, U. Atmospheric Aerosols: Composition, Transformation, Climate and Health Effects. *Angew. Chemie - Int. Ed.* **2005**, *44* (46), 7520–7540. https://doi.org/10.1002/anie.200501122.

(271) Poon, W. S.; Liu, B. Y. H. Dust Loading Behavior of Engine and General Purpose Air Cleaning Filters. *SAE Tech. Pap.* **2016**, No. 412. https://doi.org/10.4271/970676.

(272) Endo, Y.; Chen, D. R.; Pui, D. Y. H. Effects of Particle Polydispersity and Shape Factor during Dust Cake Loading on Air Filters. *Powder Technol.* **1998**, *98* (3), 241–249. https://doi.org/10.1016/S0032-5910(98)00063-1.

(273) Thomas, D.; Contal, P.; Renaudin, V.; Penicot, P.; Leclerc, D.; Vendel, J. Modelling Pressure Drop in HEPA Filters during Dynamic Filtration. *J. Aerosol Sci.* **1999**, *30* (2), 235–246. https://doi.org/10.1016/S0021-8502(98)00036-6.

(274) Thomas, D.; Penicot, P.; Contal, P.; Leclerc, D.; Vendel, J. Clogging of Fibrous Filter by Solid Aerosol Particles Experimental and Modelling Study. *Chem. Eng. Sci.* **2001**, *56*, 3549–3561.

(275) Wang, C. Sen; Otani, Y. Removal of Nanoparticles from Gas Streams by Fibrous Filters: A Review. *Ind. Eng. Chem. Res.* **2013**, *52* (1), 5–17. https://doi.org/10.1021/ie300574m.

(276) Wang, J.; Tronville, P. Toward Standardized Test Methods to Determine the Effectiveness of Filtration Media against Airborne Nanoparticles. *J. Nanoparticle Res.* **2014**, *16* (6). https://doi.org/10.1007/s11051-014-2417-z.

(277) Montgomery, J. F.; Rogak, S. N.; Green, S. I.; You, Y.; Bertram, A. K. Structural Change of Aerosol Particle Aggregates with Exposure to Elevated Relative Humidity. *Environ. Sci. Technol.* **2015**, *49* (20), 12054–12061. https://doi.org/10.1021/acs.est.5b03157.

(278) Abdolghader, P.; Brochot, C.; Haghighat, F.; Bahloul, A. Airborne Nanoparticles Filtration Performance of Fibrous Media: A Review. *Sci. Technol. Built Environ.* **2018**, *24* (6), 648–672.

(279) Poon, W. S.; Liu, B. Y. H.; Drive, C.; Pa, U. S. A. A Bimodal Loading Test for Engine and General Purpose Air Cleaning Filters. *SAE Tech. Pap.* **2016**, No. 412. https://doi.org/10.4271/970674.

(280) Biskos, G.; Vons, V.; Yurteri, C. U.; Schmidt-Ott, A. Generation and Sizing of Particles for Aerosol-Based Nanotechnology. *KONA Powder Part. J.* **2008**, *26* (March), 13–35. https://doi.org/10.14356/kona.2008006.

(281) Edwards, J.; Kinnear, D. I. Flame Generation of Sodium Chloride Aerosol for Filter Testing.

(282) Vijayakumar, R.; Whitby, K. T. Flat Flame Ultrafine Aerosol Generator. *Aerosol Sci. Technol.* **1984**, *3* (1), 17–24. https://doi.org/10.1080/02786828408958989.

(283) Zhang, Z.; Jiang, F. In-Place HEPA Filter Testing by the Sodium Flame Method. *Powder Technol.* **2016**, *301*, 615–621. https://doi.org/10.1016/j.powtec.2016.06.046.

(284) Olfert, J. S.; Collings, N. New Method for Particle Mass Classification - The Couette Centrifugal Particle Mass Analyzer. *J. Aerosol Sci.* **2005**, *36* (11), 1338–1352. https://doi.org/10.1016/j.jaerosci.2005.03.006.

(285) Mikhailov, E.; Vlasenko, S.; Niessner, R.; Pöschl, U. Interaction of Aerosol Particles Composed of Protein and Saltswith Water Vapor: Hygroscopic Growth and Microstructural Rearrangement. *Atmos. Chem. Phys.* **2004**, *4* (2), 323–350.

(286) Shin, W. G.; Mulholland, G. W.; Kim, S. C.; Wang, J.; Emery, M. S.; Pui, D. Y. H. Friction Coefficient and Mass of Silver Agglomerates in the Transition Regime. *J. Aerosol Sci.* **2009**, *40* (7), 573–587.

(287) Shin, W. G.; Mulholland, G. W.; Pui, D. Y. H. Determination of Volume, Scaling Exponents, and Particle Alignment of Nanoparticle Agglomerates Using Tandem Differential Mobility Analyzers. *J. Aerosol Sci.* **2010**, *41* (7), 665–681.

(288) Eggersdorfer, M. L.; Gröhn, A. J.; Sorensen, C. M.; McMurry, P. H.; Pratsinis, S. E. Mass-Mobility Characterization of Flame-Made ZrO2 Aerosols: Primary Particle Diameter and Extent of Aggregation. *J. Colloid Interface Sci.* **2012**, *387* (1), 12–23.

(289) Leskinen, J.; Ihalainen, M.; Torvela, T.; Kortelainen, M.; Lamberg, H.; Tiitta, P.; Jakobi, G.; Grigonyte, J.; Joutsensaari, J.; Sippula, O.; et al. Effective Density and Morphology of Particles Emitted from Small-Scale Combustion of Various Wood Fuels. *Environ. Sci. Technol.* **2014**, *48* (22), 13298–13306. https://doi.org/10.1021/es502214a.

(290) Charvet, A.; Bau, S.; Coy, N. E. P.; Bémer, D.; Thomas, D. Characterizing the Effective Density and Primary Particle Diameter of Airborne Nanoparticles Produced by Spark Discharge Using Mobility and Mass Measurements (Tandem DMA/APM). *J. Nanoparticle Res.* **2014**, *16* (5), 2418.

(291) Kulkarni, P.; Baron, P. A.; Willeke, K. *Aerosol Measurement: Principles, Techniques, and Applications*; John Wiley & Sons, 2011.

(292) Pich, J. Theory of Gravitational Deposition of Particles from Laminar Flows in Channels. *J. Aerosol Sci.* **1972**, *3* (5), 351–361.

(293) Gormley, P. G.; Kennedy, M. Diffusion from a Stream Flowing through a Cylindrical Tube. In *Proceedings of the Royal Irish Academy. Section A: Mathematical and Physical Sciences*; JSTOR, 1948; Vol. 52, pp 163–169.

(294) Crane, R. I.; Evans, R. L. Inertial Deposition of Particles in a Bent Pipe. *J. Aerosol Sci.* **1977**, *8* (3), 161–170.

(295) Zelenyuk, A.; Cai, Y.; Imre, D. From Agglomerates of Spheres to Irregularly Shaped Particles: Determination of Dynamic Shape Factors from Measurements of Mobility and Vacuum Aerodynamic Diameters. *Aerosol Sci. Technol.* **2006**, *40* (3), 197–217. https://doi.org/10.1080/02786820500529406.

(296) Wang, Z.; King, S. M.; Freney, E.; Rosenoern, T.; Smith, M. L.; Chen, Q.; Kuwata, M.; Lewis, E. R.; Pöschl, U.; Wang, W. The Dynamic Shape Factor of Sodium Chloride Nanoparticles as Regulated by Drying Rate. *Aerosol Sci. Technol.* **2010**, *44* (11), 939–953.

(297) Craig, A.; McIntosh, R. The Preparation of Sodium Chloride of Large Specific Surface. *Can. J. Chem.* **1952**, *30* (5), 448–453.

(298) Krämer, L.; Pöschl, U.; Niessner, R. Microstructural Rearrangement of Sodium Chloride Condensation Aerosol Particles on Interaction with Water Vapor. *J. Aerosol Sci.* **2000**, *31* (6), 673–685.

(299) Chindapan, N.; Niamnuy, C.; Devahastin, S. Physical Properties, Morphology and Saltiness of Salt Particles as Affected by Spray Drying Conditions and Potassium Chloride Substitution. *Powder Technol.* **2018**, *326*, 265–271.

(300) Lo, J.; Massling, A.; Swietlicki, E.; Vaclavik, E.; Ketzel, M.; Pagels, J.; Loft, S.; Swietlicki, E. Experimentally Determined Human Respiratory Tract Deposition of Airborne Particles at a Busy Street Experimentally Determined Human Respiratory Tract Deposition of Airborne Particles at a Busy Street. **2009**, 4659–4664. https://doi.org/10.1021/es803029b.

(301) Xue, H.; Khalizov, A. F.; Wang, L.; Zheng, J.; Zhang, R. Effects of Coating of Dicarboxylic Acids on the Mass− Mobility Relationship of Soot Particles. *Environ. Sci. Technol.* **2009**, *43* (8), 2787–2792.

(302) Johnson, T. J.; Olfert, J. S.; Cabot, R.; Treacy, C.; Yurteri, C. U.; Dickens, C.; McAughey, J.; Symonds, J. P. R. Transient Measurement of the Effective Particle Density of Cigarette Smoke. *J. Aerosol Sci.* **2015**, *87*, 63–74. https://doi.org/10.1016/j.jaerosci.2015.05.006.

(303) Johnson, T. J.; Olfert, J. S.; Cabot, R.; Treacy, C.; Yurteri, C. U.; Dickens, C.; McAughey, J.; Symonds, J. P. R. Steady-State Measurement of the Effective Particle Density of Cigarette Smoke. *J. Aerosol Sci.* **2014**, *75*, 9–16. https://doi.org/10.1016/j.jaerosci.2014.04.006.

(304) Markowicz, P.; Löndahl, J.; Wierzbicka, A.; Suleiman, R.; Shihadeh, A.; Larsson, L. A Study on Particles and Some Microbial Markers in Waterpipe Tobacco Smoke. *Sci. Total Environ.* **2014**, *499*, 107–113.

(305) Vu, T. V.; Ondracek, J.; Zdímal, V.; Schwarz, J.; Delgado-Saborit, J. M.; Harrison, R. M. Physical Properties and Lung Deposition of Particles Emitted from Five Major Indoor Sources. *Air Qual. Atmos. Heal.* **2017**, *10* (1), 1–14. https://doi.org/10.1007/s11869-016-0424-1.

(306) Frenklach, M. Reaction Mechanism of Soot Formation in Flames. *Phys. Chem. Chem. Phys.* **2002**, *4* (11), 2028–2037.

(307) Sgro, L. A.; De Filippo, A.; Lanzuolo, G.; D'Alessio, A. Characterization of Nanoparticles of Organic Carbon (NOC) Produced in Rich Premixed Flames by Differential Mobility Analysis. *Proc. Combust. Inst.* **2007**, *31* (1), 631–638.

(308) Sgro, L. A.; Barone, A. C.; Commodo, M.; D'Alessio, A.; De Filippo, A.; Lanzuolo, G.; Minutolo, P. Measurement of Nanoparticles of Organic Carbon in Non-Sooting Flame Conditions. *Proc. Combust. Inst.* **2009**, *32* (1), 689–696.

(309) Wang, H. Formation of Nascent Soot and Other Condensed-Phase Materials in Flames. *Proc. Combust. Inst.* **2011**, *33* (1), 41–67.

(310) Johansson, K. O.; Head-Gordon, M. P.; Schrader, P. E.; Wilson, K. R.; Michelsen, H. A. Resonance-Stabilized Hydrocarbon-Radical Chain Reactions May Explain Soot Inception and Growth. *Science (80-.).* **2018**, *361* (6406), 997–1000.

(311) Shin, W. G.; Wang, J.; Mertler, M.; Sachweh, B.; Fissan, H.; Pui, D. Y. H. The Effect of Particle Morphology on Unipolar Diffusion Charging of Nanoparticle Agglomerates in the Transition Regime. *J. Aerosol Sci.* **2010**, *41* (11), 975–986.

(312) Ouf, F.-X.; Sillon, P. Charging Efficiency of the Electrical Low Pressure Impactor's Corona Charger: Influence of the Fractal Morphology of Nanoparticle Aggregates and Uncertainty Analysis of Experimental Results. *Aerosol Sci. Technol.* **2009**, *43* (7), 685–698.

(313) Oh, H.; Park, H.; Kim, S. Effects of Particle Shape on the Unipolar Diffusion Charging of Nonspherical Particles. *Aerosol Sci. Technol.* **2004**, *38* (11), 1045–1053.

(314) Maricq, M. M. Bipolar Diffusion Charging of Soot Aggregates. *Aerosol Sci. Technol.* **2008**, *42* (4), 247–254.

(315) Hospodsky, D.; Qian, J.; Nazaroff, W. W.; Yamamoto, N.; Bibby, K.; Rismani-Yazdi, H.; Peccia, J. Human Occupancy as a Source of Indoor Airborne Bacteria. *PLoS One* **2012**, *7* (4), e34867.

(316) Yamamoto, N.; Hospodsky, D.; Dannemiller, K. C.; Nazaroff, W. W.; Peccia, J. Indoor Emissions as a Primary Source of Airborne Allergenic Fungal Particles in Classrooms. *Environ. Sci. Technol.* **2015**, *49* (8), 5098–5106.

(317) Täubel, M.; Rintala, H.; Pitkäranta, M.; Paulin, L.; Laitinen, S.; Pekkanen, J.; Hyvärinen, A.; Nevalainen, A. The Occupant as a Source of House Dust Bacteria. *J. Allergy Clin. Immunol.* **2009**, *124* (4), 834–840.

(318) Rintala, H.; Pitkäranta, M.; Täubel, M. Microbial Communities Associated with House Dust. In *Advances in applied microbiology*; Elsevier, 2012; Vol. 78, pp 75–120.

(319) O'meara, T.; Tovey, E. Monitoring Personal Allergen Exposure. *Clin. Rev. Allergy Immunol.* **2000**, *18* (3), 341–395.

(320) Fahlbusch, B.; Hornung, D.; Heinrich, J.; Dahse, H.; Jäger, L. Quantification of Group 5 Grass Pollen Allergens in House Dust. *Clin. Exp. Allergy* **2000**, *30* (11), 1646–1652.

(321) Hunt, A.; Johnson, D. L.; Griffith, D. A. Mass Transfer of Soil Indoors by Track-in on Footwear. *Sci. Total Environ.* **2006**, *370* (2–3), 360–371.

(322) Meadow, J. F.; Altrichter, A. E.; Kembel, S. W.; Kline, J.; Mhuireach, G.; Moriyama, M.; Northcutt, D.; O'Connor, T. K.; Womack, A. M.; Brown, G. Z. Indoor Airborne Bacterial Communities Are Influenced by Ventilation, Occupancy, and Outdoor Air Source. *Indoor Air* **2014**, *24* (1), 41–48.

(323) Reponen, T.; Lockey, J.; Bernstein, D. I.; Vesper, S. J.; Levin, L.; Hershey, G. K. K.; Zheng, S.; Ryan, P.; Grinshpun, S. A.; Villareal, M. Infant Origins of Childhood Asthma Associated with Specific Molds. *J. Allergy Clin. Immunol.* **2012**, *130* (3), 639–644.

(324) Pringle, A. Asthma and the Diversity of Fungal Spores in Air. *PLoS Pathog.* **2013**, *9* (6).

(325) Taylor, P. E.; Jacobson, K. W.; House, J. M.; Glovsky, M. M. Links between Pollen, Atopy and the Asthma Epidemic. *Int. Arch. Allergy Immunol.* **2007**, *144* (2), 162–170.

(326) Schmidt, C. W. Pollen Overload: Seasonal Allergies in a Changing Climate. National Institute of Environmental Health Sciences 2016.

(327) Davies, J. M.; Beggs, P. J.; Medek, D. E.; Newnham, R. M.; Erbas, B.; Thibaudon, M.; Katelaris, C. H.; Haberle, S. G.; Newbigin, E. J.; Huete, A. R. Trans-Disciplinary Research in Synthesis of Grass Pollen Aerobiology and Its Importance for Respiratory Health in Australasia. *Sci. Total Environ.* **2015**, *534*, 85–96.

(328) Bisgaard, H.; Hermansen, M. N.; Buchvald, F.; Loland, L.; Halkjaer, L. B.; Bønnelykke, K.; Brasholt, M.; Heltberg, A.; Vissing, N. H.; Thorsen, S. V. Childhood Asthma after Bacterial Colonization of the Airway in Neonates. *N. Engl. J. Med.* **2007**, *357* (15), 1487–1495.

(329) Man, W. H.; de Steenhuijsen Piters, W. A. A.; Bogaert, D. The Microbiota of the Respiratory Tract: Gatekeeper to Respiratory Health. *Nat. Rev. Microbiol.* **2017**, *15* (5), 259.

(330) Hilty, M.; Burke, C.; Pedro, H.; Cardenas, P.; Bush, A.; Bossley, C.; Davies, J.; Ervine, A.; Poulter, L.; Pachter, L. Disordered Microbial Communities in Asthmatic Airways. *PLoS One* **2010**, *5* (1).

(331) Karlsson, E.; Berglund, T.; Strömqvist, M.; Nordstrand, M.; Fängmark, I. The Effect of Resuspension Caused by Human Activities on the Indoor Concentration of Biological Aerosols. *J. Aerosol Sci.* **1999**, *30*, S737–S738.

(332) Chen, Q.; Hildemann, L. M. The Effects of Human Activities on Exposure to Particulate Matter and Bioaerosols in Residential Homes. *Environ. Sci. Technol.* **2009**, *43* (13), 4641.

(333) Raja, S.; Xu, Y.; Ferro, A. R.; Jaques, P. A.; Hopke, P. K. Resuspension of Indoor Aeroallergens and Relationship to Lung Inflammation in Asthmatic Children. *Environ. Int.* **2010**, *36* (1), 8–14.

(334) Goebes, M. D.; Boehm, A. B.; Hildemann, L. M. Contributions of Foot Traffic and Outdoor Concentrations to Indoor Airborne Aspergillus. *Aerosol Sci. Technol.* **2011**, *45* (3), 352–363.

(335) Adams, R. I.; Bhangar, S.; Pasut, W.; Arens, E. A.; Taylor, J. W.; Lindow, S. E.; Nazaroff, W. W.; Bruns, T. D. Chamber Bioaerosol Study: Outdoor Air and Human Occupants as Sources of Indoor Airborne Microbes. *PLoS One* **2015**, *10* (5), e0128022.

(336) Boor, B. E.; Spilak, M. P.; Corsi, R. L.; Novoselac, A. Characterizing Particle Resuspension from Mattresses: Chamber Study. *Indoor Air* **2015**, *25* (4), 441–456.

(337) Adolph, K. E. Motor and Physical Development: Locomotion. In *Encyclopedia of infant and early childhood development*; Elsevier Inc., 2008; pp 359–373.

(338) Davies, R. R.; Noble, W. C. Dispersal of Bacteria on Desquamated Skin. *Lancet* **1962**, 1295–1297.

(339) Pöhlker, C.; Huffman, J. A.; Pöschl, U. Autofluorescence of Atmospheric Bioaerosols–Fluorescent Biomolecules and Potential Interferences. *Atmos. Meas. Tech.* **2012**, *5* (1), 37–71.

(340) Saari, S.; Reponen, T.; Keskinen, J. Performance of Two Fluorescence-Based Real-Time Bioaerosol Detectors: BioScout vs. UVAPS. *Aerosol Sci. Technol.* **2014**, *48* (4), 371–378.

(341) Saari, S. E.; Putkiranta, M. J.; Keskinen, J. Fluorescence Spectroscopy of Atmospherically Relevant Bacterial and Fungal Spores and Potential Interferences. *Atmos. Environ.* **2013**, *71*, 202.

(342) Savage, N. J.; Krentz, C. E.; Könemann, T.; Han, T. T.; Mainelis, G.; Pöhlker, C.; Huffman, J. A. Systematic Characterization and Fluorescence Threshold Strategies for the Wideband Integrated Bioaerosol Sensor (WIBS) Using Size-Resolved Biological and Interfering Particles. *Atmos. Meas. Tech.* **2017**, *10* (11), 4279–4302.

(343) Bliznakova, I.; Borisova, E.; Avramov, L. Laser-and Light-Induced Autofluorescence Spectroscopy of Human Skin in Dependence on Excitation Wavelengths. *ACTA Phys. Pol. Ser. A* **2007**, *112* (5), 1131.

(344) Mackintosh, C. A.; Lidwell, O. M.; Towers, A. G.; Marples, R. R. The Dimensions of Skin Fragments Dispersed into the Air during Activity. *Epidemiol. Infect.* **1978**, *81* (3), 471–480.

(345) Bhangar, S.; Huffman, J. A.; Nazaroff, W. W. Size-Resolved Fluorescent Biological Aerosol Particle Concentrations and Occupant Emissions in a University Classroom. *Indoor Air*. **2014**, *24*, 604.

(346) Burg, A. W.; Rohovsky, M. W.; Kensler, C. J.; Wogan, G. N. Current Status of Human Safety and Environmental Aspects of Fluorescent Whitening Agents Used in Detergents in the United States. *Crit. Rev. Environ. Sci. Technol.* **1977**, *7* (1), 91–120.

(347) Leaver, I. H.; Milligan, B. Fluorescent Whitening Agents—a Survey (1974-82). *Dye. Pigment.* **1984**, *5* (2), 109–144.

(348) Hewett, P. Limitations in the Use of Particle Size-Selective Sampling Criteria in Occupational Epidemiology. *Appl. Occup. Environ. Hyg.* **1991**, *6* (4), 290.

(349) Reponen, T. Aerodynamic Diameters and Respiratory Deposition Estimates of Viable Fungal Particles in Mold Problem Dwellings. *Aerosol Sci. Technol.* **1995**, *22* (1), 11–23.

(350) Venkataraman, C. Comparison of Particle Lung Doses from the Fine and Coarse Fractions of Urban PM-10 Aerosols. *Inhal. Toxicol.* **1999**, *11* (2), 151.

(351) Cho, S.-H.; Seo, S.-C.; Schmechel, D.; Grinshpun, S. A.; Reponen, T. Aerodynamic Characteristics and Respiratory Deposition of Fungal Fragments. *Atmos. Environ.* **2005**, *39* (30), 5454.

(352) Koivisto, A. J.; Aromaa, M.; Mäkelä, J. M.; Pasanen, P.; Hussein, T.; Hämeri, K. Concept to Estimate Regional Inhalation Dose of Industrially Synthesized Nanoparticles. *ACS Nano* **2012**, *6* (2), 1195.

(353) Gao, M.; Jia, R.; Qiu, T.; Han, M.; Song, Y.; Wang, X. Seasonal Size Distribution of Airborne Culturable Bacteria and Fungi and Preliminary Estimation of Their Deposition in Human Lungs during Non-Haze and Haze Days. *Atmos. Environ.* **2015**, *118*, 203.

(354) Manigrasso, M.; Buonanno, G.; Fuoco, F. C.; Stabile, L.; Avino, P. Aerosol Deposition Doses in the Human Respiratory Tree of Electronic Cigarette Smokers. *Environ. Pollut.* **2015**, *196*, 257.

(355) Hubal, E. A. C.; Sheldon, L. S.; Burke, J. M.; McCurdy, T. R.; Berry, M. R.; Rigas, M. L.; Zartarian, V. G.; Freeman, N. C. Children's Exposure Assessment: A Review of Factors Influencing Children's Exposure, and the Data Available to Characterize and Assess That Exposure. *Environ. Heal. Perspect.* **2000**, *108* (6), 475.

(356) Saari, S. E.; Mensah-Attipoe, J.; Reponen, T.; Veijalainen, A. M.; Salmela, A.; Pasanen, P.; Keskinen, J. Effects of Fungal Species, Cultivation Time, Growth Substrate, and Air Exposure Velocity on the Fluorescence Properties of Airborne Fungal Spores. *Indoor Air* **2015**, *25* (6), 653.

(357) Saari, S. E.; Niemi, J.; Rönkkö, T.; Kuuluvainen, H.; Järvinen, A.; Pirjola, L.; Aurela, M.; Hillamo, R.; Keskinen, J. Seasonal and Diurnal Variations of Fluorescent Bioaerosol Concentration and Size Distribution in the Urban Environment. *Aerosol Air Qual. Res.* **2015**, 572.

(358) Velazco-Roa, M. A.; Dzhongova, E.; Thennadil, S. N. Complex Refractive Index of Nonspherical Particles in the Visible near Infrared Region--Application to Bacillus Subtilis Spores. *Appl. Opt.* **2008**, *47* (33), 6183–6189.

(359) Balaev, A. E.; Dvoretski, K. N.; Doubrovski, V. A. Determination of Refractive Index of Rod-Shaped Bacteria from Spectral Extinction Measurements. In *Saratov Fall Meeting 2002: Optical Technologies in Biophysics and Medicine IV*; International Society for Optics and Photonics, 2003; Vol. 5068, pp 375–380.

(360) Hyytiäinen, H. K.; Jayaprakash, B.; Kirjavainen, P. V; Saari, S. E.; Holopainen, R.; Keskinen, J.; Hämeri, K.; Hyvärinen, A.; Boor, B. E.; Täubel, M. Crawling-Induced Floor Dust Resuspension Affects the Microbiota of the Infant Breathing Zone. *Microbiome* **2018**, *6* (1), 25.

(361) Grinshpun, S.; Willeke, K.; Kalatoor, S. A General Equation for Aerosol Aspiration by Thin-Walled Sampling Probes in Calm and Moving Air. *Atmos. Environ. Part A. Gen. Top.* **1993**, *27* (9), 1459–1470.

(362) Hofmann, W.; Martonen, T. B.; Graham, R. C. Predicted Deposition of Nonhygroscopic Aerosols in the Human Lung as a Function of Subject Age. *J. Aerosol Med.* **1989**, *2* (1), 49–68.

(363) US EPA. Exposure Factors Handbook 2011 Edition (Final). *Washington, DC* **2011**.

(364) Madelin, T. M.; Johnson, H. E. Fungal and Actinomycete Spore Aerosols Measured at Different Humidities with an Aerodynamic Particle Sizer. *J. Appl. Bacteriol.* **1992**, *72* (5), 400–409.

(365) Reponen, T.; Willeke, K.; Ulevicius, V.; Reponen, A.; Grinshpun, S. A. Effect of Relative Humidity on the Aerodynamic Diameter and Respiratory Deposition of Fungal Spores. *Atmos. Environ.* **1996**, *30* (23), 3967.

(366) Reponen, T.; Grinshpun, S. A.; Conwell, K. L.; Wiest, J.; Anderson, M. Aerodynamic versus Physical Size of Spores: Measurement and Implication for Respiratory Deposition. *Grana* **2001**, *40* (3), 119–125.

(367) Zhou, J.; Fang, W.; Cao, Q.; Yang, L.; Chang, V.; Nazaroff, W. W. Influence of Moisturizer and Relative Humidity on Human Emissions of Fluorescent Biological Aerosol Particles. *Indoor Air* **2017**, *27* (3), 587–598.

(368) Bhangar, S.; Adams, R. I.; Pasut, W.; Huffman, J. A.; Arens, E. A.; Taylor, J. W.; Bruns, T. D.; Nazaroff, W. W. Chamber Bioaerosol Study: Human Emissions of Size-Resolved Fluorescent Biological Aerosol Particles. *Indoor Air* **2015**, 1–14. https://doi.org/10.1111/ina.12195.

(369) Thatcher, T. L.; Lai, A. C. K.; Moreno-Jackson, R.; Sextro, R. G.; Nazaroff, W. W. Effects of Room Furnishings and Air Speed on Particle Deposition Rates Indoors. *Atmos. Environ.* **2002**, *36* (11), 1811–1819.

(370) You, R.; Cui, W.; Chen, C.; Zhao, B. Measuring the Short-Term Emission Rates of Particles in the "Personal Cloud" with Different Clothes and Activity Intensities in a Sealed Chamber. *Aerosol Air Qual Res* **2013**, *13* (3), 911e21.

(371) Qian, J.; Ferro, A. R. Resuspension of Dust Particles in a Chamber and Associated Environmental Factors. *Aerosol Sci. Technol.* **2008**, *42* (7), 566–578.

(372) Huffman, J. A.; Treutlein, B.; Pöschl, U. Fluorescent Biological Aerosol Particle Concentrations and Size Distributions Measured with an Ultraviolet Aerodynamic Particle Sizer (UV-APS) in Central Europe. *Atmos. Chem. Phys.* **2009**, *9* (4), 17705.

(373) Toprak, E.; Schnaiter, M. Fluorescent Biological Aerosol Particles Measured with the Waveband Integrated Bioaerosol Sensor WIBS-4: Laboratory Tests Combined with a One Year Field Study. *Atmos. Chem. Phys.* **2013**, *13* (1), 225.

(374) Valsan, A. E.; Ravikrishna, R.; Biju, C. V; Pöhlker, C.; Després, V. R.; Huffman, J. A.; Pöschl, U.; Gunthe, S. S. Fluorescent Biological Aerosol Particle Measurements at a Tropical High-Altitude Site in Southern India during the Southwest Monsoon Season. *Atmos. Chem. Phys.* **2016**, *16* (15), 9805.

(375) Hernandez, M.; Perring, A. E.; McCabe, K.; Kok, G.; Granger, G.; Baumgardner, D. Chamber Catalogues of Optical and Fluorescent Signatures Distinguish Bioaerosol Classes. *Atmos. Meas. Tech.* **2016**, *9* (7).

(376) Noble, W. C.; Davies, R. R.; Place, D. A. Studies on the Dispersal of Staphylococci. *J. Clin. Pathol.* **1965**, *18* (1), 16–19.

(377) Lighthart, B. Mini-Review of the Concentration Variations Found Inthe Alfresco Atmospheric Bacterial Populations. *Aerobiologia (Bologna).* **2000**, *16* (1), 7–16.

(378) Gorny, R. L.; Dutkiewicz, J.; Krysinska-Traczyk, E. Size Distribution of Bacterial and Fungi Bioaerosols in Indoor Air. *Ann. Agric. Environ. Med.* **1999**, *6*, 105.

(379) Huffman, J. A.; Sinha, B.; Garland, R. M.; Snee-Pollmann, A.; Gunthe, S. S.; Artaxo, P.; Martin, S. T.; Andreae, M. O.; Pöschl, U. Size Distributions and Temporal Variations of Biological Aerosol Particles in the Amazon Rainforest Characterized by Microscopy and Real-Time UV-APS Fluorescence Techniques during AMAZE-08. *Atmos. Chem. Phys.* **2012**, *12* (24), 11997–12019.

(380) Qian, J.; Hospodsky, D.; Yamamoto, N.; Nazaroff, W. W.; Peccia, J. Size-resolved Emission Rates of Airborne Bacteria and Fungi in an Occupied Classroom. *Indoor Air* **2012**, *22* (4), 339–351.

(381) Hospodsky, D.; Yamamoto, N.; Nazaroff, W. W.; Miller, D.; Gorthala, S.; Peccia, J. Characterizing Airborne Fungal and Bacterial Concentrations and Emission Rates in Six Occupied Children's Classrooms. *Indoor Air* **2015**, *25* (6), 641–652.

(382) Kanaani, H.; Hargreaves, M.; Smith, J.; Ristovski, Z.; Agranovski, V.; Morawska, L. Performance of UVAPS with Respect to Detection of Airborne Fungi. *J. Aerosol Sci.* **2008**, *39* (2), 175–189.

(383) Hussein, T.; Norros, V.; Hakala, J.; Petäjä, T.; Aalto, P. P.; Rannik, Ü.; Vesala, T.; Ovaskainen, O. Species Traits and Inertial Deposition of Fungal Spores. *J. Aerosol Sci.* **2013**, *61*, 81.

(384) Custovic, A.; Woodcock, H.; Craven, M.; Hassall, R.; Hadley, E.; Simpson, A.; Woodcock, A. Dust Mite Allergens Are Carried on Not Only Large Particles. *Pediatr. allergy Immunol.* **1999**, *10* (4), 258–260.

(385) Montoya, L. D.; Hildemann, L. M. Size Distributions and Height Variations of Airborne Particulate Matter and Cat Allergen Indoors Immediately Following Dust-Disturbing Activities. *J. Aerosol Sci.* **2005**, *36* (5–6), 735–749.

(386) Pereira, M. L.; Knibbs, L. D.; He, C.; Grzybowski, P.; Johnson, G. R.; Huffman, J. A.; Bell, S. C.; Wainwright, C. E.; Matte, D. L.; Dominski, F. H. Sources and Dynamics of Fluorescent Particles in Hospitals. *Indoor Air* **2017**, *27* (5), 988.

(387) Górny, R. L.; Reponen, T.; Willeke, K.; Schmechel, D.; Robine, E.; Boissier, M.; Grinshpun, S. A. Fungal Fragments as Indoor Air Biocontaminants. *Appl. Environ. Microbiol.* **2002**, *68* (7), 3522.

(388) Pazmandi, K.; Kumar, B. V; Szabo, K.; Boldogh, I.; Szoor, A.; Vereb, G.; Veres, A.; Lanyi, A.; Rajnavolgyi, E.; Bacsi, A. Ragweed Subpollen Particles of Respirable Size Activate Human Dendritic Cells. *PLoS One* **2012**, *7* (12), e52085.

(389) Tian, Y.; Sul, K.; Qian, J.; Mondal, S.; Ferro, A. R. A Comparative Study of Walking-induced Dust Resuspension Using a Consistent Test Mechanism. *Indoor Air* **2014**, *24* (6), 592–603.

(390) Rosati, J. A.; Thornburg, J.; Rodes, C. Resuspension of Particulate Matter from Carpet Due to Human Activity. *Aerosol Sci. Technol.* **2008**, *42* (6), 472–482.

(391) Boor, B. E.; Siegel, J. A.; Novoselac, A. Monolayer and Multilayer Particle Deposits on Hard Surfaces: Literature Review and Implications for Particle Resuspension in the Indoor Environment. *Aerosol Sci. Technol.* **2013**, *47* (8), 831–847.

(392) Thio, B. J. R. *Characterization of Bioparticulate Adhesion to Synthetic Carpet Polymers with Atomic Force Microscopy*; 2009.

(393) Ferro, A. R.; Kopperud, R. J.; Hildemann, L. M. Source Strengths for Indoor Human Activities That Resuspend Particulate Matter. *Environ. Sci. Technol.* **2004**, *38* (6), 1759–1764.

(394) Shalat, S. L.; Stambler, A. A.; Wang, Z.; Mainelis, G.; Emoekpere, O. H.; Hernandez, M.; Lioy, P. J.; Black, K. Development and In-Home Testing of the Pretoddler Inhalable Particulate Environmental Robotic (PIPER Mk IV) Sampler. *Environ. Sci. Technol.* **2011**, *45* (7), 2945–2950.

(395) Wang, Z.; Shalat, S. L.; Black, K.; Lioy, P. J.; Stambler, A. A.; Emoekpere, O. H.; Hernandez, M.; Han, T.; Ramagopal, M.; Mainelis, G. Use of a Robotic Sampling Platform to Assess Young Children's Exposure to Indoor Bioaerosols. *Indoor Air* **2012**, *22* (2), 159–169.

(396) Sagona, J. A.; Shalat, S. L.; Wang, Z.; Ramagopal, M.; Black, K.; Hernandez, M.; Mainelis, G. Evaluation of Particle Resuspension in Young Children′ s Breathing Zone Using Stationary and Robotic (PIPER) Aerosol Samplers. *J. Aerosol Sci.* **2015**, *85*, 30–41.

(397) Gomes, C.; Freihaut, J.; Bahnfleth, W. Resuspension of Allergen-Containing Particles under Mechanical and Aerodynamic Disturbances from Human Walking. *Atmos. Environ.* **2007**, *41* (25), 5257–5270.

(398) Jamieson, K. S.; ApSimon, H. M.; Jamieson, S. S.; Bell, J. N. B.; Yost, M. G. The Effects of Electric Fields on Charged Molecules and Particles in Individual Microenvironments. *Atmos. Environ.* **2007**, *41* (25), 5224–5235.

(399) Zhang, X.; Ahmadi, G.; Qian, J.; Ferro, A. Particle Detachment, Resuspension and Transport Due to Human Walking in Indoor Environments. *J. Adhes. Sci. Technol.* **2008**, *22* (5–6), 591–621.

(400) Lacks, D. J.; Sankaran, R. M. Contact Electrification of Insulating Materials. *J. Phys. D. Appl. Phys.* **2011**, *44* (45), 453001.

(401) Foos, B.; Marty, M.; Schwartz, J.; Bennett, W.; Moya, J.; Jarabek, A. M.; Salmon, A. G. Focusing on Children's Inhalation Dosimetry and Health Effects for Risk Assessment: An Introduction. *J. Toxicol. Environ. Heal. Part A* **2007**, *71* (3), 149–165.

(402) Bennett, W. D.; Zeman, K. L.; Jarabek, A. M. Nasal Contribution to Breathing and Fine Particle Deposition in Children versus Adults. *J. Toxicol. Environ. Heal. Part A* **2007**, *71* (3), 227–237.

(403) Baldacci, S.; Maio, S.; Cerrai, S.; Sarno, G.; Baïz, N.; Simoni, M.; Annesi-Maesano, I.; Viegi, G. Allergy and Asthma: Effects of the Exposure to Particulate Matter and Biological Allergens. *Respir. Med.* **2015**, *109* (9), 1089.

(404) Phalen, R. F.; Phalen, R. N. *Introduction to Air Pollution Science*; 2012.

(405) Patrick, S. K.; Noah, J. A.; Yang, J. F. Developmental Constraints of Quadrupedal Coordination across Crawling Styles in Human Infants. *J. Neurophysiol.* **2012**, *107* (11), 3050–3061.

(406) Sturm, R. Bioaerosols in the Lungs of Subjects with Different Ages-Part 1: Deposition Modeling. *Ann. Transl. Med.* **2016**, *4* (11).

VITA

TIANREN WU

Ph.D., Lyles School of Civil Engineering, Purdue University (2020)

M.S., Lyles School of Civil Engineering, Purdue University (2016)

B.S., School of Municipal and Environmental Engineering, Shenyang Jianzhu University (2013)

PUBLICATIONS

In Referred Journals

1. **Wu, T.**, Täubel, M., Holopainen, R., Viitanen, A.K., Vainiotalo, S., Tuomi, T., Keskinen, J., Hyvärinen, A., Hämeri, K., Saari, S.E., and Boor, B.E. (2018). Infant and Adult Inhalation Exposure to Resuspended Biological Particulate Matter. *Environmental Science & Technology*, 52(1):237-247.
2. **Wu, T.** and Boor, B.E. (2020). Characterization of a Thermal Aerosol Generator for HVAC Filtration Experiments (RP-1734). *Science & Technology for the Built Environment*, DOI:10.1080/23744731.2020.1730661.
3. Haines, S.R., Adams, R.I., Boor, B.E., Bruton, T.A., Downey, J., Ferro, A.R., Gall, E., Green, B.J., Hegarty, B., Horner, E., Jacobs, D.E., Lemieux, P., Misztal, P.K., Morrison, G., Perzanowski, M., Reponen, T., Rush, R.E., Virgo, T., Alkhayri, C., Bope, A., Cochran, S., Cox, J., Donohue, A., May, A.A., Nastasi, N., Nishioka, M., Renninger, N., Tian, Y., Uebel-Niemeier, C., Wilkinson, D., **Wu, T.**, Zambrana, J., and Dannemiller, K.C. (2020). Ten Questions Concerning the Implications of Carpet on Indoor Chemistry and Microbiology. *Building & Environment*, 170:10658.
4. **Wu, T.** and Boor, B.E. Urban Aerosol Size Distributions: A Global Perspective. *Atmospheric Chemistry & Physics*, In Review.

In Referred Conference Proceedings

1. **Wu, T.** and Boor, B.E. (2018). Real-Time Monitoring of Microbes and Mold in Buildings. In Proceedings of *Indoor Air Quality Association (IAQA) 21st Annual Meeting*, Chicago, IL, January 2018 (also a Podium Presentation).
2. Jiang, J., **Wu, T.**, Wagner, D.N., Stevens, P.S., Huber, H., Tasoglou, A., and Boor, B.E. (2020). Investigating How Occupancy and Ventilation Mode Influence the Dynamics of Indoor Air Pollutants in an Office Environment. In Proceedings of *2020 American Society of Heating, Refrigerating & Air Conditioning Engineers (ASHRAE) Winter Conference*, Orlando, FL, February 2020 (also a Podium Presentation).

Conference Podium and Posters Presentations

1. **Wu, T.** and Boor, B.E. (2016). Real-Time Measurements of Fluorescent Biological Aerosol Particles in the Infant Near-Floor Microenvironment in a Child Development Laboratory School. *American Association for Aerosol Research (AAAR) 35th Annual Conference*, Portland, OR, October 2016 (Podium).
2. **Wu, T.** and Boor, B.E. (2019). Urban Atmospheric Aerosol Size Distributions: A Global Perspective. *American Association for Aerosol Research (AAAR) 37th Annual Conference*, Portland, OR, October 2019 (Podium).
3. **Wu, T.** and Boor, B.E. (2019). Size Distributions and Emissions of Fluorescent Biological Aerosol Particles in an Office. *American Association for Aerosol Research (AAAR) 37th Annual Conference*, Portland, OR, October 2019 (Poster).
4. Jiang, J., **Wu, T.**, Wagner, D.N., Stevens, P.S., Huber, H., Tasoglou, A., and Boor, B.E. (2019). Spatiotemporal Trends in Concentrations of Ozone and Ozone-Skin Oil Oxidation Products in an Occupied Office and HVAC System. *American Association for Aerosol Research (AAAR) 37th Annual Conference*, Portland, OR, October 2019 (Poster).
5. **Wu, T.**, Stevens, P.S., Huber, H., Tasoglou, A., and Boor, B.E. (2019). Indoor Measurements of Nanocluster Aerosols and New Particle Formation. *American Association* for Aerosol Research (AAAR) 37th Annual Conference, Portland, OR, October 2019 (Podium).
6. **Wu, T.**, Wagner, D.N., Jiang, J., Stevens, P.S., Huber, H., Tasoglou, A., and Boor, B.E. (2019). Dynamics of Volatile Organic Compounds in a Living Laboratory Office and HVAC System. *American Association for Aerosol Research (AAAR) 37th Annual Conference*, Portland, OR, October 2019 (Poster).
7. Jiang, J., **Wu, T.**, and Boor, B.E. (2019). In-Situ Time- and Size-Resolved Particle Removal Efficiency of a HVAC Filter Bank in an Office Building. *American Association for Aerosol Research (AAAR) 37th Annual Conference*, Portland, OR, October 2019 (Poster).
8. Sundar Patra, S., Ramsisaria, R., Du, R., **Wu, T.**, and Boor, B.E. (2019). Improving the Performance of Low-Cost Optical Particle Counters with Machine Learning: Applications for Indoor Aerosol Measurements. *American Association for Aerosol Research (AAAR) 37th Annual Conference*, Portland, OR, October 2019 (Podium).